UNIVERSIDADE DE LISBOA

FACULDADE DE CIÊNCIAS

DEPARTAMENTO DE ENGENHARIA GEOGRÁFICA,
GEOFÍSICA E ENERGIA

HYDROCHEMICAL WATER PREDICTION (WATER QUALITY) WITH TRANSIENT ELECTROMAGNETIC SOUNDINGS (TEM)

Rui Manuel Domingos Gonçalves

DOUTORAMENTO EM CIÊNCIAS GEOFÍSICAS
E DA GEOINFORMAÇÃO

(Geofísica)

2012

UNIVERSIDADE DE LISBOA

FACULDADE DE CIÊNCIAS

DEPARTAMENTO DE ENGENHARIA GEOGRÁFICA,
GEOFÍSICA E ENERGIA

PREDIÇÃO DA HIDROQUÍMICA DA ÁGUA (QUALIDADE DA ÁGUA) USANDO SONDAGENS ELECTROMAGNÉTICAS TRANSIENTES (TEM)

Tese orientada pelos Prof. Doutor Fernando Acácio Monteiro Santos
e Prof. Doutor Maxwell Azuka Meju

Rui Manuel Domingos Gonçalves

DOUTORAMENTO EM CIÊNCIAS GEOFÍSICAS
E DA GEOINFORMAÇÃO

(Geofísica)

2012

To Gisela, Inês and Rodrigo
In memory of my Father

CONTENTS

ABSTRACT

This work aims the applicability of the Transient electromagnetic method at an arid and semi-arid environmental condition in the Santiago Island – Cape Verde. Some seashore areas of this island show an increasing salt contamination of the groundwater. The main objective of present work is to relate this water-quality condition with parameters taken from the transient sounding's data.

In this context, transient soundings have been acquired from 2005 through 2009, at several chosen valleys near the sea, in a mean rate of one field campaign each year.

The first phase of this work was the understanding of the geophysical method details, problems and applicability, as the chosen and acquired equipment was the first one to be permanently available to the Portuguese geosciences community. This first phase was also accomplished with field tests.

Interpretation of the transient sounding's data curves were done by application of 1-D inversion methods already developed and published, as also with quasi 2-D and quasi 3-D inversion algorithms, where applicability was feasible. This was the second phase. The 2-D and 3-D approximation results are satisfactory and promising; although a higher spatial sounding's density should certainly allow for better results.

At phase three, these results have been compared against the available lithologic, hydrologic and hydrochemical data, in the context of Santiago's island settings. The analyses of these merged data showed that two distinct origins for the observed inland groundwater salinity are possible; seashore shallow mixing with contemporary seawater and mixing with a deep and older salty layer from up flow groundwater. Relations between the electric resistivity and the salt water content distribution were found for the surveyed areas.

To this environment condition, the electromagnetic transient method proved to be a reliable and powerful technique. The groundwater quality can be accessed beyond the few available watershed points, which have an uneven distribution.

Keywords: TEM, Salt water, Hydrologic relations, Santiago Island (Cape Verde)

RESUMO

Este trabalho tem como finalidade a aplicação do método de prospecção geofísica no domínio electromagnético, conhecido como Transiente, em regiões áridas e semi-áridas da ilha de Santiago – Cabo Verde. Algumas áreas costeiras desta ilha apresentam um aumento de salinidade na sua água subterrânea, que se vem agravando no tempo. O principal objectivo do presente trabalho é relacionar a condição de qualidade desta água subterrânea com os parâmetros adquiridos a partir dos dados das sondagens electromagnéticas transientes.

Neste contexto, foram efectuadas sondagens electromagnéticas transientes entre os anos de 2005 e 2009, em alguns vales costeiros da ilha, à razão média de uma campanha de trabalho de campo por ano.

A primeira fase deste trabalho foi a compreensão dos detalhes do método geofísico em causa, tal como a sua aplicabilidade e suas limitações, uma vez que este tipo de método e o equipamento escolhido foi o primeiro a estar permanentemente disponível para a comunidade portuguesa de geociências. Esta primeira fase foi também acompanhada com a realização de testes de campo.

A Interpretação dos dados das sondagens transientes foi efectuada através da aplicação de métodos de inversão 1D já desenvolvidos e publicados, e também com algoritmos de inversão quasi-2D e quasi-3D, sempre que possível. Esta foi a segunda fase do trabalho. Os resultados das aproximações quasi-2D e quasi-3D são satisfatórios e promissores, embora se verifique que uma maior densidade especial de sondagens transientes trará e certamente permitirá melhores resultados.

Na fase três, estes resultados foram comparados com os dados litológicos, hidrológicos e hidroquímicos disponíveis, no contexto das condições da ilha de Santiago. As análises conjuntas destes dados mostram que devem existir duas origens distintas para a salinidade observada nas águas subterrâneas das zonas costeiras; uma mistura com a água actual do mar nas zonas sub-superficiais perto do mar, e uma mistura com uma mais profunda e antiga água ascendente que atravessa uma camada com maior conteúdo salino. Foram estabelecidas relações entre a resistividade eléctrica e a distribuição de conteúdo salino da água para as regiões pesquisadas.

Nestas condições ambientais, o presente método electromagnético transiente provou ser uma técnica fiável e de fácil aplicabilidade. A qualidade das águas subterrâneas pode assim ser inferida indirectamente, mesmo em áreas no qual não existam poços ou furos de captação com distribuição uniforme nos vales.

Keywords: TEM, Água salgada, Relações hidrológicas, Ilha de Santiago (Cabo Verde)

LIST OF FIGURES

Chapter 2

Chapter 4

Chapter 8

LIST OF TABLES

LIST OF EQUATIONS

Chapter 2

Chapter 3

Chapter 4

Chapter 5

Chapter 6

Chapter 7

LIST OF SYMBOLS

a – Tortuosity factor

b , **B** – Magnetic induction vector

$\mathbf{C}$ – Laplacian roughening matrix

C^* – Fluid concentration

d , **D** – Dielectric displacement current vector

$\mathbf{D}$ – Dispersion tensor (chapter 7)

d – Diffusion length (diffusion depth)

D_m – Molecular diffusion coefficient

dm – Infinitesimal dipole moment

d_L – Longitudinal dispersion coefficient

d_T – Transverse dispersion coefficient

e , **E** – Electric field vector

e – Data error vector (chapter 3)

E(t) – Transient decay signal voltage

F – Schelkunoff potential

F – Formation factor

$\boldsymbol{f}(\mathbf{m})$ – Functional relating model parameters to model response

g – Gravity acceleration

h , **H** – Magnetic field vector

j , **J** – Electric conductive current density vector

J – Jacobean matrix (chapter 3)

$\mathbf{J_n}$ – Bessel function of *n* order

K – Hydraulic conductivity

k_s – Hydraulic permeability

L – Antenna Inductance

m – Cementation index

m – Model parameter vector

M – Magnetic moment, Mutual inductance of antennas

n – Unitary normal vector

p – Model parameters

P – Pressure

Q – Objective function

Q_v – Cation exchange capacity

r – Position vector

S_p – Specific surface area

S_w – Saturation index

t – Time

T – Temperature

T – Tortuosity (chapter 5)

u – Data vector

$\hat{y}$ – Admittivity

Y – Reflection coefficient

Y_0 – Intrinsic admittance of free space

$\hat{z}$ – Impedivity

Z – Reflection coefficient

Z_0 – Intrinsic impedance of free space

α_L – Longitudinal dispersivity coefficient

α_T – Transverse dispersivity coefficient

δ – Skin depth

δ_w – Fluid density

ε – Relative error

$\hat{\boldsymbol{\varepsilon}}$ – Dielectric permittivity tensor

η – Chargeability (polarizability)

k – Wave number

λ – Anisotropy factor (chapter 2)

λ – Lagrange multiplier (damping factor) (chapter 3)

μ – Fluid dynamic viscosity

$\hat{\boldsymbol{\mu}}$ – Magnetic permittivity tensor

ρ – Electric charge density

ρ – Electric resistivity

ρ_a – Apparent electric resistivity

σ – Electric conductivity

$\hat{\boldsymbol{\sigma}}$ – Electric conductivity tensor

τ – Time constant

Φ – Porosity

χ – Magnetic Susceptibility

ω – Angular frequency

LIST OF ABBREVIATIONS

A – Assomada Formation

ADC – Analog-to-Digital Converter)

AEMR – Applied Electromagnetic Research Ltd.

amsl – above mean sea level

APE – Antenna Polarization effect

CA – Internal Ancient Eruptive Complex

CB – Órgãos Formation

CEC – Cation Exchange Capacity

CSEM – Controlled Source ElectroMagnetic

DC – Direct Current, Continuous Current

EC – Electrical Conductivity

EDC – Effective Distance Constrain

EM – Electromagnetic

EN – Electroneutrality

ET – Evapotranspiration

FDEM – Frequency Domain Methods

FL – Flamengos Formation

GMWL – Global Meteoric Water Line

GPR – Ground Penetrating Radar

GPS – Global Positioning System

HMTEM (or HiTEM) – High Moment TEM Method

IAEA – International Atomic Energy Agency

INGRH – Instituto Nacional de Gestão dos Recursos Hídricos (Cape Verde)

INMG – Instituto Nacional de Meteorologia e Geofísica (Cape Verde)

IP – Induced Polarization

ITCZ – Inter Tropical Convergence Zone

KG – Köppen-Geiger climate classification system

LCI – Lateral Constrained Inversion

LF – Leaching Fraction

LMWL – Local Meteoric Water Line

LTCB – Lower Tagus Cenozoic Basin

LTV – Lower Tagus Valley

meq – Milliequivalent

msl – mean sea level

MT – Magnetotelluric

MV – Monte das Vacas Formation

PA – Pico da Antónia Complex

PATEM – Continuous TEM Method

PET – Potential Evapotranspiration

R – Precipitation

RET – Real Evapotranspiration

RH – Relative Humidity

rms – root-ean-square

SA – Simulated Annealing

SAR – Sodium Adsorption Ratio index

SCI – Spatially Constrained Inversion

SNR – Signal to Noise Ratio

SP – Spontaneous Potential

SPM – Superparamagnetic effect

SUTRA – Saturated-Unsaturated TRAnsport code

SVD – Singular Value Decomposition

TDEM – Time Domain Methods

TDS – Total Dissolved Salts

TEM – Transient Electromagnetic Method

TEMRES – TEM

VES – Vertical Electric Sounding

VLF – Very Low Frequency

WGS84 – World Geodetic System 1984

ACKNOWLEDGEMENTS

I want to thank Prof. Fernando Santos for all the support throughout the duration of the thesis, for providing useful suggestions, literature and especially for his skills with the inversion programs' codes. His friendship is always worth mentioning.

I want to thank Prof. Maxwell Meju for introducing me to the electromagnetic transient method, providing initial literature and also helping with the field equipment selection.

I want to thank Prof. Eugénio Almeida, a long-time friend and colleague, for the fundamental support he managed to supply from Instituto Politécnico de Tomar, providing the necessary transient field equipment. Without the equipment, this work would be impossible to fulfil.

I want to thank to Cape Verde authorities, namely the Instituto Nacional de Meteorologia e Geofísica (INMG) and Instituto Nacional de Gestão dos Recursos Hidrícos (INGRH), for the support with the meteorological and climatic data series as also with the hydrochemical data.

I want to thank to Prof. António Pina and Prof. Mota Gomes for they support on my first field trip to Santiago Island. Their knowledge of Santiago's geology was fundamental to me, as also were they commitment and help at this survey.

Many thanks to all friends and colleagues who have been at Santiago with me doing the important field work; Eugénio Almeida, Fernando Santos, João Coroado and last but not least special thanks to Patricia Represas for her commitment to this Santiago work.

To "my" Faculdade de Ciências da Universidade de Lisboa (FCUL) for the support throughout the duration of this thesis, especially to the Centro de Geofísica da Universidade de Lisboa.

I want to thank the Fundação para a Ciência e a Tecnologia (FCT) for the PhD scholarship financial support SFRH/BD/24640/2005 and also they support with the project HYDROARID (POCI/CTE/GEX/55399/ 2004).

1
INTRODUCTION

The worldwide available freshwater to human needs for direct consumption or for the many fundamentals human activities (agriculture, industry, etc.) are in a fast decline face to the growing population natural demands. By consequence of human activities, water's quality is accordingly getting depleted, with very adverse effects over populations, ecosystems and economy. The knowledge and control of water quantity and quality is vital and fundamental to the planning and management of this priceless resource to Earth life and health. This is even more difficult to achieve when groundwater is concerned. To probe the quantity and especially the quality of groundwater, specific actions have to be made, and some background conditions are mandatory, other than a simple superficial water sampling for physical-chemical (or biological) analyses. The traditional direct method, i.e. *in-situ* measurement of water's electric conductivity or water sampling is only possible if springs, wells and boreholes do exist in the field. Nevertheless, the information will be limited to those sampling spots. The number of these sampling places is for most of the situations very limited. To overcome this, indirect methods can be very useful, like the geophysical methods have prove since the beginning of last century.

The present thesis deals with the applicability of one method, between many geophysical electromagnetic prospection methods, known as Transient Method to the characterization of groundwater reservoirs. It was applied to the particular problem of groundwater quality assessment at Santiago Island – Cape Verde Republic. The work was done under the scope of FCT project HYDROARID – "Evaluation of the hydrological potential and seawater intrusion monitoring at semi-arid regions, by a multidisciplinary approach. Application to the islands of Santiago and Maio (Cabo Verde)", POCI/CTE/GEX/55399/2004. Briefly the thesis is organized in nine chapters, including this first one devoted to a general introduction.

Chapter 2 describes the physical electromagnetic principles behind the transient electromagnetic method. The signal problems and special effects over it are also included, together with the equipment description at field work.

Chapter 3 describes the transient electromagnetic modelling theory, with description and testing of the several different methods to invert measured data and obtain a useful physical model.

Chapter 4 describes the field work test to the equipment used thereafter, with comparison to other geophysical data acquired with different methods over the same location.

Chapter 5 describes the electrical/hydrogeological relationships that can be established between the transient electromagnetic modelled data and some useful hydrogeological parameters of groundwater quality.

Chapter 6 includes the most important Santiago Island settings, with geological and climatological description, as also the most-recent hydrochemical and isotopic available data.

Chapter 7 describes the transient electromagnetic method (TEM) surveys at Santiago Island, as also the interpretation of data by several different methods, and its relation with the observed groundwater chemistry. Assessment to groundwater salinity is advanced.

Chapter 8 describes the interpretation of the results and observed changes on the transient electromagnetic repetition surveys.

In the chapter 9, the conclusions and recommendations are described.

2
TEM METHOD

The purpose of this second chapter is to give an introduction to the Transient Electromagnetic Method (TEM). The basic principles of the method, used equipment and sources of errors will be also presented here. Special effects like Induced Polarization and Superparamagnetic effect are discussed also.

2.1 – Electromagnetic methods

Electromagnetic (EM) geophysical exploration method is one of the many tools now available and applied to obtain information about the subsurface of the Earth. There is an EM variety of techniques, survey methods, applications and interpretation procedures. All of them, however, involve the measurement of one or more electric and/or magnetic-field component by an EM Receiver, from some natural or man-made Controlled Source ElectroMagnetic (CSEM) energy source - the EM Transmitter. Examples of techniques using natural EM field propagation at the Earth are Magnetotelluric (MT) and Spontaneous Potential (SP). One classification of the several techniques is given at table 2.1. Table's first entry, is the resistivity method, also known as direct current (DC). This fundamental and well establish EM method was the first one to be successfully applied to earth interior's study, at the XX century. It is a subset of the EM methods, which arise when zero frequency (continuous current - DC) are applied by the transmitter.

Electromagnetic methods are based and ruled by Maxwell's laws. An alternating current EM source induces always a secondary current in conductive earth materials. These secondary currents then generate secondary magnetic fields. EM receivers measure this secondary field, and sometimes, also the primary (initial) source field. The relation between the primary and secondary fields is just the way earth reacts to the applied stimulus – "the transfer function of the Earth". Proprieties of the earth's interior are interpreted from these transfer functions, being electrical resistivity (or electrical conductivity, EC) one of the most-used propriety.

The success and evolution of EM methods stand from the wide range of available targets, and the almost any scale applicability of it; starting from the small natural sample at the laboratory to regional and global distribution of anomalously conductive mantle. However the "driven force" behind the EM method was the mineral exploration surveys, because most base metal massive sulfides ores are very conductive, providing a strong contrast to their host rocks. This exploration began in the 1950-60 period, with the advent of airborne systems. For long time, it was the prime application of EM methods. In the last century 70', the application of EM to other targets, besides traditional mineral exploration, together with a growing development of EM exploration equipment, gave the possibility to search, for instance, the conductive influx seawater into a resistive aquifer (Auken *et al*., 2006, Swift, 1988).

Not included on Table 2.1 is the GPR (Ground-Penetrating Radar) technique. It is a relatively new tool, with typically a two twin antenna system, one being the EM Transmitter and the other one being the EM Receiver. The EM frequency ranges from 50 MHz to the 1-2 GHz, allowing a high resolution and detail at the near surface, with a small size and portable equipment. This EM technique output is similar to seismic method, and many working tools are just adapted from the latter. The major difference, to exclude GPR from Table 2.1, is the applied frequency domain. At these high frequencies, EM earth material's behaviour is very different from the diffusive techniques included on Table 2.1.

Table 2.1 – Electrical and electromagnetic systems classification (adapted from Swift (1988)).

EM Transmitter	**EM Receiver**			
grounded wire	**grounded wire**	**wire and small coil**	**small coil (ground)**	**small coil (air)**
Galvanic	Resistivity, IP		Magnetometric resistivity (MMR), Magnetic IP (MIP)	
Inductive	Eltran	Controlled source AMT (CSAMT)	Some TEM systems	
Small loop			Slingram, Horizontal loop EM, Vertical loop EM, Tilt angle method, Some TEM systems coincident loop, Borehole configurations	Airborne EM; Time domain towed-bird, Helicopter rigid-boom
Large loop (long wire)			Large loop systems Turam, many TEM systems, Borehole configurations	
Plane Wave				
Vertical antenna		VLF-Resistivity	VLF	VLF
Natural geomagnetic field	Telluric currents SP	Magnetotellurics		

2.2 – The TEM method

Electromagnetic methods are divided into two categories: Frequency Domain methods (FDEM) and Time Domain methods (TDEM). Only this latter one will be described here.

Transient Electromagnetic Method is a time-domain method which was originally designed in the seventies of last century, as a way of finding ore deposits, mainly sulfides. At Portugal, it was and still is applied throughout the Iberian pyritic main belt with that purpose. It is an inductive method, and its ability to find low-resistivity layers has also made it one of the preferred methods for locating the bottom of aquifers, in the last decades. Nowadays, it is becoming very popular for hydrogeological mapping, replacing the traditional DC resistivity method, to some extent, by its easy application and less man power, being cheaper than DC method. It is best suited to groundwater prospecting at arid and hard-rock environments. However there are some natural limitations, inherent to the method. For instance, according to Jørgensen *et al*. (2003), layers with resistivity higher than 80-120 Ω.m cannot be expected to be mapped correctly if they are surrounded by layers with a lower resistivity value.

At present, TEM is under continuous development, which has resulted in the development of systems like the airborne SkyTEM method, the continuous TEM method (PATEM) and the high moment TEM method (HMTEM or HiTEM). (Danielsen *et al*., 2001 and 2003). Reference texts and descriptions for geological exploration and environmental investigation problems; such as mineral, groundwater and geothermal explorations, engineering geology and applied environmental geophysics investigations can be found at (Fittermann and Stewart, 1986; Buselli *et al*., 1990; Hoekstra and Blohm, 1990; Nabighian and Macnae, 1991; Zhdanov and Keller, 1994; Christensen and Sorensen, 1998).

As described the TEM is part of the Time Domain Electromagnetic Method geophysical prospection technique, contrary to the Frequency Domain Electromagnetic Method. Time Domain methods use a direct current, usually passed through an ungrounded loop laying down at earth's surface. Applying a continuous current to a coil creates a magnetic field, which is stable after some time. Stopping this current originates a variable magnetic field, which intensity decreases rapidly. The changing magnetic field induces currents in the ground.

Previous reviews of CSEM studies, including TEM method, for near-surface applications have been carried out by Nobes (1996) and Tezkan (1999). Tutorial articles specifically concerned with the CSEM method have been written by McNeill (1980 a, b) and West and Macnae (1991), while deeper theoretical treatments are available in the books by Grant and West (1965), Ward and Hohmann (1987), Wait (1982), Nabighian (1989) and Zhdanov and Keller (1994). Introduction level exploration textbooks such as Telford *et al*. (1990), Sharma (1997) and Kearey *et al*. (2002) provide just a brief overview of the CSEM method, along with some case studies.

At figure 2.1, the nomenclature and basic principles behind this method are summarized. Depicted theoretical waveform is called square wave (blue line). Red line represents the real current signal in the transmitter loop. The EM transmitter repeats this on-time – off-time cycles for a few minutes, to grab and enhance the registered signal. Each cycle last typically a couple of seconds.

After the initial continuous field has stabilized, the current is turned off very rapidly (thus the term transient EM) and this induces a primary magnetic field, which is proportional to the

effective area of the loop and the current amount. The current can be turned off in several ways, and for theoretical studies, the turn-off ramp can even be a true 'step-off' response (blue line at figure 2.1). Just after the current is turned off, eddy (ring smoke like) currents are instantly generated near the transmitting wire, as a reaction to maintain the magnetic field. With the passage of time these horizontal currents diffuse down and outward (figure 2.2). As a result of the finite electrical conductivity of the ground (and also nearby targets) these current's decay with time. The decay of the currents induces a secondary magnetic field, which is only dependent on the electric conductivity of the ground (and nearby targets), and can be measured by an induction receiver coil or loop (McNeill, 1990). Ideally, the primary field is absent while measuring earth's response.

The data is usually recorded in time windows (often called time gates) with increasing interval time length. That improves the signal to noise ratio (SNR) at late times, were the signals are weak. This recording happens at the off-time part of the cycle, following the turn-off instant (zero time for the time gates counting). The current direction's shift due to the unwanted signal from power lines if the repetition frequency is chosen as a multiple of a sub harmonic of the usual 50 Hz (or 60 Hz) power line frequency.

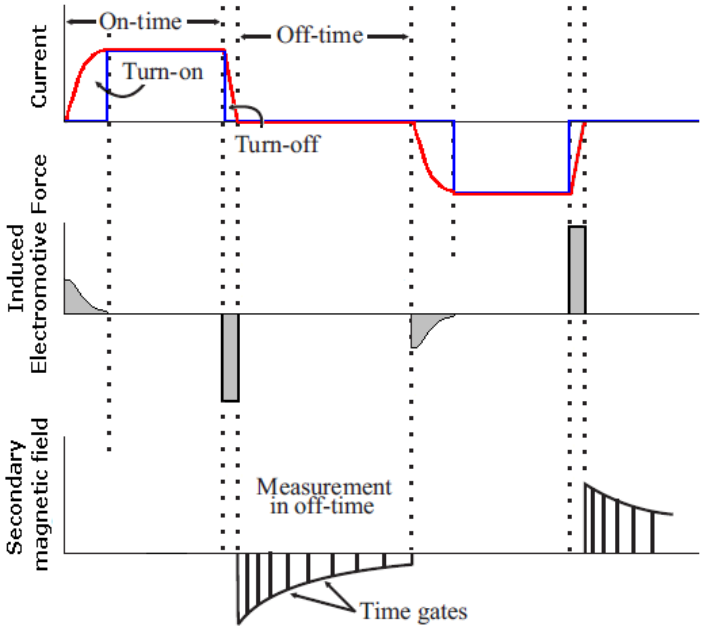

Figure 2.1 - The basic measuring principles of the TEM method, with theoretical current (blue line) and real current (red line) over time. This is for a central (in loop) system. The relative lengths of the turn-on ramp and the turn off-ramp are not to scale, (adapted from Christiansen (2003)).

The common TEM system used in environmental studies consists of a transmitter and a receiver unit. The transmitter unit is usually a large square loop made of standard flexible electrical cable with a side length varying between 10-20 and 100-150 meters. The current signal applied to the transmitter loop can be high as 30 ampere, but typically is about a few ampere in a 50 m × 50 meter single-turn square loop transmitter. The receiver is usually a rigid multi-turn coil with a diameter between a half and one meter, with an effective area of around 40-50 m^2. Alternatively, the same transmitter loop cable can also be used as the receiver loop, one of the configurations at figure 2.3. The receiver can be placed either inside

the transmitter (central-loop or in-loop configuration) or outside the transmitter (offset configuration). For most ground TEM systems, only the vertical component of the secondary field is measured in a central loop configuration, but in recent years steps have been taken to use other configurations, and with receiver coils, all three components of the field can be used to gain information about the conductivity of the underground. For airborne systems, an offset configuration is used, and all three components of the field are recorded.

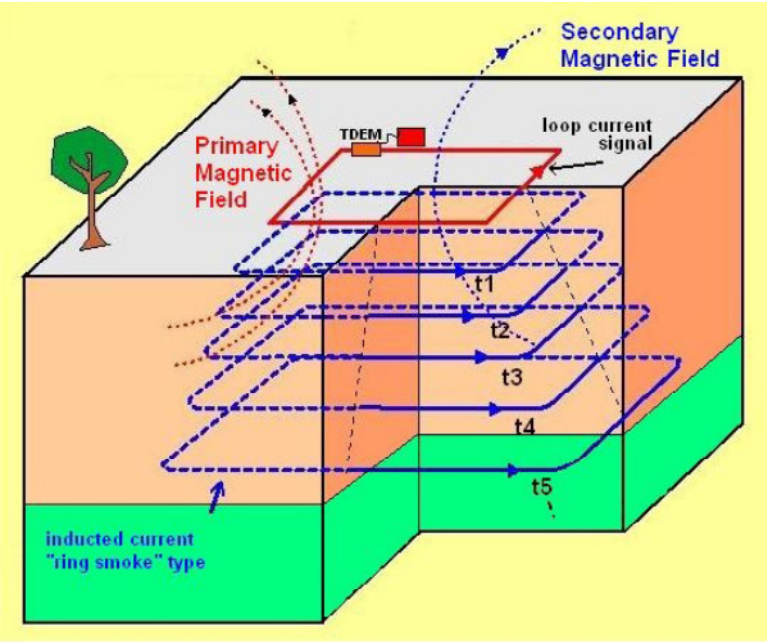

Figure 2.2 - The flow of TEM eddy current below the transmitter at successive times, from early times (t1, t2) to late times (t5,…).

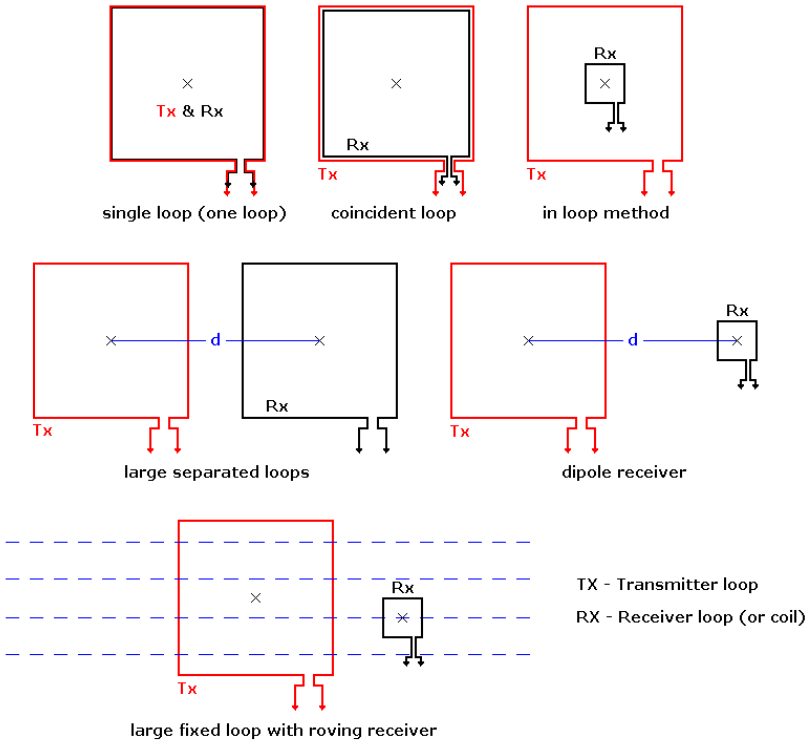

Figure 2.3 – Some usual field Tx-Rx configurations for TEM surveys, (adapted from Nabighian and Macnae (1991)).

2.3 – The Physics of the TEM method

The following description is a short overview of the electromagnetic theory behind the TEM method. The applied notation is as follows: lowercase-letters concern to functions expressed over time domain, and upper case-letters to functions expressed in the frequency domain (Harrington 1961). Where possible, the presentation of the relevant equations is kept in the time domain, although some arguments require equations stated in the frequency domain.

2.3.1 – Maxwell Equations and constitutive relations

The physics behind all electromagnetic phenomena is contained in the Maxwell Equations, which are first-order linear differential equations. Those equations are uncoupled, but they can be coupled by empirical constitutive relations, which reduce the amount of basic vector field functions from five to just two. Maxwell Equations are empirical equations based on experimental data and observations, performed, for instance, by Faraday and Ampere (Ward and Hohmann, 1988). All known electromagnetic phenomena obey to these equations, described in the time domain as;

$$\nabla \cdot \mathbf{d} = \rho \qquad (2.1a)$$

$$\nabla \cdot \mathbf{b} = 0 \qquad (2.1b)$$

$$\nabla \times \mathbf{e} + \frac{\partial \mathbf{B}}{\partial t} = 0 \qquad (2.1c)$$

$$\nabla \times \mathbf{h} - \frac{\partial \mathbf{D}}{\partial t} = \mathbf{j} \qquad (2.1d)$$

in which **e** is the electric field vector [$V.m^{-1}$],
b is the magnetic induction vector [$Wb.m^{-2}$],
h is the magnetic field vector [$A.m^{-1}$],
j is the electric conductive current density vector [$A.m^{-2}$],
d is the dielectric displacement current vector [$C.m^{-2}$]
and ρ is the electric charge density [$C.m^{-3}$].

Maxwell's equation (2.1c) is the Faraday's Law, which states that a changing over time magnetic field generates an electric field. This electric field is perpendicular to the magnetic induced field. Equation (2.1d) is known as modified Ampere's Law, which states that magnetic fields are perpendicular to the electrical current and that the total current is the sum of the conductive current and the displacement current. The remaining two equations are both the laws of Gauss, describing the electric displacement (2.1a) and magnetic induction (2.1b). The later states that the divergence of the magnetic field is zero. That means a solenoid geometry field and ultimately that magnetic mono-poles do not exist. The former equation states that the divergence of the displacement current is equal to the electric charge density.

The usual way to solve this boundary-value problem is by field vector functions conversion to the scalar potential functions must.

These Maxwell's Equations (2.1a to 2.1d), are coupled through the following constitutive relations, in the frequency-domain. They are;

$$\mathbf{D} = \hat{\boldsymbol{\varepsilon}}(\omega,\mathbf{E},\mathbf{r},t,T,P,...)\mathbf{E} \qquad (2.2a)$$

$$\mathbf{B} = \hat{\boldsymbol{\mu}}(\omega,\mathbf{H},\mathbf{r},t,T,P,...)\mathbf{H} \qquad (2.2b)$$

$$\mathbf{J} = \hat{\boldsymbol{\sigma}}(\omega,\mathbf{E},\mathbf{r},t,T,P,...)\mathbf{E} \qquad (2.2c)$$

where $\hat{\boldsymbol{\varepsilon}}$, $\hat{\boldsymbol{\mu}}$ and $\hat{\boldsymbol{\sigma}}$ are tensors describing, respectively, the dielectric permittivity, the magnetic permittivity and the electric conductivity, as a function of ω (angular frequency), **E** (electric field), **r** (position vector), t (time), T (temperature) and P (pressure), These tensors are complex (in the general case), meaning that phases of **D** and **E**, of **H** and **B** and of **J** and **E** are different (Ward and Hohmann, 1988).

Together with these two sets of expressions (2.1 and 2.2), the physic's fundamental equation of charge conservation is always present:

$$\frac{\partial \rho}{\partial t} + \nabla \cdot \mathbf{j} = 0 \qquad (2.3)$$

For homogeneous earth materials with electric conductivities equal or greater than 10^{-4} S.m^{-1}, free electric charge dissipates in less than 10^{-6} s (Stratton, 1941). Thus for the stand of view of geophysical prospecting, in which frequencies less than 10^5 Hz are employed, the first term of the left-hand side of equation (2.3) vanish, remaining just:

$$\nabla \cdot \mathbf{j} = 0 \qquad (2.4)$$

This equation (2.4) does not hold true at inhomogeneous regions, for instance, at the interface between two different media a surface charge does accumulate.

At most of the electromagnetic earth problems, and to simplify the analysis, a number of assumptions are made:

- All media are considered linear, isotropic, homogeneous, and electrical properties are taken independent of time, temperature or pressure,
- The magnetic permeability μ is assumed to be that of free space, $\mu = \mu_0$ (that couldn't be the case over some eruptive formations).

At some conditions, anisotropic media must be necessarily considered to aid in interpretation of observed data. At deep crustal surveys, temperature and pressure are also taken into account. Furthermore, in shallow geotechnical surveys, the time dependence of electric conductivity due to changes in soil moisture cannot always be neglected.

In the following considerations and derived relations, the simplification of the set of three expressions (2.2) in the time domain will suffice. The relations are restricted to non-dispersive media where ε, μ and σ are time independent.

$$\mathbf{d} = \boldsymbol{\varepsilon}\mathbf{e} \tag{2.5a}$$

$$\mathbf{b} = \boldsymbol{\mu}\mathbf{h} \tag{2.5b}$$

$$\mathbf{j} = \boldsymbol{\sigma}\mathbf{e} \tag{2.5c}$$

The last relation (2.5c) is the very well known Ohm's law, connecting the prevailing conductive electric current to the applied electric field, over a conductive body.

2.3.2 –The Electromagnetic Wave Equations

The wave equations describe the wave properties of electric and magnetic fields as they travel across any conductive media. One arrive at the wave equation using the Maxwell equations (2.1) shows upon and taking the curl of each Faraday and Ampere equation and applying the constitutive relations (2.5).

$$\nabla \times \nabla \times \mathbf{e} + \mu \frac{\partial}{\partial t}(\nabla \times \mathbf{h}) = 0 \tag{2.6a}$$

$$\nabla \times \nabla \times \mathbf{h} - \varepsilon \frac{\partial}{\partial t}(\nabla \times \mathbf{e}) = \sigma \nabla \times \mathbf{e} \tag{2.6b}$$

It is assumed that the vector functions **e** and **h** are piecewise continuous and have continues first and second derivatives, allowing interchanging between $\nabla\times$ and $\partial/\partial t$.

By use of Maxwell's equations (2.1c) and (2.1d), and taking into account the known vector identity $\nabla \times \nabla \times \mathbf{a} \equiv \nabla\nabla \cdot \mathbf{a} - \nabla^2\mathbf{a}$, and that for homogeneous regions we have $\nabla \cdot \mathbf{e} = \mathbf{0}$ and $\nabla \cdot \mathbf{h} = \mathbf{0}$, equations (2.6) turn out to be:

$$\nabla^2\mathbf{e} - \mu\varepsilon \frac{\partial^2\mathbf{e}}{\partial t^2} - \mu\sigma \frac{\partial \mathbf{e}}{\partial t} = 0 \tag{2.7a}$$

$$\nabla^2\mathbf{h} - \mu\varepsilon \frac{\partial^2\mathbf{h}}{\partial t^2} - \mu\sigma \frac{\partial \mathbf{h}}{\partial t} = 0 \tag{2.7b}$$

These are the time-domain wave equations for the electric and magnetic fields. Physically (2.7) equation's terms are as follows; the second term is the energy storage term, describing wave propagation (Powers, 1997). The third one is the energy dissipation term describing electromagnetic diffusion. As stated before, most CSEM methods operate at low frequencies (100 Hz to 1 MHz range), alternatively, slow time disturbances of the source current (~1 μs to 10 ms range). This condition leads that $|\mu\sigma\,\partial\mathbf{e}/\partial t|$ ($|\mu\sigma\,\partial\mathbf{h}/\partial t|$) are larger by several orders of magnitude than $|\mu\varepsilon\,\partial^2\mathbf{e}/\partial t^2|$ ($|\mu\varepsilon\,\partial^2\mathbf{h}/\partial t^2|$). It is then safe to ignore the wave propagation terms from (2.7) equations, and dielectric permittivity (***ε***) play no further role in this discussion. But, if the electrical conductivity is low enough (like σ = 0.0001 S.m^{-1}, electric resistivity of 10000 Ω.m) and the angular frequency high enough (like $\omega = 2\pi\times10^6$ rad.s^{-1})

than $\sigma \sim \varepsilon\omega$, the electromagnetic response of the earth is fully described by Equations (2.7) with all terms kept.

These simplifications are generally referred as the quasi-stationary approach and are best considered in the frequency-domain version of the wave equations. Applying Fourier Transformation to these wave equations, with respect to time leads to:

$$\nabla^2\mathbf{E} + (\mu\varepsilon\omega^2 - i\mu\sigma\omega)\mathbf{E} = 0 \qquad (2.8a)$$

$$\nabla^2\mathbf{H} + (\mu\varepsilon\omega^2 - i\mu\sigma\omega)\mathbf{H} = 0 \qquad (2.8b)$$

with

$$k^2 = \mu\varepsilon\omega^2 - i\mu\sigma\omega = -\hat{z}\hat{y} \qquad (2.9)$$

where k is the wave number as defined by Ward and Hohmann (1988). The *admittivity* $\hat{y} = \sigma + i\varepsilon\omega$ and the *impedivity* $\hat{z} = i\mu\omega$ is such defined (Harrington, 1961).

Equations (2.8) can be now rewritten as;

$$\nabla^2\mathbf{E} + k^2\mathbf{E} = 0 \qquad (2.10a)$$

$$\nabla^2\mathbf{H} + k^2\mathbf{H} = 0 \qquad (2.10b)$$

Both sets of equations (2.8) and (2.10) are known as Helmholtz equations. The expression in the brackets (equations 2.8a and 2.8b) describes the differences between the electric displacement currents and the electric conducting currents. As stated, frequencies less than 10^5 Hz mean that conducting currents are much larger than the displacement currents, when real earth materials are considered. Once $\mu\varepsilon\omega^2 \ll \mu\sigma\omega$ it is fulfilled, and expressions (2.8) do become:

$$\nabla^2\mathbf{E} - i\mu\sigma\omega\mathbf{E} = 0 \qquad (2.11a)$$

$$\nabla^2\mathbf{H} - i\mu\sigma\omega\mathbf{H} = 0 \qquad (2.11a)$$

The equivalent equations set (2.7) in time domain, as stated before, thus becomes;

$$\nabla^2\mathbf{e} - \mu\sigma\frac{\partial\mathbf{e}}{\partial t} = 0 \qquad (2.12a)$$

$$\nabla^2\mathbf{h} - \mu\sigma\frac{\partial\mathbf{h}}{\partial t} = 0 \qquad (2.12b)$$

Under this circumstance, the wave number k simplifies to:

$$k = \sqrt{-i\mu\sigma\omega} \qquad (2.13)$$

These equations set (2.11) and (2.12), represent diffusion equations (TEM is strictly a diffusive phenomenon method) that apply to real earth materials and lead to the attendant lack of resolution in EM prospecting methods (Ward and Hohmann, 1988).

2.3.3 – Boundary conditions

The boundary conditions are important as they relate and rule out the behaviour of the electric and magnetic fields, when crossing in between regions of different electric and magnetic properties. They are stated as follows (Ward and Hohmann, 1988);

Normal B: the normal component of the magnetic induction vector $\mathbf{B}$ is continuous over an interface between two regions (media 1 and 2) with different electrical properties.

$$(\mathbf{B}_1 - \mathbf{B}_2) \cdot \mathbf{n} = 0 \tag{2.14}$$

n is the unitary normal vector at boundary.

Normal D: the normal component of the dielectric displacement vector **D** is discontinuous over an interface due to the accumulation of a surface charge density ρ_s.

$$(\mathbf{D}_1 - \mathbf{D}_2) \cdot \mathbf{n} = \rho_s \tag{2.15}$$

Normal J: the normal component of the current density vector $\mathbf{J}$ is continuous over an interface.

$$(\mathbf{J}_1 - \mathbf{J}_2) \cdot \mathbf{n} = 0 \tag{2.16}$$

Tangential E: the tangential component of the electrical field vector $\mathbf{E}$ is continuous.

$$\mathbf{n} \times (\mathbf{E}_1 - \mathbf{E}_2) = 0 \tag{2.17}$$

Tangential H: the tangential component of the magnetic field vector $\mathbf{H}$ is continuous assuming that no surface currents exist at boundary. This is true for most non-metallic media.

$$\mathbf{n} \times (\mathbf{H}_1 - \mathbf{H}_2) = 0 \tag{2.18}$$

2.3.4 – Wave equations derived solutions

The wave equations are of second order, linear and homogenous differential equations. To solve them, two sets of basic solutions are considered (Ward and Hohmann, 1988). The first set describes the sinusoidal dependence while the second set describes the impulsive, electric and magnetic fields in a full-space.

First set solution – assuming plane waves with a sinusoidal time dependence, $e^{i\omega t}$:

$$\mathbf{e} = \mathbf{e}_\mathbf{0}^+ e^{-i(\overline{k}z - \omega t)} + \mathbf{e}_\mathbf{0}^- e^{i(\overline{k}z + \omega t)} \tag{2.19a}$$

$$\mathbf{h} = \mathbf{h}_\mathbf{0}^+ e^{-i(\overline{k}z - \omega t)} + \mathbf{h}_\mathbf{0}^- e^{i(\overline{k}z + \omega t)} \tag{2.19b}$$

$\mathbf{e}_\mathbf{0}^+$ ($\mathbf{h}_\mathbf{0}^+$) and $\mathbf{e}_\mathbf{0}^-$ ($\mathbf{h}_\mathbf{0}^-$) are the initial time amplitudes (t = 0 s) of the electric (magnetic) field propagating, in the positive and negative z-direction, respectively.

$$\overline{k} = \alpha - i\beta \tag{2.20}$$

with α and β being identical quantities (as conductive currents dominate over displacement currents), defined as:

$$\alpha = \beta = \sqrt{\frac{\mu\sigma\omega}{2}} \tag{2.21}$$

This implies that quasi-static case waves propagating, in the positive z-direction, are just reduced to:

$$\mathbf{e} = \mathbf{e_0^+} e^{-i\alpha z - \beta z + i\omega t} \tag{2.22a}$$

$$\mathbf{h} = \mathbf{h_0^+} e^{-i\alpha z - \beta z + i\omega t} \tag{2.22b}$$

Since β is a real value, the $e^{-\beta z}$ factor decreases as z increases. This factor represents the attenuation of the electromagnetic wave. As a result, the electromagnetic wave amplitude is reduced by a factor of 1/*e* at a distance called the *skin depth*, δ:

$$\delta = \sqrt{\frac{2}{\mu\sigma\omega}} \cong 503.3\sqrt{\frac{2}{f\sigma}} \tag{2.23}$$

The known skin depth expression put into evidence, that attenuation depends on both the frequency and the conductivity of the media. Relatively high conductivity and frequency result in a faster attenuation with respect to depth.

Second set solution - is derived by inverse Fourier transformation of the positive part of equations set (2.19) (neglecting displacement currents). It describes the behaviour of impulsive electric and magnetic fields at the surface of a media (z = 0 m), i.e. a plane wave propagating in a whole space. It yields that:

$$\mathbf{e} = \mathbf{e_0^+} \frac{\mathbf{z(\mu\sigma)^{1/2}}}{\mathbf{2\pi^{1/2}t^{3/2}}} e^{-\frac{\mu\sigma z^2}{4t}} \tag{2.24a}$$

$$\mathbf{h} = \mathbf{h_0^+} \frac{\mathbf{z(\mu\sigma)^{1/2}}}{\mathbf{2\pi^{1/2}t^{3/2}}} e^{-\frac{\mu\sigma z^2}{4t}} \tag{2.24b}$$

Figures 2.4 (a and b) shows the calculated electric (magnetic) field in a 100 Ω.m (0.01 $S.m^{-1}$) whole space due to a 1D impulse in the field. As a function of time (figure 2.4a) the field exhibits a modest short peak followed by a long decreasing tail. As a function of space, it is also possible to follow the electric (magnetic) field at each given time (figure 2.4b).

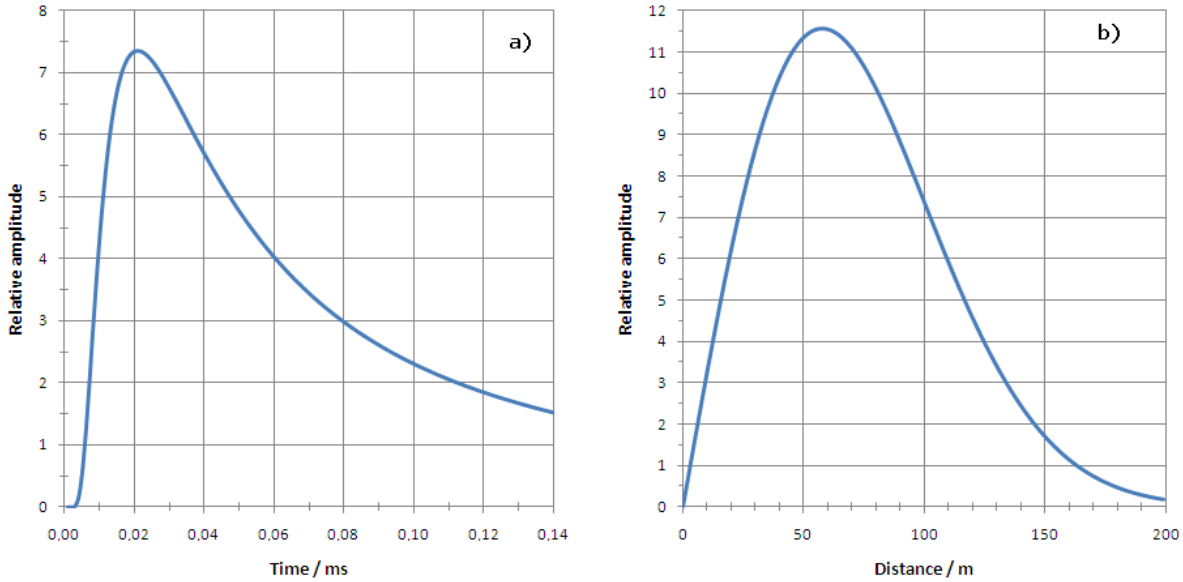

Figure 2.4 – a) Electric (magnetic) field as a function of time, 100 m from a 1D impulse, in a 100 Ω.m whole space. b) Electric (magnetic) field from a 1D impulse as a function of distance, at 0.0209 ms time.

For a given spatial position, it's possible to get the time of maximum field intensity in (2.24), doing the time derivative and finding the corresponding extreme peak (t_{max}), which is given by:

$$t_{max} = \frac{\mu\sigma z^2}{6} \tag{2.25}$$

At figure 2.4a) this intensity's peak occur at 0.0209 ms time (z = 100 m).

Similarly, setting the spatial derivative (with respect to z) of expressions (2.24), and extracting the maximum, result at:

$$z_{max} = \left(\frac{2t}{\mu\sigma}\right)^{1/2} \tag{2.26}$$

where z_{max} is the penetration depth.

At figure 2.4b) this intensity's peak occur at z ≈ 57.7 m (t = 0.0209 ms).

Having the penetration depth, it's possible, by differentiating the expression (2.26) with respect to time, to know the travel velocity expression of that maximum peak (V_{max}):

$$V_{max} = \left(\frac{1}{2\mu\sigma t}\right)^{1/2} \tag{2.27}$$

Figure 2.5 displays the fast velocity decay of that maximum peak with time.

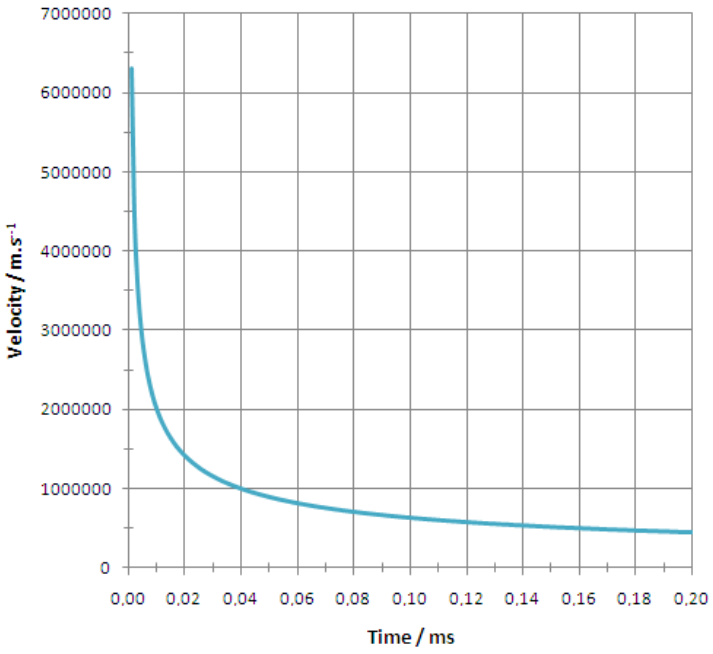

Figure 2.5 – Electric (magnetic) field maximum peak velocity values with time, from a 1D impulse, in a 100 Ω.m whole space.

As seen from expression (2.26) the penetration depth is proportional to $t^{1/2}$. This is similar to the skin depth described by expression (2.23), which is proportional to $1/\omega^{1/2}$.

Maxwell's equations are homogenous in the frequency domain and apply only to source-free regions, and can be rewritten as:

$$\nabla \times \mathbf{E} + \hat{z}\mathbf{H} = 0 \qquad (2.28a)$$

$$\nabla \times \mathbf{H} - \hat{y}\mathbf{E} = 0 \qquad (2.28b)$$

If the region contains a source, equations (2.28) must be replaced by the following, which takes into account the non-homogeneity that is introduced:

$$\nabla \times \mathbf{E} + \hat{z}\mathbf{H} = -\mathbf{J}_m^S \qquad (2.28c)$$

$$\nabla \times \mathbf{H} - \hat{y}\mathbf{E} = +\mathbf{J}_e^S \qquad (2.28d)$$

where $\mathbf{J}_m^S$ and $\mathbf{J}_e^S$ are the magnetic and electric sources currents, respectively.

According to Ward and Hohmann (1988), these equations can be solved for infinite homogenous regions, provided that $\mathbf{J}_m^S$ and $\mathbf{J}_e^S$ can be described explicitly. If **E** and **H** are described in terms of potentials, i.e functions from which **E** and **H** may be solved by differentiation; the equations are more easily solved. To accomplish this, Schelkunoff **A** and **F** potentials are introduced.

TEM methods use a magnetic source $\mathbf{J}_m^S$, transmitting a transverse electric field to the surrounding mean. This simplifies the situation because only the Schelkunoff potential **F** is necessary to express $\mathbf{E_m}$ and $\mathbf{H_m}$.

$\mathbf{E_m}$ is defined as:

$$\mathbf{E_m} = -\nabla \times \mathbf{F} \tag{2.29}$$

From upon $\mathbf{H_m}$ ends up as:

$$\mathbf{H_m} = -\hat{y}\mathbf{F} + \frac{1}{\hat{z}}\nabla(\nabla \cdot \mathbf{F}) \tag{2.30}$$

When this short electric pulse is emitted in a TEM square or circular transmitter loop, the observed induction response at receiver coil or loop can be thus computed. The response of a square (rectangular) or circular loop (with the same area) are similar (Poddar, 1982). The calculation of the circular loop response solution is easier because the integration along the loop can be carried out analytically.

2.3.5 – General solutions

A vertical magnetic dipole is a good approximation of a circular (square) loop, and the **F** Schelkunoff potential can be written. Assuming a circular loop at a height of h over a half-space earth surface, with a current intensity *I* and radius *a*, the **F** potential at a point P(x,y,z) is:

$$\mathbf{F}(\rho, z) = \frac{\hat{z}_0 \mathbf{m}}{4\pi} \int_0^\infty \frac{\lambda}{u_0} \left[e^{-u_0(z+h)} + r_{TE} e^{u_0(z-h)} \right] \mathbf{J_0}(\lambda\rho) d\lambda \tag{2.31}$$

where m is the magnetic moment of the vertical dipole, $\lambda = \left(k_x^2 + k_y^2\right)^{1/2}$, $\rho = (x^2 + y^2)^{1/2}$, $u_n = (\lambda^2 - k_n^2)^2$ and $\mathbf{J_n}$ is the Bessel function of *n* order, k_x and k_y are the wavenumbers. Assuming that magnetic permeability is that of free space, the reflection coefficient, obtained by recursion from the bottom layer of the model, can be written like (Ward and Hohmann, 1988):

$$r_{TE} = \frac{\lambda - \hat{u}_1}{\lambda + \hat{u}_1} \tag{2.32}$$

The infinitesimal dipole moment is;

$$dm = I\rho' d\rho' d\phi \tag{2.33}$$

where $\rho' d\rho' d\phi$ the elemental area contribution from the loop area, as show in figure 2.6.

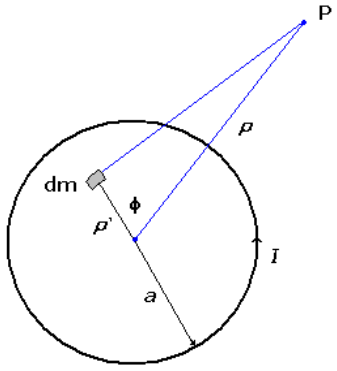

Figure 2.6 – Plan view of a circular loop at the earth's surface, elemental moment dipole contribution.

If this last (2.33) expression is substituted into (2.31) and one integrates it over the loop, the result is the TE_z potential:

$$\mathbf{F}(\rho, z) = \frac{\hat{\mathbf{z}}_0 \boldsymbol{Ia}}{\mathbf{2}} \int_0^\infty \frac{\mathbf{1}}{\mathbf{u_0}} \left[e^{-u_0(z+h)} + r_{TE} e^{u_0(z-h)} \right] \mathbf{J_1}(\lambda a)\, \mathbf{J_0}(\lambda \rho) d\lambda \qquad (2.34)$$

The corresponding field value $\mathbf{H_z}$ is found, applying definition (2.30) to the previous one;

$$\mathbf{H_z} = \frac{\boldsymbol{Ia}}{\mathbf{2}} \int_0^\infty \frac{\boldsymbol{\lambda^2}}{\mathbf{u_0}} \left[e^{-u_0(z+h)} + r_{TE} e^{u_0(z-h)} \right] \mathbf{J_1}(\lambda a)\, \mathbf{J_0}(\lambda \rho) d\lambda \qquad (2.35)$$

If measurements are taken at the center of a horizontal loop, the response can be found by just setting ρ equal to zero. Furthermore, if the measurements are made at the surface of a homogeneous earth, under the quasi-static approximation (valid when distances are much less than a wavelength in free space), equation (2.35) becomes (Ward and Hohmann, 1988):

$$\mathbf{H_z} = Ia \int_0^\infty \frac{\boldsymbol{\lambda^2}}{\boldsymbol{\lambda + u}} \mathbf{J_1}(\lambda a)\, d\lambda \qquad (2.36)$$

and so the vertical component of the magnetic field at the surface of the earth is given by:

$$\mathbf{H_z} = -\frac{I}{k^2 a^3} \left[3 - (3 + 3ika - k^2 a^2) e^{-ika} \right] \qquad (2.37)$$

2.3.6 – Transient response

The analytic expression of the response for a step field excitation can be found by inverse Laplace transformation of (2.37) equation (divided by iω) (Ward and Hohmann, 1988):

$$\mathbf{h_z} = \frac{I}{2a} \left[\frac{3}{\sqrt{\pi}\theta a} e^{-\theta^2 a^2} + \left(1 - \frac{3}{2\theta^2 a^2} \right) \mathrm{erf}(\theta a) \right] \qquad (2.38)$$

where erf is the known error function, and θ given as:

$$\theta = \sqrt{\mu_0 \sigma / 4t}\ . \qquad (2.38a)$$

The time derivative of this magnetic field, also called the impulse response, can be found by differentiation (2.38) with respect to time:

$$\frac{\partial \mathbf{h_z}}{\partial t} = -\frac{I}{\mu_o \sigma a^3} \left[3\, \mathrm{erf}(\theta a) - \frac{2}{\sqrt{\pi}} \theta a (3 + 2\theta^2 a^2) e^{-\theta^2 a^2} \right] \qquad (2.39)$$

The behaviour of the magnetic-field intensity and of the time derivative of the magnetic field, given by equations (2.38) and (2.39), are plotted at figure 2.7. At late times, θ becomes small and the magnetic-field intensity decays with a time dependency like $t^{-3/2}$, while the magnetic field's time derivative decays with a time dependency of $t^{-5/2}$. Decay slope for both fields is almost constant beyond 0.01 ms time (10 μs) (figure 2.7 example). Slope angular values are ≈ 56.3º and ≈ 68.2º, for magnetic field and its time derivative, respectively.

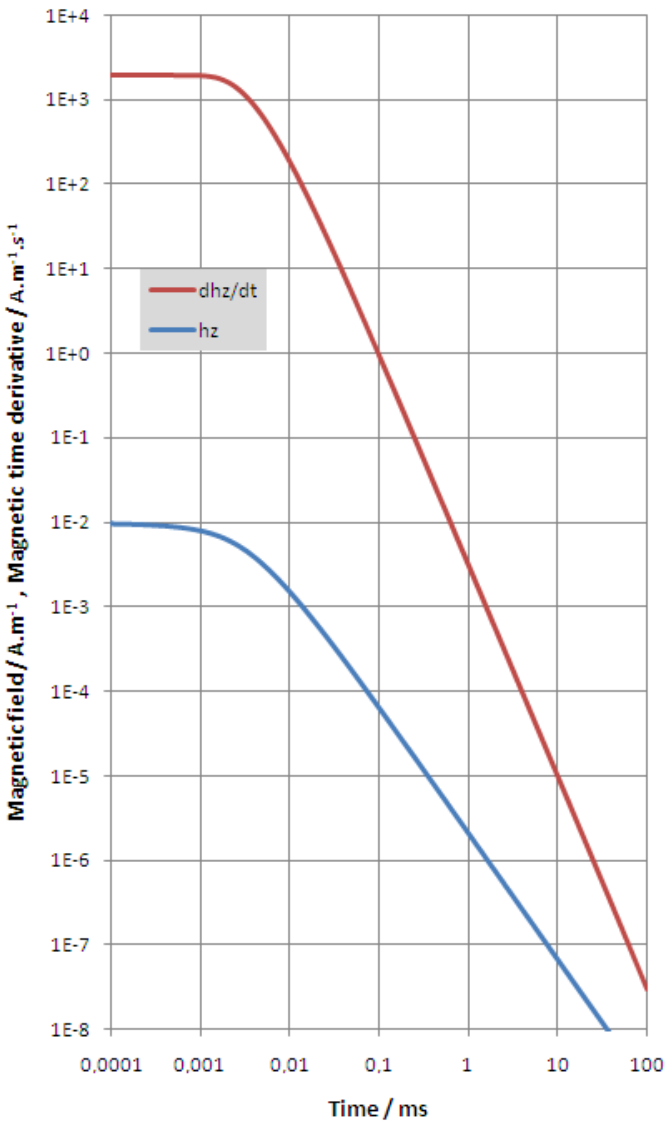

Figure 2.7 – The behaviour of the magnetic field and its time derivative, at circular loop's center (with 50 m radius) over a 100 Ω.m homogeneous earth. The applied current of 1 A has been turned off abruptly at t = 0 s (adapted from Ward and Hohmann, 1988).

The receiver in TDEM equipments is usually an induction-coil or loop sensor. So, it is therefore, better to handle with magnetic induction, **b**, instead of just work with magnetic-field intensity, **h**. This is easily accomplished, as the relation between these two fields is given by $\mathbf{b} = \mu_0 \mathbf{h}$.

The two equations (2.38) and (2.39) can also be simplified to;

$$\lim_{t\to\infty} \mathbf{b}_z \approx \frac{I\sigma^{3/2}\mu_0{}^{5/2}a^2}{30\sqrt{\pi}} t^{-3/2} \qquad (2.40)$$

$$\frac{\partial \mathbf{b}_z}{\partial t} \approx -\frac{I\sigma^{3/2}\mu_0{}^{5/2}a^2}{20\sqrt{\pi}} t^{-5/2} \qquad (2.41)$$

as θ becomes smaller at late times stages.

The apparent resistivity expression can now be taken from this last equation (2.41), representing the impulse response, and thus valid to late times of signal, as can be seen at figure 2.8.

$$\rho_a \approx \left(\frac{Ia^2}{20\frac{\partial b_z}{\partial t}}\right)^{2/3} \frac{{\mu_0}^{5/3}}{\pi^{1/3}} t^{-5/3} \qquad (2.42)$$

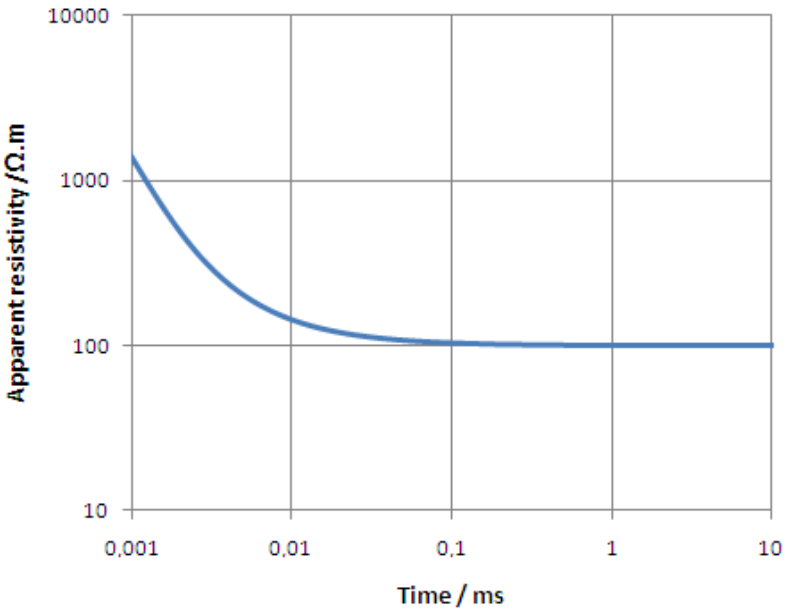

Figure 2.8 – Apparent resistivity curve with a circular in loop central measure (50 m radius) over a homogeneous 100 Ω.m earth. The applied current of 1 A has been turned off abruptly at t = 0 s.

2.4 – Application of the TEM method

The TEM method, as previously derived, is sensitive to electrical conductivity averaged over the volume of ground in which induced electric currents are caused to flow. Among the surface applied geophysical methods that sense bulk electrical properties of the subsurface of the earth, this CSEM offers deeper penetration capability than GPR techniques and greater resolving power than DC resistivity methods. The method performs substantially better in conductive soils or high radar reflectivity zones where GPR often encounters difficulties. As mention before, TEM also performs well in highly resistive terrains where it's difficult to establishing a good electrode contact with the ground, as required for most DC methods (Everett and Meju, 2005).

Nowadays, it's easy to operate TEM equipment at the field, with the available generation of commercial inexpensive instruments. The output power signal can reach several hundred watt, with the applied electric current from 1 A to several tens of ampere, allowing loop's diameters to the hundred meters level. However, most of the TEM data is extensively acquired with the central loop or coincident (single) loop configurations. That is because most of the developed have been made for those geometries (Morrison *et al.*, 1969; Patra, 1970; Lee and Lewis, 1974; Kaufman, 1979; Nabighian, 1979; Verma and Mallick, 1979; Spies and Raiche, 1980; Raiche and Spies, 1981; Hoversten and Morrison, 1982; Rai and Sarma, 1986; Newmann *et al.*, 1987; Goldman and Fittermann, 1987; Smith and West, 1988,

1989; Buselli *et al*., 1990; Hoekstra and Blohm, 1990; Nabighian and Macnae, 1991; Karmis *et al*., 2003, Zhdanov, 2009), because of the computational intricacies and difficulties associated with the TEM response for arbitrary in-loop and offset-loop receiver locations. As a matter of fact, only a few analytical or semi-analytical TEM response expressions have been published yet for the arbitrary source receiver offsets at the surface of the homogeneous earth model (Singh *et al*., 2009). The problem arises due to the computational complexities resulting from the product of Bessel's functions in frequency-domain expressions (Ward and Hohmann, 1988).

The processing of field data can be done throughout a variety of available options, ranging from construction of apparent conductivity curves based on simple asymptotic derived formulas, for rapid subsurface evaluation, like expression (2.42), to 1-D, 2-D and a few advanced 3-D forward modelling and inversion, for more detailed analyses.

2.4.1 – Transient diffusion distance

To implement the derived equation's theory, a typical transmitter current waveform with a "slow rise" to a steady-on value is applied to the transmitter loop (figure 2.1). That just induces a static magnetic field, the primary field. This contains no information about the earth, but is proportional to the magnetic moment, M, given by:

$$\mathrm{M} = InA_{loop} \qquad (2.43)$$

with n being the number of turns of the loop, A_{loop} the area of the loop [m^2] and I the direct current intensity [A].

This steady current is followed by a rapid shut-off, as exemplified by the linear ramp decay at figure 2.1. This disturbance through the loop breaks the initial primary magnetic-field that begins to decay and generates a primary magnetic-field that is in-phase with, or proportional to the corresponding transmitter loop current. This current causes an electric-field to be induced and eddy currents to begin running in the ground near the coil, (figure 2.2). Due to ohmic loss by heat dissipation at the medium, these currents will soon begin to decay, thereby inducing a secondary magnetic field. This secondary magnetic is weak, and produced in proportion to the waning strength of those eddy currents. Immediately, after the current had been turned off, the strength of the secondary and primary fields are of the same order. Since the decay of these currents is a function of earth's conductivity, the same happens with the secondary magnetic-field intensity. The decay of the secondary magnetic field induces an electromotive force in the receiver loop or coil that is measured trough time. Most TEM systems take voltage measurements during the transmitter off-time, when the primary field is already absent. The off-time measure's advantage is that the relatively too much weak secondary field signal is not swamped by the stronger primary field signal.

This induction process at the earth subsurface is equivalent to the diffusion of the transmitter loop image into a conducting medium. The similarity of the equations governing electromagnetic induction and hydrodynamic vortex motion was first noticed by Helmholtz

(Everett and Meju, 2005). This has lead directly to the association of this current image with a “smoke ring”, but care must be taken as the latter is not “blown”, as usually thought, but instead moves by self-induction with a velocity (maximum value given by 2.27 equation) that is generated by the smoke ring’s own vorticity and described by the famous Biot-Savart law. An electromagnetic smoke ring dissipates in a conductive medium much as the strength of a hydrodynamic eddy is attenuated by the viscosity of its host fluid. The medium property that dissipates the electromagnetic smoke ring is the electrical conductivity.

During the ramp-off, the induced current assumes the shape of the horizontal projection of the transmitter loop on the surface of the conducting earth. This “smoke ring current like”, advances and diffuses downward and outward through the ground and time, at an angle of approximately 30º with horizontal, while decrease in amplitude. Current always flows horizontally with no downward component. The sense of the circulating induced currents is such that the secondary magnetic field tends to maintain the total magnetic field at its original steady-on value prior to the transmitter ramp-off situation (Lenz law). Therefore, the induced currents flow in the same direction as the transmitter current, to compensate for transmitter current decrease.

The penetration depth, Z_d, at a given time t was already deduced at expression (2.26). This depth corresponds to the vertical location of the surface current maximum (Nabighian and Macnae, 1991) and is also known as *diffusion length* or *diffusion depth*. Often the *diffusion distance* is defined as:

$$\mathrm{d} = 2\pi Z_d \tag{2.44}$$

The maximum depth, to which measurements can be obtained, Z_{last}, is not only a function of the applied magnetic moment, but also of the noise level, V_{noise} acquisition at the measuring coil or loop (Christensen, 1995):

$$Z_{last} = \left(\frac{2}{25\pi^3}\right)^{1/10} \left(\frac{\mathrm{M}}{\sigma \mathrm{V_{noise}}}\right)^{1/5} \tag{2.45}$$

At this depth, the measurements are greatly noise influenced, and became unsatisfactory. According to Christensen (1995) a practical limit could be when the SNR (Signal to Noise Ratio) equals the unit. This distance corresponds to the t_{last} time, by the expression (2.25):

$$t_{last} = \mu \left(\frac{\sigma}{\pi}\right)^{3/5} \left(\frac{\mathrm{M}}{20\mathrm{V_{noise}}}\right)^{2/5} \tag{2.46}$$

As already mentioned, the maximum penetration depth is a function of the applied magnetic moment. Equation (2.45) expresses that dependency, Z_{last} is proportional to $M^{1/5}$. Thereby a dramatic increase in magnetic moment is always needed to increase the maximum penetration depth.

The magnetic-field configuration, for a given time, is shown at figure 2.9, with the “smoke ring” current superimposed. A conductive homogeneous half-space is considered.

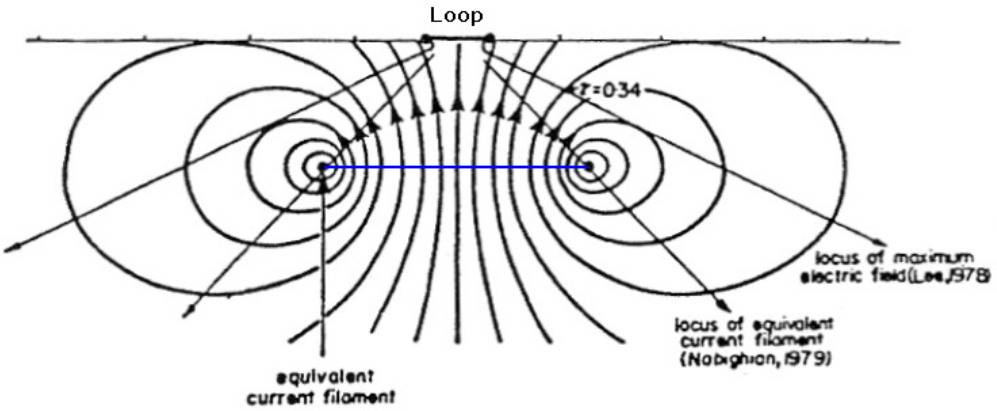

Figure 2.9 – Magnetic field cross-section representation bellow a square loop, for a given time (after shut-off). The “smoke ring” like current is also added. (Adapted from Nabighian and Macnae, 1991).

For each time, the vertical profile of current density is calculated from the electric field at the earth by Ohm’s law. That current density decays rapidly with depth at any given instant in time, as plotted at figure 2.10, for tree time instants. The corresponding equivalent penetration depth (skin depth) is also represented.

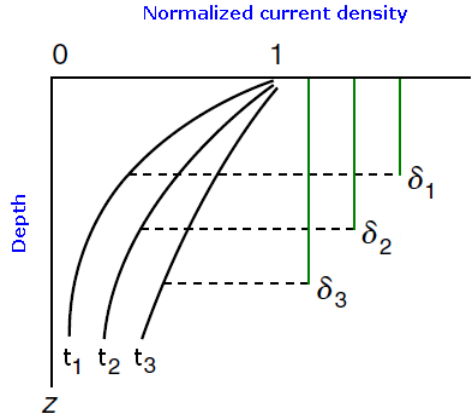

Figure 2.10 – Change in current density as a function of depth for several time instants (adapted from Zhdanov, 2009).

2.4.2 –Time stages in the diffusion process

Previous expressions (2.40 to 2.42) have been derived upon the assumption of a small θ, (2.38a). That means a late time (or late stage) behaviour. Let’s take a characteristic geometric dimension of the loop, such as r, the distance between the center of the transmitter and receiver loops or the transmitter-receiver loop radius for a coincident (or single) one loop. The stages can be defined as (Nabighian and Macnae, 1991):

- early time (early stage) for $d \ll r$
- intermediate time (intermediate stage) for $d \approx r$
- late time (late stage) for $d \gg r$

For each of these stages, simple asymptotic formulas can be derived, and thus solely valid and applicable in that same range. Deduced expressions (2.40) to (2.42) are the asymptotic

ones when t → ∞ , and consecutively θ → 0, a late stage condition. That means greater distances from the loop. For t → 0 , and consecutively θ → ∞ , early stage asymptotic expression also exist:

$$\lim_{t\to 0} \mathbf{b_z} \approx -\frac{I\mu_0}{4a}\left(1-\frac{18t}{\mu_0\sigma a^2}\right) \tag{2.47}$$

$$\frac{\partial \mathbf{b_z}}{\partial t} \approx \frac{9I}{2\sigma a^3} \tag{2.48}$$

and

$$\rho_a \approx \frac{2a^2}{9I}\left(\frac{\partial \mathbf{b_z}}{\partial t}\right) \tag{2.49}$$

The early stage apparent resistivity expression (2.49) it's then independent of time, t. At figure 2.11, the early and late stage apparent resistivity is plotted against time. It shows clearly that asymptotic approximation to apparent resistivity values are only valid at first beginning of early stage and to the end of late stage, diverging otherwise. To avoid miscalculations of the apparent resistivity, it is therefore necessary to use the exact formula, given by expression (2.39), especially at the stages not covered by asymptotic expressions. The differences are notorious when comparing the full and late asymptotic apparent resistivity (figure 2.12).

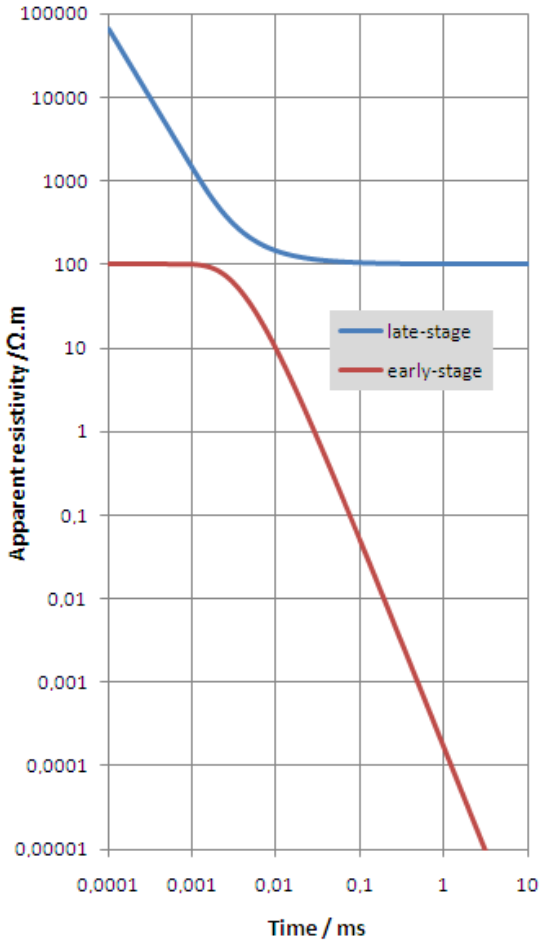

Figure 2.11 – Apparent resistivity curves for early and late stage for a circular in loop central measure (50 m radius) over a homogeneous 100 Ω.m half-space earth. The applied current of 1 A has been turned off abruptly at t = 0 s.

Characteristics of early and late-stage TEM vertical magnetic-field can be thus summarized as follows. Receiver measures with a central coil or coincident (or single) loop.

Early time:

diffusion distance is much less than transmitter-receiver separation,
diffusion current is concentrated near transmitter loop,
measured voltage $\left(\frac{\partial b_z}{\partial t}\right)$ is independent of time,
measured voltage $\left(\frac{\partial b_z}{\partial t}\right)$ is linearly proportional to ρ.

Intermediate time:

complex behaviour,
measured voltage $\left(\frac{\partial b_z}{\partial t}\right)$ relationship to ρ is changing.

Late time:

diffusion depth greater than transmitter-receiver separation,
measured voltage $\left(\frac{\partial b_z}{\partial t}\right)$ relationship is proportional do $1/ t^{5/2}$,
measured voltage $\left(\frac{\partial b_z}{\partial t}\right)$ relationship is proportional do $1/ \rho^{3/2}$.

In contrast to the incident EM plane wave response of a homogenous conductive half-space which yields equations that can be easily solved for the true resistivity (therefore, defining a unique apparent resistivity result, e.g., in magnetotellurics), the usual time-domain response equations do not allow a single to all-time apparent resistivity solution. Nevertheless, it is customary to use the derived asymptotic relations to define early time and/or late time formulations to calculate those two apparent resistivities. That is still assumed as first approach, especially with some acquisition field equipment used for deeper TEM soundings.

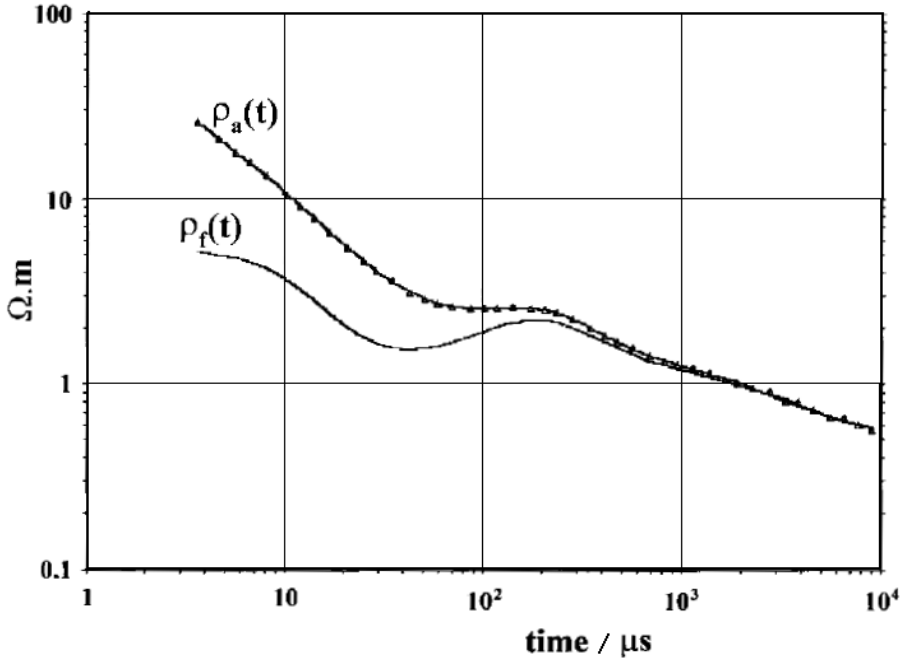

Figure 2.12 – Example of apparent resistivity from calculated asymptotic $\rho_a(t)$ and exact $\rho_f(t)$ expressions (adapted from Barsukov *et al.* (2007)).

2.5 – TEM-FAST 48 equipment

Transient electromagnetic data acquisition within this thesis framework was accomplished with the equipment from the Applied Electromagnetic Research Ltd. (AEMR). This electromagnetic prospecting tool it's the TEM-FAST 48, a very small, compact and portable unit, easy to deploy and apply at field work, even under hard conditions (figure 2.13). It was developed and builds under the chosen strategy of being a "simple - fast - robust" system. The complete set, with a single main transmitter-receiver unit, cables and loop weights about 5 kg. External gel power batteries can be used, adding a couple more kilograms to be carried at the field.

Figure 2.13 – TEM FAST 48 set with main unit (103 mm × 27 mm × 310 mm), loop cables and small pocket personal computer, (original photography from AEMR).

One of the most important features of any TEM equipment is the time duration of the self-transient process. That process is only dependent on the transmitter-antenna-receiver system properties. Obviously, proper quality TEM signals measures, and results are feasible only within the time interval where that self-transient process of the system is missing. The shorter the self-transient process is, earlier are the time delays and measures becomes feasible, allowing also the minimum depth of study.

2.5.1 – TEM-FAST 48 technical specifications

The 48 at TEM-FAST 48's name stand for the maximum allowed number of acquisition channels. Those 48 time gate channels range from 4,1 μs to 15,4 ms, spanning over four decades at the ratio of 12 channel/decade. This very short beginning time of 4,1 μs after

turn-off, offer one to get information about the first few meter's depth, when using small loops (1-10 meter size). The following characteristics are described at TEM-FAST 48 own manual. The transmitter unit output current amplitude pulses can be selected as one or four ampere. This is the maximum current allowed values. At the 4 A option, this extreme value is not usually reached. The achieved output current is only limited by the loop load resistivity value. The resistive loop values spans from a few to 20 ohm, with typically less than 0.01 H inductance and around 3 nF capacity (1 A output). The time of turning off the current's pulse, with a square single loop and 1 A option, is less than 3 μs (25 m × 25 m side size loop), 8 μs (50 m × 50 m) and 20 μs (100 m × 100 m). The ratio pulse/pause output current "square wave" is of 3 to 1. This special sequence of unipolar rectangular current pulses, provides at registration of long slow processes in well conducting media the minimal dynamic error caused by imposing of transients from both fronts of current pulses in transmitting loop antenna. Transmitted current pulse form, both theoretical and real, is given at figure 2.14.

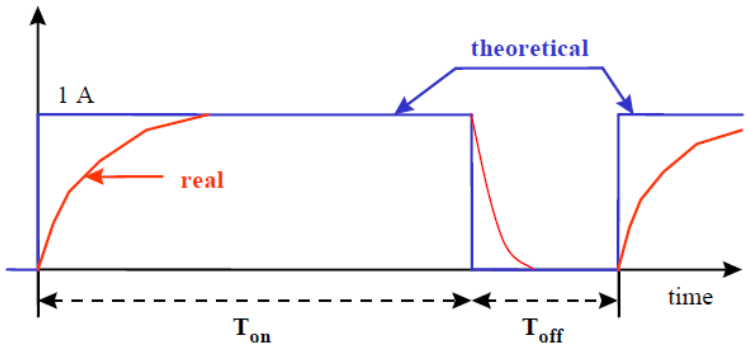

Figure 2.14 – Applied rectangular current pulses form of TEM FAST 48 (adapted from AEMR, 2006).

Real voltage and current output test measures at loop are also shown at figures 2.15 and 2.16, respectively. Those figures express the known fact that, useful data it's postponed to increased times with the loop size dimensions. It is also expected some distortion at the output signal, especially at the maximum current value of 4 A (as seen at figure 2.17), as the extreme output voltage of the transistor used in the unit is equal to about 850 V. This effect can distort the measured transient process at a time less than 6-7 μs (20 m × 20 m size loop), 15-20 μs (50 m × 50 m) and until 40 μs (100 m ×100 m).

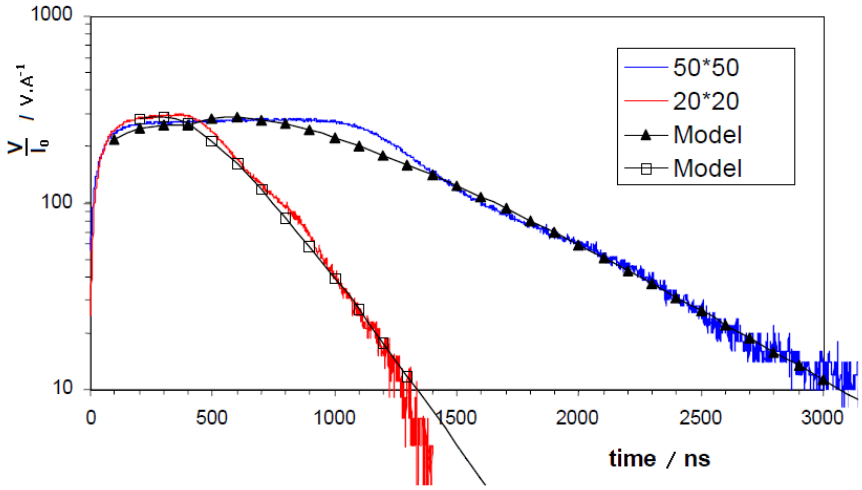

Figure 2.15 – Expected and measured loop antenna normalized voltage after turn off, for 20 m and 50 m side square loop (adapted from AEMR, 2006).

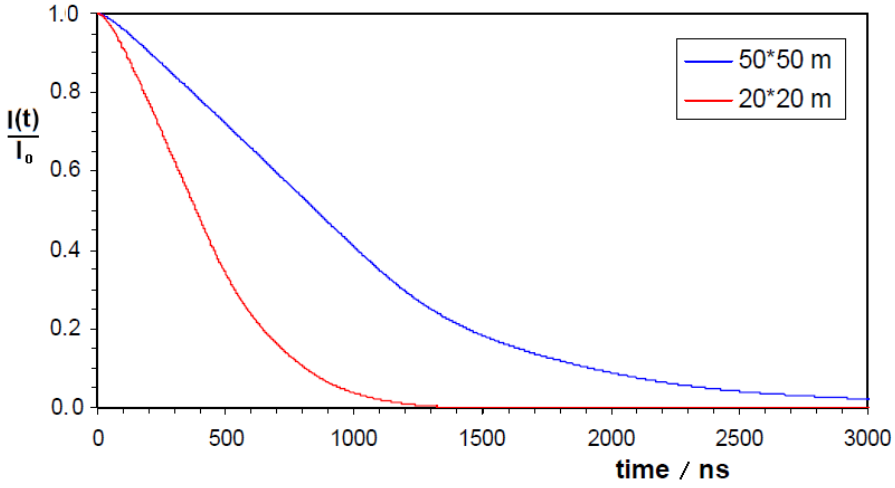

Figure 2.16 – Measured loop antenna normalized current after turn off, for 20 m and 50 m side square loop (adapted from AEMR, 2006).

The input voltage to power on the unit is done by the internal 12 V, 2 Ah battery. External power can be provided with a 12 or 24 V option, being the 24 V the best and maximum power unit choice.

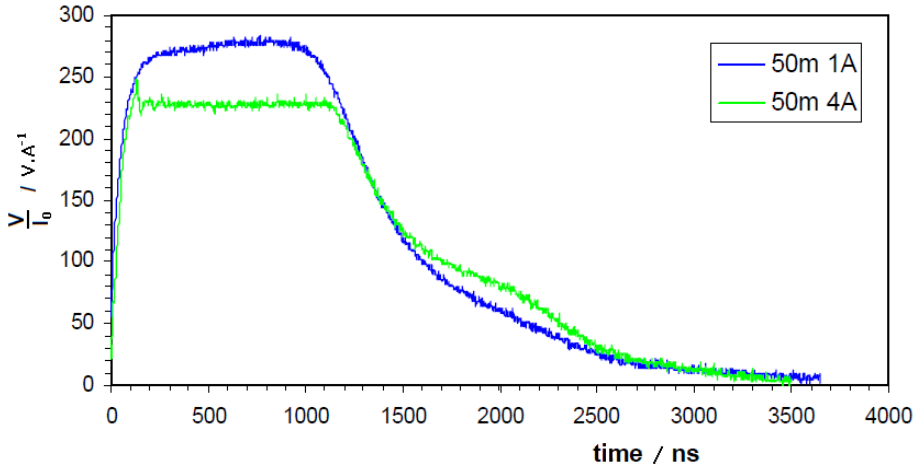

Figure 2.17 – Measured loop antenna normalized voltage after turn off, for the 50 m × 50 m loop with an applied current of 1 A and 4 A (adapted from AEMR, 2006).

The receiver frequency band is greater than four MHz, allowing a correct time signal measure starting from the μs level. The number of automatically registered delays (time gates) spans from 16 to 48. The complete description and definition of these time gates are given at table 2.2, table 2.3 and figure 2.18. The electromagnetic cultural noise suppression is implemented with the 50 Hz or 60 Hz option, and is greater than 60 dB. The internal noise measure is at the 1 μV level (rms), with a dynamic range of 10^7 (10 V to 1 μV) or 140 dB. A 10 times signal amplification can be turned on. That can be necessary when in loop configuration is used. Constructor reported overall systematic voltage errors are 1 %. This is done in the operational temperature range -20 ℃ to +65 ℃, as the acquisition system provides stable results of measurements at sharp changes of temperature, up to 3 ℃/minute. The unit performs also auto-calibrating and testing, tracing a correctness of work of the device during measurements, even in case when the noise level at input of the receiver achieves 1 V to 2 V.

Table 2.2 – TEM-FAST 48 time gates and time integration signal definition of strobe pulses, (adapted from AEMR, 2006).

Time gate	t_{start}	t_{finish}	t_{center}	Δt	Time gate	t_{start}	t_{finish}	t_{center}	Δt
	μs					μs			
1	3.6	4.6	4.06	1	**25**	255.6	319.6	285	64
2	4.6	5.6	5.07	1	**26**	319.6	383.6	350	64
3	5.6	6.6	6.07	1	**27**	383.6	447.6	414	64
4	6.6	7.6	7.08	1	**28**	447.6	511.6	478	64
5	7.6	9.6	8.52	2	**29**	511.6	639.6	570	128
6	9.6	11.6	10.53	2	**30**	639.6	767.6	699	128
7	11.6	13.6	12.55	2	**31**	767.6	895.6	828	128
8	13.6	15.6	14.56	2	**32**	895.6	1023.6	956	128
9	15.6	19.6	17.44	4	**33**	1023.6	1279.6	1152	256
10	19.6	23.6	21.46	4	**34**	1279.6	1535.6	1408	256
11	23.6	27.6	25.49	4	**35**	1535.6	1791.6	1664	256
12	27.6	31.6	29.50	4	**36**	1791.6	2047.6	1920	256
13	31.6	39.6	35.28	8	**37**	2047.6	2559.6	2304	512
14	39.6	47.6	43.30	8	**38**	2559.6	3071.6	2816	512
15	47.6	55.6	51.40	8	**39**	3071.6	3583.6	3328	512
16	55.6	63.6	59.41	8	**40**	3583.6	4095.6	3840	512
17	63.6	79.6	71.60	16	**41**	4095.6	5119.6	4608	1024
18	79.6	95.6	87.60	16	**42**	5119.6	6143.6	5632	1024
19	95.6	111.6	103.6	16	**43**	6143.6	7167.6	6656	1024
20	111.6	127.6	119.6	16	**44**	7167.6	8191.6	7680	1024
21	127.6	159.6	143.6	32	**45**	8191.6	10239.6	9216	2048
22	159.6	191.6	175.6	32	**46**	10239.6	12287.6	11264	2048
23	191.6	223.6	207.6	32	**47**	12287.6	14335.6	13312	2048
24	223.6	255.6	239.6	32	**48**	14335.6	16383.6	15360	2048

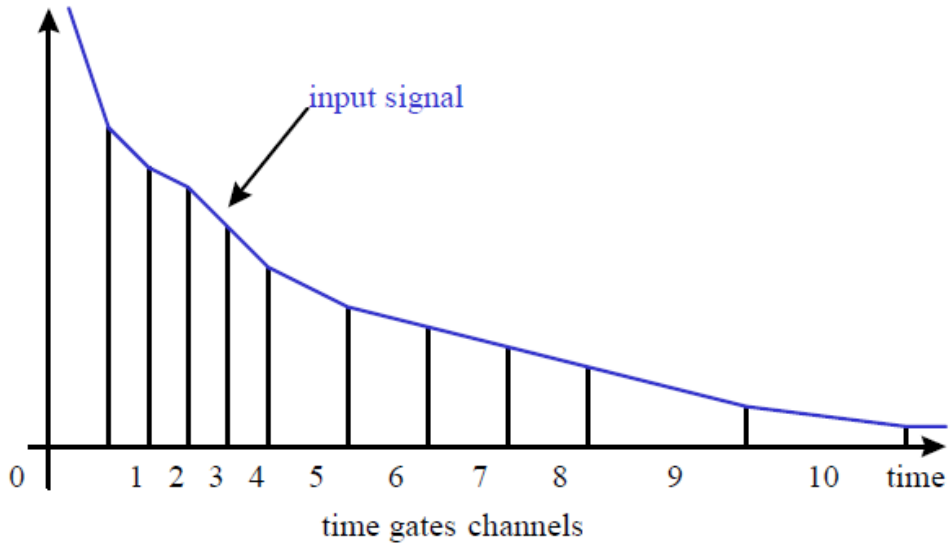

Figure 2.18 – Growing channel integration time with time amount and decreasing signal intensity. after turn off (adapted from AEMR. 2006).

Table 2.3 – TEM-FAST 48 number of active channels (time range), for the 50 Hz and 60 Hz option, (adapted from AEMR, 2006).

TEM-FAST 48 Time Range	Maximum time μs	Number of active time gates	Signal analog stack	$T_{on}+T_{off}$ 50 Hz ms	Total	$T_{on}+T_{off}$ 60 Hz ms	Total
1	64	16	1024	0.3125	320	0.26	266
2	128	20	512	0.625	320	0.52	266
3	256	24	256	1.25	320	1.042	266
4	512	28	128	2.5	320	2.08	266
5	1024	32	64	5	320	4.17	266
6	2048	36	32	10	320	8.33	266
7	4096	40	16	30	480	25	400
8	8192	44	8	50	400	41.67	333
9	16384	48	4	90	360	75	300

Measurements of transient decay signal voltage E(t) for some channels is schematically shown at figure 2.19. For each strobe at each consecutive channel, the signal is grabbed and stored, to be analog stacked on the next run. Thus, the transient is gated practically continuously without "dead zones". This is done by the internal algorithm known as DAS (multi-channel strobe system, integration and storage of the analog information). After termination of DAS processes, the output signals are digitized by the ADC (Analog-to-Digital Converter), transferred to the control block, and the integrators reset into initial condition. The number of strobe-pulses at the analog stacking phase is given at Table 2.3, for the several modes of the unit operations. ADC dynamic range is 16 bits, with smallest unit being 1 μV. The joint work DAS plus ADC provides measurement of sizes E(t)/I in the already described dynamic range of 1 μVA^{-1} to 10 VA^{-1}. The dynamic range of the signals E(t)/I depends on the value of the input parameters “Time Range”.

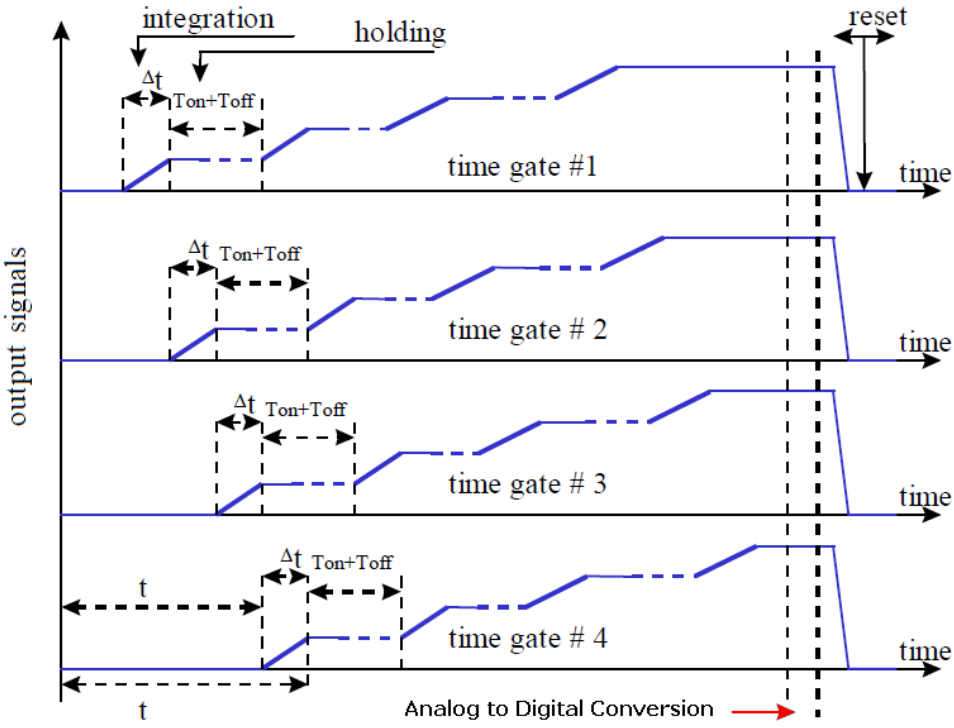

Figure 2.19 – Multi-channel data acquisition holding and integration DAS scheme, after turn off, (adapted from AEMR, 2006).

This procedure is automatically repeated for several times, to a maximum number of 20 stacks. Each stack corresponds to 13 complete work cycles of DAS algorithm system. At full stack and with all 48 channels, acquisition time of a single TEM sounding can last almost 10 minutes. The collected and grabbed data is saved into a small pocket personal computer (iPAQ), linked to the TEM-FAST 48 unit. This piece of equipment runs the program (AEMR, 2006) that supply and controls the main unit's selective parameters.

Stacking the measured signals not only enhances the SNR, but also outputs the associated error to each channel measure. Typically, the higher channels (that correspond to signal late stages) are always more noisy when compared to the early ones, as seen at figure 2.20.

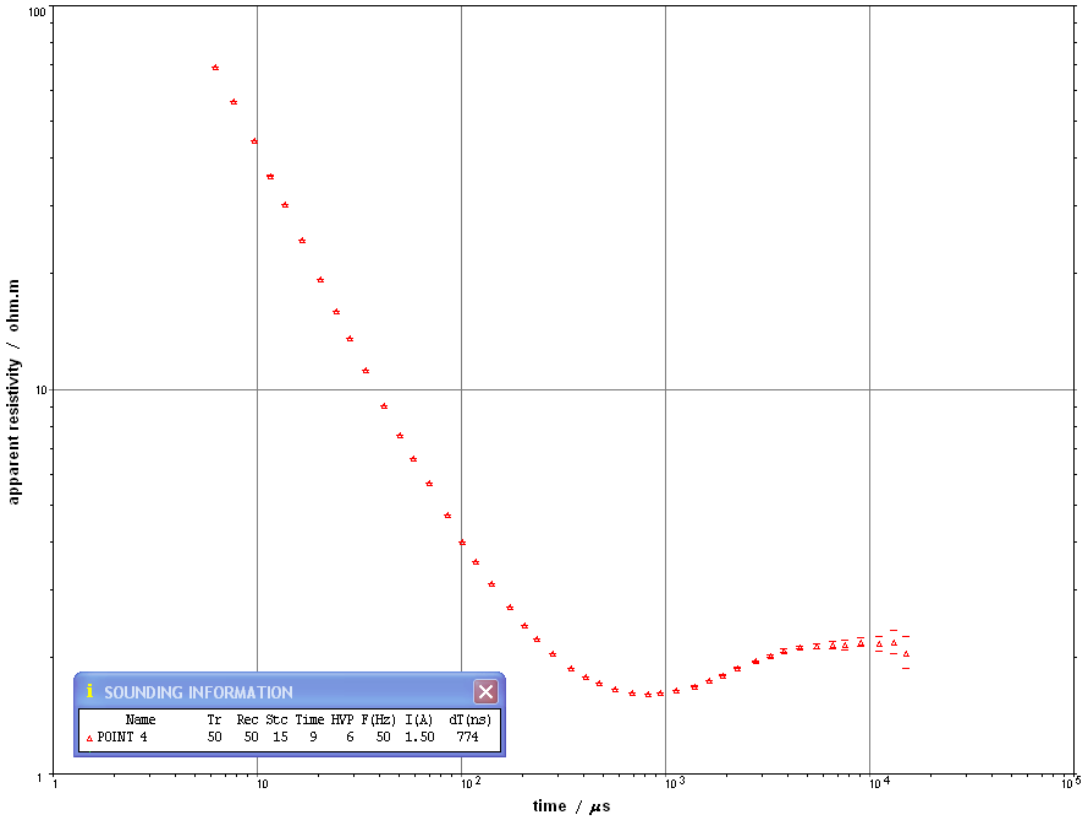

Figure 2.20 – A typical TEM sounding curve with data points and corresponding error band.

2.6 – Transient signals noise origin

The TEM method measures the magnetic flux in the induction coil or loop. For accurate, correct and reliable interpretation of the responses in terms of subsurface geology, it's important to recognize the various electromagnetic noise sources that may be present in TEM responses.

There are natural and "artificial" (man-made) sources of EM noise. Within these two kinds of sources it is also essential to differentiate between what is coherent and what is incoherent EM noise (figure 2.21). Incoherent noise is, by definition, temporally uncorrelated with the TEM transmitted source current. Coherent noise will significantly change the shape of the TEM data curve.

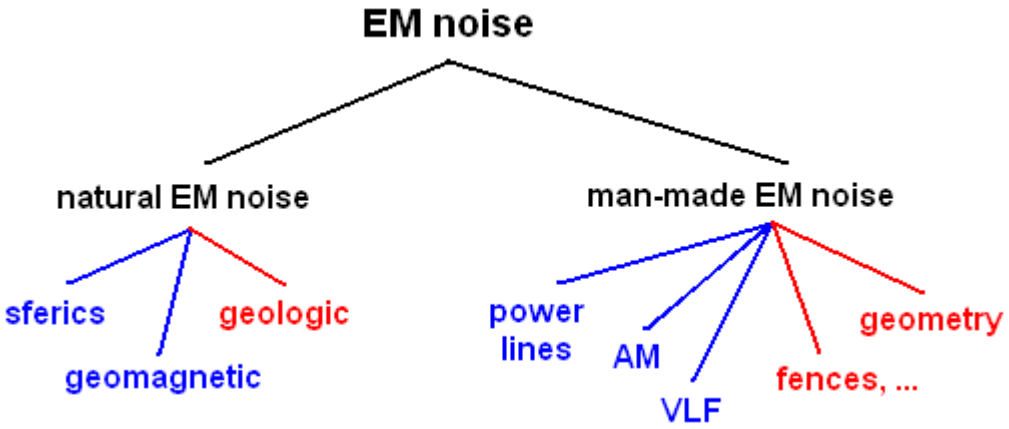

Figure 2.21 – EM noise classification; Incoherent noise (at blue colour) and coherent (at red colour) for the TEM acquisition data's stand view.

Environmental sources of incoherent noise in the frequency range (10^2 Hz to 10^6 Hz) in hydrogeophysical studies with EM methods, can be identified in the electromagnetic noise spectrum, (figure 2.22), spanning from 10^{-2} Hz to 10^5 Hz frequencies.

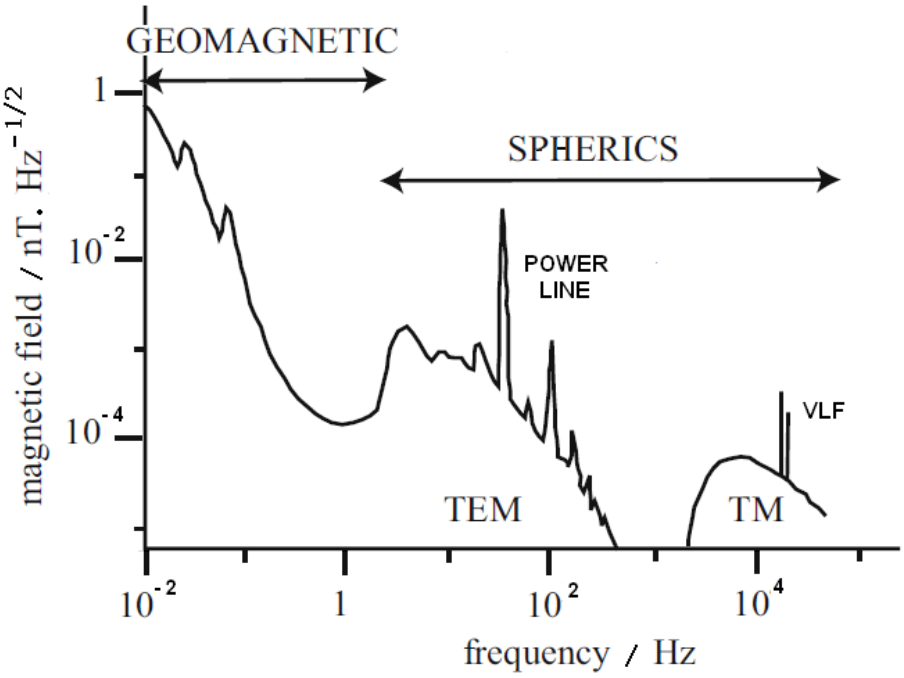

Figure 2.22 – EM noise spectrum intensity in the frequency range of interest to TEM hydrogeophysical investigations (adapted from Palacky and West (1991)).

2.6.1 – EM incoherent noise

The predominant environmental noise sources (called spherics) are caused by impulsive lightning discharges whose EM radiation can propagate over thousands of kilometres within the earth-ionosphere waveguide. The sources of this EM radiation are the lightning discharges occurring all over the world. The continuous thunderstorms at the equatorial and

tropical regions of the earth's globe, like Brazil, Central Africa or Malaysia, are the major contributors to this random character noise. The labels "TEM" and "TM" under spherics designation, refer to different waveguide modes of propagation (Wait, 1962), whereas the shape of the background continuum within the spherics band is determined by the cut-off frequencies of this two modes (Porrat *et al*., 2001). Usually noise from spherics has a frequency above 1 Hz. The lower continuum below 1 Hz frequency is caused by large-scale geomagnetic pulsations that arise in the response to the solar wind interaction with Earth's magnetosphere. The fluctuations in the Earth's magnetic field due to the solar wind, Earth's rotation and the magnetic field are large-scale ones, do not interfere significantly with the measurements since they contribute only to the low-frequency noise, below 1 Hz (Spies and Frischknecht, 1991).

The transient measured data is always an averaging of the induced electromotive force in the receiver loop or coil within the time gate channels. TEM equipments usually have logarithmic gating, that means that gate's length is proportional to delay time (table 2.2). When the environmental noise is "white" (i.e., stochastic through all frequencies), this logarithmic gating result in an effective noise decay of $t^{-1/2}$. However, the surrounding noises are not a "white spectrum", as seen at figure 2.22. At a local scale, we can have superimposed spectra of AM transmitters with high amplitudes at single frequencies around 200 kHz. At these conditions, averaging and stacking such monochromatic signal results in an effective noise decay of t^{-1} (Effersø *et al*. 1999). This contribution will dominate at early times, whereas the stochastic noise will dominate at late time stages. That's also the case with the superimposed spikes on the background continuum spectrum at figure 2.22, caused by the 50 Hz and 60 Hz (and harmonics) supply power lines and radio signals from very low frequency (VLF) transmitters, used primarily by the navy military communication. The near-surface VLF hydrogeophysical investigation method uses these emissions (around 15 kHz to 24 kHz) as a signal source (Newman *et al*., 2003) (table 2.1), but for the most part, these transmissions are rather a source of noise. These are considered cultural noise, and will be next described. Other types of incoherent noise can include electronic and thermal noise in the receiver amplifiers of the signal.

2.6.2 – EM coherent noise

Coherent noise, however, is much more problematic. This kind of noise is temporally correlated with the transmitted source current and can include transmitter or receiver loop misalignment (when other then single loop geometry is used) or instrumental drift. Also, geometrical errors are introduced if the transmitter-receiver single loop is not perfectly squared. These geometric errors may also be induced by topography, but even if the ground is not flat the smoke rings currents will soon begin to travel downwards as if it was (Nabighian and Macnae, 1991). These effects are reduced by careful experimental and data processing procedures. Other sources of coherent noise are induced currents in conductive structures not classified as the primary target of the hydrogeophysical investigation. The two major classes are geologic and cultural noise.

Geological noise can be defined as the electromagnetic field generated by induced currents flowing in fine-scale geological heterogeneities that are too small, too numerous and complicated to be described in detail and hence accounted in the numerical simulations to by done (Everett and Weiss, 2002). That includes anisotropy, frequency-dependent conductivity, dipping layers and near-surface inhomogeneities. Layers are commonly assumed to be homogeneous and parallel to the surface, and because this is obviously not always the case, errors are introduced. Small inhomogeneities disturb more the early times measures than the late times one, due to the smaller earth volume covered by the measurements at early times. Electrical conductivity may even vary with direction, as it is seen in sedimentary rocks where it is typically higher parallel to bedding than perpendicular to bedding. This is the called anisotropy, and a measure of this is the anisotropy factor (Spies and Frischknecht, 1991):

$$\lambda = \sqrt{\sigma_L/\sigma_T} \tag{2.50}$$

where σ_L and σ_T are the longitudinal and transverse conductivity, respectively.

Furthermore, electrical conductivity is not always independent of frequency, giving rise to induced polarization (IP) effects. After currents are turned off in the transmitter loop, vortex currents are induced in the ground beneath it. After signal turn-off, ions in the pore space fluids will begin to move in the same direction as the created vortex currents, thereby creating an additional current, the **polarization current**. The result is a decreasing resistivity at early times. These ions will begin ”piling up” at places of low mobility, the ”charged state” (Flis *et al.*, 1989). As the vortex currents begin to decay, these ions will move back into their original place, to the equilibrium position, but now at a much slower rate. This movement gives rise to a second polarization current, this time of opposite direction. Given a sufficiently polarizable earth, the polarization current may dominate the vortex current at late times, thereby possibly reversing the signal (Flis *et al.*, 1989). The IP effect will be detailed further on this chapter.

Cultural noise is man-made. Major contributors are the 50 Hz or 60 Hz human power-lines supply. Associated to this situation, we have transient signals from switching on and off electric equipment, especially at densely human populated areas. Cultural noise is also the electromagnetic field generated by currents induced in man-made electrical conductors such as buried pipes, tanks and drums, fences, pipelines and power lines scaffoldings, or other objects (Qian and Boerner, 1995). These electrical conductors must be, if possible, included in numerical simulations so that their distorting effects on the TEM response can be properly evaluated. VLF transmitters and AM radio signals can be and are filtered out by low pass filters.

The action at all these objects creates a measurable secondary magnetic field if they are in the vicinity of the sounding. The time constants of direct induction in these features are usually negligible as a result of the relatively small cross-section, so the main contribution comes from the ability to channel currents induced in the surrounding media (Danielsen *et al.*, 2003), (Spies and Frischknecht, 1991). Coupling noise with TEM loop can be either capacitive or galvanic in origin, as can be seen, respectively in figure 2.23 and 2.24.

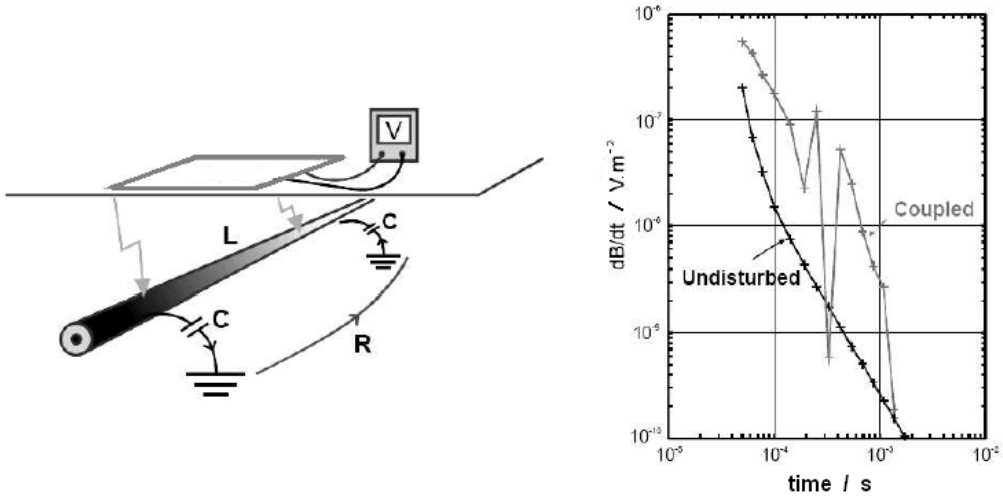

Figure 2.23 – Sounding whit capacitive coupling noise (adapted from Danielsen *et al*. (2003)).

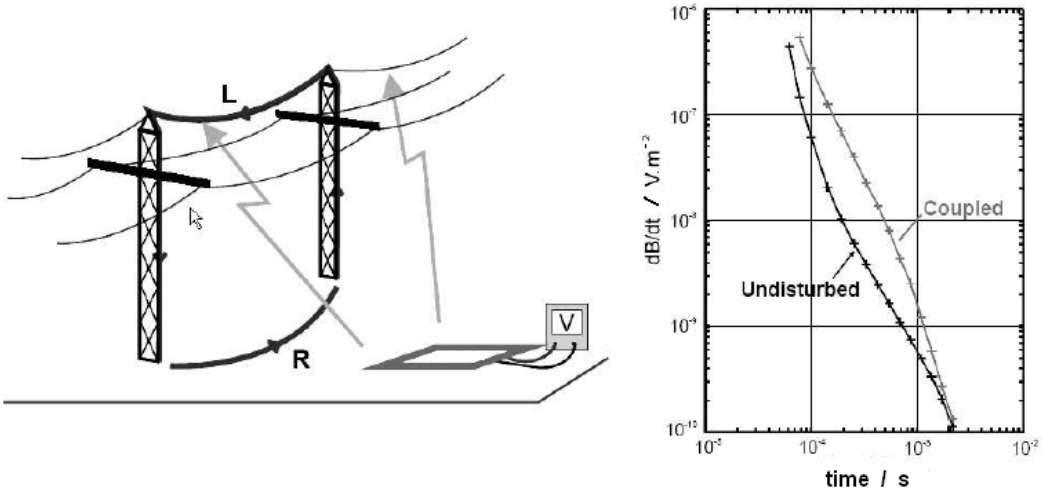

Figure 2.24 – Sounding whit galvanic coupling noise (adapted from Danielsen *et al*. (2003)).

The former situation happens when the conductor is isolated, i.e. there is no contact between this and the surrounding media. The earth plus the insulator conductor system, work as an L-C-R electrical circuit, giving rise to a secondary magnetic field in the conductor. Capacitive couplings may be easily recognized as fluctuations in the TEM sounding curves. They are related to modern high-power lines, insulated underground cables and telephone cables (Danielsen *et al.*, 2003), (Spies and Frischknecht, 1991).

Galvanic coupling requires galvanic contact with the conductor. The current runs from the surrounding media into the electric conductor and back, so the system can be regarded as an L-R electrical circuit. Galvanic couplings result only in a change of shape (bump) in the sounding curve, making them difficult to recognize, although the resulting attained model often contains an anomalously high conductivity. They are related to metallic fences, power line's earthed connection, pipes or old type power cables with a metallic protection shielding (Danielsen *et al.*, 2003), (Spies and Frischknecht, 1991).

The intensity effect of a coupling depends on the shape of the conductor and his distance to the transmitter-receiver loop, r. The shape of conductors may be three-dimensional (3D),

two-dimensional (2D) or elongated with ends (referred to as 2.5D). The response of a 3D conductor decays proportional to r^6 while the response of 2.5D and 2D conductors decay proportional to r^4 and r^2, respectively. A safety distance of 100-200 m from those noisy sources is often suggested. The safety distance increases with increasing resistivity (Danielsen *et al.*, 2003).

Geological and cultural noise like capacitive and galvanic coupling cannot be filtered or stacked out of TEM data easily, because of the mutual induction between the causative structures and the host geology.

2.7 – Induced Polarization and Superparamagnetic effects

As earlier referred, sometimes the TEM measured signals can be affected by means of frequency dependence of dielectric permittivity (ε), known as the induced polarization (IP) effect, i.e. a dispersive phenomenon. It can occur also that magnetic permittivity (μ) of some earth layer or body is not that of free space. When such situation takes place, we can have a sow called superparamagnetic effect (SPM).

2.7.1 – Induced Polarization effect

Induction polarization is a complex phenomenon controlled by many physical and physicochemical reactions associated with the current passage through earth rocks. The effect was initially observed and discovered at galvanic measurement's data in the middle of last century, and it was thereafter systematically studied and incorporated into many geophysical researches (Antonov and Shein, 2008). This natural phenomenon was widely observed at various geological media, essentially due to the influence on results at practically all EM researches. There is a great and positive experience of the IP effect use in classical researches of mineral deposits with direct and quasi-direct current methods, to achieve petrophysical properties of rocks with it. The applicability of the effect still is not fulfilled from a "practical" point of view in induction EM. IP is considered as "noise" and the recipes to overcome with it are yet under developed, e.g., Pelton *et al.* (1983 and 1984), Oldenburg and Li (1994), Effersø (2000), Routh and Oldenburg (2001), El-Kaliouby (2001), Antonov and Shein (2008).

Some relationships do exist to account for this dispersion effect on TEM data. Most of IP models came from a phenomenological approach implying boundary-value solutions of Maxwell's equations, for frequency-dependent resistivity. The Cole-Cole expression is one of the commonly applied to account for this polarization effect (Cole and Cole, 1941), and is written as;

$$\rho(\omega) = \rho_0 \left[1 - \eta \left[1 - \frac{1}{1+(i\omega\tau)^c}\right]\right] \qquad (2.51)$$

where η is the chargeability (or polarizability) defined as $\eta = 1 - \rho_\infty/\rho_0$, the ρ_∞ is the high frequency (infinite) resistivity and ρ_0 the low frequency (DC) resistivity, τ is the time constant

of IP process (relaxation time), c is the so-called "logarithmic speed" or "parameter c", describing the variation of phase with frequency. The concepts of high and low frequency is not strictly determined, as in TEM practice, ρ_0 is the resistivity on a constant current, and the ρ_∞ is the resistivity at frequency range of 50 kHz to 100 kHz (which is actually the really measured limiting research frequency for TEM-FAST48 equipment).

The IP effect comes because, when a displacement occurs in a material, there is a displacement current represented by the charge's movement from the rest positions to the displaced positions. This current persists for only a limited amount of time, lasting from the moment at which the charge is first caused to move by the applied electric field to the moment at which the elastic restoring force brings the motion of the charge to a virtual halt. Over this time span, both the electric conductivity (resistivity) and the dielectric permittivity of the medium will vary with frequency. One of the simpler frequency-dependent behaviours in those electrical properties is caused by electron's resonance, which can be characterized by simple harmonic motion of an electron in its "orbit" when an oscillatory field is applied. That is given by (von Hippel, 1954a, b):

$$\varepsilon' = \varepsilon_\infty + \frac{\varepsilon_s - \varepsilon_\infty}{1+\omega^2\tau^2} \qquad (2.52)$$

where the ε_∞ is the high-frequency limit of dielectric constant, and ε_s is the low-frequency limit, and τ is the time constant of electron resonance. The low frequency can be even zero (DC or "static"), ε_0. The dielectric value is $\varepsilon = \varepsilon' - i\varepsilon''$, with ε' and ε'' the real (storage part) and imaginary (loss part) of it (Cole and Cole, 1941).

This behaviour is traditionally characterized by a plot in the complex plane (the Cole-Cole plot), shown in figure 2.25. On this plot, the imaginary response is considered to be the dielectric permittivity and the real response is considered to be the dielectric loss. The form of the plot is a semicircle centred on the horizontal axis. Each point along this semicircle represents a specific frequency, increasing from right to left. The intercepts of the circle on the dielectric permittivity axis occur at the values for dielectric permittivity at very high and very low frequencies, where the displacement has not yet started and where the displacement is complete, respectively.

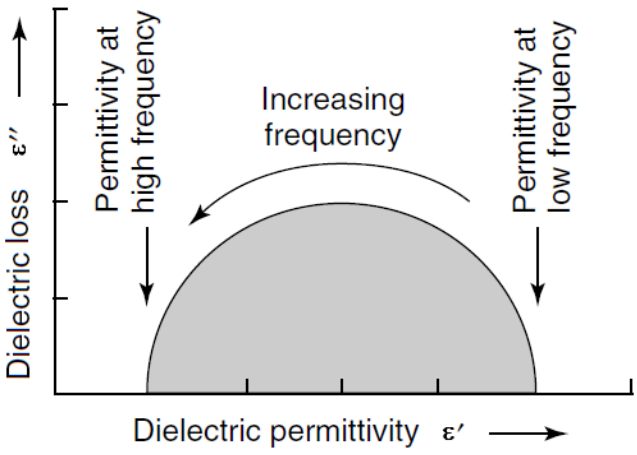

Figure 2.25 – The Cole-Cole plot of the frequency-dependent behaviour of the dielectric permittivity in the complex plane. ε'' is plotted as positive (adapted from Zhdanov, 2009).

In this simple and ideal polarization mechanism, the real conduction term is then zero at extremely high and low frequencies, meaning that no conduction takes place. In real materials, there is always an independent conduction term. The complexity of physical law governing dispersion is far more than that for simple harmonic motion. It can be described by equation:

$$\varepsilon = \varepsilon_\infty + \frac{\varepsilon_0 - \varepsilon_\infty}{1+(i\omega\tau)^{1-\alpha}} \tag{2.53}$$

where α is a characteristic parameter of the material ($0 < \alpha \leq 1$) and ε_0 is the zero-frequency value of dielectric constant (Cole and Cole, 1942). This is the Debye dielectric relaxation expression;

$$\varepsilon = \varepsilon_\infty + \frac{\varepsilon_0 - \varepsilon_\infty}{1+i\omega\tau} \tag{2.54}$$

with $\alpha = 0$, (expression (2.52) is the real part of present one).
It is also a particular case of the Havriliak-Negami expression;

$$\varepsilon = \varepsilon_\infty + \frac{\varepsilon_0 - \varepsilon_\infty}{((1+i\omega\tau)^{\alpha})^{\beta}} \tag{2.55}$$

when the symmetry parameter β is equal to unit, (when the relaxation peaks are symmetric).

In real materials, some electric conduction by free charge carriers takes place in addition to the displacement currents. Total conduction is the sum of these two components, one being by free charge carriers (which is largely independent of frequency) and the other one being by the displacement of bound charge carriers, which is strongly frequency dependent:

$$\sigma_{\text{full}} = \sigma_{\text{DC}} + \sigma_{\text{AC}} \tag{2.56}$$

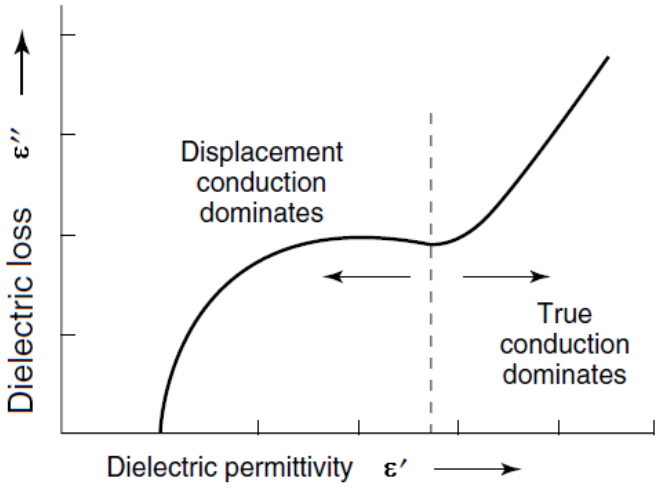

Figure 2.26 – The Cole-Cole plot for a material which exhibits both currents; displacement and ohmic one. ε'' is plotted as positive (adapted from Zhdanov, 2009).

The new Cole-Cole plot, has a pattern like the one in figure 2.26; it consists of a portion of a circular arc for high-frequency behaviour, with a transition to a rising straight line for low

frequency behaviour. The transition from the circular plot to the linear plot depends on the relative importance of displacement and conduction currents. With strong conduction currents, the linear portion of the plot becomes dominant.

Expression (2.51) describes the frequency characteristics of "infinitesimal" media cells, and generally speaking, does not contain any restrictions to parameters included in it. From a physical point of view, the question on those restrictions is more complicated. That expression describes a passive electrical system with the distributed parameters, however, having a "zeroth volume", it is then possible to assume the system only consists of the distributed resistors R and capacitors C, because the inductance is connected to volumetric magnetic interactions of fields, i.e. it is a function of volume, which considered cell have not, by definition. The (2.51) expression describes the characteristic of a passive RC-circuit, according to the classical theory of electrical circuits, impedance or admittance, as the complex function of frequency $p = s + i\omega$ (has poles and zeros only at $s < 0$). The $\rho(\omega)$ function as the following restrictions; parameter c must be $0 < c \leq 1$ and $\rho_0/\rho_\infty > 1$ and $|\rho(\omega)|$ is a monotonously decreasing function of frequency (these restrictions are practically all confirmed at laboratory and field experiments), (AEMR, 2006).

For homogeneous half-space with dispersive conductivity, the reaction of media to step power off the magnetic field consists approximately of two added parts (AEMR, 2006), as stated before:

$$E(t)/I = E_0 + E_{ip} \tag{2.57}$$

with $E(t)/I$ the “normalized” emf value at R radius circular coincident loop,

$$E_0 = \frac{\pi^{1/2}{\mu_0}^{5/2}R^4}{20\,\rho_0^{3/2}}t^{-5/2} \tag{2.58}$$

describes induction process in media with conductivity ρ_0 at constant current, and

$$E_{ip} = \frac{q\pi{\mu_0}^2R^3}{8\,\rho_t(t)\tau} \tag{2.59}$$

determines the process of polarization with constant time $\tau = \tau_{ip}$ and $\rho_t(t) = F^{-1}[p\rho(p)]$ the time Fourier-image of function $\rho(p)$.
The particular cases are:

with $c = 1$ $$\frac{1}{\rho_t(t)} = \sigma_t(t) = -\frac{\rho_0}{\rho_\infty\tau}e^{-t/\tau} \tag{2.60a}$$

with $c = 1/2$ $$\frac{1}{\rho_t(t)} = \sigma_t(t) = -\frac{1}{2\pi^{1/2}}\frac{\rho_0}{\rho_\infty\tau}\left(\frac{\tau}{t}\right)^{5/2} \tag{2.60b}$$

with $0 < c \leq 1$ $$\frac{1}{\rho_t(t)} = \sigma_t(t) = \frac{1}{\Gamma(-c)}\frac{\rho_0}{\rho_\infty\tau}\left(\frac{\tau}{t}\right)^{c+2} \tag{2.60c}$$

$\Gamma(-c)$ is the known Gamma-function.

It is possible, this way, to consider induction and polarizing signals additive in near zone of TEM (at $\rho t/\mu_0 R^2 \gg 1$). However, as exact calculations for horizontal layered media shown, this conclusion is only valid when $\rho t/\mu_0 R^2$ is grater then 20-30. At earlier stages, the close interaction of induction and polarization signals is observed, and the additive summation is inconvenient. Usually, for calculations of IP in TEM, a rather simple mode is used. The conductivity of each layer (in integration expressions of the TEM processes), is replaced to frequency dependent according to $k = (e^{-t/\tau_1} - e^{-t/\tau_2})/\ln(\tau_1/\tau_2)$ (TEM time constants values $\tau_1 \gg \tau_2$ depend on many factors and usually can be taken as $\tau_1 = 1\ s$ and $\tau_2 = 1\ \mu s$) then make Fourier and Hankel transformation.

In many cases, the IP effect is adequately described by the well-known Cole-Cole dispersive resistivity relation (2.51). But in a series of cases, Cole-Cole is not sufficient to explain the materials frequency dependence. More empirical relations do exist, like the Classical Dielectric Dispersion, Special Dielectric Dispersion, Cole-Davidson Dispersion (King and Smith, 1981), (Pelton *et al.*, 1983, 1984), all of them implemented at the TEM-FAST 48 inversions sounding algorithms.

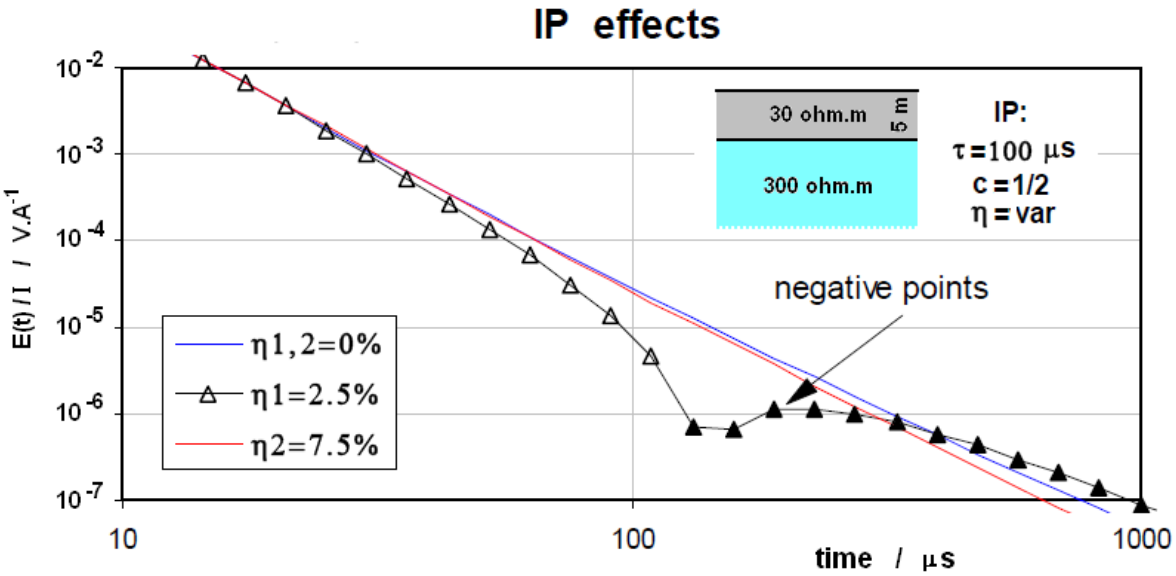

Figure 2.27 – The IP effect responses from a two layered earth model. Cole-Cole dispersive relation is applied to layers, with assigned values (adapted from AEMR, 2006).

The classical example of IP effect is shown in figure 2.27. It is the output of a 25 m coincident single square loop size, over a horizontal layered earth with a superficial resistivity of 30 ohm.m and 5 m thick, over a 300 ohm.m half-space. Relaxation time is 100 µs, and c = 0.5. Three responses are given; a first one without any IP effect (η = 0%), a second with located polarizability at first layer (η_1 = 2.5%) and a third one with polarizability at deep poorly conducting layer (η_2 = 7.5%).

Distortion from shallow first layer is very significant, in spite of the fact that the thickness is just 5 m, and polarizability is rather small, compared with third response, were the observable distortions are hardly appreciable. At this first layer IP effect response, the late stages of the process have a negative sign, the typical signature at these polarized environments.

Conclusions about the IP effect can be summarized as:

- polarizing effect $E_{ip}(t)$ is proportional to time derivative from the transient characteristic of conductivity ($\sim d/dt[\sigma(t)]$),
- at any values of parameter c ($0 < c \leq 1$) the $E_{ip}(t)$ sign signal is opposite to $E_0(t)$, and monotonously decreases in time,
- greatest speed of decrease at c = 1 ($E_{ip}(t) \sim -e^{-t/\tau}$) and at $0 < c \leq 1$ is $E_{ip}(t) \sim -(\tau/t)^{c+2}$,
- at some polarization's parameters, the measured signal $E(t)/I = E_0 + E_{ip}$ can change sign at least twice,
- polarizing signal E_{ip} is proportional to R^3, while induction signal E_0 is proportional to R^4,
- with single coincident loop, the ratio E_0/E_{ip} is increased proportionally to the perimeter of the receiving-transmitting antenna ~ R,
- apparent resistivity curve ρ(t) for different size of loop, have essentially different form,
- sounding curves ρ(t) and E(t), sharply change at rise of loop above the ground surface,
- effect is minimal in the coincident loop configuration,
- reduction of IP influence can be achieved by the increase of the loop size. The ratio of induction and polarizing signals is proportional to the size of the coincident antenna ~ R.

The IP effects are frequently very hard diagnosed on the TEM data. Exceptions are cases when the very intense manifestations of the polarization, at low levels of induction processes, repeatedly invert the sign of the observable signals. Cases occur when all observable signals (single coincident loop) from 4 μs to 4-10 ms time has a negative sign. Much more often the polarizing process just distorts measured sounding curve, without sign inversion of data points. At interpretation in these cases, false poorly conducting horizons come to light (Barsukov *et al.*, 2007).

With TEM-FAST 48 equipment, investigations have shown that most adverse interpretative situations (in which IP effect takes place) arise with the following conditions (AEMR, 2006):

- thin, well conducting horizon of subsurface clay deposits with electric resistivity smaller than 20-40 ohm.m, over rather high resistive layer of rocks with 300-500 ohm.m. At polarization of first layer (η = 1 - 3%), late stages of transient will be IP deformed.
- glaciers, permafrost rocks and superficial deposits intensively polluted with industrial wastes, (including petroleum pollution),
- weathering cores in crystal rocks and fault zones.

The IP effect popup also at resistivities above 100 ohm.m when a significant polarizability does exist (η > 10%) and the time constant (τ_{ip}) spans a very wide range (1-1000 μs). As a layer superficial effect, c is approximately unitary ($E_{ip}(t) \sim -e^{-t/\tau}$) and distortions are observed in a narrow range of times. "Deep" IP effect is characterized by a c value around 1/3 to 1/2, and distorts all the late stages of the signal. With the presence of IP in superficial and deep horizons of section, two negative minimums on early and late times are observed simultaneously.

It is important to emphasise that since IP effect is linked to the presence of polarisable bodies (or fluids), it can thus be used in prospecting, tracing and monitoring those targets.

2.7.2 – Antenna Polarization effect

The antenna polarization effect (APE) has been detected in TEM data soundings by many researchers (Bishop and Reid, 2003). No explanation was given to this effect, until recently (Barsukov *et al.*, 2003). In practice, the transient characteristics (or their time derivatives) often show a sign reversal (usually called “negative anomalies”), which is solely due to the frequency dependence of electric conductivity of rocks, as previously described.

With some TEM sounding’s experimental data, discrepancies are often observed that do not fit theoretical models of polarizable media, and the negative anomaly’s value depends on the resistivity of the loop wire (antenna). These differences between the experiment and theory cannot be explained by horizontal inhomogeneities of the studied medium or imperfection of modelling technique (Bishop and Reid, 2003).

Distributed antenna capacity and ever-persisting resistance in the devices employed in geological media showing frequency-dependent dielectric permeability – produces the APE. This effect manifests themselves at later stages of transient process and is detected as a slow time decaying process $\sim t^{-(0,3-0,7)}$ with phase opposite to the induction transient characteristic phase. APE depends on the dispersion parameters of the medium at a fixed current value; it is proportional to the squared resistivity value of the antenna (loop) wire, as the plotted example at figure 2.28. APE is detected both with coincident (single) loop and with all the offset (separated) antennas, and should be taken into account in the field data interpretation (Barsukov *et al.*, 2003 and 2007).

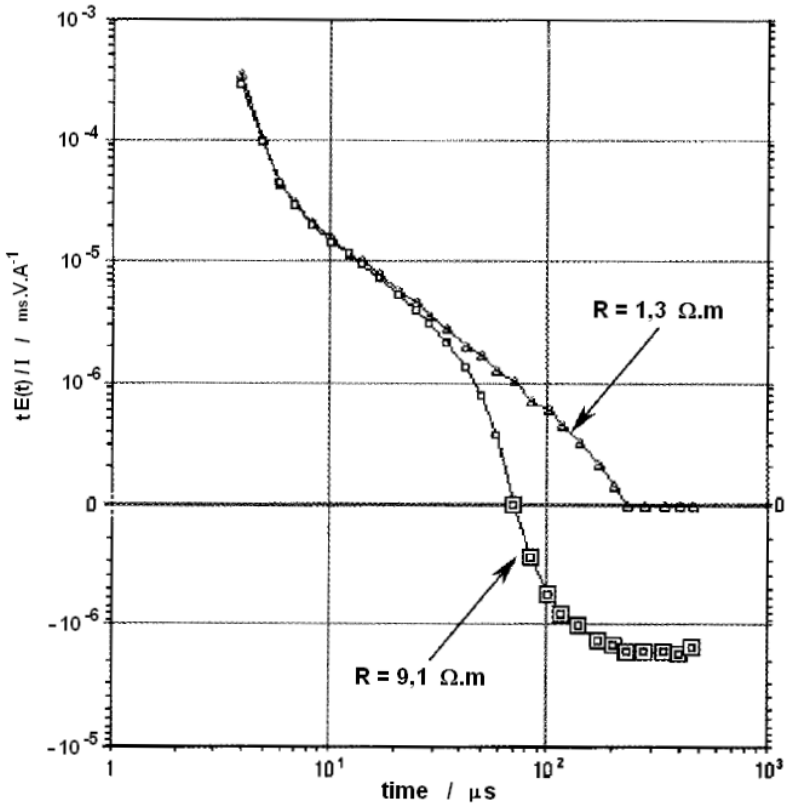

Figure 2.28 – The APE dependency signal response on wire resistance. Coincident single loop (10 m ×10 m). Square points have negative values (adapted from Barsukov *et al.*, 2007).

2.7.3 – Superparamagnetic effects

Superparamagnetic (SPM) effect was studied by many researchers since last century, starting with Néel's pioneering work (Néel 1949), followed by many more, directly connected to EM soundings (Nagata 1961, Averyanov 1965, Lee 1981, Buselli 1982, Barsukov and Fainberg 2001, etc.). In some publications, SPM effect is also called by "effect of magnetic viscosity".

SPM effect in rocky material is connected with the processes of orientation/disorientation of the magnetic moments of very fine scale particles (10^{-10} m order size) of magnetic minerals in the initial moments of turn on/turn off of exciting magnetic field. The researches of SPM effects in various areas of the world with TEM-FAST (predecessor of actual TEM-FAST 48 system) between 1985 and 1998 have shown the following facts:

- most intensive SPM effects exist in areas of effusive and volcanic-sedimentary rocks. Superficial clay formations covering parent rocks are most superparamagnetic,
- SPM effects take place in conditions of long-term permafrost and usually are located on the border of zones of thawing frozen rocks,
- significant SPM effects are observed on glaciers,
- SPM is created, as a rule, by particles (radius of 10^{-9} to 10^{-7} m) of magnetite and maghemite. In practice, a SPM effect in TEM is usually treated as frequency dispersion of the rocks magnetic susceptibility, by analogy with frequency dispersion of conductivity (IP effect). The transient characteristic (reaction to step-type power off a magnetic field) of magnetic susceptibility χ_{SPM} it is conveniently simulated as a relaxation model of SPM in TEM.

$$\chi_{SPM}(t) = k \times \chi_{SPM}/t \qquad (2.61)$$

with $k = (\mathrm{e}^{-\mathrm{t}/\tau_1} - \mathrm{e}^{-\mathrm{t}/\tau_2})/\ln(\tau_1/\tau_2)$ (as already described taking $\tau_1 = 1$ s and $\tau_2 = 1$ μs).

The characteristic signature of SPM effect is the slow speed of the transient decay in time, with E(t) ~ t^{-1}. For induction processes, E(t) decreases not slower than ~ $t^{-5/2}$, as described early (expression 2.39). The usual identification of SPM in the TEM registered data is normally done with a t.E(t) versus t plot, as the late stages of transient signal containing SPM component, will show an almost constant behaviour in time (figure 2.29). In practice, because of different reasons the observable SPM processes decrease as E(t) ~ $t^{-(1+\delta)}$, where $-0{,}2 < \delta < 0{,}2$ (Barsukov and Fainberg, 2001).

For coincident circular antenna (with radius R), located at earth's surface and above a SPM half-space, SPM effect is described by the expression:

$$E(t)/I = \mu_0 \chi_{SPM}(t) L \qquad (2.62)$$

and *L* is the antenna's inductance.

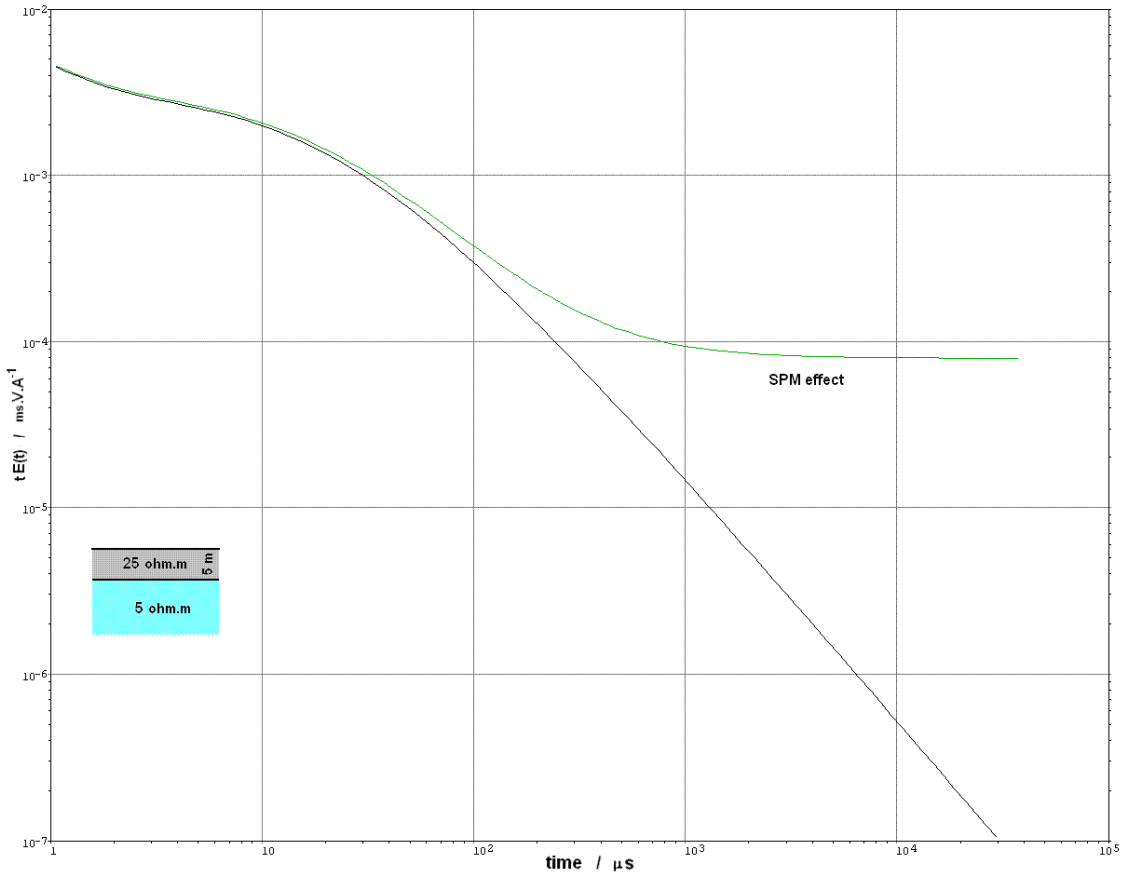

Figure 2.29 – Half earth model response without and with SPM effect from top layer, (k = 0.1 at 0.5-2.5 m depth influence).

The precise calculations of transient's response of horizontal layered conductive and SPM media, have shown, that the interaction of induction currents and SPM effects can be neglected, i.e. it is possible to consider these effects as purely additive. Reduction of SPM effect influencing TEM sounding data at the acquisition level is possible by doing the following operations:

- Reduce mutual inductance of antennas (M), when offset configuration is applied. Using two identical antennas shifted at some distance, ensuring practically zero stream coupling (mutual inductance of antennas M), can provide 50-100 times suppression of SPM signal. However in real field conditions, applicability can be tricky, and it is rather time-consuming.
- Increase the size of the coincident loop.

The signal in the coincident configuration is proportional to the square of the loop's area ~R^4, while the SPM effect at small depth of bedding of magnetic layers, is proportional to size of antenna ~R. Thus, at the increase of the antenna's size from 50 to 100 m, the ratio between "useful" induction and "harmful" SPM effects will increase as a minimum at 8 times (~R^3).

- Uplift the coincident antenna above the surface of media.

If SPM effect to a soil layer is not too intensive (that's the case at 80% of situations) using small coincident antennas with a size not more than 50 m × 50 m is a rather effective way both from the point of view of results, and from the point of view of minimization of work time. The rising of a 25 m × 25 m loop antenna at 1 to 1.5 meters aboveground is easily realizable and allows a SPM effects reduction of 3 to 4 times.

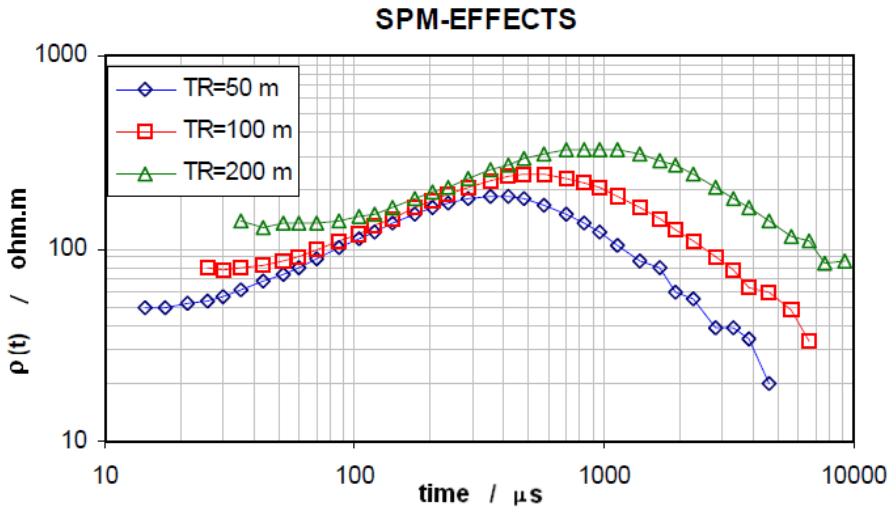

Figure 2.30 – SPM effect with three different sizes square loop, over sedimentary rocks in permafrost conditions at Norilsk, Russia (adapted from AEMR, 2006).

At field acquisition, it is necessary to do analysis of registered data to control SPM signal distortions and if necessary, change the antenna's configuration. This analyses is done under the assumption that SPM distortions act at late stages of the process with $E(t) \sim t^{-1}$. The observed resistivity $\rho(t)$ sharply decreases to "unreal low" values and the apparent resistivity curves $\rho_a(t)$, on late times for different loop sizes, show parallel abruptly falling down branches, like the given example at figure 2.30. The SPM effect can be taken, not as a harmful signal, but as useful information about researched media, which can be accessed with different configurations of loops. It is also possible to measure SPM in rock samples at the laboratory (or directly in-field conditions, using special portable sensors) (AEMR, 2006).

3
TEM MODELLING THEORY

This third chapter presents an overview of TEM data modelling. The forward (direct problem) solution for a layered half-space (1D problem) is described. Inversion methods are also discussed, including joint TEM and VES soundings.

3.1 – Layered half-space TEM response

The conductive half-space TEM response, with their full and asymptotic formulation has been given on previous chapter. We have seen that with a loop source over a horizontal ground, the only field transmitted in the TEM method is a transverse electric field (TE). Hence, only the Schelkunoff scalar potential **F** is necessary for a derivation of the vertical magnetic field in the loop's centre. Under this one-dimensional (1D) layered earth assumption, potential **F** consists of one component only, the z-component. The z-direction is the vertical (positive downward), x and y defines the horizontal planes. The TE mode of this potential **F** is:

$$\mathbf{F} = F_z \mathbf{u_z} \quad ; \quad \mathrm{TE_z} \tag{3.1}$$

where F_z is a scalar function of x, y and z ($\mathbf{u_z}$ is the unit vector in the z-direction). $\mathrm{TE_z}$ denotes the transverse electric field, which is the field propagating in the xy-plane.

Substituting expression (3.1) into chapter 2 equations (2.29) and (2.30) enables the expression of the field components;

$$\mathbf{H_x} = \frac{\mathbf{1}}{\hat{\mathbf{z}}} \frac{\partial^2 F_z}{\partial x \partial z} \quad ; \quad \mathbf{E_x} = -\frac{\partial F_z}{\partial \mathrm{y}} \tag{3.2a}$$

$$\mathbf{H_y} = \frac{\mathbf{1}}{\hat{\mathbf{z}}} \frac{\partial^2 F_z}{\partial y \partial z} \quad ; \quad \mathbf{E_y} = \frac{\partial F_z}{\partial \mathrm{x}} \tag{3.2b}$$

$$\mathbf{H_z} = \frac{\mathbf{1}}{\hat{\mathbf{z}}} \left(\frac{\partial^2}{\partial z^2} + k^2 \right) F_z \quad ; \quad \mathbf{E_z} = 0 \tag{3.2c}$$

For a parallel plane 1D model consisting of source-free regions, as well as regions containing sources, the derived general Schelkunoff **F** potential has been written as an expression (2.31). From expression (2.34), a circular loop (radius a and current *I*) with a vertical dipole magnetic moment m, is then (Ward and Hohmann, 1988):

$$\mathbf{F}(\rho, \mathrm{z}) = \frac{\hat{\mathbf{z}}_\mathbf{0} \boldsymbol{Ia}}{\mathbf{2}} \int_\mathbf{0}^\infty \frac{\mathbf{1}}{\mathbf{u_0}} \left[\mathrm{e}^{-\mathrm{u_0(z)}} + \mathrm{r_{TE}} \mathrm{e}^{\mathrm{u_0(z)}} \right] \mathbf{J_1}(\lambda a)\, \mathbf{J_0}(\lambda \rho) \mathrm{d}\lambda \tag{3.3}$$

The derived vertical magnetic component at the centre of the loop, with the loop position on the earth's surface (height null for z and h), by (3.2c) application, became:

$$\mathbf{H_z} = \frac{\boldsymbol{Ia}}{\mathbf{2}} \int_{\mathbf{0}}^{\infty} \frac{\boldsymbol{\lambda^2}}{\mathbf{u_0}} [1 + \mathrm{r_{TE}}] \mathbf{J_1}(\lambda a)\, \mathrm{d}\lambda \tag{3.4}$$

with $\mathrm{r_{TE}}$ the already mention reflection coefficient.

The **reflection coefficient** relates the amplitude amount of the plane-wave EM components that are reflected to the original travel media, when an interface exists (between two different media). It can be written in terms of the plane-wave impedance or admittance (Ward and Hohmann, 1988), which is defined as the ratios of the amplitudes of the orthogonal electric and magnetic-field pairs:

$$Z = \frac{\mathrm{E_x}}{\mathrm{H_y}} = -\frac{\mathrm{E_y}}{\mathrm{H_x}} \tag{3.5a}$$

$$Y = \frac{\mathrm{H_y}}{\mathrm{E_x}} = -\frac{\mathrm{H_x}}{\mathrm{E_y}} \tag{3.5b}$$

These relations hold for wave propagation in the positive z-direction. If waves are traveling in negative z-direction, the relations reverse their sign.

The reflection coefficient, for normal wave incidence, is written as:

$$\mathrm{r_{TE}} = \frac{Y_n - Y_m}{Y_n + Y_m} \tag{3.6a}$$

$$\mathrm{r_{TM}} = \frac{Z_n - Z_m}{Z_n + Z_m} \tag{3.6b}$$

Wave traveling from medium *m* and reflected at medium *n*.
At earth surface that becomes:

$$\mathrm{r_{TE}} = \frac{Y_0 - \hat{Y}_1}{Y_0 + \hat{Y}_1} \tag{3.7a}$$

$$\mathrm{r_{TM}} = \frac{Z_0 - \hat{Z}_1}{Z_0 + \hat{Z}_1} \tag{3.7b}$$

with the intrinsic admittance and impedance of free space, respectively as:

$$Y_0 = \frac{u_0}{\hat{z}_0} = \frac{u_0}{i\omega\mu_0} \tag{3.8a}$$

$$Z_0 = \frac{u_0}{\hat{y}_0} = \frac{u_0}{i\omega\varepsilon_0} \tag{3.8b}$$

For the present analyses, to calculate the $\mathrm{r_{TE}}$ coefficient for an *N* layer's medium, as shown in figure 3.1, the surface admittance is determine by a recursive relation, starting at the deepest layer (*N*) and iterating upward (Ward and Hohmann, 1988):

$$\hat{Y}_1 = Y_1 \frac{\hat{Y}_2 + Y_1 \tanh(u_1 h_1)}{Y_1 + \hat{Y}_2 \tanh(u_1 h_1)} \quad , \quad \hat{Y}_n = Y_n \frac{\hat{Y}_{n+1} + Y_n \tanh(u_n h_n)}{Y_n + \hat{Y}_{n+1} \tanh(u_n h_n)} \quad , \quad \hat{Y}_N = Y_N \tag{3.9}$$

and

$$Y_n = \frac{u_n}{\hat{z}_n} \tag{3.10}$$

with $u_n = \left(k_x^2 + k_y^2 - k_n^2\right)^{1/2} = (\lambda^2 - k_n^2)^{1/2}$ and $k_n^2 = -\hat{\mathrm{z}}_\mathrm{n}\hat{\mathrm{y}}_\mathrm{n} = \omega^2\mu_n\varepsilon_n - i\omega\mu_n\sigma_n$

quantities already introduced at chapter 2. Knight and Raiche (1982), have found that for greater numerical stability, this recursive relation works better if formulated with e^{-2uh} instead of $\tanh(uh)$.

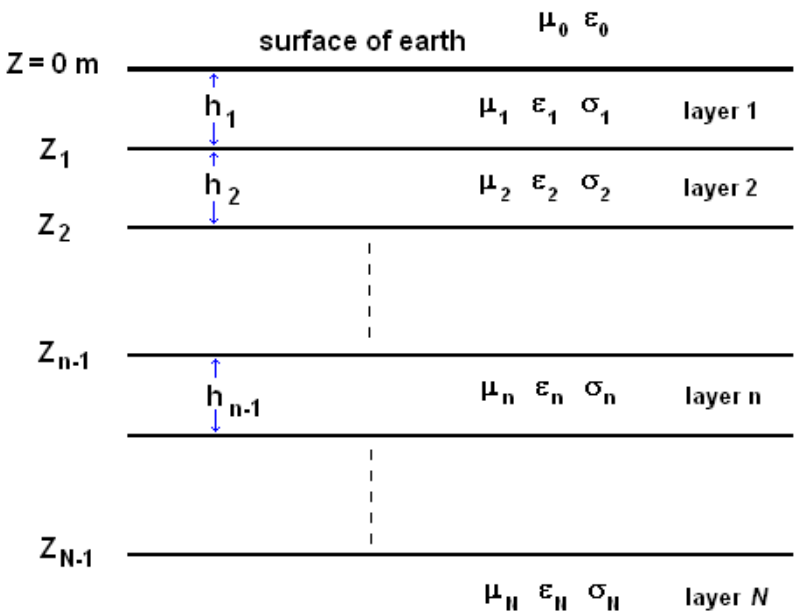

Figure 3.1 – Horizontal and parallel *N*-layered half-space earth, with defined physical parameters at each layer.

Equation (3.4) is expressed in the frequency domain (r_{TE} is a function of frequency). The response in the time-domain (transient response), is obtained by inverse Laplace transform or inverse Fourier transform. The integral in (3.4) is called a Hankel integral. There is no analytical solution for this integral, and it must be evaluated by numerical methods. That task is faster if digital filtering is applied, instead of just compute the numerical integration of the Hankel transform (Bessel function decays slowly and set direct numerical integration to be a time-consuming task). The integration function (3.4) is the product of two functions; Bessel function times a kernel function, the latter with model and signal information. An alternative method to Bessel function evaluation was given by Koefoed *et al*. (1972) by digital filtering. Anderson (1979) defines latter digital filters to this problem. The linear relation between the kernel function and the magnetic field is used. The magnetic field is given by linear filtering. With this procedure, it's not necessary to re-compute the kernel function every time, speeding numerical calculations. Applying the natural logarithmic transforms as stated by Koefoed *et al*. (1972), results into a convolution between the input function and output filter response. The input function can be taken as the adding of sinc functions. The output function is given by the integral adding of the sinc filter response. (Koefoed *et al*., 1972). The sinc filter spectrum response is the sinc spectrum times the filter spectrum. The final result is given by inverse Fourier transform of the sinc filter response.

Modelling TEM responses includes sometimes convolutions with low-pass filter, like specified by Effersø *et al*., (1999) and turn-on and turn-off ramps effects (Fitterman and Anderson, 1987). Each equipment has its own acquisition specifications, and those parameters must be taken into account for a perfect modelling and comparison with field data.

3.1.1 – Forward 1D TEM response

For the *N* layer model, we have the usual 2*N*-1 number of model parameters, if we just take the *N* layers electric conductivity and the *N*-1 layer's thickness, with permeability and permittivity equal to their free space values. With this parameters set, a response at the earth surface can now be computed.

Three models are presented at figure 3.2; a uniform half-space and two 3 layers models. The forward solution to these models is given at figure 3.3. It expresses basic different behaviour between a half-space to a layered one. The responses are for a single 50 m × 50 m square loop.

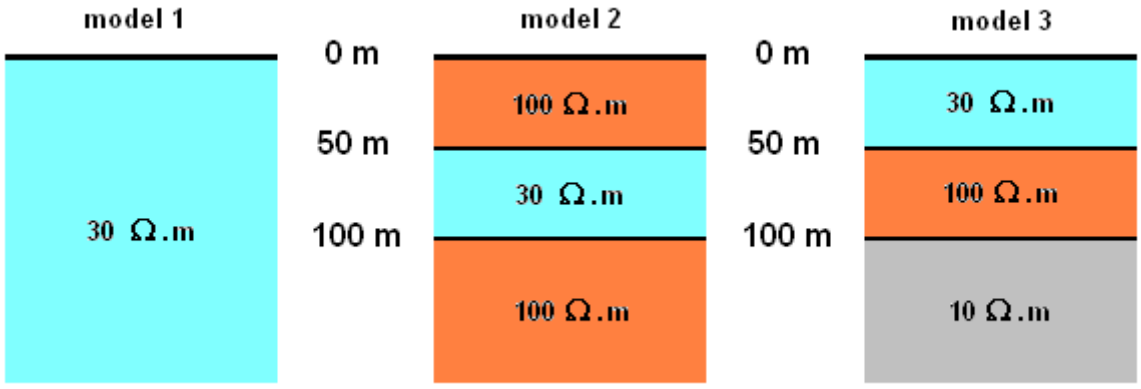

Figure 3.2 – Uniform half-space (model 1) and three-layer models; one with a low-resistivity layer embedded in a high-resistive background (model 2) and one with a high-resistivity layer embedded in a low-resistivity background (model 3).

The emf signal offset between model 2 and model 1 response is greater than offset between models 3 and 1 response (figure 3.3a). Model 2 and 3 signals do not decay anymore with $t^{-5/2}$. The apparent resistivity plot exhibit also great differences. The top layers definitely perturb the sounding curve, and no uniform half-space can represent this behaviour anymore. Regardless of these, later stages points converge asymptotically to the bottom layer resistivity (figure 3.3b).

Figure 3.4 plots the spatial current density at three different times after transmitter signal turn-off, for the same set of models. Only one side section of the current system is shown. Figure 3.4a) shows the current density in the homogeneous half space. For the 1D half-space the current flows cylindrically and symmetrically around the vertical axis through the centre of the transmitter loop. The current maximum moves downwards and outwards as time passes. The current densities are normalized to the maximum value at that time giving the same maximum amplitude in all plots. Although the real values are very different, with maximum amplitude at time 10 μs some 10^6 times larger than at 1000 μs. The darker grey regions indicate larger current densities.

For model 2 (low-resistivity layer embedded in high-resistivity layers) at figure 3.4b) we see that already at 100 μs after the turn-off of the current pulse, the maximum of the current density is located in the low-resistivity layer (layer 2). Later at 1000 μs the maximum stays in

that layer. Later at 1000 µs the maximum stays in that layer. When compared to the homogeneous half-space (figure 3.4a), the low-resistivity layer interrupts the normal diffusion pattern and acts as a shield for the high resistivity layer below.

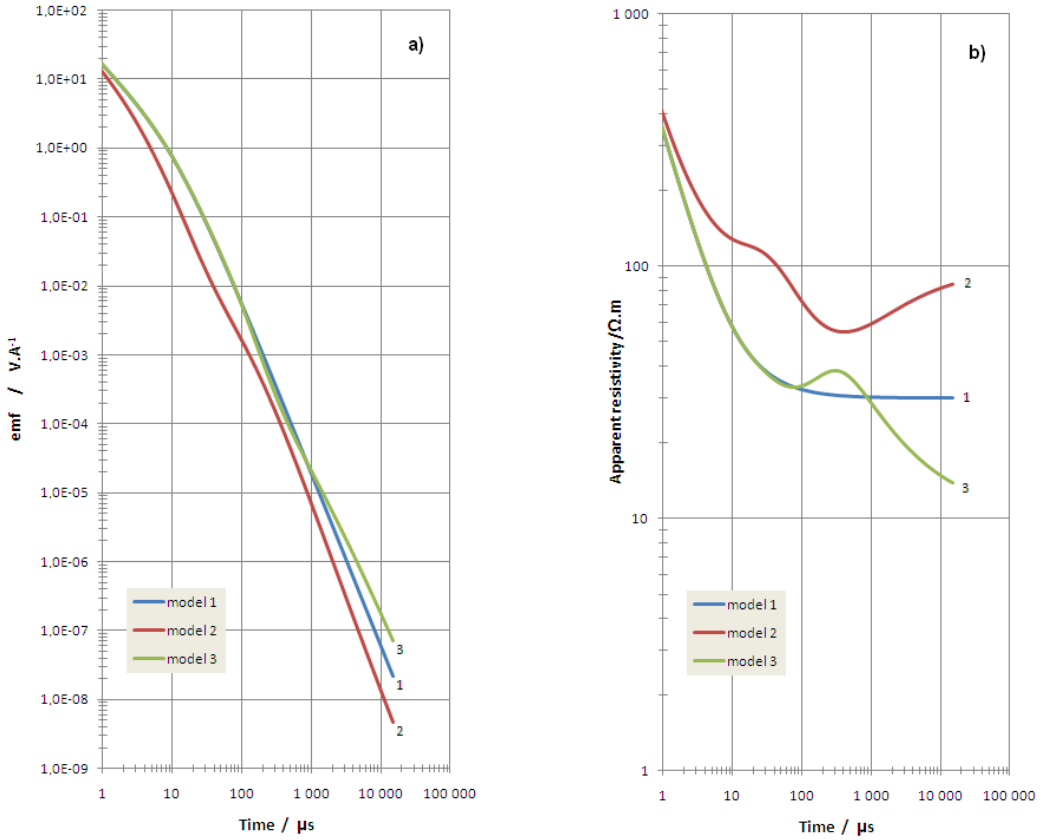

Figure 3.3 – Models response; a) emf current normalized signal, b) apparent resistivity, with TEMRES software (AEMR)

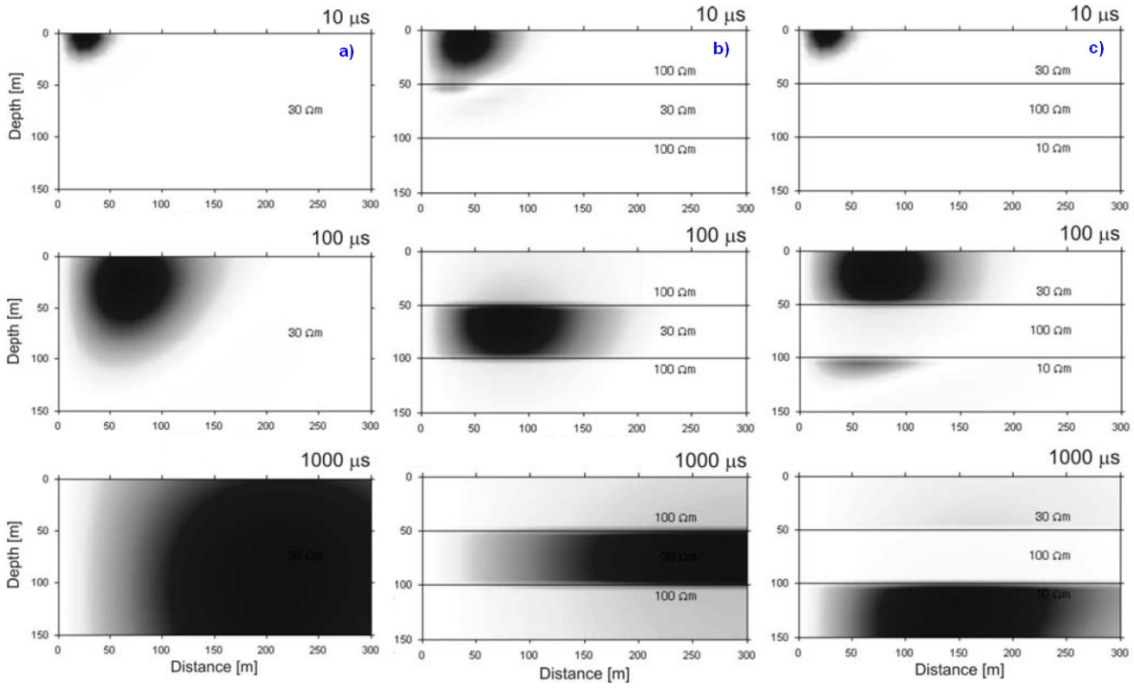

Figure 3.4 – Current density models response for; a) model 1, b) model 2, c) model 3. (Adapted from Christiansen *et al*, 2006)

For model 3 (high-resistivity layer embedded in low-resistivity layers) at figure 3.4c) we see that at 100 μs the current density exists and is divided between the top and the bottom layers. The current density in the high-resistivity layer is very low. At 1000 μs the current density distribution is “entirely at the bottom layer skipping the high-resistivity layer” in the middle. The implication to this is that the resulting sounding curve retains very limited information on this resistive layer.

These different responses put into evidence that TEM method is highly sensitive to low-resistivity layers (conductive layers) simply because a larger amount of the current flows in these layers. The diffusion speed depends on the resistivity of the layers, i.e. the diffusion speed is high for high-resistivity layers and low for low-resistivity layers, as given by expression (2.27).

3.2 – Inversion methods

To analyse the field data sounding curve, we need to compare it against an output curve from a give forward model result, for instance a 1D layer model. There are several schemes proposed for direct problem or approximate analysis of TDEM data, e.g. (Nekut, 1987), (Smith *et al.*, 1994). Meju (1995) proposes a simple approximate scheme for electromagnetic data analysis. The scheme for transforming TDEM apparent resistivity data into approximate resistivity-versus-depth information is an adaptation of the Niblett-Bostick transformation used in magnetotelluric data analysis (Bostick, 1977).

If the field and computed curves have a good match, then the suggested model is a (possible) model to explain the field data. This is a trial-and-error process that is a kind of inverse problem. Many techniques have been developed, and the underlying theory of the inverse problem is well described in the geophysical literature from several authors, e.g. Jackson (1972 and 1979), Twomey (1977), Tarantola and Valette (1982), Menke (1984), Constable *et al.*, (1987), Meju (1994a and 1994b), Parker (1994), Newman and Alumbaugh (1997), Scales *et al.* (2001), Tarantola (2005), Aster *et al.* (2005).

3.2.1 – General data inversion

Knowledge of the subsoil properties by data acquired on earth’s surface is a typical case of the inverse problem’s geophysical applications. For a given set of model’s parameters and values, response must fit the observed data at discrete points. This model is not unique and equivalence problems can exist. The number of solutions (models) is also enhanced by the addition of data errors.

To solve the inverse problem it’s necessary to:

1 - Parameterize the model, i.e. split the earth domain under study to discrete and uniform proprieties’ regions. Assuming 1D models these are just thickness layers with some physical attributed parameters (resistivity or conductivity). At 2D we have cells and at 3D volumetric defined blocks.

2 - Express a relation between the model parameters and observational data – direct problem issue for the used array.

3 - Apply a satisfactory method that finds the closest model response to observed data. At this stage, two kinds of methodologies can be used; local and global search methodologies. The local methods seek solutions from the start model. At the global one, solution search is done at a wider solution space. The former can be the **least-square** adjustment and the later the **simulated annealing** method.

3.2.2 – Model parameterization

The complexity of a discrete model is a function of the given dimension. Any finite space $\mathbb{D}$, were some variable physical properties do exist, can be divided into a limited number of discrete geometric elements, with constant physical properties of each element. Taken the classical 1D TEM approach, the physical property under study is the electric resistivity (ρ) and geometric thickness (h) of each horizontal layer. These comprise the **m** vector's parameter of the problem with M elements.

Being $\boldsymbol{f}(\mathbf{m})$ the functional relating model parameters to model response (direct problem), the model response over $\mathbb{D}$ space is then:

$$\int_D f(m)dv \approx \sum_{j=1}^{\mathrm{M}} f(m_j) = \boldsymbol{u} \qquad (3.11)$$

Where $\boldsymbol{u}$ is the data vector.

The corresponding matrix equation is:

$$\boldsymbol{u} = \mathbf{F}\mathbf{m} \qquad (3.12)$$

and $\mathbf{F}$ is the matrix relating the $\boldsymbol{u}$ data line matrix to the **m** parameters column matrix.

3.2.3 – Least-square linear inverse problem

When a linear relation prevails between $\boldsymbol{u}$ and **m**, when expression (3.12) can be written for discrete data and model regions:

$$u_i = \sum_{j=1}^{\mathrm{M}} F_{ij} m_j \qquad (3.13)$$

In reality, the collected data have always an associated error, leading to the impossibility of a model response to perfectly match it. To account for this, the data error vector **e** is added to the problem,

$$\boldsymbol{u} = \mathbf{Fm} + \mathbf{e} \tag{3.14}$$

"Finding a solution" is the same as to minimize the difference between the observed data and calculated values from the direct problem. The way is to reach a minimal value to the added residual squares – the least squares' method (Menke, 1989). That is accomplished with minimization of the objective function Q, that quantifies misfit.

$$\mathrm{Q} = \mathbf{e}^{\mathbf{T}}\mathbf{e} = (\boldsymbol{u} - \mathbf{Fm})^{\mathbf{T}}(\boldsymbol{u} - \mathbf{Fm}) \tag{3.15}$$

Where **u** represents the observed data and **Fm** the model response. The minimization, against parameters m_j , is given by:

$$\frac{\partial \mathbf{Q}}{\partial m_j} = 0 \tag{3.16}$$

with solution:

$$\mathbf{m} = \left(\mathbf{F}^{\mathbf{T}}\mathbf{F}\right)^{-\mathbf{1}}\mathbf{F}^{\mathbf{T}}\boldsymbol{u} \tag{3.17}$$

This is the least square solution to the linear problem, without any constrains, and $\left(\mathbf{F}^{\mathbf{T}}\mathbf{F}\right)^{-\mathbf{1}}\mathbf{F}^{\mathbf{T}}$ is the known ***generalized inverse matrix operator***, which applied to the data vector ***u*** recover the **m** vector of parameters. This is true if the number of model parameters equals the number of observed data points. In this linear case, the model can be found from data in just one step. On the other hand, if the number of data exceeds the number of model parameters, the problem is over-determined and there will be an infinite number of solutions.

3.2.4 – Least-square non-linear inverse problem

With a non linear situation, expression (3.12) is still valid if a conversion to a linear approximation is found. The usual way is to expand the model response by Taylor's series, around a starting initial model ($\mathbf{m^0}$);

$$\boldsymbol{f}(\mathbf{m^0}) \tag{3.18}$$

Taken $\boldsymbol{f}(\mathbf{m})$ to be linear around the $\mathbf{m^0}$ model, the Taylor expansion becomes:

$$\boldsymbol{f_i}(\mathbf{m^0}) + \frac{\boldsymbol{\partial f_i}}{\boldsymbol{\partial m_1}}\boldsymbol{\delta m_1} + \frac{\boldsymbol{\partial f_i}}{\boldsymbol{\partial m_2}}\boldsymbol{\delta m_2} + \cdots + \frac{\boldsymbol{\partial f_i}}{\boldsymbol{\partial m_p}}\boldsymbol{\delta m_p} + \text{higher order terms} \tag{3.19}$$

In short condensed form;

$$\boldsymbol{f}(\mathbf{m}) = \boldsymbol{f}(\mathbf{m^0}) + \left(\sum_{j=1}^{M} \frac{\partial f_i(m)}{\partial m_j}_{|\mathrm{m}=\mathrm{m}^0} \delta m_j\right) + \mathrm{O}(\|\delta m\|^2) \tag{3.20}$$

regardless of superior order terms. This approximation is only valid to converging series; that is, δm_j must be small for all *j* indexes.

Like previously result, the misfit between data and model response must become:

$$\boldsymbol{e} = \boldsymbol{u} - \boldsymbol{f}(\mathbf{m}) \tag{3.21}$$

is the difference vector between observed data (***u***) and model response.

If the Jacobean matrix **J** with partial derivatives of $\boldsymbol{f}$ against m_j parameter is:

$$\mathbf{J} = \begin{bmatrix} \frac{\partial f_1(m)}{\partial m_1} & \cdots & \frac{\partial f_1(m)}{\partial m_M} \\ \vdots & \ddots & \vdots \\ \frac{\partial f_n(m)}{\partial m_1} & \cdots & \frac{\partial f_n(m)}{\partial m_M} \end{bmatrix} \tag{3.22}$$

and

$$\mathbf{b} = \delta\mathbf{m} \tag{3.23}$$

is the adjustment vector to be applied at each m_j parameter, misfit vector **e** can now be rewritten as:

$$\boldsymbol{u} - \boldsymbol{f}(\mathbf{m}) = \mathbf{u} - \left[\mathbf{f}\left(\mathbf{m^0}\right) + \mathbf{Jb}\right] = \mathbf{y} - \mathbf{Jb} \tag{3.24}$$

Again, by least square method, a similar expression to (3.17) is found:

$$\mathbf{b} = \left(\mathbf{J^T J}\right)^{-1}\mathbf{J^T}\boldsymbol{y} \tag{3.25}$$

b represent the small change over the **m** parameters to gets a better fit to the starting model response.

$$\mathbf{m^1} = \mathbf{m^0} + \mathbf{b} \tag{3.26}$$

If the new model $\mathbf{m^1}$ is still far from the "true model", i.e., if the model response does not fit to a certain degree the observed data, the process is repeated, but now taking as new starting model the $\mathbf{m^1}$. These operations are repeated iteratively until a reasonable solution with a good fit is found. The next expression gives the generic iterative process scheme:

$$\mathbf{m}^{k+1} = \mathbf{m}^k + \left(\mathbf{J^T J}\right)^{-1}\mathbf{J^T}\boldsymbol{y} \tag{3.27}$$

and to each iterative step a new Jacobean matrix **J** must be calculated. New model is always found from previous one. This iterative method is known as ***Gauss-Newton method*** (Meju, 1998).

The method is simple and powerful, but can be tricky producing solutions with no physical meaning when the $\mathbf{J^T J}$ matrix is singular (or almost singular). That is, when eigenvalues are near zero. When the $\mathbf{J^T J}$ matrix is not singular, very slow convergence can take place or even diverging situations, due to a wrong chosen starting model. To overcome this, any previous information – *a priori* information, like former processed data, logging data and geologic knowledge can be incorporated to have a better start model.

3.2.5 – Smoothed inverse problems

It's possible to impose certain limitation to the **m** parameter values. That is done, for instance, to 1D inversion, by fixing lower and higher limits to each of the electric resistivity and thickness layer's values. In 2D and 3D inversion, the assigned parameter values of each domain cell or block element can be "closely" related with the neighborhood ones by the *roughness* quantity. Smooth constrains methodology applications are published from various authors like Constable *et al.* (1987), Sasaki (1989, 1992 and 1994), DeGroot-Hedlin and Constable (1990), Sasaki *et al.* (1992), Zhang and Hobbs (1992).

A similar methodology for 1D inversion, taken into account nearby soundings to construct a quasi-2D pseudo-section, is known as Lateral Constrained Inversion (LCI), and has been applied over galvanic and EM data, (Auken *et al.*, 2001, 2002 and 2005a), (Santos, 2004), (Auken and Christiansen, 2004), (Mansoor *et al.*, 2006). Viezzoli *et al.*, (2008) have presented a new methodology, Spatially Constrained Inversion (SCI), which produces quasi-3D modeling by taken into account not only soundings along a given profile, but also from across profiles.

The *roughness* of the model parameters can be expressed as:

$$\mathbf{r} = \mathbf{C}\mathbf{m} \tag{3.28}$$

where $\mathbf{C}$ is the Laplacian roughening matrix.

The objective function Q, must now include not only the data misfit term $(\mathrm{Q_d})$ but the smoothness one also $(\mathrm{Q_r})$.

$$\mathrm{Q} = \mathrm{Q_d} + \lambda \mathrm{Q_r} = \mathbf{e}^{\mathbf{T}}\mathbf{e} + \lambda \mathbf{r}^{\mathbf{T}}\mathbf{r} \tag{3.29}$$

$\boldsymbol{\lambda}$ is the Lagrange multiplier (damping factor) that controls the amplitude of the parameter corrections and oscillations and the fastness of convergence. Too high λ value means a very smooth model and a worse data fitting. Too low λ vanish with the smooth constrain. The usual procedure is to start with a relatively high λ value and diminish it throughout the iteration process.

With this new formulation, the solution of the inversion using the linear approach becomes (Menke, 1989):

$$\mathbf{m} = \left(\mathbf{F}^{\mathbf{T}}\mathbf{F} + \lambda \mathbf{C}^{\mathbf{T}}\mathrm{C}\right)^{-1}\mathbf{F}^{\mathbf{T}}\boldsymbol{u} \tag{3.30}$$

and the parameters correction for the non-linear case are calculated by:

$$\mathbf{b} = \left(\mathbf{J}^{\mathbf{T}}\mathbf{J} + \lambda \mathbf{C}^{\mathbf{T}}\mathrm{C}\right)^{-1}\mathbf{J}^{\mathbf{T}}\boldsymbol{y} \tag{3.31}$$

3.2.6 – Matrix equations solving methods

There are several different methods to solve the (3.12) equation system. The ***conjugate gradient*** is an iterative method to search local minimum by gradient method analyses of minimizing function (Hestenes and Stiefel, 1952). Converging process ends by reaching a predefined limited number of steps or to a predefined misfit value. The implemented code algorithm it's easily found in the literature, like Press *et al.* (1992). From this method, several others do exist, e.g. the *biconjugate gradient method*.

The ***singular value decomposition*** (SVD) (or spectral decomposition) is an important factorization method of a rectangular real (or complex) matrix. It's an excellent method to perform the least square's data fitting, and is nowadays most applied at geophysical data analyses, because is mathematically robust and numerically stable giving also tools for analyses of the model results. Applied computing SVD data methods back to the fifths of last century, and a detailed description is given by Lanczos (1958) and Jackson (1972). Today the computing most-used code is the one from Golub and Reinsch (1970). The decomposition of the matrix F is written as:

$$\mathbf{F} = \mathbf{U}\mathbf{W}\mathbf{V}^{\mathbf{T}} \tag{3.32}$$

where $\mathbf{U}$ is an orthogonal data space eigenvector matrix with the same dimension ($m \times n$ as $\mathbf{F}$), $\mathbf{W}$ is a diagonal matrix ($n \times n$) of nonnegative elements (singular values of $\mathbf{F}$, usually listed in descending order) and $\mathbf{V}$ is a singular orthogonal parameters space eigenvector matrix ($n \times n$) (Meju, 1998), and:

$$\mathbf{U}^{\mathbf{T}}\mathbf{U} = \mathbf{V}^{\mathbf{T}}\mathbf{V} = \mathbf{V}\mathbf{V}^{\mathbf{T}} = \mathbf{I} \tag{3.33}$$

where $\mathbf{I}$ is the identity matrix.

Whit this formulation, expression (3.17) becomes then;

$$\mathbf{m} = \mathbf{V}\mathbf{W}^{-\mathbf{1}}\mathbf{U}^{\mathbf{T}}\boldsymbol{u} \tag{3.34}$$

and the damped equivalent expression (3.31) becomes;

$$\mathbf{m} = \mathbf{V}\left(\mathbf{W}^{\mathbf{2}} + \lambda\mathbf{C}^{\mathbf{T}}\mathrm{C}\right)^{-\mathbf{1}}\mathbf{I}\mathbf{W}\mathbf{U}^{\mathbf{T}}\boldsymbol{u} \tag{3.35}$$

The advantage of the SVD is that it also gives the inversion statistics, with the *importance* value of each model parameter. A unitary *importance* means that parameter has strong importance on the model's fit output, and a smaller value (near zero) means that parameter has little influence on the model's fit (Strack, 1992).

3.2.7 – Simulated Annealing method

The Simulated Annealing (SA) it's a global minimization method (Monte Carlo class), with the ability to lock for the solution over a wider solution space. The process is similar, and its name comes from the annealing in metallurgy, a technique involving heating and controlled cooling of a material to reorient internal particles and reduce their defects. This method is controlled by the initial temperature ($T_0 > 0$ and generally high) and cooling rate of T. With a high-temperature value the model parameters are allowed to have a greater variability (like kinetic energy of the particles in the metal), but as temperature drops those values freezes around the absolute minimum of it. To avoid falling at a local minimum, even with a rise in the objective function, a comparison is made between the acceptance probably function, defined as:

$$\psi = \mathbf{e}^{(-\Delta \mathbf{E}/\mathbf{T})} \tag{3.36}$$

and a generated random number χ (between 0 and 1). ΔE is the objective function variation. If $\psi > \chi$ then the variation of the parameters is accepted. This is the basis of the ***Metropolis algorithm*** proposed at Metropolis *et al.* (1953). From (3.36) equation we see when T is high (at beginning) almost all variations are taken, but with low T the chance to be accepted is less and less probable. Application and introduction of this process in the framework of inverse theory was done by Rothman (1985a, 1985b, 1986).

To be efficient, the cooling temperature rate must be small, to allow a correct search over the model parameters' space (which is normally limited). But if this is too small, and if initial T is also too high, we get a long computing time. With this method, and because the process is randomly established, each run output a different model. The final model is usually calculated from the analysis of several runs (e.g. 10) to check coherency between all of them.

3.2.8 – Joint inversion method

The acquired geophysical data over the earth have the signature of the structures beneath it, and each method sample only some physiochemical state of geological and/or man-made targets. Upon this, conclusions can be drawn about the structures. However, each applied method as its own practical and theoretical limitations. For instance, no single conductivity sounding technique provides complete, consistent and sufficient data to characterize completely the subsurface. Moreover, the effectiveness of each technique varies from one geological environment to another, as the various measurements' sets are influenced differently by the presence of small-sized three-dimensional bodies in the very near-surface (Meju, 2005).

When different sets of geophysical data do exist from the same area, taken with different methodologies or techniques, a joint inversion can be done if they share some (or not) common physical propriety. The resulting model's parameters must give a good solution

replicating the different data sets. There are basically two approaches to the joint inversion problem. The first one is the structural approach, where the inversion seeks for a common structure of the models. In the second one the inversion seeks for values of parameters that are related through empirical relationships. For example, the joint inversion of seismic and resistivity data can only be done using the structural approach (Gallardo and Meju, 2003 and 2004).The parametric approach is commonly used with electromagnetic and electrical resistivity data. In this case, both the geometry (thickness) and resistivity values are taken as parameters into the inversion process. The integration of these data (e.g. DC and TEM) can improve the robustness of model interpretation and the cumulative probability of detection of subsurface targets. Several authors have developed joint inversion with DC resistivity, magnetotelluric (MT) and TEM data, e.g. Vozoff and Jupp (1975), Jupp and Vozoff (1977), Meju (1996), Harinarayana (1999).

The 1D joint inverse problem can be accomplished by the use of a least-square criterion with SVD as a solving method (sections 3.2.4 and 3.2.6) or by SA approach (section 3.2.7.). Concerning the DC and TEM joint inversion, besides the parameters' calculation, attention must be taken also to the well know "static shift" effect of the DC data. This effect arises from small-scale irregularities around the source and readings' electrodes, and gives a constant (logarithmic) resistivity shift to the same aperture MN/2 segment data (DC soundings). That can be known and corrected comparing the TEM and DC apparent resistivity curves. To perform such comparison, we can use the empirical relation from Meju (2005) in order to plot them together:

$$t = \frac{\pi \mu_0 L^2}{2\rho} \tag{3.37}$$

with t the transient time (in s) and *L* the half electrode-array length (AB/2 distance, in m).

Sometimes TEM data soundings' acquisition is exclusively used to quantify and correct the static shift over DC and MT data sets.

3.2.9 – Lateral and spatially constrained joint TEM inversion

The joint inversion of nearby soundings, usually stitched-together along a profile, was originally developed for inverting continuous DC data sets (Sørensen, 1996). The 1D-LCI technique, already mentioned at 3.2.5 section, uses sharp layer boundaries and solves a number of 1D problems simultaneously with constraints between neighboring models. The limitations are that it requires all separate 1D models have the same model parameters' subset, and it works best at environments with relatively smooth lateral resistivity variations, like sedimentary areas. All the models and the corresponding data sets are inverted simultaneously; minimizing a common object function (Auken and Christiansen, 2004) thereby creating a quasi-2D image from a 1D based forward solution. The lateral constraints and constraints from a-priori information are all part of the data vector together with the measured apparent resistivity data. Due to the lateral constraints' algorithm, the model parameter's information will spread smoothly to the neighbours models so the parameters in those near models have to be equal within certain limits.

Auken and Christiansen (2004) have also introduced the 2D-LCI algorithm. It uses the same formulation as the 1D-LCI inversion scheme, but the difference is that the forward model is 2D. This means that 2D formulation can handle larger lateral variations in the subsurface resistivity. With the 1D-LCI method approach, inversion of TEM data in a 3D environment is possible. Studies show that if the geological environment consists of gently varying 3D structures with moderate resistivity contrasts, the 1D inversion approach in most cases will give a good recovery of the true model. When environments with high-resistivity contracts and strong 3D features exist the 1D based inversion algorithm is strongly influenced by 3D effects and will in many cases provide unreliable models. These 3D structures' effects in 1D interpretation of TEM data have been dealt by; e.g. Newmann *et al*, (1987), Goldman *et al*. (1994), Auken (1995), Hördt and Scholl (2004) and Auken *et al*. (2008).

The quasi-3D inversion, the mathematical formulation of the SCI method is very similar to that of the LCI method (Auken and Christiansen, 2004). It is a least-squares inversion of a layered earth regularized through spatial constraints, which gives the smoothed lateral transitions. Main difference between the SCI and LCI methodologies are the entries in the roughening matrix $\mathbf{C}$. In SCI, the constraints are also applied to offline soundings so each model parameter is connected to many other model parameters of the same kind, not only to neighboring along-line soundings. Nevertheless, in both LCI and SCI, $\mathbf{C}$ is sparse. Another major difference is that over the spatial domain, the constraining points have to follow a Delaunay triangulation (Viezzoli *et al.*, 2008).

Upon this SCI methodology, a spatially constrained 1D inversion algorithm for quasi-3D TEM response was tested over synthetic data models. The algorithm code was implemented by Fernando Santos (personal communication) and details are given at Santos *et al*. (2011), Santos and El-Kaliouby (2011). The forward 1D calculation is based on the single loop configuration for a layered earth (Raiche, 1984). Care was taken to accurately calculate the early times' response and this forward TEM algorithm account for the ramp time effect. The data are the logarithms of the apparent resistivity values (versus time) at sounding's sites. The model parameters are the resistivity logarithms of the hexahedral model blocks beneath each sounding measurement site. The block thickness increases to depth following an exponentially rule, with an initial value (Z_0) and an increase factor (step) given by:

$$Z_0 e^{step(n-1)} \quad \text{m} \tag{3.38}$$

to the nth thickness layer. The number of layers (vertical blocks) is chosen by user.

The minimization of an appropriate objective function allows the estimation of the corrections to the model parameters at each iteration. At this code, the defined objective function is:

$$\mathrm{Q} = \|\mathbf{W_d}(\delta\mathbf{d} - \mathbf{J}\delta\mathbf{p})\|^2 + \lambda\|\mathbf{C}(\mathbf{p} - \mathbf{p_0})\|^2 \tag{3.39}$$

where $\mathbf{W_d}$ is a diagonal matrix, consisting of the reciprocal of data error standard deviations, $\delta\mathbf{d}$ is the vector of the differences between the logarithms of the apparent resistivity of the calculated model responses and of the observed measured data, $\mathbf{J}$ is the Jacobian (derivative matrix) containing the derivatives of the model responses with respect to the model

parameters, $\delta\mathbf{p}$ is the vector containing the corrections to the model parameters, and $\mathbf{p_0}$ is the a priori defined model. Damping factor λ it is set (empirically) at beginning and decreased by a factor of 0.8 at each iteration. The elements of the matrix $\mathbf{C}$ are the roughness coefficients of each parameter (block resistivity); defined in terms of the neighbor's proximity. Minimization of expression (3.39) yields the normal equations:

$$\delta\mathbf{p} = \left(\mathbf{J^T W_d^T W_d J} + \lambda\mathbf{C^T C}\right)^{-1}\left(\mathbf{J^T W_d^T W_d}\delta\mathbf{d} + \lambda\mathbf{C^T C}(\mathbf{p} - \mathbf{p_0})\right) \qquad (3.40)$$

After solving this equations set, the model parameters $\mathbf{p}$ are then updated by adding the vector $\delta\mathbf{p}$. The iteration procedure continues until the misfit is reduced to an acceptable level (user defined) or an iteration limit number is reached.

Firstly, over the inversion of data acquired over a uniform 10 ohm.m resistivity half-space was tested. Apparent resistivity TEM curve response was computed for a single 25 m × 25 m side square loop sounding (figure 3.5). The numbers of soundings were set to 5; one at each corner of a 100 m side square and at its centre. This response curve was decimated to just 21 data points, from 5.07 μs to 7.65 ms time. The number of layers to be inverted was 15. Shallow layer was set to 2 m (Z_0) and the incremental step to 0.121.

The computed outcome, from an initial damping factor of 2.0 and stopping criteria of 40 maximum convergence iteration or 0.02 model to data misfit error, it's below at figures 3.5 and 3.6. All the computed five soundings 1D quasi-3D models are equal (as they had started from the same model and data set).

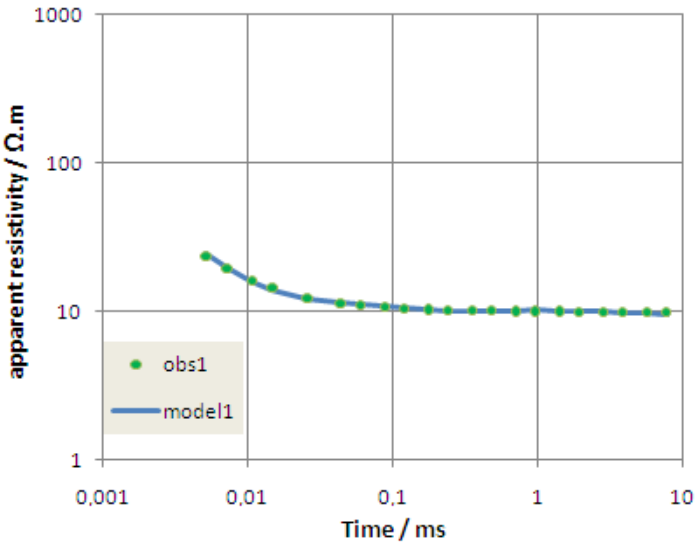

Figure 3.5 – Synthetic apparent resistivity data points and model inversion response, to 10 ohm.m uniform half-space model.

To quantify the misfit between the true model and the quasi-3D inversion calculated model, a measure root-mean-squared (rms) misfit error is defined:

$$\varepsilon = \left[\frac{1}{M-N}\sum_{i=1}^{M}\left(\frac{\rho_{oi}-\rho_{ci}}{\rho_{oi}}\right)^2\right]^{1/2} \times 100\% \qquad (3.41)$$

with ρ_{oi} the observed apparent resistivity M data points and ρ_{ci} are the computed apparent resistivity model response, were N is the number of model parameters to fit.

For this first test, the initial starting model was set uniform with 20 ohm.m. The difference between the computed model and the true model is high, 29.6% (after 21 iterations). Half this misfit value comes from the last layer. With this inversion methodology, all models are to be greatly smoothed when compared against usual 1D inversion, as the fixed layers' depth inhibits sharp and high resistivity contrast layers.

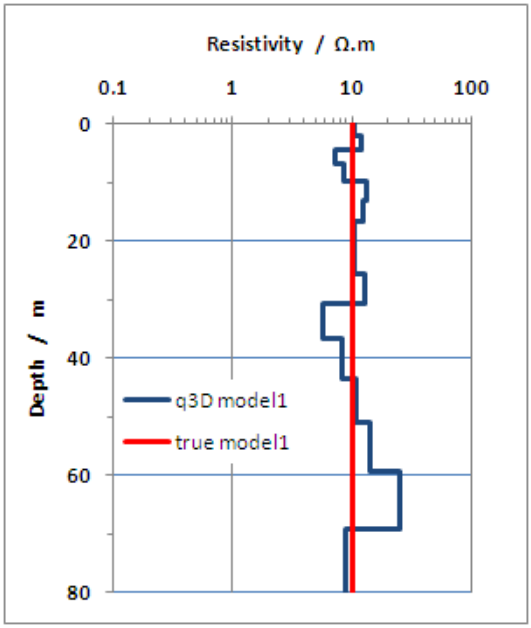

Figure 3.6 – Inversion model against true model (corresponding to figure 3.5 data).

Next step was to recovery the resistivity values for a three-layer model with the same TEM geometry (see Table 3.1). The two tested models decrease their resistivity values with depth. Figure 3.7 shows the responses of those models.

Table 3.1 – Test model2 and model3 parameters settings.

Model	Layer	Resistivity / ohm.m	Thickness / m
model2	1	100	10
	2	20	20
	3	5	∞
model3	1	50	10
	2	10	30
	3	2	∞

The starting model was again set uniform to 20 ohm.m with the same 15 layers and initial damping factor equal to 2.0. The difference between the calculated model and the true one is 16.6% (14 iterations) and 39.7% (27 iterations), respectively to model2 and model3. Model3 misfit drops to 18.4% if the second layer is not accounted for (figure 3.8). All five soundings calculated from the models are accordingly equal and fit well the data. With the layer thickness increased a better step and contrast response is achieved. The last layer resistivity value is very well established for these two test models.

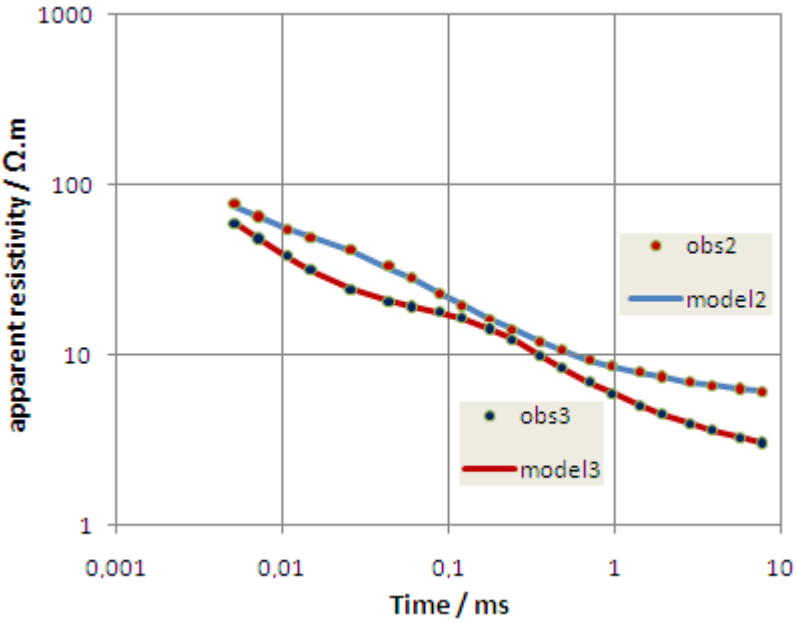

Figure 3.7 – Synthetic apparent resistivity data points and model inversion response, to model2 and model3 test, (Table 3.1).

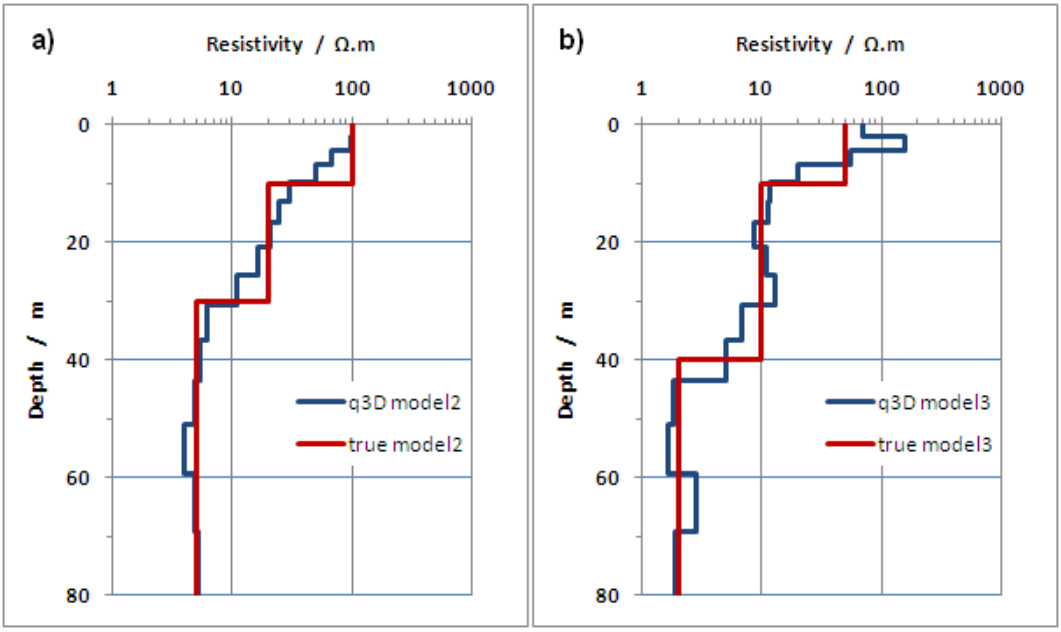

Figure 3.8 – Inversion models against true models, for a) model2 and b) model3, (corresponding to figure 3.7 data).

The fourth model test has a dipping initial layer. 1D models beneath TEM soundings 1 and 2 are designed as model4a, beneath TEM sounding 3 as model4b and beneath TEM soundings 4 and 5 as model4c, as described at Table 3.2 and presented at figure 3.9, with the same size loops. The starting uniform model was set to 20 ohm.m with 15 layers and initial damping factor equal to 1.0. Outputs of the inversion are given at figure 3.10 and 3.11. Results after 38 iterations show differences to the true model of 19.5%, 16.1% and 18.2%, respectively at TEM 1 and 2 (model4a), TEM 3 (model4b) and TEM 4 and 5 (model4c). The dipping layer is detected and represented by layers with smooth resistivity transition between the top and lower model layers when in between those there is a thinner layer.

Table 3.2 – Test model4a to model4c parameters settings.

Layer	Resistivity ohm.m	Thickness / m		
		model4a	model4b	model4c
1	50	20	30	40
2	10	40	30	20
3	2	∞	∞	∞

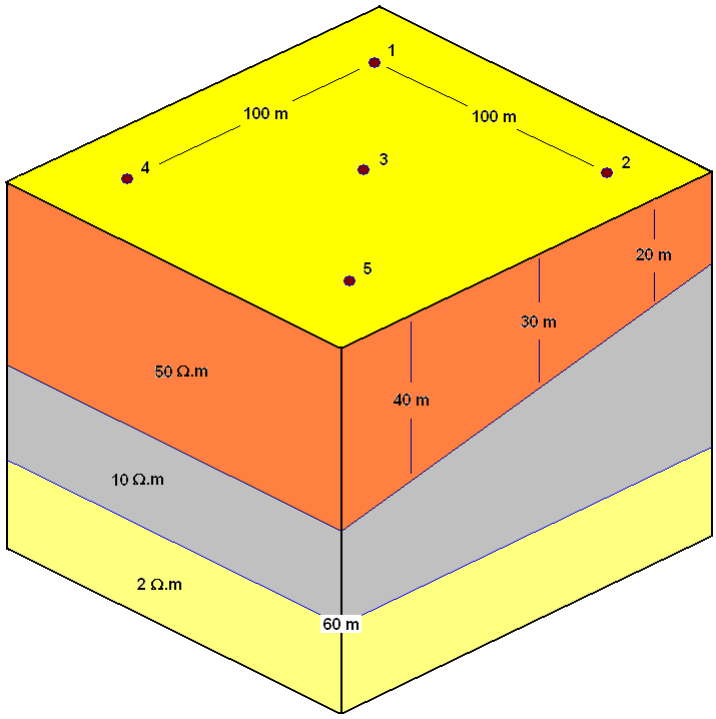

Figure 3.9 – Schematic model4 settings and TEM soundings location.

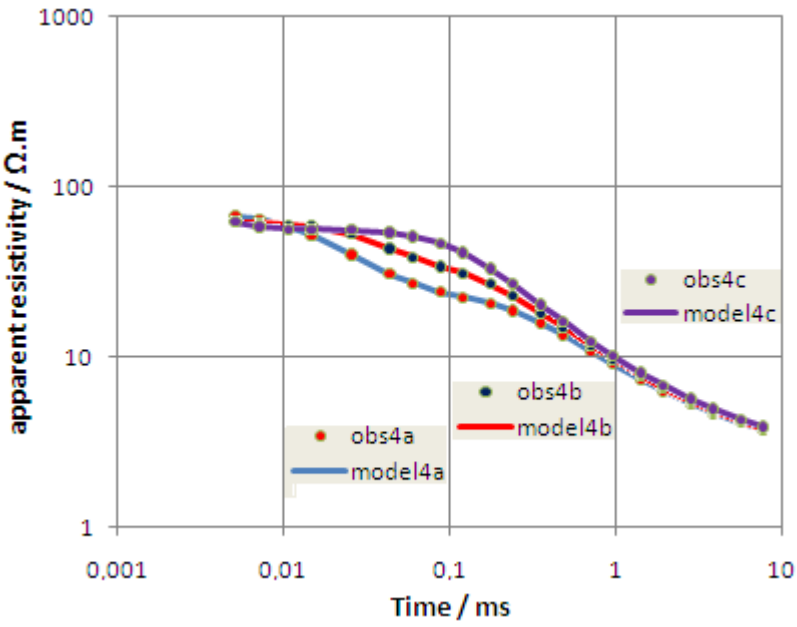

Figure 3.10 – Synthetic apparent resistivity data points and models inversion response, from model4a to model4c, (Table 3.2).

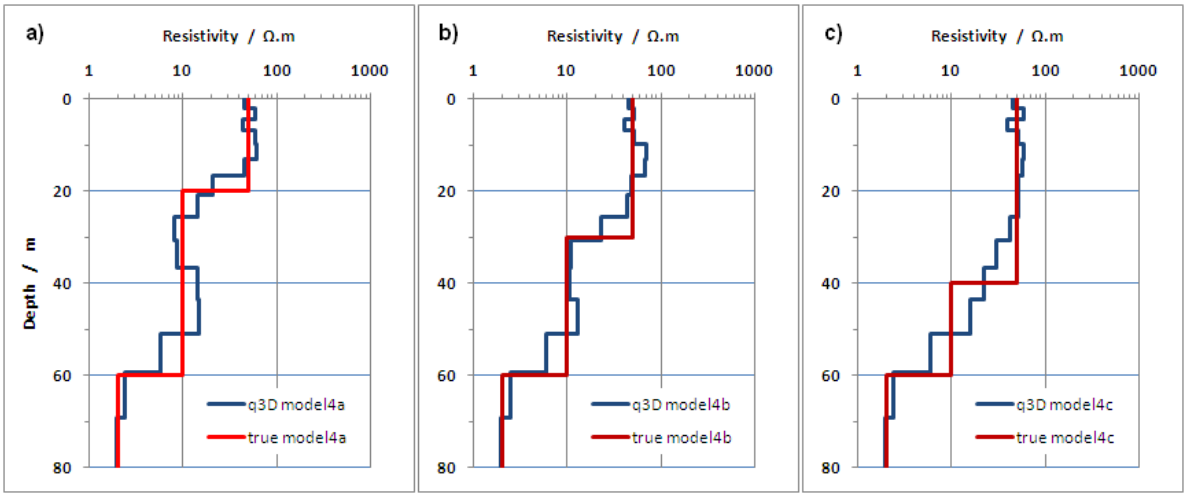

Figure 3.11 – Inversion models against true models, for a) model4a, b) model4b and c) model4c, (corresponding to figure 3.10 data).

With the same TEM data sounding inputs the quasi-3D models beneath TEM 1 and 2 soundings are almost the same ones (the same is true with TEM 4 and 5). The fifth quasi-3D test was done with the same previous settings, but adding a maximum 5% random noise to each TEM data sounding. The quasi-3D pair models' TEM 1 and 2 results are much alike and similar to the model than those from earlier test (figure 3.12). After 30 iterations, the difference between true and calculated models is 17.9% and 16.2%, for TEM 1 and 2 respectively.

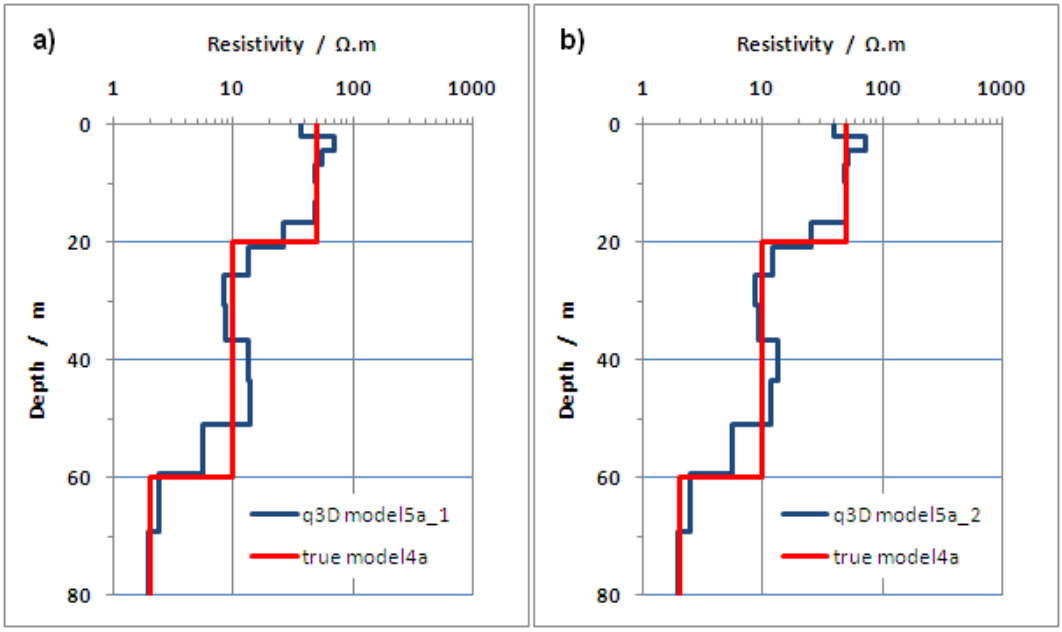

Figure 3.12 – Inversion models against true models, for a) TEM 1 and model4a, b) TEM 2 and model4a.

A comparable result is obtained from TEM 3. With this noise level, the model is much alike the previous one (figure 3.13). After 30 iterations, the difference between true and calculated models is 19.1%, slightly higher than that from early test.

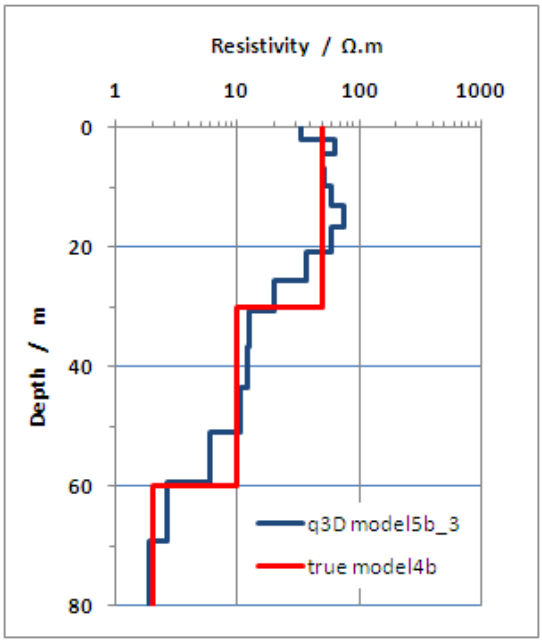

Figure 3.13 – Inversion model against true model, for TEM 3 and model4b.

The quasi-3D models from TEM 4 and 5 results are also much alike and similar to the previous models (figure 3.14). After the same 30 iterations, the difference between true and calculated models is 18.9% and 19.3%, for TEM 4 and 5 respectively.

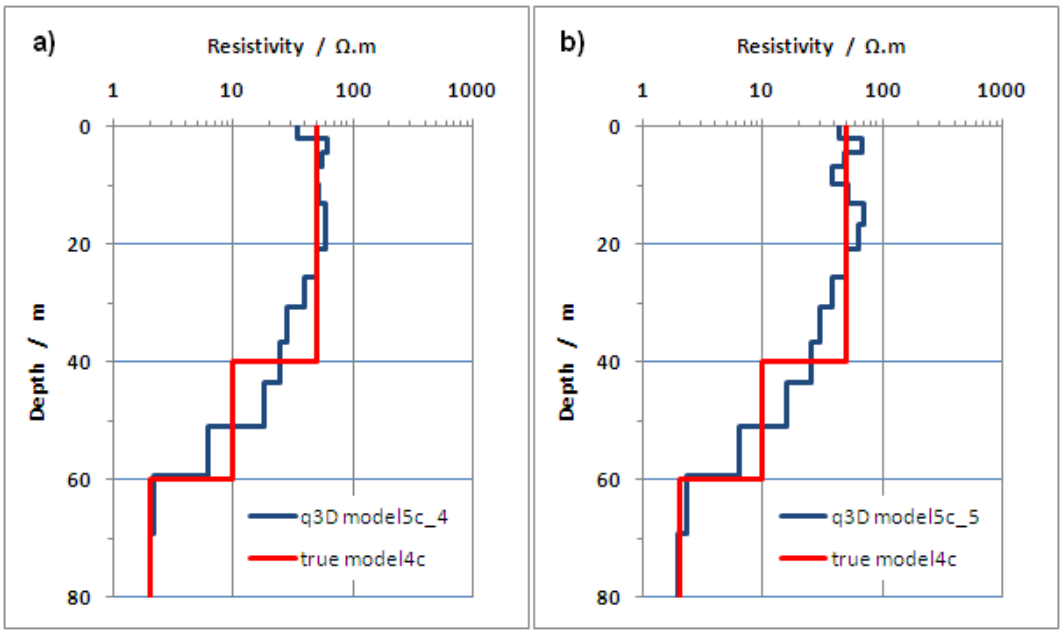

Figure 3.14 – Inversion models against true models, for a) TEM 4 and model4c, b) TEM 5 and model4c.

These tests showed that the quasi-3D algorithm successfully recovers the existing resistivity structure with 20% error level, just starting with an initial uniform half-space resistivity model. The higher number of model layers greatly smoothes the resistivity contrast results, as expected. The resistivity of the last layer is usually very well calculated at all tested models.

4
TEM-FAST 48 TESTS

On this chapter, the TEM-FAST 48 equipment and some software are tested over a known conductive environment where DC geoelectric soundings have also been acquired. Results are compared between each method and with seismic profiles. Joint inversion of TEM with VES (Vertical Electric Sounding) and TEM to VES data conversion was also tested.

4.1 – Test site description

To test the TEM-FAST 48 equipment system a wide open and flat land space was chosen, at the Lower Tagus Cenozoic Basin (LTCB). It is a tectonic depression filled with Cenozoic sediments that hosts the lower reach of the Tagus River which flows along the Lower Tagus Valley (LTV), figure 4.1.

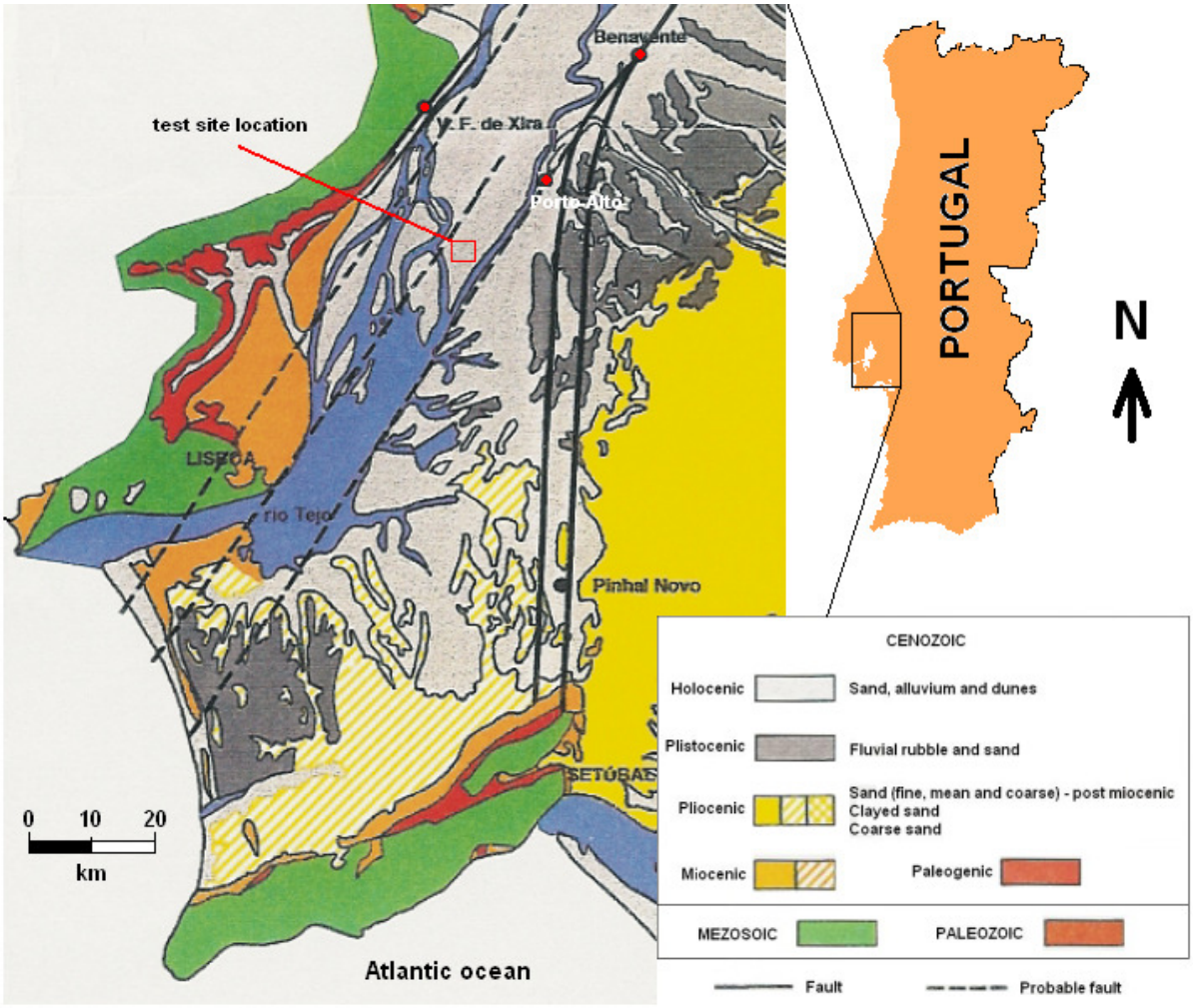

Figure 4.1 - Test site location.
Synthetic geological onset description of LTCB (adapted from Simões, 1998).

4.1.1 – Test site geologic description

The test site geology is characterized by recent (plisto-holocenic and quaternary) sedimentary deposits of yellowish gravel with intercalated grey clay and an expected thickness of 60-70 meter (figure 4.2). Above this we have recent soil and silt filling in the many natural and man-made channels that drain the water from these flat and low lands (2 to 3 m above the Tagus river water surface). Bellow these initial formations are 150 m thickness pliocenic yellow and whitish coarse sandy with rubble and small brown clay intrusion, followed by the miocenic one composed by shells limestone sandstone. Miocenic formation attains some 200-400 m thickness in the southwest part of the basin.

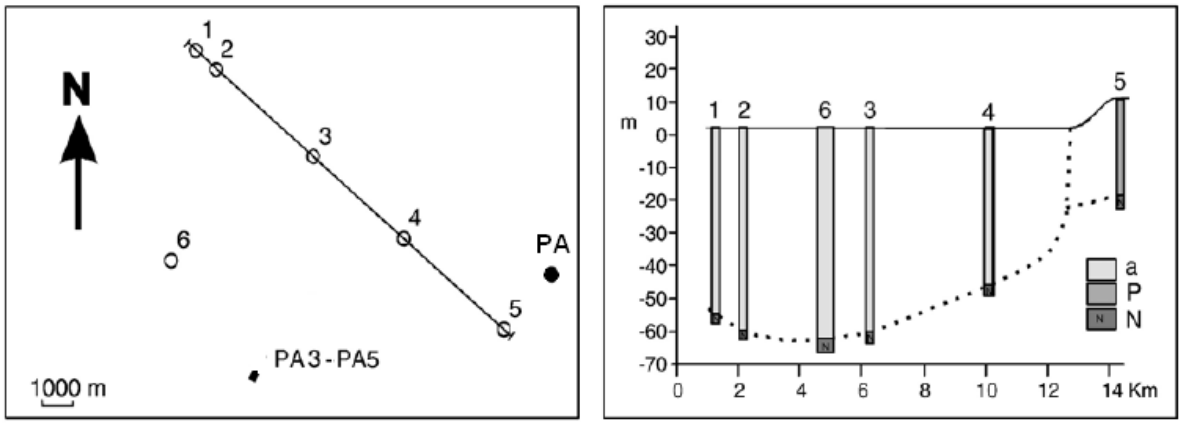

Figure 4.2 - Well locations and available logs in the Porto Alto area (at northeast of test area), drilled for water supply. a: Holocene; P - Pleistocene; N - Neogene. Profiles locations are also shown. (Adapted from Carvalho *et al.*, 2006).

The underground water free level is very near the surface, some 0.5 to 1 m depth. This groundwater is highly conductive because all the area is under estuarine water influence, a mixture of fresh waters from the river and Atlantic ocean salty water. The measured water electric conductivity value at the surface drainage channels was 9300 $\mu S.cm^{-1}$ (1.08 Ω.m) at 20 ºC.

4.2 – Test field work

The locations of the TEM and VES soundings are given at figure 4.3. They were conducted over three nearby and parallel north-30-east profiles. The centres of VES arrays are coincident with TEM square loop centres. The VES array direction is also along the profile's orientation. TEM single square loops are 50 m × 50 m and loops centre are contiguous 25 m apart each other. Profile PA3 comprises 16 TEM soundings. Profiles PA4 and PA5 have both 10 TEM soundings. Over each profile, five VES have been done, also spaced by 25 m. Westwards the PA5 profile is 50 m apart from PA4 profile (at the west side of the country road), and the latter is 85 m from the eastern PA3 profile (at the east side of the road). The fieldwork was conducted during 2005 summer's beginning; with a dry soil condition (2005 was a very dry year in Portugal).

All these profiles have been done coincident with seismic lines, named PA3 to PA5 (Porto Alto), acquired in a previous work concerning the application of high-resolution seismic reflection method to detection near-surface faulting in two major tectonic structures at Tagus Valley (Carvalho *et al.*, 2006). At that time, VES with larger AB/2 distances were also acquired nearby the seismic profiles.

The region is a wild life protected area, but many places are still mainly used to bovine cattle production, and the land is usually grass covert. Some of these wide areas have metallic fences stacked to the ground by wood pools. That was the situation at the tested place, with a border fence along each side of the road. The nearest high-power transmission lines are far way, 10 km north and also 8 km to the west.

Figure 4.3 – VES (yellow circles) and TEM (white squares) soundings disposition at the field. North is up at this image (adapted from Google images).

4.2.1 – VES data

The VES data acquisition followed the traditional and standard field procedure for the Schlumberger array. Field equipment belongs to the Geophysics Group (Lisbon Science Faculty), and it is self-made equipment. Current electrode separation (AB/2) varied from 1 m

up to 200 m, giving eight apparent resistivity values per logarithmic decade. The measured electric potential (MN) was done with the gradual step spreading, from 0.5 m to 8 m. The VES soundings' data (apparent resistivity) are shown in figure 4.4.

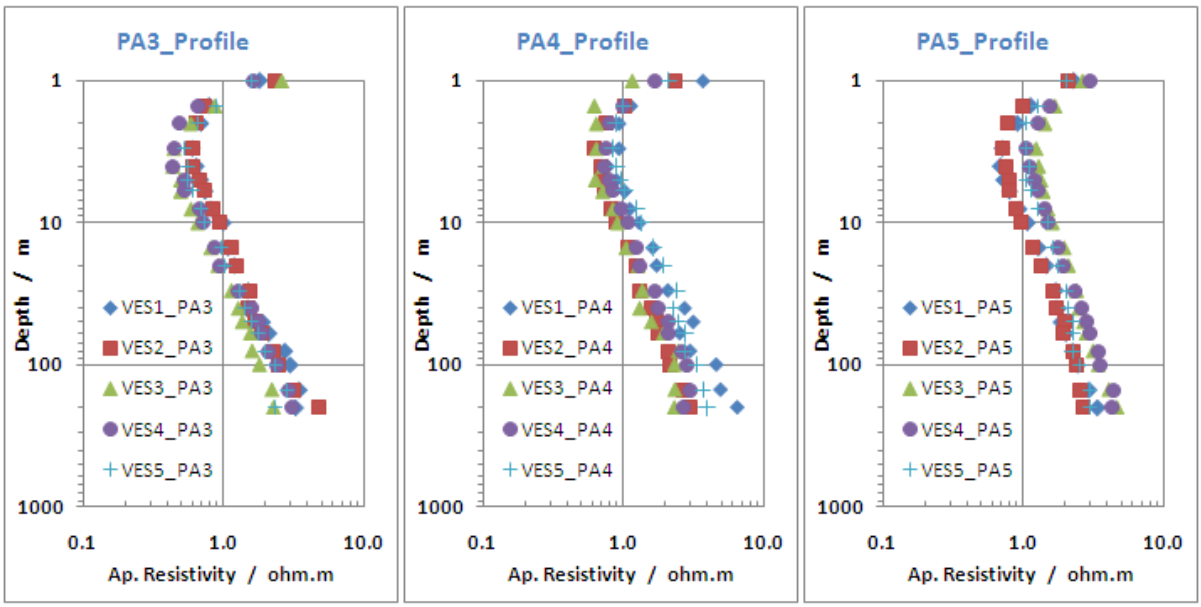

Figure 4.4 – VES sounding curves data points at each profile, apparent resistivity versus depth (AB/2).

The VES curves are of the H type, starting at a mean apparent resistivity value of 3-5 Ω.m, decreasing to mean value of 0.6-0.8 Ω.m and increasing afterwards to higher apparent resistivities. The last couple points exhibit greater experimental errors, at 20% order. With these low apparent resistivity values, effective depth of investigation is much less than real AB/2 distances, as most current density flows and stays at the near surface.

4.2.2 – VES data modelling

1D inversion of the VES data was done with the classical horizontal layers' inversion tools. The forward problem is solved calculating the electric field created by a point source over a homogeneous and isotropic horizontal layer earth (Stefanesco *et al.* 1930). The digital filtering theory (Ghosh, 1971a, 1971b) is applied to relate the apparent resistivity to the resistivity transform as defined by Koefoed (1970, 1979). In this way, the apparent resistivity response of a model (with specific layer's resistivity and thickness) is computed.

The inversion problem is solved as stated at previous section (3.2), by the SVD method. The starting model to initiate the process is taken from the asymptotic analyses of the data field curve. From all possibilities, the simpler (fewer number of layers) model is chosen. At some VES, the misfit of the five layers model was the smallest, but the corresponding geoelectric model makes nonsense when compared with the surrounding ones. At this level, we are just modelling the noise data features, as higher scattering is present at the last VES data points. The number of the layer that best satisfy all VES data is four. The observed shift between different constant MN segments is smaller, and correction was made to the initial MN branch. VES curves are similar, but a slight shift does exist among them.

The four layer models with the best fit are shown in figures 4.5 to 4.7. Minimum and maximum equivalent models were also computed. The mean values of the parameters and their bound's errors (Raiche *et al*. 1985) are included in Tables 4.1 to 4.3. These Tables include also the computed root-mean-squared misfit error between the observed and computed apparent resistivity data, defined previously by the expression (3.31).

Table 4.1 – PA3 profile VES models parameters; value, variation and global misfit result.

Layer	VES 1	VES 2	VES 3	VES 4	VES 5
1 ρ_a / Ω.m	10.5 ± 2.0	35.7 ± 4.3	3.0 ± 1.2	6.8 ± 0.5	3.6 ± 0.4
2 ρ_a / Ω.m	0.57 ± 0.02	0.57 ± 0.01	0.53 ± 0.01	0.38 ± 0.01	0.48 ± 0.01
3 ρ_a / Ω.m	1.4 ± 0.1	1.5 ± 0.1	2.0 ± 0.1	1.3 ± 0.1	1.3 ± 0.2
4 ρ_a / Ω.m	4.7 ± 0.2	4.5 ± 0.1	4.2 ± 0.1	6.0 ± 0.3	3.7 ± 0.2
1 h / m	0.30 ± 0.01	0.25 ± 0.01	0.70 ± 0.07	0.34 ± 0.01	0.42 ± 0.02
2 h / m	3.1 ± 0.3	3.9 ± 0.2	3.4 ± 0.2	3.1 ± 0.2	3.8 ± 0.5
3 h / m	17.7 ± 1.9	21.6 ± 1.7	25.7 ± 1.8	21.8 ± 1.5	16.5 ± 3.0
misfit / %	**8.97**	**6.60**	**5.65**	**7.23**	**6.08**

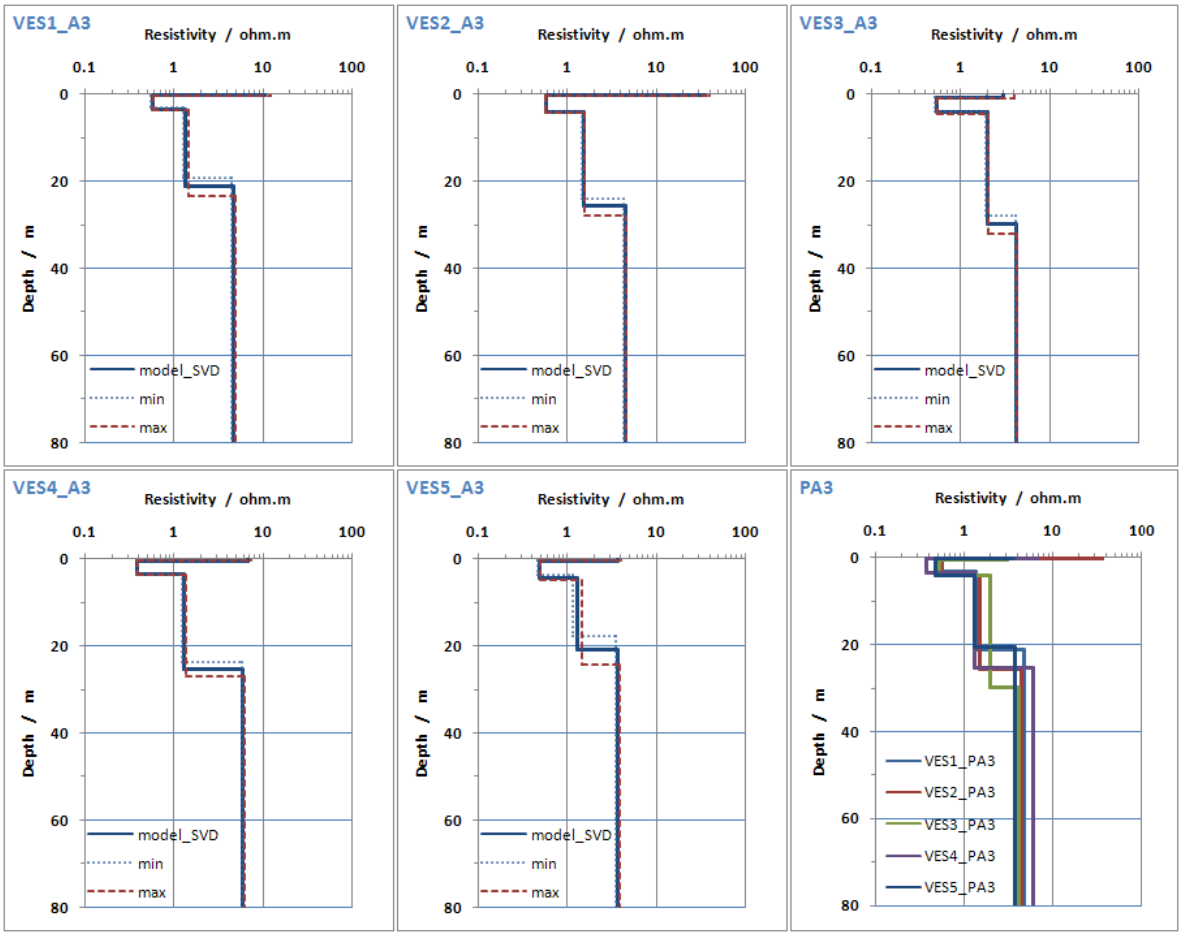

Figure 4.5 – PA3 profile VES models. Mean, minimum and maximum models.

Table 4.2 – PA4 profile VES models parameters; value, variation and global misfit result.

Layer	VES 1	VES 2	VES 3	VES 4	VES 5
1 ρ_a / Ω.m	49.4 ± 15.3	9.1 ± 0.5	65 ± 20	3.8 ± 0.3	14.6 ± 2.2
2 ρ_a / Ω.m	0.83 ± 0.02	0.60 ± 0.01	0.59 ± 0.02	0.61 ± 0.02	0.77 ± 0.02
3 ρ_a / Ω.m	2.9 ± 0.5	1.6 ± 0.1	2.4 ± 0.2	1.9 ± 0.1	2.8 ± 0.1
4 ρ_a / Ω.m	8.9 ± 1.2	3.9 ± 0.1	4.4 ± 0.4	4.0 ± 0.4	4.4 ± 0.2
1 h / m	0.26 ± 0.02	0.35 ± 0.01	0.18 ± 0.04	0.40 ± 0.02	0.28 ± 0.01
2 h / m	4.6 ± 0.6	4.2 ± 0.2	3.4 ± 0.3	2.7 ± 0.2	3.5 ± 0.1
3 h / m	25.2 ± 8.6	31.7 ± 2.2	32.3 ± 12.0	33.6 ± 5.4	30.8 ± 6.2
misfit / %	**14.35**	**6.99**	**17.81**	**8.02**	**6.23**

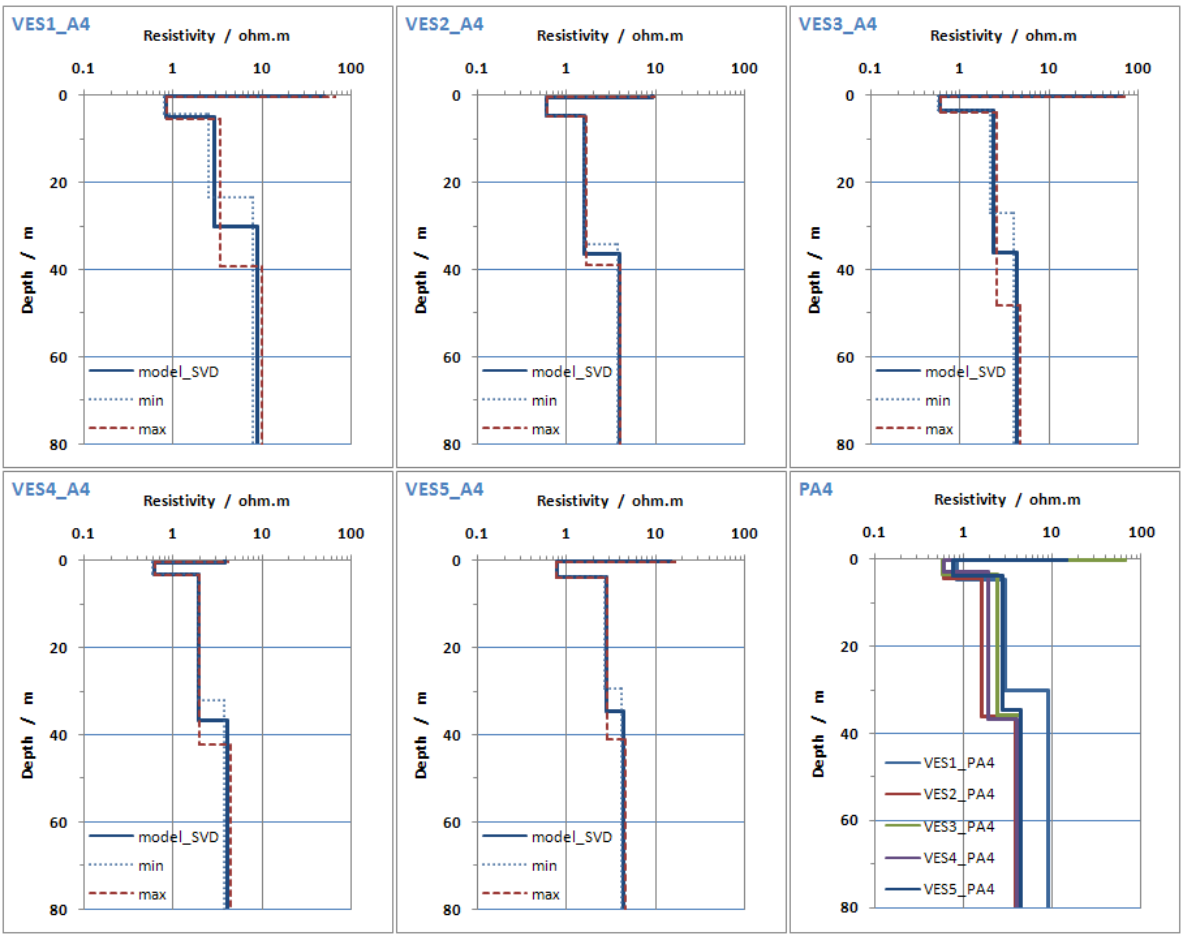

Figure 4.6 – PA4 profile VES models. Mean, minimum and maximum models.

The first and very shallow layer is not well solved, with thickness always better solved as uncertainty is bigger to the computed resistivity. An S-equivalence (conductance equivalence) happens at several VES for the second layer. The third layer exhibits also equivalence, with thickness the worse constrained parameter. The first layer resistivity value and the third layer thickness are very bad resolved parameters.

In the profile PA3 the bottom of the third layer varies from the profile edges to the centre, getting thicker at the middle of the profile. This behaviour can be accounted for the scattering of the data or can reflect a real feature as stated ahead. Note, however, that the third layer in profile PA4 and PA5 have less variation.

Table 4.3 – PA5 profile VES models parameters; value, variation and global misfit result.

Layer	VES 1	VES 2	VES 3	VES 4	VES 5
1 ρ_a / Ω.m	5.0 ± 0.35	10.5 ± 0.6	4.0 ± 0.3	6.0 ± 0.7	6.3 ± 0.8
2 ρ_a / Ω.m	0.59 ± 0.02	0.69 ± 0.01	0.77 ± 0.01	0.71 ± 0.01	0.88 ± 0.02
3 ρ_a / Ω.m	2.3 ± 0.1	2.0 ± 0.1	1.8 ± 0.1	1.9 ± 0.1	2.2 ± 0.1
4 ρ_a / Ω.m	3.6 ± 0.2	3.5 ± 0.2	3.8 ± 0.2	4.8 ± 0.3	3.1 ± 0.1
1 h / m	0.44 ± 0.01	0.31 ± 0.01	0.38 ± 0.01	0.38 ± 0.02	0.32 ± 0.01
2 h / m	3.3 ± 0.2	4.7 ± 0.1	4.1 ± 0.2	3.5 ± 0.3	3.9 ± 0.2
3 h / m	32.2 ± 8.4	32.4 ± 5.8	35.1 ± 3.1	30.7 ± 3.7	33.2 ± 7.3
misfit / %	**5.25**	**5.58**	**2.59**	**6.01**	**5.73**

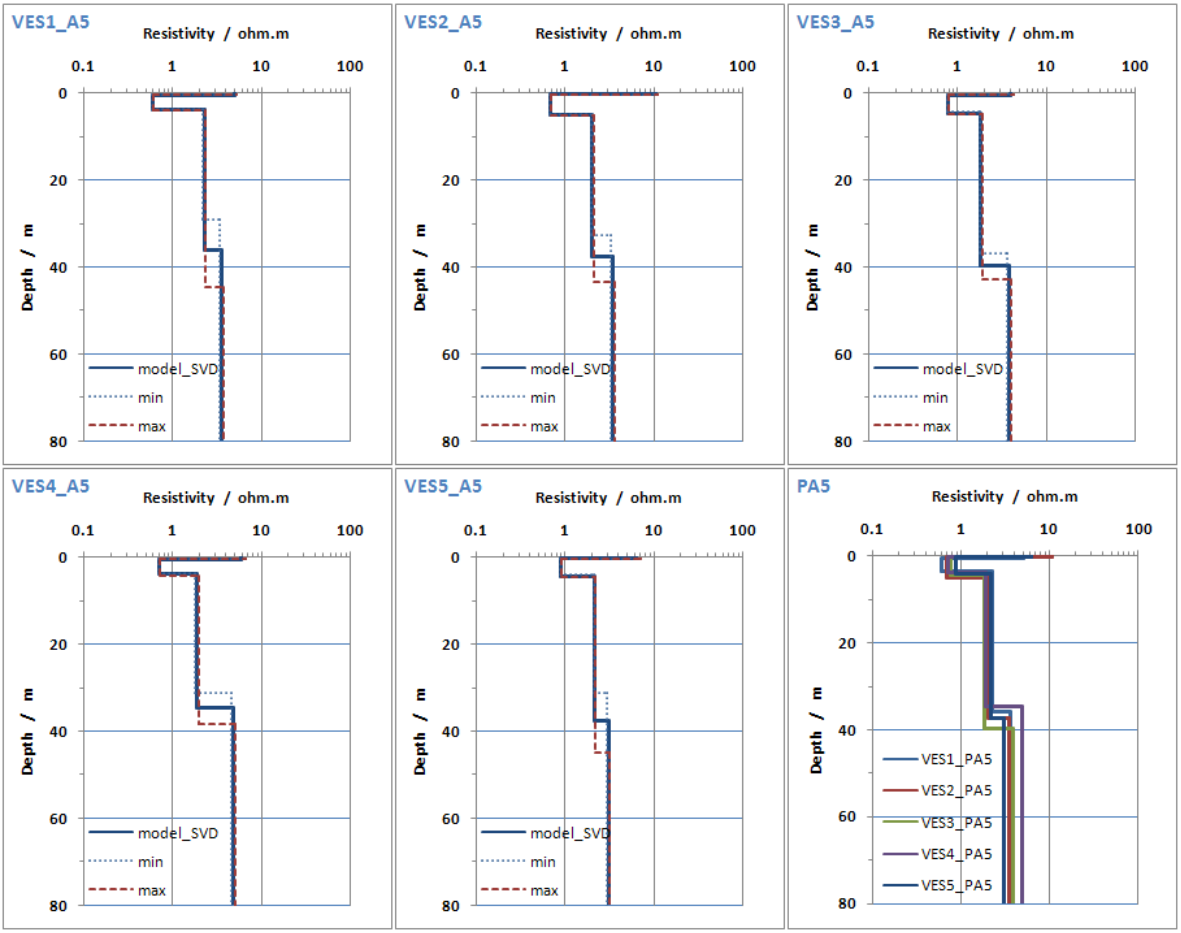

Figure 4.7 – PA5 profile VES models. Mean, minimum and maximum models.

Looking to the third layer bottom position mean values; 24.6, 36.0 and 37.1 m, respectively from PA3 to PA5 profile, a bending interface can be inferred, deepping towards west. These values are in relatively good agreement with seismic refraction interpretation of a change in the seismic character of the reflectors at an average depth of 35 m to 45 m and correspond to the Quaternary base, figure 4.8 (Carvalho *et al.*, 2006).

The variations of the misfit error difference values between VES are justified by data quality of each curve. Curve model fit response against VES data points is plotted in figures 4.9 to 4.11. The mean model at each profile was also computed, and parameters are very similar to each other, as can be seen at table 4.4.

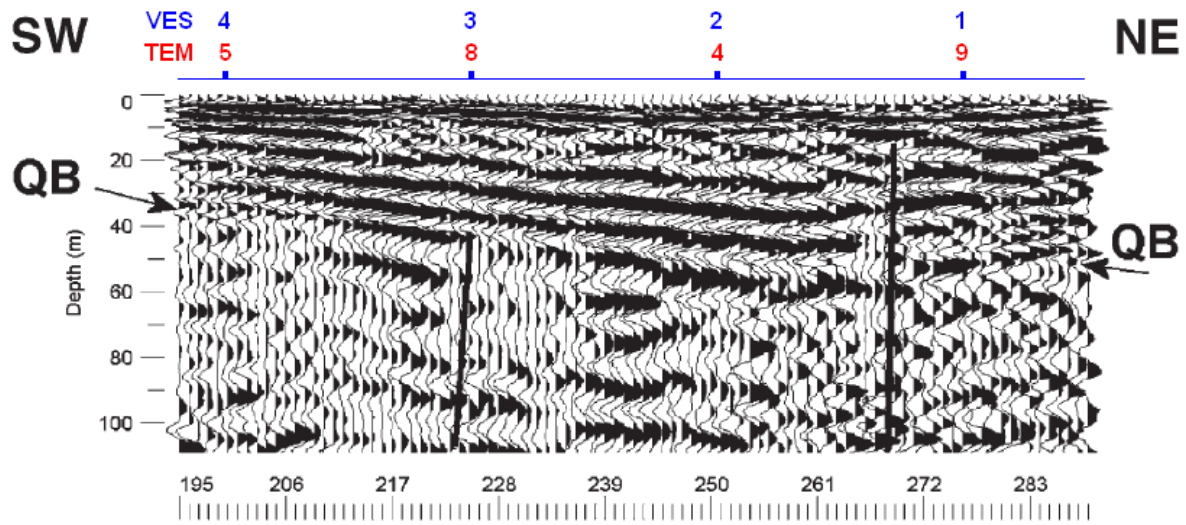

Figure 4.8 – Seismic profile PA4. QB - base of Quaternary. (Adapted from Carvalho *et al.*, 2006).

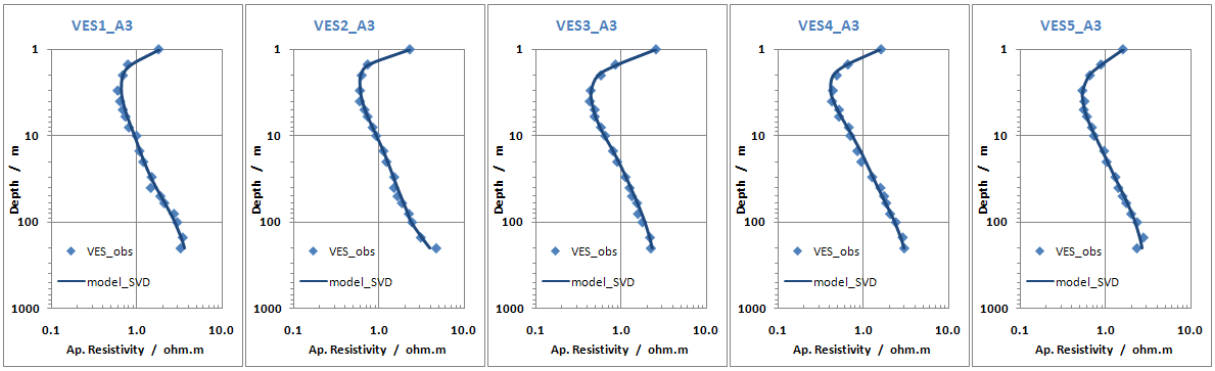

Figure 4.9 – PA3 profile VES data points and models fit curve.

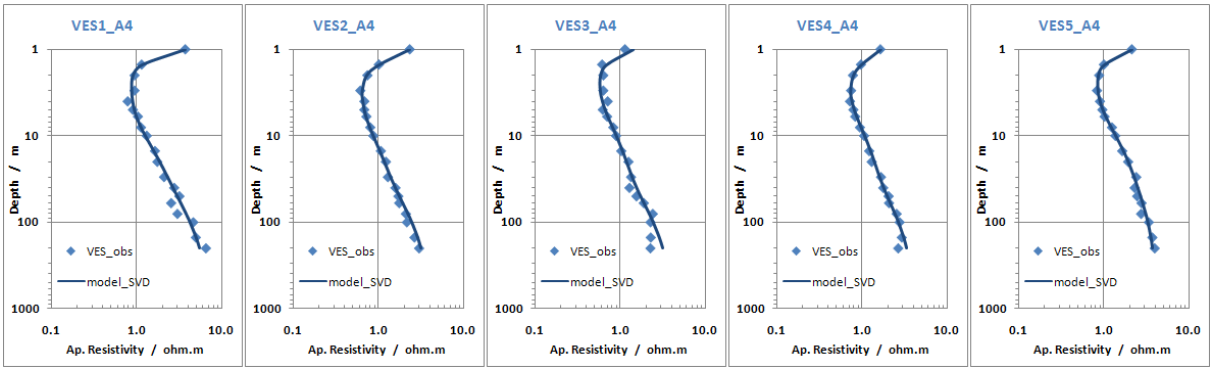

Figure 4.10 – PA4 profile VES data points and models fit curve.

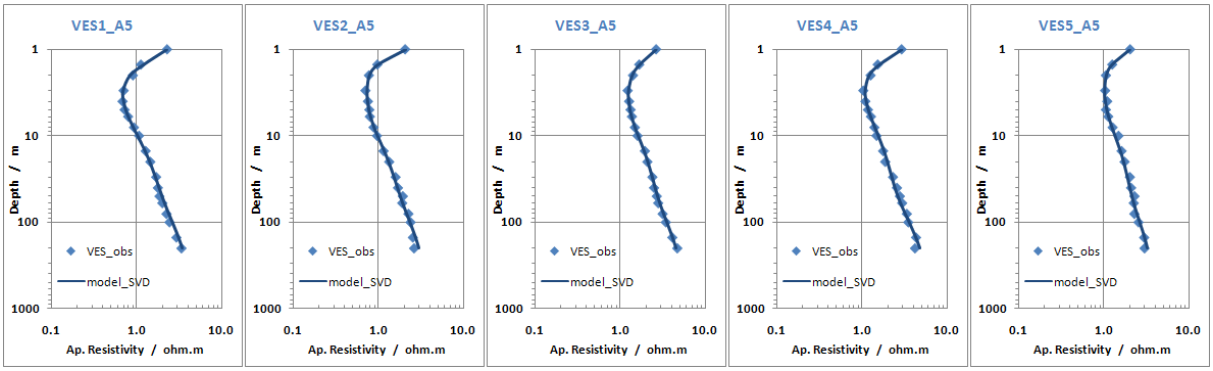

Figure 4.11 – PA5 profile VES data points and models fit curve.

Table 4.4 – Mean VES model to each profile.

Layer	PA3	PA4	PA5
1 ρ_a / Ω.m	11.9 ± 4.9	9.2 ± 2.3	6.4 ± 1.3
2 ρ_a / Ω.m	0.51 ± 0.03	0.68 ± 0.04	0.72 ± 0.03
3 ρ_a / Ω.m	1.5 ± 0.3	2.3 ± 0.6	2.0 ± 0.2
4 ρ_a / Ω.m	4.6 ± 0.4	5.1 ± 1.3	3.8 ± 0.5
1 h / m	0.40 ± 0.07	0.29 ± 0.05	0.37 ± 0.03
2 h / m	3.5 ± 0.7	3.7 ± 0.7	3.9 ± 0.5
3 h / m	20.7 ± 4.6	32.0 ± 8.5	32.8 ± 13.4

Model tests have been also made with the SA inversion method. Results are comparable to the ones with SVD solving method, as illustrated at figure 4.12 (VES 1 in profile PA3). Ten runs with different starting models, and random seeds were applied.

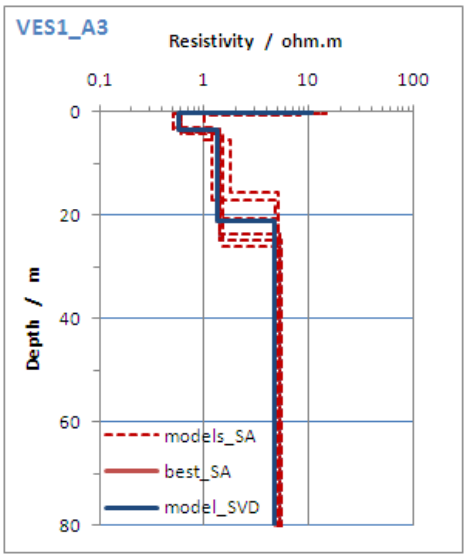

Figure 4.12 – SA model test results; 10 models and best one.
SVD model is also included.

4.2.3 – TEM data

TEM data acquisition with TEM-FAST 48 was done with one external 12 V power battery. The EM induction signals were grabbed at full 48 time gate channels, with 15 stacks. That is 3/4 of allowed maximum number of stack parameter. Registered mean output current value was 1.40 A, with a 200 m long electric cable (50 m × 50 m single, one turn loop). Most of TEM curve data points have very small residual errors (below 1%), except the last ones, above the 10 ms time mark, with more than 5% errors. The measured average noise level at 1 ms time mark is around 2 to 3 nVm^{-2}. The first three points, till the 6.07 μs are distorted by the antenna self-process at turn-off time. The curves are all very similar with small differences at first glance. The normalized emf measured values for selected time range channels are given at figures 4.13 to 4.15. The figures 4.16 presents some of the TEM soundings at profiles PA3 to PA5, corresponding to the VES positions.

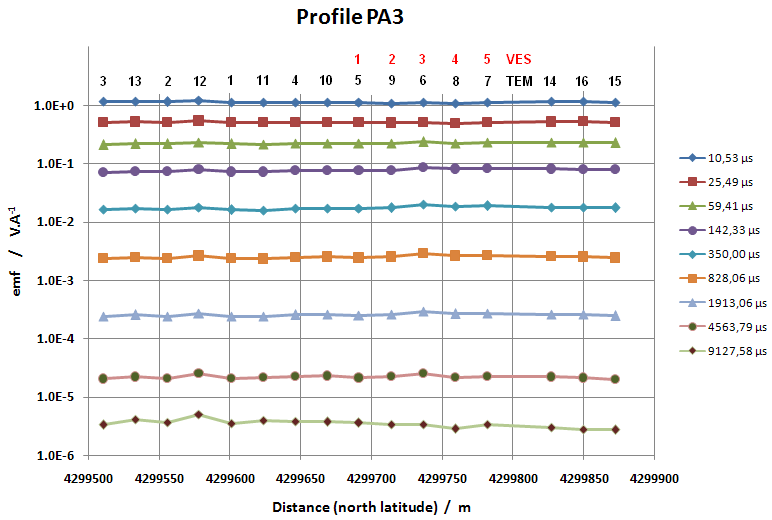

Figure 4.13 – Measured emf TEM signal for some time channels. Profile PA3.

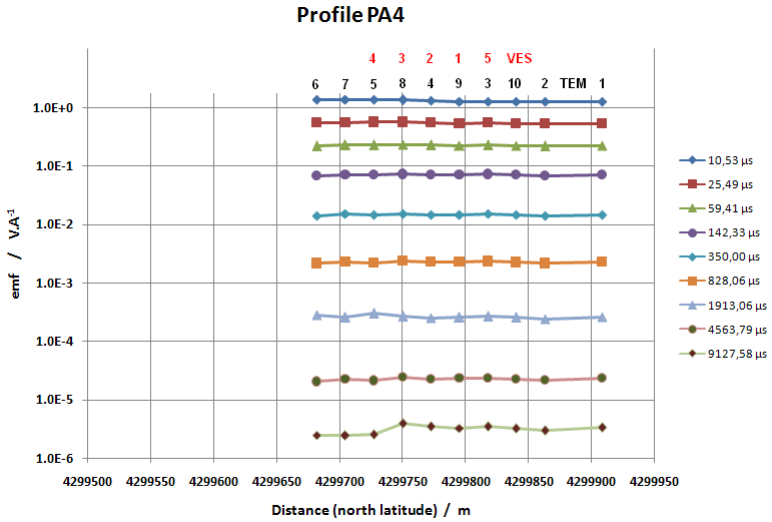

Figure 4.14 – Measured emf TEM signal for some time channels. Profile PA4.

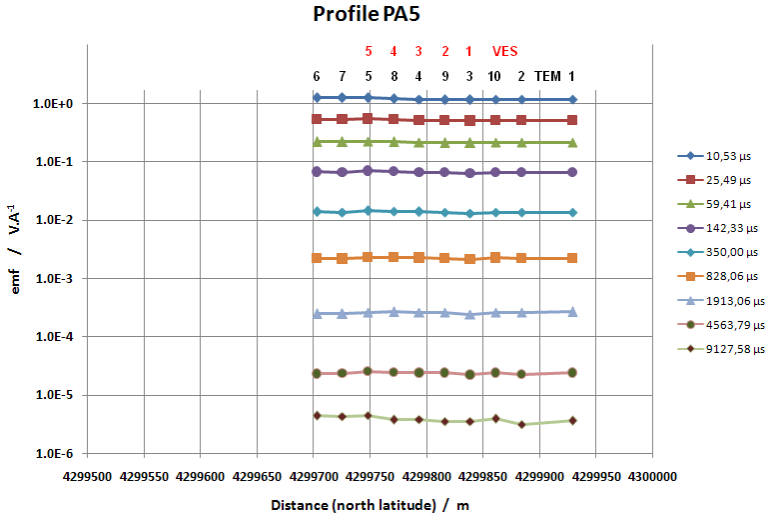

Figure 4.15 – Measured emf TEM signal for some time channels. Profile PA5.

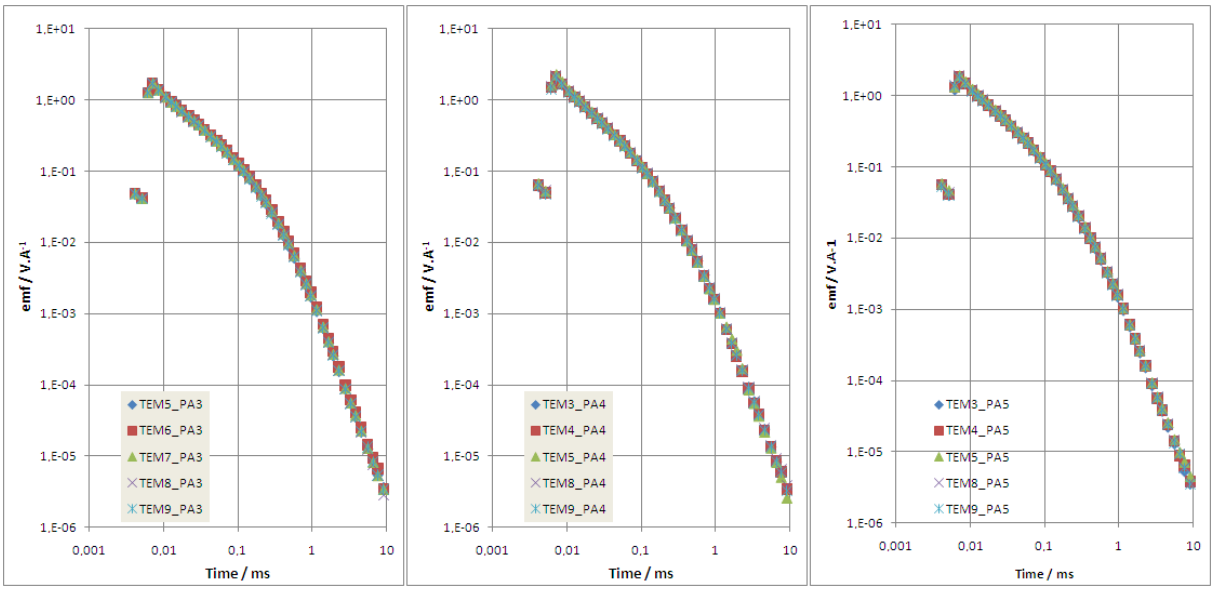

Figure 4.16 – Measured TEM data points signals. Profiles PA3 to PA5.

Those intensity values are very similar in sounding to sounding and also between the different profiles, with minor differences. The apparent resistivities of these soundings are consequently, very similar too and are plotted at figure 4.17. Minimum apparent resistivity value is near 1.5 Ω.m, and curve mimics the VES observed ones, as expected.

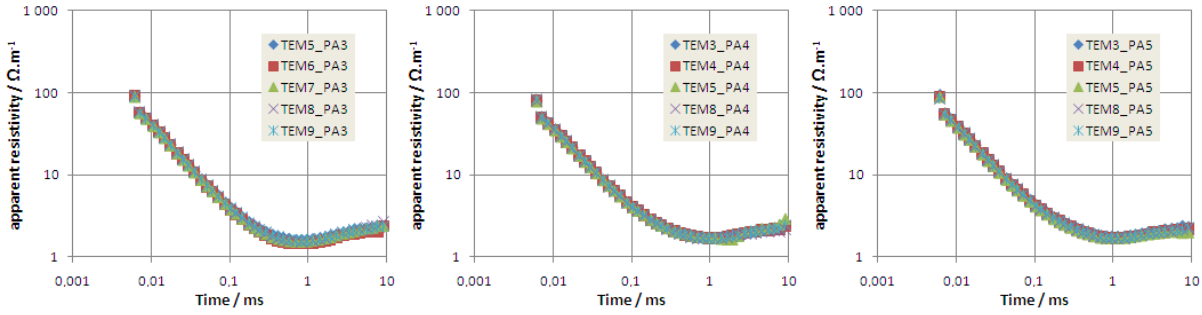

Figure 4.17 – TEM sounding apparent resistivity curves. Profiles PA3 to PA5

4.2.4 – TEM data modelling

The 1D inversion of TEM soundings was done using the smaller layers' number that gave best rms misfit error. The number of achieved layers (6) is greater than those ones found with VES, as TEM data exhibit greater quality. Side by side, comparison shows that TEM data point's quality is higher than of VES, with very small scattering, except at the very last points (late time channels).

Tables 4.5 to 4.7 contain TEM best models in profiles PA3, PA4 and PA5 respectively. Those soundings are at the same location of the VES soundings at each profile. The models are shown in figures 4.18 to 4.20, again respectively for profiles PA3, PA4 and PA5. Also included in each figure are all TEM soundings' models for each profile.

Table 4.5 – PA3 profile TEM models parameters; value and global misfit result.

Layer	TEM 5	TEM 9	TEM 6	TEM 8	TEM 7
1 ρ_a / Ω.m	2.8	2.8	2.4	2.8	2.5
2 ρ_a / Ω.m	0.51	0.49	0.45	0.47	0.48
3 ρ_a / Ω.m	1.3	1.3	1.3	1.2	1.3
4 ρ_a / Ω.m	2.2	2.0	2.2	2.4	2.2
5 ρ_a / Ω.m	5.8	8.5	5.3	6.1	5.5
6 ρ_a / Ω.m	1.6	2.5	1.3	2.1	2.8
1 h / m	3.0	3.0	2.6	2.9	2.7
2 h / m	1.9	2.0	2.3	2.2	2.3
3 h / m	11.4	10.9	11.3	9.7	10.6
4 h / m	22.0	18.9	21.2	23.4	16.1
5 h / m	52.0	29.0	47.2	51.0	35.3
misfit / %	**2.46**	**2.74**	**2.45**	**2.60**	**2.59**

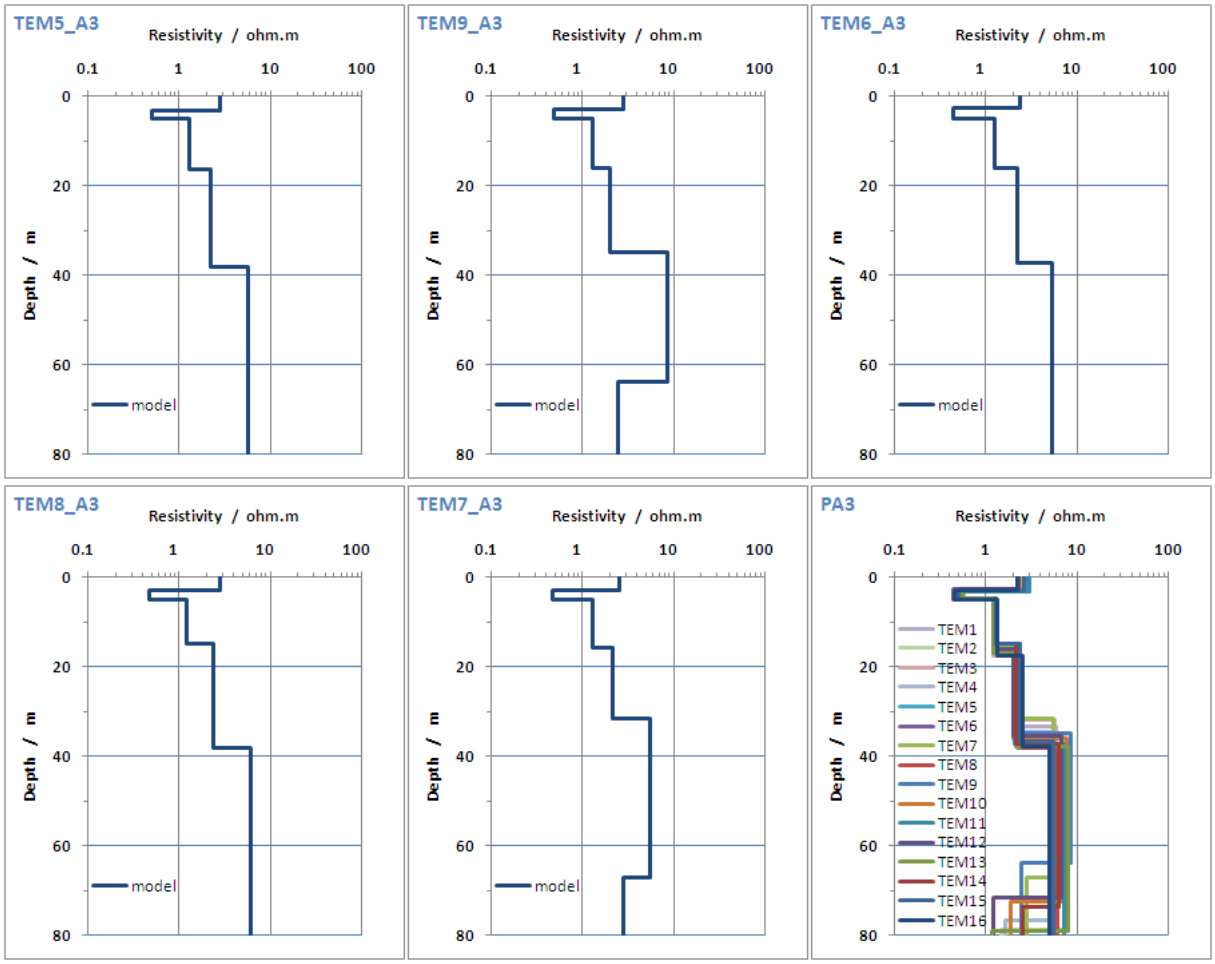

Figure 4.18 – PA3 profile TEM sounding models.

Table 4.6 – PA4 profile TEM models parameters; value and global misfit result.

Layer	TEM 3	TEM 4	TEM 5	TEM 8	TEM 9
1 ρ_a / Ω.m	2.2	2.2	1.9	2.0	2.3
2 ρ_a / Ω.m	0.61	0.64	0.61	0.67	0.64
3 ρ_a / Ω.m	1.5	1.5	1.6	1.5	1.5
4 ρ_a / Ω.m	1.9	1.9	2.0	1.8	1.9
5 ρ_a / Ω.m	10.8	13.6	20.0	11.9	13.1
6 ρ_a / Ω.m	2.7	1.9	2.3	2.0	2.0
1 h / m	3.1	3.1	3.3	2.9	3.2
2 h / m	1.9	1.9	1.6	2.0	1.9
3 h / m	17.7	15.3	21.2	15.4	16.5
4 h / m	19.0	22.8	17.9	20.8	22.0
5 h / m	25.6	29.5	40.6	26.8	31.1
misfit / %	**2.81**	**2.84**	**4.49**	**2.90**	**2.75**

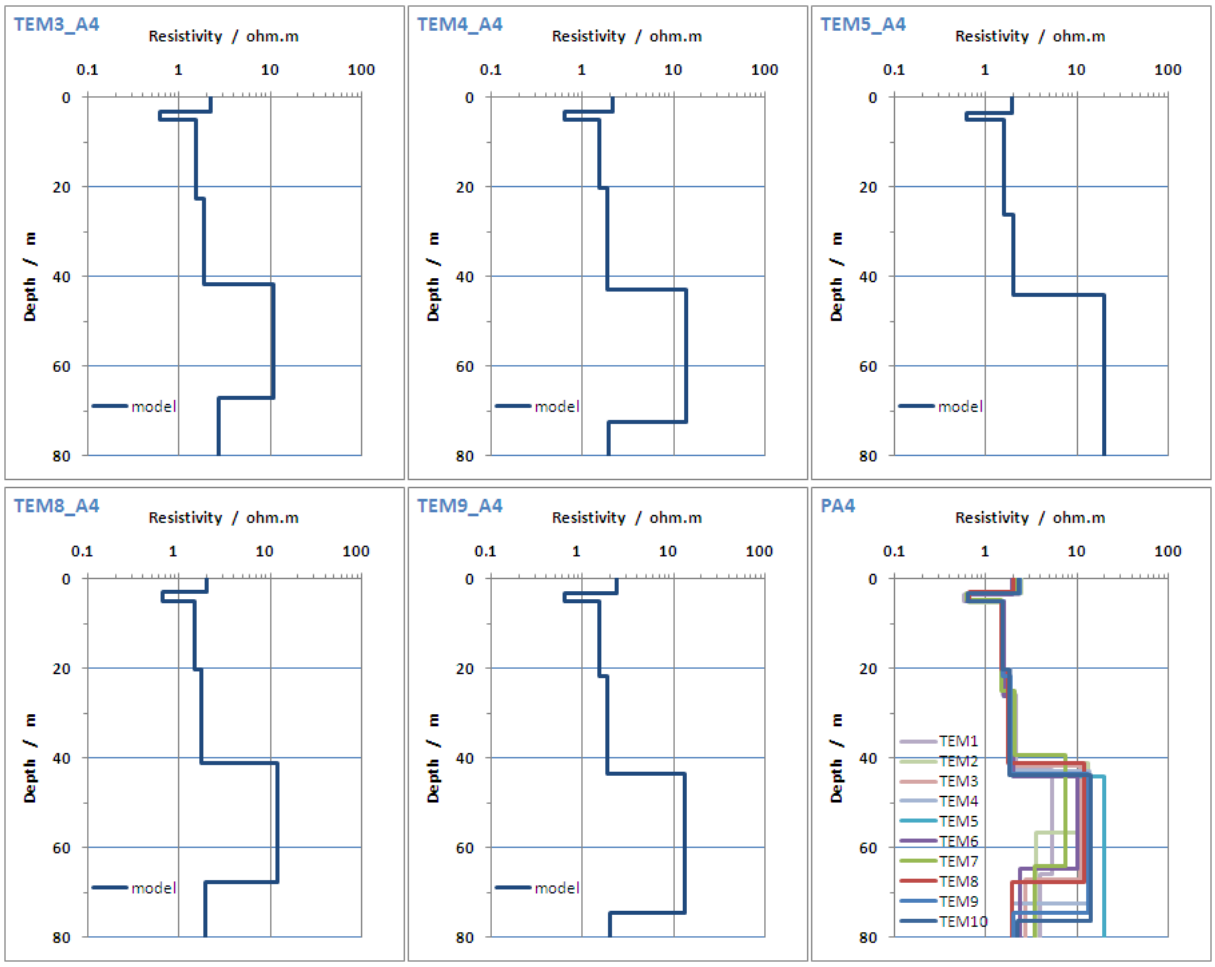

Figure 4.19 – PA4 profile TEM sounding models.

Table 4.7 – PA5 profile TEM models parameters; value and global misfit result.

Layer	TEM 3	TEM 4	TEM 5	TEM 8	TEM 9
1 ρ_a / Ω.m	3.2	2.9	2.4	2.7	3.1
2 ρ_a / Ω.m	0.57	0.55	0.54	0.57	0.55
3 ρ_a / Ω.m	1.7	1.6	1.6	1.6	1.6
4 ρ_a / Ω.m	1.2	1.2	1.3	1.2	1.2
5 ρ_a / Ω.m	38.9	13.9	9.9	23.2	12.0
6 ρ_a / Ω.m	2.6	1.4	1.5	2.0	1.9
1 h / m	3.6	3.4	3.2	3.2	3.6
2 h / m	1.6	1.5	1.5	1.6	1.5
3 h / m	20.0	20.5	19.5	19.6	19.7
4 h / m	11.0	11.6	11.2	10.7	11.5
5 h / m	24.5	39.6	34.3	27.6	36.0
misfit / %	**2.58**	**2.63**	**2.50**	**2.85**	**2.75**

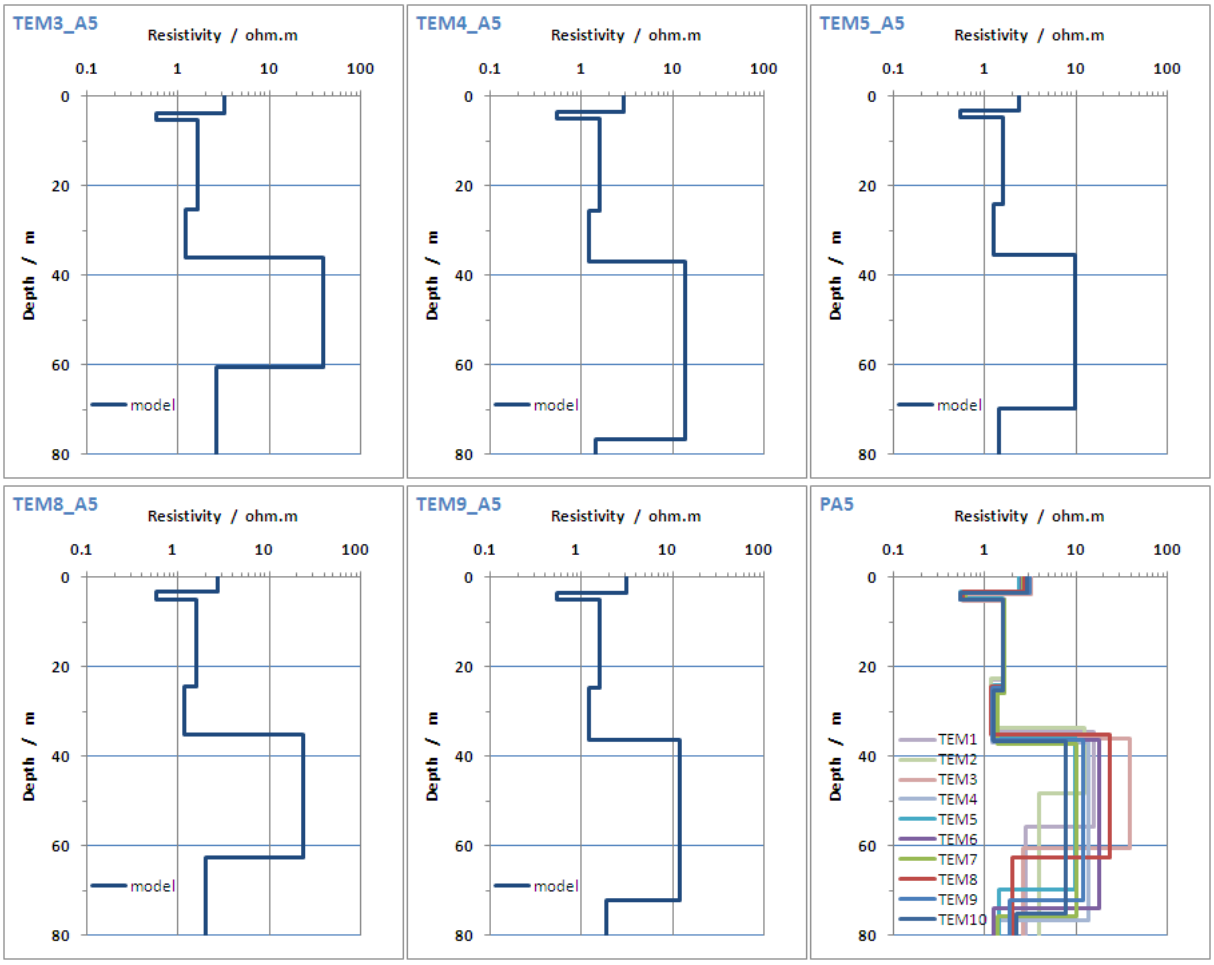

Figure 4.20 – PA5 profile TEM sounding models.

The model response curve and the data for sounding TEM5 at profile PA3 is shown in figure 4.21. All the other's TEM soundings have similar features.

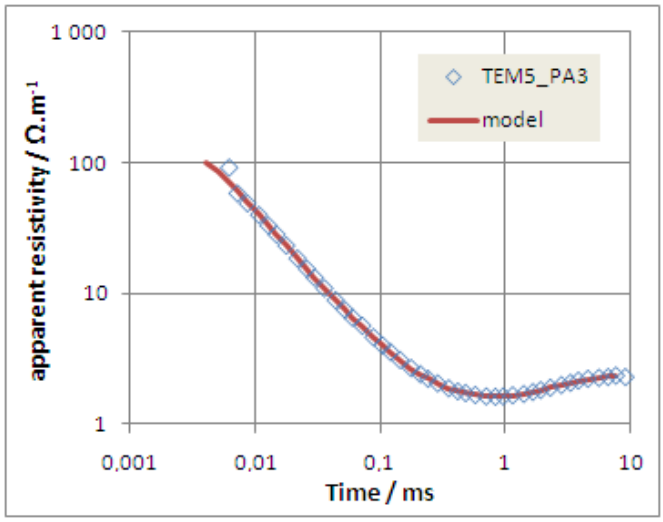

Figure 4.21 – TEM5 sounding data point and model fit curve. Profile PA3.

The mean model at each profile is given in the next table (4.8), and parameters are very similar to each other.

Table 4.8 – Mean TEM model to each profile.

Layer	PA3	PA4	PA5
1 ρ_a / Ω.m	2.6 ± 0.2	2.1 ± 0.2	2.9 ± 0.5
2 ρ_a / Ω.m	0.48 ± 0.03	0.63 ± 0.04	0.56 ± 0.02
3 ρ_a / Ω.m	1.3 ± 0.1	1.5 ± 0.1	1.6 ± 0.1
4 ρ_a / Ω.m	2.2 ± 0.4	1.9 ± 0.1	1.2 ± 0.1
5 ρ_a / Ω.m	6.2 ± 2.3	13.9 ± 6	19.6 ± 10
6 ρ_a / Ω.m	2.1 ± 0.8	2.2 ± 0.5	1.9 ± 0.7
1 h / m	2.8 ± 0.2	3.1 ± 0.2	3.4 ± 0.2
2 h / m	2.1 ± 0.2	1.9 ± 0.3	1.5 ± 0.1
3 h / m	10.8 ± 1.1	17.2 ± 4	19.9 ± 0.6
4 h / m	20.3 ± 4.2	20.5 ± 2.5	11.2 ± 0.5
5 h / m	42.9 ± 14	30.7 ± 10	32.4 ± 7

TEM method can detect the first two layers, but as they are very shallow ones compared to the loop square length side, the corresponding thickness is not well solved. That is also true for the last but one layer thickness (fifth one), were a T-equivalence do exist between layers' parameters. This fifth layer thickness is related to the last layer resistivity values that come from less quality data points (late time points with low SNR).

The bottom of fourth layer with mean depth of about 35, 42 and 35 meters, at PA3, PA4 and PA5 profiles respectively, match the Quaternary base position taken from the seismic data. All the TEM models show also a low resistivity contrast between layer three and layer four. This interface exhibits a mean position value of 15.8, 22.2 and 24.8 meters, at PA3, PA4 and

PA5 profiles respectively. This finding agrees very well with the interpretation of the reflection seismic data from profiles PA3 to PA5, where the interface mean position is placed at 17, 20 and 23 meters depth, respectively, as seen in figure 4.22.

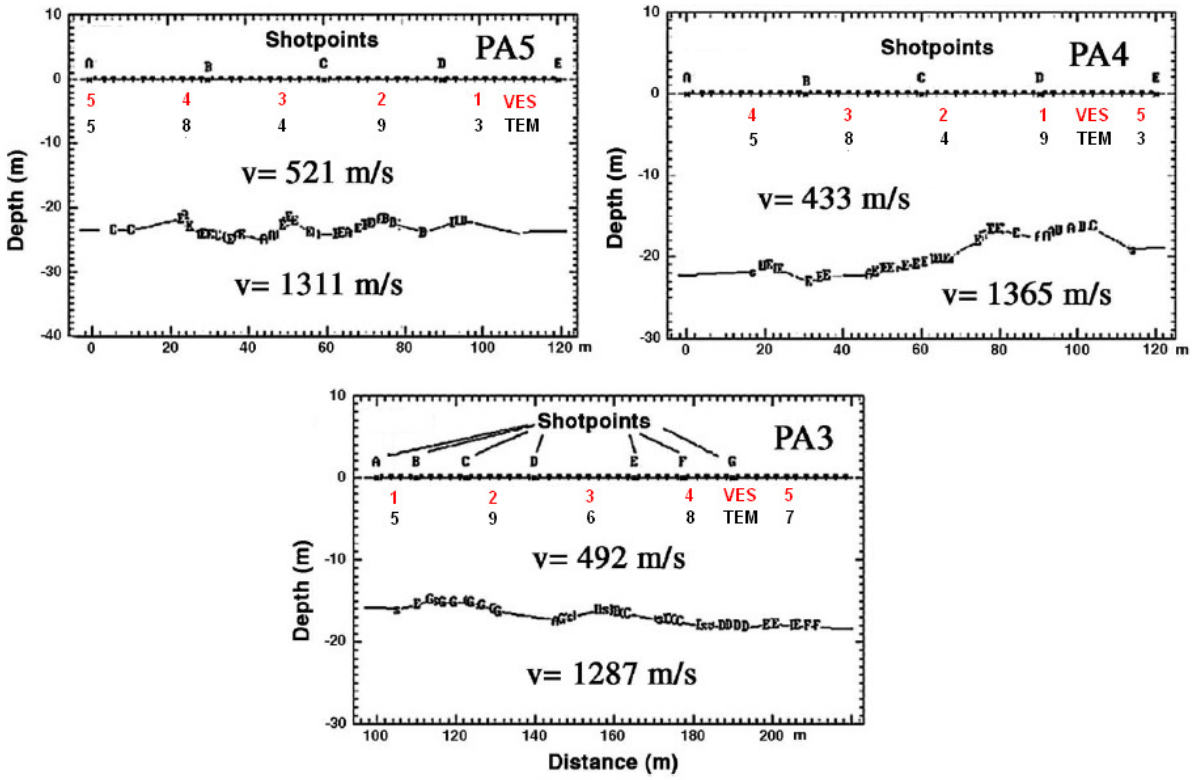

Figure 4.22 – Refraction interpretation of the reflection seismic data from profiles PA3 to PA5. Interface letters represent emerging rays from the respective surface shot. P-wave velocities are indicated for each layer. Also shown are the locations of the VES and TEM soundings over the seismic profiles. (Adapted from Carvalho *et al.*, 2006).

With these few seismic P-wave velocity values, it's impossible to properly quantify the relationship between velocity to electric resistivity relation, as stated e.g. by Meju *et al.* (2003) and references therein. The common link is that resistivity and velocity are both functions of porosity. At present situation, one can conclude that the resistivity is more uniform in shallow layers than in the deeper one. These resistivity values of the deepest layer decrease from profile PA3 (east) to profile PA5 (west side), along with increasing deep. The explanation is a change of the stratigraphic unit parameters from east to west, namely the clay content, having upper layers higher porosity. TEM method performs a volumetric integration response and it smoothes all the small-scale and small contrast geologic variations. As a consequence, the perfect match between TEM models and seismic data is not achieved. The latter is only affected by ray path and lateral velocity variations.

4.3 – TEM versus VES comparison

The models from VES and TEM soundings are roughly the same, although with few differences, especially between profiles, as exposed in tables 4.4 and 4.8 .VES gives better solution to the very shallow first layers, and TEM a better resolution to the small variations between low resistivity layers. Figure 4.23 shows the resistivity cross-section and figure 4.24 the side by side collocated VES and TEM models.

Profile PA3 - Both models give similar resistivity values for the bottom layer. The major differences are at the thickness of two first layers (as stated before) and VES third layer depth interface position which is approximately in the middle of the fourth TEM layer. The resistivity of the third VES layer matches that one calculated from TEM data for the third layer at most of the sites.

Profile PA4 - At this profile the same pattern is seen, but resistivity values seem to be somewhat shifted.

Profile PA5 - The major difference between this profile and the previous two profiles is that the interface position of the third layer calculated from VES is approximately the same of fourth TEM layer. This has to do with resistivity contrast between third and fourth TEM layers, as fourth layer resistivity value is in-between more resistive upper and lower layers.

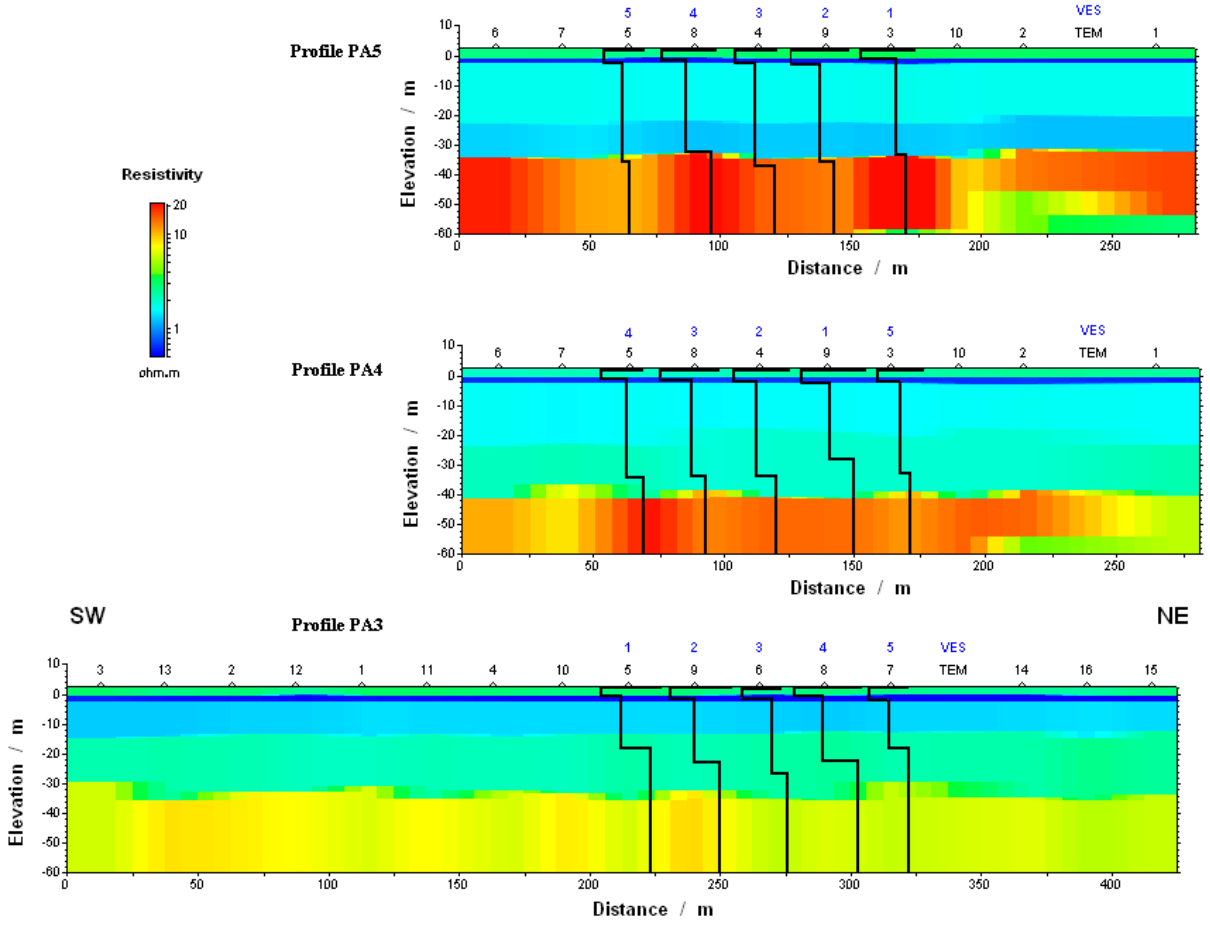

Figure 4.23 – TEM resistivity profiles cross-section with superimposed VES models.
Cross-sections stitched-together output from AEMR software.

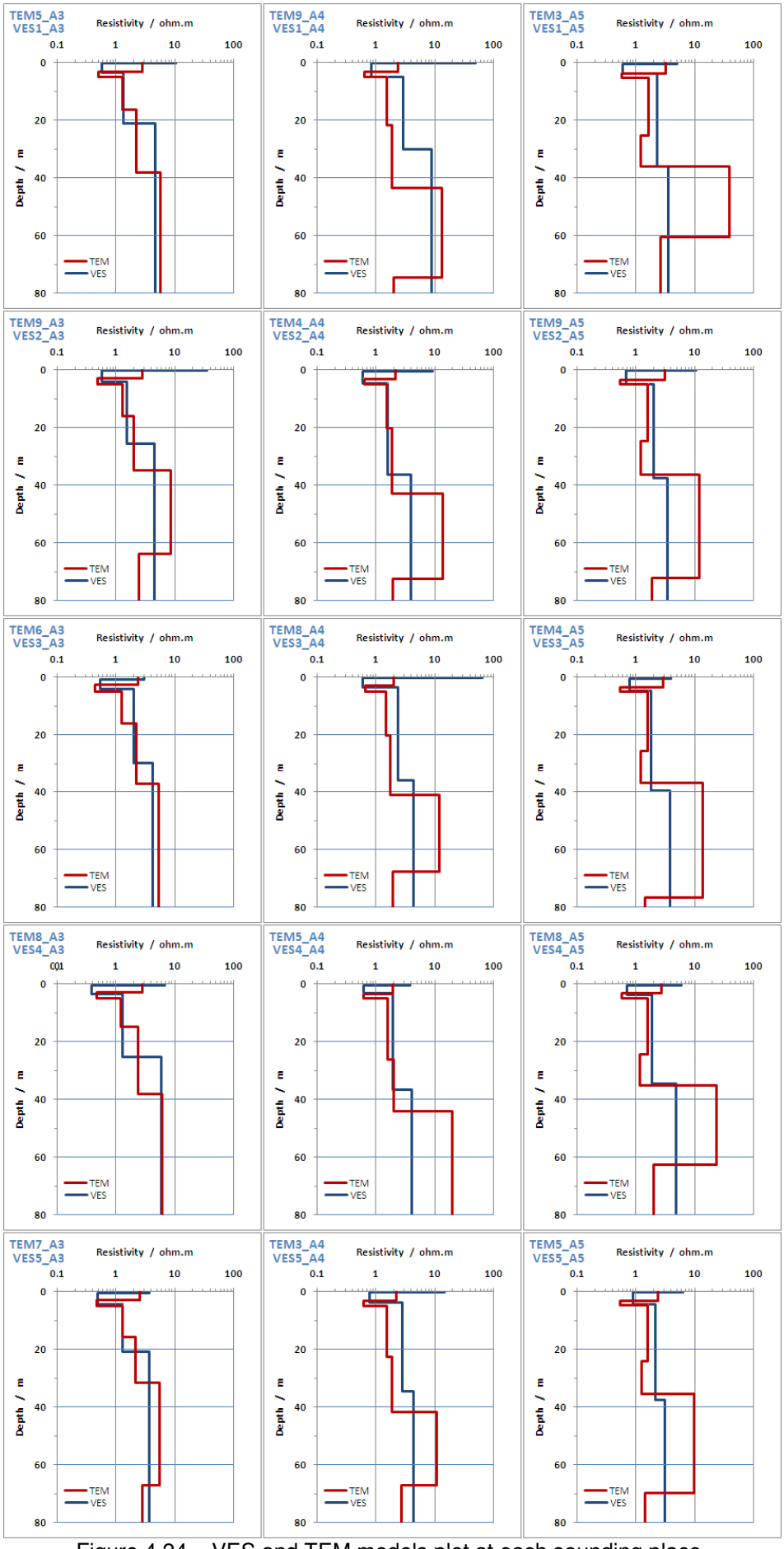

Figure 4.24 – VES and TEM models plot at each sounding place.

It seems clear that over this geologic sedimentary environment, with high conductive electric layers, TEM method as the ability to detect interfaces between layers with small contrast very near the surface (at half one of the loop sides). Closer to the surface, where the loop is laid down, the method detects low resistivity layers, but it's impossible to ascribe a correct thickness to them. These findings are in accordance with technical descriptions and specifications of TEM-FAST 48. Equipment's manual states that investigation depth, with an L side square single loop, ranges from L/10 to 3L below the surface (AEMR, 2006). With a loop 50 m × 50 m this will correspond from 5 m to 150 m.

The upper limit it's confirmed with this test data. If a better resolution is intended at the shallow surface, we have just to decrease the loop size.

The lower limit is not fulfilled although the last layer's model (sixth layer) is within the "theoretical limit". However, the last data points' quality does not clearly support it. That can be explained by the loop low magnetic moment input signal. Loop's current stays always around 1,4 A, below the possible equipment's maximum of 4 A. Being so, the lower limit is in the L to 2L range at present situation test.

4.3.1 – Resistivity static shift

The DC resistivity method values could be affected by an offset, called electric static shift (or galvanic distortion). This is due to the presence of small-scale heterogeneities, near the ground surface at the sounding place. The result is a distorted or shifted curve (e.g. Barker 1981; Bahr 1991; Spitzer 2001) and that must be (when possible) accounted before interpretation. If not, it will lead to erroneous interpretations, especially at resistivity values.

To have the quantitative static shift value, a scaling relationship between the spatial (VES) and temporal (TEM) sounding configurations must be applied. That relation is given by Meju (2005), as:

$$t = \mu\pi\sigma L^2/2 \qquad (4.1a)$$

or

$$L = 711{,}8\sqrt{t\rho} \qquad (4.1b)$$

with *t* the transient time (in seconds) and *L* the one-half electrode-array length (AB/2). Material's magnetic permeability is taken to be equal to that of free-space.

Those relations were applied to collocated VES and TEM data, as plotted at figure 4.25. As it can be seen, most of the VES soundings present any or meaningless static shift, namely at profile PA3, but several ones are notoriously shifted against the TEM data scaled values. Contiguous VES 5 and 1 at profile PA4, and also contiguous VES 3, 4 and 5 at profile PA5 exhibit an upper and non negligible shift.

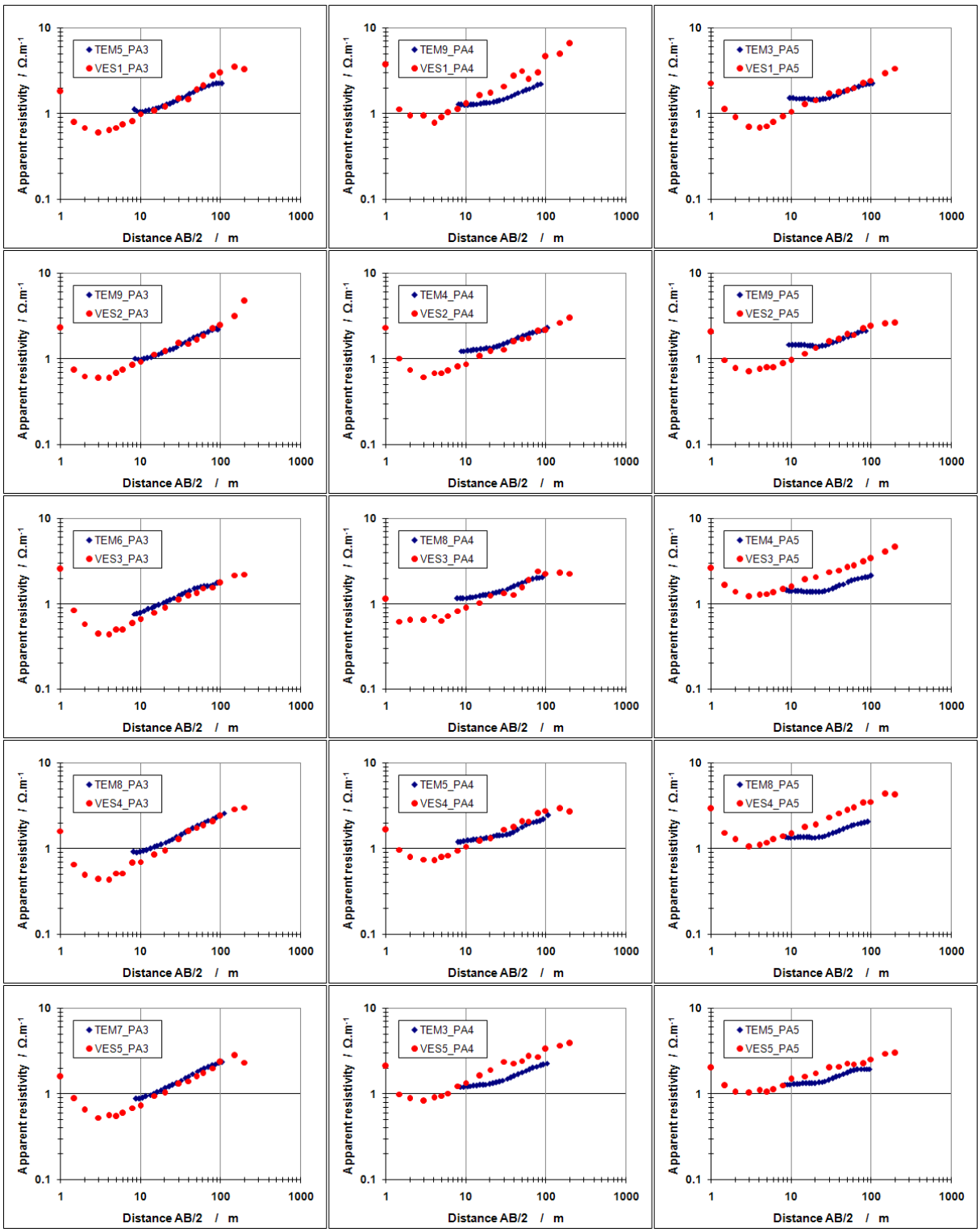

Figure 4.25 – Apparent resistivity VES and TEM scaled data, at each profile sounding position.

4.3.2 – TEM – VES joint inversion

The VES and TEM soundings' data were modelled all together with a spatially constrain inversion (SCI) method, based on the algorithm mention at previous chapter. The resistivity cross sections to each profile are shown in figure 4.26. The thickness of the model's blocks

increases with depth; that is, are thinner at the surface. The computational tests started always with a uniform resistivity model. The obtained resistivity values and interfaces (Santos *et al.*, 2010) are very similar to the 1D model inversions, which proven the validity of both inversion algorithms.

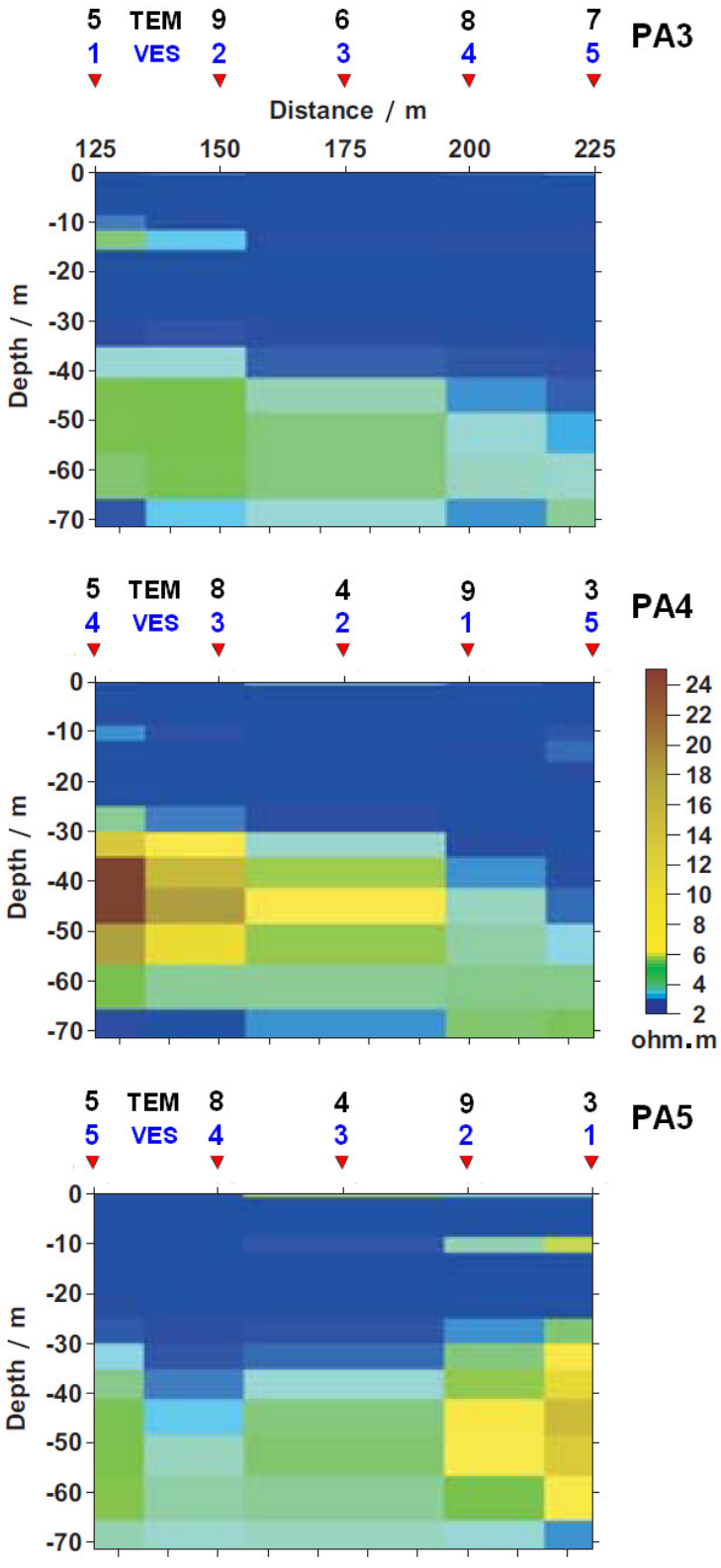

Figure 4.26 – Joint VES and TEM block resistivity cross sections inversion. Profiles PA3 to PA5.

5
ELECTRICAL-HYDROGEOLOGICAL RELATIONSHIP

On this fifth chapter, the relations between the measured geophysical data, namely the resistivity and the hydrogeological properties of rocks, soils and groundwater chemical characteristics is studied.

5.1 – Introduction

To be useful, the geophysical data, most times acquired at the surface, must be correlated with subsurface properties. That's the main goal of most hydrogeophysical studies. Estimation of subsurface porosity and hydraulic conductivity is often the primary objective at water-saturated environments. The usual difficulty arises by the fact that hydraulic conductivity at geologic formations can span's orders of magnitude over relatively small spatial scales. It is then a challenge to accurately characterize the subsurface aquifer properties by just working piecewise information from networks of widely spaced boreholes or at worse cases only a few ones.

A more accurate and complete underground characterization can be achieved by using an integrated exploration approach in which wells, boreholes and geophysical data sets are interpreted together. The necessary key step is the transformation of measured geophysical properties into the desired hydrogeological parameters, not only qualitatively but especially quantitatively. This conversion typically relies on petrophysical relationships. These relationships can be developed at the field-scale level, by co-located hydrogeological-geophysical data sets or through laboratory experimentation over rock and soil samples. It can come also from theoretically based models.

However, even with joint analyses, the generic hydrogeophysical site characterization can be a difficult problem. The subsurface geology may contain much localized features such as weathered areas, bedding planes, bedrock, faults, joints and fracture zones, in addition to continuously distributed textural and composite variations. This gives rise to an expected multiscale complexity, and the geological medium can be viewed like a discrete hierarchy (Vogel *et al.*, 2002), were different length scales possess different patterns of spatial variability and correlation or like a fractal (Mandelbrot, 1988), in which each length scale possesses a similar pattern of spatial variability and correlation. The corresponding spatiotemporal response by EM controlled source over a discrete hierarchical or fractal geological medium is surely a complicated one, characterized by some broadband, power-law spatial wave number spectrum (Everett and Weiss, 2002).

The behaviour of the different geological scale, affects most of the measured hydrogeologic property' values, principally the hydraulic conductivity (Neuman, 1994; Winter and Tartakovsky, 2001). This important parameter increase to increasing measurement scale, as seen in figure 5.1. At Basin-scale, the hydraulic conductivity estimates are often one to two orders of magnitude higher than aquifer pumping test determinations, which by turn are

larger than laboratory measurements on core samples of the same aquifer material. The electric conductivity (EC) like the hydraulic conductivity are both transport properties of the geological medium. They depend on geometric parameters at many length scales, such as the fracture's networks connectivity and the tortuous microstructure of the pore space. Thus, EC should also exhibit similar scale effect. Field-based studies on these subjects are scarce (Purvance and Andricevic, 2000).

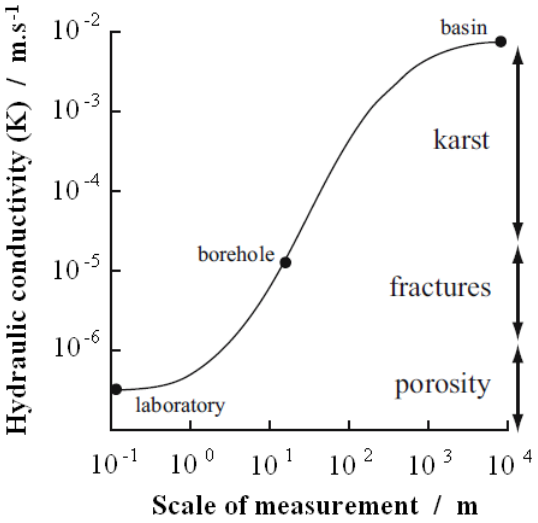

Figure 5.1 - Dependence of hydraulic conductivity with measurement scale, (modified after Person *et al.*, 1996).

The geophysical electromagnetic field data, acquired by different methods, can provide high-resolution information about underground conditions. Both the structural and the electrical property information, by spatial mapping, can provide important models constraints to hydrogeology. Structural geometric information can be used to define and delineate hydrostratigraphic units as well as the locations of fractures and faults. The EC values are used to qualitatively characterize the rock and soil type as well as the pore fluid properties estimation. Petrophysical models can often be used to make quantitative predictions about the rock and soil properties, such as water content, water conductivity, porosity, clay content and hydraulic conductivity.

These petrophysical models of the EC and hydrogeological properties of rocks and soils are usually formulated in terms of intrinsic properties of the geological material, like pore and grain topology and of the chemical and physical properties of the pore fluids. Relationships are often non-unique, even with some common controlling factors. The use of multiple source data can be used to constrain results, knowing, for instance, the pore fluid conductivity, porosity, and other relevant geological information. In general several simplifications have to be done before empirical relationship's application between the hydrogeological and electrical properties. These empirical relations are typically based on correlations made between the electrical and hydrogeological measured data from a specific site. The problem with these empirically relations between electrical and hydraulic parameters, is that they often work reasonably well only to the specific study site or to sites with similar characteristics (e.g., Huntley, 1986; Purvance and Andricevic, 2000).

5.2 – Hydrological and electrical properties

The most important and relevant parameters used to characterize the aquifer and fluid behaviour, that are usually estimated from or measured in the fields collected data are next described.

5.1.1 – Hydrological properties

The underground soil and the rocks are composed by solid mineral grains and the corresponding pore space. The porosity (Φ) is defined as the ratio of pore volume (or non solid space of soil) (V_p) to the total volume of the sample (V_t). A distinction has to be given in the materials who contain isolated (not connect) pores. In these cases, the effective (open) porosity of the connected pore space is less than the total porosity. Fractured systems like some basaltic ones can be seen (at-large scale) as a porous medium, although geometry of pore space is rather different from a common sand or sandstone aquifer system. The porosity associated to this fractured system is considered as a secondary porosity overlaying the primary pore space network, and can surpass primary one. Table 5.1 gives measured range porosity values for most geologic environments, collected from several literature sources.

Table 5.1 – Representative porosity ranges for soils, materials and rocks.
(after Lesmes and Friedman, 2005)

Geologic medium / material	**Porosity range**
Peat and diatomaceous earth	0.80 - 0.90
Shell fragments	0.62 - 0.72
Soil	0.50 - 0.60
Clay	0.40 - 0.70
Shaley sand	0.41 - 0.48
Silt	0.35 - 0.50
Mean to coarse mixed sand	0.35 - 0.40
Uniform sand	0.30 - 0.40
Fine to mean mixed sand	0.30 - 0.35
Gravel	0.25 - 0.40
Gravel and sand	0.20 - 0.35
Sandstone	0.05 - 0.30
Fractured basalt	0.05 - 0.50
Karst limestone	0.05 - 0.50
Limestone	0.01 - 0.20
Shale	0.01 - 0.10
Fractured crystalline rock	0.01 - 0.10
Dense crystalline rock	0.01 - 0.05

In saturated media, from where most data concerns, the rate of fluid flow through porous materials is controlled by the saturated hydraulic conductivity (*K*). For homogeneous and isotropic materials, *K* (in $m.s^{-1}$) is given by (e.g., Fetter, 2001):

$$K = k_S \frac{g \delta_w}{\mu} \qquad (5.1)$$

with; k_s the hydraulic permeability (m^2), *g* the gravity acceleration ($m.s^{-2}$), δ_w the fluid density ($kg.m^{-3}$) and μ the fluid dynamic viscosity (Pa.s).

The flow rate is proportional to *K* and to the hydraulic gradient through classical Darcy's relation, for laminar flow. The range of values for the hydraulic conductivity is given below in table 5.2.

Table 5.2 – Hydraulic conductivity of several formations, (after Hölting, 1989).

Lithologic formation or rock	***K*** **/ m.s^{-1}**
Gravel, clean	10^{-1} - 10^{-2}
Sand, coarse	≈10^{-3}
Fractured basalt	10^{-3} - 10^{-4}
Sand, medium	10^{-3} - 10^{-4}
Sand, fine	10^{-4} - 10^{-5}
Sand, silty	10^{-5} - 10^{-7}
Silt, clayey	10^{-6} - 10^{-9}
Clay	<10^{-9}

The traditional (empirical) expressions to predict hydraulic permeability of saturated sands from just particle grain size was formulated by the end of XIX century, e.g. Seelheim (1880) and Hazen (1895) (Matthess and Ubell 2003). Both are power law based expressions. The Hazen original formulation (*K* in $cm.s^{-1}$) is given by:

$$K = C_H D_{10}^2 \qquad (5.2)$$

with C_H the Hazen empirical coefficient and D_{10} the particle size for witch 10 % are finer (in cm). Published value of C_H ranges from 1 to 1,000 and Hazen formula's applicability is generally limited to $0.01 < D_{10} < 0.3$ cm (Hazen 1892, 1911; Holtz and Kovacs 1981; Coduto 1999).

Many variants of this power law had been establish, most of them having exponent values in the 1.10 to 2.05 range, with most values significantly less than 2 (e.g. Shepherd, 1989). All these empirical formulations are less accurate when compared with latter developed semi-empirical and semi-theoretical expressions (Carrier, 2003). As the hydraulic permeability, is a function of the existing pore size distribution, they connectivity and tortuosity of pore network. In granular materials, the topology of the pore space is given by the grain size distribution, their packing and cementation.

The formulations of hydraulic permeability models can either be in terms of the pore space characteristics or in terms of the solid mineral grains (e.g., Nelson, 1994). The equivalent channel fundamental model developed by Kozeny (1928) and Carman (1937), known as K-C model, assumes that flow through a porous medium can be represented by the flow through a bundle of capillaries (Carman, 1939). Each of this capillary is assumed to represent an independent flow path through the medium. The fractured mediums can act and can be thought accordingly. The effective path length (L_a) is greater than (or equal) to the macroscopic sample length (L). The tortuosity (T) is defined as the square of effective path length to sample length ratio. The relation between these parameters is given and follows experimental considerations of laminar viscous flow through tubes, (e.g., Scheidegger, 1974);

$$k_s = \frac{\phi r_h^2}{fT} \tag{5.3}$$

with; r_h the effective hydraulic radius (in m) and f the tube shape or form factor (a dimensionless number between 1.7 and 3.0). Φ is porosity.

The more common indication of the hydraulic radius is given by reciprocal of the specific surface area (S_p) (in m^{-1}), the ratio of pore inner surface area to its volume. Furthermore, the defined tortuosity can be related to electrical (resistivity) formation factor (F) through the following relationship (e.g., Nelson, 1994);

$$T = \left(\frac{L_a}{L}\right)^2 = \phi F \tag{5.4}$$

with formation factor defined as:

$$F = \frac{\sigma_w}{\sigma_b} = \frac{\rho_b}{\rho_w} \tag{5.5}$$

were σ_w and σ_b are the fluid and system bulk EC (ρ_w and ρ_b the corresponding resistivity values), respectively. It is a purely geometric parameter, describing how the porous medium obstructs transport processes. Thus, it is often assumed to be an indicator of the hydraulic tortuosity (Archie, 1942). It is detailed further on this chapter. Table 5.3 presents the range value of the formation factor of several media.

Table 5.3 – Formation factor of different lithologic media.
(after Heiland 1968).

Lithologic formation or rock	Formation factor
Peat and Diatomaceous earth	1.0 - 1.5
Marl, loess, clay and sandy soils	1.5 - 4
Porous clay, sand, sandstone and dolomites	3 - 20
Clay and sand in general	20 - 40
Dense limestone and sandstone	50 - 100
Igneous and metamorphic rocks	100

The K-C equation (5.3) is more practical when expressed like:

$$k_s = \frac{1}{fFS_p^2} = \frac{\phi r_h^2}{fT} \tag{5.6}$$

because the F and S_p are well-defined physical parameters that can be measured, whereas T and r_h are theoretical ones that cannot be directly measured.

More relationships like those ones expressed by equations (5.1) and (5.6) have been identified and also updated by many authors. Relationships between porosity and hydraulic properties are usually proposed by semi-log and log-log regression's analyses with physical basis in a set of geometric and hydrodynamic considerations. Those correlations were obtained empirically, often aided by dimensional analysis and theoretical considerations, and are known as phenomenological models (Dullien, 1979). Those relationships with hydraulic properties include particle's dependence on pore sizes for both mean values as well as the entire distribution of values. At grain-scale permeability, models can predict k_s to be dependent and function of the square of an effective grain size and grain sorting, (e.g., Fetter, 2001). Those based on particle size are typically empirical or phenomenological, while the models based on pore sizes more often include assumptions regarding pore structure, shape, connectivity (or tortuosity). A rather complete list of these relationships is given by Flint and Selker (2003). A common and generalized applied expression is the one from Georgi and Menger (1994);

$$k_s = \frac{r_h^2}{fT^2}\frac{\phi^3}{(1-\phi)^2} \tag{5.7a}$$

from previous K-C relation,

$$k_s = \frac{D_{50}^2}{180}\frac{\phi^3}{(1-\phi)^2} \tag{5.7b}$$

D_{50} is the grain diameter (in cm) of the 50 % grain fraction size distribution (geometric mean).

All these K-C models, often called hydraulic radius theory, are closest to a geometric model because assumptions on pore structure are made, whereas a purely phenomenological theory based on empirical tests often makes no such assumptions. When particles deviate strongly from spherical, broad particle size distribution, the K-C model often gave worse results. The disagreement's reasons between k_s predictions and experimental values are primarily due to the fact that natural porous mediums are not composed of well-connected, tubular flow conduits, or constant-diameter pores, which is the basis for many of the theories and proposed models. The empirical coefficients are introduced to account for the following situations. Anomalously high tortuosity (in high porosity media), the assumption of conduit flow is rather and more appropriately a ''flow around submerged objects''. The friction drag mechanisms are dominant over viscous shear mechanisms that determine the friction in conduit flow. If pores of different sizes are present and operate in parallel, the k_s is dominated by the largest pores rather than if all pores had the same diameter. If pores of different sizes are operating serially, the sequential variation in the effective cross-section of flow channels tends to result in a k_s linked with the smaller cross section. These two last

assumptions operate oppositely, and there may be some cancellation effects in a porous medium (Flint and Selker, 2003).

Better results are expected when knowledge of tortuosity is introduced. Pape *et al.* (1987) had shown that tortuosity behaves as a fractal and depends on the effective radius of pore to grain radius ratio relation (r_h/r_{grain}) with an exponent involving the fractal dimension (D) of media. Tortuosity increases with increasing fractal dimension in the range of $2.0 < D < 2.4$. Strongly fractured and claystones rocks show a fractal dimension in the range of $2.4 < D < 3.0$. These later rocks are characterized by a high degree of connectivity of the pore space system, which in turn reduces their tortuosity (Pape and Schopper, 1988).

5.1.2 – Electrical properties

The observed and measured electric conductivity of soils and rocks is essentially a function of the: water (electrolyte) content, the conductivity of the electrolyte saturated solution and the lithology. The electrical conductivity of aqueous solution increases with the concentration, mobility and electronic charge of the ions in the solution, as well as with the temperature of the solution. Considering pure water, it has a relatively very low electrical conductivity of about 0.04 $\mu S.cm^{-1}$ (or 250000 Ω.m electric resistivity) (Weast, 1983). The conductivity of natural groundwater with dissolved salts and other ionic components is much larger. The pore water conductivities range from about 100 $\mu S.cm^{-1}$ (100 Ω.m) for freshwater aquifers to 200000 $\mu S.cm^{-1}$ (0.05 Ω.m) for oil field brines (e.g., Schön, 1996) being the seawater EC around 50000 $\mu S.cm^{-1}$ (0.2 Ω.m). Thus, groundwater EC value can give us directly the quality condition. That is, the salt content amount, as described later on. Table 5.4 shows the range of EC values for several waters found in nature.

Table 5.4 – Natural water EC and quality classification.

Water natural source	EC / $\mu S.cm^{-1}$	Water quality
Meteoric waters (precipitation)	10 - 300	Fresh
Surface waters (lakes and rivers)	3 for very pure waters	Fresh
	20 - 300 in igneous regions	Fresh
	100 - 1000 in sedimentary regions	Fresh to Brackish
	10^5 for salt lakes	Saline
Soil and ground waters	60 - 300 in igneous regions	Fresh
	Up to 2×10^5 (average around 200)	Fresh to Saline
Mine waters (copper, zinc, i.e. sulphates)	not usually less than 3×10^4	Brackish to Brine

Classification of water quality can be on salt content amount or EC values, (see table 5.5 and 5.6), respectively. Higher salinity upper limit description for fresh water is also found varying between 1 to 3 $g.L^{-1}$, but the standard drinkable level is 0.5 g L^{-1}.

Table 5.5 – Natural water salt content quality classification ($mg.L^{-1}$).

Fresh water	Brackish water	Saline water,	Brine
< 500	500 – 30000	30000 – 50000	> 50000

Table 5.6 – Natural water salinity EC rating classification (μS.cm^{-1}).

Low	Moderate	High	Very high	Extremely high
< 650	650 – 1300	1300 – 2900	2900 – 5200	> 5200

The EC of an aqueous solution containing *m* ionic component is given by the following expression, valid for low salt concentrations, when ion-ion interactions can be neglected:

$$\sigma_w = \sum_{i=1}^{m} \alpha_i c_i z_i \mu_i \quad (5.8)$$

were α_i is the degree of dissociation, c_i the ionic concentration (C.m^{-3}), z_i the ionic valence and μ_i the ionic mobility (m^2.s^{-1}V^{-1}) for the ith component of solute, (e.g., Schön, 1996).

The mobility values of the most common water ions are illustrated in table 5.7. Water components, the hydroxide (OH^-) and the hydron (H^+) have the highest mobility values.

Table 5.7 – Mobility of water's common ions at 25 ℃.
(Adapted from (Vanysek, 2002)).

Ion	Mobility / m^{2}s^{-1}V^{-1}
H^+	36.2×10^{-8}
OH^-	20.5×10^{-8}
SO_4^-	8.3×10^{-8}
Na^+	5.2×10^{-8}
Cl^-	7.9×10^{-8}
K^+	7.6×10^{-8}
NO_3^-	7.4×10^{-8}
Ca^{2+}	3.1×10^{-8}
Mg^{2+}	2.7×10^{-8}
HCO_3^-	4.6×10^{-8}

The EC temperature dependence of the electrolyte is almost entirely due to the liquid viscosity temperature dependence, which in turn affects directly the ionic mobility of water components and the degree of dissociation (Lesmes and Friedman, 2005).

The observed and measured EC variations with temperature are approximately linear over the range of normal ambient temperatures. Temperature dependence of pure Sodium Chloride (NaCl) solutions has been studied and described by several authors (e.g., Arps, 1953; Worthington *et al*., 1990). They empirical equations gave a slope temperature coefficient variation of 0.022 ℃$^{-1}$. This value is also valid for other ions. For natural waters, the actual slope value is very similar. That is, around a mean value of 0.019 ℃$^{-1}$ (Hayashi, M., 2004). Thus, the electrolyte groundwater conductivity for a temperature other than standard can be computed by:

$$\sigma_w(T) = \sigma_{25}[1 + 0{,}020(T - 25)] \quad (5.9)$$

were σ_{25} is the water solute EC value at standard 25 ℃.

This means a 2.0% EC change per Celsius degree and a doubling EC value with a 50 ºC temperature increase. A groundwater aquifer system with a temperature variation of just a couple of degrees throughout the year exhibits only a minor EC temperature induced variation.

Empirical relationships also exit relating EC of aqueous solutions to the total dissolved solids (TDS) content (e.g., Fishman and Friedman, 1989);

$$\sigma_w \cong \beta \times \mathrm{TDS} \qquad (5.10)$$

with water EC unit in $\mu S.cm^{-1}$ and TDS in $mg.L^{-1}$.

Depending on ionic composition of water solution the constant β can ranges from 1.2 to 2.0 (at normal ambient temperatures). The average value for β is 1.5, usually applied to predict the electric conductivity of natural waters at 25 ºC (Fishman and Friedman, 1989).

The major salt component of seawater is NaCl with an 85.6% total salt mass content (salinity of 35). In figure 5.2 the EC (and resistivity) dependence with NaCl mass concentration is shown.

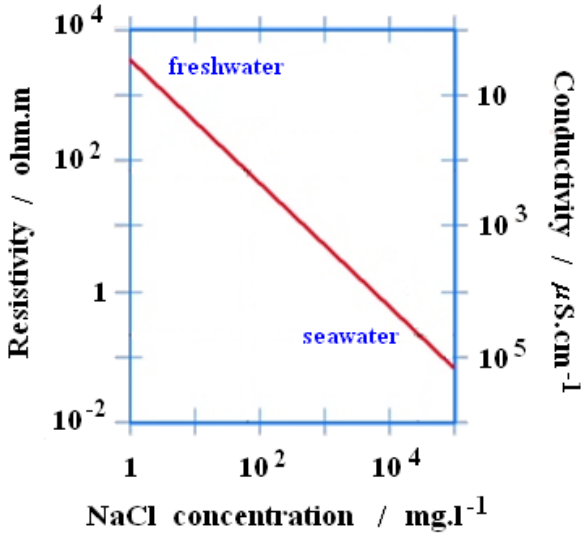

Figure 5.2 – Sodium Chloride concentration *versus* EC, at 20 ºC, (after Worthington *et al.*, 1990).

The effective shape of the grains (or pores) and orientation also affects the conductivity response. Solid matrix surface conductivity at the grain interface can have a significant importance in fine-grained materials, especially when solution conductivity is low. In this case, the surface conductivity models are dependent on the amount of surface area and the surface chemical properties of the solid to liquid interface (Lesmes and Friedman, 2005).

If the water solution conductivity is known, for instance, from field borehole measures, electrical conductivity measurements can be used to estimate the effective porosity of water-saturated formations or the water content of partially saturated formations. The most widely used relationship to predict the effective electrical conductivity response of water-saturated geological materials is the famous Archie's empirical 1st equation (Archie, 1942), or the modified version to under-saturated formations, 2nd equation. Although being an empirically

based expression, it has been also derived from a fractal model for porous rocks by Pape and Schopper (1988) and Shashwati and Tarafdar (1997).

The empirical Archie's law (1st equation) is expressed by:

$$\sigma_w = a\sigma_b \phi^{-m} \quad (5.11a)$$

or

$$F = a\phi^{-m} \quad (5.11b)$$

linking the porosity to formation factor. The constant a, named tortuosity factor (or lithology coefficient) it's applied to correct and account for variation in compaction, pore structure and grain size of the sample. Tortuosity factor varies in the range 0.5 to 2.0 (Serra, 1984). Archie found that exponent *m* ranges from 1.3 for unconsolidated sand to 1.8-2.0 for consolidated sandstones, naming this parameter as the cementation index.

Table 5.8 resumes some measured cementation index values for several materials and rocks found in published literature (e.g., Stefansson *et al.*, 1982; Lesmes and Friedman, 2005). Experimental measures and theoretically derived petrophysical models, relate this cementation index to the effective grain shape. The index increases as the grains became less round (spherical), but keeps almost unchanged to variations in grain size and sorting (Jackson *et al.*, 1978).

Table 5.8 – Archie's cementation index parameter for several medium.
(after Lesmes and Friedman, 2005)

Geologic medium / material	**Cementation index *m***
Clean sand	1.3
Consolidated sandstone	1.6 - 2.0
Shaley sand	1.52
Quartz sand	1.44
Limestone	1.9 - 2.3
Fractured basalt	1.0
Glass beads (spheres)	1.20 - 1.38
Prisms	1.63
Cylinders, Cubes	1.47
Disks	1.46

This Archie's law implicitly assumes that the effective porosity and total porosity are equal, and that all electrical conduction in a water-saturated rock or soil results from the ion's migration in the bulk pore-solution. If there are non interconnected pores through which ions cannot migrate, then Archie's relation will be over predicting electric conductivity.

As stated before, in fine-grained materials or at saturated materials with resistive pore solutions, surface conduction can be of a significant amount, causing Archie's law to under predict the EC. That's the situation when clay minerals are present due to clay's structure and cation exchange capacity. This means that the formation factor as defined by expression (5.5) is strictly valid only to a certain class of petrophysically rocks (Archie rocks). Formation

factor is known as the apparent formation factor when it varies with solute EC, temperature and ion type solution. Archie's 1st equation has been modified to include this surface conduction term (σ_s) in parallel with the bulk conduction term, which results from the migration of ions through the bulk pore solution (e.g., Schön, 1996) and also to be applied under unsaturated areas (2nd equation):

$$\sigma_b = \frac{\sigma_w}{F} S_w^n + \sigma_s \qquad (5.12)$$

with S_w the saturation index of material, *n* the saturation exponent value, usually close to 2. Departures from this value are variously attributed to the influence of wettability and nature of desaturating fluid (Schön, 1996).

Although not being expected that bulk and surface conduction mechanisms act strictly in parallel (e.g., Friedman, 1998), the simple parallel-conduction model consideration has several practical advantages. One is that differentiation, and estimation can easily be done between *F* and σ_s by analysis of the plot σ_b versus σ_w (e.g., Waxman and Smits, 1968; Nadler, 1982).

The effects of lithology and solution chemistry on the surface conductivity term in (5.12) were introduced and accounted for by Waxman and Smits (1968), (W-S models) like:

$$\sigma_s = \frac{BQ_v}{F} \qquad (5.13)$$

where Q_v is the cation exchange capacity (CEC) per unit pore volume, a measure of the effective clay content, and *B* the equivalent ionic conductance of the clay exchange cations.

Waxman and Smits empirically obtained formulas for the dependence of *B* on the solution conductivity. Sen *et al.* (1988) developed one version in which the empirical parameter *B* is a function of; the solution conductivity (in μS.cm^{-1}) and also the cementation index (*m*).

$$B = \frac{1{,}93m}{1+7000/\sigma_w} \qquad (5.14)$$

The advantage of this Sen *et al.* formulation (based upon saline solutions) is that it accounts for lithologic effects on the surface conductivity response. However, the empirical parameters at expression (5.14) are still dependent upon the solution type. The Q_v value can be expressed by:

$$Q_v = \frac{\rho_{mat}(1-\phi)}{\phi} \times \mathrm{CEC} \qquad (5.15)$$

with ρ_{mat} the material matrix density.

Ground and soils CEC range values are naturally linked to the clay mineral composition. The critical parameter for conductivity of clayey material is thus not the clay content, but is CEC value (Kirsch, 2006). CEC unit is usually provided as milliequivalent of hydrogen per 100 g (meq$^+$/100g), Many such values have been measured and are listed, for example; Kaolinite (3 to 15 meq$^+$/100 g), Chlorite (10 to 40 meq$^+$/100 g) or Volclay Bentonite (80 meq$^+$/100 g).

6
SANTIAGO ISLAND SETTINGS

On this sixth chapter, the principal settings of Santiago Island (Cape Verde) are given, namely the geology, climatology, hydrogeology and hydrochemistry ones.

6.1 – Santiago island location

Santiago Island belongs to the Cape Verde archipelago. It is the southernmost archipelago of the Macaronesia system, at the North Atlantic Ocean. Santiago is the biggest of the ten major islands, five smaller desert islands and several islets, composing the Cape Verde archipelago. The major town and capital of the country, Praia, is located in the southern side of the island. Praia had 100000 inhabitants and total island's populations were 235000, according to the last population's CENSOS (INE, 2000). This CENSOS also indicates a total 432000 inhabitant in the archipelago.

Cape Verde is a volcanic archipelago located at the eastern north Atlantic border 450 km from Africa western coast of Senegal and 1400 km south-south-west from the Spanish Canary island's archipelago, at the Sahel region. It is limited by north parallels 14º 48' and 17° 13', and by the west meridians 22° 42' and 25° 22'. The archipelago is divided into three sectors; the north one, the western one and the eastern and south one. Santiago belongs to this latter and it's located between 14º 54' and 15º 20' north latitudes and between 23º 48' e 23º 27' west longitudes. Total Isle surface is 991 km^2 with a maximum length of 54.9 km by 28.8 km maximum wide, north-west to a south-east oriented (figure 6.1). The island summit is 1394 meters above mean sea level and is the third highest island of the archipelago.

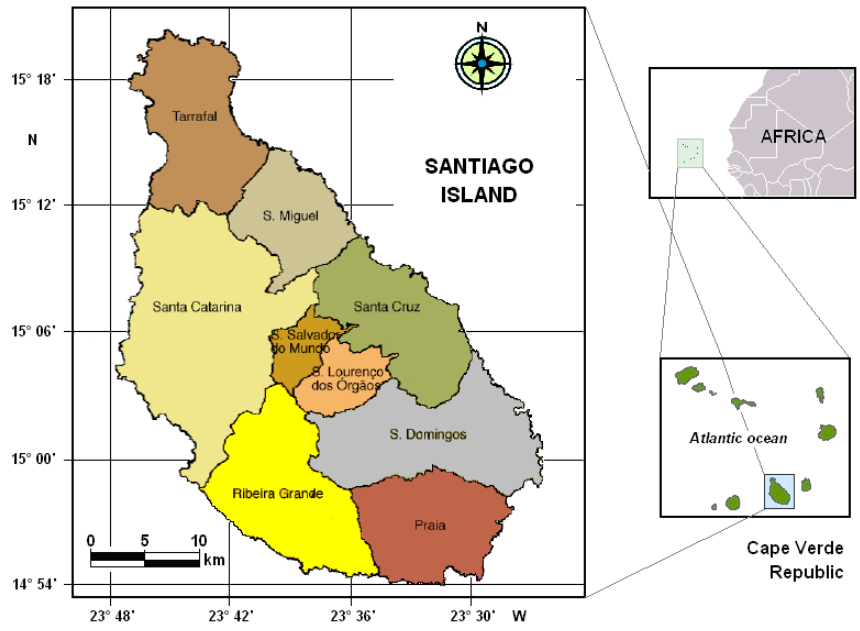

Figure 6.1 – Cape Verde archipelago and Santiago island location, with actual counties. (Modified from MIF (2006)).

6.1.1 – Geologic regional settlement

The Cape Verde archipelago is an emerged portion of a Mesozoic-Cenozoic volcanic accretion in the form of a westward-facing horseshoe along fracture zones converging from the mid-Atlantic ridge toward Africa (figure 6.2). The interior abyssal plain slopes westward, increasing in depth from 2.7 to 4.5 km (Duprat *et al.*, 2007). The archipelago is located on the southwestern part of the Cape Verde Rise, a swell about 2.2 km high and 1400 to1600 km wide that is considered the largest oceanic intra-plate bathymetric anomaly (Lodge and Helffrich, 2006). Islands stand on 120 to 140 Million years (Ma) old (Williams *et al.*, 1990, Müller *et al.*, 2008) and about 85 km thick (Cazenave *et al.*, 1988) oceanic lithosphere. The crustal thickness is anomalously high beneath the islands (reaching 22 km), but have a normal 7 km between them (Lancelot, Y. and Seibold, E., 1977, Ali M. Y. *et al.*, 2003; Lodge and Helffrich, 2006; Pim J. *et al.*, 2008).

An important residual geoid gravimetric and heat flow anomaly is present (Dash *et al.*, 1976; Courtney and White, 1986). These features are believed to result from mantle plumes (Sleep, 1990). The Cape Verde genesis from a deeply anchored mantle plume seems to be supported by seismic tomography studies (Montelli *et al.*, 2006; Zhao, 2007) and by He isotope signatures obtained both from silicate and carbonatitic rocks (Christensen *et al.*, 2001, Doucelance *et al.*, 2003, Mourão *et al.*, 2007, Mata *et al.*, 2010). This underneath plume explains the observed volcanic activity and the associated geothermal anomalies. Off-shore seismic refraction line's results indicate a 2 to 3 km of semi consolidated sediments underlining a 3 to 6 km of basalt and 6 to 8 km of plutonic rocks (Duprat *et al.*, 2007).

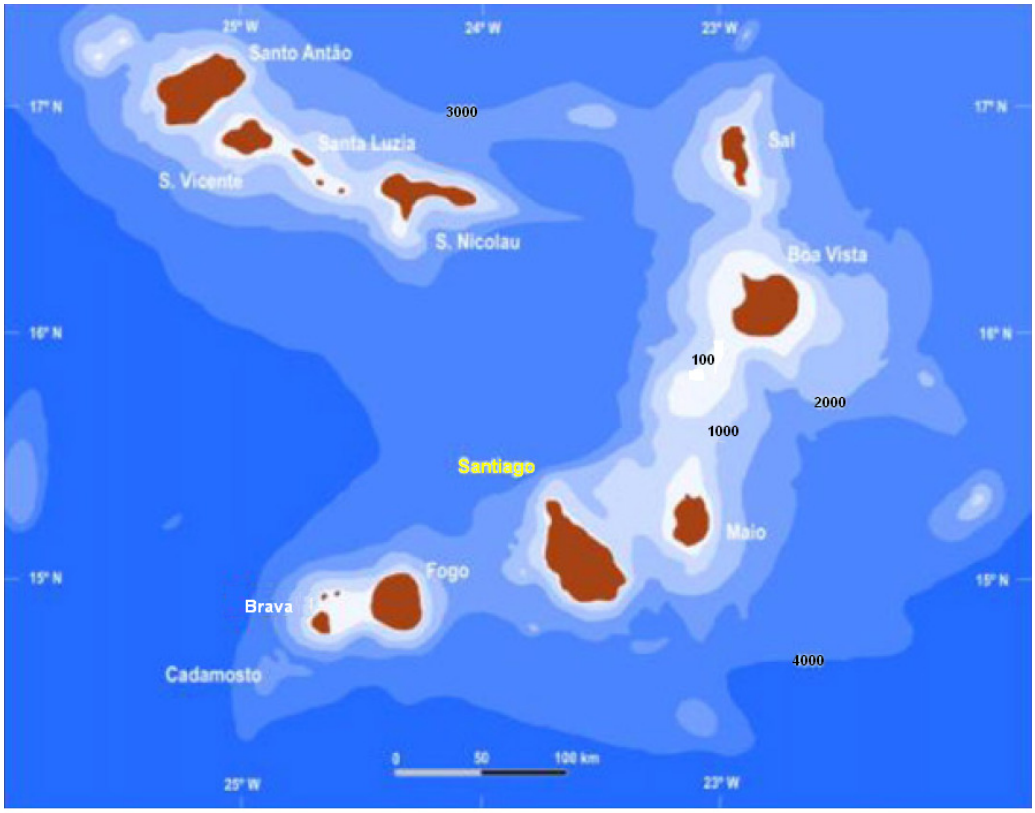

Figure 6.2 – Cape Verde archipelago horseshoe structure with bathymetry values. (Modified from Madeira *et al.* (2010)).

The archipelago island's formation as been linked to a hotspot mechanism (Holm *et al*., 2008) and the oldest published date for the Cape Verde hotspot (about 26 Ma) was obtained for a submarine basalt from the basal complex of the Sal Island (Torres *el al*., 2002).

The island's formation had begun with an initial underwater volcanic core, lately completed by a network of small-scale faults, seen at the outcrops (Serralheiro, 1976a, Alves *et al*., 1979). All the region have been subjected to important vertical movements (De Paepe *et al*., 1974; Gerlach *et al*., 1988; Millet *et al*., 2008) with measured values in the 0.2 to 0.4 mm per year range (Madeira *et al*., 2010, Ramalho *et al*., 2010a and b).

Though Cape Verde's islands are all volcanic in origin, they show a widely variety of terrain and geomorphology aspect. The first geological report and account study was from Charles Darwin's epic voyage at the "Beagle" (Darwin, 1844). The following geology report of these islands (except Fogo one) comes with Bebiano (1932) monograph. A comprehensive and detailed description of these early works can be found from Mitchell-Thomé (1972 and 1976) respective article and book and references therein.

The archipelago islands are principally composed of igneous rocks, with basic volcanic and pyroclastics comprising the majority of the total volume (Bebiano, 1932). The archipelago is an example of a soda-alkaline petrographic province, with a petrologic succession which is similar to that found in other mid Atlantic islands of the Macaronesia system. The archipelago currently exposed volcanic sequences ranging from the Miocene to the present (Madeira *et al*., 2010). Some islands are flat with just small elevations, like Sal (406 m high) and Maio (436 m). Others have relatively high central mountains, like Fogo (2829 m), Santo Antão (1978 m), Santiago (1394 m) and São Nicolau (1304 m).

6.2 – Santiago geology

The most ancient Cape Verde archipelago formations are from Mesozoic era (late Jurassic and early Cretaceous periods), found at island of Maio (Rigassi, 1975, Serralheiro, 1976a, Alves *et al*., 1979). Santiago's formation is slightly posterior and like all other islands, has borne from a central volcanic system. The principal island and the main structure were created by several times stages episodes, with a changing volcanic activity rate. At low volcanic activity periods, erosion took place. Lately, the eroded valleys have been again refilled with new basaltic flows. The oriented axe of Santiago seems to be related to an overtime volcanic activity migration.

6.2.1 – Volcanostatigraphic: a brief description

Eruptive rocks are the dominant in Santiago, responsible for the building of is morphology. Sedimentary formations do exist at several small portion areas. Metamorphic rocks are almost inexistent (Serralheiro, 1976a). Santiago's geologic map was done by Serralheiro (1976b), at a 1:25000 scale. The 1:100000 scale map was published one year later

Serralheiro (1977). After this, Matos Alves team did the petrologic and volcanologic study, in connection and linked to the other islands (Alves *et al.*, 1979).

Serralheiro assigned several important historical evolution stages at Santiago Island:

First Stage – Palaeogene (65 to 23 Ma)
The initial undersea water eruptions take place followed by the aerial emersion of the volcanism. This stage created the ancient internal eruptive complex.

Second Stage – Palaeogene to Neogene (Oligocene to lower Miocene epochs, 36 to 20 Ma)
Lower volcanic activity with hard erosive action takes place, with destruction of previous superficial volcanic systems. Large underwater deposits have been originated with those eroded materials.

Third Stage – Neogene (Lower Miocene epoch, 20 to 16 Ma)
Seamount stage takes place. Rise of the sea level above the 450 m actual mark.

Fourth Stage – Neogene (Middle Miocene epoch, 16 to 12 Ma)
Very intense extrusive activity along with great extends of land covert areas. This corresponds to “Flamengos Formation”. At present days only the submarine facies is known.

Fifth Stage – Neogene (Middle to upper Miocene epochs, 12 to 5 Ma)
Regression period to a level not smaller than 250 m high takes place. Break off volcanic activity and thick sedimentary deposits formation with marine and terrestrial facies. This corresponds to “Órgãos Formation”.

Sixth Stage – Neogene to Quaternary (5 Ma to present)
Before the last extrusive period, the generalized erosion and sedimentation process give raises to dune and beach deposits some tens of meters above the sea level (Plistocene epoch). Last volcanic activity creates many scoria and pyroclastic cones. At the Halocene epoch, the terrestrial deposits are generalized, as like the sand beach one.

The volcano-statigraphic description is summarized at table 5.1, with principal mineralogical specimens included (Martins, 2003), following the Serralheiro (1976a) and Matos Alves *et al.* (1979) proposed sequence characterization. Detailed description can be found at those authors’ works and also at the recent thesis about the hydrochemistry of the island, by Mota Gomes (Gomes, 2007) and António Pina (Pina, 2009).

The X-ray diffraction mineralogical analyses from former authors (Serralheiro, 1976a, Matos Alves *et al.*, 1979 and Martins, 2003), revealed similar compositions between the principal mineralogical associations, from the different formations on the island. The mineralogy of basanits essentially formation is olivine, pyroxene and plagioclase, with small quantities of iron and titan oxides. The mineralogy of melanefelinits formations is feldspatoids (nefeline), together with olivine, pyroxene and iron and titan oxides.

Table 6.1 – Main geologic formations and associated mineralogical specimens, at Santiago Island. (Modified from Martins (2003)).

Eruptive formation	Mineralogy
I - Internal ancient eruptive complex (CA)	Plagioclase calcite, dolomite, feldspats-k, biotite, amphibole, pyroxene, olivine, zeolits, feldspatoids
II - Pre-"Flamengos" formation conglomerates	
III - "Flamengos" formation (FL)	**Basanits:** plagioclase, olivine, pyroxene, plagioclase, feldspatoids and oxides. **Melanefelinits:** olivine, pyroxene, feldspatoids and oxides Usual presence of xenoliths peridotitics and gabbroic at lavas **Submarine lava:** carbonates, idingsite, zeolits, serpentine
IV - "Órgãos" formation (CB)	
V - Post-"Órgãos" formation	
VI - Pre-"Pico da Antónia" sediments	
VII - "Pico da Antónia" complex (PA)	**Basanits:** olivine, pyroxene, plagioclase and oxides **Melanefelinits:** olivine, pyroxene, oxides, mica, nefeline. **Nefelinits:** pyroxene, nefeline, oxides. Usual presence of xenoliths peridotitics and gabbroic at lavas **Submarine lava:** carbonates, idingsite, zeolits, serpentine
VIII - "Assomada" formation (A)	**Basanits:** olivine (altered to idingsite), pyroxene, plagioclase, oxides. **Melanefelinits:** olivine, pyroxene, oxides, mica, nefeline.
IX - "Monte das Vacas" formation (MV)	**Basanits:** olivine, pyroxene e oxides (titanomagnetits).
Sedimentary Formations	
X - Quaternary sedimentary formations	Plagioclase, feldspate, magnetite / maghemite, hematite.

The brief statigraphic formations' description is given bellow, from the most ancient to the most-recent ones. The corresponding geologic map is plotted at figure 6.3.

I – Internal ancient eruptive complex (CA)

This is the most ancient rock formation of the island. They are essentially basic dikes and fono-traquits, with some silicate granular rock intrusions. It corresponds to the evolutionary first stage. They are mostly visible to west-central part of the island, with vertical and near vertical dikes, corroborating the central genesis of Santiago. The low permeability and productivity of this formation give it a reduced hydrogeologic importance.

II – Pre-"Flamengos" formation conglomerates

These are conglomeratic formations covering the CA formation (and very alike the "Flamengos" formation). They are visible to south, with a small extent. Lower deposits start by thin layers and evolve to broad sediments. No assigned hydrogeologic activity exists to this formation.

III – “Flamengos” formation (FL)
This formation covers discordantly the CA formation, and corresponds to basic breeches and pyroclastics, with great extent and uniformity, with submarine genesis. It is found all over the island except to the north. Formation occurrence is over the 250 m altitude mark. The hydrogeologic productivity of this formation is relatively low, except at the areas where pillow lavas do exist, giving then pumping rates over the 20 $m^3.h^{-1}$. This formation corresponds to evolutionary fourth stage.

IV – “Órgãos” formation (CB)
This formation essentially shows thick basaltic blocks (sharp to round ones) from secondary volcanic phenomena. CB formation corresponds to fifth stage of the historical evolution, with great extent erosion. It is highly heterogeneous with sand intercalations and purely conglomeratic. Deposits can be thick by more than 100 m. Most of this formation outcrop at Santiago central region (S. Jorge dos Órgãos) and north and west, to a small extent. This formation is packed to a high degree and as no hydrogeologic importance, except at areas containing pyroclastics cones and high number veins.

V – Post-“Órgãos” formation
This formation belongs to post CB traquitic phase, with a limit extent. Its major expression is seen at Monte Branco, located at the centre of the island. There are endogenous domes greatly disassembled but cutting and metamorphing the old submarine lavas, FL sedimentary and CA formation. There is no important assigned hydrogeologic specification to this formation.

VI – Pre-“Pico da Antónia” sediments
This formation shows small sedimentary outcrops, with fossil sandstone-limestone and conglomerates. This formation is found at island south locations. With a limited extent, this formation has also no hydrogeologic importance.

VII – “Pico da Antónia” complex (PA)
This is one of the most important geologic formations, filling more than half of the island area, spanning over a long time period with a great volumetric content. It is responsible by high-altitude relief as also the main structural platforms of Santiago. Formation spans’ materials from effusive and explosive activities, submarine and terrestrial. Older PA formation does exist at the south and southeast (Vailleux *et al.*, 1974) and at the east side (Serralheiro, 1976a) with a predominant terrestrial facies. Sedimentary layers do exist among magmatic events, but it is sometimes difficult to clearly differentiate and identify these episodes between locations. This sedimentary stage is more expressive at the north side of Santiago. After this initial period, an important erosion process took over followed by a partial immersion with substantial submarine emissions. All this process is repeated once more and ends with an important explosive phase. Resulting materials have high relative porosity, which gives them a good hydrologic productivity – becoming the island most important aquifer system.

VIII – “Assomada” formation (A)
This formation corresponds to a new eruptive period, exclusively terrestrial with basaltic facies lava flows and a few pyroclastics, after an important erosive time. Formation is located at Santiago’s central west side with large horizontal layers, and has good hydrological characteristics.

IX – “Monte das Vacas” formation (MV)
These formations correspond to island’s last volcanic episodes. The produced pyroclastics basaltic cones (tufts and scoria) and small flows through the island, have high porosity ones. Although direct MV groundwater exploration is not feasible (formation is very shallow), it has an important hydrological roll by leaking to the underling PA formation.

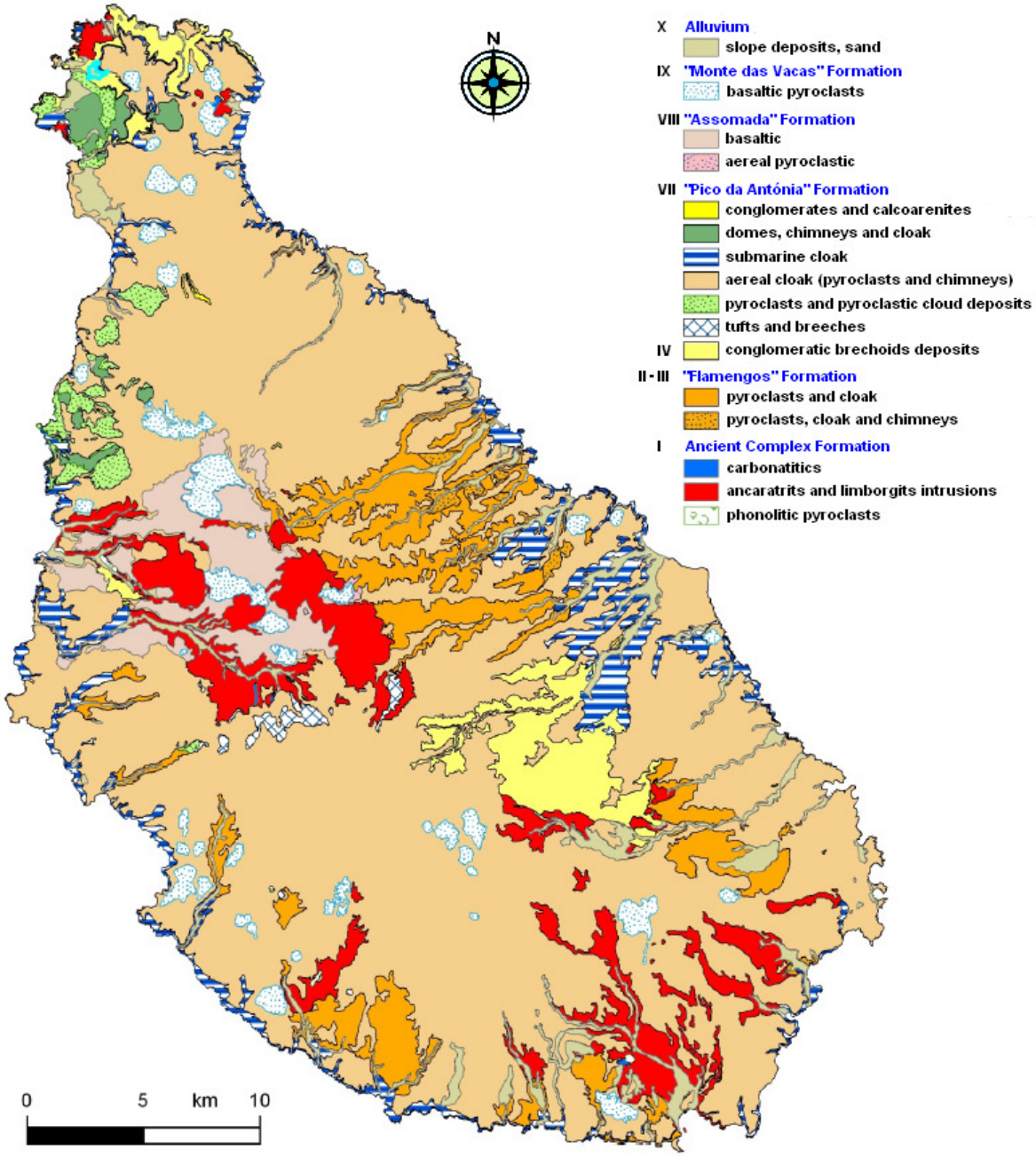

Figure 6.3 – Santiago geologic map after Serralheiro (1976b, 1977). (Modified from Pina (2009)).

X – Quaternary sedimentary formations
These recent formations cover 8.5% of the island land total surface, and are mainly formed by alluvium, slop or runoff flow deposits, dune sands and maritime beaches at several levels to the 100 m elevation mark (Serralheiro, 1976a). They are very important units, especially at the major valleys of the east coast island side, with some 40 m thick layers (Vailleux *et al.*, 1974). Local boreholes and wells provide most of the groundwater to inhabitants and especially to land irrigation, as these formation's soils are the islands suited ones for agriculture. These Quaternary formations are plotted at figure 6.4, and match the main and principal transient creeks of the island, as they fill most of the eroded valleys.

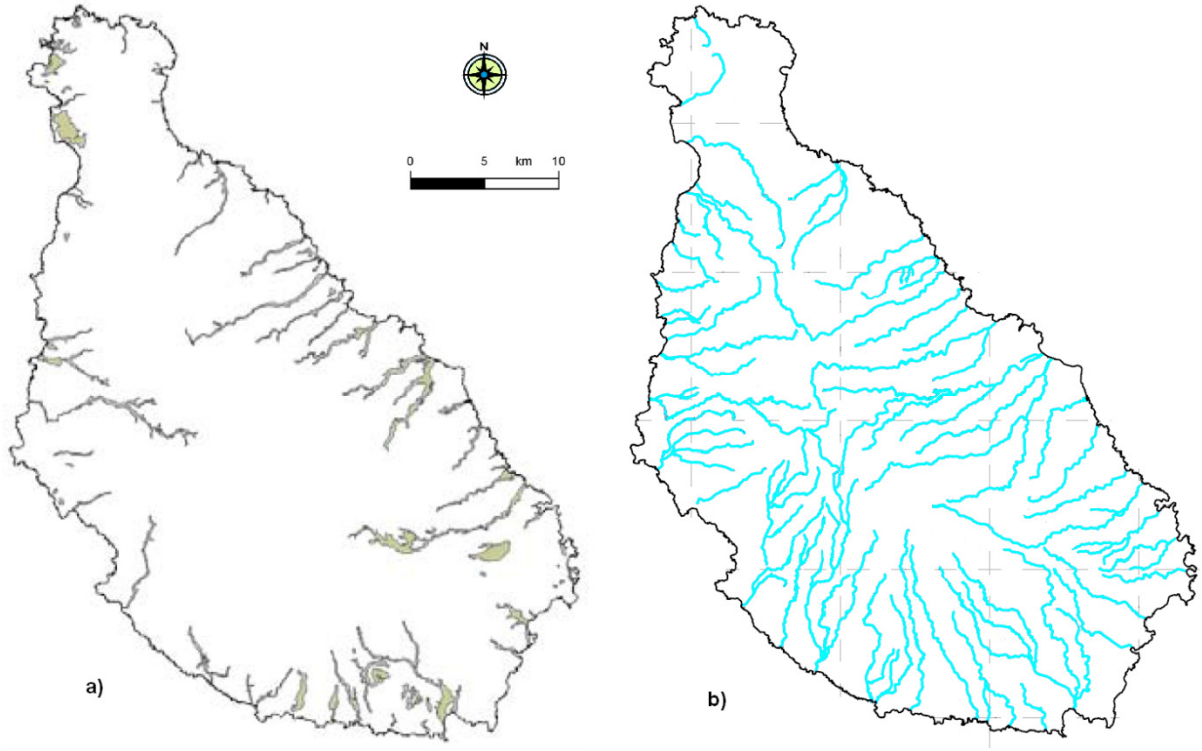

Figure 6.4 – a) Santiago Quaternary sedimentary formations, b) major transient creeks location, (modified from Pina (2009)).

6.2.2 – Geomorphology

The morphology of Santiago Island is linked to geology and is the outcome of the evolutionary process. It is dominated by steep topographic gradients and eroded valleys. There has been assigned seven geomorphologic units, although at some areas, the limit between them could be difficult to define. Sub classification as been also assigned to some of these units. Detailed geomorphology account can be found at Marques (1987, 1990). Location and limits of those units are shown at figure 5.5. The next brief description is based on Marques (1990).

I – South volcanic plateau (Achadas Meridionais)
Unit extension is from Pico da António south side mountain to the coast. It covers roughly one-third of the island. It is a PA basaltic flow with tuffs intrusions and having slope's ranges from 2 to 12%.

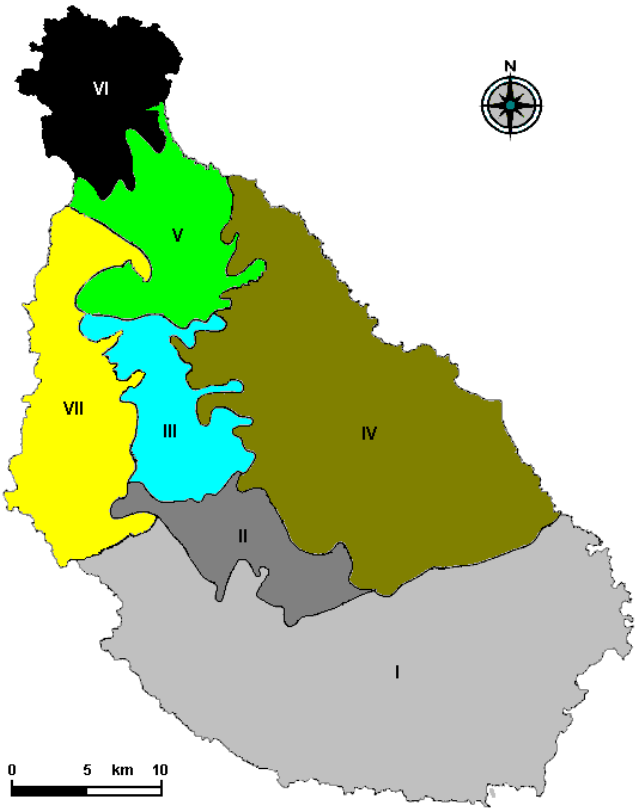

Figure 6.5 – Geomorphology map of Santiago (modified from Marques (1990)).
Units: I - South volcanic plateau, II – Pico da Antónia mountain massif,
III – Santa Catarina plateau, IV – East side border, V – Malagueta mountain massif,
VI – Tarrafal plateau, VII – West side border

II – Pico da Antónia mountain massif

This unit is located at the southwest central part. The highest point is the Pico da Antónia, at 1392 m. The system is highly eroded with sharp summits. It is almost formed by PA eruptive complex and represents the south rim of the last big volcanic crater. Observed slopes have more than 25%. It is a natural water recharge system to the island.

III – Santa Catarina plateau

This plateau is located in the middle of the island, surrounded at south by Pico da Antónia mountain, at north by the Serra Malagueta mountain. It is an almost flat area with a mean elevation of 500 m. This unit seems to represent the eroded bottom of the volcanic crater that as created the PA eruptive complex (Serralheiro, 1976a).

IV – East side border

This unit extends from São Domingos creek valley, at south, to the São Miguel creek valley, at north. All sporadic streams born at Santa Catarina plateau, Pico da Antónia or Malagueta mountains, have at the start, high slopes, that decrease to a 7% mean value at halfway distance to the coastline. Observed lithologies are tuffs and breccias with lava flows. At eroded areas, the succession from the CA, Flamengos, Orgãos and PA formations are seen. This unit is completely exposed to predominant northeast trade winds that blow throughout the year.

V – Malagueta mountain massif
This unit is the north rim of the ancient big volcanic crater. The summit is at Serra da Malagueta with 1064 m, and is entirely a PA formation. It is between the Tarrafal plateau unit (at north) and Santa Catarina plateau (to the south). The mountain exhibits mean slopes of 25%. It's north flank is exposed to the predominant northeast trade winds.

VI – Tarrafal plateaux
It's the north side unit, with several plateaux between 20 and 300 m high, with gentle mean slopes of 4%. This unit is formed by PA formation. The Monte Graciosa is the local higher mountain (605 m) formed by fonolits and traquits. At this unit, the areas of Tarrafal and Chão Bom are covered by recent flood flow deposits, coming from debris of lava flow erosion. The predominant northeast trade winds affect only the northeast side of the unit.

VII – West side border
This unit is located between the Santa Catarina plateau and the sea, at the west coast. Some CA outcrops exist, but PA lava flows and tuffs dominate the landscape as basaltic layers of Assomada formation. It is a very arid region with high slopes between 12 and 25%. The shoreline is high over the ocean. This region is one of the most naturally eroded of the island (and archipelago) with the lowest inhabitant's density, in contrast to the island east side.

6.3 – Santiago climatic settings

The superficial and groundwater dynamics are greatly, if not entirely, connected to the geomorphology of the island (Custodio, 1975). Superficial water path is driven by topography, as the establishment of water circulation lines and the observed flow regime is fully a function of local slopes (Meneses, 1977; Rodrigues F., 1993; Rodrigues C., 1995; Azevedo, 1998; Fontes, 1999). But to have water running we need to collect water from the atmosphere. Again, the island's morphology and topography play a key role (figure 6.6). The maritime moisture air masses, mostly from the east, interacted with island landscape differently. Air masses flowing over the low altitude gentle slopes have a different action than upper air masses at the higher mountains and valleys, as rainfall is convective in origin (Correia, 1998). Precipitation and evapotranspiration (ET) have a strong gradient between inland and coastal areas. A major difference exists also between the east and west sides of the island (Rodrigues C., 1995; Azevedo, 1998). Landscape flora is also of great importance; to the water infiltration process and soil protection, to evapotranspiration and to runoff. (Falkland and Custodio, 1991, Rodrigues F., 1993, Meneses, 1993).

Cape Verde is located between the subtropical Atlantic north high pressure (Azores anticyclone) and West Africa inter tropical convergence zone (ITCZ). The orientation and position of those systems have a great impact over the archipelago (Amaral, 1964). When this later atmospheric system is shifted to the south, precipitation drops dramatically when the archipelago stays exposed to the northeast dry winds from Sahara desert. The variability of the West Africa inter tropical convergence position drives the observed variability of the Cape Verde rain amount. Some years the rain amounts can be 2 to 3 plus the mean value. Others can be waterless.

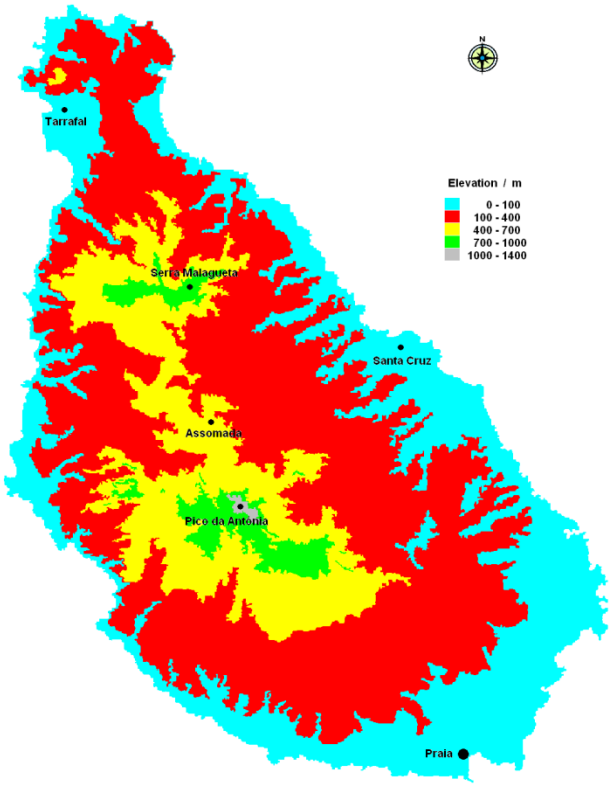

Figure 6.6 – Santiago five layers topographic map.

6.3.1 – Precipitation

Cape Verde is characterized by two annual main weather conditions; the “wind season” from November-December to June-July and the “rain season” from July-August to October-November, each year – the equatorial monsoon, with July and November the transition months between those epochs. Although annual and monthly rainfall amounts in Cape Verde are invariably low, daily or storm precipitation values can be very high (Rocha Faria, 1971). To quantify the rain amount, there are on the island several measure points (figure 6.7). The total amount of meteorological and hydrological stations is nowadays of 17. They had started collecting data from 1940 onward, but only less than half have complete time series. They belong to Cape Verde’s National Meteorological Intitute (Instituto Nacional de Meteorologia e Geofísica - INMG). Station’s spatial distribution is not uniform and is smaller than the required minimal, necessary in this kind of mountain island (Linacre, 1992), which is one station per 25 km^2. Island’s west side is badly sampled.

Precipitation time series from 1961 to 2009 yields a 363 mm annual mean value. This amount changes greatly from year to year, but especially with altitude and distance to the sea. Inland and higher locations are the rainy ones. For instances, the Chão Bom (16 m amsl) at extreme north, and Praia Airport (64 m) at extreme south, have annual mean precipitation of 197 and 164 mm respectively. At Assomada (462 m) this value is 466 mm and at S. Jorge dos Orgãos (310 m) is 430 mm. Higher locations like Serra da Malagueta (765 m) has 670 mm. Rainfall intensity is another important factor. Precipitation is not uniform all over the “rain season”, with August and September being the rainiest months

(figure 6.8). Traditionally, there are episodes of high-intensity precipitation with heavy storms. Rainfall days range from 3 to 20. For most of the years, 45% of mean annual rain falls on very short time periods. It is normal to have at the higher areas 200-300 mm per day after these storm events (Mannaerts and Gabriels, 2000), which leads to intense superficial runoff water and floods in the creek valleys. Surface water resources exist only on those days. The storm episodes have little effect to aquifer's recharge, but a dramatic impact to the soil, producing heavy erosion and destruction at the farmed valleys' areas.

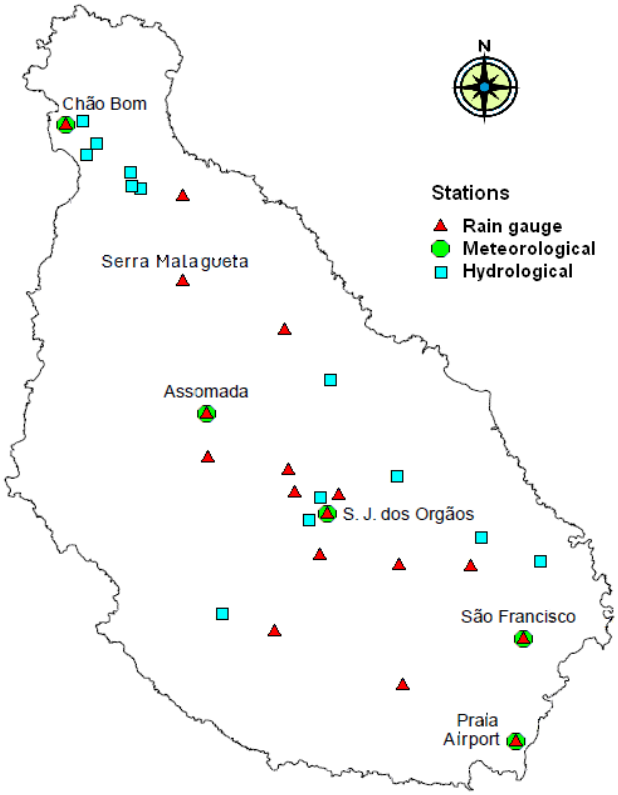

Figure 6.7 – Santiago rain gauge, meteorological and hydrological stations location (INMG).

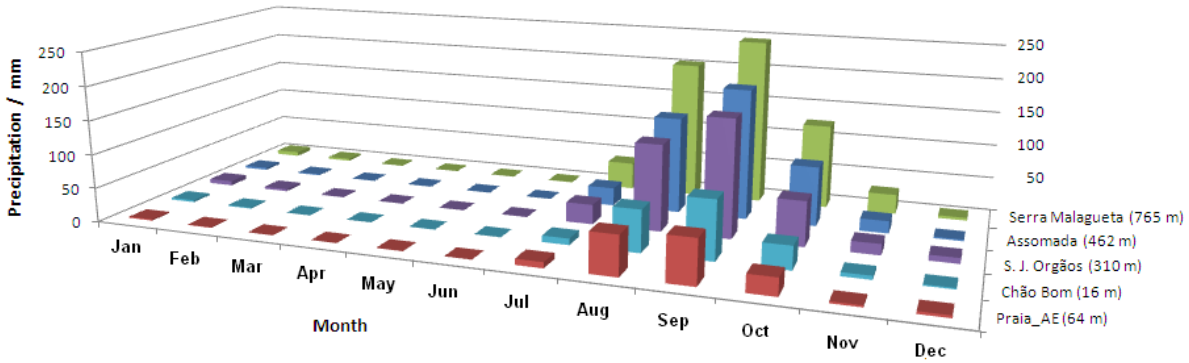

Figure 6.8 – Mean monthly rainfall for some Santiago's locations (1961-2009), (INMG).

Time rainfall variability can be seen at figure 6.9. Data from five stations is plotted from north to south, top to bottom, down the island axis. It's evident a strong annual variability and that lower altitude locations have much less rainfall than higher ones. Mean rainfall spatial distribution is given at figure 6.10. Accuracy is limited by stations spatial locations.

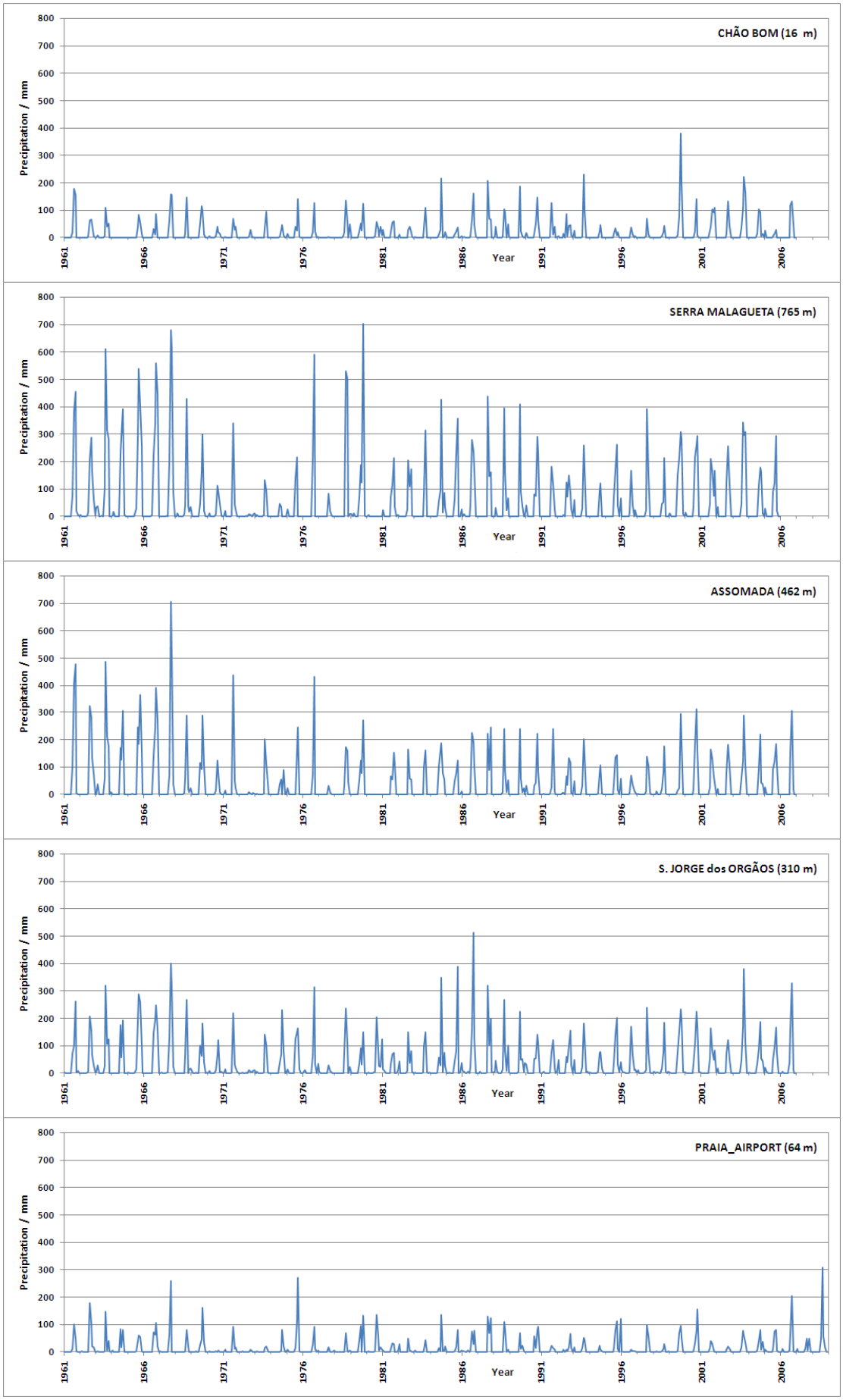

Figure 6.9 – Santiago's monthly rainfall for some locations, from 1961 to 2009, (INMG).

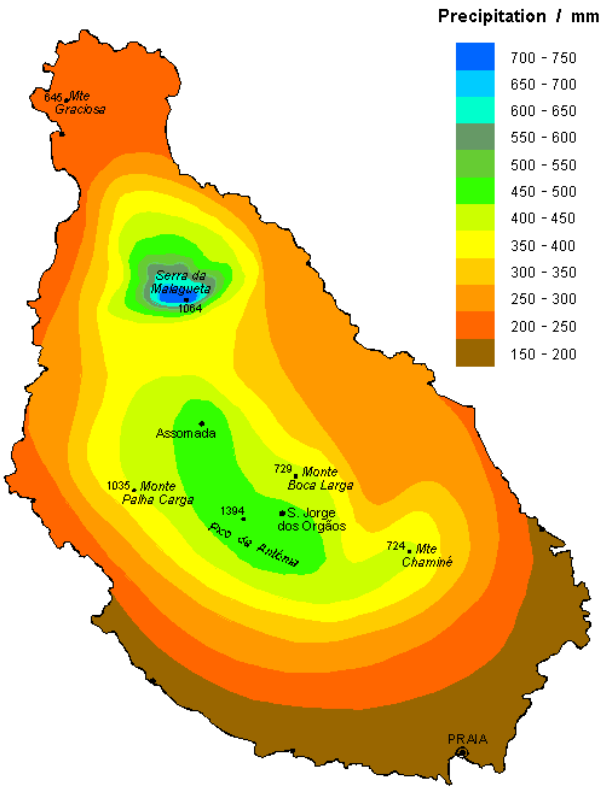

Figure 6.10 – Santiago's mean annual precipitation (1961-2000), (INMG).

6.3.2 – Temperature

Air temperature at Santiago is conditioned by relief exposition and orientation, elevation and distance from the sea. From the few available temperature time series, it's possible to assign a annual mean value of 24.2 ºC to the island, with a small amplitude range from 21.0 ºC to 25.1 ºC. The higher mean temperatures are at stations near the sea at low altitude, Praia airport (at south) and Tarrafal (at north) with respectively, 25.2 ºC and 24.7 ºC. At a high place such as Assomada, the mean annual value is 21.1 ºC with an amplitude of just 4.6 ºC. This last value is roughly the main island amplitude.

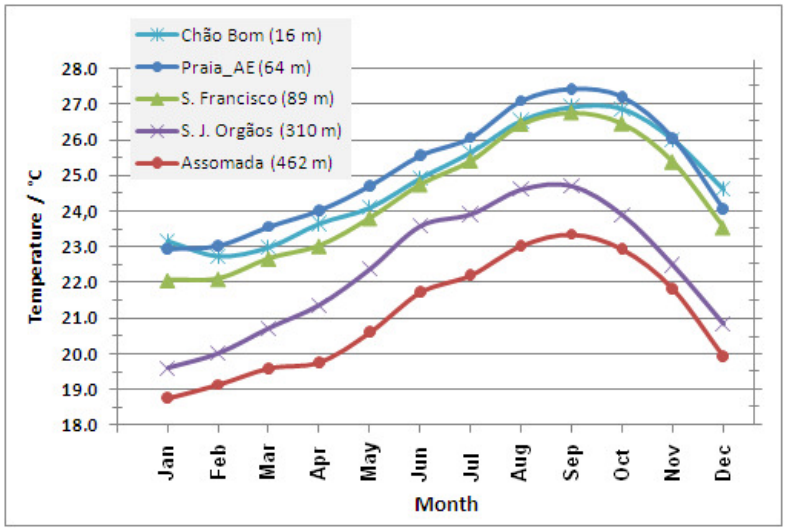

Figure 6.11 – Monthly temperature mean values (1973-2005), (INMG).

All island's locations have minimum annual temperatures in January-February and maximum ones in September. That can be seen from the monthly temperature values, figure 6.11. The annual temperature starts rising slowly and steadily from January onward until September's maximum and followed by a fast decline to the minimum. The daily temperature variations don't show large amplitudes, too. The daily minimum is reached at dawn (5 - 6 hour local time) and maximum at afternoon (13 - 14 hour local time), as expected.

6.3.3 – Relative Humidity

Santiago relative humidity (RH) mean values are always above the 60% mark. That's because for the most part of the time, the island is under a cloudy sky condition. RH time series only exist for five meteorological stations. Overlapping data spans only two decades (1981 to 2001). The island mean RH value is 74%. Mean minimum value is 68% and maximum 79%. The mean value increases and temperature decrease as we go inland to high locations. Annual variations are plotted at figure 6.12, for the five meteorological stations.

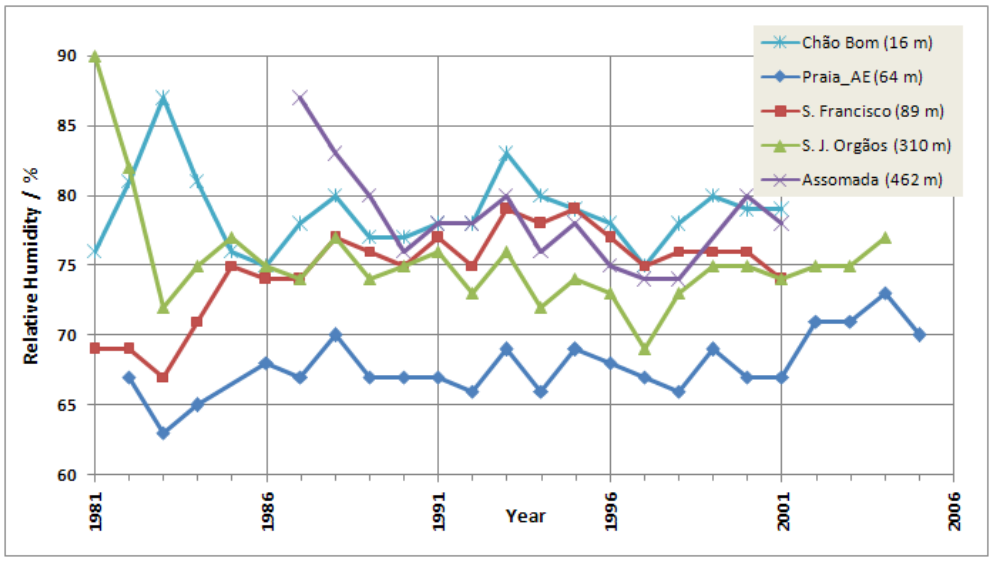

Figure 6.12 – Relative humidity mean annual values (1981-2005), (INMG).

Trough the year, the mean monthly value of RH increases steadily from the minimum in March to its maximum value in September and then decreases again, closing the annual cycle, in good correlation with the temperature patterns. Monthly values are plotted at figure 6.13.

The importance of these almost constant RH values on the island, trough the year, is considerable. Not only, it reduces the ET amount but also adds water, by "horizontal precipitation", to the high regions of the island. Several studies and experiments have measured the total amount of this recharge for the usual 3 km^2 foggy area of Santiago, at 1000 m high. The obtained values range over from 1500 to 3500 m^3 per day (Cunha, 1964; Juvik, 1988, Sabino, 2004).

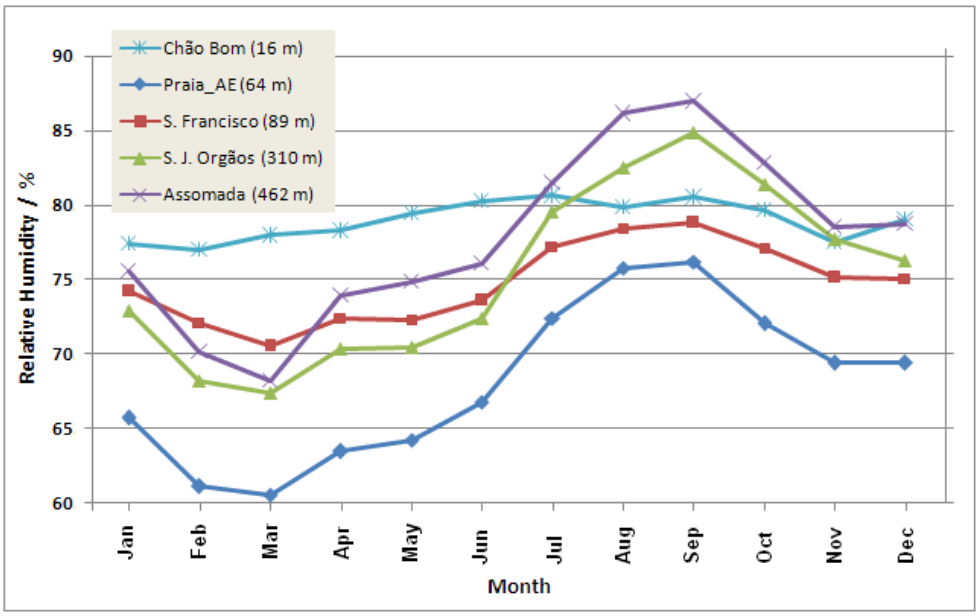

Figure 6.13 – Monthly relative humidity mean values (1981-2005), (INMG).

6.3.4 – Wind

The wind is one of the most important factors to the island rain amount. The three prevailing winds at Santiago are (table 6.2);

- the northeast trade that blows for most of the year, but brings almost no rainfall yet being very wet. They normally produce foggy conditions at high northeast side regions.
- the dry and hot east that blows from continental Africa at winter months, usually with immense dust content.
- the south and southwest monsoon that blow between July and September, responsible for the “rain season”.

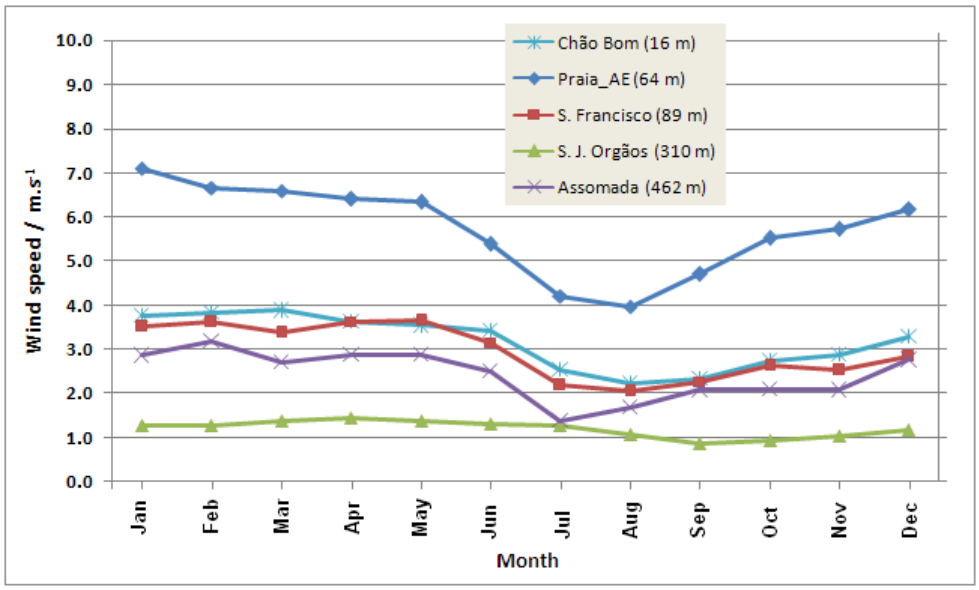

Figure 6.14 – Monthly wind speed mean values (1981-2004), (INMG).

The average measured wind speed is higher at the lower and southern regions, enhancing ET effect at southern regions. The mean annual value at Praia Airport is 5.8 $m.s^{-1}$ (at 2 m high) and 1.2 $m.s^{-1}$ at S. Jorge dos Orgãos. The wind speed is almost constant trough the year, decreasing from June-July to September-October, at the "rain season". The monthly wind speed values are plotted at figure 6.14, for the five meteorological stations.

Table 6.2 – Percentage measured wind direction at Praia Airport meteorological station (INMG).

Wind direction	Number of measures (%)
N	42.7
NE	35.0
E	6.1
SE	2.2
S	3.5
SW	1.5
W	0.5
NW	1.6
no wind condition	6.9

6.3.5 – Sunshine

Sunshine at Santiago Island has a mean annual amount of about 7 h per day. Lower regions have a higher sun exposition. That is, have more daily hours of clear sky than highlands of the island (figure 6.15). Throughout the year, the brightness months are at the springtime beginning, with a minimum at the August-September "rain season" (figure 6.16). As happen to the temperature, RH and wind speed parameter, the insulation values at Chão Bom (at Tarrafal, extreme north) exhibits local topographic effects, probably influenced by the nearby Serra da Malagueta.

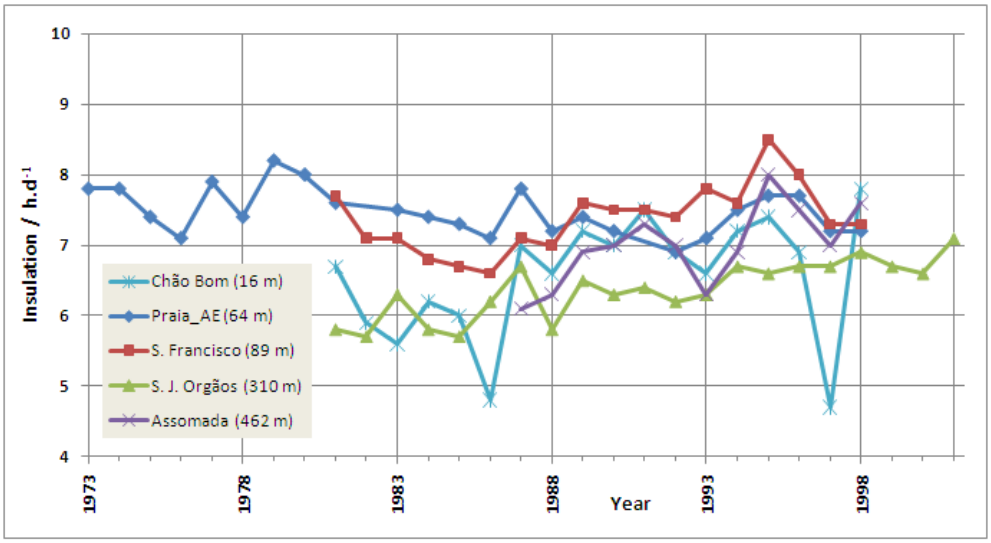

Figure 6.15 – Sunshine mean annual values (1973-2001) (INMG).

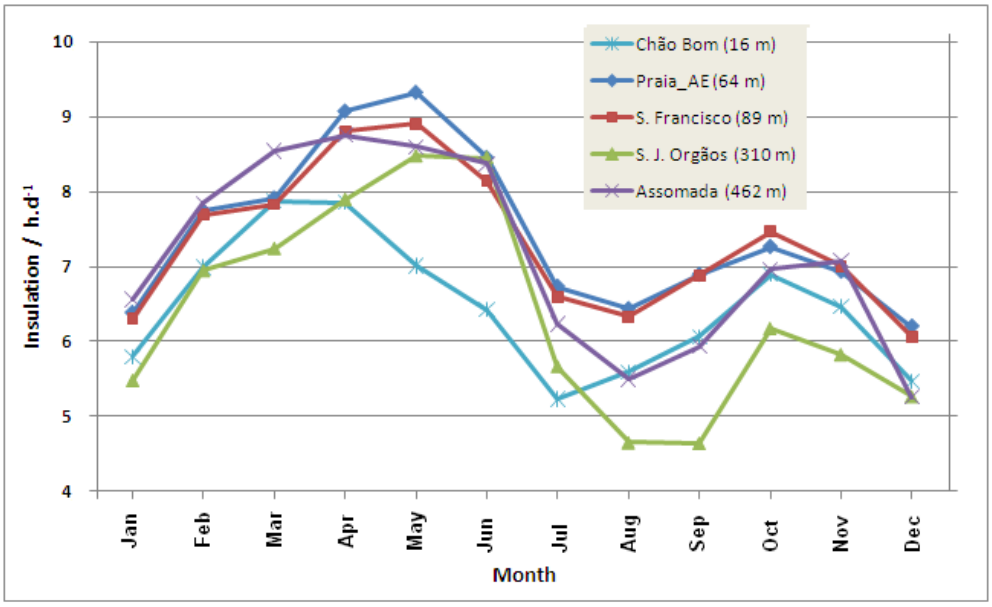

Figure 6.16 – Monthly sunshine mean values (1973-2001), (INMG).

6.3.6 – Soil and vegetation

Most part of Santiago's soil is volcanic by nature, rocky and thin, with little evolution. They are slightly alkaline with low organic matter content, but have altered minerals (Costa, 1995). Soil's field capacity values vary in the range 50 to 200 mm per year (Fernandopullé, 1977) and mean infiltration's rates values vary between the 40 mm per hour at alluvium and 40 to 80 mm per hour at basalts (BURGEAP, 1974). The wild vegetation is adapted to these climatic conditions, and is mainly composed by gramineae, bushes and woody specimens like *Acacia nilotica*.

6.3.7 – Evapotranspiration

The potential evapotranspiration (PET) can be measured or estimated using several methods. Data have been collected by evaporimetric and Piche's tank. With this available data, Pina (2009) reached the following annual PET values, at three different stations, with three different methods (table 6.3)

Table 6.3 – Annual PET values (units are in mm), (adapted from Pina (2009)).

Method	Praia Airport	S. Jorge Orgãos	Serra Malagueta
Piche tank	1034	939	705
Penman	1298	714	811
Thornthwaite	1687	1204	1203

These monthly values are plotted at figure 6.17 (for a mean hydrological year) and show increased PET variations at low altitude. At Summer time, the PET values are higher. The minimum values occur at winter beginning. Of these three methods, the Penman seems to be the closest to reality, and Thornthwaite the less adequate to this climatic characterization.

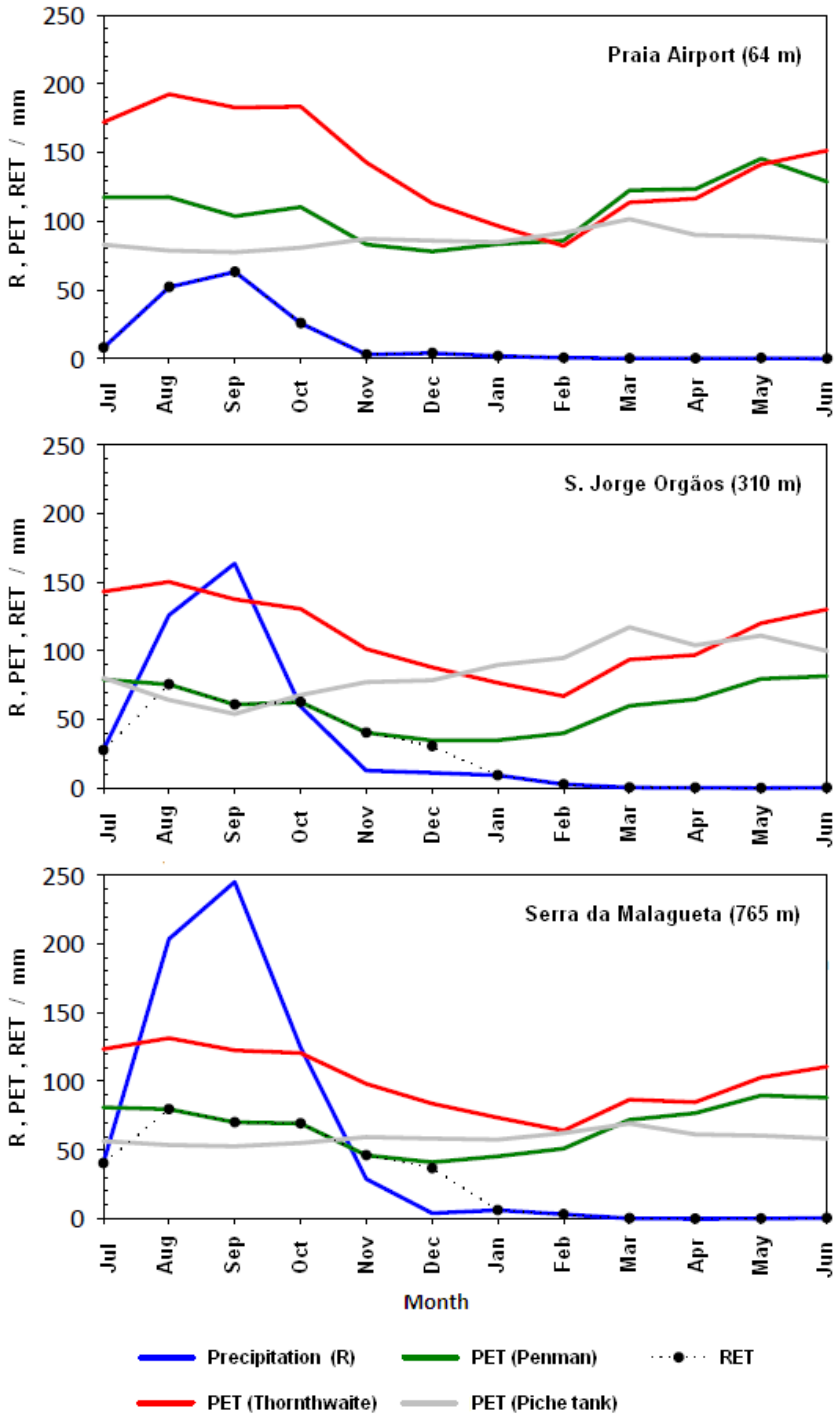

Figure 6.17 – Monthly rainfall, potential evapotranspiration and real evapotranspiration values at three meteorological stations (modified from Pina (2009)).

Data analysis shows a different scenario at all these three stations. In Praia, a low altitude and shoreline location, there is no water surplus at any time of the year. The real evapotranspiration (RET) is always equal to the precipitation (R). At S. Jorge dos Orgãos, an intermediate altitude place, precipitation exceeds the RET only in August and September "rain season" months. At Serra da Malagueta, a high-altitude location, precipitation exceeds RET trough all "rain season". These two last locations attain the necessary direct conditions to runoff and soil infiltration waters.

6.4 – Santiago recharge

With these climatologically settings, a bioclimatic classification can be assigned to the several regions of Santiago, according to their altitude. The corresponding Köppen–Geiger (KG) climate classification system is shown in figure 6.18 for Santiago.

I - Arid zone: from shoreline to 200 m altitude. Rainfall is less than 300 mm per year. Landscape is covered by herbaceous. KG: BWh

II - Semi-Arid zone: between the 200 m and 400 m high. Rainfall is between the 300 mm to 400 mm per year. Landscape is covered by herbaceous, like arid zone, but with more species. KG: BSh

III - Sub-Humid zone: between the 400 m and 600 m high. Rainfall is between the 400 mm to 600 mm per year. Landscape is covered by bushes and woody trees. Extreme dry conditions are very rare. KG: CWa

IV – Humid zone: above the 600-700 m high. Rainfall is more than 600 mm per year. It never reaches a dry condition. KG: CWa

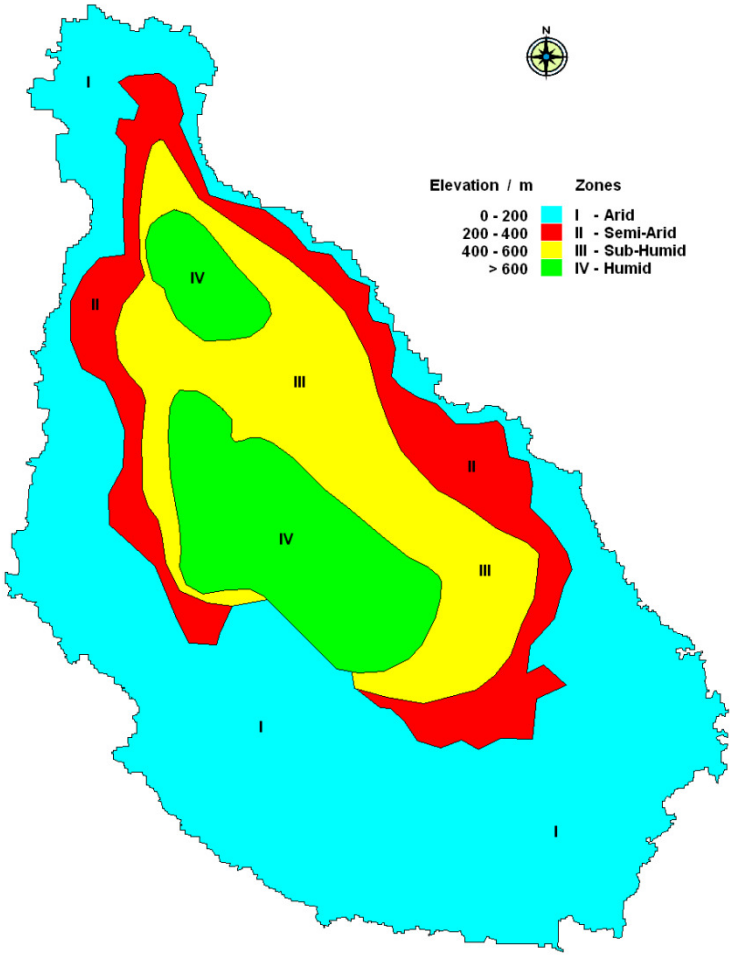

Figure 6.18 – Bioclimatic zones at Santiago (modified from INGRH).

6.4.1 – Recharge value estimation

Studies have been carried on to quantify Santiago's ground water recharge. Empirical methods have been applied (BURGEAP, 1974, Fernandopullé, 1979, Bossher, 1981, Dittrich, 1982, BURGEAP, 1983, PNUD, 1992), and also water balance calculations (Fernandopullé, 1979, BURGEAP, 1983, PNUD, 1992). The results are not in accordance, and express the difficulty to achieve a good estimation with the available data, (table 6.4).

Table 6.4 – Studies recharge values with actual mean rainfall value (R = 363 mm per year).

Study Author	Recharge	
	mm per year	hm^3
BURGEAP (1974)	16	16
	54 to 182	54 to 180
Fernandopullé (1979)	36 to 62	36 to 61
PNUD (1992)	11 to 65	11 to 64

António Pina (2009) has done recent recharge estimation by two different methods; a physical - the classical Penman-Grindley soil water balance equation (Penman, 1950, Grindley, 1967) and a chemical - the water-saturated zone Chloride budget.

To do that, Pina had measured the total area of bioclimatic zones with recharge abilities, and assigned a rainfall value from the most representative weather station at zone. Arid and Semi-Arid zone area amounts to 573 km^2. Sub-Humid zone area amounts to 152 km^2 and Humid zone area amounts to 77 km^2. The three main hydrogeological units in Santiago have been defined from the geological formations, BURGEAP (1974). They are; the Recent Unit - Quaternary sedimentary and "Monte das Vacas" formations, the Middle Unit - "Assomada" and "Pico da Antónia" eruptive complex formations and the Bottom Unit - Órgãos", "Flamengos" and Internal ancient eruptive complex formations. This last hydrogeology unit area wasn't accounted for, as it has a very low permeability. These units will be detail latter on the chapter.

On the first method using the classical balance equation (6.1), the climatologic input parameters come from the meteorological station's data;

$$\bar{Q}_r = \bar{R} - \overline{RET} - \bar{S}_w \qquad (6.1)$$

where $\bar{Q}_r$ is the mean recharge value, $\bar{R}$ the mean precipitation, $\overline{RET}$ the mean real evapotranspiration and $\bar{S}_w$ the mean superficial runoff water.

Penman-Grindley method works better at humid regions where soil never gets dry. At arid and semi-arid zones, RET is less then PET and equal to precipitation, which leads to no recharge condition. Nevertheless, occasional water recharge can happen with storms and by the indirect leaks from high central island areas. Mean superficial runoff water assigned values are 50 and 150 mm to III and IV zones, respectively. These values agree with

observations and local inhabitant descriptions about the maximum flood high in-stream valleys and time durations after traditional big storm events.

Recharge values are given at table 6.5. Total annual recharge amount with Penman PET method is 19 hm^3 (9.0% of estimated rainfall) and with Piche's tank PET method is 27 hm^3 (12.8% of rainfall). These are mean values corresponding to climatological time series (average values). Year to year there is recharge variability, mostly driven by rainfall quantity and less by temperature, sunshine, humidity and wind speed, more constants over time.

Table 6.5 – Bioclimatic zones annual Penman-Grindley method recharge values, (modified from Pina (2009)).

Bioclimatic Zone	**Area km^2**	**Precipitation mm per year**	**PET method**	**Recharge per year**		**Recharge/ Precipitation**
				mm	**hm^3**	**%**
I - Arid zone and II - Semi_Arid	573	164	Penman	0	0	0
			Piche tank	0	0	0
III - Sub-Humid	152	430	Penman	55	9	12.8
			Piche tank	74	11	17.2
IV - Humid	77	670	Penman	143	10	21.3
			Piche tank	204	16	30.4

The second method - the water-saturated zone Chloride budget - applies to Chloride measures at incoming rain and at groundwater. It was implemented originally at Israel's coastal plains in the 60' of last century (Eriksson and Khunakasem, 1969). It recently was successfully applied at some volcanic islands (Custodio, 1997; Lameli, 2001; Custodio, 2004). This method assumes that the Chlorine ion is conservative in the system, which has vertical flux at recharge area and horizontal flux within aquifer, and that groundwater Chloride comes only from rainwater. It is assumed that the Chloride input is constant over the time covered by the analyses, and that the groundwater is taken sufficiently deep to prevent evaporation. The mean recharge value is given by (e.g. Allison and Hughes, 1978):

$$\bar{Q}_r = \bar{R}\,\frac{(\overline{Cl}_R + \overline{Cl}_{DR})}{\overline{Cl}_w} \qquad (6.2)$$

where $\overline{Cl}_R$ is the mean Chloride rainwater concentration, $\overline{Cl}_{DR}$ is the mean Chloride dry deposition and $\overline{Cl}_w$ is the groundwater mean Chloride concentration.

Recharge values obtained with this method are given at table 6.6. Total annual recharge amount estimated with this chemical method is 40 hm^3 (19.0% of rainfall). The volume is greater than the one given by the previous method. That's because the method cannot give good recharge estimation at the arid and semi-arid zones. The two method's results are in very good agreement at Sub-Humid and Humid zones.

From these two methods, the estimated average recharge value can be given as 30 ± 10 hm^3 per year. Recharge is necessarily smaller at dry years. But at unusual rainy years, with more storm events, superficial runoff increases accordingly preventing high recharge values.

Table 6.6 – Bioclimatic zones annual Chloride budget method recharge values, (modofied from Pina (2009)).

Bioclimatic Zone	Precipitation mm per year	$\overline{Cl}_R + \overline{Cl}_{DR}$	$\overline{Cl}_w$	Recharge per year		Recharge/ Precipitation
		p.p.m.		mm	hm^3	%
I - Arid zone and II - Semi_Arid	164	36.2	163.0	36	21	21.9
III - Sub-Humid	430	27.1	177.7	65	10	15.2
IV - Humid	670	17.9	99.3	121	9	18.0

6.5 – Santiago hydrological units

The characterization of the hydrologic system volcanic islands like Santiago is difficult due to the observed heterogeneity and complexity of geologic formations. Nevertheless, the principal features of the system settings are the volcanism type, size and distance to main emission source, tectonic activity, age and non volcanic intruded materials (Custodio, 1986). Volcanic Groundwater path in Volcanic Islands is mostly linked to lithology formations. Empty spaces within rocks (porosity), vary in volume and shape, frequency and connectivity, being responsible by hydraulic properties, especially at most-recent formations (Rodrigues, 2002). The basaltic rocks typically have higher permeability (mainly those of acid type), and more recent lava flows are also more permeable then ancient flows (Custodio and Llamas, 2001). Porosity can range between 10 and 50% in pyroclastics rock type, to less than 5% at heavy lavas (Custodio, 1978). Hydrological units at Santiago have been grouped by their common formation's behavior. Data comes from geologic, borehole logging and pumping test's data studies (BURGEAP, 1974). Figure 6.19 shows the spatial distribution of the three main units; Bottom, Middle and Recent.

6.5.1 – Bottom Unit

The bottom unit is composed by the internal ancient eruptive complex (CA), the "Flamengos" (FL) and "Órgãos" (CB) formations. It is a compact unit, with strong altered outcrops and consequently, has a relatively low permeability against more recent units. The top 20 to 30 m CA formation are in general fractured and altered, with roughly 5 to 10 % porosity. The formation is compact below this layer without any groundwater on it. At this shallow layer, boreholes and wells have 5 to 15 m^3h^{-1} productions (8 to 10 hours per day extraction). Mean value of transmissivity (T) of this formation range from 0.2 to 5×10^{-5} m^2s^{-1}. The FL formation has hydraulic properties similar to those of CA. The exceptions are the pillow lavas' areas where mean production can reach the 20 m^3h^{-1} (10 to 12 hours per day), with small water level withdraw. The behaviour of the CB formation is like the others two, with general mean production of 5 m^3h^{-1}. The Value can be higher than that in CB formation (up to 10 m^3h^{-1}) with pyroclastics content, dikes and fractures' presence. This hydrological unit shows high a degree of mineralization waters.

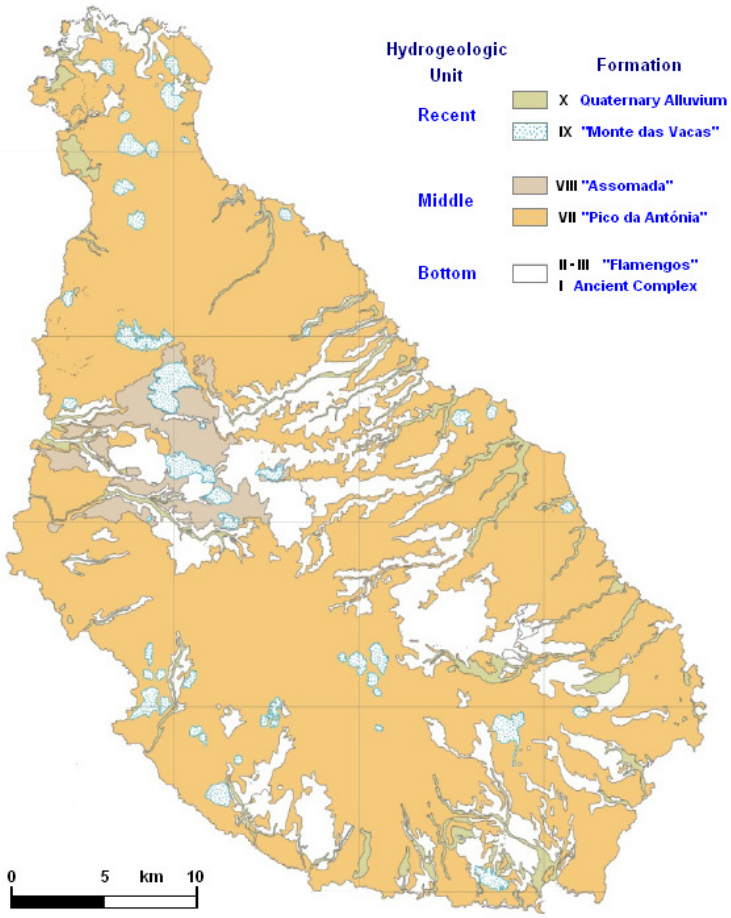

Figure 6.19 – Hydrogeologic Units at Santiago. (Modified from Serralheiro, 1976a).

6.5.2 – Middle Unit

This unit is composed by "Pico da Antónia" eruptive complex (PA) and Assomada formation (A). The PA formation is mainly a structure of basalt (submarine and aerial) with some pyroclasts showing some tens of meter's thickness. This is the main aquifer system, although shows a broad permeability, decreasing with depth. With the presence of pillow lavas, the PA formation has transmissivity values from 10^{-1} to 2×10^{-2} m^2s^{-1}. Pumping at these areas can be high as 40 m^3h^{-1} (12 or more hours per day). Mean extraction, is, however, of about 3 to 5 m^3h^{-1} with transmissivity values from 10^{-4} to 5×10^{-4} m^2s^{-1}. The Assomada formation has also some tens of meters, and is located at Assomada plateau. Mean extraction at this formation area is 20 to 25 m^3h^{-1} (10 to 12 hours per day), with transmissivity values ranging from 10^{-4} to 5×10^{-4} m^2s^{-1}.

6.5.3 – Recent Unit

This unit is composed by the "Monte das Vacas" (MV) formation and by Quaternary alluvium deposits. The former is essentially composed by basaltic pyroclastic cones and is extremely permeable. They are very important recharge areas liking groundwater to the system underneath. At the alluvium formation, hydraulic parameters are a function of grain size, thickness and clay content. When these Quaternary formations are thick, coarse and clay free, they can present high porosity and permeability values, with transmissivity ranging from

10^{-1} to 2×10^{-2} m^2s^{-1}. The productive boreholes at the several eastern downstream valleys (like Flamengos, Picos, Seca and São Domingos creeks) can reach 40 m^3h^{-1} (12 hours per day). Upstream the same valleys, where formation's thickness is smaller and materials are thinner, transmissivities range from 10^{-4} to 10^{-5} m^2s^{-1} and the mean extraction rate drops to 8 m^3h^{-1} (12 hours per day).

Table 6.7 – Main hydrologic units hydraulic parameters, (adapted from BURGEAP (1974)).

Hydrologic Unit	Geologic formation	Extraction / (m^3h^{-1})		T m^2s^{-1}
		limits	useful	
Bottom	CA	0 to 10	3	0.2 to 5×10^{-5}
	FL	0 to 25	5	0.2 to 5×10^{-5}
	CB	0 to 10	3	0.2 to 5×10^{-5}
Middle	PA	0 to 10 (basalt with pyroclasts)	5	10^{-4} to 5×10^{-4}
		0 to 5 (tufts and breeches)	3	0.2 to 3×10^{-4}
		20 to 100 (pillaw lavas)	40	10^{-1} to 2×10^{-2}
		10 to 60 (breeches)	30	10^{-1} to 2×10^{-2}
	A	0 to 10 (basalt with pyroclasts)	5	10^{-4} to 5×10^{-4}
		5 to 40 (thick areas)	25	10^{-4} to 5×10^{-4}
Recent	MV	-	-	-
	Alluvium	2 to 15 (upstream valley)	8	10^{-4} to 10^{-5}
		20 to 100 (downstream valley)	40	10^{-1} to 2×10^{-2}

6.6 – Santiago watershed points

The number of registered watershed points at Santiago is nowadays more than 3000 (INGRH). This number comprises natural springs (1199), manmade wells (1074) and boreholes (880). First census was done in the 70s of the last century and by end of 1979; the watershed points were already 2287. The initial knowledge of the hydrologic parameters came from the analyses of those data. With the growing and demanding of population, the water resources increasing is almost entirely due to new borehole facilities, at a present-day mean rate of ten boreholes by year. Not all this watersheds is still active. Many wells had become dry and only seven hundred are useful. The number of working borehole is around three hundred. The valuable springs are about to 264, but only 41 have a really important water flow rate. To overcome water needs, the Poilão water dam at Seca stream was finished by 2008 (Gomes, 2007). It is a medium rainfall catchment structure with an 1.2 hm^3 volume capacity. A few desalinization power plants exist also. Nowadays, 70% of Praia's waters consumption comes from desalinization.

6.6.1 – Springs

Springs are related to geology, especially to fractures and dike's location. Most of them are found at island central plateau, between Pico da Antónia and Serra da Malegueta mountains. Springs are found from 3 m to 804 m high, and they have a seasonal variability trough the hydrologic year. The most productive springs have a 300 m^3 per day mean flow that can be higher as 1000 m^3 per day after "rain season". Springs total water flow estimation exceeds certainly 5 hm^3 reaching perhaps 10 hm^3 a year.

6.6.2 – Wells

Wells are the manmade oldest way to extract water, existing since archipelago occupation. Typically, they have 2 to 4 m diameter with 3 to a maximum of 15 m depth. They are settled at alluvium formation, and made with stone walls. Most of them are located at the eastern side of the island, figure 6.20a), but can also be found at central and higher locations, at Bottom Unit basalt fractured layer or receiving water from some perched water body. They usually provide small water quantities, between 10 to 15 m^3 per day, at Bottom Unit formations. At the alluvium that quantity can easily grow to 100 m^3 per day. Wells represent a water-quality problem as they are extremely vulnerable to contaminations by standing on high permeable formations near the shoreline. The over-exploitation and diffuse contaminations by human activities are a constant at many locations.

6.6.3 – Boreholes

Boreholes have a more uniform distribution over the island, and have been made from the sea level to 700 m high, figure 6.20b). Their location is related to local hydrogeological settings and also to sea distance, to prevent seawater intrusion. Boreholes depth varies from 30 to 270 m, with deeper ones at higher locations. INGRH controls annually 150 boreholes that make a groundwater extraction of 4.5 hm^3. It is reasonable to consider a maximum total amount of 9.0 hm^3 by all the 300 operational boreholes on the inland.

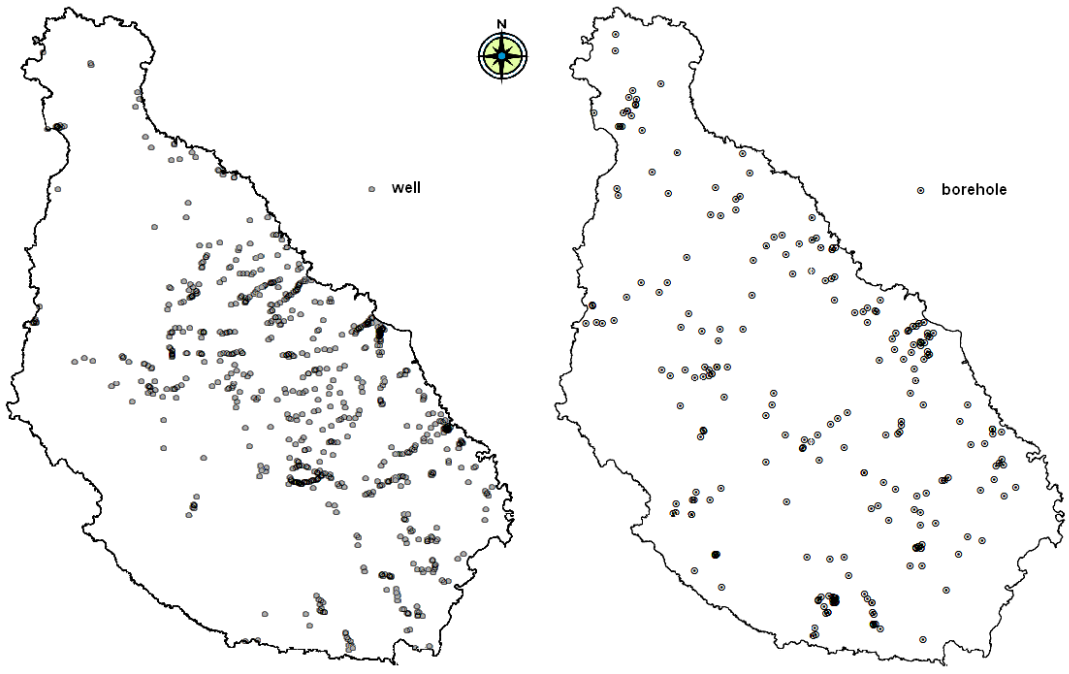

Figure 6.20 – Location of active and controlled wells a) and boreholes b), (INGRH).

6.6.4 – Piezometric head

From INGRH water level regular measure's data set (not covering all databases points, but just a couple hundred) it's possible to map the groundwater piezometric head surface of the island.

The analysis of the time evolution of springs discharges, plus the groundwater level at wells and boreholes have shown that piezometric level seems to be reasonable continuous all over the island. There is a direct, as also an indirect observed seepage (a few months after "rain season"). Springs discharge amount can vary a lot after precipitation. Piezometric level variations aren't significant over the last decade, at island scale dimension, (Pina, 2009). The piezometric map is presented at figure 6.21, with plotted flow direction, driven by the hydraulic gradient, (care must be taken especially at areas where no data exist to support krigging interpolation or same outlier data point). From level lines, clearly that the piezometric surface follows the topographic one (see figure 6.6) and have the same island axis symmetry. Groundwater flows naturally outwards, and drains to gully valleys and sea. Hydraulic gradient is higher (around 0.05 $m.m^{-1}$) at high-altitude locations, and much smaller at lower ones (around 0.008 $m.m^{-1}$).

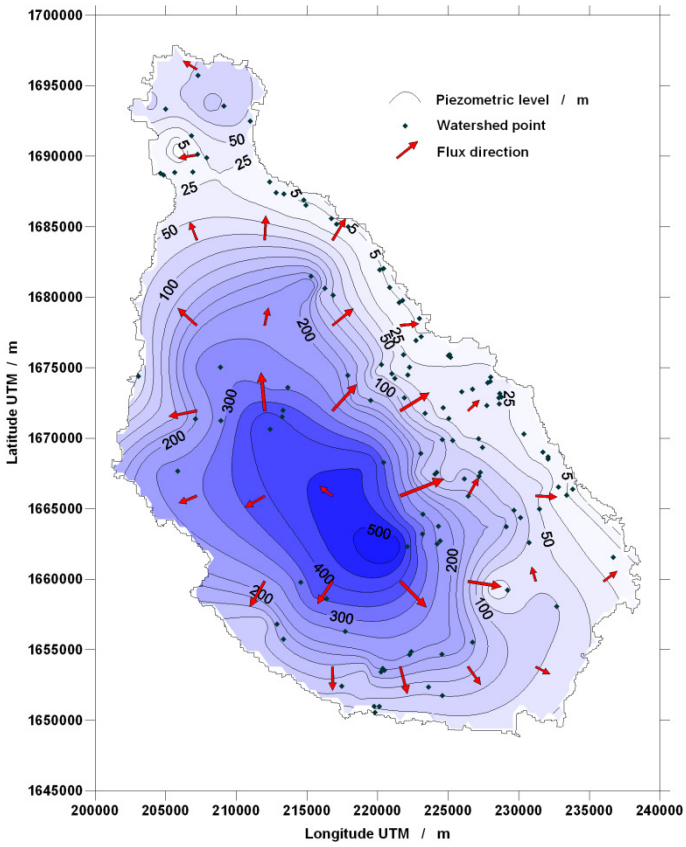

Figure 6.21 – Santiago piezometric map, 2004 (INGRH data).

6.6.5 – Conceptual hydrogeologic island model

As described, Santiago (like all Cape Verde islands) has predominantly made by basaltic lava flows, interspersed with pyroclastics and breccias and intruded by near-vertical mafic dikes. The current conceptual understanding of recent volcanic oceanic island hydrogeology is based primarily on Hawaiian studies (Peterson 1972, Macdonald *et al.*, 1983, Oki *et al.*, 1999, Hildenbrand *et al.*, 2005). On this high topographic relief, shallow soils, and rapid runoff or infiltration islands, the conceptual hydrogeologic model consists of a regional low-gradient water table aquifer with overlying perched and dike-confined groundwater bodies. The vertical and steeply dipping intrusive feeder dikes form as magma moves upward through both the central caldera and along fissures at volcano's flank (through pre-existing

lava flows). These denser and low-permeability intrusive feeder dikes often act as barriers to horizontal flow, creating large groundwater reservoirs (Mink, 1963; Peterson, 1972; Jackson and Lenat, 1989). At the same time, low-permeability clay layers intercalated with and formed by the weathering of the upper surfaces lava flows may also act as hydraulic barriers (Barmen *et al.*, 1990). Such horizontal and vertical flow barriers produces perched groundwater bodies, the highland springs, and by compartment of groundwater, can create a stepped and discontinuous water table (figure 6.22).

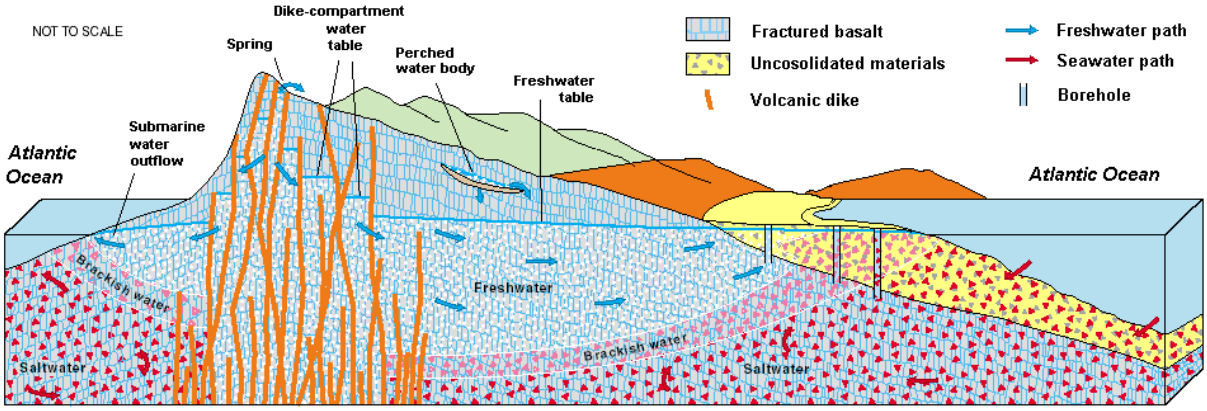

Figure 6.22 – Generalized conceptual model of volcanic islands hydrogeology, (modified from Macdonald *et al.*, 1983).

The admitted model for Santiago is that the majority of infiltration and groundwater recharge occurs at the highest areas, as they have many times more precipitation than coastal areas, high-permeability basalts, and closed-basin calderas (Barmen *et al.*, 1984, 1990; Kallrén and Schreiber, 1988). Application of this conceptual model to Santiago Island is compatible with the existence of a major groundwater central reservoir at Middle Unit, the PA and Assomada formations being the catch area the closed-basin of Santa Catarina plateau (Pina, 2009). The reservoir could have a lens shape being thicker in the middle, resting over the much more impermeable Bottom Unit, figure 6.23. At this central region, the many intrusive near-vertical dikes can create independent groundwater bodies. Groundwater movement at the central region is essentially vertical downward, but the many fractures, faults and dikes play a key role to the local groundwater path. At lower regions, near the surface the water movement is roughly sub-horizontal to the sea, but an upward flow can be present from deeper groundwater.

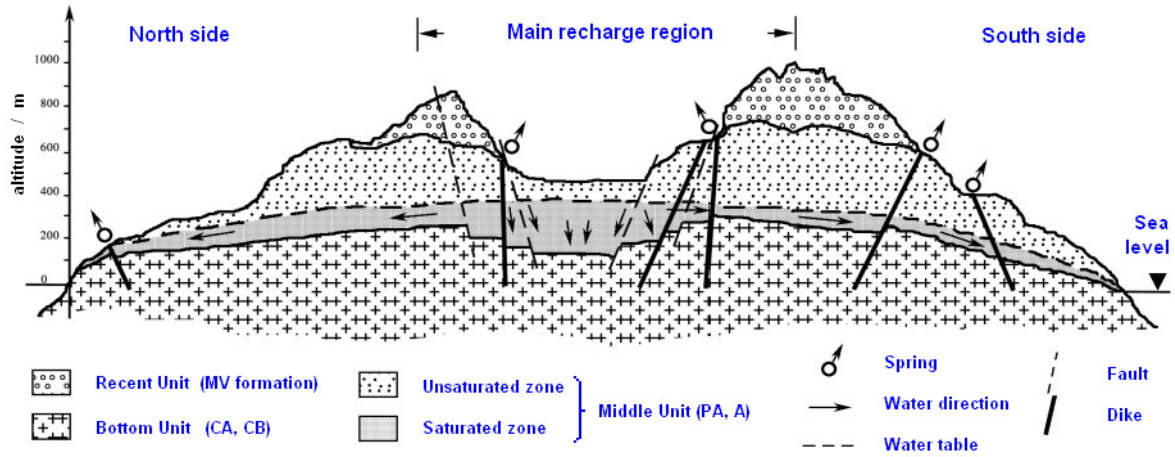

Figure 6.23 – Santiago conceptual model (modified from Pina (2009)).

The low-density lens shape freshwater reservoir stands over the higher-density brackish and saltwater. Under steady-state conditions, the freshwater hydraulic head above sea level should be balanced by an approximately 40-fold thickness of fresh water beneath sea level, as given by the Ghyben-Herzberg principle. Boundary between fresh and brackish waters isn't even sharp or fixed. It is controlled by pressure and density and is balanced by groundwater recharge and groundwater discharge (Peterson 1972). Aquifer drawdown due to excessive extraction will lower water levels and move the fresh/brackish water interface upward and inland, producing a salt-water intrusion (Gingerich and Oki, 2000). Springs are the manifestation of groundwater natural discharge at Santiago. The others are wells and boreholes withdrawals, occasional seepage to streams, and shallow water table evapotranspiration. Groundwater discharges most probably also includes a sub-surface outflow to the ocean. Such submarine groundwater discharge (SGD) has been documented in other volcanic island sites (Izuka and Gingerich 2003; Hildenbrand et al. 2005; Prada et al. 2005) and could represent a substantial fraction of total groundwater discharge from the island aquifer.

6.7 – Santiago hydrochemistry

The properties of groundwater are very limited and piecewise if we just stay at the knowledge of water table depth (or the hydraulic head), flow amount, temperature or electric conductivity (EC), for instance. With chemical and isotope hydrology, many more parameters data are available, allowing the access to the concealed nature of groundwater.

Starting with pure water, it is composed by the most common Hydrogen and Oxygen atoms, but also with more rare isotopes, like Deuterium (^{2}H or D) and heavy Oxygen ^{17}O (very rare) and ^{18}O. A sample of pure water will be mostly H_2O with some heavier rare molecules HDO and $H_2{}^{18}O$.

Natural water has also dissolved salts, dissociated into cations and anions. The most common cations are Sodium (Na^+), Calcium (Ca^{2+}), Magnesium (Mg^{2+}) and Potassium (K^+). The most common anions are Chloride (Cl^-), Bicarbonate (HCO_3^-), and Sulphate (SO_4^{2-}). Water contains also dissolved gases. The major source is the atmosphere with molecular Nitrogen (N_2), Oxygen (O_2), and noble gases; Helium (He), Neon (Ne), Argon (Ar), Krypton (Kr), and Xenon (Xe). Many more can be of biogenic origin, added to the water in the ground, like Carbon Dioxide (CO_2), Methane (CH_4), and Hydrogen Sulphide (H_2S).

Cosmic rays interact with our upper atmosphere and produce a variety of radioactive isotopes. Three of them have a special interest to hydrology; Tritium (^{3}H or T) the heaviest hydrogen isotope, Carbon-14 (^{14}C), the heaviest isotope of carbon, and Chlorine-36 (^{36}Cl), a rare Chlorine isotope. The half-life rate of radioactive decay gives us the time of permanence at saturated zone since incorporated into groundwater, and they are 12.32 ± 0.022, 5730 ± 40 and 301000 ± 4000 years, respectively to Tritium, Carbon and Chlorine radioactive isotopes. Those rates allow investigation period values from a few decades, to 25000 years, and 100000 to one million years, respectively. All these isotopes have also been produced by nuclear bomb tests, providing additional inputs to natural systems (Mazor, 2004).

Water with all these (and more) components will infiltrate into the ground, and react chemically with underground rocks that have minerals and biologic materials. Physical factors are also important, for instance, to rock rupture and hence more area available to reactions. At Santiago Island, most rocks are basaltic by nature, mostly with siliceous minerals. This rock type is extremely favourable to chemical alteration process, like dissolution, hydrolyse and oxidation. Not only, rock type, but also the climatic condition, water constituents, rock-water interaction time and soil existence are factors that control chemical rock changing degree. At scarce rain regions, like the arid and semi-arid areas of Santiago, the chemical alteration processes are naturally slower. Rock's influence depends on its texture, structure and mineral composition. The structure and texture are decisive to water path and solely by the surface rock area – water interaction. Cationic groundwater content is then changed, as some of these rock elements, like Na, Ca, Mg and K dissolves easily, function of pH and temperature (Custodio and Llamas, 2001).

Several hydrochemistry investigations have been done at Santiago Island. Barmen *et al.* (1984) made principal groundwater elements studies and Tritium determinations at north, central and eastern locations. Akiti (1985), has done stable isotope's determinations (^{2}H, ^{18}O, ^{13}C), Tritium and ^{14}C at Tarrafal and Achada Baleia locations. The INGRH (1994) has done a similar study, including the first rain water chemical and isotopic analyses at Santiago Island. Recent studies have been from Hydroarid project. Under the scope of this project, a new chemical campaign has been done, sampling uniformly the island at 133 points. (Gomes, 2007; Pina, 2009), and ^{2}H, ^{18}O, and ^{3}H isotopic analyse to 60 points (a subset of the 133) have been also accomplished (Carreira *et al.*, 2007a). Last hydrochemical and stable isotopic study was about potential recharge areas and salinization groundwater mechanism at eastern seashore, Condesso de Melo *et al.* (2008).

The following descriptions are mostly based on the Hydroarid project data. Chemical analyses are from samples taken in June-July 2003 (before the "rain" season), in November-January, 2003-2004 (after the "rain" season) and throughout the year 2004. Isotopic analyses are from December 2005, February 2006 and November 2006, altogether with chemical samples analyses. The number of samples by watershed and hydrogeologic unit are given at the table 6.8, and plotted at figure 6.24.

Table 6.8 – Chemical and isotopic analyses by hydrologic unit and watershed type.

Hydrogeologic Unit	Spring		Well		Borehole	
	Chemical	Isotopes	Chemical	Isotopes	Chemical	Isotopes
Bottom	10	1	-	-	18	3
Middle	30	15	-	-	49	32
Recent	-	-	25	-	1	9
Total	**40**	**16**	**25**	**-**	**68**	**44**

All these water sampling and analysis's procedures are described at the Gomes (2007) and Pina (2009) thesis. The analysis's electroneutrality (EN) value is under 4% for 33% of total samples and between 4 to 10% for the remaining 77%. The acceptable error should be less than 5% (Appelo and Postma, 2005) or 4% to "high" electric conductivity waters (Custodio and Llamas, 2001). Groundwater samples total mean EN value is 6.45%.

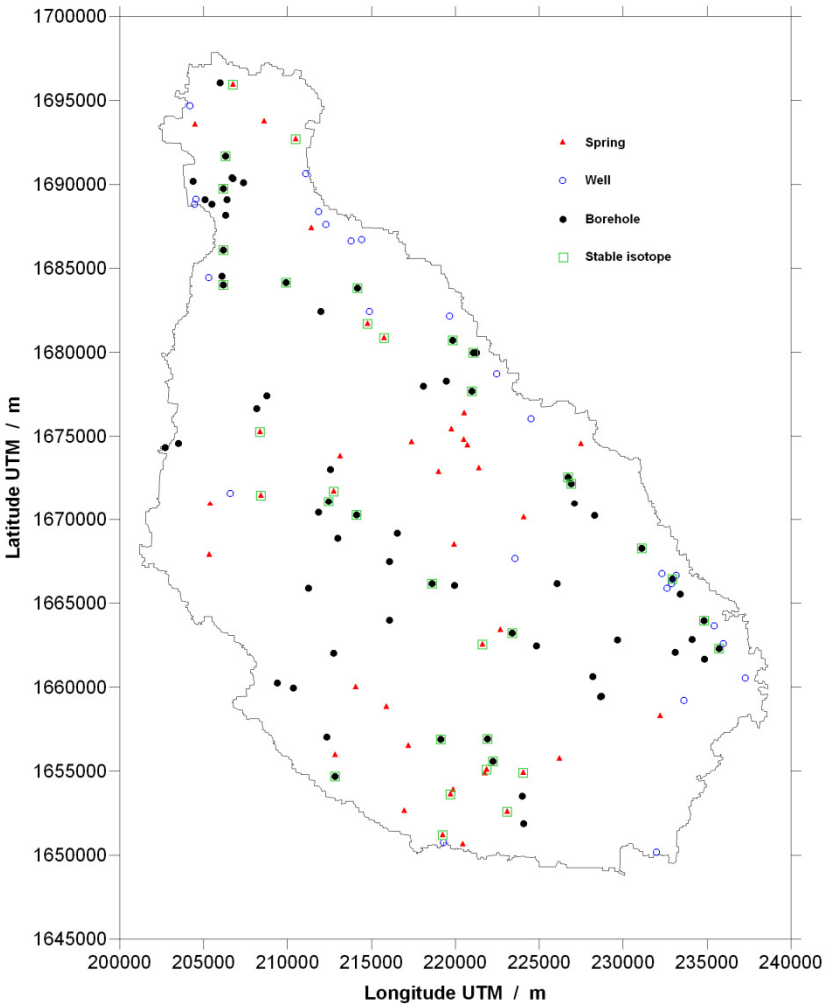

Figure 6.24 – Chemical and isotopic sampled watersheds.

6.7.1 – Groundwater temperature

Water and rock temperature is important because it enhances significantly the mineral and gases' solubility. However, temperature data analyses have shown that no significant difference exists between shallow and depth groundwater, and between the different hydrogeological units. Temperature remains almost the same throughout the year, with small amplitude, less than 1 to 2 ºC. Several boreholes follow the seasonal atmospheric temperature variation being always warmer than air. Figure 6.25a) plots the mean measured temperatures. Mean temperature is around 26 ºC, with some spurious watershed points. Minimum and maximum temperatures (20.3 and 34.9 ºC) were measured at Middle Unit formation. The Recent Unit as the smallest amplitude between extreme temperatures.

Table 6.9 – Temperature mean values at hydrogeologic units.

Temperature ºC	**Hydrogeologic Unit**		
	Bottom	**Middle**	**Recent**
Mean	26.2	26.1	26.0
Standard deviation	1.8	1.9	1.4

6.7.2 – Groundwater pH values

The pH parameter is very important because it controls chemical reactions, like acid-base equilibrium, hydrolyze, adsorption, redox (Langmuir, 1997). At Santiago, a clear difference can be seen; the eastern region groundwater are slightly acid to neutral (6.75 to 7.25) and western regions more alkaline (> 7.25). A possible explanation can be related to the predominant winds at this island side, with bigger moisture content and also were most groundwater extraction happens, water time residence and rock-water interaction being smaller. Figure 6.25b) shows the mean measured pH values. Minimum and maximum pH (5.7 and 8.2) were measured at Middle Unit formations. Like temperature values, the Recent Unit has the smallest amplitude between extreme pH values (6.5 to 7.5). Lowest and highest pH areas in figure 6.25b) are due to some pH "outlier" measured single points. The problem always happens when the spatial distribution is non-uniform and extreme data points are present, creating an "eye pattern" (closed lines around a single point).

Table 6.10 – pH mean values at hydrogeologic units.

pH	Hydrogeologic Unit		
	Bottom	Middle	Recent
Mean	7.1	7.1	7.0
Standard deviation	0.3	0.4	0.2

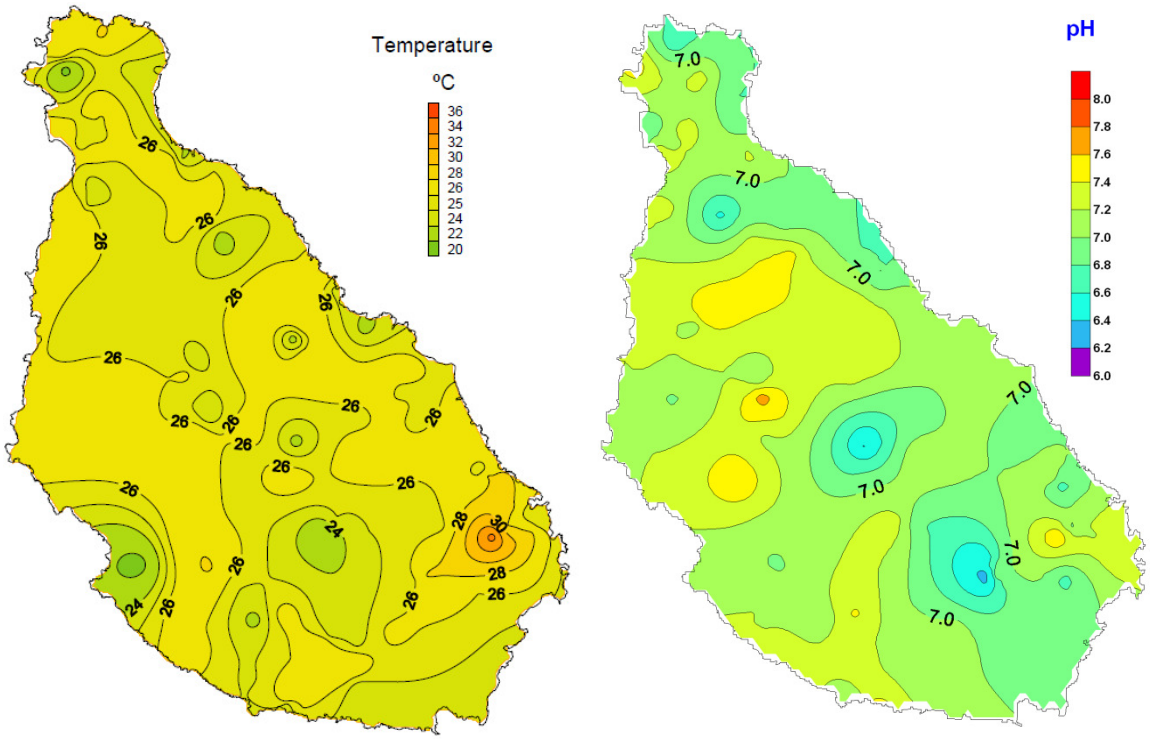

a) **b)**

Figure 6.25 – Temperature a) and pH b) Santiago's maps, (temperature map modified from Pina (2009)).

6.7.3 – Groundwater electric conductivity

Groundwater electric conductivity (EC) it's a function of ionic content and also temperature. It is a measure of mineralization degree, e.g. by rock dissolution, or can result from industrial, agriculture, domestic and salt intrusion contaminations. At Santiago, high EC values are found near the sea, decreasing inland and in altitude. Eastern island side shows grater EC values than the western side. This later coastline is higher above the sea with fewer inhabitants and consequently, smaller water extraction needs. Areas with smaller EC at north and south correspond to springs and boreholes at Middle Unit. Although some variability in EC values has been observed, the majority of sampled points haven't changed significantly over the time of this study, especially between dry and rain epochs. Exceptions have been detected at some points in Recent Unit formations, near the sea, with smaller EC values after "rain season", certainly due to the increase in the inland freshwater content. The EC distribution is shown at figure 6.26.

Table 6.11 – EC mean values at hydrogeologic units (20 ºC).

Electric conductivity µS.cm^{-1}	**Hydrogeologic Unit**		
	Bottom	**Middle**	**Recent**
Mean	1353	1226	2895
Median	1261	741	2215

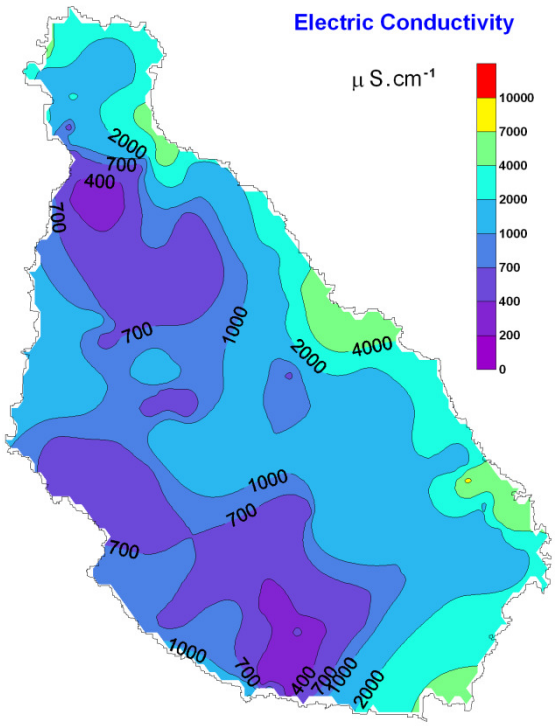

Figure 6.26 – Electric conductivity distribution map (20 ºC), (modified from Pina (2009)).

For the Bottom Unit, the minimum and maximum values were 440 and 2750 µS.cm^{-1}. Middle Unit shows much greater amplitude, from 362 to 53500 µS.cm^{-1} (seawater) and Recent Unit from 503 to 8550 µS.cm^{-1}. These very high EC were observed in wells close to the sea. If we exclude these outlier points (with explained cause), the mean EC values (table 6.11)

between the Bottom and Middle Units are similar but smaller than those in Recent Unit measured values. The sampled watersheds at this last Unit are mostly wells in alluvium formations. At the Bottom Unit the EC mean value stays constant over the distance to shoreline. For the Middle and Recent Units, that not holds. EC values grow significantly starting from 1.5 km to shoreline.

6.7.4 – Groundwater cations

In Santiago Island, the relation between major cation's abundances has as follows; [Na] > [Mg] ≥ [Ca] > [K]. Cations are the groundwater constituents who have major affinity and interaction with environment rocks and came from this rock-water interaction process and also from human activities and seawater intrusion. Mean observed values are given in table 6.12.

Sodium (Na^+)

This is by far the predominant cation in the island groundwater, with 55% of the total cation's amount. Sodium can have different sources; Halite (sodium chlorine) maritime aerosol deposition at dry season (incorporated to soil in "rain season"), alkaline type rock with plenty of Sodium, Calcium and Magnesium, and ultimately from seawater intrusion. Groundwater Sodium distribution seems almost constant throughout the island, with a 100 to 150 mg per liter mean content. It is the natural background concentration, presumable from rain and rock minerals dissolution origin. Exceptions to these are the north and eastern regions. At those locations, the values are much higher, presumable from seawater intrusion origin. At the Bottom Unit hydrogeological unit the Sodium mean value stays constant with distance to shoreline. For the Middle and Recent Units, the Sodium concentration grows significantly, starting 1.5 km to shoreline, figure 6.27a). That mimics the EC behavior because this parameter is a function of water salt concentration. Range values are from 19.7 to 438 $mg.L^{-1}$ at Bottom Unit, 22.6 to 652 $mg.L^{-1}$ at Middle Unit and 67.6 to 1349 $mg.L^{-1}$ at the Recent Unit.

Magnesium (Mg^{2+})

For most of Santiago areas, Magnesium content surpasses the 25 mg per liter. At the eastern coastal region, that value is much higher. Magnesium origin must come from dolomite and magnesite dissolution (Martins, 2003) or olivine hydrolyzes (Matos Alves *et al.*, 1979). Range values are from 4.1 to 51.7 $mg.L^{-1}$ at Bottom Unit, 1.8 to 64.6 $mg.L^{-1}$ at Middle Unit and 6.0 to 347.9 $mg.L^{-1}$ at Recent Unit. Magnesium distribution is plotted at figure 6.27b).

Calcium (Ca^{2+})

The highest values of Calcium concentration do exist at the east and north island side. Origin can be from Calcite dissolution (Calcite exists at the major volcanic formations), carbonate rock dissolution at Tarrafal region (at north), by plagioclase hydrolyze and pyroxene's mineral alterations or by seawater intrusion with Sodium cationic exchange. Range values are from 8.0 to 126.4 $mg.L^{-1}$ at Bottom Unit, 6.4 to 1280 $mg.L^{-1}$ at Middle Unit and 32.0 to an extreme

value of 3496 mg.L^{-1} at Recent Unit (last value comes from one seawater intruded well). Molar ratio between Ca/Mg is less than one at most samples. That means that there is a major dissolution of magnesium minerals over calcium ones. Calcium distribution is given in figure 6.28a).

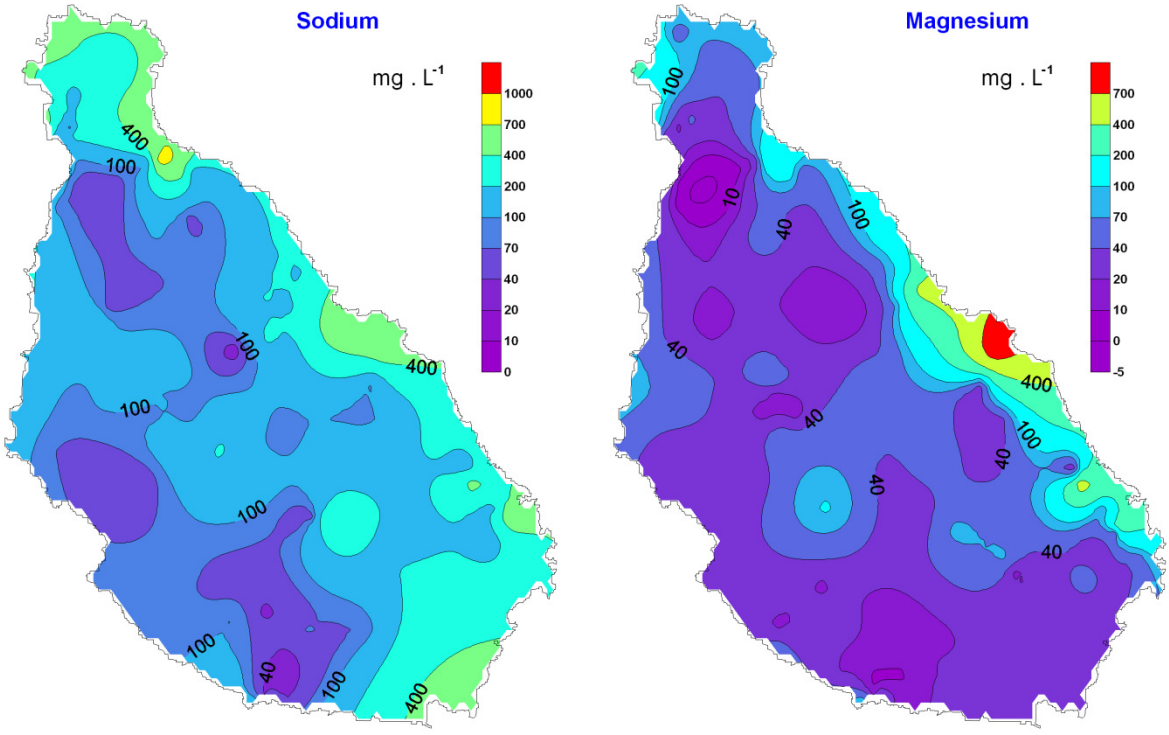

a) **b)**

Figure 6.27 – Sodium a) and Magnesium b) distribution maps.

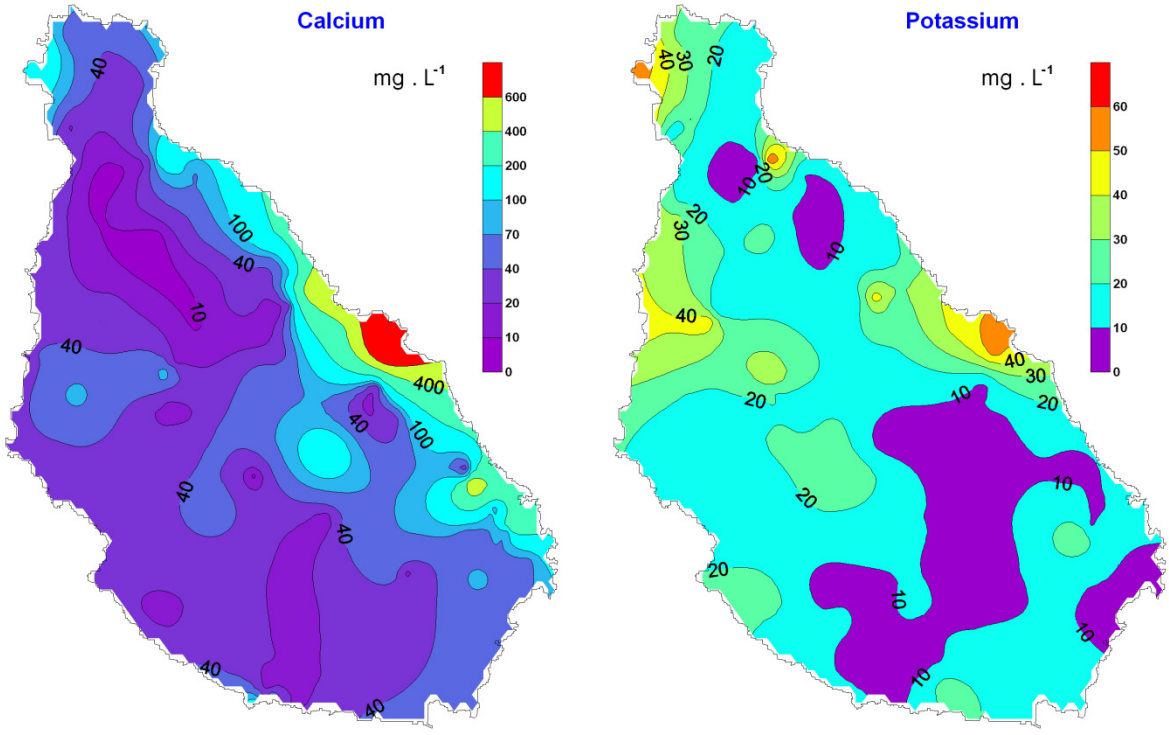

a) **b)**

Figure 6.28 – Calcium a) and Potassium b) distribution maps.

Potassium (K^+)

Groundwater Potassium distribution is enhanced in the northwest, west and east regions of the island. The Potassium origin must be related to potassium feldspats interactions. They have been identified in fractures at CA formations, with frequent well developed crystals (Matos Alves *et al.*, 1979). Another Potassium origin is surely the fertilizer application at farmed valley's soils, although the limited Potassium mobility caused by soil retention at clay layers. Range values are from 4.1 to 51.7 $mg.L^{-1}$ at Bottom Unit, 1.8 to 64.6 $mg.L^{-1}$ at Middle Unit and 6.0 to an extreme value of 348 $mg.L^{-1}$ at Recent Unit (last value is from a seawater intruded well). Potassium distribution is given at figure 6.28b).

Table 6.12 – Mean values of major cations at hydrogeologic units.

Mean concentration $mg.L^{-1}$	Hydrogeologic Unit		
	Bottom	Middle	Recent
Sodium	165.8	133.1	333
Magnesium	54.4	53.4	195
Calcium	45.0	59.8	211
Potassium	18.6	16.3	29.5

6.7.5 – Groundwater anions

The relation between major anion's abundances in Santiago Island is as fallowing; $[HCO_3] > [Cl] \geq [SO_4] > [NO_3]$. These compounds, Bicarbonate, Sulphate and Nitrate reveal less affinity with environment rock than observed cations. These anions came from natural rock-water interaction process and also from human contamination, like agriculture activities. Mean values are given at table 6.13.

Chloride (Cl^-)

This groundwater anion specimen comes directly or indirectly from seawater, as rock source chloride has a small expression. It reaches the groundwater by sodium chlorine maritime aerosol deposition (like sodium) and by seawater intrusion at the seashore. Inland, the groundwater mean chloride concentrations is less than 150 $mg.L^{-1}$. The major groundwater Chloride distribution happens at eastern and northwest shoreline, figure 6.29a). The Bottom Unit has the smaller concentration and Recent Unit the highest. Range values are from 49.6 to 535 $mg.L^{-1}$ at Bottom Unit, 26.2 to 5,708 $mg.L^{-1}$ at Middle Unit and 42.5 to a extreme value of 14003 $mg.L^{-1}$ at Recent Unit (last value is from a seawater intruded well).

Bicarbonate (HCO_3^-)

The highest concentrations of Bicarbonate are located inland at central island major recharge areas, figure 6.29b). For most samples, it is the major anion. In addition to rainwater origin, it comes also from carbonate dissolution or minor silicate weathering. The Bottom Unit has the highest concentration and the Recent Unit has the smallest. Range values are from 146 to 708 $mg.L^{-1}$ at Bottom Unit, 78 to 566 $mg.L^{-1}$ at Middle Unit and 78 to 372 $mg.L^{-1}$ at Recent Unit.

Sulphate (SO_4^{2-})

The anion Sulphate is one of the less abundant in Santiago's water samples. Distribution is rather uniform except near the east coast and at "Órgãos" formation (Bottom Unit), figure 6.30a). These inland higher concentrations are related to marine facies carbonate rocks. It's roughly the same region were high bicarbonate values also take place. At shoreline, it may be related to seawater intrusion, as Sulphate is one of the major seawater anions. This explains the small concentration values observed at the Middle Unit. Range values are from 4.6 to 296 $mg.L^{-1}$ at Bottom Unit, residual to 364 $mg.L^{-1}$ at Middle Unit and 18.2 to 546 $mg.L^{-1}$ in Recent Unit.

Nitrate (NO_3^-)

At Santiago, Nitrates doesn't exist naturally. They leach into groundwater by overfertilization at farmed soils, especially in the stream valleys' closest to the ocean. The other contaminant sources are manure, at some punctually intensive goat's areas and nonagricultural sources such as septic systems and cesspools (Santiago Island hasn't yet a developed residual drainage network). The majority of groundwater samples (98%) show Nitrates contends. 15% of all samples surpass the human consumption legal admitted maximum. Values range from <0.1 to 23.0 $mg.L^{-1}$ at Bottom Unit, <0.1 to 20.6 $mg.L^{-1}$ at Middle Unit and <0.1 to 66.6 $mg.L^{-1}$ in Recent Unit. At this Unit highest values are observed at farmed areas; westwards of Praia (Cidade Velha), in the eastern side (S. Domingos, S. Cruz and S. Catarina) and at the east side, figure 6.30b).

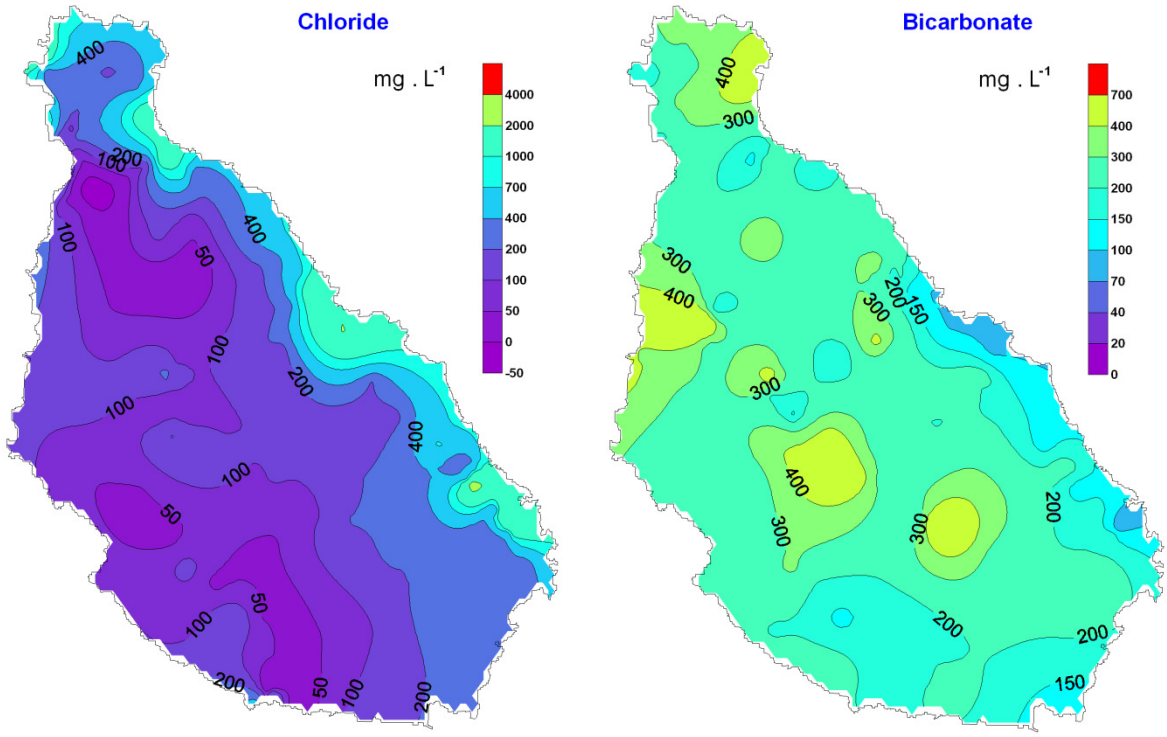

a) **b)**

Figure 6.29 – Chloride a) and Bicarbonate b) distribution maps.

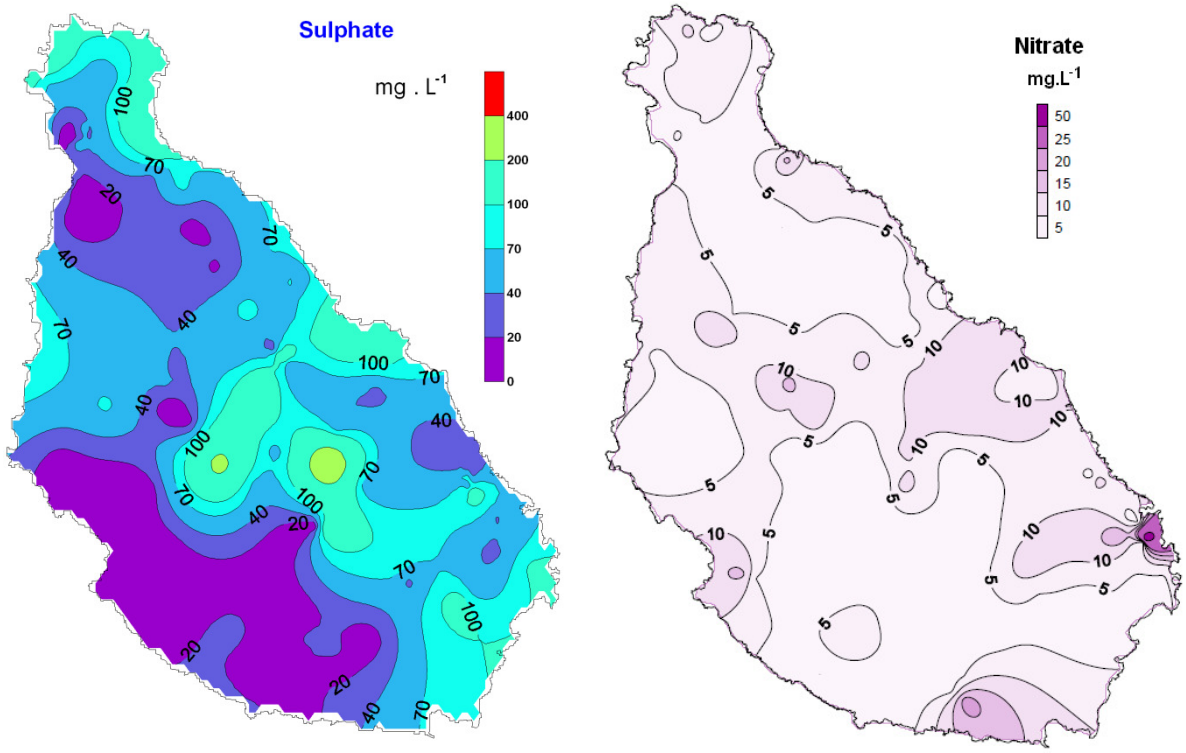

a) **b)**

Figure 6.30 – Sulphate a) and Nitrate b) distribution maps, (nitrate map modified from Pina (2009)).

Table 6.13 – Mean values of major anions at hydrogeologic units.

Mean concentration mg.L^{-1}	Hydrogeologic Unit		
	Bottom	Middle	Recent
Bicarbonate	327	226	205
Chloride	197	254	1,080
Sulphate	70.9	38.7	91.9
Nitrate	6.9	5.9	7.9

The know Br/Cl ratio is an invaluable tracer of groundwater processes and origin (e.g., Simpson and Herczeg, 1994; Herczeg *et al.*, 2001). Oceans have a constant molar Br/Cl ratio of 0.00154 (e.g., Drever, 1997; Davis *et al.*, 1998, 2001). Small islands and coastal rainfall commonly have similar Br/Cl ratios. However, inland rainfall at arid or semi-arid climates may have lower ratios due to the tendency for Chloride to be removed by deposition of marine aerosols in coastal areas (Edmunds, 2001).

At Santiago, the major part of the groundwater samples (for the three hydrogeologic units), have a Br/Cl ratio that fits to the ocean molar ratio (figure 6.31a), confirming groundwater origin. A few groundwater samples have a reduced ratio that could be due to interaction with Chloride bearing contaminants such as some fertilizers (Cartwright *et al.*, 2006). However, the plot of molar Na/Cl ratio, figure 6.31b) (seawater as a constant ratio of 0.85) shows for higher concentration samples, that Sodium seems to be arrested by clay minerals. That's predominant at Recent Unit formations and an indication of a seawater intrusion process, (Pina, 2009).

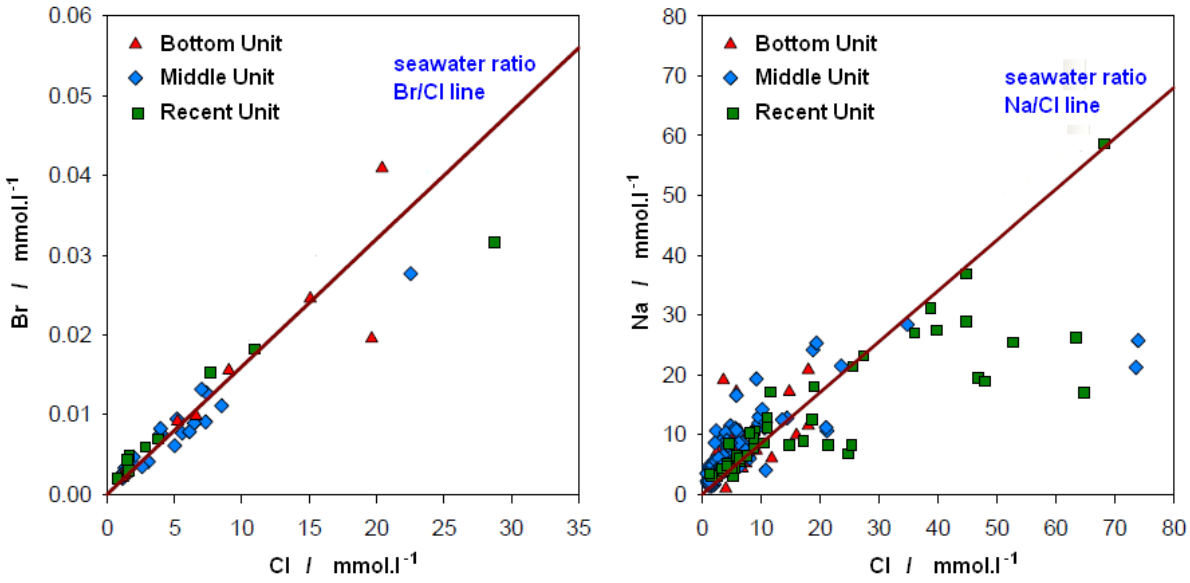

a) b)

Figure 6.31 – Groundwater samples against seawater ratios: a) Br/Cl ratio, b) Na/Cl ratio. (Modified from Pina (2009)).

A strong correlation, with a fit regression of 99%, exist between the EC values and the major cations and anion's summation, the calculated water total dissolved salts (TDS) or total salinity, figure 6.32. Although water samples have much more dissolved ions, their total weight amount is at least two orders of magnitude lesser than those major ones.

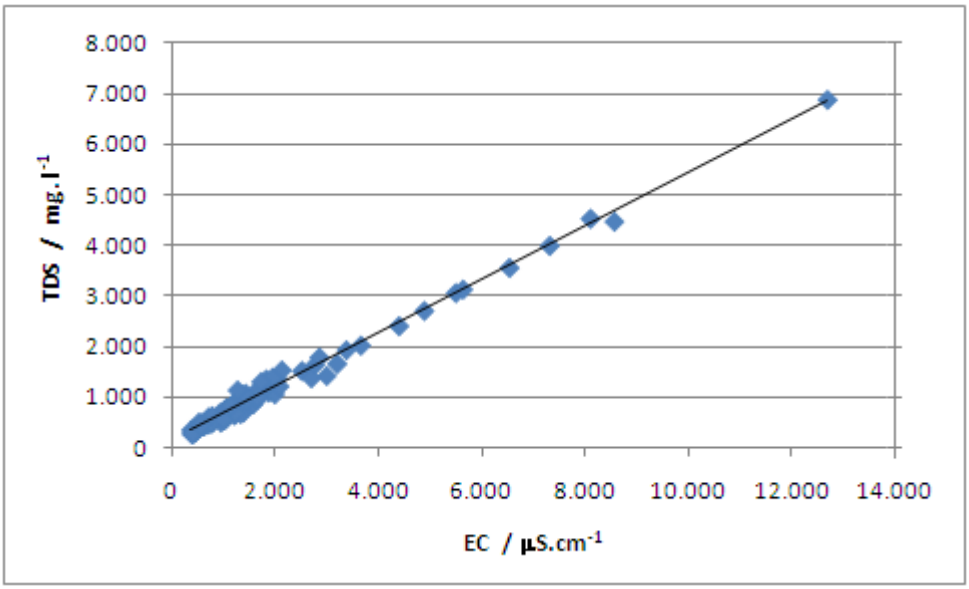

Figure 6.32 – Groundwater electric conductivity versus total dissolved salts.

The good correlation (R^2 = 0.99) gives confidence about chemical data. The general relation EC versus TDS (expressed at equation (5.10)) is:

$$\mathrm{TDS} = 0.528 \times \mathrm{EC} \qquad (6.3)$$

with $1/\beta = 0.528$

6.7.6 – Mineral saturation indices

Previous studies about saturation indices (SI) of calcite, dolomite, magnesite and silica have been published (Akiti, 1985; Pina 2009). SI is defined as the logarithm of the ratio of the ion activity product to the solubility product.

At northwest area (Tarrafal region), the springs show an undersaturation condition of calcite and dolomite, meaning that water hasn't been enough time to get into equilibrium with those minerals. That could represent a mixture of different origin waters. Concerning borehole waters, some are supersaturated with respect to dolomite and some are undersaturated with respect to calcite. This saturation index variation can be due to different waters contributions.

At Eastern side (Achada Baleia region) most of the wells are undersaturated with respect to calcite, and a few are supersaturated with respect to dolomite. Calcite minerals appear to dominate as the majority of wells have Ca/Mg molal ratio greater than unity. In boreholes, most of the waters are supersaturated with respect to dolomite and only half of them are supersaturated with respect to calcite. The Ca/Mg molal ratio is generally lower than unity, showing a greater presence of magnesium over calcite minerals. The basic rocks of Middle formation are responsible for the dissolution of magnesium (Akiti, 1985). Deeper waters are older than superficial waters, because they had sufficient time to become in equilibrium with dolomite and calcite. These are the ones which SI values cannot be attributed to different waters mixing. Both borehole and well waters are silica saturated (typical at this crystalline rock environmental).

As a rule, boreholes waters have a saturated and supersaturated condition related to dolomite and magnesite. This is also verified for calcite, but to a lesser extent. The majority of the water from springs and wells are undersaturated to those minerals (Pina, 2009). This means that superficial groundwater is younger than the deeper groundwater.

6.7.7 – Chemical groundwater facies

Groundwater chemical is usually described by plotting data in special diagrams, for instance, the Stiff and Piper patterns. The observed groundwater facies type it's a consequence of water origin - rainfall, followed by its land deposition and variable interaction with underground rock minerals, and lately by human activity's impact and / or seawater interconnection. All this factors, trough time, had influence over the observed water composition and quality, at the natural and manmade seepages.

Island Stiff patterns (figure 6.33) show a distinct behaviour by hydrogeological unit and consequently, by watershed location. The central, south and southwest regions with Bottom and Middle units have an ionic amount (salts) much smaller than seashore ones at Recent Unit formations (eastern and north sides).

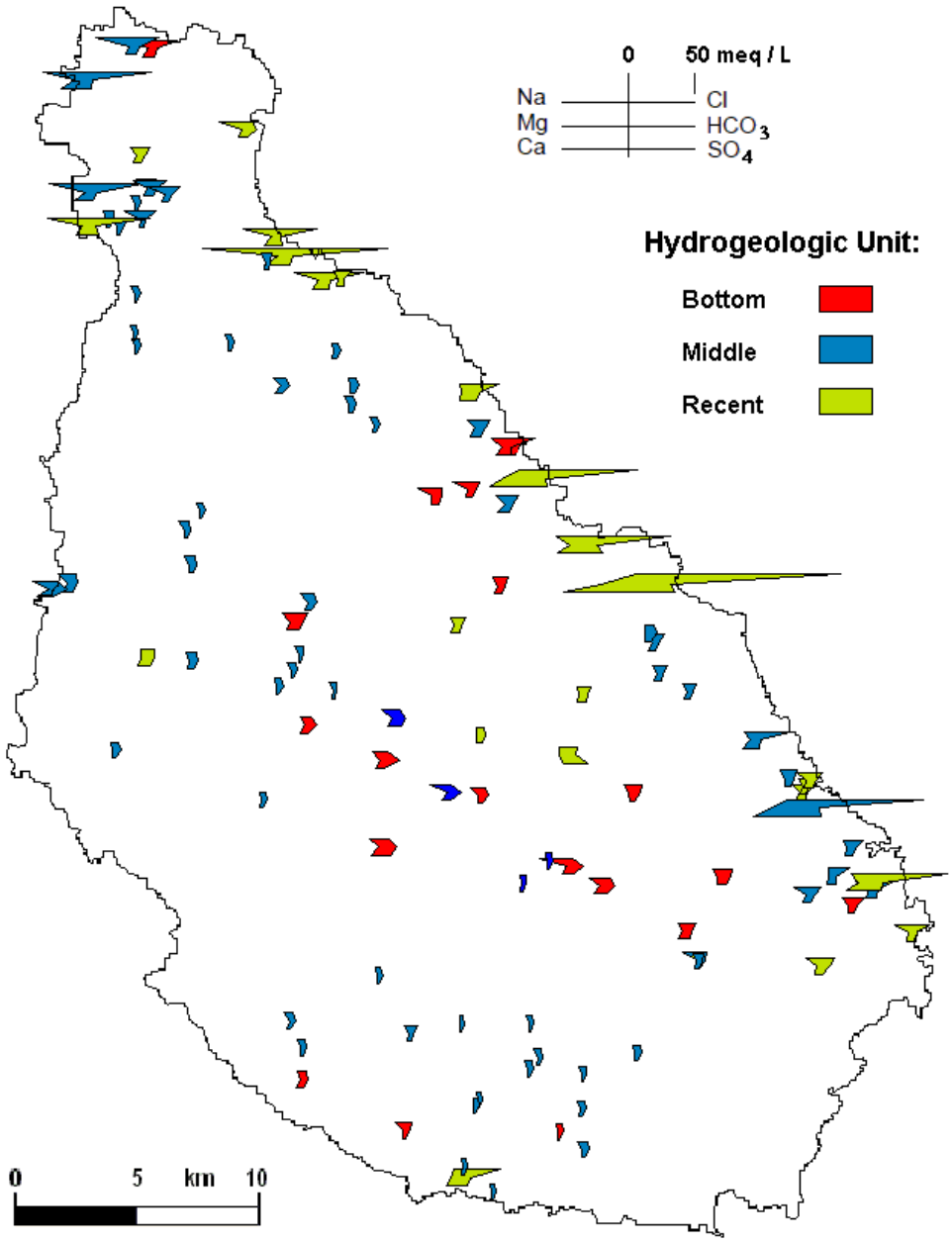

Figure 6.33 – Santiago's groundwater Stiff pattern distribution, by hydrogeologic unit.

The water samples from the central region of Santiago belong to the Na-HCO_3 type, revealing the refereed influence of the geological matrix volcanic rocks. That's where Bottom and Middle hydrogeologic Units dominate the landscape and most rainfall occurs. With low EC samples, marine aerosol influence was detected at recent underground shallow waters. Bicarbonate existences are related to the Carbon Dioxide (CO_2) reaction at unsaturated zone infiltration and by dissolution of carbonate minerals and weathering silicate, later. That's compatible with slightly acid and low EC new waters, (Pina, 2009).

Over time, by gravity, water goes deeper and reacts with hosting siliceous rocks, becoming bicarbonate enriched and increasing pH value. The remaining ions also increase but water facies stays similar. EC ranges from 440 to 2750 $\mu S.cm^{-1}$ which is a low to medium value. Sodium is the dominant cation, Bicarbonate and Chloride the dominant anions, by that order.

The Island's most productive hydrogeological unit, the Middle Unit, have poor mineralized groundwater with HCO_3-Cl-Na facies type. At pyroclastics deposit areas (MV formation) Sodium enrichment is observed. Near the sea, water's facies from PA formation with intense pumping boreholes is Cl dominated (> 2000 $mg.L^{-1}$) plus Na (> 1300 $mg.L^{-1}$).

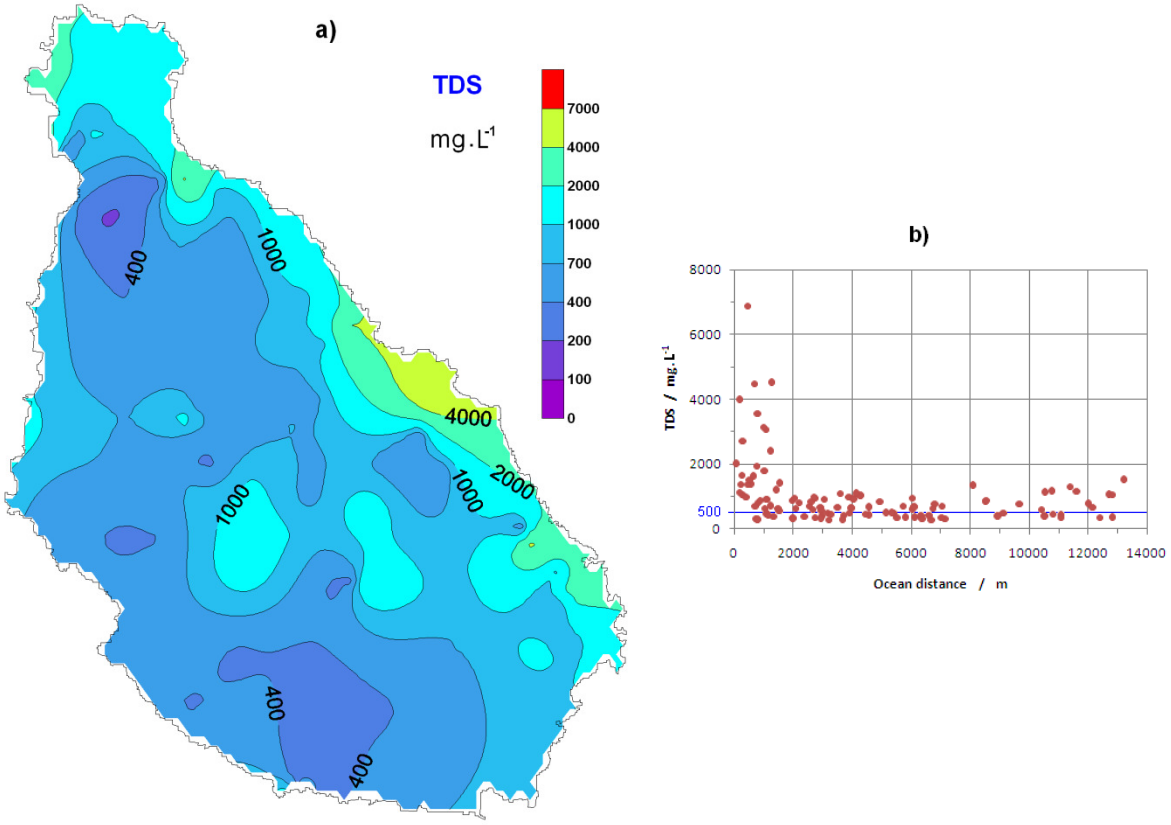

Figure 6.34 – a) Santiago's groundwater total dissolved salts distribution map, and b) TDS *versus* seashore distance.

The Recent Unit has made by permeable and non consolidated materials, mostly in the stream valleys, where intense agriculture practices exist (e.g. sugar cane, banana and papaya fields). They are at low altitudes near the ocean, and some boreholes extraction screens are under sea level. The dominant hydrochemical facies is Cl-Na, with high to very high EC values (2500 to 3000 $\mu S.cm^{-1}$) and TDS (figure 6.34a and b). At this unit, some samples have a Cl-Mg facies.

Although, the Recent Unit has a limited storage capacity and most groundwater leak to deeper levels (Middle Unit formations) or flows to the ocean, the valleys act as a recharge sue when strong rainfall happens. Throughout the valleys, there is some rainfall manmade catchment structures, with 2 to 4 meter high walls to retain incoming superficial waters. Most of these small dams are nowadays already filled with sediment and rocky debris. Boreholes at these formations usually have a high-water production and non controlled over-extraction is becoming a problem, especially at dry years.

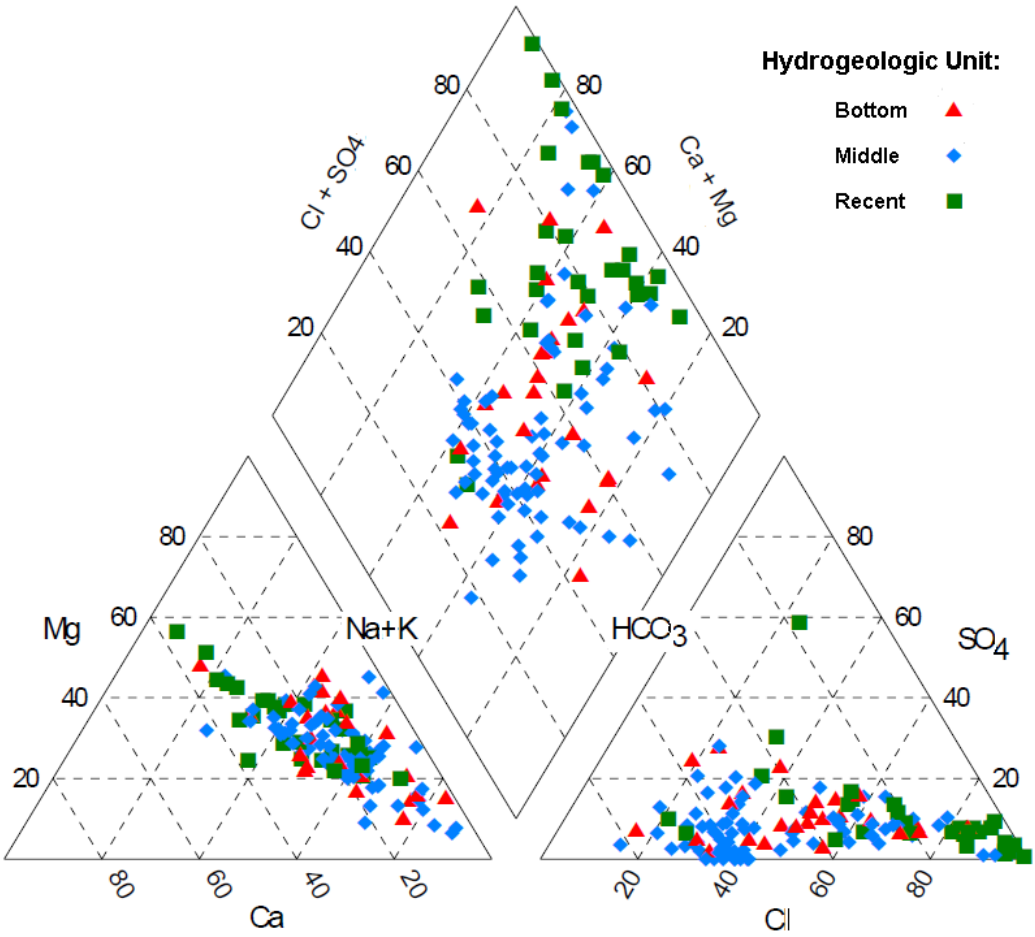

Figure 6.35 – Santiago's groundwater chemical composition Piper pattern distribution by hydrogeologic unit, (modified from Pina (2009)).

Island groundwater composition can be also represented by Piper Diagram. The same overall dissolved solids concentration increasing can be observed. At figure 6.35 the analyses are shown for all three hydrogeologic units.

Figure 6.36 only includes those from the subset (isotopic and chemical sampling), belonging exclusively to Bottom and Middle Units. At this figure, the two evolution trend lines are found and inserted, corresponding to the two major processes. The water-rock interaction processes, representing the major mechanism in the hydrochemical aquifer system evolution at Santiago Island and the groundwater evolution/mineralization controlled by the seawater spraying and by mixing with underlying seawater in the Recent Unit Quaternary formations, particularly in the valley zones.

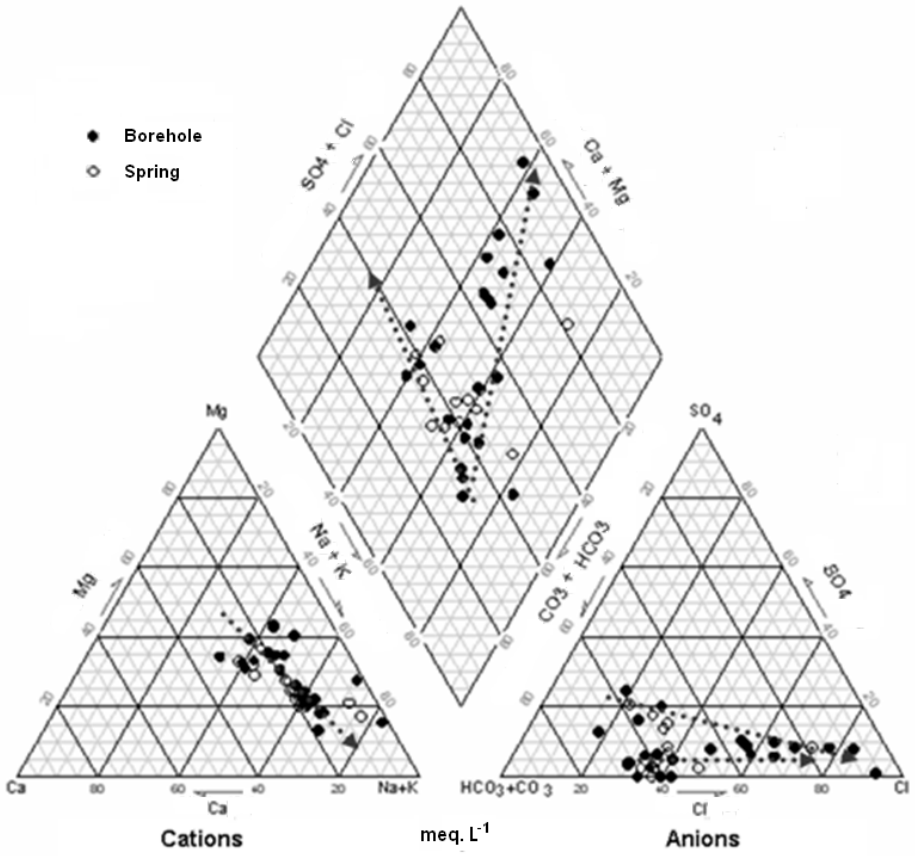

Figure 6.36 – Santiago's groundwater chemical composition Piper pattern, Bottom and Middle Units, (modified from Carreira *et al.* (2007a)).

Chemical species data were plotted versus total salinity of the water samples. No especial correlation was found between the chemical evolution and the specific hydrogeologic unit. Figure 6.37 represents the diagrams of the major cations and anions. In the Na, Cl, and SO_4 data versus TDS graphs, only one evolution trend line is recognized, pointing out to mixture with seawater or marine aerosol influence. However, in the Mg, Ca, HCO_3 diagrams two evolution lines are identified after groundwater reach the 500 $mg.L^{-1}$ TDS value, reflecting one the water-rock interaction processes and the other, with a lower slope value, the influence of the seawater composition (mixing and/or aerosol), (Carreira *et al.*, 2007a).

The high salt content within the groundwater systems appears to be restricted to agricultural areas in the valleys near the sea. The observed deterioration of the water quality limits its use for Human supply and for irrigated agriculture. This brackish water leads to potential soil salinization and alkalinisation, with the inherent soil deterioration and loss of productivity. Santiago's water supply is almost entirely from groundwater source origin (exceptions are several desalinization units used for towns supply and Poilão catchment, used in the agriculture). Only one-third of those watersheds have freshwater (TDS < 500 $mg.L^{-1}$), figure 6.34b), the remaining sources surpass greatly that amount, remarkably the wells closest to the sea.

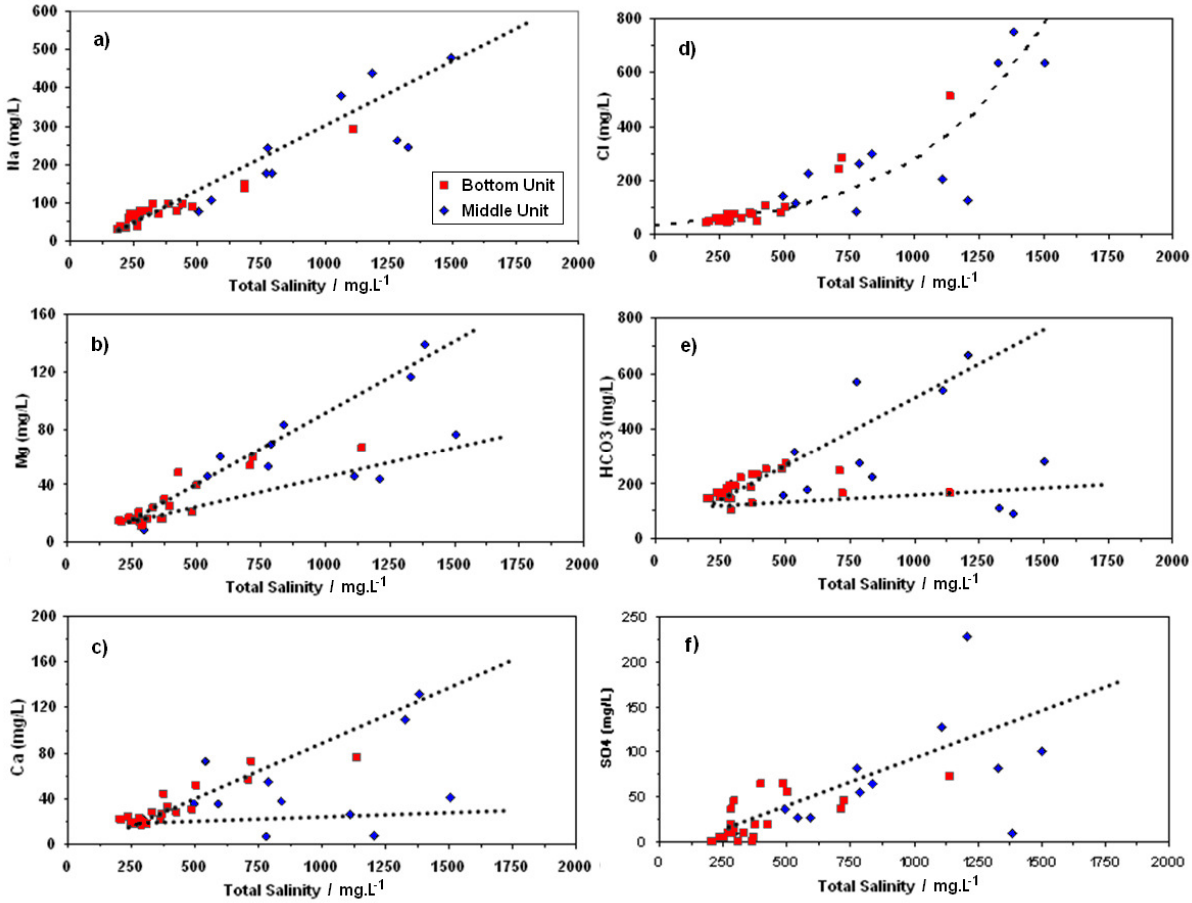

Figure 6.37 – Santiago's major ions evolution in the groundwater samples as function of TDS. (Modified from Carreira *et al.* (2007a)).

6.7.8 – Environmental isotopes groundwater signature

Isotopic hydrogeology uses environmental or artificial sources to outline water and groundwater. One of the most used environmental isotopic analyses is the ^{2}H and ^{18}O pair. They usually allow groundwater paths and fractioning to be followed. The fraction is mostly by evaporation and condensation process, (Custodio and Llamas, 2001). The ^{3}H isotope measure is a technique to check recent age groundwater recharge. The piston-flow method can be used, assuming that the tritium peak migrates through the aquifer and retains its shape when isotope time series measures are not available (Siegel and Jenkins, 1987).

$\delta^{2}H$ versus $\delta^{18}O$

The ^{2}H and ^{18}O measure results are reported in δ notation, sample relative deviation against standard VSMOW (Craig, 1961) and are given with the accuracy of 1‰ for $\delta^{2}H$ and 0.1‰ for $\delta^{18}O$. The $\delta^{2}H$ and $\delta^{18}O$ were determined by the Instituto de Tecnologia Nuclear (ITN) equipment using the methods proposed by Friedman (1953) to ^{2}H measures and by Epstein and Mayeda (1953) to ^{18}O measures (Carreira *et al.*, 2007a). The observed groundwater mean isotopic composition at Santiago Island is given at table 6.14. The isotopic contents obtained are close to the average isotopic composition over the Island as discussed by Akiti (1985), suggesting that the infiltrated meteoric waters were not subjected too much

evaporation, at most locations. Akiti as defined the isotopic composition of precipitation in Santiago (Akiti, 1985). In São Nicolau and Fogo islands similar studies and results have been also published, by Olivry (1981) and Heilweil (2009), respectively. Studies show that Local Meteoric Water Line (LMWL) is given by $\delta^2\mathrm{H} = 8.32 \times \delta^{18}\mathrm{O} + 10.54$ with mean weighted value of -36‰ for δ^2H and -5.5 for δ^{18}O. The Global Meteoric Water Line (GMWL) (Craig, 1961) given by $\delta^2\mathrm{H} = 8.13 \times \delta^{18}\mathrm{O} + 10.8$ is slightly above LMWL.

Table 6.14 – Groundwater measured isotopes values from Carreira *et al.* (2007a).

Isotope	minimum	maximum	averange
	‰		
δ^2H	-44.6	-14.9	-25.43
δ^{18}O	-4.98	-2.61	-3.94

The isotopic groundwater composition data shows no strong correlation to watershed's altitude (with 600 m variations). But data can be shifted by a small amount. The altitude δ^{18}O meteoric gradient at tropical regions is known to be of –1 to –3‰ by km (e.g. Gonfiantini *et al.*, 2001). This increase in isotopic depletion is generally attributed to the Rayleigh adiabatic condensation process. Diagram of δ^{18}O versus δ^2H (figure 6.38) exhibit two groups of groundwater samples: one group is composed by samples collected in the eastern side of Santiago Island (figure's lower group), in most cases located near the shoreline. The other group is ascribed to higher altitude and inland sampled locations.

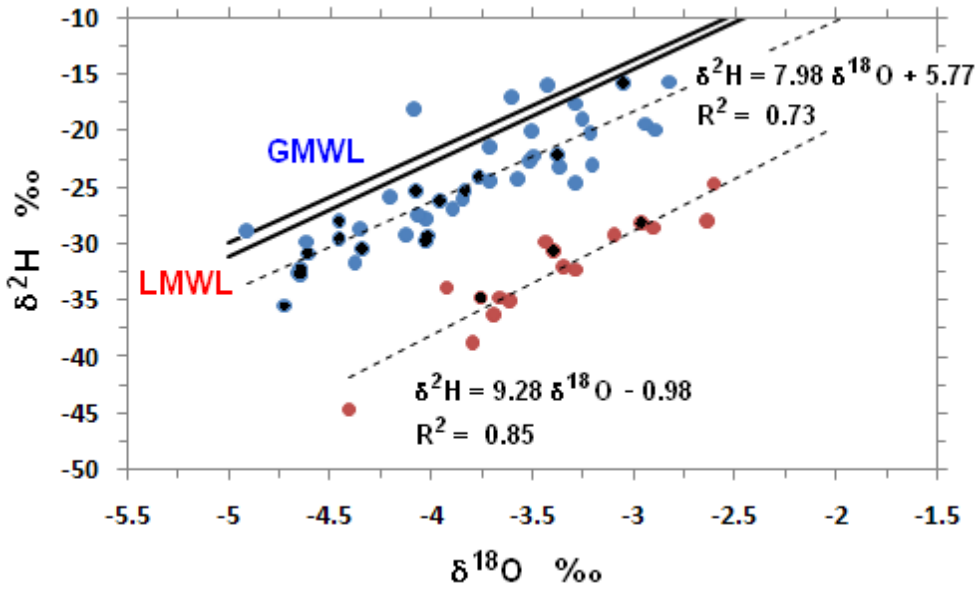

Figure 6.38 – δ^{18}O versus δ^2H plot. Two group samples trend lines are fitted, with GMWL and LMWL as guidelines. Black filed dots - boreholes, (modified from Carreira *et al.* (2007a)).

Both group samples have values under the GMWL and LMWL. The inland groundwater isotopic group's data can be explained by recharge's intensive meteoric events. Those events have increased isotopic depletion. At the lower locations, the isotopic values suggest a recharge mixture of rainfall and runoff water partially evaporated. It is not to exclude a strong evapotranspiration through the unsaturated zone at agricultural land areas and the consequent soil salt increase. This type of isotopic pattern was also mentioned by Akiti

(1985). According to this author, the inland waters have similar isotopic history but different geochemical history, which depend on the weathering and permeability of the hosting rocks.

The analyze of isotopic ^{18}O data against the EC, TDS, Cl, SO_4, Na and temperature content of the groundwater samples is plotted at figure 6.39. In these diagrams, two evolution lines can be observed, one showing the influence/mixture with seawater with a progressive enrichment in ^{18}O and in the mineralization where the influence of marine aerosol cannot be excluded. No significant variation is detected with groundwater temperature.

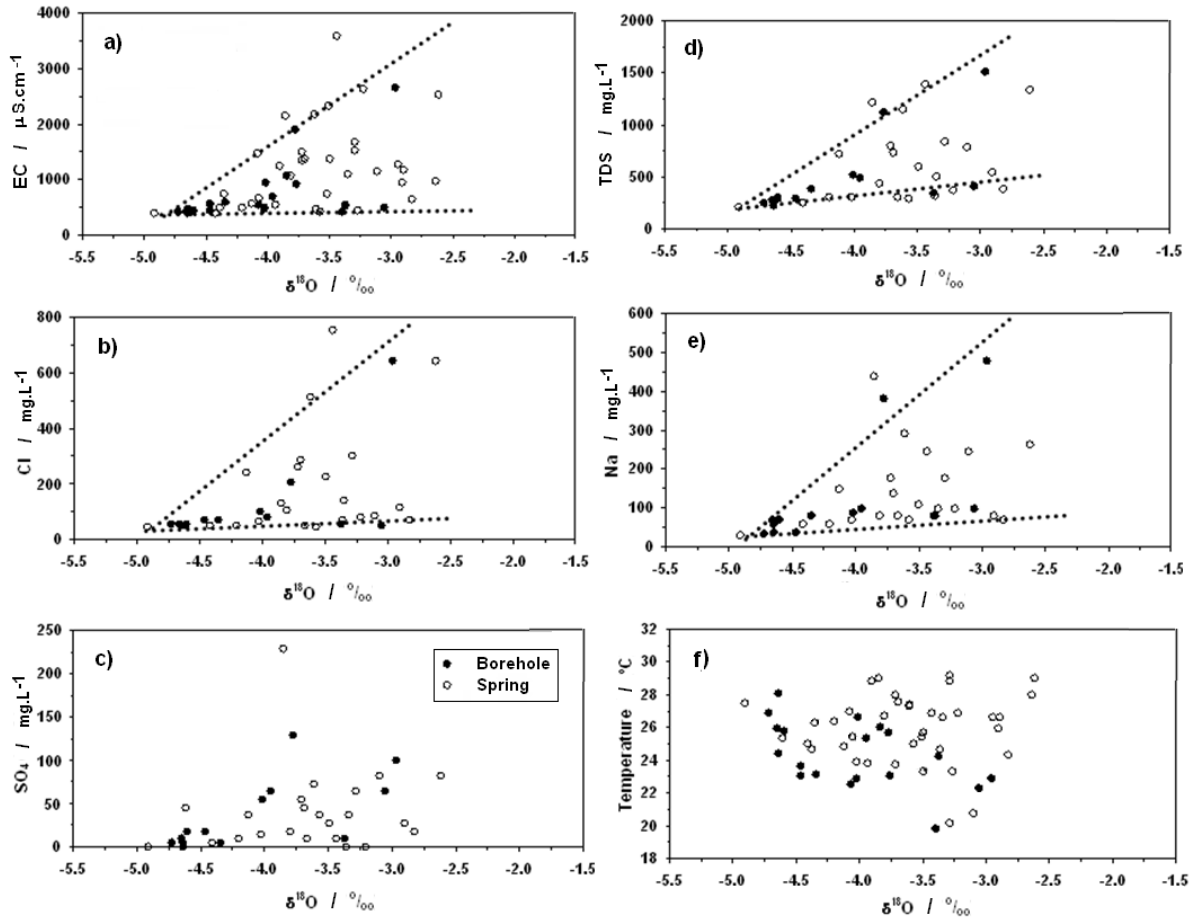

Figure 6.39 – $\delta^{18}O$ *versus* a) EC, b) Cl, c) SO_4, d) TDS, e) Na and f) temperature. (Modified from Carreira *et al.* (2007a)).

Tritium measures and ^{14}C values

Tritium was also analyzed altogether with ^{2}H and ^{18}O isotope's analysis. Measures were carried out at ITN laboratory. The error associated with the ^{3}H measurements varies with the ^{3}H sample's concentration, although usually is around 0.6 to 0.7 TU (Tritium Unit). Hydroarid project measured values range between 0 ± 0.7 TU and 3 ± 0.7 TU (2005-2006 measures), (Carreira *et al.*, 2007b).

Unfortunately, no long series of ^{3}H content in rainfall are available on the archipelago of Cape Verde. In fact, face to the absence of ^{3}H and the lower content found it is difficult to point the turnover rates of the groundwater. To overcome this gap, ^{3}H are usually compared

on the basis of International Atomic Energy Agency (IAEA) network stations records at similar latitudes islands; Barbados, Ascension Island, St. Helena. Barmen et al. (1990) estimation of the natural background concentration of ^{3}H in Cape Verde's precipitation was less than or equal to about 3 TU prior to 1953 and after 1990. Relatively large quantities of man produced ^{3}H were introduced into the atmosphere by many thermonuclear testing in the 1950s and 1960s. The estimated peak precipitation ^{3}H concentrations in Cape Verde are about 175 TU in 1964 (Kallrén and Schreiber 1988). Observations show atmospheric ^{3}H concentrations at Santiago decreasing rapidly to less than about 5 TU during the 1980s, as indicated by five precipitation samples collected during 1984, with values from 2.3 ± 0.1 to 4.4 ± 0.2 TU (Akiti 1985). One sample collected on nearby island of Fogo in 1987 had a ^{3}H concentration of 3.0 ± 1 TU (Barmen et al. 1990). Recent values (2005) are from rain-fed only agricultural products analyses at Fogo Island, with 3.0 and 1.0 TU (Heilweil *et al*., 2009)

The measured maximum value of 3 ± 0.7 TU can reflect water's age with a few years or a mixture with ^{3}H enriched older water. Low Tritium values waters indicating even younger waters. Tritium measures versus electric conductivity shows this trend, with younger groundwater having high EC values (more salt content), figure 6.40. With this ^{3}H data, no correlation was found against sampling altitudes and lithologic or hydrogeologic units.

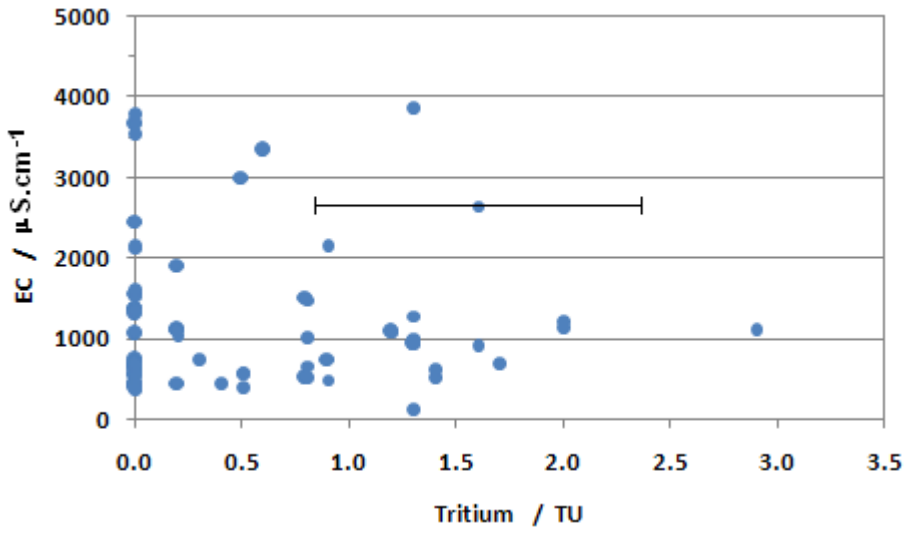

Figure 6.40 – Groundwater Tritium versus electric conductivity.
The associated error bar is plotted, (modified from Carreira *et al.* (2007b)).

The previous work of Akiti at Santiago, from 1984 to 1985, included measures of ^{3}H and ^{14}C. In the north part of the island (Tarrafal region) Akiti obtain 0.2 ± 0.2 and 1.0 ± 0.2 TU at springs and deep boreholes (150 to 200 m), showing that recharge water was prior to year 1952. It means at least a residence time of 30 years and consequently, a limited groundwater renewing capability. This result was confirmed by ^{14}C borehole measures at the same region, with groundwater ages greater than 30 years. In the eastern side (Achada Baleia), Akiti has measured 0.0 ± 0.2 to 7.1 ± 1.0 TU, respectively in boreholes and wells, (equivalent to a decay-correction concentration of 2 TU by 2005). That means that wells received recent recharge while the boreholes were receiving water slowly coming from joints and fractures. The corresponding ^{14}C analyses show that the major boreholes have relatively contemporary waters.

Conclusions from the isotopic and hydrochemical waters composition is that groundwater at Santiago are naturally recharged by precipitation, which has not been subjected to evaporation (or was just minimal). The infiltration process is fast and existing fractures play a very important role in that process. Shallow waters from wells are partly recharged by water coming from runoff episodic floods in the stream valleys. The higher salt content and EC values observed at wells located very near the ocean are due to seawater intrusion. The high salt content and EC values at deep borehole waters could mean also a salt water intrusion or solid salt dissolution, as the groundwater movement at these lowest valley's regions, near the sea, must have an upward component.

6.7.9 – SAR index

A significant amount of the groundwater extraction is applied into land irrigation. With only an annual short period of precipitation, irrigation is needed to support useful agriculture practices, especially to overcome the evaporation and transpirations' losses. The percentages of water in public distributions are: 44.2% to human consumption, 53.5% to irrigation (27.6 and 25.9%, respectively to traditional and drip irrigation) and only 2.3% to industrial activities (INGRH). These are values of 2005, but percentages are roughly the same throughout the decade, with an increasing trade between drip irrigation to traditional one. Total official water amount was 4.479×10^6 m^3. To this we have to add individual owners' water extraction, mainly to irrigation purposes also.

The major concern with this groundwater used for irrigation are the decrease crop yields and land degradation as a result of excess salts present in water and in the soils. One of the parameters that can be useful to the agriculture land use management is the water sodium content, given by the Sodium Adsorption Ratio (SAR) index, altogether with groundwater EC and soil type. The SAR index value is a measure of the relative concentration of sodium to calcium and magnesium. SAR is defined by the following expression, with cation's quantities given in meq per liter (Richards, 1954):

$$\mathrm{SAR} = \frac{\mathrm{Na}^+}{\sqrt{\frac{\mathrm{Ca}^{2+}+\mathrm{Mg}^{2+}}{2}}} \qquad (6.4)$$

This measure of "water irrigation sodium hazard" is important as the high sodium ion's presence in water affects the permeability of soil and causes infiltration problems. This happens because sodium when present in the soil in the exchangeable form replaces the calcium and magnesium adsorbed on the soil clays and causes dispersion of soil particles. That is, if calcium and magnesium are the predominant cations adsorbed on the soil exchange complex, the soil tends to be easily cultivated and has a permeable and granular structure. With this dispersion, the result is a breakdown of soil aggregates. The soil becomes hard and compact when dry. This will reduce water infiltration to the soil surface and down the profile, and limit aeration, leading to reduced crop growth. (Adapted from ANZECC).

When a high sodium concentration takes place it become a problem as the infiltration rate is reduced to such a rate that the vegetation and crop do not have enough water available. Furthermore, the hydraulic conductivity of the soil profile could become too low to provide adequate drainage. The plant extracts water from the soil by exerting an absorptive force greater than that which holds the water to the soil particles. If the plant cannot make sufficient internal adjustment and exert enough force, it is not able to extract sufficient water and will suffer water stress. This happens when the soil becomes at a dry condition. Salt in the soil-water increases the force the plant must exert to extract water (the osmotic effect or osmotic potential). Other problems caused by an excess of sodium is the formation of crusting seed beds, temporary saturation of the surface soil, high pH and the increased potential for diseases, weeds, soil erosion, lack of oxygen and inadequate nutrient availability, (Adapted from ANZECC).

An infiltration problem occurs if the irrigation water does not enter the soil rapidly enough during a normal irrigation cycle to replenish the soil with water needed by the crop before the next irrigation and to avoid water stress. The reduced infiltration rate, if due to quality of applied water, is usually a problem within the upper few centimeters. The water infiltration problem reduces the quantity of water put into the soil for later use by the crop. The soil and water salinity reduces the availability of the water in storage (Rhoades, 1977; Oster and Schroer, 1979).

But sodium himself is not a discriminator. The SAR index needs to be associated to groundwater EC and thus related with soil type. At the figures 6.41 and 6.42 are stated, those relationships between SAR and EC measured values at Santiago Island springs, wells and boreholes groundwater, to the infiltration rate problem and soil structure stability.

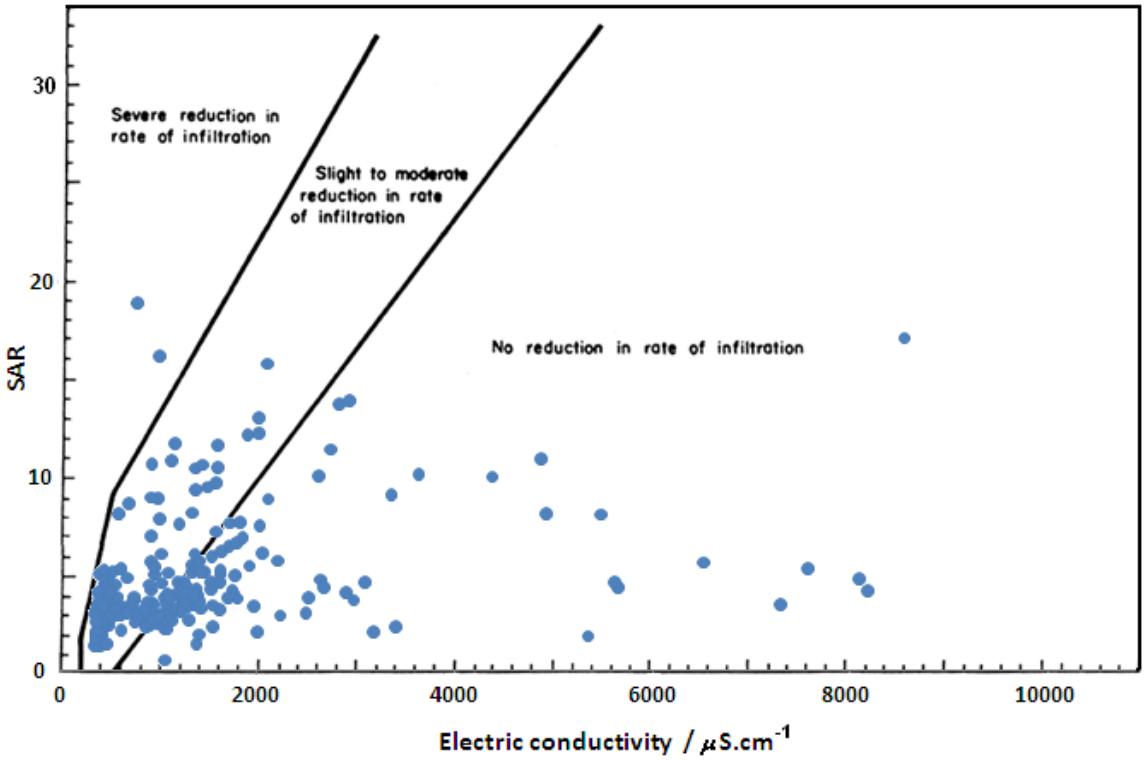

Figure 6.41 – Relative rate of water infiltration as affected by Santiago's groundwater calculated SAR and measured EC. (After Rhoades (1977); Oster and Schroer (1979)).

Actually, a newer index, the adjusted SAR (adj SAR) is defined (Suarez, 1981). It encompasses and offers a better insight into the change in calcium in the soil-water due to addition by dissolution of calcium from soil carbonates and silicates, or loss of calcium from soil-water by precipitation as carbonates. The SAR value underpredicts by 10 to 20% the adj SAR value, but SAR index still are acceptable to irrigation problems analyses.

Figure 6.41 shows that about half (55%) the groundwater characteristics have an “infiltration rate reduction problem”, increasing the water loss by evaporation at irrigation. The same data is plotted against soil stability and the potential impact of irrigation water quality on soil structure can be thus detected. Furthermore, about half the groundwater is suitable to land irrigation, not changing the soil structure stability. Comparison is done against standard curves from DNR (1997).

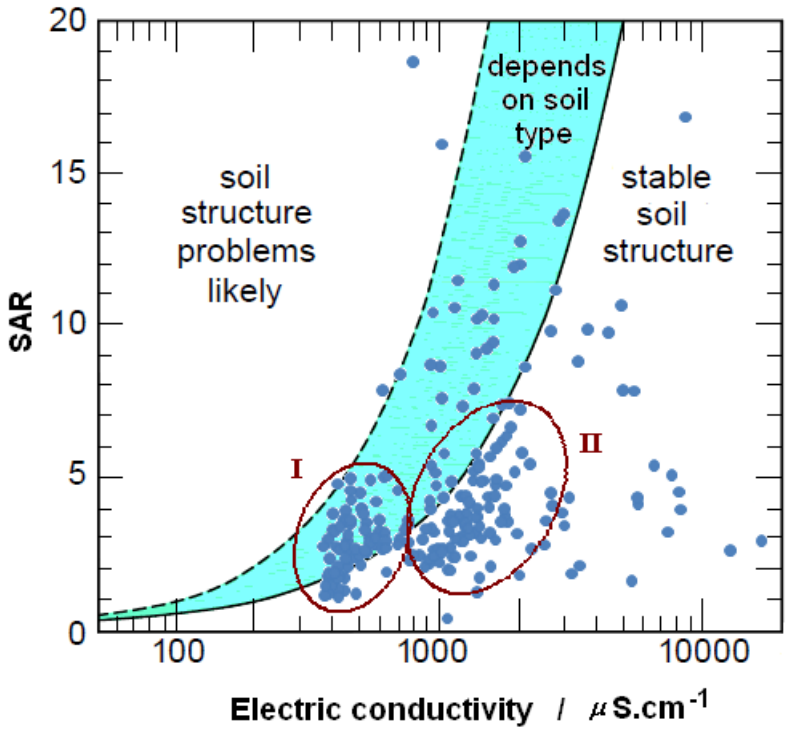

Figure 6.42 – Santiago’s groundwater EC versus SAR to soil stability, with two samples group identification, (adapted from DNR (1997)).

SAR values range from 0.5 to 18.5 and EC from 362 to 16600 μS.cm^{-1}. Although some scattering points, two distinct clusters are recognized at figure 6.41 and 6.42 (group, I and II). A closer analysis for each one reveals that group I data come from higher locations (75% are above 100 m altitude) and group II data come mostly from lower regions (65% are below 100 m high). Threshold altitude difference is that below 100 m, soils belong to the alluvium Quaternary formation. Group II is in a stable soil condition but group I is conditioned by soil type and problems can arise with irrigation.

With this observed SAR and EC groundwater values, the soil and crop types are essential to yield values. The salt content of the soil groundwater in the crop’s root zone (the average root zone salinity, EC_R) is important in assessing which crops are suitable for growing in specific soils and depend on those soils. The EC_R is given at expression (6.5), function of

irrigation water EC and soil type by the average root zone leaching fraction (LF). The last value represents the proportion of applied water moving below the root zone, i. e. it represents the applied surface irrigation water fraction that percolates below the root zone. The remaining value (1 - LF) replaces water used by the crop to meet its evapotranspiration demand and water lost by surface evaporation. The LF value is higher at sand and sandy soils (0,6) and lower to loam, light clay and heavy clay soils (0.33 to 0.2).

$$\mathrm{EC_R} = \frac{\mathrm{EC}}{2{,}2 \times \mathrm{LF}} \qquad (6.5)$$

after Rhoades (1974) and Rhoades and Merrill (1976).

Table 6.15 reports the EC_R common accepted limits and rating for plant salt tolerance. Taking a mean value of 0.5 for the LF parameter (mixture of sandy and clayed soil), it gives that about half data points locations (52%) can support sensitive to moderately sensitive crops. Unfortunately, those places are located at higher altitudes. There the infiltration problem is more intense (figure 6.43) and were a significant crop amount is irrigation rain dependent.

Table 6.15 – Soil and water salinity criteria based on plant salt tolerance groupings, (after Maas, (1984)).

Plant salt tolerance grouping	**Water or soil salinity rating**	**Average root zone salinity, EC_R / µS.cm^{-1}**
sensitive crops	very low	< 950
moderately sensitive crops	low	950 to1900
moderately tolerant crops	medium	1900 to 4500
tolerant crops	high	4500 to 7700
very tolerant crops	very high	7700 to 12200
generally too saline	extreme	> 12200

Crop salt tolerance needs to be taken into account when assessing the suitability of water and soil for irrigation. Table 6.16 includes some plants usually found at Santiago's farm lands. Crossing this data with irrigation groundwater results that most vegetables have some yield reduction as the majority of these plantations are located at the lower valleys' areas, near the shoreline (figure 6.35), were EC_R is higher.

Table 6.16 – Tolerance of some plants to salinity in irrigation. Threshold for yield reduction, (after Maas, (1984)).

Plant common name	**Average root zone salinity, EC_R / µS.cm^{-1}**
Papaya	3000
Tomato	2300
Corn and Sugarcane	1700
Potato	1700
Sweet potato	1500
Onion	1200
Bean and Carrot	1000

Figure 6.43 represents the calculated root zone electric conductivity EC_R distribution and also the locations of infiltration rate problems. Spatial distribution of the areas with irrigation problems related to groundwater hydrochemical composition has two distinct origins. Inland higher locations and also at west and southwest, soil infiltration problems occur. At the eastern side of Santiago, the EC_R values are mostly above the allowed maximum and diminish the mean production of vegetables.

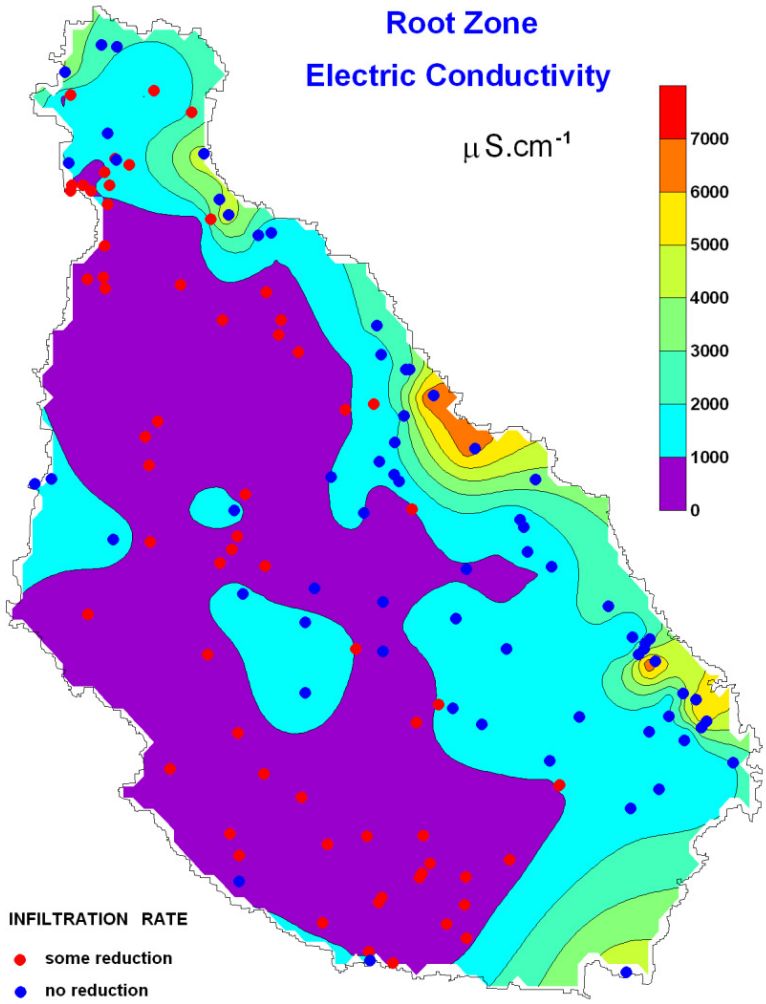

Figure 6.43 – Santiago Island map with root zone electric conductivity values and infiltration rate condition at watershed irrigation points.

7
TEM MEASUREMANTS AND RESULTS

This seventh chapter describes the TEM acquired soundings and their modelling. The relation of hydrogeologic parameters to the obtained geoelectric models is advanced, as also the relation with groundwater quality.

7.1 – TEM soundings at Santiago

Transient electromagnetic soundings were acquired at the most important creek valleys and agricultural areas of Santiago Island, figure 7.1. The majority of these sampled valleys are located at island east side; S. Domingos (near Achada Baleia village), Seca and Picos (near Pedra Badejo village), Salto, Flamengos and S Miguel (near Calheta de S. Miguel village). At the northwest island side near Tarrafal village, two more sites were covert; at Chão Bom plateau (a one kilometre square agricultural area near the sea) and Ribeira Grande creek valley. All these creeks only possess superficial waters at the "rain season" from respective hydrographic basin catchment runoff. Near the ocean, valleys are filled with alluvium Quaternary sediments and these soils are the best ones for agriculture. Most of these chosen valleys are intensely farmed throughout the year (S. Miguel and Ribeira Grande to a lesser extent) as the irrigation water is mostly from local wells and borehole groundwater extraction. At the remaining island rural areas, where no groundwater pumping or net distribution water exists, the agriculture practices are rain-fed based only.

The TEM soundings have been acquired at several campaigns, between the year 2005 and 2009 (see table 7.1). The principal areas were surveyed at June 2005, November 2005 and September 2006. At every next campaign, repetitions at some of the previous places have been also done. From year 2007 onward only this sounding's repetitions took place. A few more soundings were done; at Campelo (to the south of Salto valley) over some previous VLF-EM profiles (Summer 2005) and at Assomada central plateau for static shift magnetoteluric correction (September 2006), (Santos *et al.*, 2006). When possible, repetitions were exactly at the same sounding spot. Not being so, as closest as possible. The major and principal surveys took 4 to 5 days field work. Repetitions last only just 2 to 3 days.

Table 7.1 – Calendar for the several TEM campaigns, surveyed places and amounts.
(R marks the repetition TEM soundings).

Date	S.Dom.	Picos	Seca	Tarrafal	R.Grande	Salto	Flamengos	S.Miguel
Jun 2005	47	15	21	-	-	-	-	-
Nov 2005	4 R	4 R	2 R	35	9	-	-	-
Sep 2006	2 R	4 R	3 R	5 R	-	24	8	24
Sep 2007	4 R	4 R	3 R	3 R	-	-	3 R	3 R
Mar 2008	10 R	2 R	5 R	-	-	5 R	-	3 R
Jan 2009	10 R	2 R	5 R	3 R	-	5 R	-	3 R

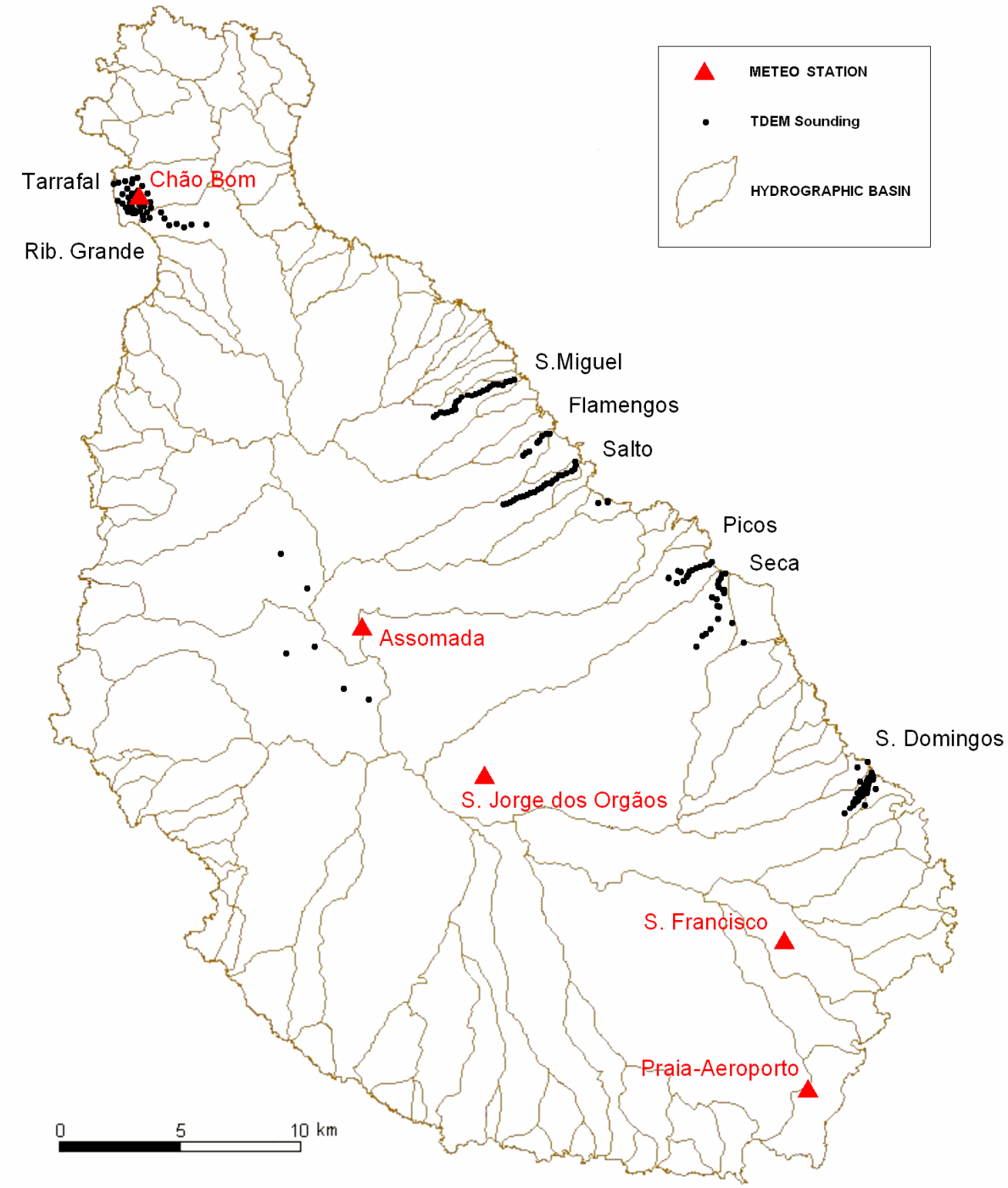

Figure 7.1 – TEM soundings locations at Santiago.

The several TEM campaigns were carrying out by different field work teams;

June 2005: Fernando Santos, Eugénio Almeida, Mota Gomes and António Pina,
November 2005: myself, Mota Gomes and António Pina,
September 2006: Eugénio Almeida, Patrícia Represas and João Coroado,
September 2007: myself and Patrícia Represas,
March 2008: myself and Patrícia Represas,
January 2009: myself and Fernando Santos.

7.1.1 – S. Domingos data

São Domingos stream valley is the southernmost of the surveyed locations. It's nearby Achada Baleia village. At surveyed area, the valley is 300 to 400 m wide with 30 to 40 m hillside and 15 to 20 degree slope walls. Soundings were taken from near the ocean, at 2 m amsl to 2100 m inland and 34 m high. Creek bed altitude grows steadily from the sea. A few soundings were done outside the valley. Hydrographic catchment basin covers 31.3 km^2.

Information from valley's borehole logs indicates a mean 12 m alluvium thickness over the PA basaltic formations, at the valley centre. The basaltic formations are fractured and have sometimes pyroclastics intrusions and clays. Deepest drilled borehole goes to 46 m below the mean sea level. No direct geologic information is known beyond this limit. Agriculture practices exist in the valley, except the last 500 m near the sea. Production of green vegetables is declining especially at this nearest to shoreline valley area.

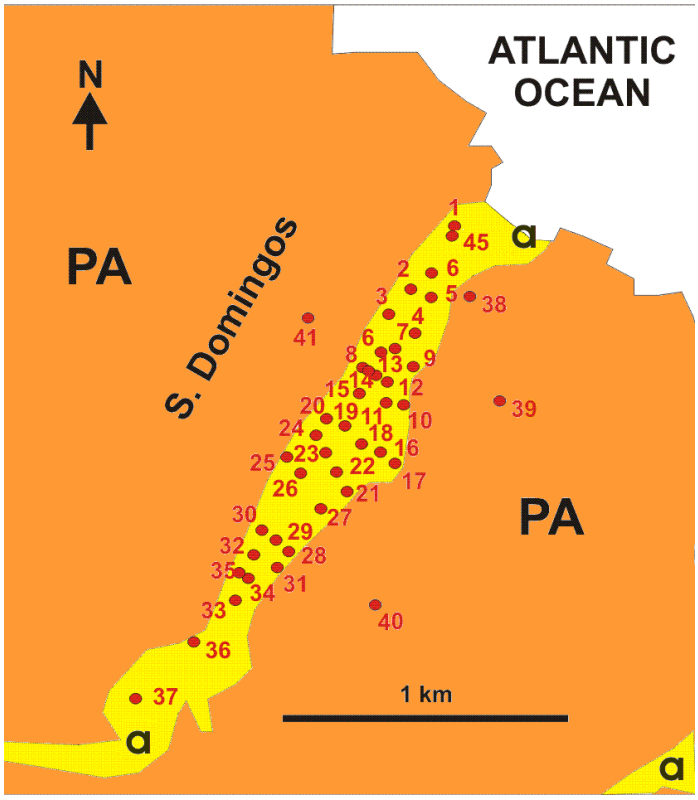

Figure 7.2 – TEM soundings number and location at S. Domingos, over simple geologic map description; PA – Pico da Antónia formation, a – Quaternary alluvium formations.

Acquisition of TEM soundings (and respective numbering) starts from the shoreline throughout the axis valley. The majority of the TEM-FAST 48 soundings were acquired with a 25 m × 25 m single loop wire, with a mean current of 3.0 ampere and time channel from 4 to 9 (maximum). The soundings' location is shown at figure 7.2 together with the simple geology sketch of the region. The loop dimension was primarily chosen to have a better superficial accuracy and smaller 3D effect over soundings (Goldman *et al.*, 1994; Rabinovich, 1995), and to survey the know aquifer. Figure 7.3 plots the TEM soundings' locations plus the boreholes and wells (with lithologic and chemical information) over a photographic image (Google image).

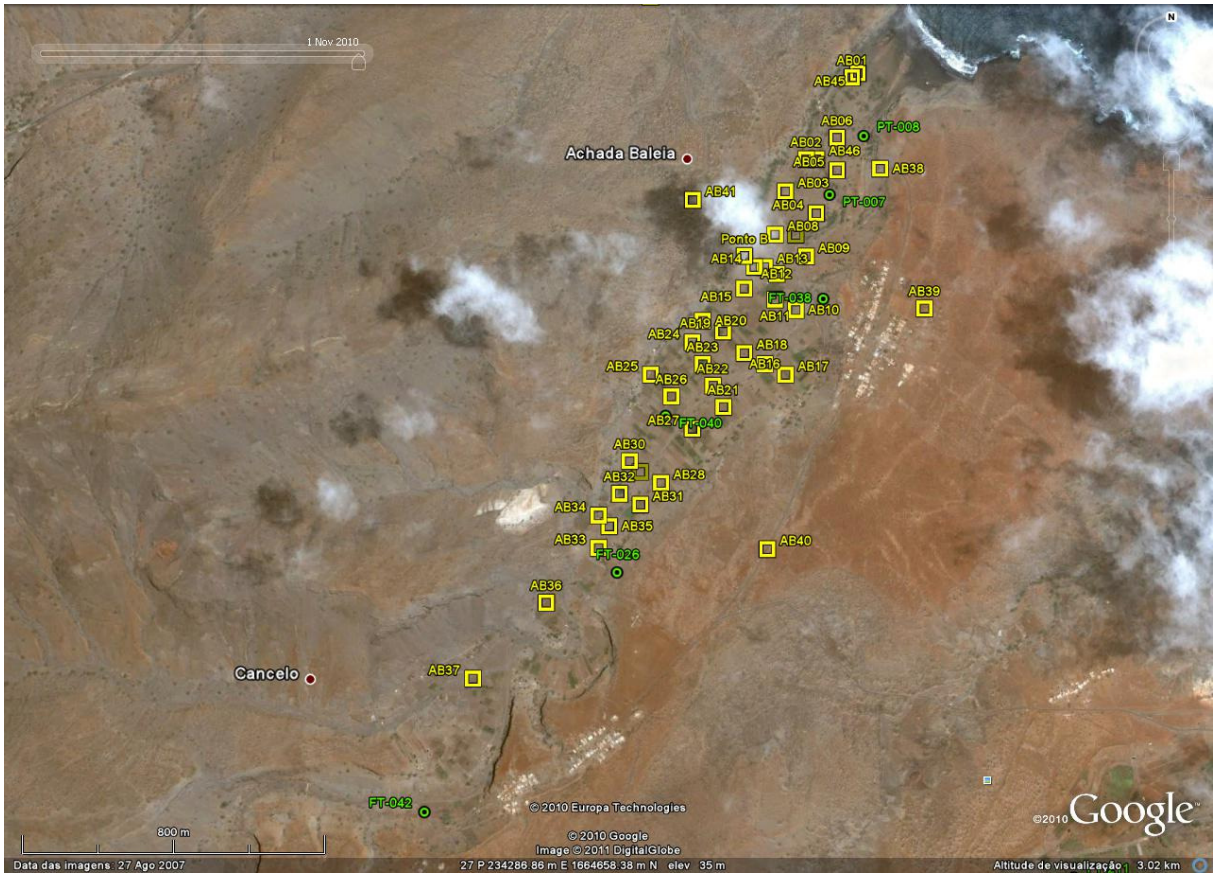

Figure 7.3 – TEM soundings, boreholes and wells location at S. Domingos valley, (adapted from Google images),

The figures 7.4 a) to c) display the characteristic S. Domingos valley landscape scenario and environment.

An initial inspection of the TEM apparent resistivity curves show that the medium is conductor to highly conductor, i.e. the measured apparent resistivity has low to very low values. Krigged overall distribution of apparent resistivity for eight increasing time windows after the turnoff (and increasingly depth) is plotted in figures 7.5 to 7.8. The measured apparent resistivity increases inland upstream. This observed effect could arise from different sources; effectively freshwater to seawater mixture, altogether with a bending alluvium substratum (thinner alluvium near the sea) or some added effect over the normal transient induction process. Notably, all these issues can be presents at this geologic scenario, plus some lateral effects, i.e. some 2D or 3D effects.

First results came from 1D data modelling and model analyses. The resistivity of the deepest layer is similar to seawater typical values of 0.3-0.4 to 1.0 ohm.m, in many models. This would imply a water brine condition or localized 3D effect at some soundings. A closer inspection of the decay induction signal reveals also that signal is affected by SPM, most probably from magnetite, maghemite or hematite content of shallow sedimentary formation near the sea. Previously studies found those minerals (Martins, 2003). A superficial sand sample (from Seca region beach) was also analyzed, confirming this magnesian based mineral's presence (João Coroado, personal communication), figure 7.9a) and 7.9b).

Figure 7.4 a) – Photography at S. Domingos TEM sounding 13 location, facing south.

Figure 7.4 b) – Photography at S. Domingos TEM sounding 13 location, facing southwest.

Figure 7.4 c) – Photography at S. Domingos TEM sounding 13 location, facing west.

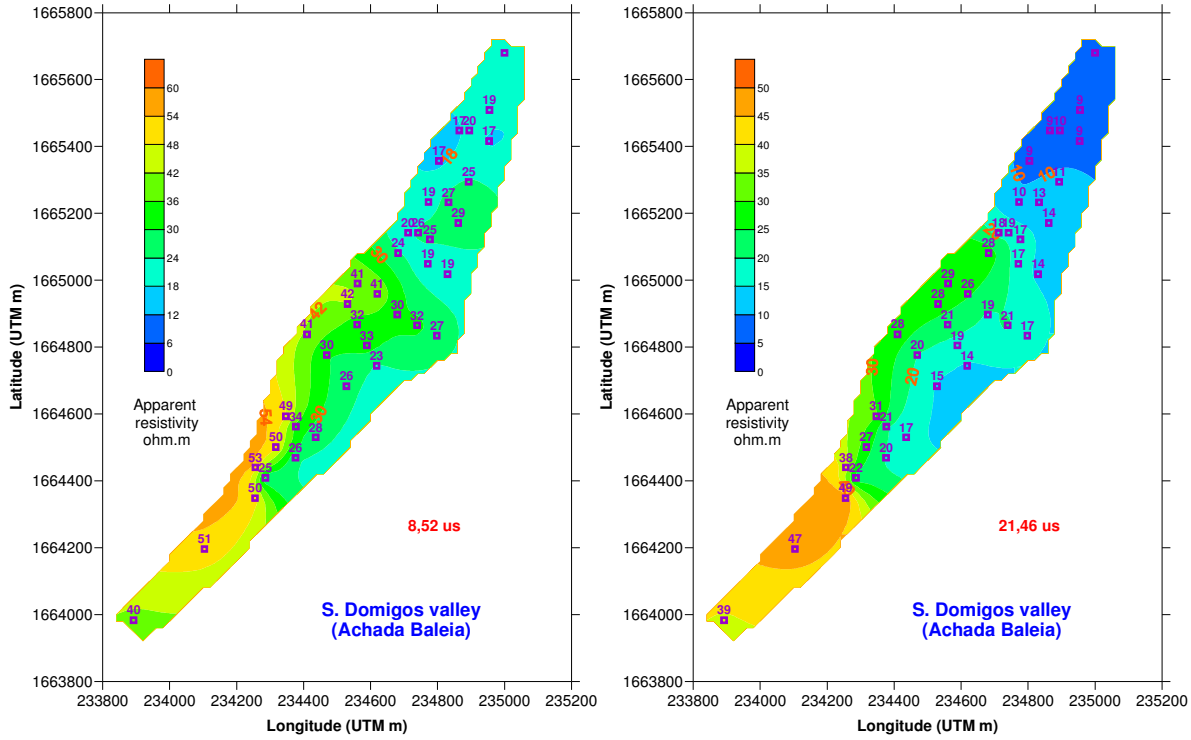

Figure 7.5 – Apparent resistivity at S. Domingos; a) at 8.52 μs, b) at 21.46 μs,

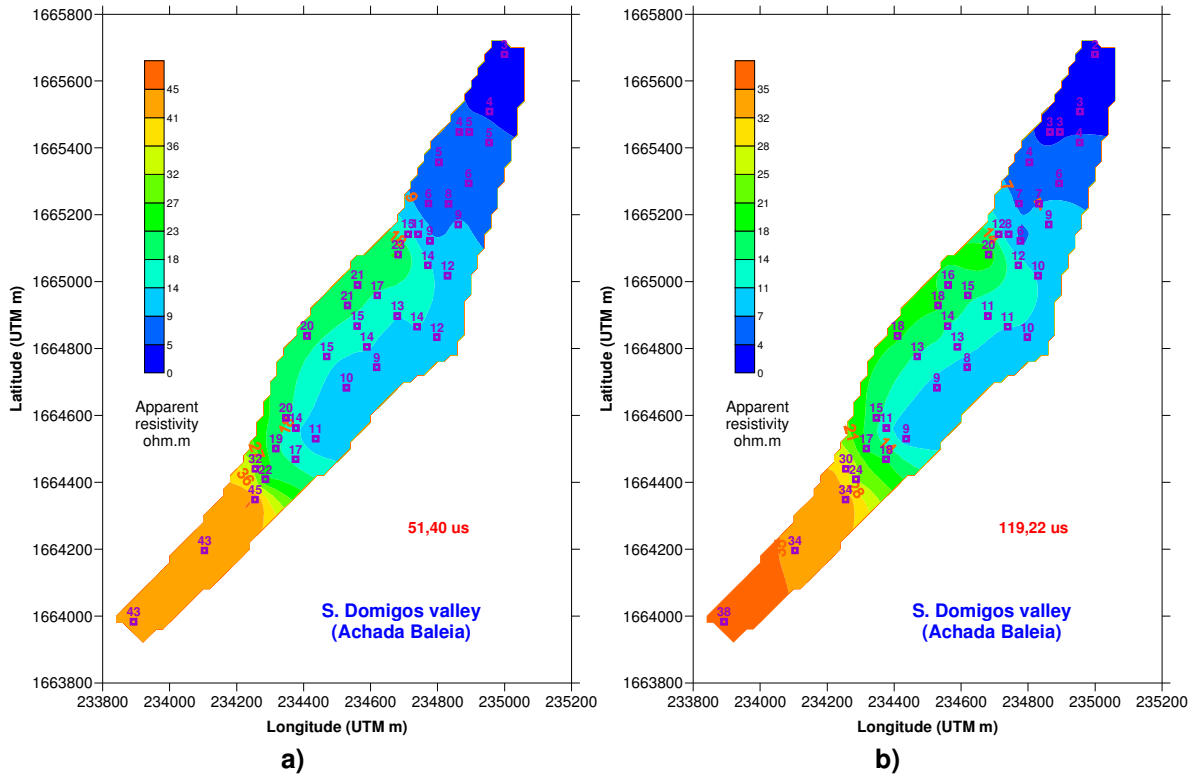

Figure 7.6 – Apparent resistivity at S. Domingos; a) at 51.40 μs, b) at 119.22 μs.

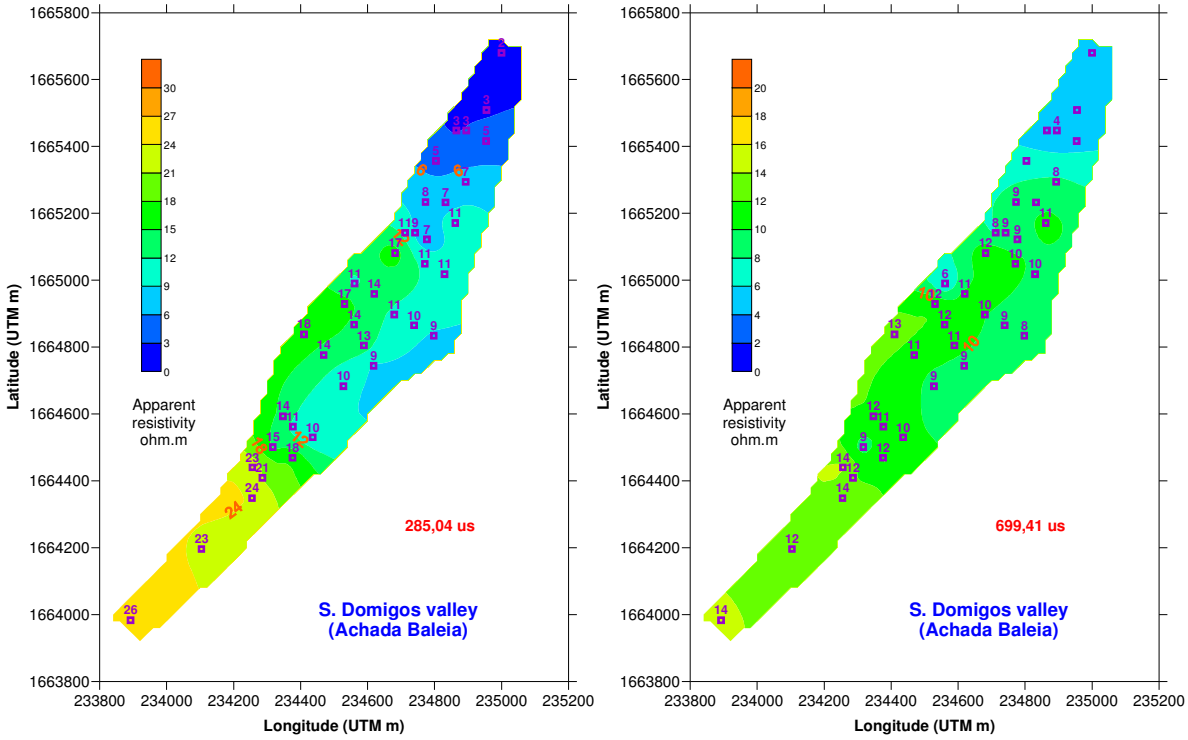

Figure 7.7 – Apparent resistivity at S. Domingos; a) at 285.04 μs, b) at 669.41 μs.

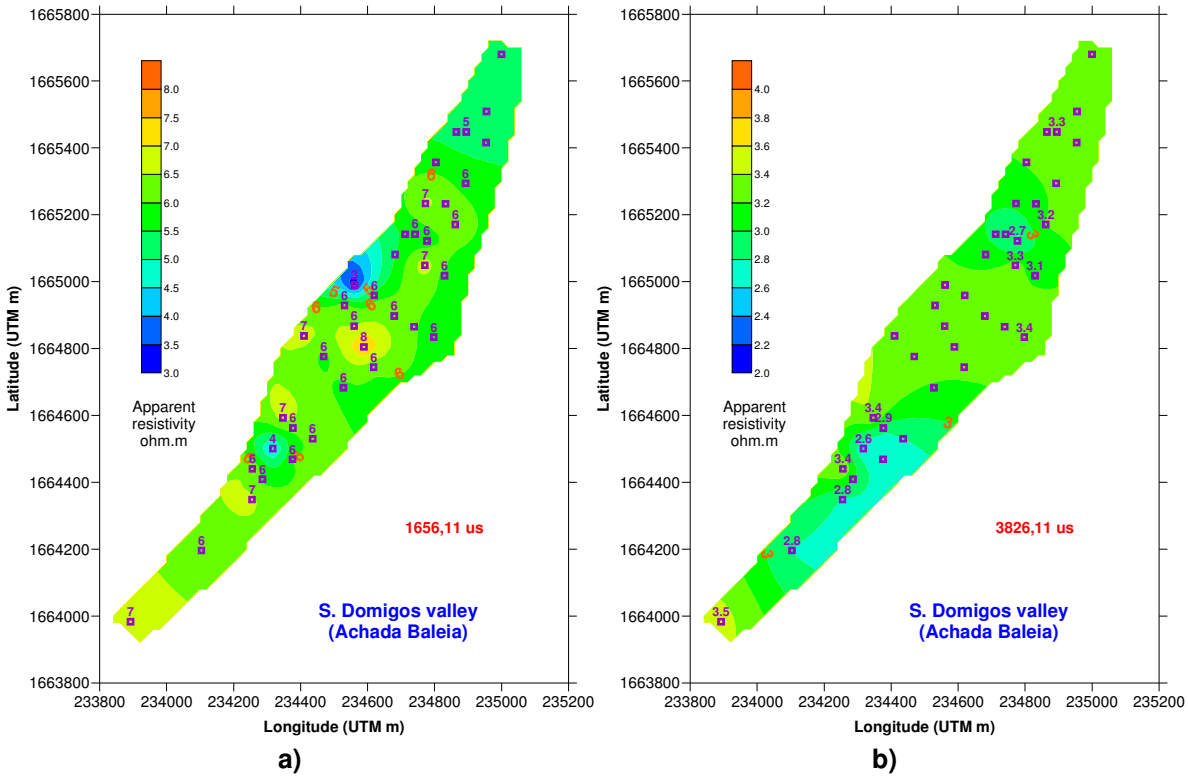

Figure 7.8 – Apparent resistivity at S. Domingos; a) at 1656.11 μs, b) at 3826.11 μs.

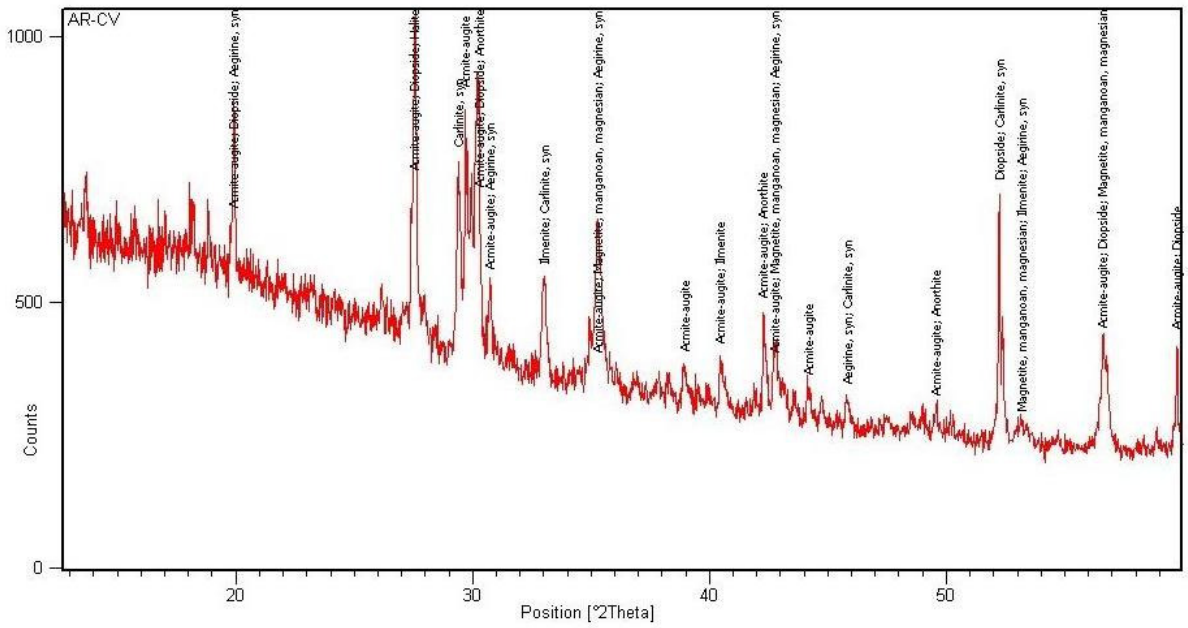

Figure 7.9 a) – Mineral composition of sampled sand.

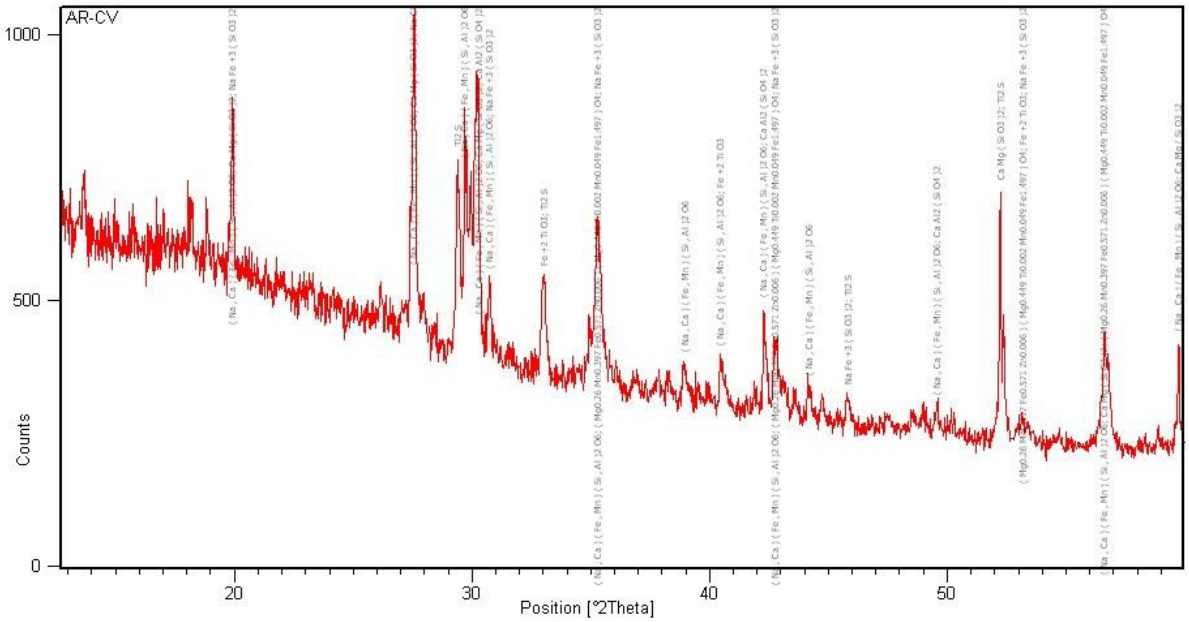

Figure 7.9 b) – Chemical composition of sampled sand.

One-dimensional modelling using the TEM-FAST48 software (AEMR) taking into account a susceptibility value of 0.001 $kg^{-1}m^3$, within the literature range values (Schön, 1998) and the influence of the shallow layer 10 m thick, corresponding to the sedimentary formation, was tested. Distinct responses are obtained from these two values variations; one gets almost no model influence (a few percent of the resistivity) when layer thickness is modified between 1 to 20 m, but changing susceptibility up and down one-magnitude order (to 0.0001 or 0.01) shows greater models variability outside the geologic accepted limits (very high and extremely low resistivity values). Figure 7.10a) show the observed SPM affect at two of the soundings, as refereed in subchapter (2.7.3). The respective models and responses are shown in figure 7.10b), taking into account this SPM effect.

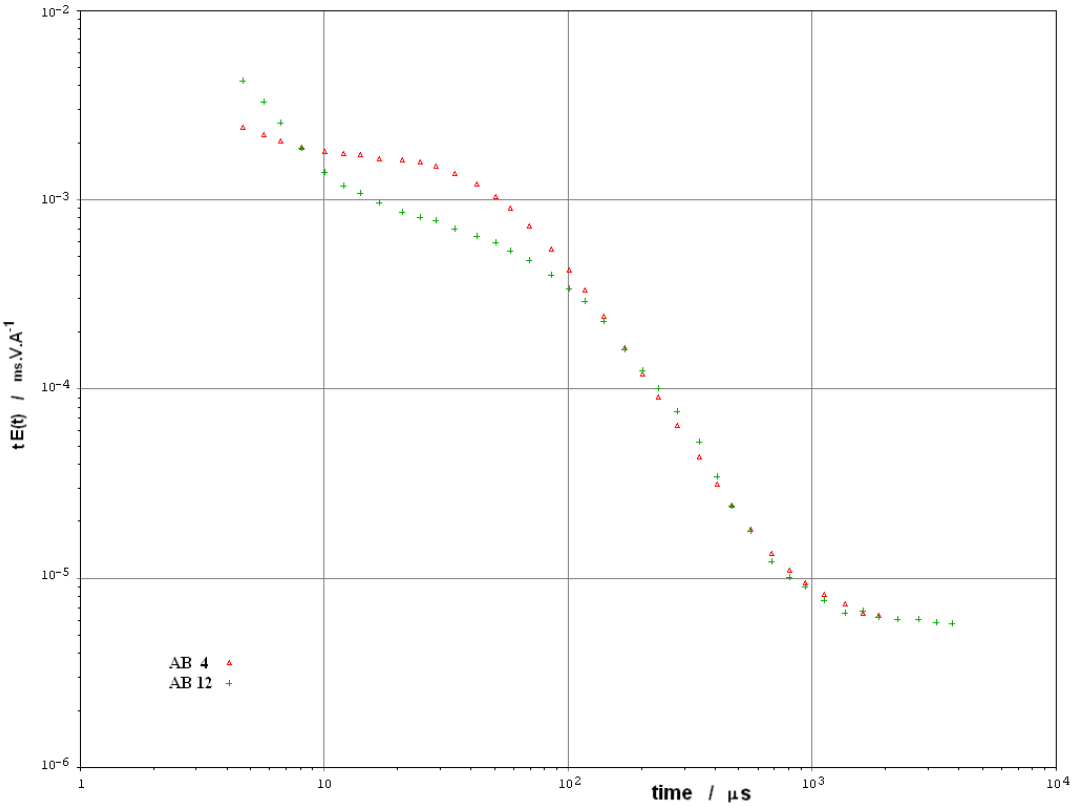

Figure 7.10 a) – SPM effect in TEM sounding curves (AB 4 and AB12 example).

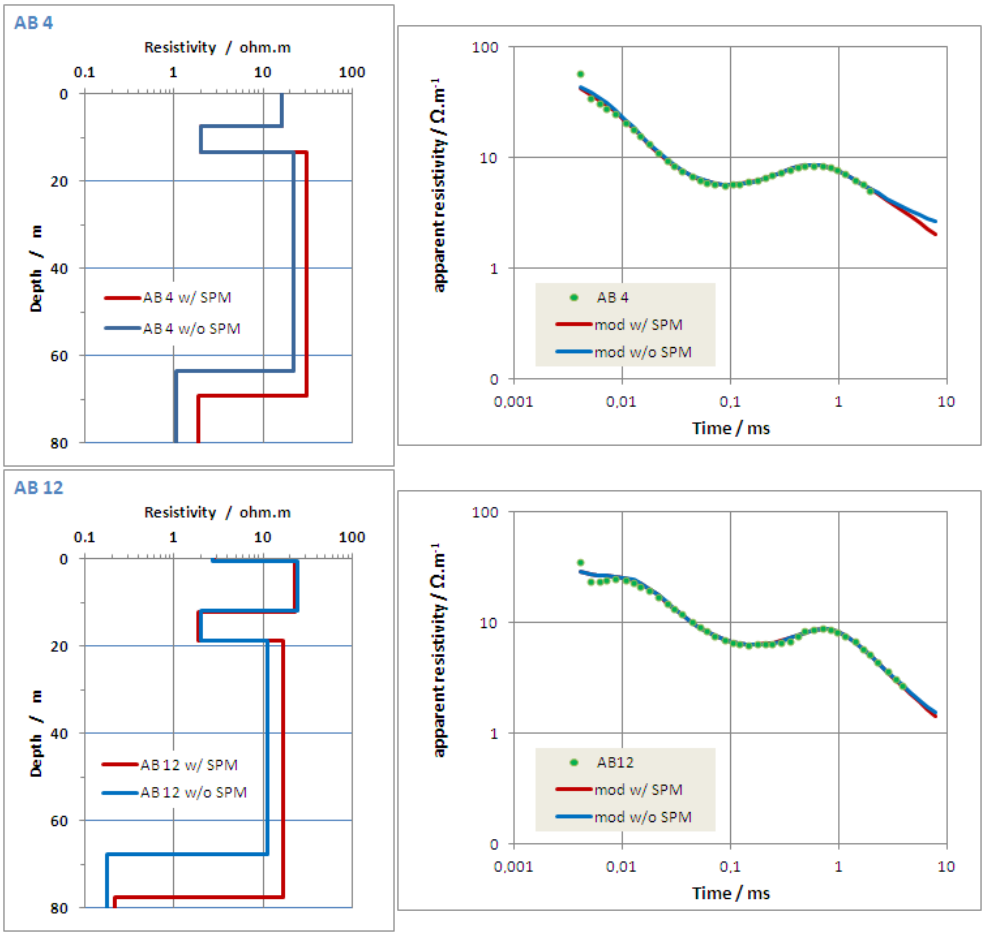

Figure 7.10 b) – Models and responses for AB 4 and AB 12 soundings, with and without SPM effect.

7.1.1.1 – 1D inversion of TEM data from S. Domingos

Taking into account this SPM effect, the valley's TEM soundings were accordingly modelled. Figure 7.11 plots the typical observed TEM curves and model fit response, from near the ocean upstream the valley. Measured noise is between 2 to 3 nVm^{-2} with any nearby major EM noise sources. Error band from stacking procedure is a few percent at last time points.

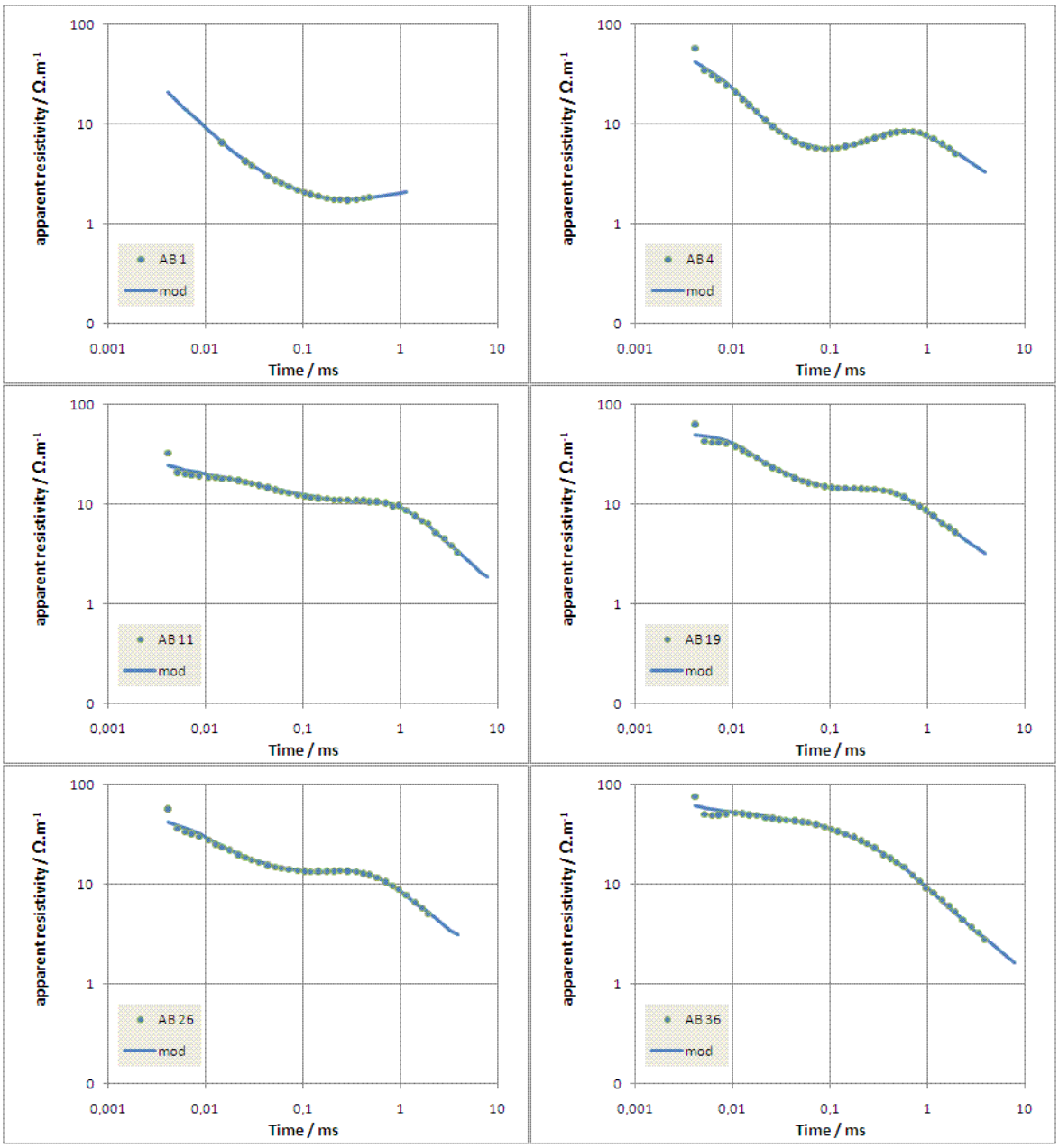

Figure 7.11 – Some S. Domingos measured TEM curves and 1D mean model fit response.

Model's errors have a mean 2 to 3% misfit to data points. Figure 7.12 shows the respective 1D mean model of TEM soundings showing in figure 7.11. With these low resistive values, equivalent models are only a few percent different from the mean values. A characteristic of some models is a conductive layer in 15 to 20 m depth. This is in accordance with lithologic

logging information at middle valley boreholes, as can be seen at figure 7.13 sketch. Below this depth, resistivity corresponding to the aquifer system is around 10 to 20 ohm.m.

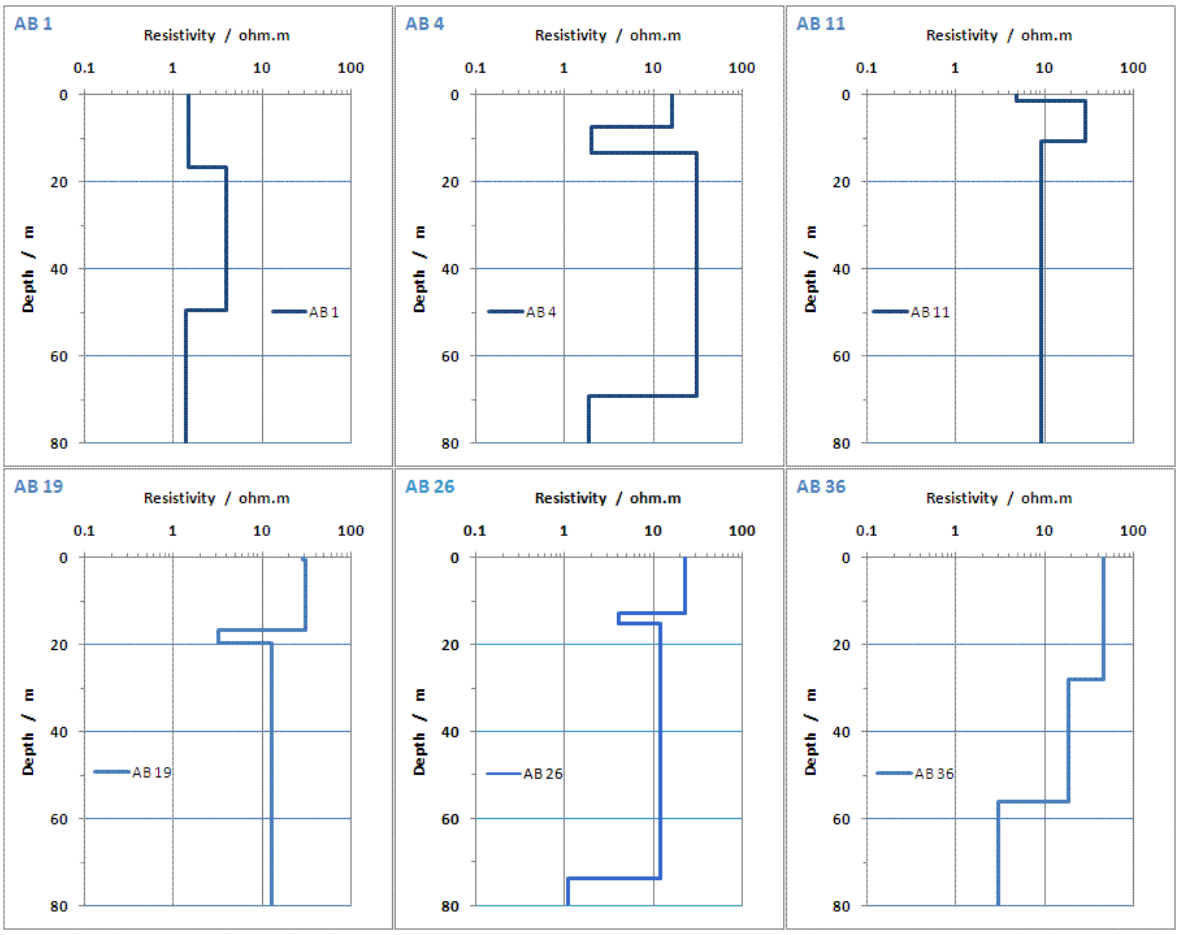

Figure 7.12 – S. Domingos 1D TEM mean models (corresponding to figure 7.10 soundings).

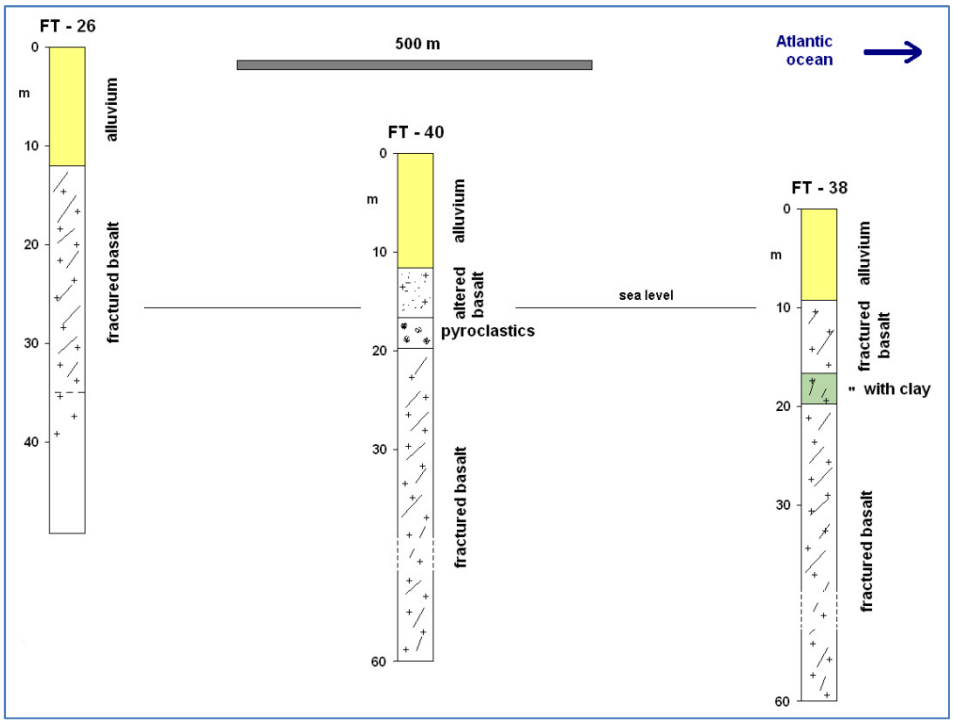

Figure 7.13 – Boreholes lithologic description data at S. Domingos valley, (from INGRH data).

At roughly 70-80 m depth (at soundings depth limit) a highly conductive substratum is detected in the majority of the soundings throughout the valley. This is the cause of the observed continuous decreasing of apparent resistivity curves. The most reasonable explanation is that this phenomenon might be related to clay saturated layer with fossil saline water (Goldman *et al.*, 1991). Clays have a very low hydraulic conductivity, and all these layer levels were under seawater in the past. This could be the cause for the high degree of salinization after long time over-extraction of boreholes far from the sea.

Near the shoreline, the typical freshwater-seawater interface is detected, as can be seen in the 1D sounding models shown in figure 7.14 (TEM sounding AB 9 is 550 m from the sea). The interface calculated by the Ghyben-Herzberg or Todd relations for stagnant seawater (Bear *et al.*, 1999) are in accordance with the measured fresh water (brackish water) levels at this area. The water table level measured in wells is around 1 to 2 m high above the sea level. The assumed interface is shown in the resistivity cross section (figure 7.15).

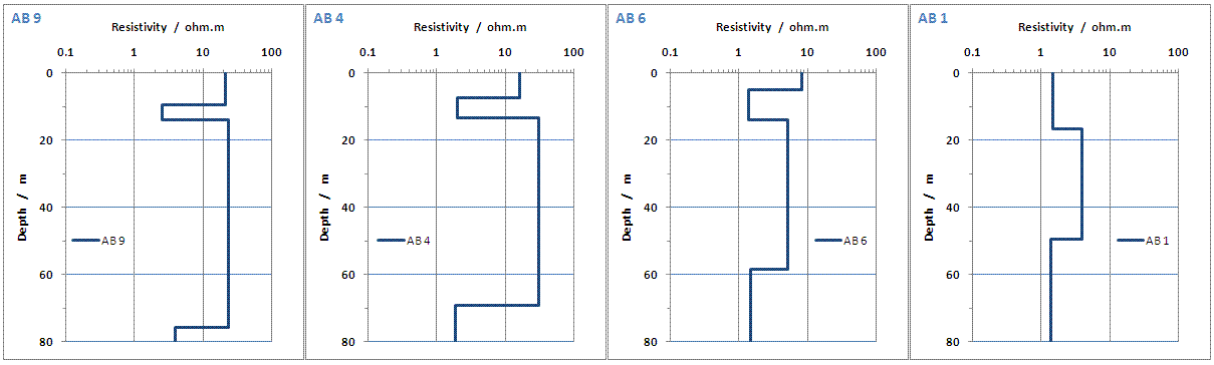

Figure 7.14 – TEM sounding mean models from near the ocean (AB 1) to inland (AB 9).

The quasi-2D cross sections were assembled from the 1D sounding models (figures 7.15 and 7.16). These cross sections are taken from AEMR TEM inversion software, and aren't really a 2D data inversion nor a 1D inversion with laterally constrains (LCI) as written at chapter 3. Models are stitched-together into a section, and lateral continuity is guarantied by simple interpolation between each model. With this procedure, it's possible to delineate the layered structures in the valley, although some local 3D effects can be present. Shallow buried small rock debris from ancient runoff events and wall's erosion effects are greatly smoothed in the TEM process.

The resistivity cross section along the axis of the valley and starting from the sea is shown in figure 7.15. The fresh sea water interface is seen at cross section right side. An upper conductive layer at roughly 15 to 20 m depth bellow surface and thicker near the sea is seen. The resistivity increases going inland and seems to have lateral continuity coming from the sea. It must be separated from bottom freshwater by an impermeable clay layer. At the bottom, 60 m bellow the mean sea level a conductive layer is present and extent all over the valley. That is shown in three perpendicular middle valley cross sections (figure 7.16 a) and b)). The BB' cross section exhibit a step like structure in the north side, that is, the conductive layer is closer to the surface. This is an uncommon behaviour and a local 3D effect is not to exclude as an explanation of this feature.

To check and confirm these resistivity values and lateral continuity of layers, a quasi-3D modelling was done with the data soundings.

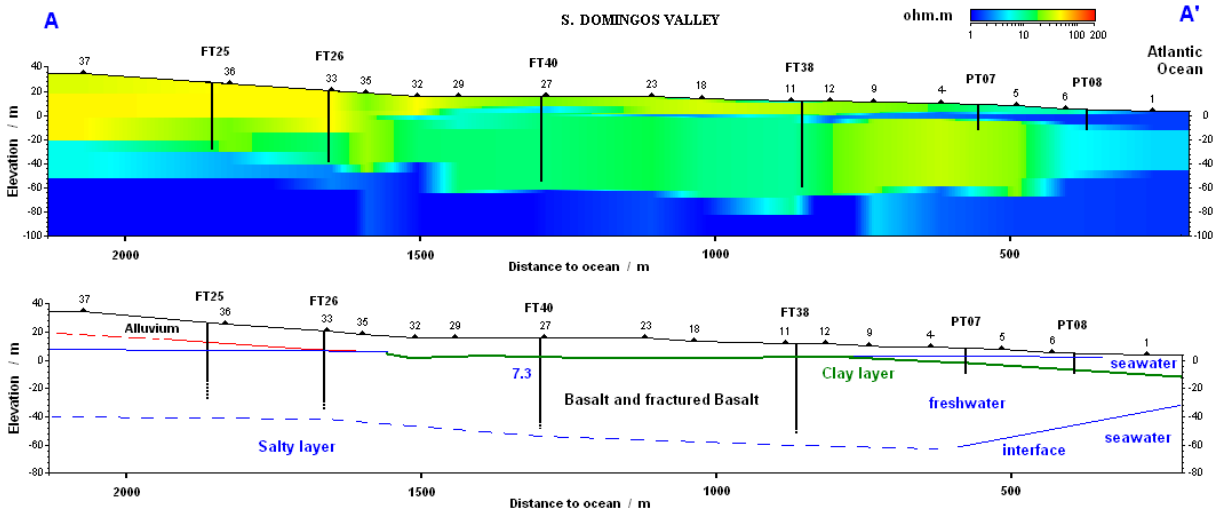

Figure 7.15 – Resistivity axial valley cross section from 1D sounding models. Groundwater level and resistivity (ohm.m), with interpreted geology at S. Domingos valley.

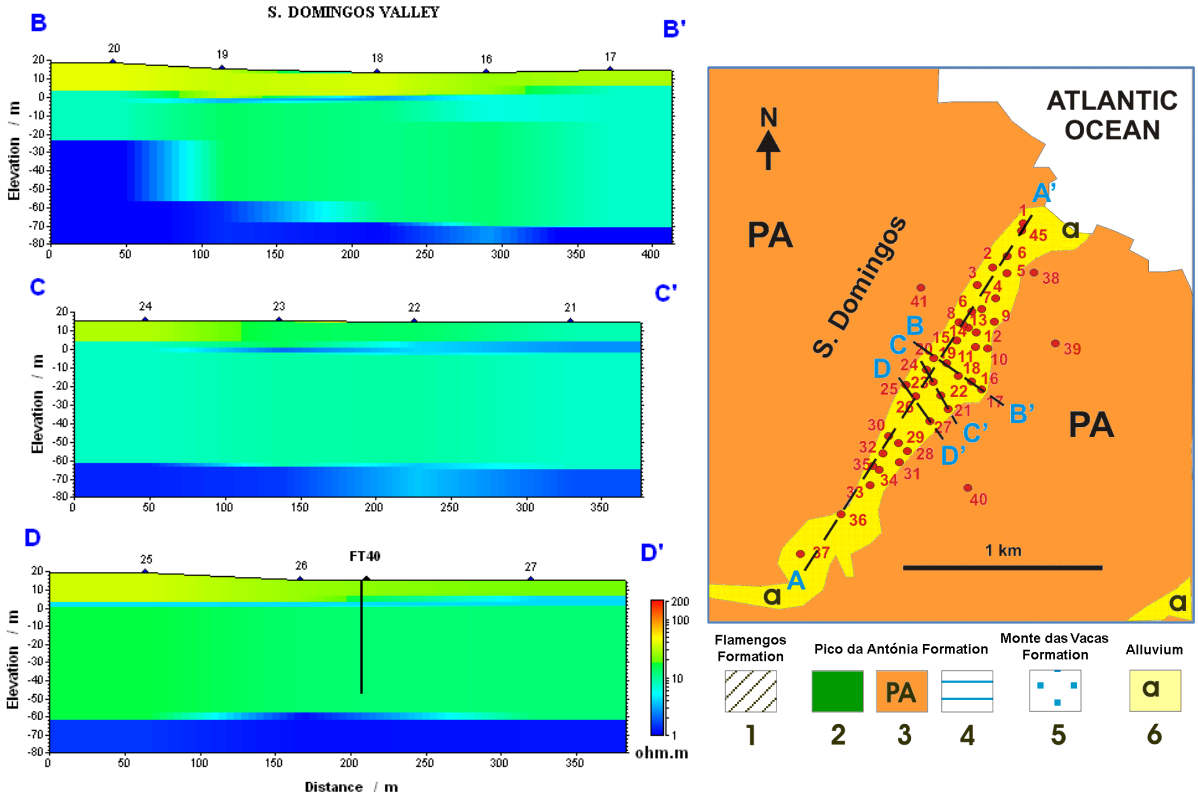

a) b)

Figure 7.16 – a) Resistivity perpendicular cross sections at S Domingos valley.
b) Cross section location map, with geologic explanation: Flamengos formation – 1, Pico da Antónia formation, Pyroclasts – 2, Aereal cloak – 3, Submarine cloak – 4, Monte das Vacas pyroclastic formation – 5, Quaternary alluvium formations – 6. (adapted from Serralheiro (1976, 1977)).

7.1.1.2 – S. Domingos quasi-3D data inversion

The quasi-3D modelling was calculated with a spatially-constrained-inversion algorithm (SCI) that uses the 1D approach in forward calculations (Santos, personal communication; Santos, 2011a and 2011b). As usual, model parameters are the logarithmic resistivity of the layers beneath each sounding site. The number of layers can be chosen. On the several modelling tests made in this thesis they have varied between 13 and 19 layers. The incremental depth is exponential, starting with a shallow 2 m layer and a step of $2e^{0,121(n-1)}$ to the n^{th} thickness layer. Total number of resistivity model parameters to fit is a function of the number of layers' and soundings.

A total of 38 TEM soundings was used at S. Domingos. The number of time channels used in the inversion and fit of each sounding was unequal. They were decimated and vary from just 10 to 21 data points per soundings. The starting initial models were always a resistivity uniform half space.

The effective distance constrain (EDC) parameter between soundings can be also modified. It can be set to zero and thus the inversion is regardless of surrounding ones. Or it can be extended (by 6 steeps) to encompass nearby models. With the spatial spreading of soundings in S. Domingos valley, the maximum constrained distance was around 320 m. Near the sea and far from it, at beginning and ending of axial profile, the number of TEM soundings is smaller, and they are far apart each other. The overall mean distance between soundings is 125 m. At mid valley they are clustered and inversion results are expected to be better in this part. Many inversion tests were carried out changing the initial damping factor parameter (λ), as also the number of layers and the maximum depth of investigation, the neighbours sounding distance and stopping convergence criteria (final iteration and *rms* numbers).

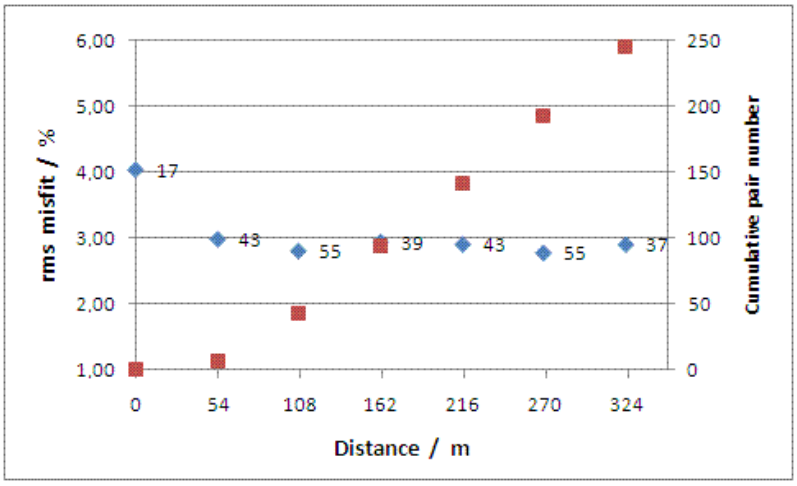

Figure 7.17 – Mean *rms* quasi-3D models misfit and iteration number (blue square), and cumulative sounding pair number (red square) for several constrained distances at S. Domingos valley. Initial damping factor set to 0.1 and 15 layers with 10 ohm.m model space.

A maximum of 60 iterations and a 0.01 *rms* value for stopping the calculations were adequate with a starting homogeneous resistivity model of 10 (or 20) ohm.m. The output results with 15 layers (till 80 m deep) are better than just only 13 layers (till 60 m deep). This

concern to edge conditions and measured data values. The global model's misfit is worse when the EDC distance parameter is turned off (around 4% error) and stays slightly under 3% when neighbours influence is considered. The smaller distance influence value was 54 m. Figure 7.17 give the mean final *rms* misfit value and iteration number to such allowed influence distances, with the same starting conditions, as also the increasingly sounding's pairs number under EDC. This behaviour might indicate a rather smooth horizontal changing medium, and that misfit are limited by data errors. Each inversion's run takes around 15 to 20 minutes maximum computing time (dual-core 2.6 GHz CPU and 2 GB memory machine).

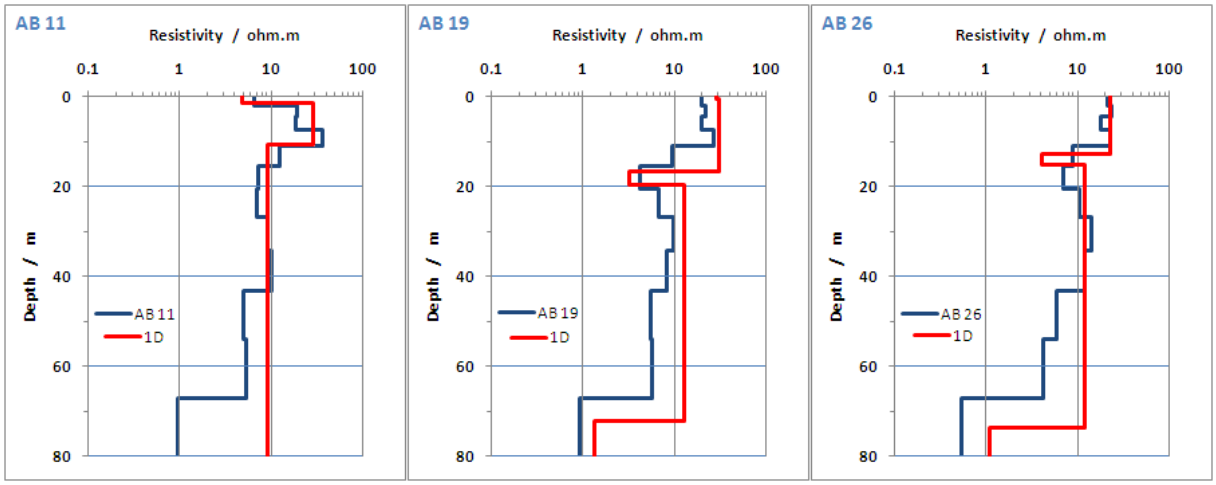

Figure 7.18 – Some S. Domingos mid valley TEM soundings 1D model from quasi-3D inversion (blue), and corresponding 1D mean model (red).

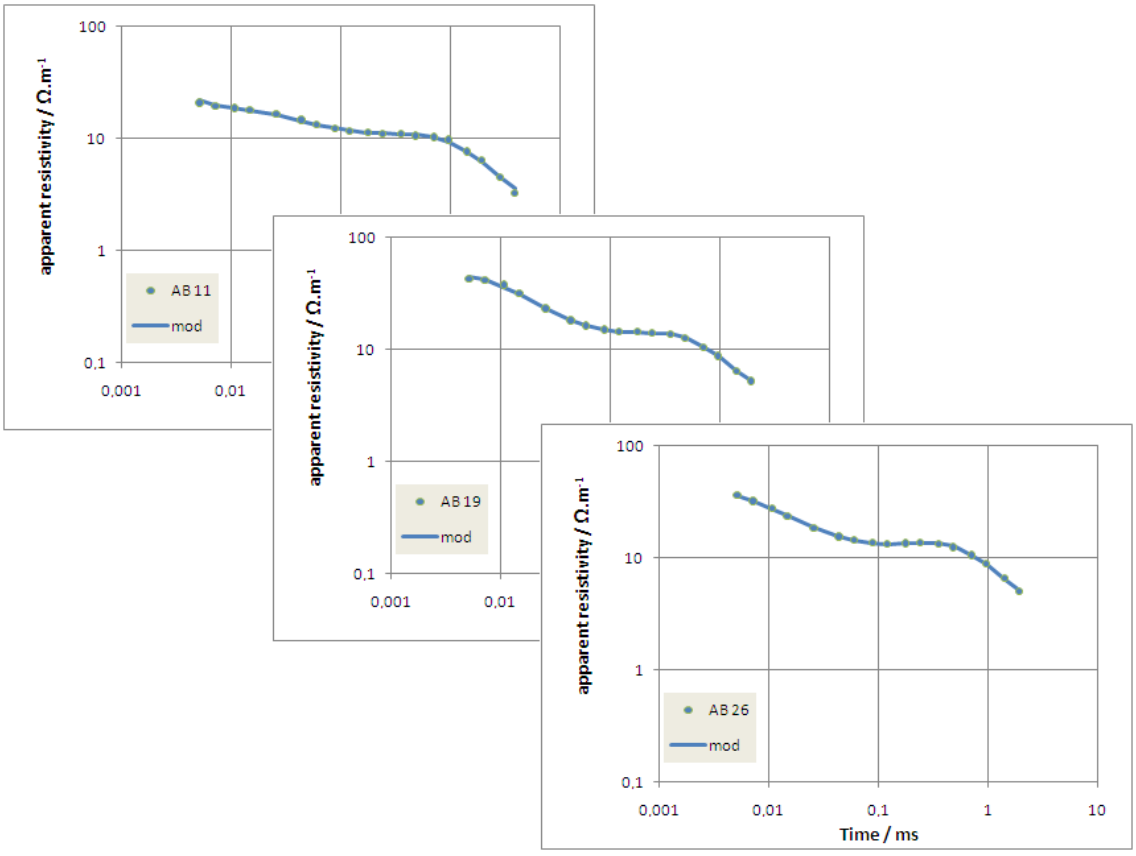

Figure 7.19 – S. Domingos mid valley TEM data points and 1D model fit response from quasi-3D inversion, (corresponding to figure 7.18 models).

Some 1D models and corresponding sounding's data fit are shown in figure 7.18 and 7.19. Although the greater vertical detail of the quasi-3D models, the results are similar to 1D single inversion, with global mean differences under 10% between both sets of models.

The figure 7.20 shows the inversion result for the AA' resistivity cross section. The quasi-2D model structure is quite similar to the previous stitched 1D results. This can also be seen in the perpendicular cross sections (figure 7.21), with the high conductive bottom layer and aquifer bulk resistivity values from 10 to 20 ohm.m. The low resistivity bottom layer is placed somewhat closer to surface beneath sounding 20 in the section BB'.

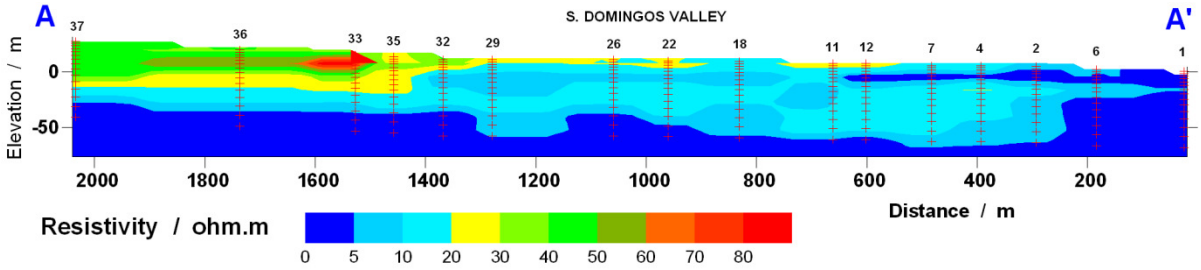

Figure 7.20 – Axial resistivity 2D cross section from quasi-3D model, at S Domingos valley.

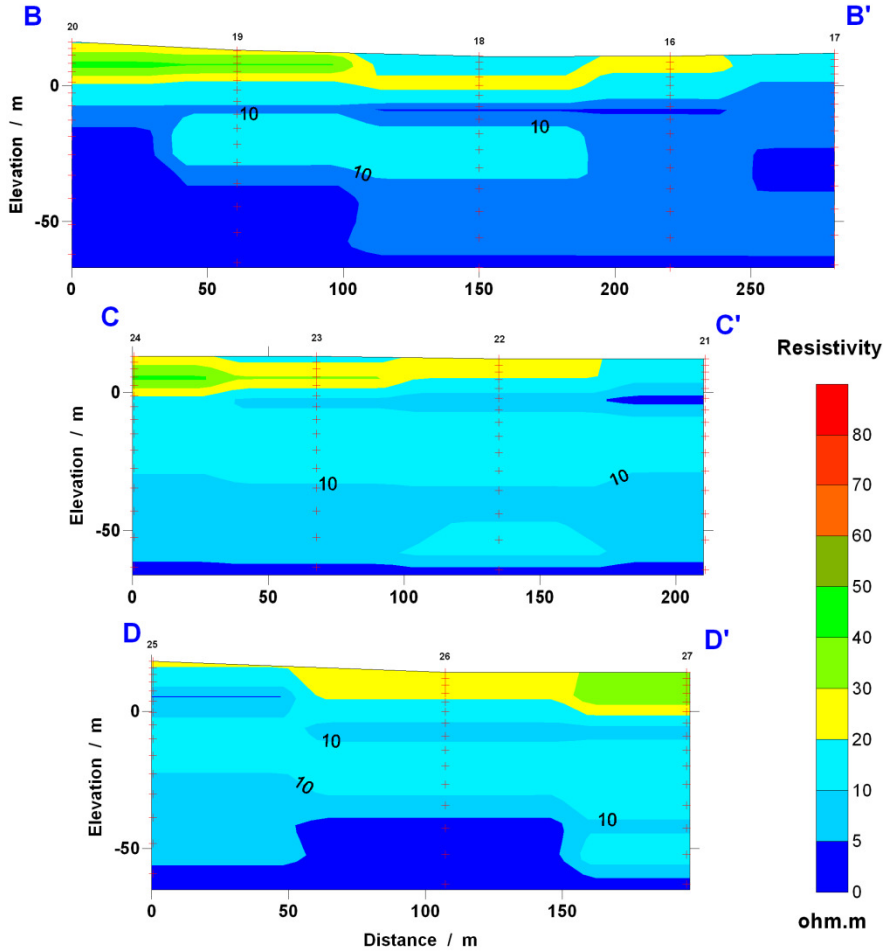

Figure 7.21 – Perpendicular resistivity 2D cross sections from quasi-3D model, at S Domingos valley.

7.1.2 – Seca and Picos data

The Seca and Picos creek valleys are located 10 km to the north of S. Domingos valley, near Santa Cruz village (figure 7.1). These two contiguous valleys show a similar morphology to the previous one with the difference of being much wider. At the coastline the joint valley end span for some 1300 m wide. A few kilometres inland, they attain together some 3500 m wide. These two hydrographic catchment basins are the biggest ones at Santiago, with 49.9 and 71.5 km^2, for Pico and Seca, respectively. Floods are frequent at rainy season, as both basins include the central mountains where intense precipitation happens as recharge areas. TEM soundings have been carried out from the shoreline (at roughly 3 to 4 m amsl) to 3300 and 2000 m inland at 29 and 25 m high, for Seca and Picos valleys, respectively. Again, the creek bed altitude grows steadily from the sea. A few soundings have also been done, to the southeast, outside the Seca valley.

Information from borehole logs in the valleys indicates a mean 25 m thick shallow basaltic alluvium with pebbles, resting over the fractured PA basaltic formation. Sandy and clayed layer's intercalations exist between these two formations. Deepest drilled boreholes reach about 55 m below the mean sea level. No direct geologic information is known beyond this limit. Intense agriculture activities take place at both valleys, except in the last couple of hundred meters from the sea. At Picos valley a considerable large area is devoted to banana production. The situation is analogous to that in the S. Domingos valley with vegetable's productivity declining near the shoreline.

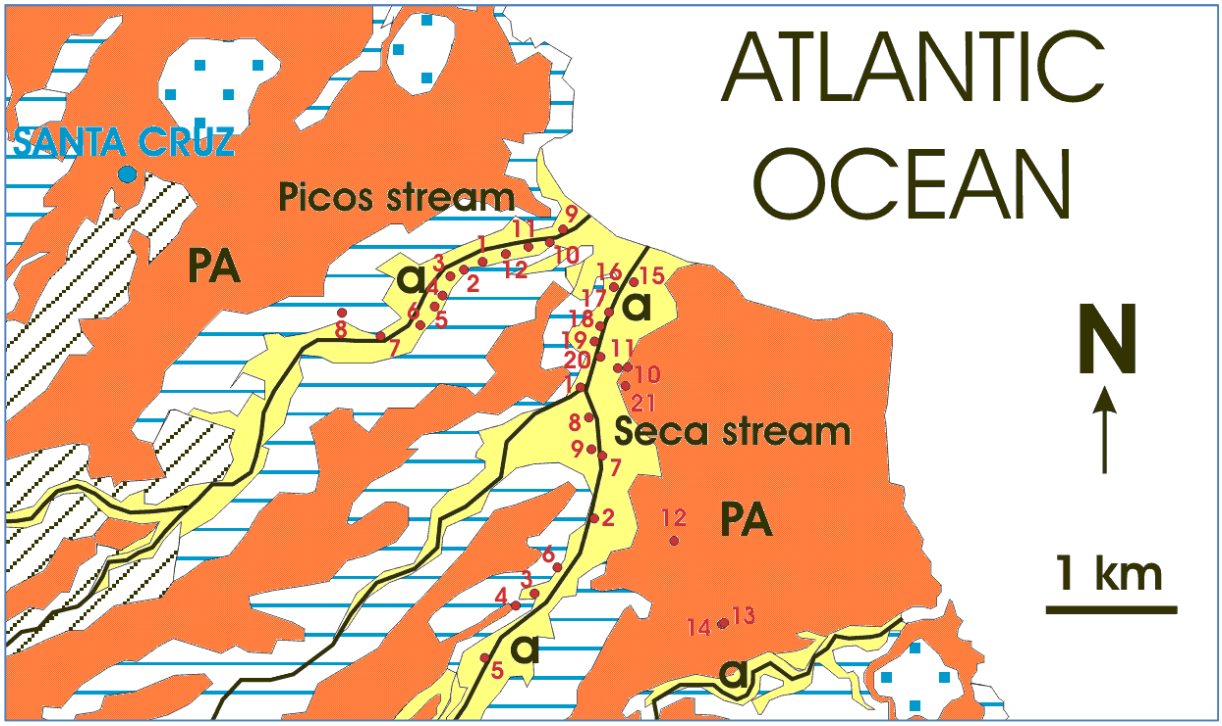

Figure 7.22 – TEM soundings location and number order at Seca and Picos valleys. Geologic map explanation is given at caption of figure 7.16 b).

TEM soundings were carried out from the shoreline throughout the axis valley. The majority of the TEM-FAST 48 soundings were acquired with a 25 m × 25 m single loop wire, with a maximum current of 3.0 ampere and time channel from 6 to 9. The sounding's location is shown at figure 7.22 together with a simple geology sketch of the region. Figure 7.23 plots the TEM sounding's locations plus the boreholes and wells (with lithologic and chemical information) over a photographic image (Google image).

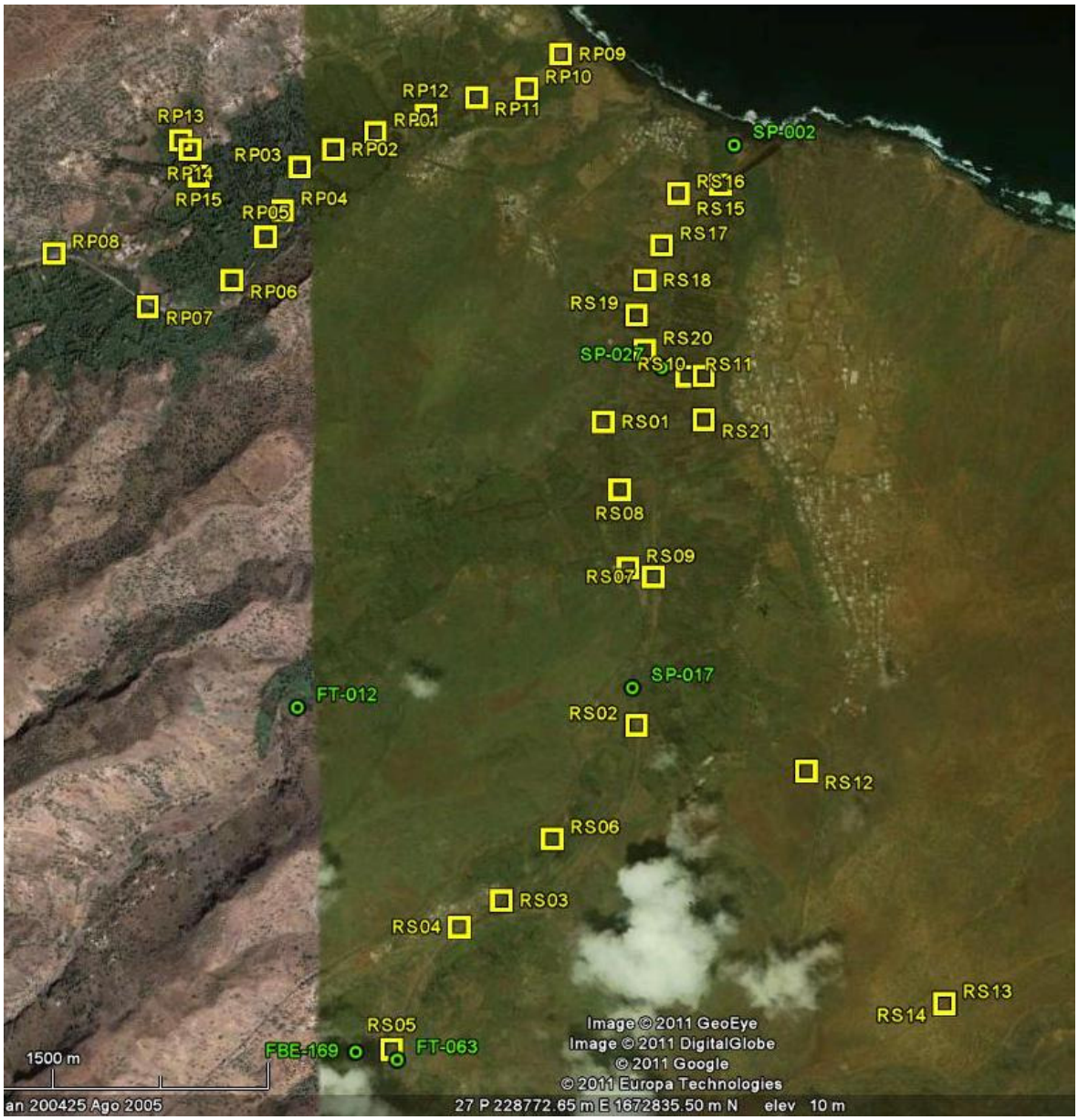

Figure 7.23 – TEM soundings, boreholes and wells location at Seca and Picos valley, (adapted from Google images).

Figures 7.24 a) to c) and 7.25 a) to c) display respectively, the typical landscape scenario and environment at Seca and Picos valleys, respectively.

Figure 7.24 a) – Photography at Seca TEM sounding 17, facing southeast.

Figure 7.24 b) – Photography at Seca TEM sounding 21, facing southwest.

Figure 7.24 c) – Photography at Seca TEM sounding 2, facing northeast.

Figure 7.25 a) – Photography at Picos, near TEM sounding 10, facing north.

Figure 7.25 b) – Photography at Picos TEM sounding 10, facing south.

Figure 7.25 c) – Photography at Picos TEM sounding 4.

7.1.2.1 – 1D inversion of TEM data from Seca

Figure 7.26 shows typical observed TEM curves and their model response fit, from near sea going upstream Seca's valley. Measured noise is again from 2 to 3 nVm^{-2} and error band from stacking procedure is at most a few percent of signal (for last time points) with no major EM noise sources at the surveyed places.

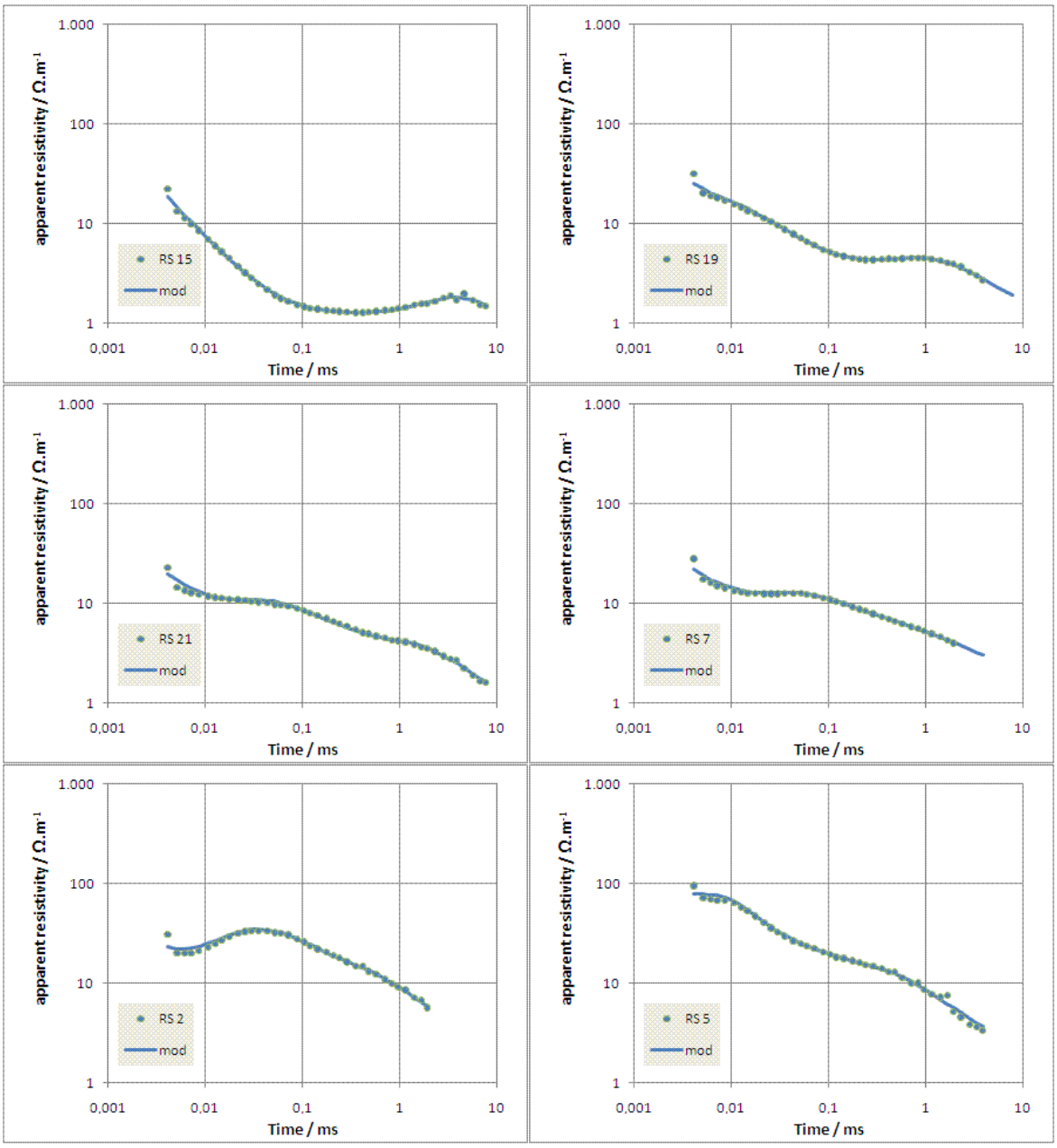

Figure 7.26 – Some Seca measured TEM curves and 1D mean model fit response.

Misfits of the models responses have a mean of 4 to 5%. Figure 7.27 shows the respective 1D mean model for the TEM soundings shown in figure 7.26. The majority of the curves decrease smoothly to low apparent resistivity values. At some locations, there is a conductive layer, roughly at 15 to 20-30 m depth. This is in accordance with some lithologic logging information from boreholes, as can be seen in figure 7.28. At and below this depth,

electric resistivity corresponding to the aquifer formations is around 10 to 20 ohm.m. Under this, a higher conductivity layer is again present, at roughly 50 m deep below mean sea level.

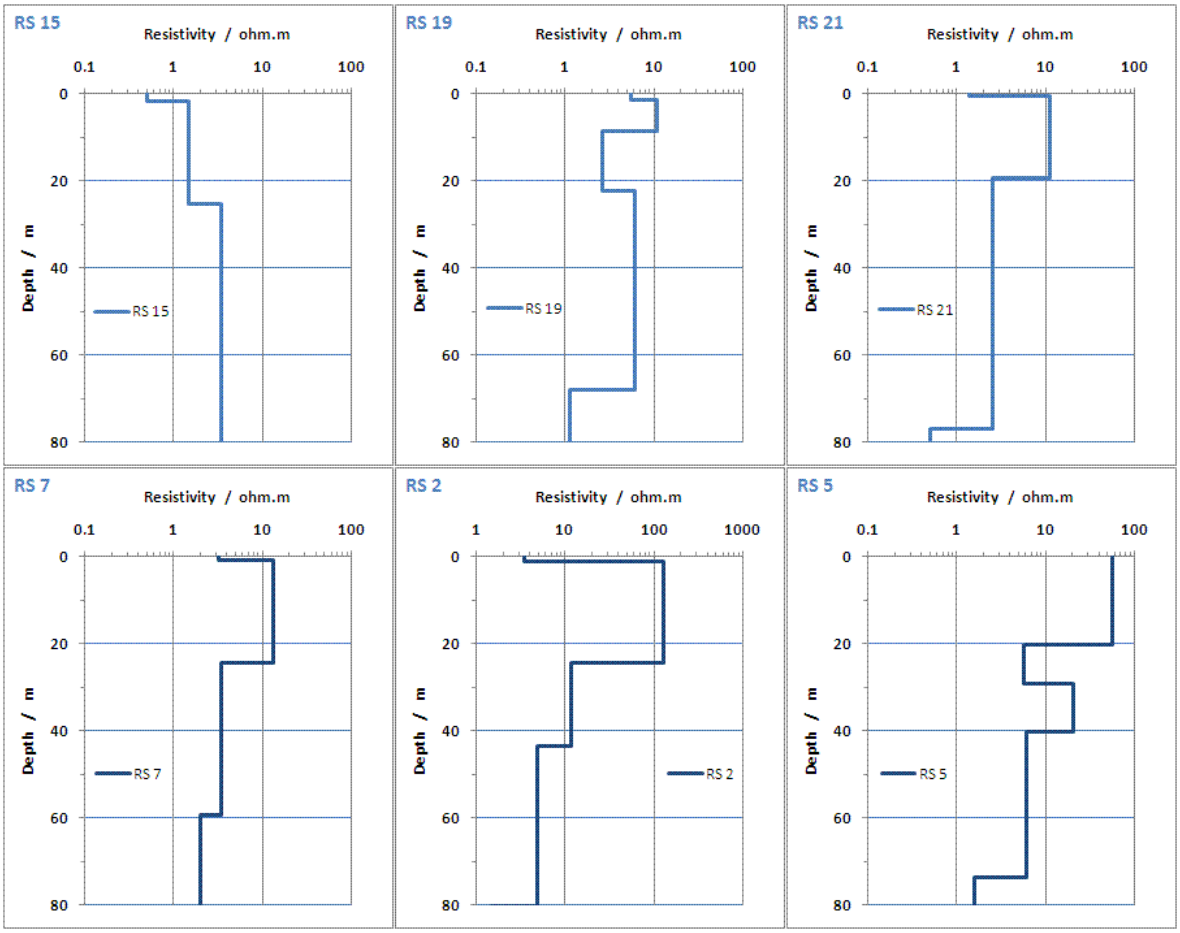

Figure 7.27 – Seca 1D TEM mean models (corresponding to figure 7.26 soundings).

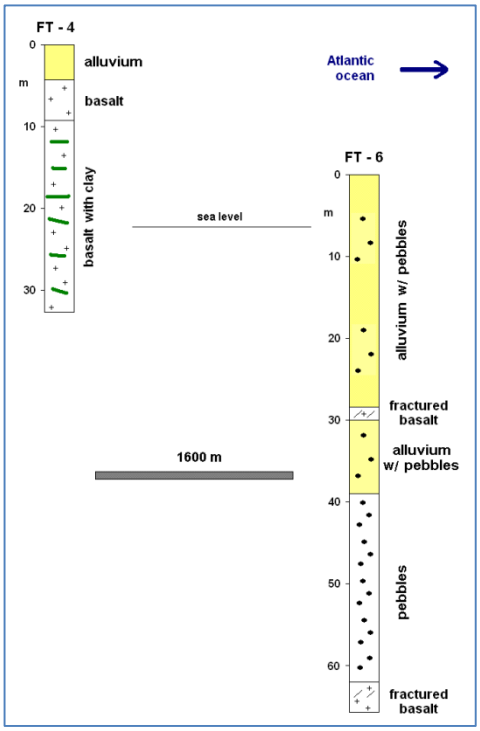

Figure 7.28 – Boreholes lithologic description data at Seca valley, (from INGRH data).

Resistivity cross sections were assembled from the valley 1D sounding models (figure 7.29). As previously, this cross section was taken from AEMR TEMRES inversion software. Borehole and wells measures show that the water level is about 9 to 10 m amsl at 3 km from the coastline (FT63 and FBE169) and almost at the sea level at the shoreline, giving a hydraulic gradient of 0.002 to 0.003.

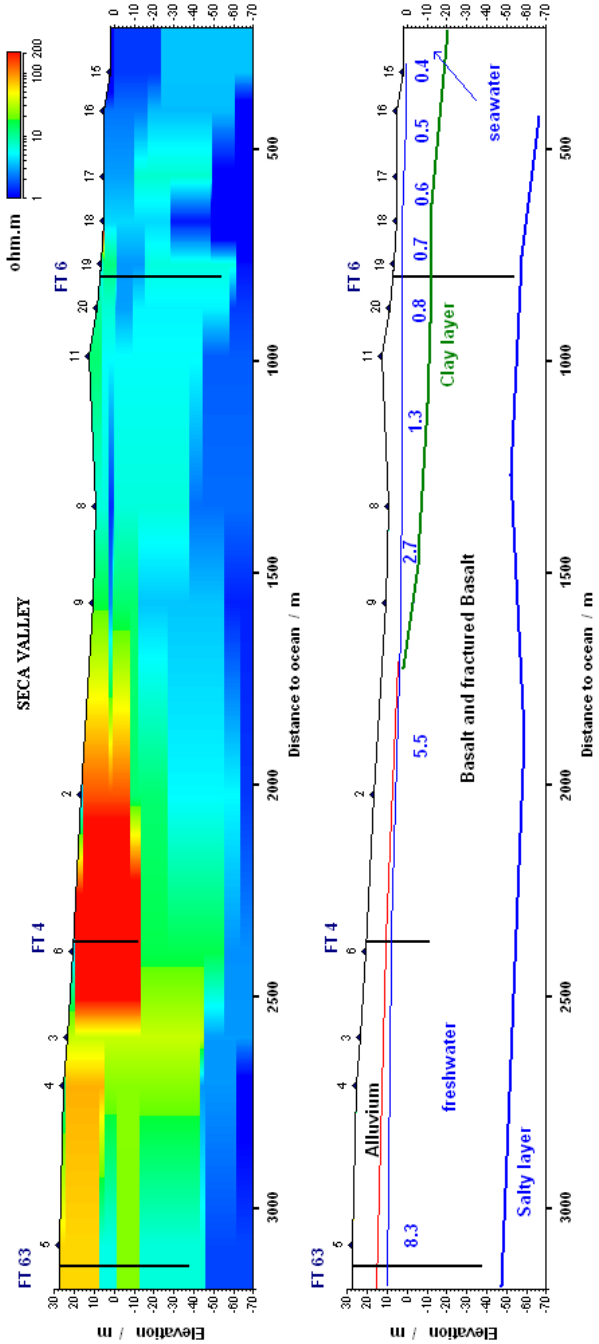

Figure 7.29 – Resistivity axial cross section at Seca valley, from 1D TEM sounding models. Groundwater level and resistivity (ohm.m) plus interpreted geology.

The same upper conductive layer roughly 20 m thicker near the sea and increasing resistivity inland can be noted. This structure seems to be separated from the lower freshwater by an impervious clay layer. Far from the coastline the superficial resistivities are higher, but at bottom, 40 to 50 m bellow the mean sea level a conductive layer is present and extent all over the valley.

7.1.2.2 – Seca 2D data inversion

The same spatially constrained algorithm has been applied to the soundings acquired in the Seca valley. As TEM soundings are along a line, the result can be approached to a 1D inversion with only laterally constrains (LCI). The overall mean distance between soundings was 175 m. Several inversion tests had been carried out, changing initial damping factor (λ), different number of layers and different EDC values.

A maximum of 40 iterations and a 0.02 *rms* value with a starting homogeneous resistivity model of 10 (or 20) ohm.m were adequate, with 15 layer model (till 80 m deep). Figure 7.30 display the mean *rms* misfit *versus* maximum iteration number and number of pairs of soundings under EDC, all with the same starting conditions. The number of soundings within EDC grows up almost linearly with that parameter. The misfit decreases accordingly to about 6% and better results occurs with more iterations.

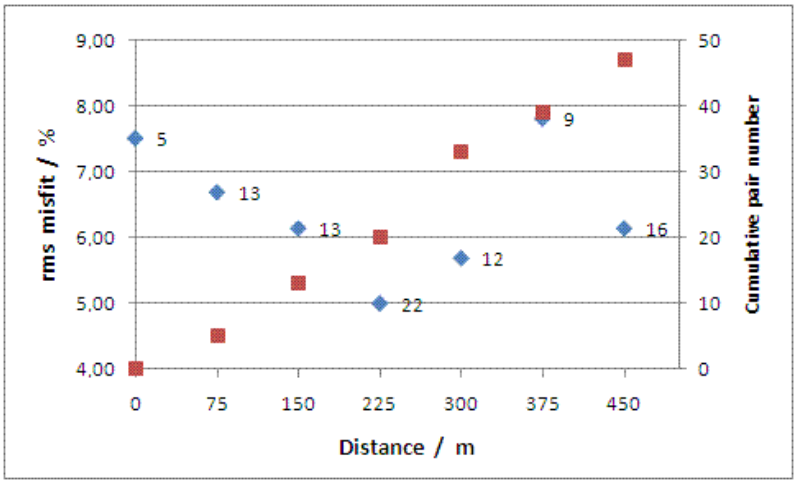

Figure 7.30 – Mean *rms* quasi-2D models misfit and iteration number (blue square), and cumulative sounding pair number (red square) for several constrained distances at Seca valley. Initial damping factor set to 0.1 and 15 layers with 10 ohm.m model space.

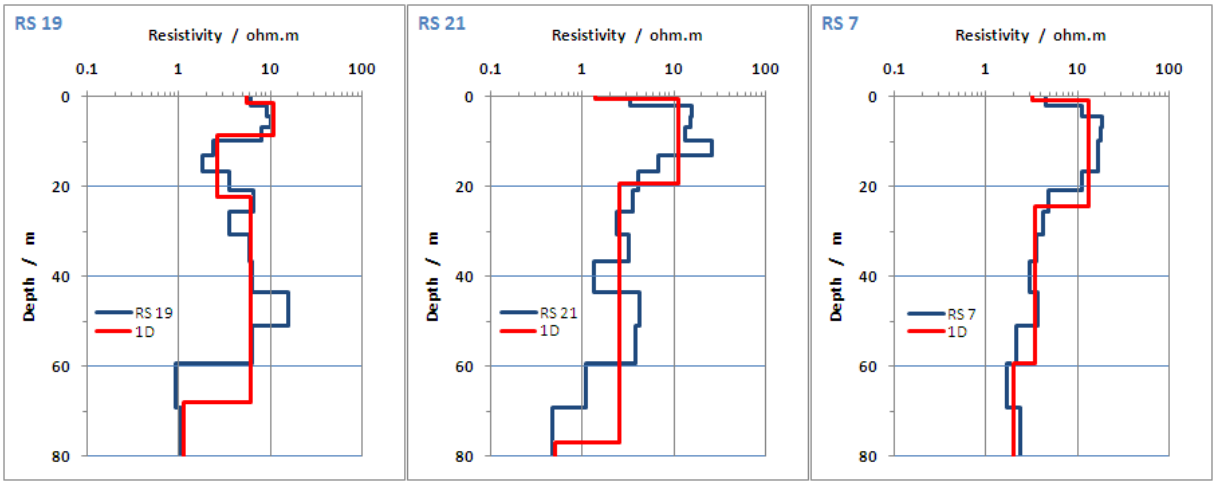

Figure 7.31 – Some Seca valley TEM soundings 1D model from quasi-2D inversion (blue), and corresponding 1D mean model (red).

The quasi 2D global mean *rms* misfit is higher than mean 1D inversion models misfit. This is a consequence of the inversion process, as TEM soundings aren't sufficiently closer to each other and because the model has layers with fixed geometry. Some 1D model's results and soundings data fit is shown in figure 7.31 and below in figure 7.32, from the EDC highest models. Differences between both modelled sets are globally smaller than 10%. The overall resulting structure is similar to previous one obtained by stitched 1D models (figure 7.29).

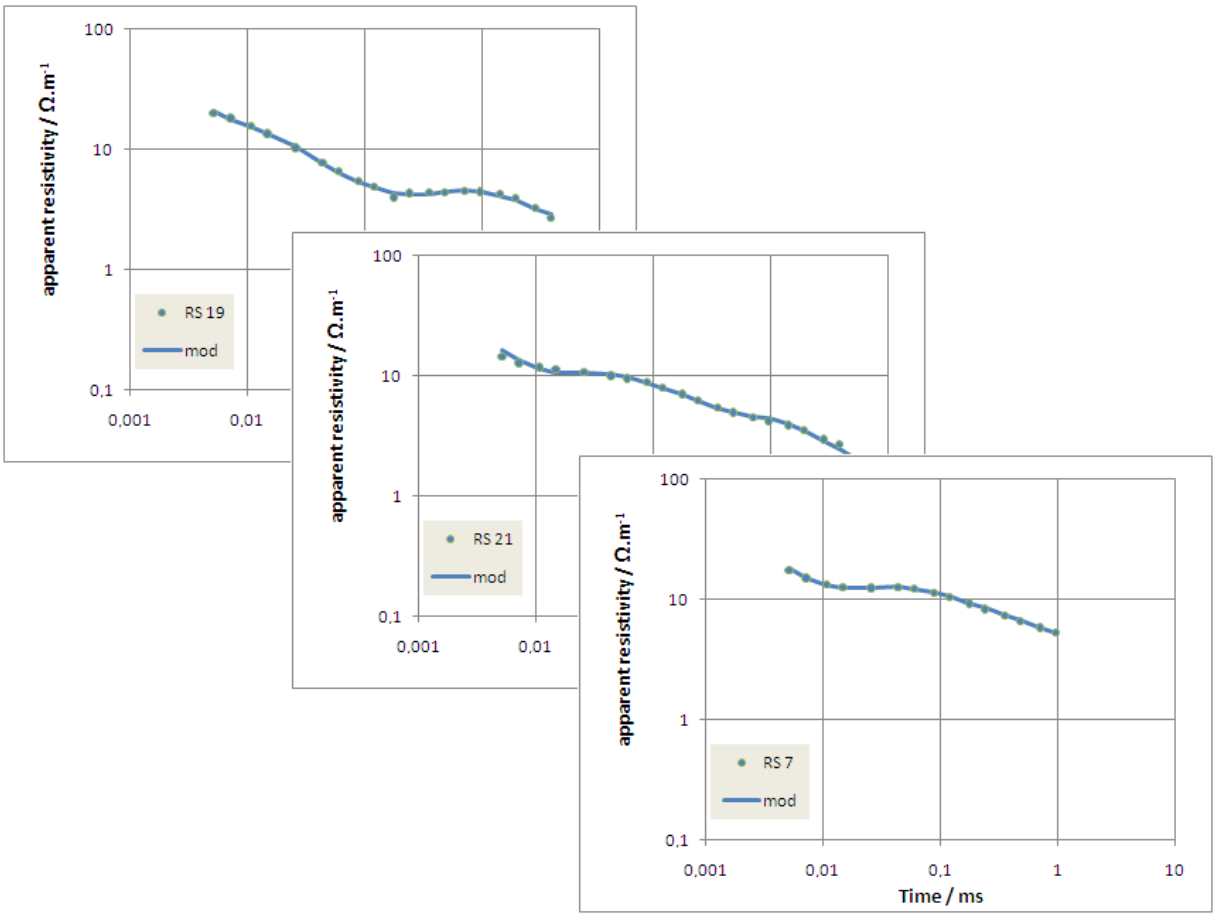

Figure 7.32 – Seca valley TEM data points and 1D model fit response from quasi-2D inversion, (corresponding to figure 7.31 models).

The plot below (figure 7.33) is the 2D cross section, and it shows the superficial influence of the near sea, the superficial high resistivities inland and the conductive bottom. The same problem of no spatially uniform data affects the plotting.

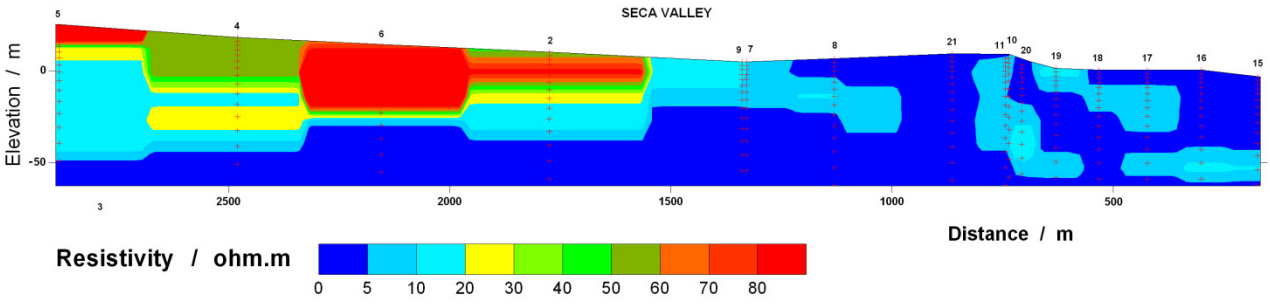

Figure 7.33 – Axial resistivity 2D cross section from quasi-2D model, at Seca valley.

7.1.2.3 – 1D inversion of TEM data from Picos

Figure 7.34 shows some of the calculated 1D models at Picos valley, from near the shoreline upstream the valley. The corresponding measured TEM data and the model response are shown in figure 7.35. Signal noise was small with data errors growing in the last measured points. No major EM noise source exists. Some borehole and well pumps (mechanical) were running during the acquisition, but no major signal influence was detected.

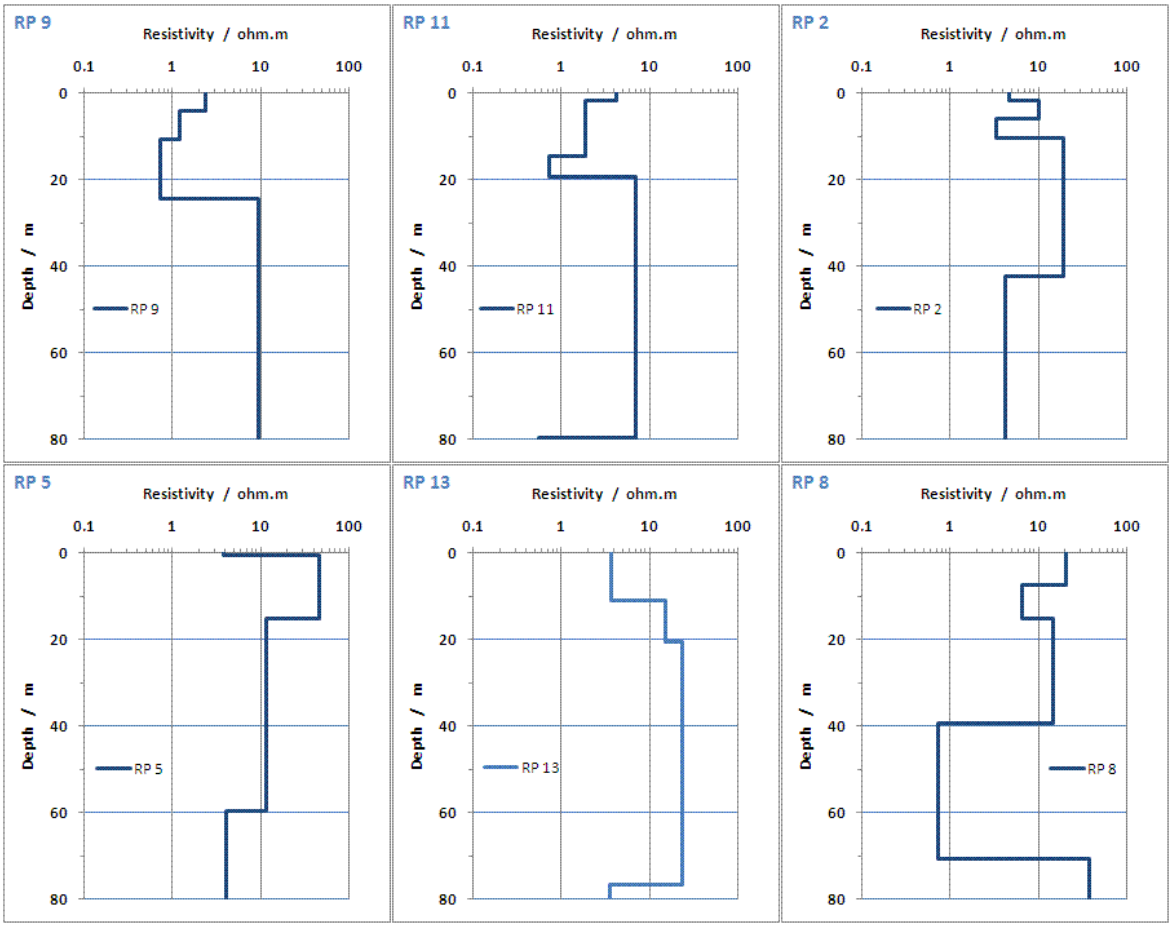

Figure 7.34 – Some 1D TEM mean models from Picos valley survey.

Model responses have a mean 3 to 4% of misfit. The majority of the sounding curves decrease smoothly to low apparent resistivity values. The observed behaviour is similar to that in Seca valley with the corresponding aquifer system having bulk resistivity around 10 to 20 ohm.m values.

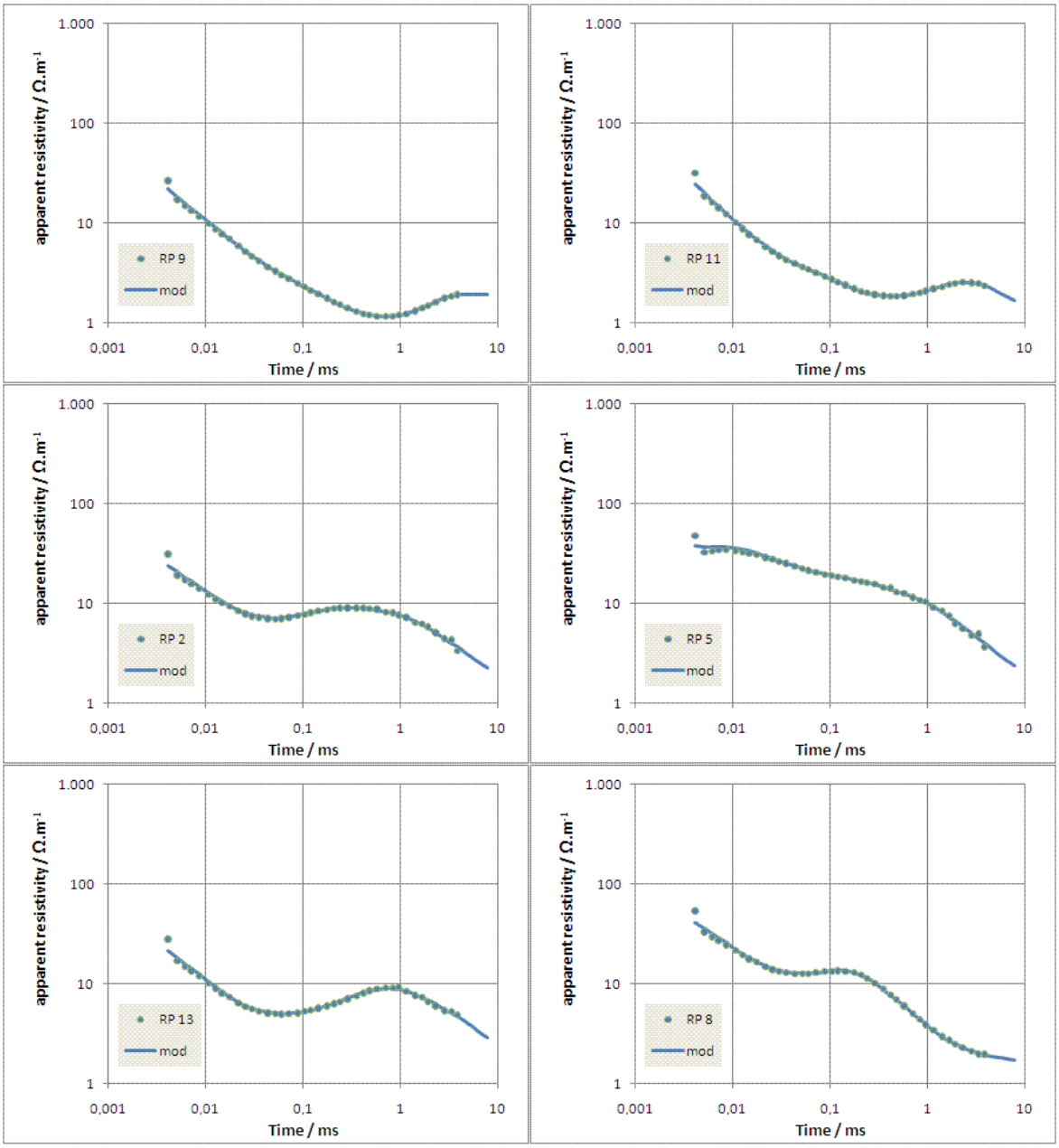

Figure 7.35 – Several Picos TEM sounding curves and 1D mean model fit response.

Like previously, the resistivity cross section was assembled from the 1D sounding models, calculated with the AEMR TEM inversion software (figure 7.36). This resistivity cross section is very similar to the Seca one, showing roughly the same resistivity values and spatial features. The corresponding deeper conductive layer is barely detected at some soundings. Near the coastline, the models and the cross section do not show the freshwater to seawater classical interface (as detected at S. Domingos). That's also true in the Seca cross section. The same low resistivity shallow layer, coming from the sea is detected. The groundwater flux and pressure heads seems to setup the freshwater-seawater interface way and deeper to be detected by TEM soundings nearest to sea.

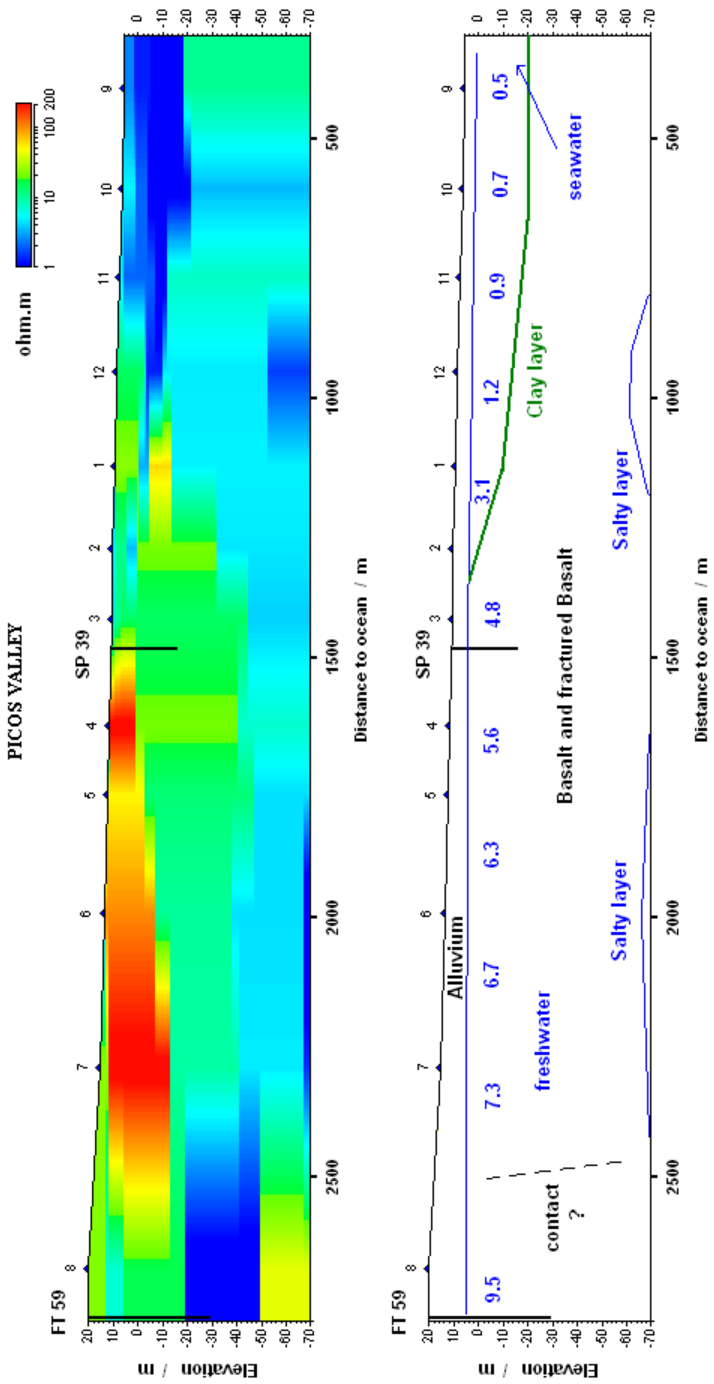

Figure 7.36 – Resistivity axial cross section at Picos valley, from 1D TEM sounding models. Groundwater level and resistivity (ohm.m) plus interpreted geology.

7.1.2.4 – Picos 2D data inversion

The spatial distribution of the TEM soundings in Picos is almost under a straight line. To that situation, the spatially constrained algorithm methodology behaves like the 1D inversion with only laterally constrains (LCI). The overall mean distance between soundings was also of 175 m. Inversion tests have been carried out like previously, changing initial damping factor (λ), the number of layers and different EDC values.

The maximum number of iterations was set to 40 and the *rms* value to 0.01 misfit. Initial model was again and always set to a homogeneous resistivity model of 10 ohm.m, with 15 layers (till 80 m deep). Figure 7.37 display the mean *rms* model's misfit to maximum iteration number and pairs of soundings in the EDC. The misfit is high with no lateral models influencing the inversion and becoming smaller, with the LCI influence, to a mean value of 5%, with better results when more iterations take place. The number of pairs of soundings within EDC grows up almost linearly, alike Seca's modelling. Again, quasi 2D global mean *rms* model's misfit is higher than 1D inversion models mean misfit, by the same already exposed reasons.

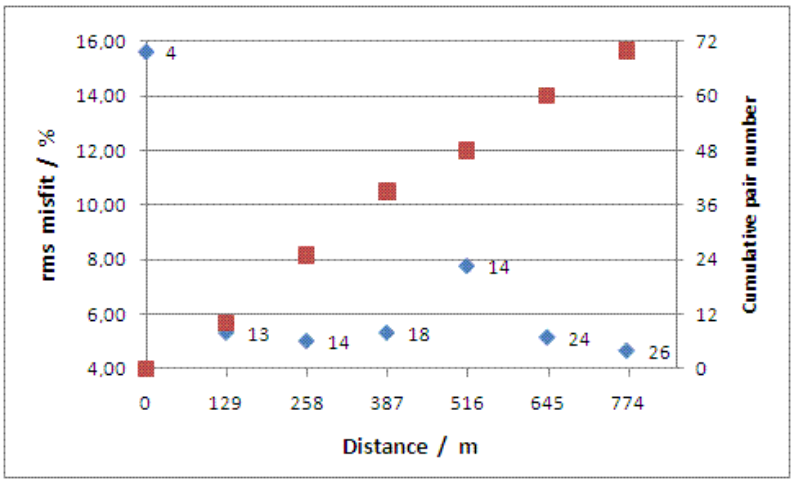

Figure 7.37 – Mean *rms* quasi-2D models misfit and iteration number (blue square), and cumulative sounding pair number (red square) for several constrained distances at Picos valley. Initial damping factor set to 0.1 and 15 layers with 10 ohm.m model space.

Some 1D models and the corresponding data fit are shown below in figures 7.38 and 7.39, from the highest EDC value. Models are similar to those obtained from 1D inversion in spite of the different approach between methods. The resistivities are much alike and differences between both single and constrained models are of the same order, as previously.

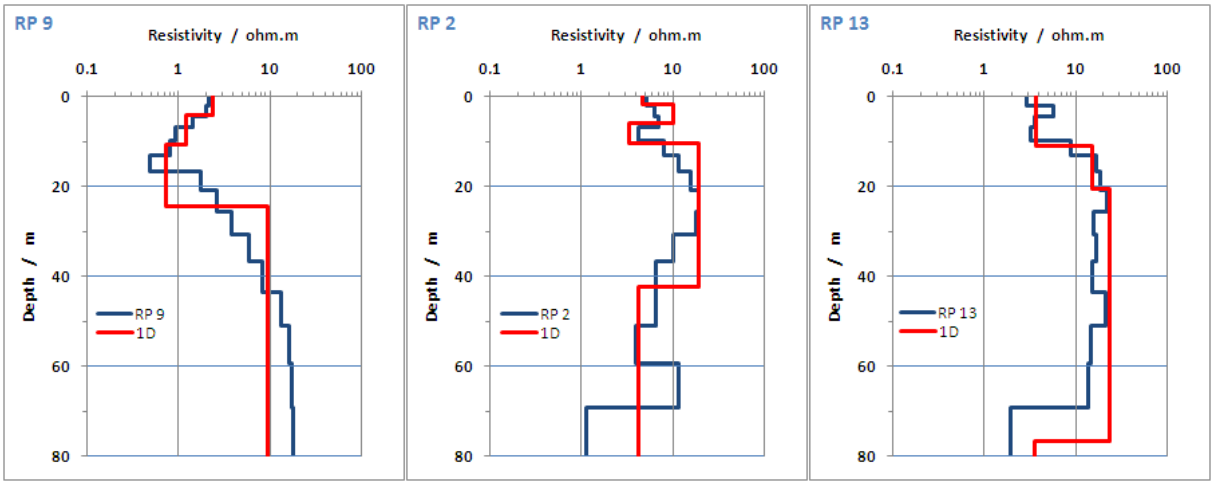

Figure 7.38 – Some Picos valley TEM soundings 1D model from quasi-2D inversion (blue), and corresponding 1D mean model (red).

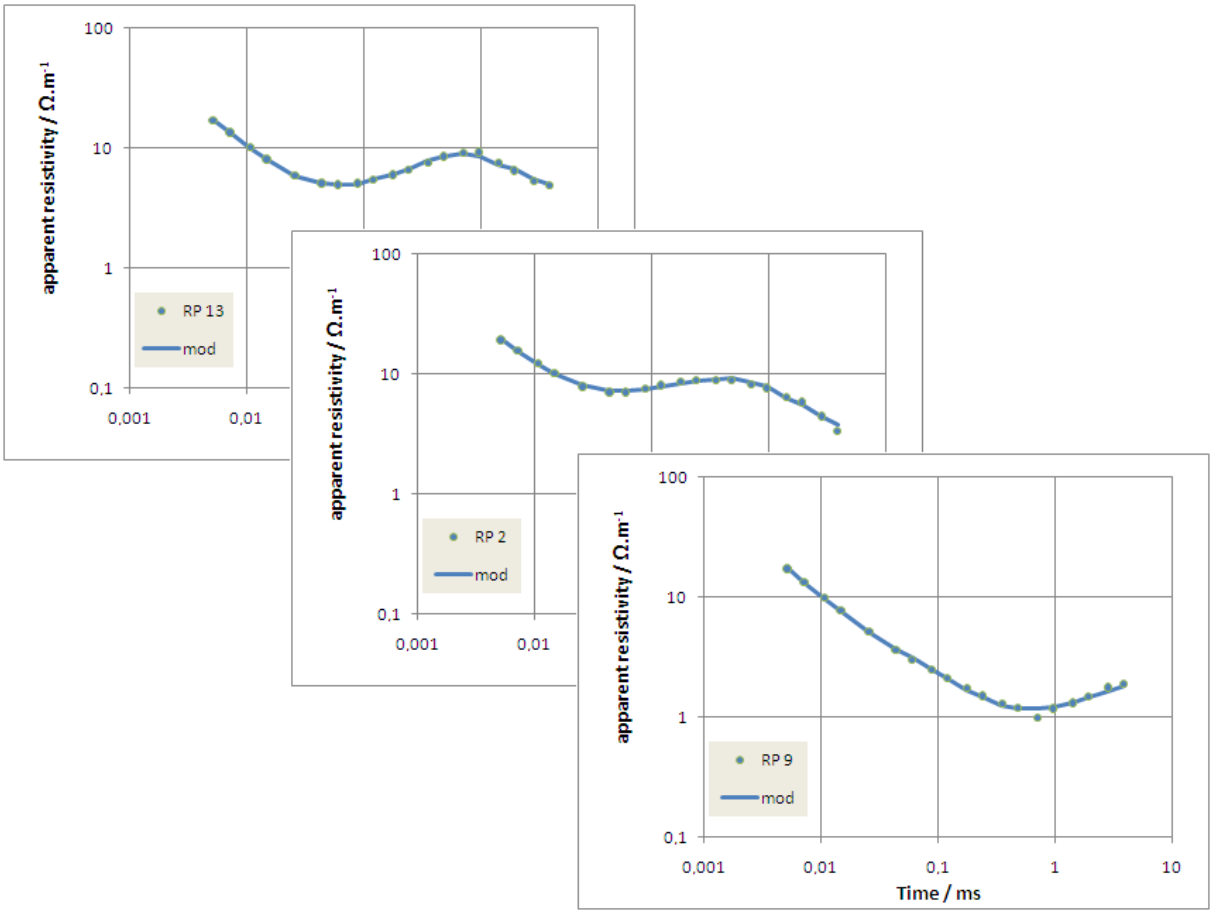

Figure 7.39 – Picos valley TEM data points and 1D model fit response from quasi-2D inversion, (corresponding to figure 7.38 models).

The resulting structure is quite similar to the one obtained by stitched 1D models (figure 7.36), with some differences at the near surface, caused by somewhat fewer resistive layers beyond the mid profile. The less resistive bottom is also barely detected.

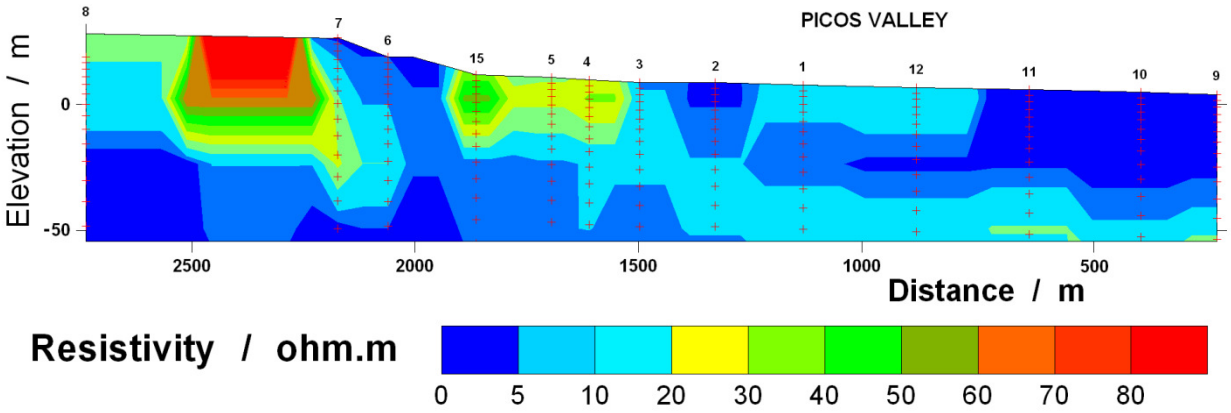

Figure 7.40 – Axial resistivity 2D cross section from quasi-2D model, at Picos valley.

7.1.2.5 – VLF and MT data comparison at Seca and Picos valleys

The Seca and Picos TEM inverted models have been compared with previous electromagnetic profiles crossing both Seca and Picos valleys. The former studies comprise a 4 km long MT profile (9 stations) and several shorter VLF-EM ones, approximately oriented SE to NW and parallel to the coastline at 1 to 2 km way from it. A full description of this work; equipment, data processing and results are given in Santos *el al.* (2006).

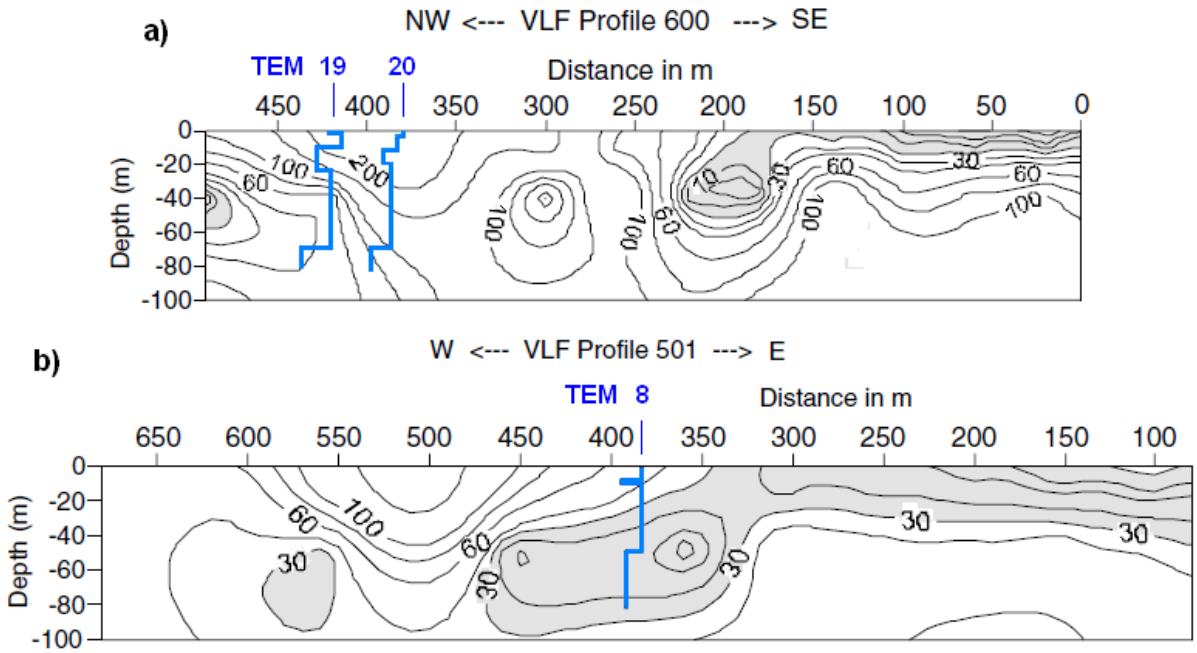

Figure 7.41 – VLF resistivity models (tipper component) for two cross sections at Seca valley and models from nearest TEM soundings. a) 750 m and b) 1400 m, from the coastline. (Adapted from figure 8, Santos *el al.* (2006)).

The VLF resistivity cross sections are shown above, in figure 7.41, with some nearby TEM models stamped over. These VLF resistivity results must be taken as relative values, rather than absolute ones, because the VLF data are only the tipper component. The low resistivity values in TEM soundings seem to be in accordance with the resistivity decreasing suggested in the VLF models.

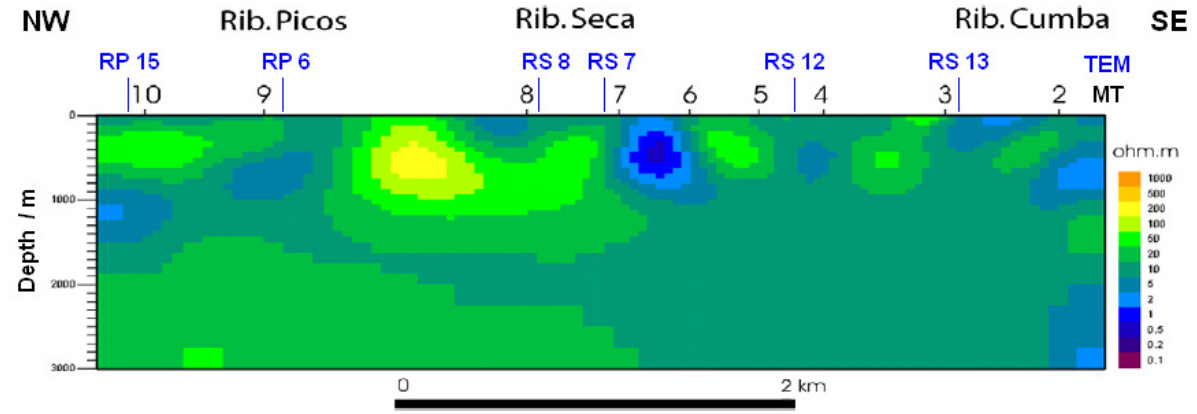

Figure 7.42 – 2D MT resistivity model cross section at Seca and Picos valleys. TE- and TM-mode data joint inversion, (adapted from figure 9, Santos *el al.* (2006)).

The 2D MT model cross section (from TE and TM-mode data joint inversion) is shown in figure 7.42. Although the broad-band MT method is being unsuited to investigate very shallow structures (less than 100 m deep), the resistivity values near the surface and also at major depths, have low values, especially beneath the valleys. The resistivity values are around 5 to 10 ohm.m, and these deeper structures could be related to the valley fault genesis and may be linked to some regional conductive groundwater up flow.

7.1.3 – Tarrafal and Ribeira Grande data

The Chão Bom in Tarrafal, is a flat area near the ocean, at the northwest side of Santiago Island. The Ribeira Grande stream valley is located just to the south of Tarrafal. The major difference to the remaining places is that Chão Bom is intensively farmed since many decades and is not crossed by any creek or stream system. It has approximately one square kilometre surface, with elevation from 5 to 20 m above msl. Several areas within Chão Bom had been severely affected by local salty water irrigation and were temporally abandoned. Nowadays, the situation is slowly reversing, with less salty water irrigation, as most of it comes from nearby mountain's sources. The corresponding hydrographic catchment basin as 7.5 km^2,

The Chão Bom area is almost entirely covered by an alluvial deposit, surrounded (and overlying) by the PA formations (figure 7.43). This alluvium is manly formed by flood debris deposits with elements of a great variety in composition as well as in size and shape. This information comes from several lithological borehole descriptions at Tarrafal region (Dahlin *et al.*, 1986 and INGRH). Superficial soil and alluvium are thinner with just a couple of meters at the south side of studied area, and have some six meters tick at the north side. In the southern area, under the initial layer, some pillow lava and scoria detritus are followed by fractured basalt until 28 m depth. From this level to 48 m depth, consolidated sandy alluvium is observed, being slightly clayey to the bottom. Bellow this, fragments of pillow lava exist. In the northern side and after the initial layer, a succession of fractured basalt with scoria and scoria layers exist until 49 m depth, sometimes with clayed inclusions. At Ribeira Grande, a stream valley with 20 to 30 m hillside high walls, the layers' successions are almost entirely formed by altered and fewer altered basalts, with some clayed inclusions. Deepest drilled borehole at area goes to 35 m below the mean sea level. No direct geologic information is known beyond this limit. The Ribeira Grande hydrographic catchment basin covers 21.0 km^2,

The TEM survey has covered the agricultural area from the Tarrafal village limits, at north and east, to the coastline. In Ribeira Grande, soundings have been carried out from the seashore upstream the valley to 2 km m inland, and to 75 m elevation. The majority of the TEM-FAST 48 soundings were acquired with a 25 m × 25 m single loop wire, with a maximum current input of 3.0 ampere and time channel set to the maximum (9). The soundings' location is shown at figure 7.43, over a regional geological map. Figure 7.44 shows the TEM soundings' location plus the boreholes and wells (with lithologic and chemical information) over a photographic image (Google image).

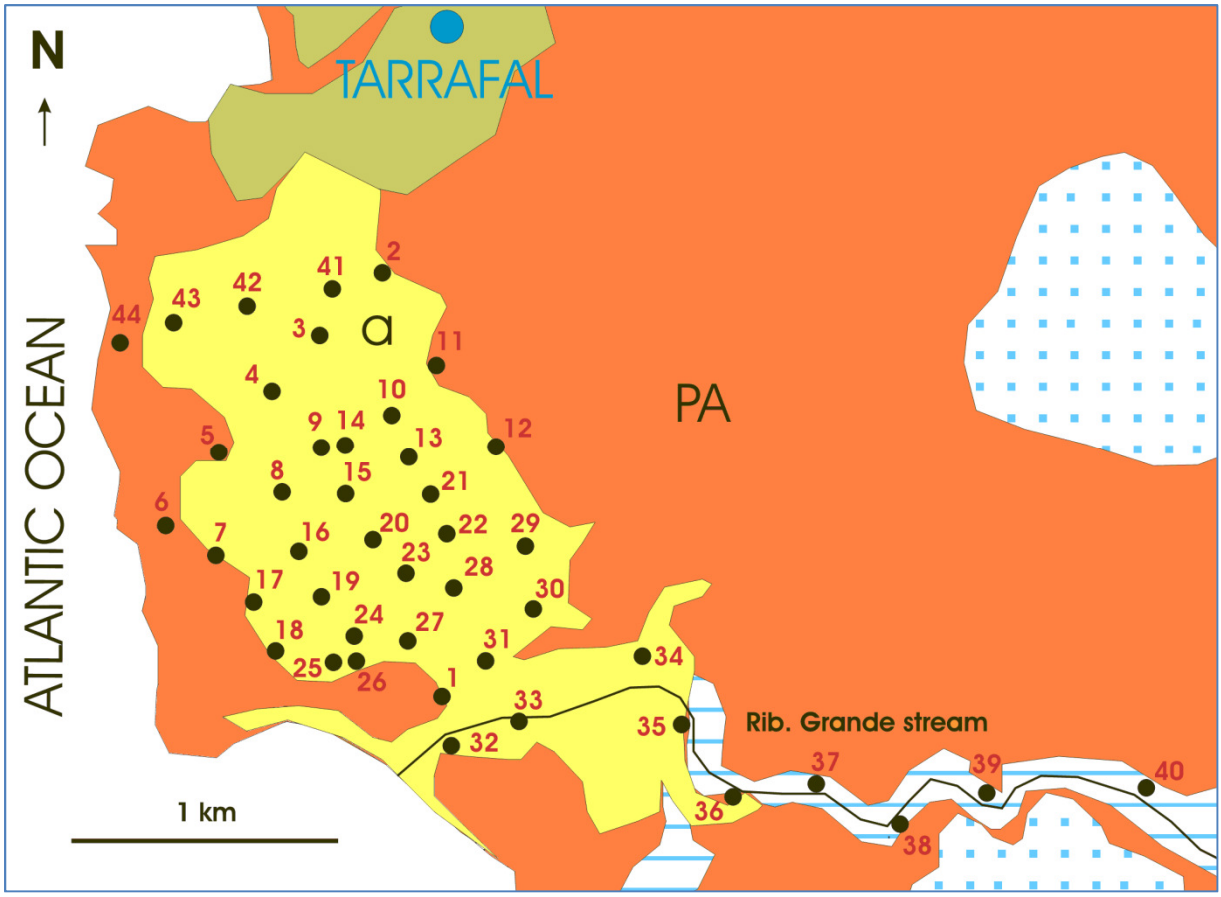

Figure 7.43 – TEM soundings number and location at Tarrafal and Ribeira Grande valley. Geologic map explanation is the same as given at caption in figure 7.16 b).

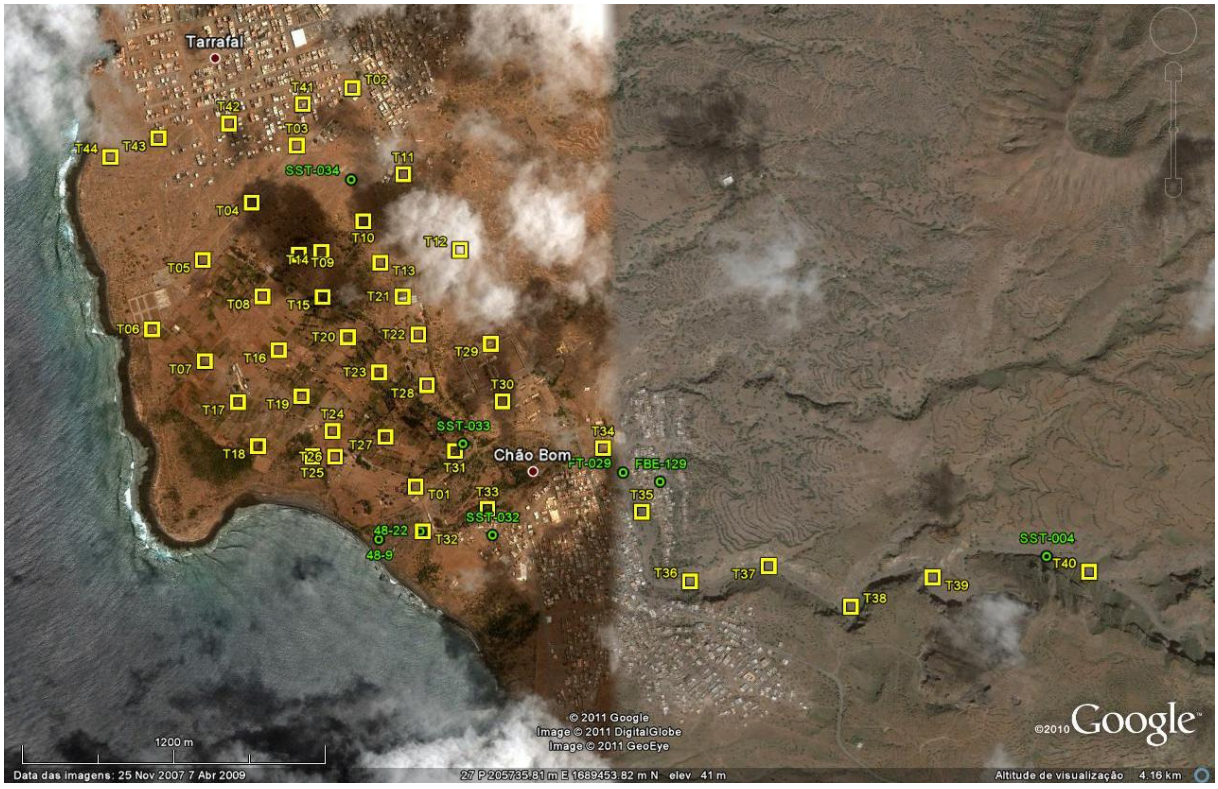

Figure 7.44 –TEM soundings, boreholes and wells location at Tarrafal and Ribeira Grande valley, (adapted from Google images).

The figures 7.45 a) and b) show the typical landscape and local environment, at the Chão Bom agricultural north area limit.

Figure 7.45 a) – Photography at Tarrafal, near TEM sounding 2, facing northeast.

Figure 7.45 b) – Photography at Tarrafal, near TEM sounding 3, facing southwest.

An analysis of the TEM apparent resistivity curves show that they have a similar behaviour, the medium is a mostly high conductor with resistivity decreasing with depth. In figures 7.46 to 7.49 the overall krigged apparent resistivity distribution is mapped for eight increasing time windows after the turnoff. Inland, far from the coastline at higher places, the apparent resistivity values are high at the shallow depths and decrease towards the shoreline (lower elevation). The late time registered windows (deeper layers) have low apparent resistivity values all over the Chão Bom area. Near the northeast extreme, the very low apparent resistivity values linked to TEM number 11 are due to a disturbing coupling effect in the late time records (figures 7.48 and 7.49). This sounding was located very near the road and to several houses under construction, with ongoing work taking place.

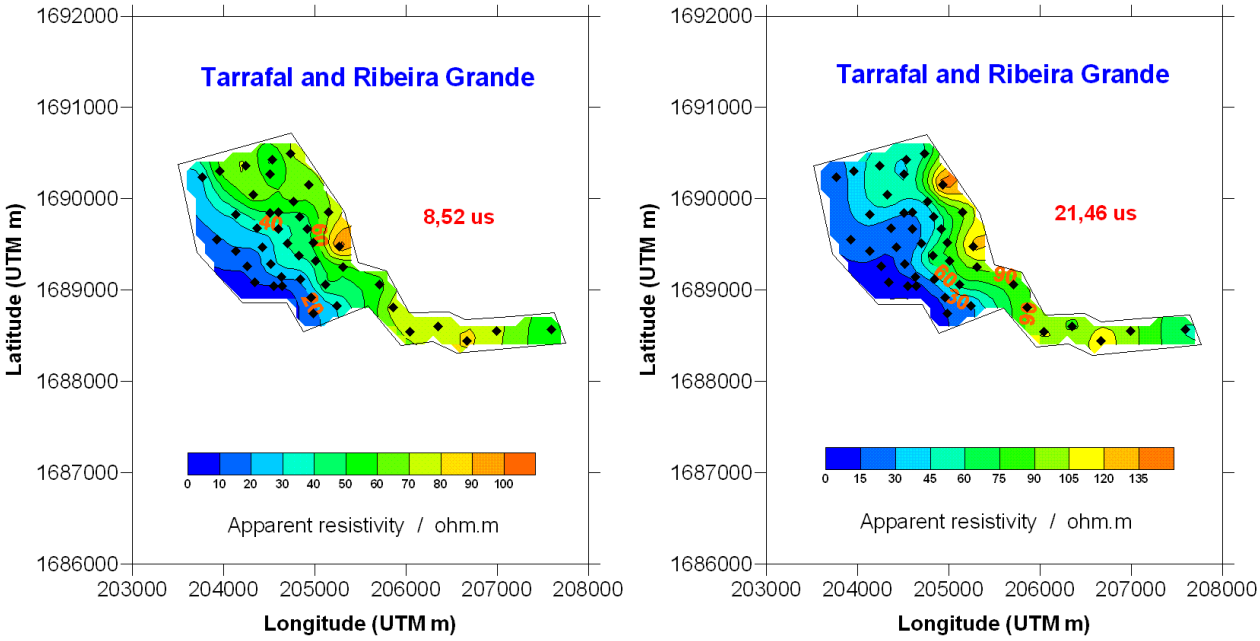

Figure 7.46 – Apparent resistivity map at Tarrafal (Cháo Bom) and Ribeira Grande; a) at 8.52 μs, b) at 21.46 μs.

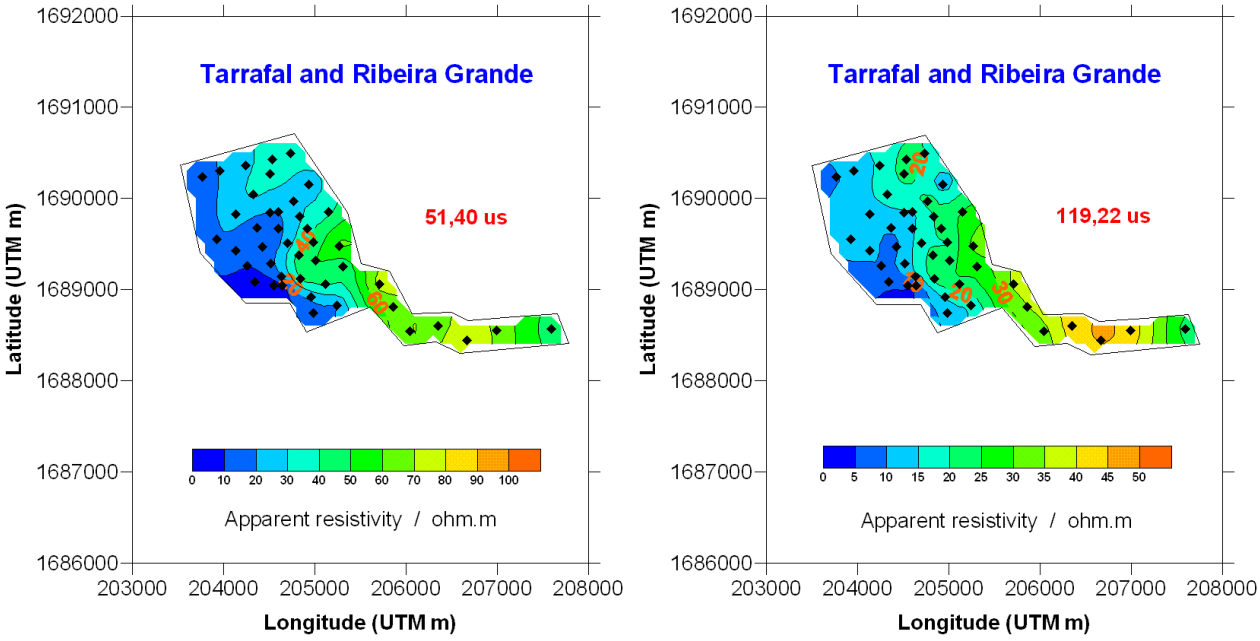

Figure 7.47 – Apparent resistivity map at Tarrafal (Cháo Bom) and Ribeira Grande; a) at 51.40 μs, b) at 119.22 μs.

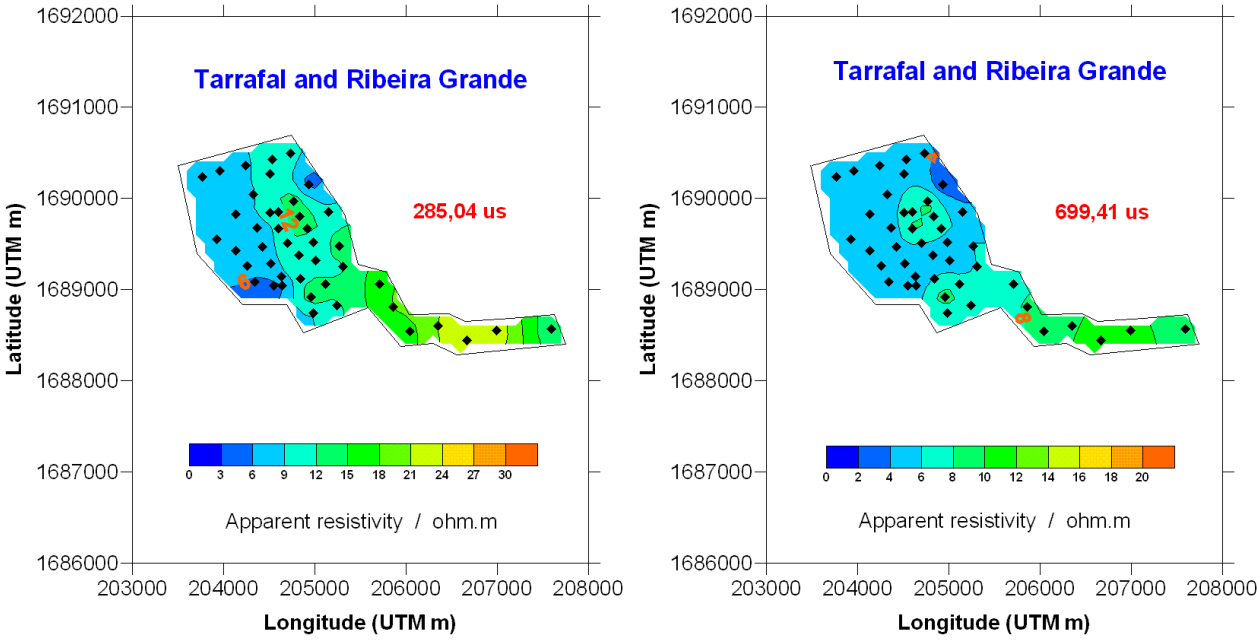

a) b)

Figure 7.48 – Apparent resistivity map at Tarrafal (Cháo Bom) and Ribeira Grande; a) at 285.04 μs, b) at 699.41 μs.

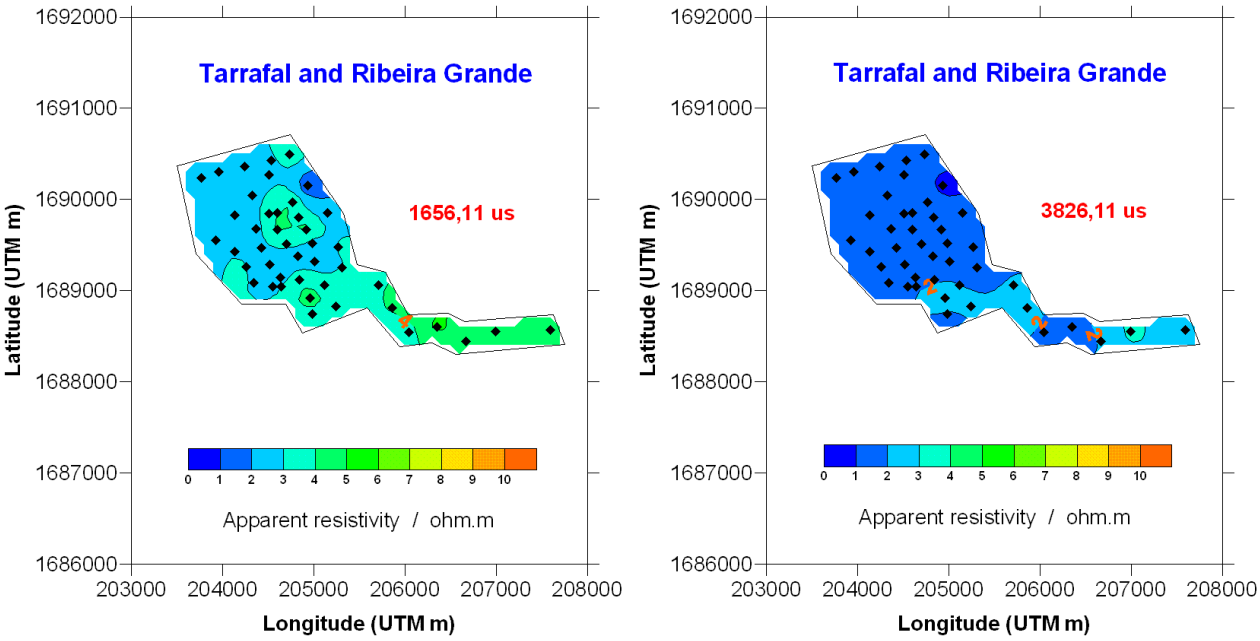

a) b)

Figure 7.49 – Apparent resistivity map at Tarrafal (Cháo Bom) and Ribeira Grande; a) at 1656.11 μs, b) at 3826.11 μs.

7.1.3.1 – 1D inversion of TEM data from Tarrafal and Ribeira Grande

Figure 7.50 shows the typical observed TEM curves at Chão Bom area (Tarrafal) and Ribeira Grande valley and their model response fitting. Measured noise was also in the 3 nVm^{-2} level but at some places unusual greater noise was registered. That's most probably caused by locally grounded metallic fences. A couple of soundings had shown a resonant signal, easily smoothed during the inversion process.

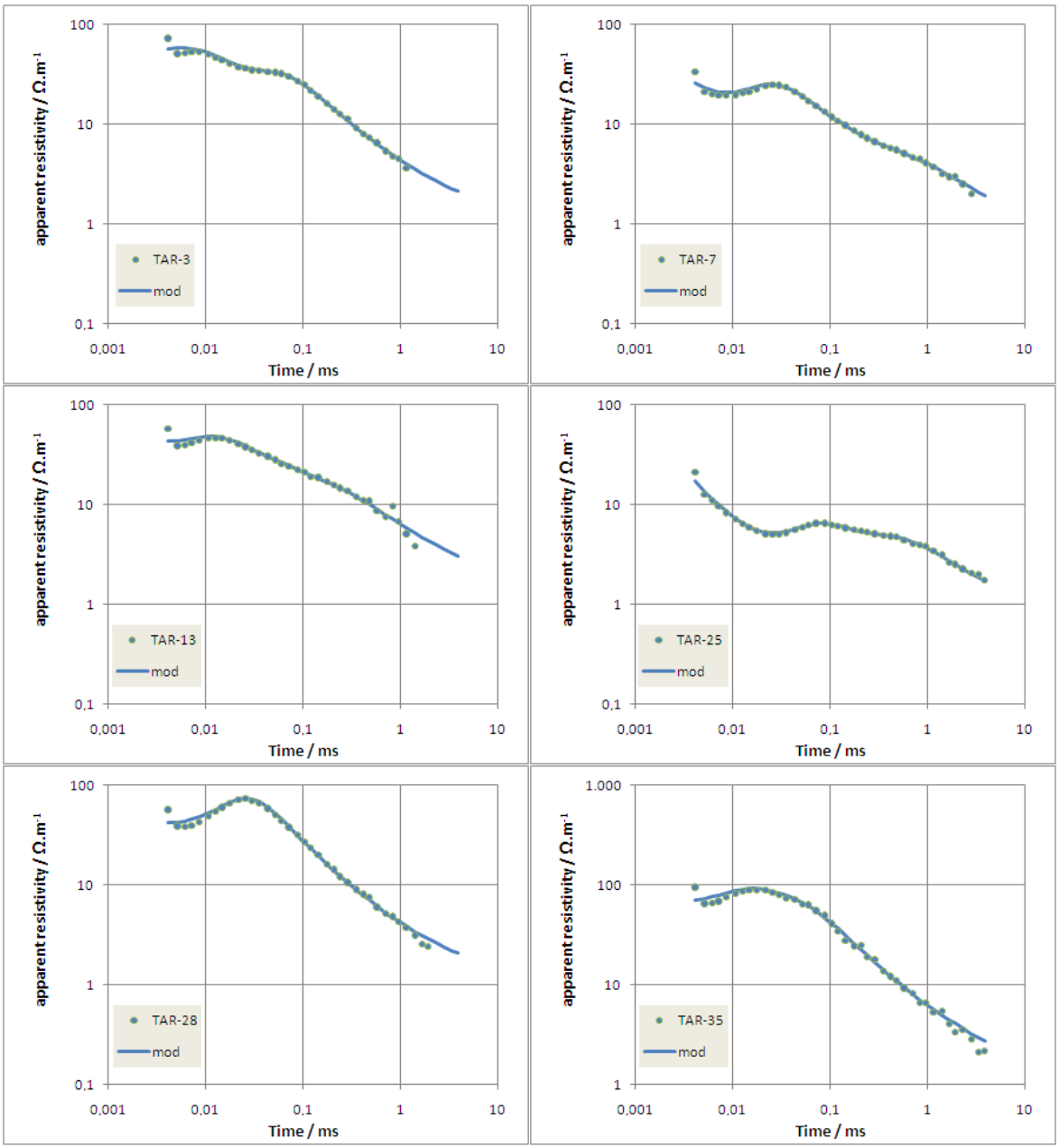

Figure 7.50 – Some Chão Bom and Ribeira Grande TEM curves and 1D mean model fit response.

Model's response misfits have a mean of 3 to 4%. Figure 7.51 shows the respective 1D mean model of the TEM soundings in figure 7.50. Most soundings exhibit high resistivity layers, with resistivity of 100 ohm.m or grater, from top to 20 to 30 m deep. Bellow this depth the bulk resistivity is clearly dominated by groundwater saturated layers. Measures at boreholes show that groundwater level is around 1 to 2 m above msl at 1 km inland (e.g.

SST-34 borehole) and near the sea level at the coastline (e.g. SST-32). The nearest sounding to borehole SST-34 is TEM 10 (figure 7.52). From the TEM model of this sounding it can be seen that the resistivity of 10 ohm.m corresponds to brackish and that deeper layer with 2.5 ohm.m resistivity corresponds to layers containing salty water. The measured groundwater resistivity was 4 ohm.m (1.3 mg.L^{-1} TDS) to less than 0.3 ohm.m.

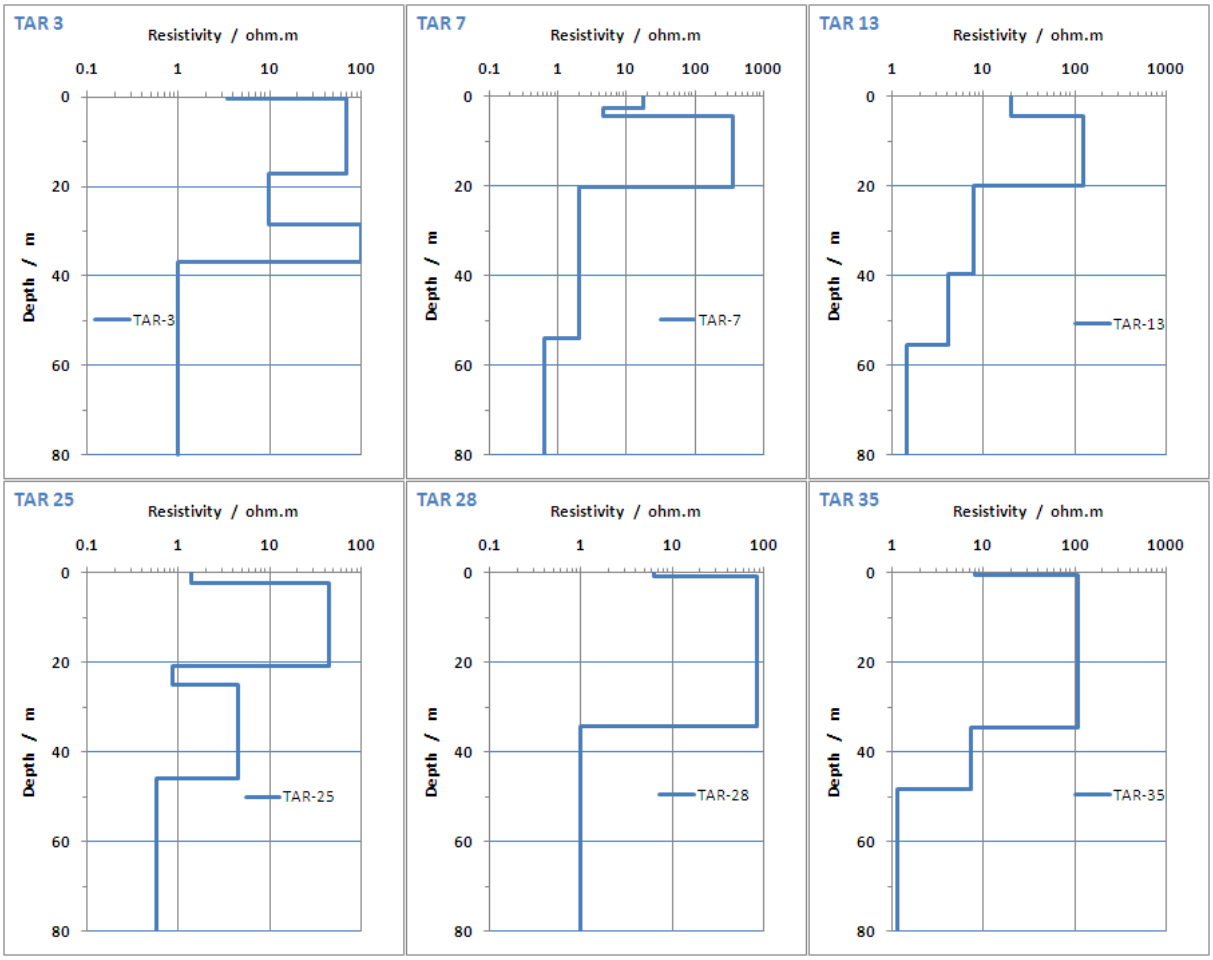

Figure 7.51 – Chão Bom and Ribeira Grande 1D TEM mean models, corresponding to figure 7.48 soundings.

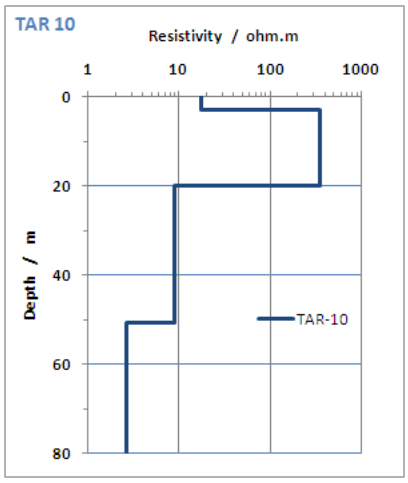

Figure 7.52 – Chão Bom TEM 10 sounding model, closet to SST-34 borehole.

The borehole lithology is represented below, in figure 7.53. As already mentioned most of the region is formed by fractured basalt, except in the southern area of Chão Bom plateaux, with some 20 m thick alluvium. Above the sea and at water saturated level, the majority of the measured and modelled high resistivity values (>100 ohm.m) correspond to unsaturated or dry fractured basalt and scoria layers with some clay inclusions. These high resistivity layer's values are usually the less determined model parameters (not well constrained) by the TEM method, with an ambiguity of 100 to 200% (e.g. Kafri and Goldman, 2005).

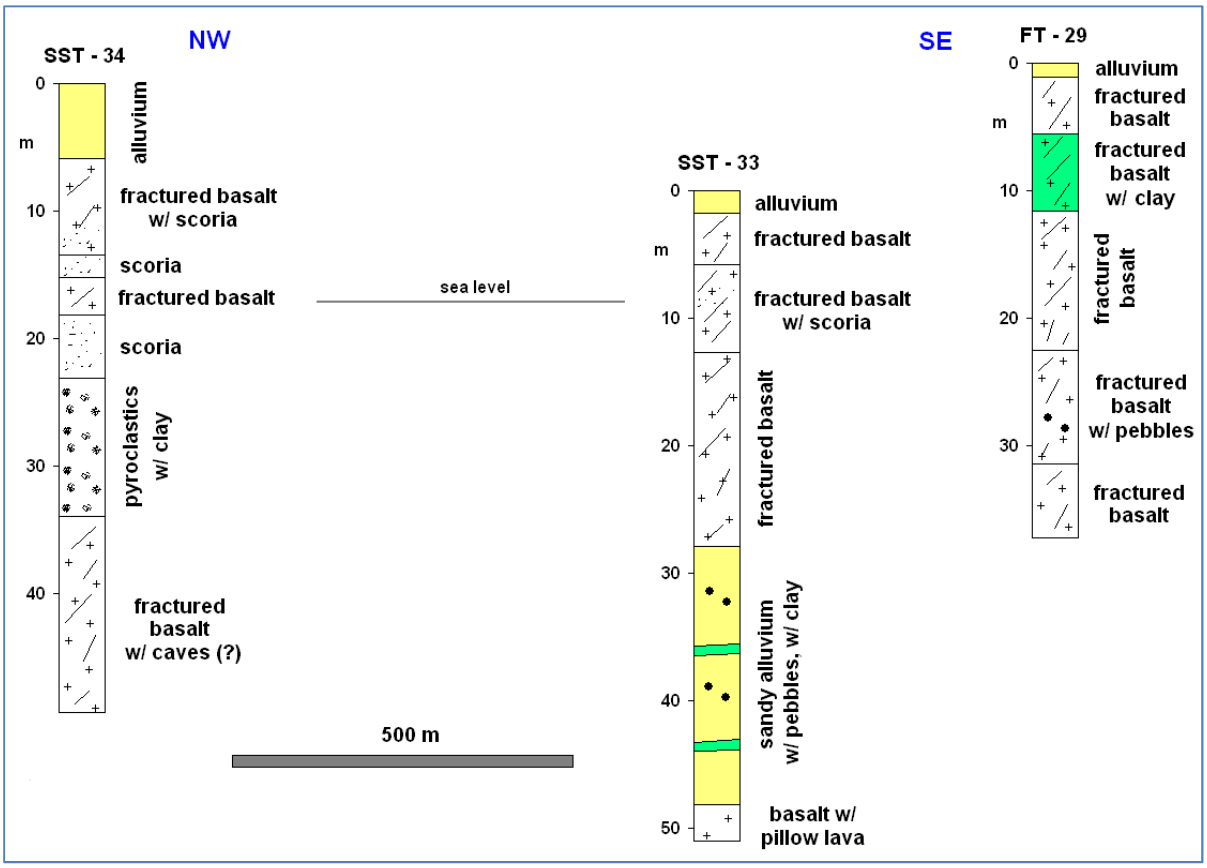

Figure 7.53 – Boreholes lithologic description at Chão Bom, (Dahlin *et al.* (1986), and INGRH data).

These high resistivity values confirm the results of a previous field study done at Chão Bom region by Dahlin *et al.* (1986). In the study (February 1986) VES resistivity measures (Schlumberger array), were done near the uncased (at that time) boreholes SST32, SST33 and SST34. Measures have been done in two perpendicular directions. Figure 7.54 shows those soundings curves as well their corresponding resistivity models, for each perpendicular direction.

The depth of the layers has been fixed by the borehole lithology data, as the two different direction's VES models show discrepancies between them (Dahlin *et al.*, 1986). These differences are due to the lateral effects originated by the inhomogeneous superficial geology, like blocks or stones, scattered throughout the area. In this (deep) conductive environment VES investigation is greatly shortened, and soundings are less effective to solve those deeper resistivity values.

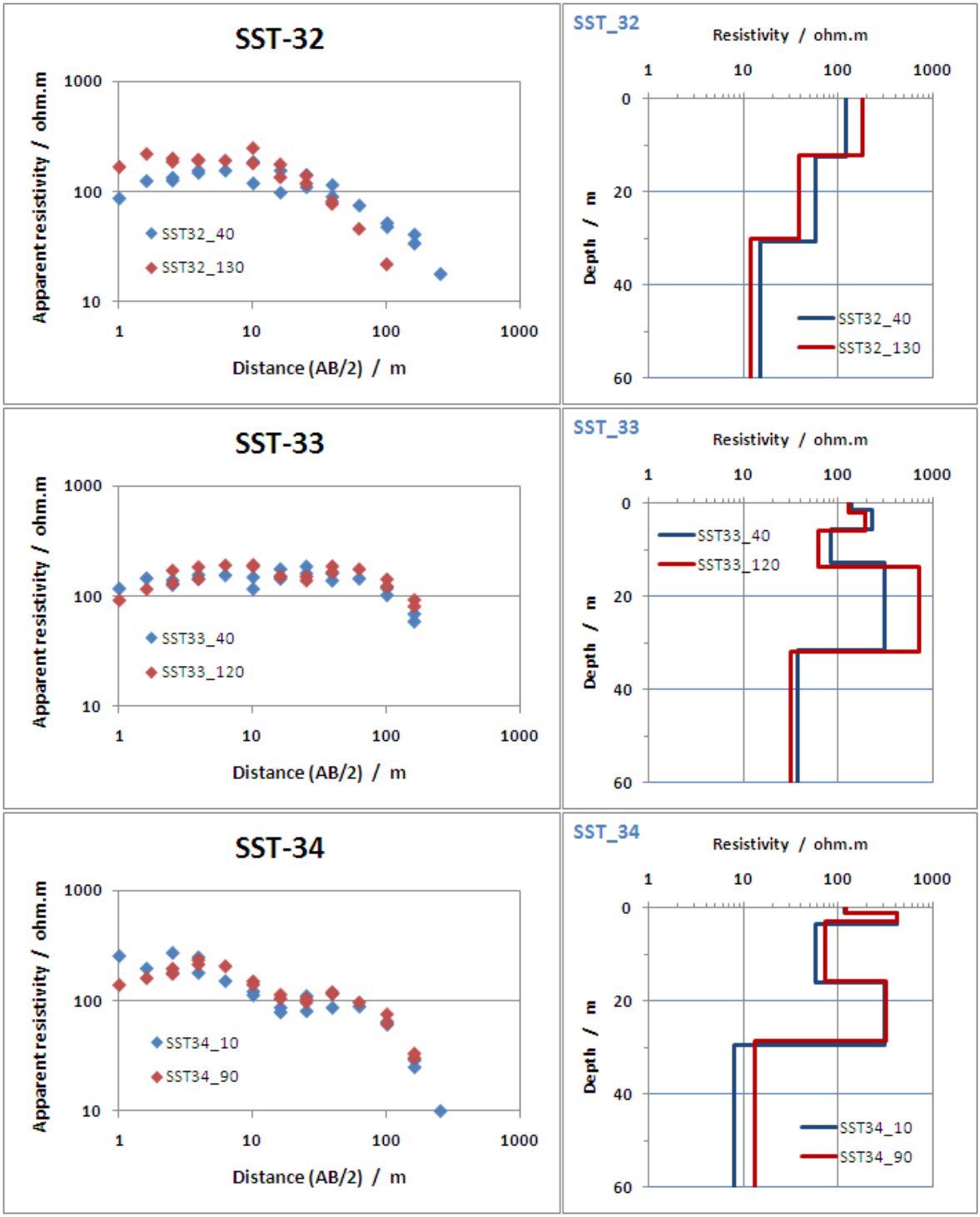

Figure 7.54 – VES data at Chão Bom (Tarrafal) and 1D resistivity models (from Dahlin *et al.* (1986)).

In these environmental conditions, where the uppermost layers are dry, it is expectable a worsen VES data quality. It's also noted a huge difference between the resistivity values assigned to the bottom layer in VES and TEM models. That is explained when a comparison between both data sets is done using Meju's scaling relationship (subchapter 4.3.1). Indeed, a considerable static shift exists as can be seen in figure 7.55, where the nearest TEM and VES soundings are compared. Although both data sets were acquired at different years and epochs, they have been done following the dry "rain season" condition of 1985 and 2005.

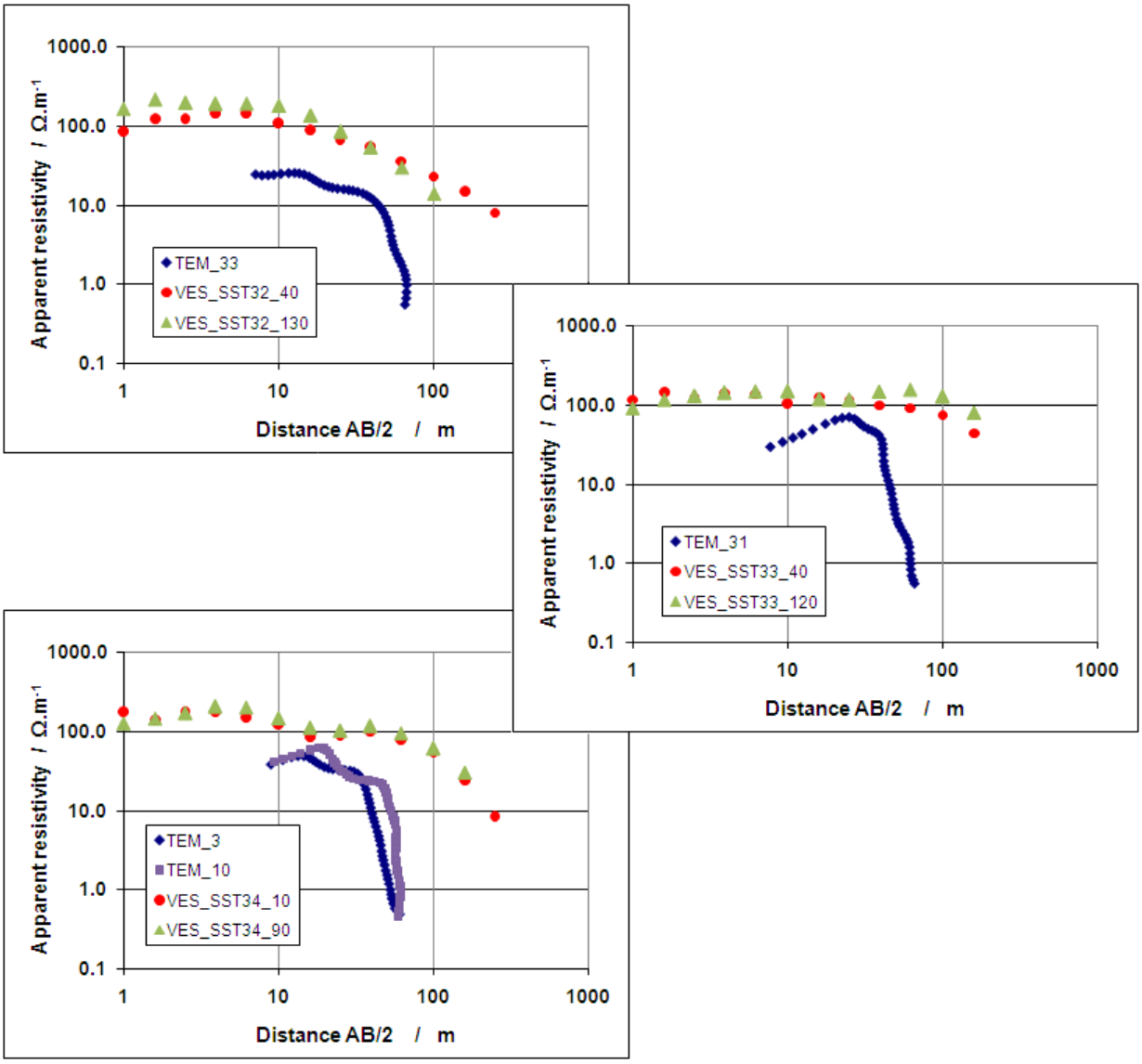

Figure 7.55 – Apparent resistivity VES (Dahlin *et al.*, 1986).and TEM scaled data points comparison at Chão Bom (Tarrafal).

Several resistivity cross sections were built using the 1D models calculated in the Chão Bom and Ribeira Grande valley. As previously, the same procedure was applied stitching together the 1D models, as can be seen in the next pages (figure 7.56 and 7.57). Resistivity cross sections are all plotted to the same resistivity colour scale. The profile location and direction are shown in figure 7.58.

The overall resistivity structure at Chão Bom starts with high values (100 to 200 ohm.m) and 20 m thick layer, matching dry basalts or quaternary alluvium. It is noted that the resistivity of this upper layer decreases towards the shoreline. The next layer, with resistivity range of 10 to 20 ohm.m is mainly associated to the brackish water. Beneath this, the resistivity drops to 1 to 2 ohm.m. This value is associated to salty water filling the pores/fractures of the rock (actual seawater or fossil water remains). As previously, the uniform horizontal continuity of resistivity layers from the first sounding towards the sea is just a graphical effect.

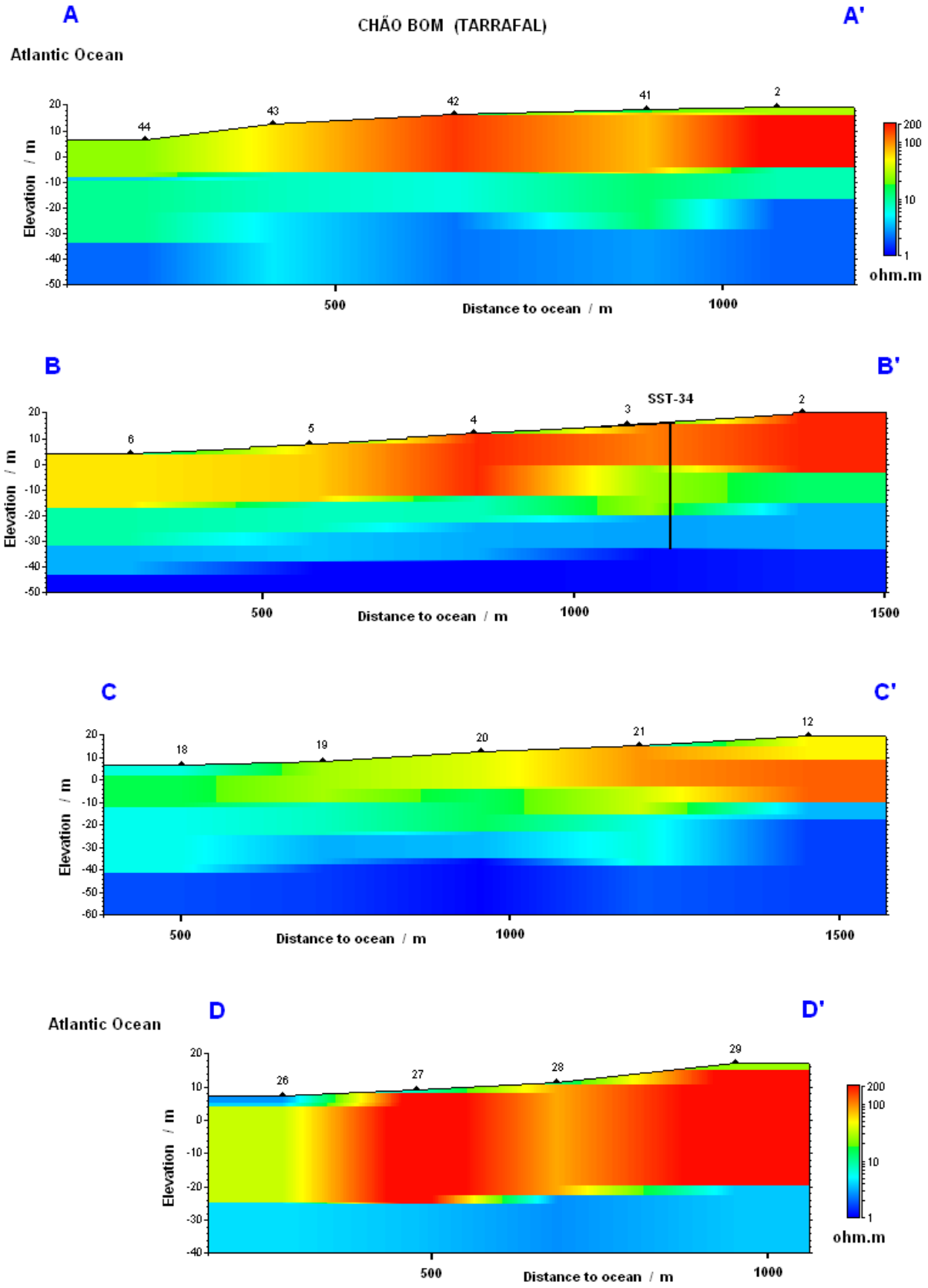

Figure 7.56 – Resistivity cross section at Chão Bom (perpendicular to the coastline), from 1D sounding models (top to bottom corresponds from north to south section).

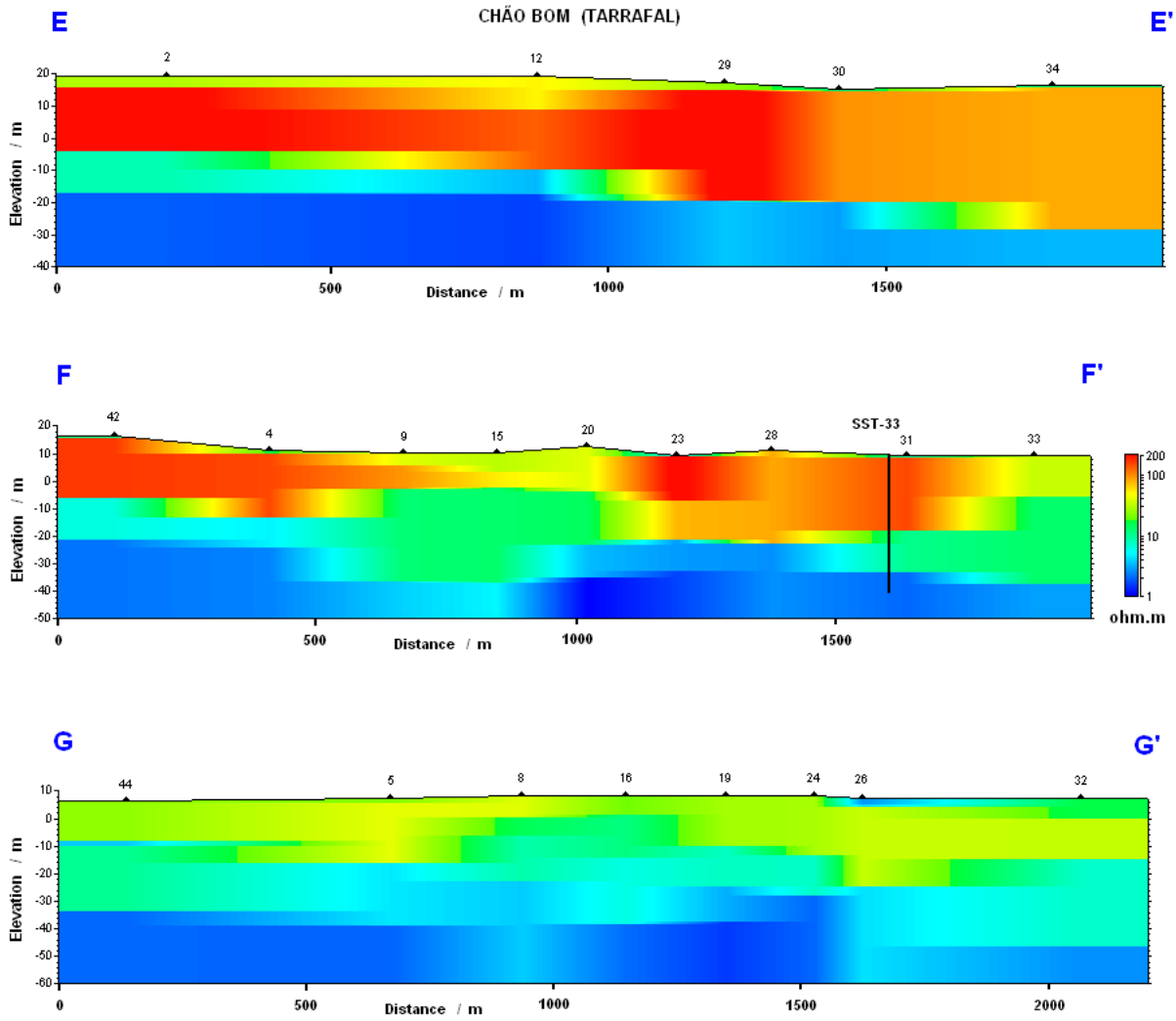

Figure 7.57 – Resistivity cross section at Chão Bom (parallel to the coastline), from 1D sounding models (top to bottom corresponds from inland to shoreline section).

There is a difference between the Chão Bom northern and southern areas. The superficial layer is thicker and resistive in the southern part decreasing its resistivity towards the coastline. The most relevant and odd structural aspect from data, is that the deeper conductive layer (1 to 2 ohm.m resistivity) absolute level seems to get shallow inland. Considering the measured groundwater level and under a steady-state water flux condition, the theoretical position of the Ghyben-Herzberg freshwater-seawater interface is about 42 m below the mean sea level at sites nearest to the coastline. As the groundwater level increases inland, that interface would be increasingly deeper.

Results from TEM soundings contradict this last assumption; they show that the conductive layer is roughly sub-horizontal and approaches the surface instead, as we go inland. Consecutively the low resistivity feature seems to be not linked to actual seawater intrusion but also to some high conductive lithologic layer. The same structure is detected upstream at Ribeira Grande valley cross section (figure 7.59). The thickness of this layer is difficult to quantify, because it is almost at the soundings' depth investigation limit. In theory, with the available field data, it could be two or three tens of meters and can overlay a more resistive

layer (≈ 10 ohm.m or more). The differences at the late time in the soundings curves would be very small and wrapped by the signal noise.

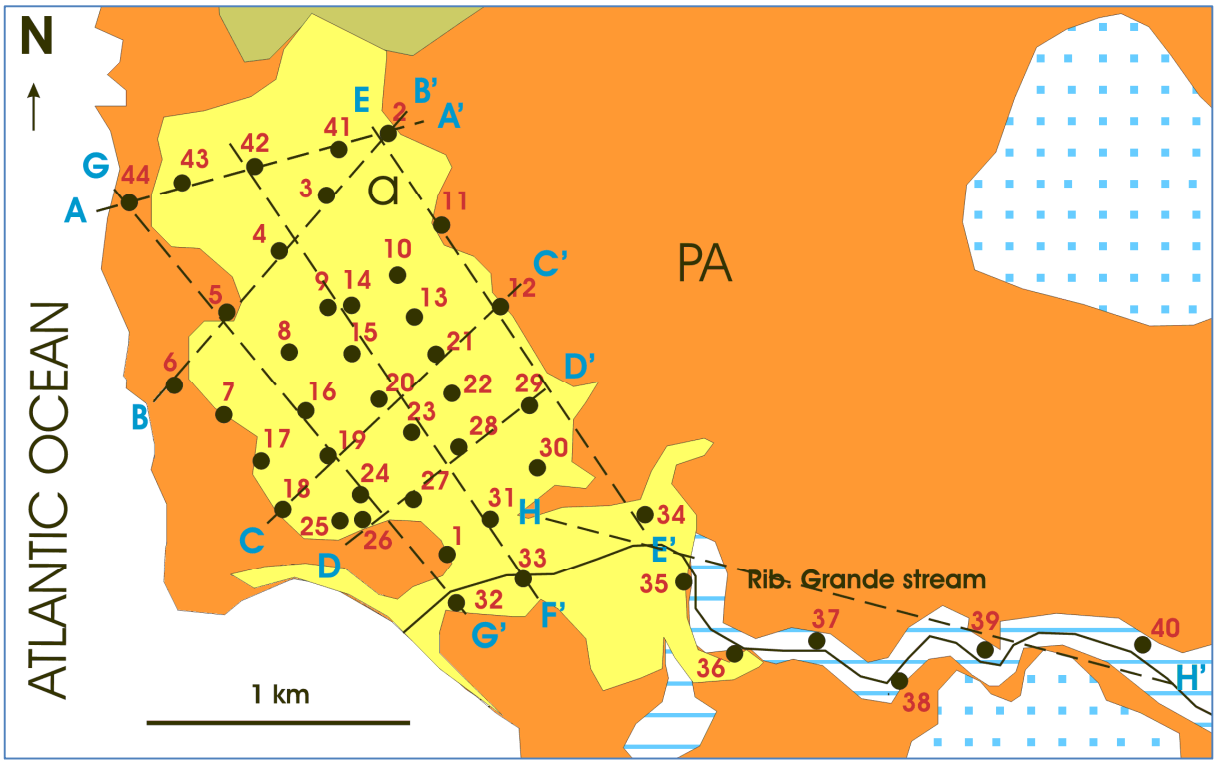

Figure 7.58 – Cross section location map at Tarrafal; Chão Bom plateaux and Ribeira Grande sream. The geologic map explanation is given at caption in figure 7.16 b).

7.1.3.2 – Chão Bom 3D data modelling

The soundings at Chão Bom have been also inverted using the spatially constrained algorithm, a quasi-3D approximation. TEM sounding's spatial locations are more or less uniform over the area. The overall mean distance between soundings was 205 m. Several modelling inversion tests had been carried out, changing the initial damping factor (λ), the different number of layer and different EDC values.

The following results were achieved with a maximum of 40 iterations, *rms* value of 0.02 and a starting homogeneous model with resistivity of 10 ohm.m and 16 layers (until 92 m deep). Figure 7.60 shows the final mean *rms* misfit variations with EDC parameter. The output for the first EDC value (45 m) is equivalent to a single sounding inversion (EDC set to zero). That's because there aren't soundings so close. With greater EDC values, models fit are slightly worsened because only a few soundings are included in the constraints. Beyond the mean inter sounding's distance much more soundings are taking into account and increasingly better model's fits outcome.

From this quasi-3D modelling a few 1D model results and corresponding soundings' data fits are presented below, in figures 7.61 and 7.62. The resulting models are similar to the 1D single inversion ones (figure 7.62). The mean global misfit between both sets around 8%.

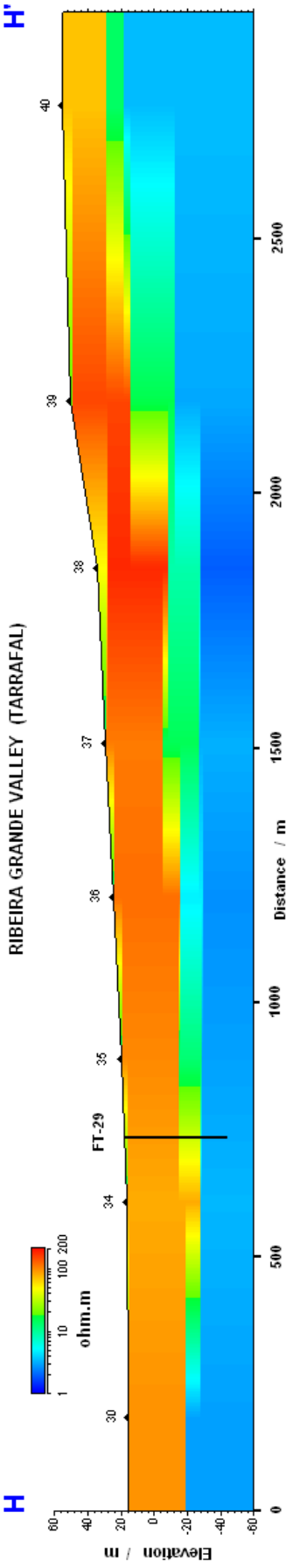

Figure 7.59 – Resistivity cross section at Ribeira Grande, from 1D sounding models.

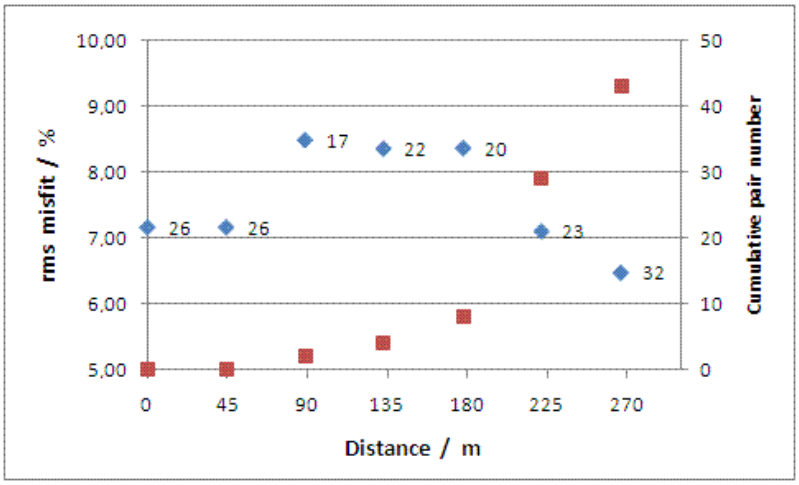

Figure 7.60 – Mean *rms* quasi-3D models misfit and iteration number (blue square), and cumulative sounding pair number (red square) for several constrained distances at Chão Bom (Tarrafal). Initial damping factor set to 0.5 and 16 layers with 10 ohm.m model space.

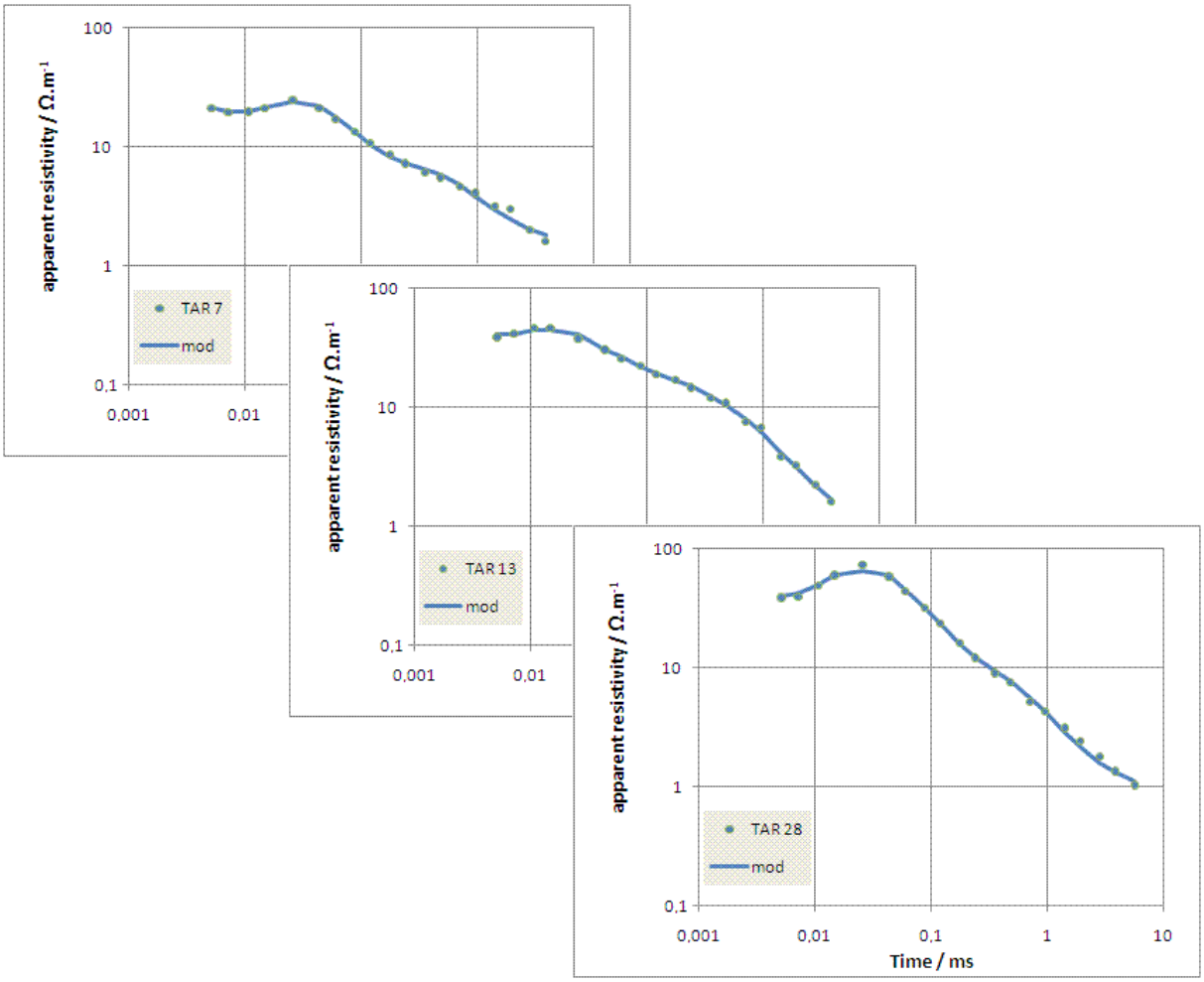

Figure 7.61 – Chão Bom TEM data points and 1D model fit response from quasi-3D inversion.

At Chão Bom, soundings are almost uniformly separated, and it is possible to draw representative resistivity maps for several depths (figure 7.62). In the 0 m slice, the lowest resistivities are found near the shoreline. In the -50 m deep the resistivity value is uniform, around 1 ohm.m. At -25 m deep, it seems to exist a difference. That is certainly related to a

changing in the lithology from north to south, at roughly the position limit between the two basins.

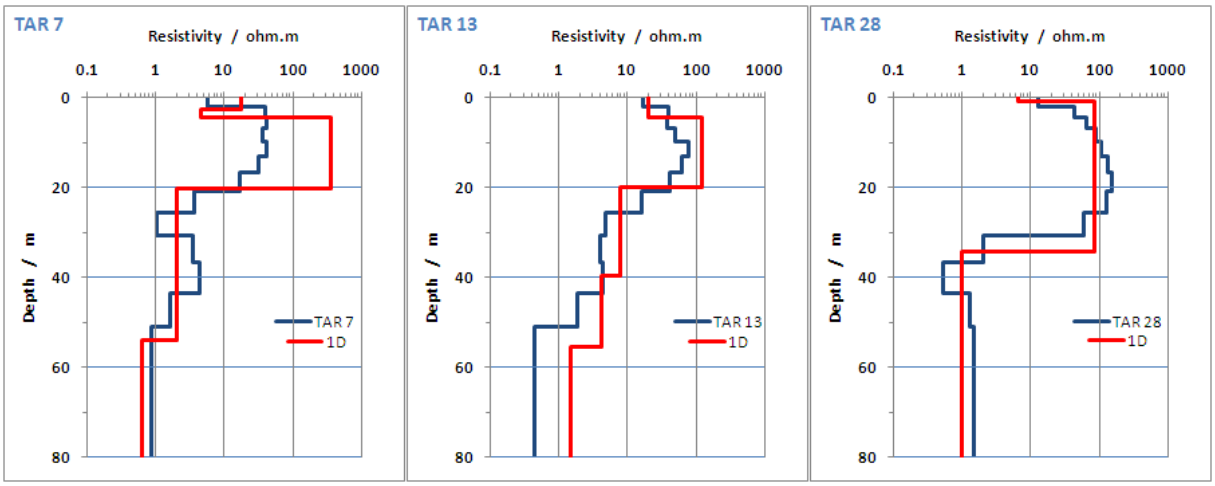

Figure 7.62 – Some Chão Bom (Tarrafal) TEM soundings 1D model from quasi-3D inversion (blue), and corresponding 1D mean models (red).

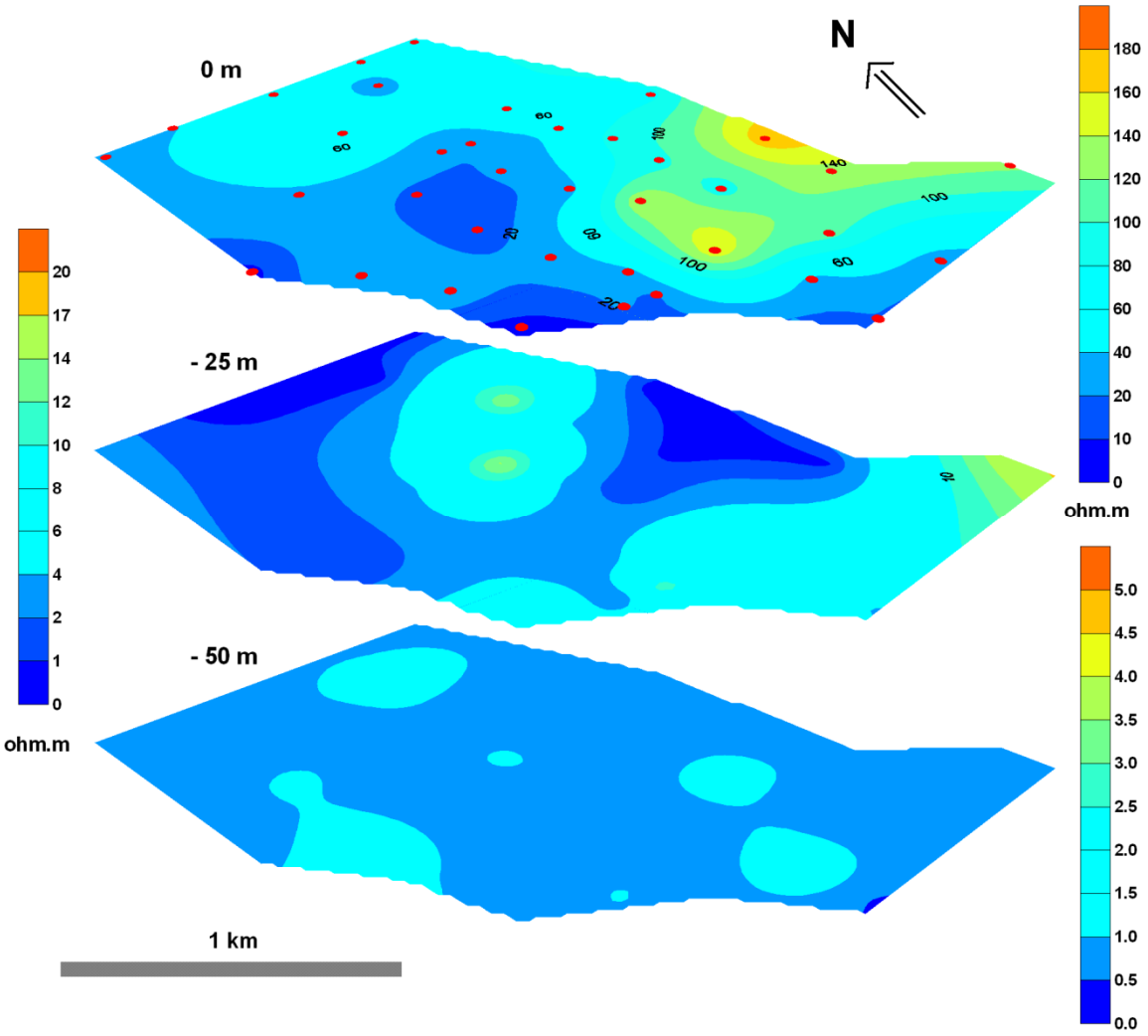

Figure 7.63 – Electric resistivity slices to three depth (below msl) from quasi-3D soundings inversion at Chão Bom (Tarrafal).

7.1.4 – Salto, Flamengos and S. Miguel data

Salto, Flamengos and S. Miguel valleys are located 10 km to the north of Seca and Picos ones, near Calheta de S. Miguel village (figure 7.1). Salto and S. Miguel valleys are very narrow near the sea, with 300 and 150 m wide, respectively. Near the shoreline, Salto valley is limited by a 70 m hillside at north with a slope of 20 to 30 degrees and a gentler slope and less high south hillside. Inland, the valley spans wide to some 1.5 km. The hydrographic catchment in Salto covers around 12.4 km^2. The S. Miguel valley is limited at both, north and south by 50 m hillside with slopes of 20 degrees. Inland, the valley spans from 500 m wide to 1.5 km wide. S. Miguel hydrographic catchment covers 14.4 km^2. The Flamengos valley has 300 m side to side at the coastline, but it is wider with 1000 m between hillsides going inland. Those hillsides can reach 100 m above the valley floor with a slope of 30 degrees. The hydrographic catchment covers 30.5 km^2. The three basins head starts are contiguous to the Serra da Malagueta mountain, one of the island regions with intense rainfall. Floods are frequent at these valleys in the course of the rainy season. All these valley creek beds are relatively flat and slowly increase the altitude with the upper creek course.

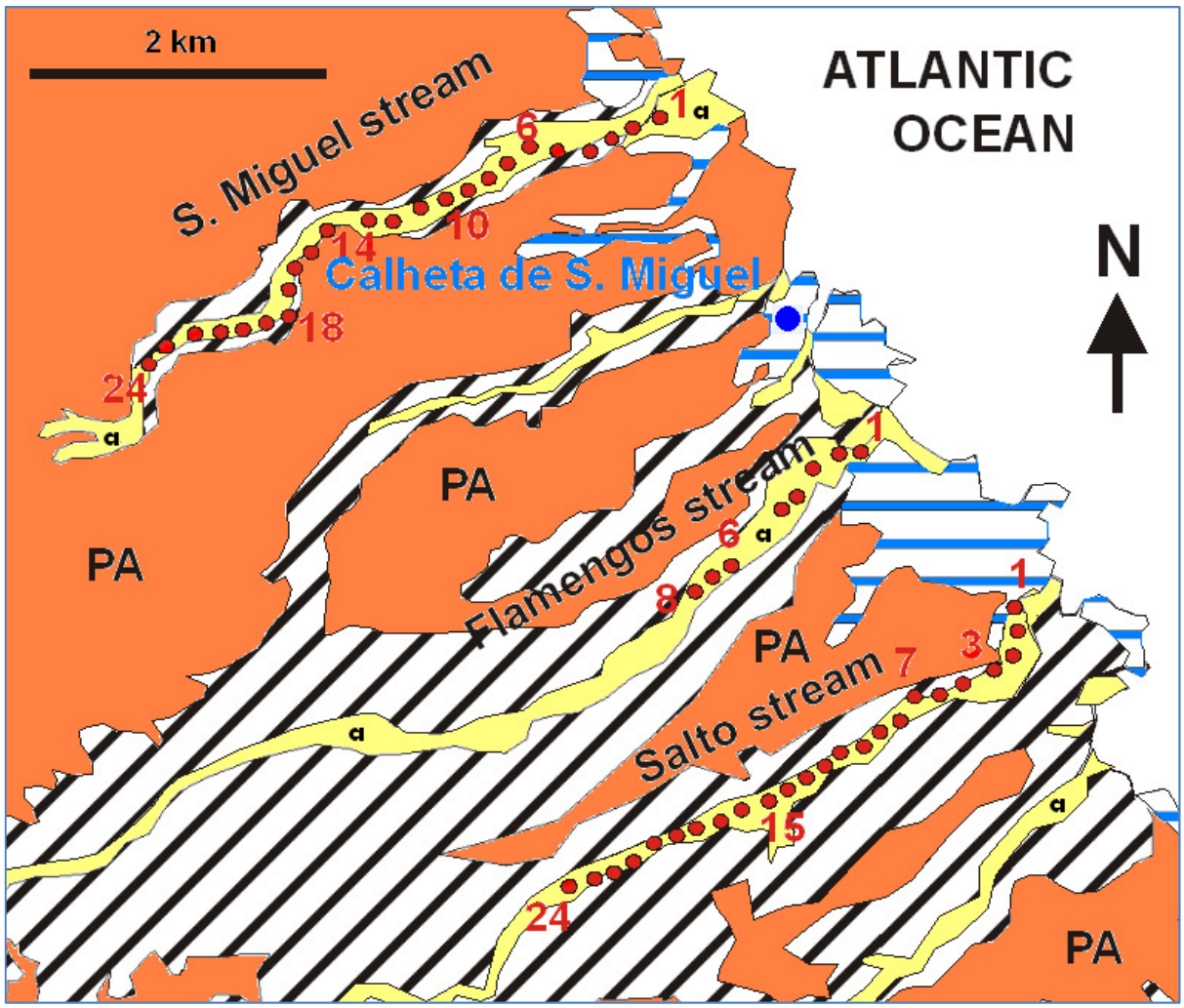

Figure 7.64 – TEM soundings number and location at Salto, Flamengos and S. Miguel valleys. Geologic map explanation is the same as given at caption in figure 7.16 b).

TEM soundings were acquired throughout the valley axis from the coastline, at roughly 6 m above msl, to 3500, 1600 and 3700 m inland, at 70, 20 and 100 m high, for Salto, Flamengos and S. Miguel, respectively. TEM sounding's locations, with the numbering order starting all from the coastline and increasing upper creek valleys, are shown in figure 7.64, over the regional geology map. Soundings are also plotted over a photographic image (Google image), with the locations of boreholes and wells where lithologic and chemical groundwater data do exist (figure 7.65).

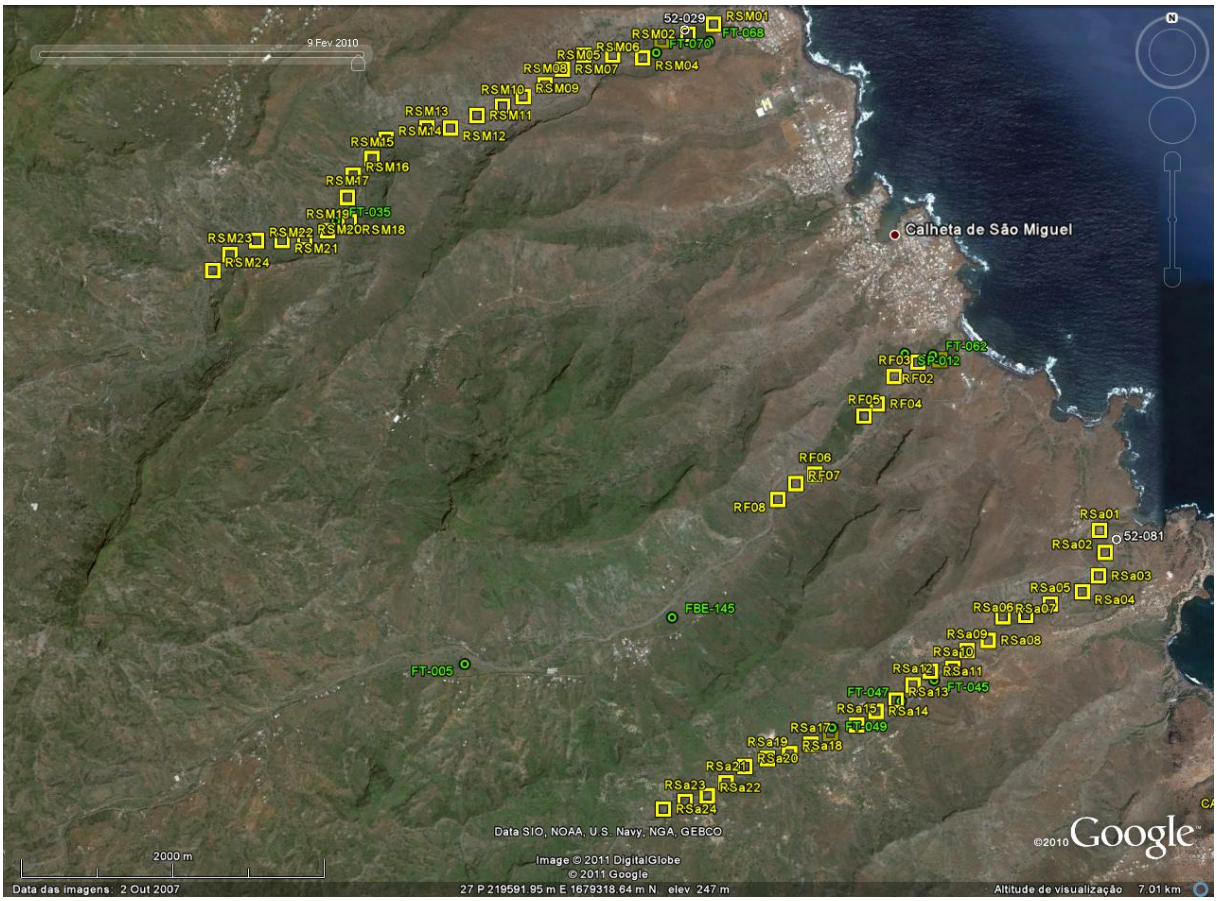

Figure 7.65 – TEM soundings, boreholes and wells location at Salto, Flamengos and S. Miguel valleys, (adapted from Google images).

Borehole logs data from these valleys indicate a somewhat different geologic setting, when compared with those previously described. The Quaternary alluvium formation is very shallow and thinner, except to the downstream locations, that is, near shoreline. Together with the common basalt structures (more or less fractured) there are also pillow lava and greenish tuff layers. The deepest drilled borehole goes to 35 m below the mean sea level, and no direct geologic knowledge exists beyond this depth.

Concerning the agriculture activities, they exist on those valleys but are restricted to the areas near the coastline at Salto and S. Miguel valleys. At Flamengos valley this agriculture practices extent further inland, to a couple of kilometres from the coastline.

In figures 7.66 a) to c) it is showed the typical Salto and S. Miguel valley landscape scenario and environment. The landscape at Flamengos valley is not too much different.

Figure 7.66 a) – Photography at Salto, near TEM sounding 5, facing southwest.

Figure 7.66 b) – Detailed photography of 0.5 m high flood debris in Salto, near TEM sounding 7.

Figure 7.66 c) – Photography at S. Miguel, near TEM sounding 4, facing south.

7.1.4.1 – 1D inversion of TEM data from Salto

TEM-FAST 48 soundings were acquired with a 25 m × 25 m single loop wire, with a maximum current input of 2.9 ampere and time channel set to 5. The observed noise was again at the same level of 3 nVm^{-2}. Signal noise was very small. The error bar in the last time data is of 1 to 2% level. No man-made sources of EM noise or metallic fences were present) to produce coupling effects. The fourth sounding was located near a running well. Sounding acquisition was done with this pump turned on and off, and no difference was detected in the TEM data signal strength and noise level. The corresponding measured TEM data field curves and also the 1D mean fit response, is shown bellow (figure 7.67), for six of the twenty four acquired soundings.

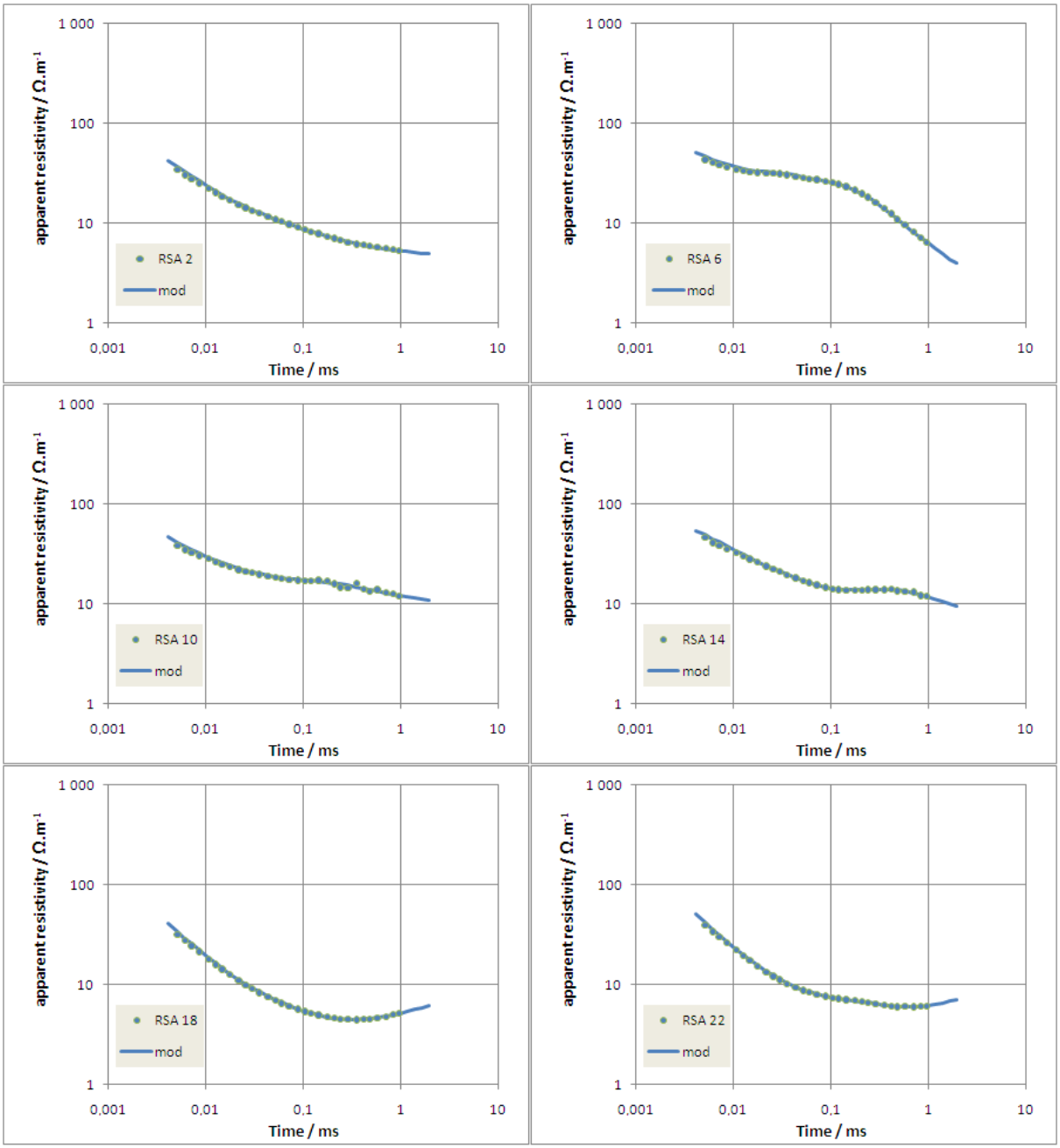

Figure 7.67 – Some Salto measured TEM curves and 1D mean model fit response.

Misfits have a mean 2 to 3%. Figure 7.68 shows the respective 1D mean model of the sounding in figure 7.67. The majority of the curves decrease smoothly to low apparent resistivity values of 7 to 10 ohm.m.

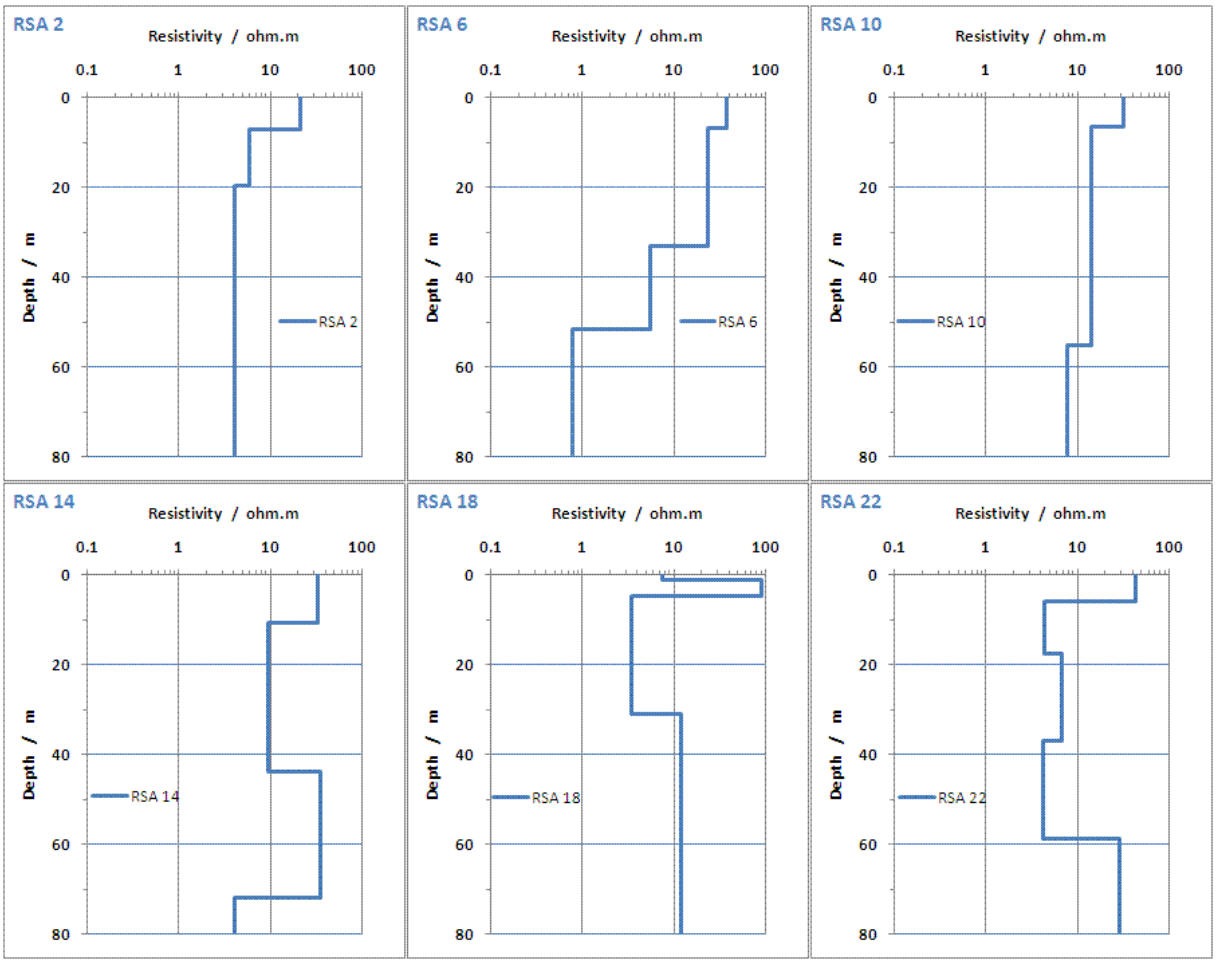

Figure 7.68 – Some Salto valley 1D TEM mean models, corresponding to figure 7.67 soundings.

The available lithologic logging information comes from three boreholes; FT 45, FT 47 and FT 49, located at mid profile, near TEM soundings 11, 13 and 16, respectively. Comparison between 1D models (figure 7.69) and the borehole lithology description (figure 7.70), shows a resistivity variation in 10 to 15 m depth, from higher to 10 ohm.m (TEM 11 and 13). This represents the groundwater level at the bottom of the superficial pillow lava layer (at unsaturated conditions). At these two soundings and bellow this position, only a deeper and less resistive layer (around 4 ohm.m) is detected, not having a correspondent geological changing in borehole description (FT 45 and TEM 11 are 100 m apart). At TEM 16 site, no pillow lava layers exist, instead we have greenish tuff, basalt and fractured basalt. Groundwater level coincides with the change in resistivity from lower to 6 ohm.m. The low resistivity values can be from altered tuff, probably with clay. Below this, at roughly 40 m depth, the resistivity increases probably due to the lithology change from tuff layer to basaltic and tuff layers.

The groundwater level measures give a mean hydraulic gradient of 0.012.

With all these 1D TEM models, a stitched cross section was built throughout the Salto valley. Figure 7.71 show the cross section, plus some groundwater resistivity values and levels, together with interpreted lithology.

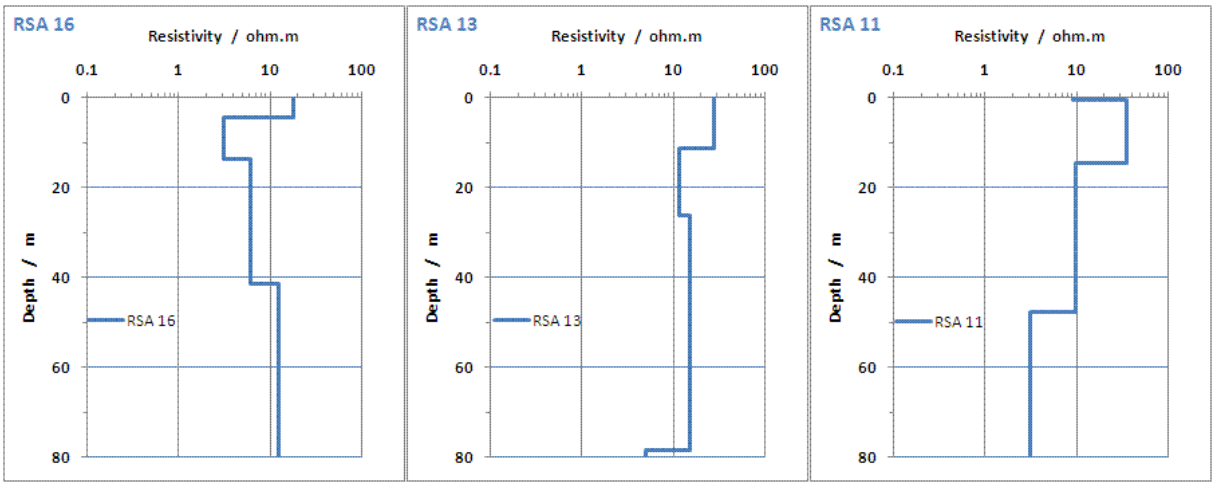

Figure 7.69 – Salto valley TEM 1D sounding mean models near the existing boreholes.

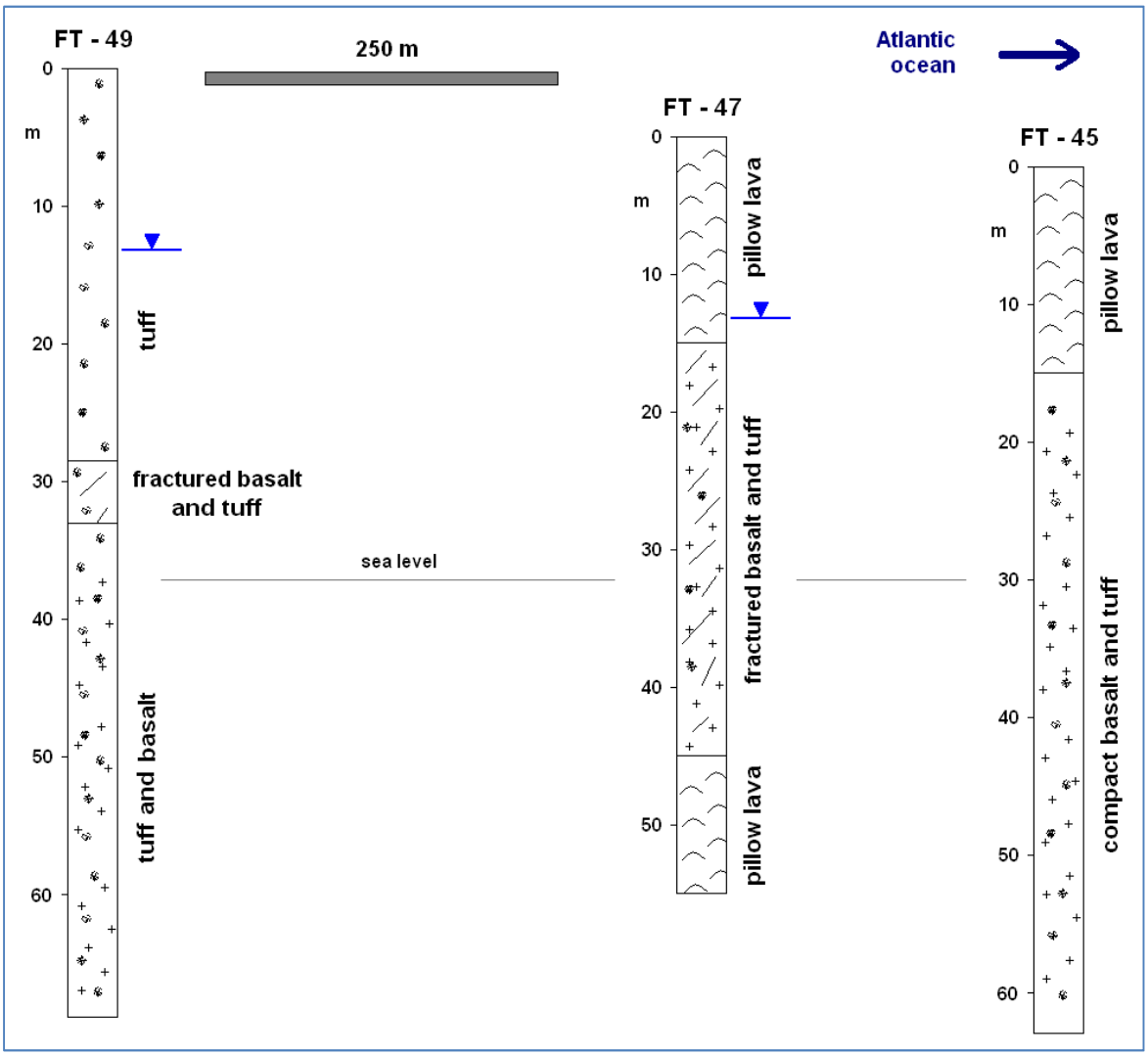

Figure 7.70 – Boreholes lithologic description at mid Salto valley (INGRH data).

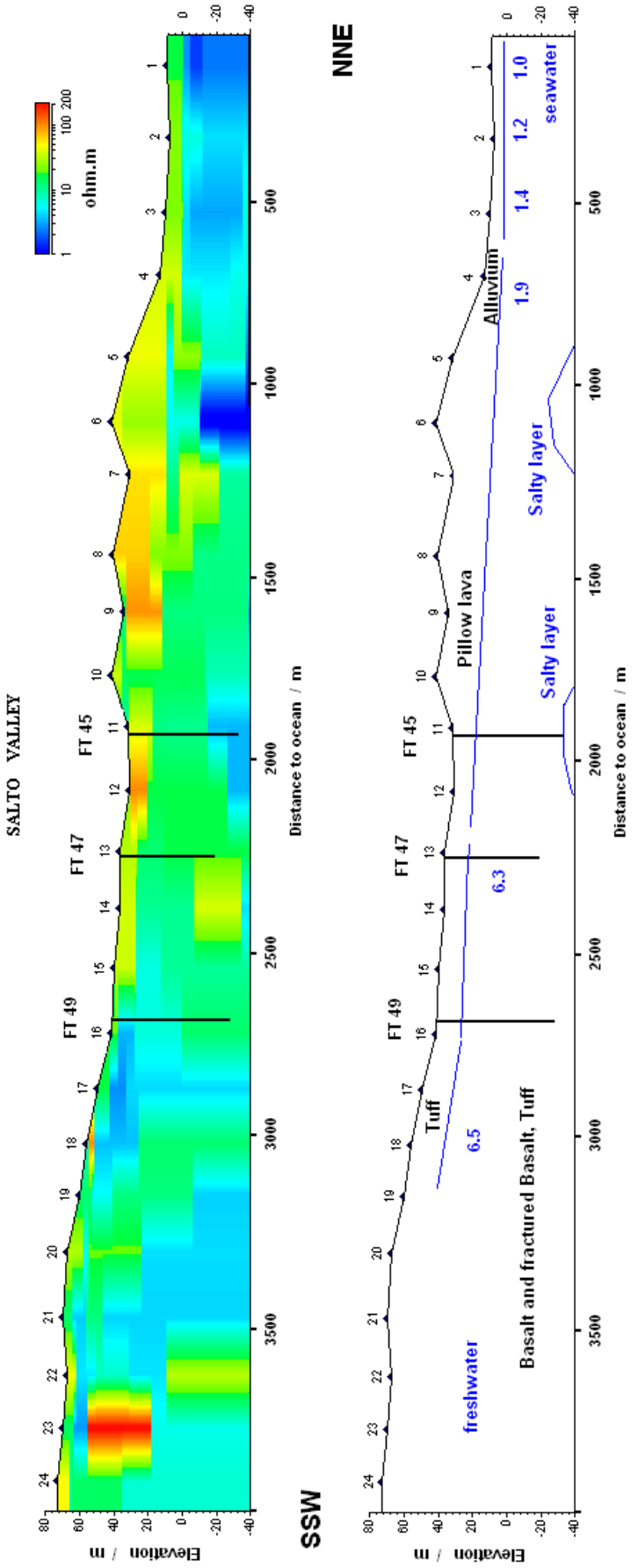

Figure 7.71 – Resistivity cross section at Salto valley, from 1D TEM sounding models, Groundwater level and resistivity (ohm.m) plus interpreted geology.

From the groundwater samples, a seawater influence is plausible, as lowest resistivity values are nearest to the ocean ones, increasing upstream. At middle profile, the shallow layers are more resistive (50 to 100 ohm.m), most certainly due to dry pillow lavas. At the end of the profile the resistivity is somewhat low (10 ohm.m). This might be due to the high porosity of tuff and fractured basalts.

7.1.4.2 – Salto 2D data inversion

TEM soundings at Salto valley were acquired on a straight line. In this conditions the spatially constrained algorithm methodology becomes a 1D inversion with laterally constrains (LCI). The overall mean distance between soundings was 155 m. The modelling inversion tests had been carried as previously, changing initial damping factor, the number of layers and different EDC values.

The maximum iteration was set to 60, and the *rms* value to 0.02. Initial model was always set to a homogeneous resistivity medium of 10 ohm.m, with 15 layers (until 80 m deep). Figure 7.72 displays the mean *rms* misfit to maximum iteration number and number of soundings in the EDC. Misfit error is high with no lateral models influence and drop with LCI influence to a mean value of 1.2%, with almost equal results and iteration. The number of soundings within EDC grows up almost linearly because soundings are evenly spaced. In this particular case, the number of pair of soundings pairs seem not to have too much influence in individual models.

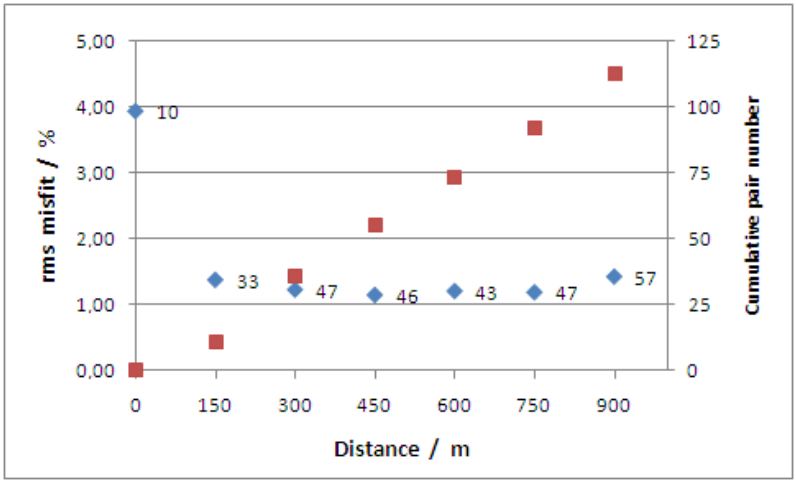

Figure 7.72 – Mean *rms* quasi-2D models misfit and iteration number (blue square), and cumulative sounding pair number (red square) for several constrained distances at Salto valley. Initial damping factor set to 1.0 and 15 layers with 10 ohm.m model space.

Some of the 1D models and corresponding soundings' data fits are shown on next page, in figures 7.73 and 7.74, (mid-range EDC value of 450 m). Models are very similar to those from 1D inversion in spite of some scatter around uniform values due to the multi layer quasi-2D method and prevailing data errors. The same multi layer method approach prevents also the sharp resistivity contrasts typical from 1D models. The mean differences between both model sets are globally smaller than 5%. The overall resulting structure presented in figure

7.75 is similar to previous one by stitched 1D models (figure 7.71). This figure shows plotting limitations by unevenly data spatial location. The mean resistivity values at aquifer depth range from 5 to 20 ohm.m, like previously given by 1D models.

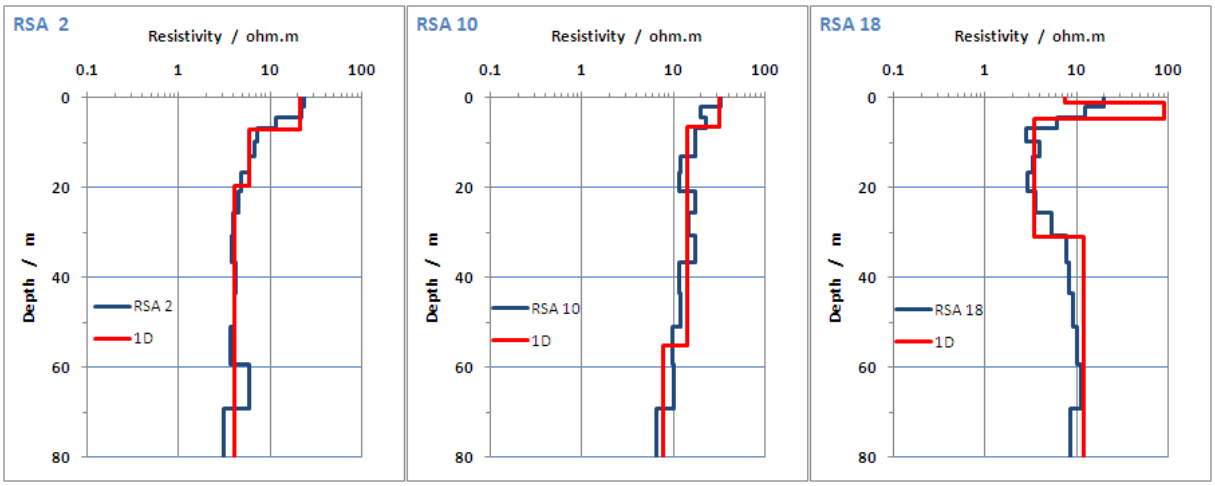

Figure 7.73 – Some Salto valley TEM soundings 1D model from quasi-2D inversion (blue), and corresponding 1D mean models (red).

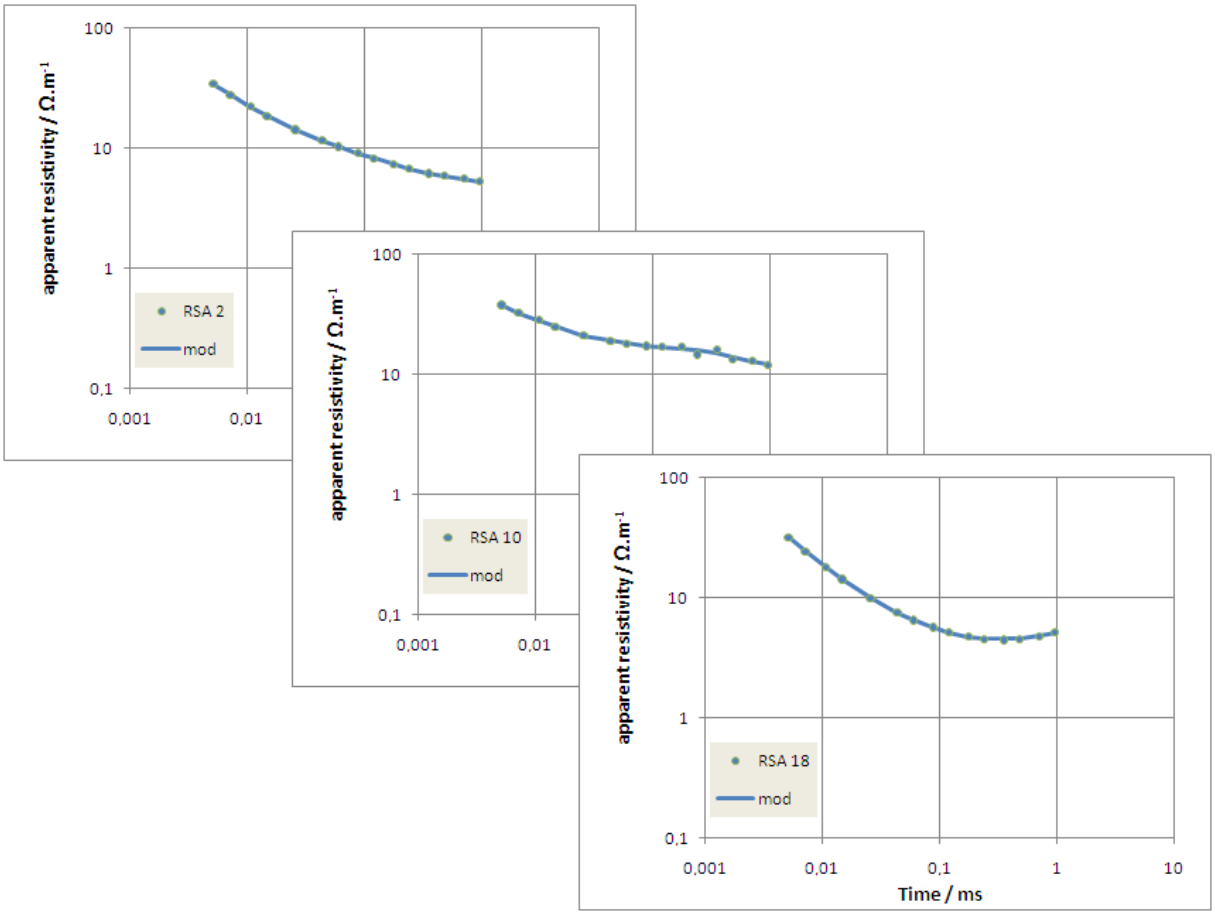

Figure 7.74 – Salto valley TEM data points and 1D model fit response from quasi-2D inversion, (corresponding to figure 7.73 models).

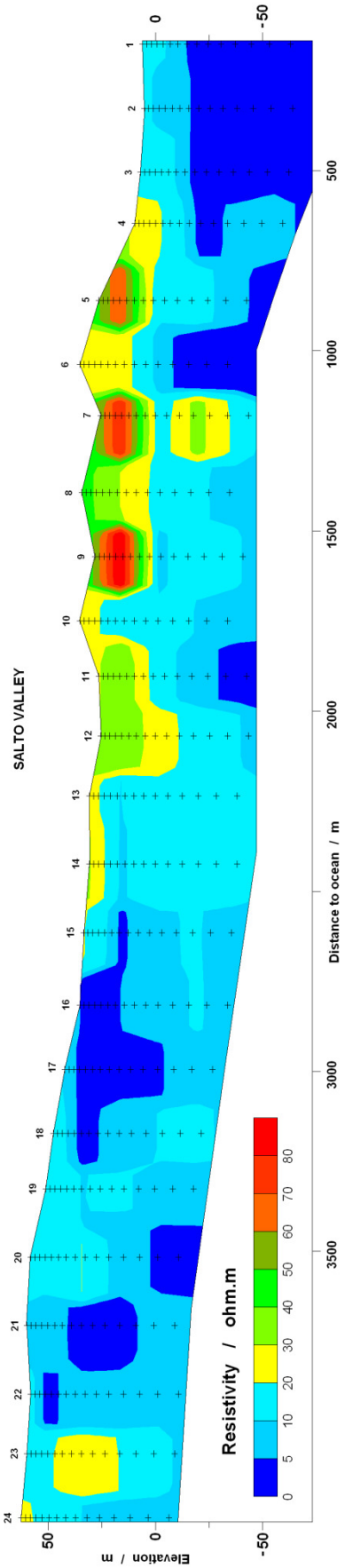

Figure 7.75 – 2D resistivity cross section from quasi-2D models, at Salto valley.

7.1.4.3 – 1D inversion of TEM data from Flamengos

TEM-FAST 48 soundings were acquired with a 25 m × 25 m single loop wire, with a current input of 1.0 ampere and time channel set to 5. The observed noise was also very small at the level of 3 nVm^{-2}. Signal noise was very small with a bar error of the 1 to 2% level. No man-made source of EM noise was present or metallic fences to produce coupling effects. The corresponding measured TEM data field curves and also its 1D mean responses, are shown bellow (figure 7.76), for six of the eight acquired soundings.

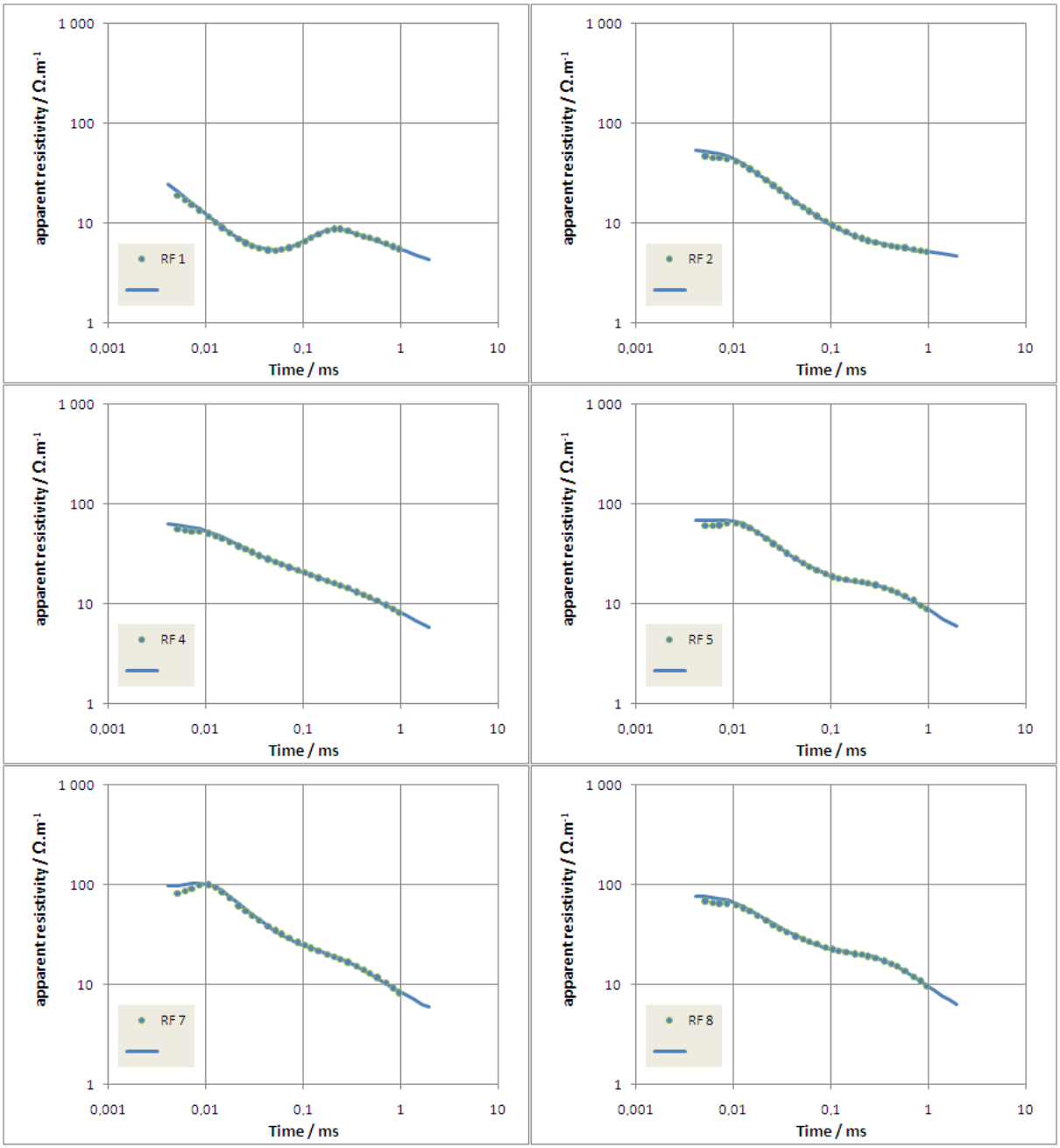

Figure 7.76 – Some Flamengos measured TEM curves and 1D mean model fit response

Model response misfits are of 2%. Figure 7.77 shows the respective 1D mean models of the soundings shown in figure 7.76. The majority of the curves decrease smoothly to low apparent resistivity values of around 5 to 6 ohm.m.

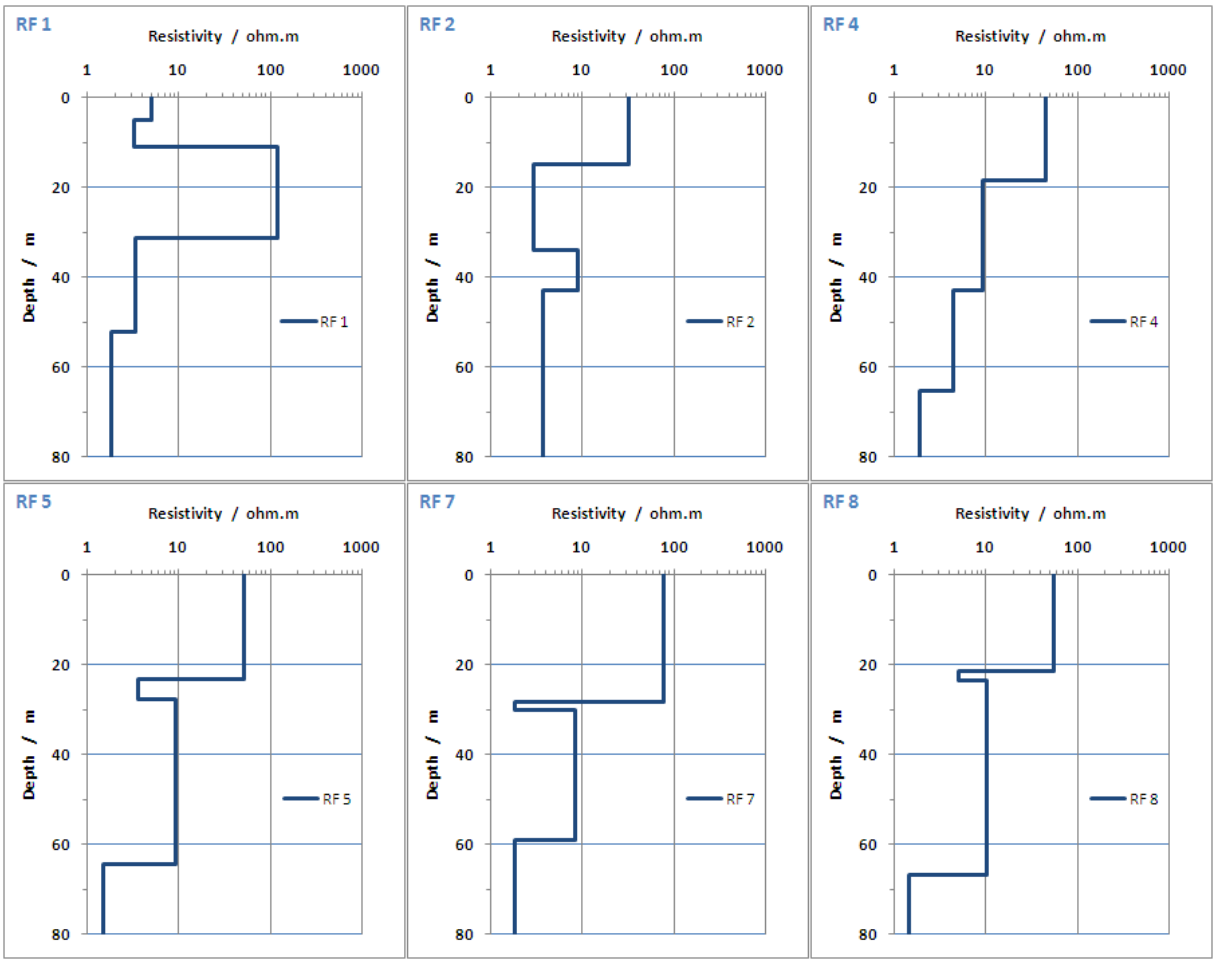

Figure 7.77 – Some Flamengos valley 1D TEM mean models, corresponding to figure 7.76 soundings.

The available lithologic logging description comes from a borehole far from the TEM profile (figure 7.78). The FT 5 borehole is located 4 km inland. Fractured basalt followed by more compact basalt with some tuff layers are the mean matrix. At mid valley and near the shoreline, a few meters thin alluvium layer exist.

Most of the soundings exhibit a resistivity change at about 20 m depth from a higher value to near 10 ohm.m, approximately at the aquifer know depth. A thin conductive layer is also detected in most of the inland soundings, most certainly of clay origin. This layer can act as an impermeable horizontal barrier, if extended laterally and thus confining the aquifer locally. Below the 10 ohm.m aquifer layer, a deeper and less resistive layer takes place. As the measured groundwater level is some 5 m to 10 m below the surface at the start and end TEM profile (corresponding to a 0.014 hydraulic gradient), respectively, those layer's interfaces cannot be linked to groundwater table and to deep fresh-seawater interface. With the given settings and considering a steady-state flux condition, the fresh-seawater interface should be deeper. The bottom conductive layer must be formed then by ancient salty layer deposits.

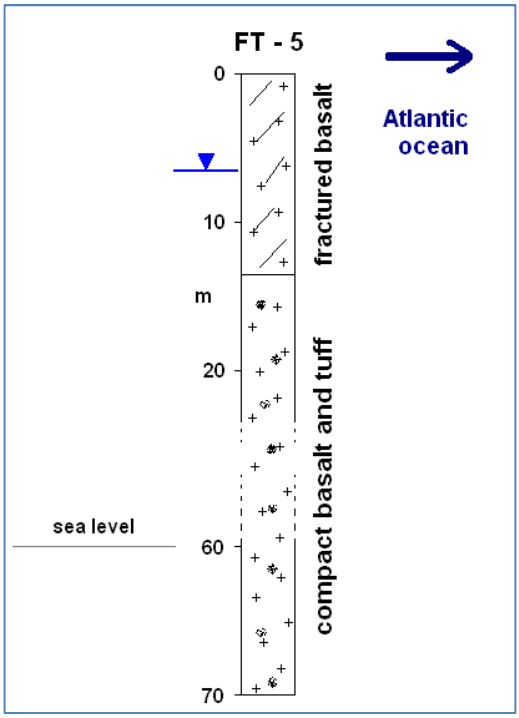

Figure 7.78 – Borehole lithologic description at Flamengos valley (INGRH data).

With the calculated 1D TEM a stitched cross section was assembled throughout the Flamengos valley. Figure 7.79, bellow, shows the cross section as also the groundwater resistivity and level below the surface, from wells and boreholes positions.

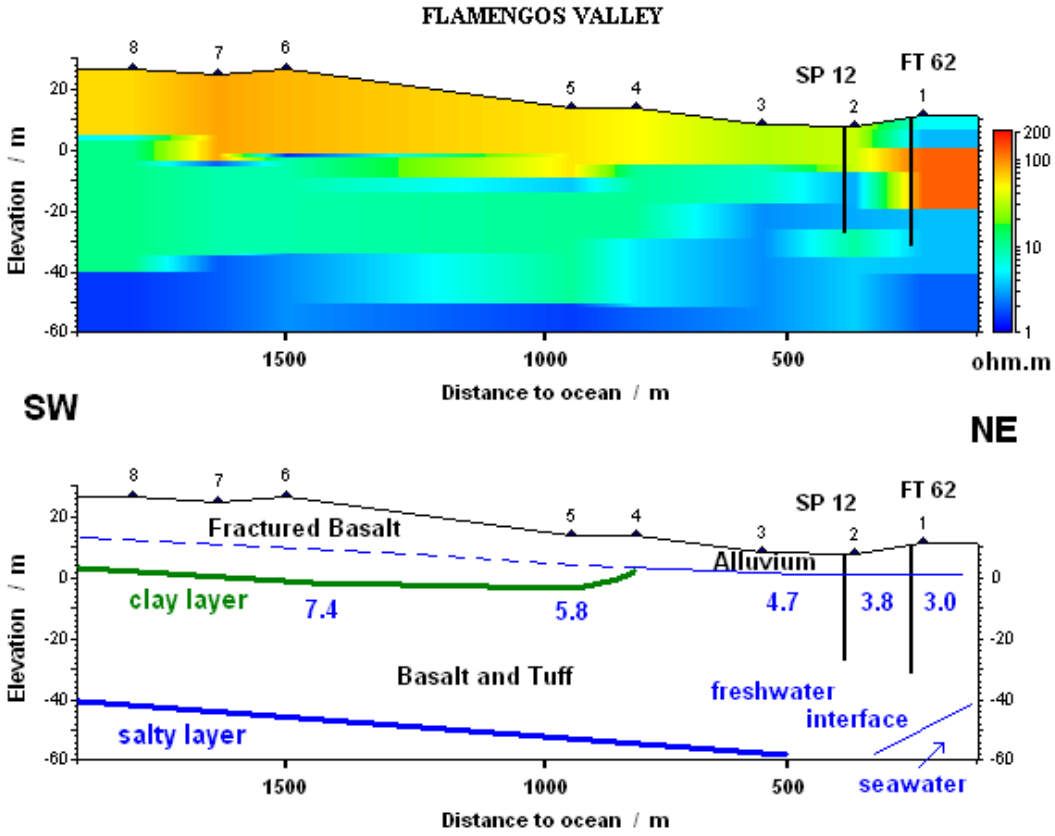

Figure 7.79 – Resistivity cross section at Flamengos valley, from 1D TEM soundings. Groundwater level and resistivity (ohm.m) plus interpreted geology.

7.1.4.4 – Flamengos 2D data inversion

At Flamengos valley, the TEM soundings have been taken almost over a straight line with a mean distance of 200 m between them, but not exactly at uniform spacing. The inversion of the all data set by the spatially constrained algorithm methodology becomes a 1D inversion with laterally constrains (LCI). The inversion tests were carried out as previously, changing initial damping factor, different number of layers and lately different EDC values.

The maximum number of iterations was set to 40 and the *rms* value to 0.02. Initial model was set with resistive top layers (30 ohm.m) over a 10 ohm.m medium. The number of layers was 11 (until 80 m deep) with an incremental step of $2e^{0,17(n-1)}$. Like previously, data points were decimated (15 at each sounding). Figure 7.80 displays the mean *rms* misfit to the maximum number of iterations and pairs of soundings in EDC. The mean misfit value is around 3.5%, almost independent of EDC. Exception happens when no EDC influence exists, and the convergence stops after only 6 steps.

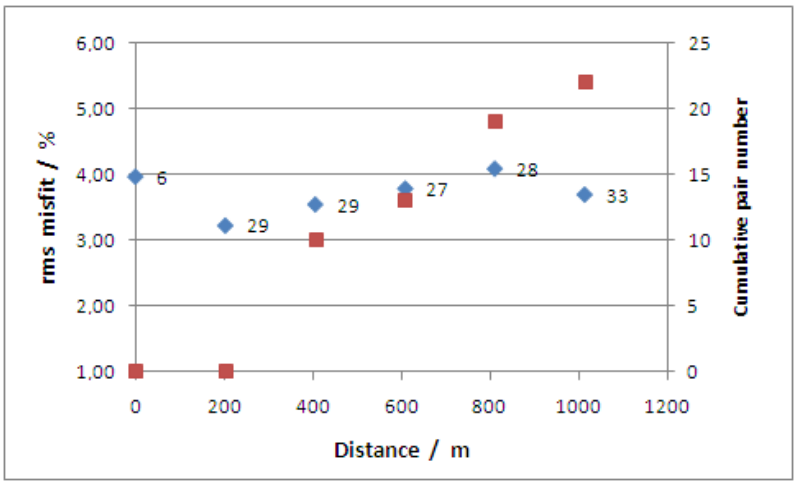

Figure 7.80 – Mean *rms* quasi-2D models misfit and iteration number (blue square), and cumulative sounding pair number (red square) for several constrained distances at Flamengos valley. Initial damping factor set to 1.0 and 11 layers with 30 to 10 ohm.m model space.

Some of the 1D models from the quasi-2D inversion and corresponding data fit are shown on the next page, in figures 7.81 and 7.82. Models' outputs are similar to those obtained from individual 1D inversion in spite of some differences mostly related to layers fixed geometry and equivalent responses. The mean differences between both modelled sets are globally around 8%. The overall resulting structure presented in figure 7.83 is similar to previous one by stitched 1D models (figure 7.79), with plotting limitations by unevenly data spatial location at mid profile. The mean resistivities values in the aquifer depth range from 10 to 20 ohm.m, likewise, the former 1D model results. Higher superficial resistivities appear inland at the end of the profile. Near the coastline, it seems to be detected a superficial and a deeper seawater influence. At 40 m depth, below mean sea level a conductive layer is also detected, as seen in other valleys.

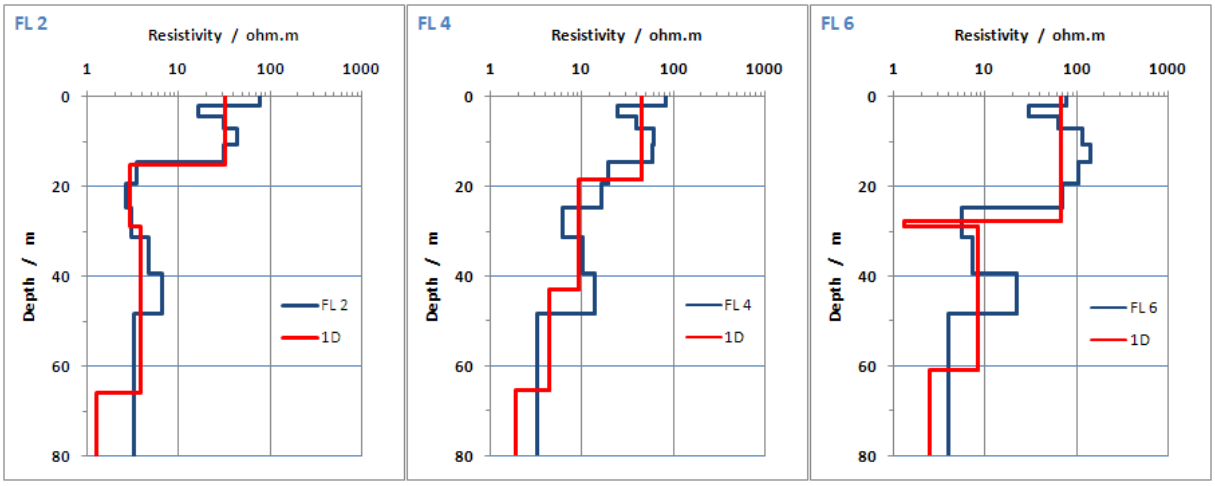

Figure 7.81 – Some Flamengos valley TEM soundings 1D model from quasi-2D inversion (blue), and corresponding 1D mean models (red).

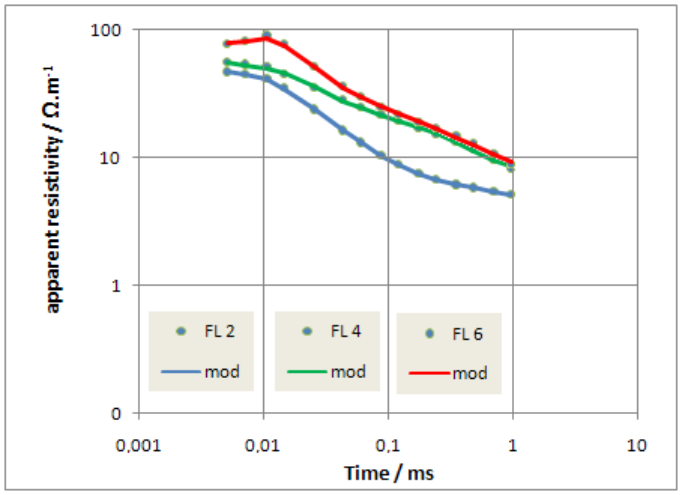

Figure 7.82 – Flamengos valley TEM data points and 1D model fit response from quasi-2D inversion, (corresponding to figure 7.81 models).

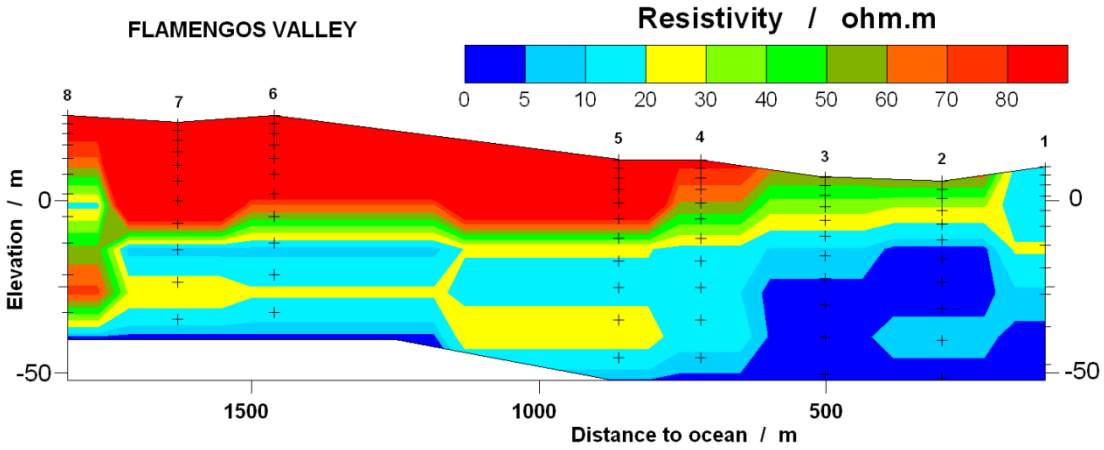

Figure 7.83 – 2D resistivity cross section from quasi-2D models, at Flamengos valley.

7.1.4.5 – S. Miguel 1D data inversion

TEM-FAST 48 soundings were acquired with a 25 m × 25 m single loop wire, with a maximum current input of 2.8 ampere and time channel set to 5. The observed noise was again at the same low level of 3 nVm^{-2}. Signal noise was very small at last time's data (error bar of 1 to 2%). No man-made source of EM noise was present (metallic fences, etc.) to produce coupling effects. The corresponding measured TEM field curves and also the 1D mean model responses, are shown bellow (figure 7.84), for six of the twenty four acquired soundings.

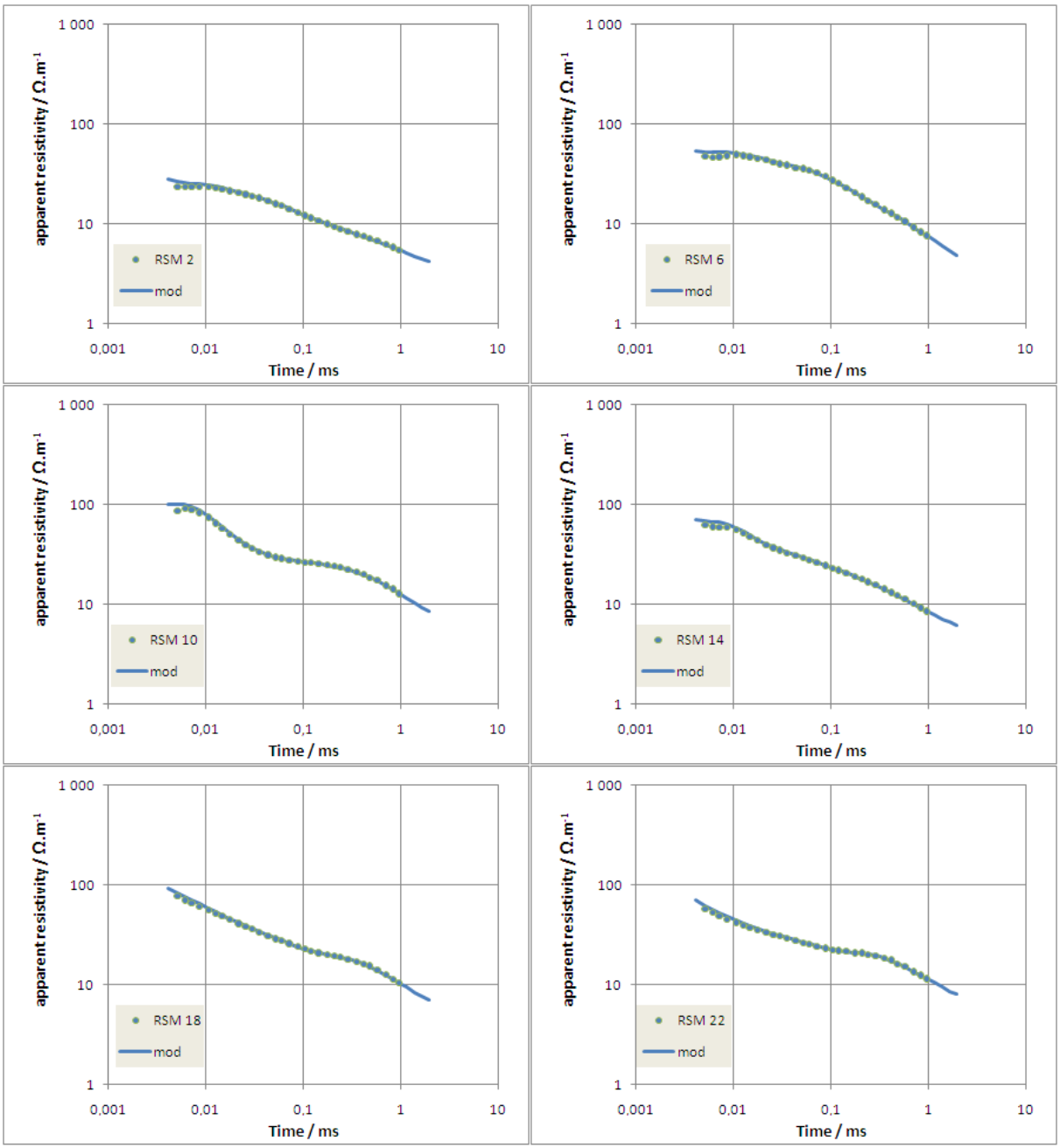

Figure 7.84 – Some S. Miguel measured TEM curves and 1D mean model fit response

The models' responses have a mean misfit of 1 to 2%. Figure 7.85 shows the 1D models of the soundings shown in figure 7.84. The behaviour of the apparent resistivity curves is analogous to those acquired in other valleys: a smooth decrease to low apparent resistivity values (less than 10 ohm.m) is observed.

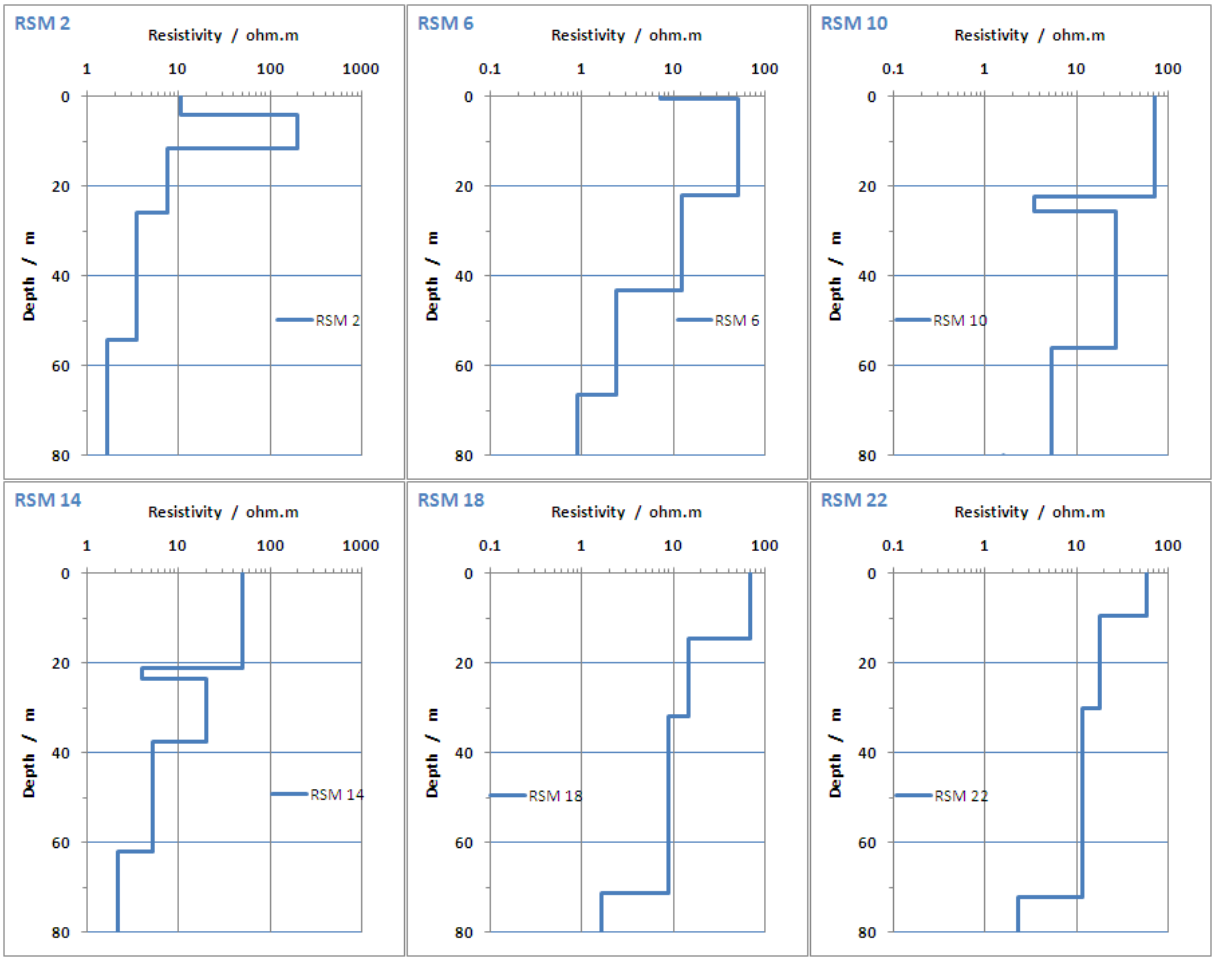

Figure 7.85 – Some S. Miguel valley 1D TEM mean models, corresponding to figure 7.84 soundings.

The available lithologic logging description comes from two boreholes (FT 68 and FT 70) near the coastline between TEM soundings 1 and 4, and one borehole located between TEM soundings 18 and 19, figure 7.86. Down course of the creek valley, near the shoreline the quaternary alluvium formation has some 30 m thick. At upper course, 3 km from the coastline, fractured basalt is again the main formation. Groundwater level in borehole and wells is about 5 m below the surface at TEM profile beginning and about 10 m at the profile end. Those levels correspond to a 0.020 hydraulic gradient throughout S. Miguel valley.

Most of the soundings have an initial changing resistivity from a higher value (80 ohm.m) to about 10 to 20 ohm.m value, corresponding to the aquifer. The depth of this resistivity change match the water table at both TEM profile limits, were groundwater levels do exist. Similar to the previous Flamengos valley, the models at the middle profile also show a thin conductive layer between the uppermost and aquifer layers, probably of clay origin. This can again act out like an impervious horizontal barrier at mid valley. Below this 10 to 20 ohm.m

layer, a deeper and less resistive one exist from mid profile towards inland. With the given settings and assuming a steady-state flux condition, this bottom layer cannot be connected to the fresh-seawater interface as it should be much deeper. The bottom conductive layer must then be formed by ancient salty layer deposits.

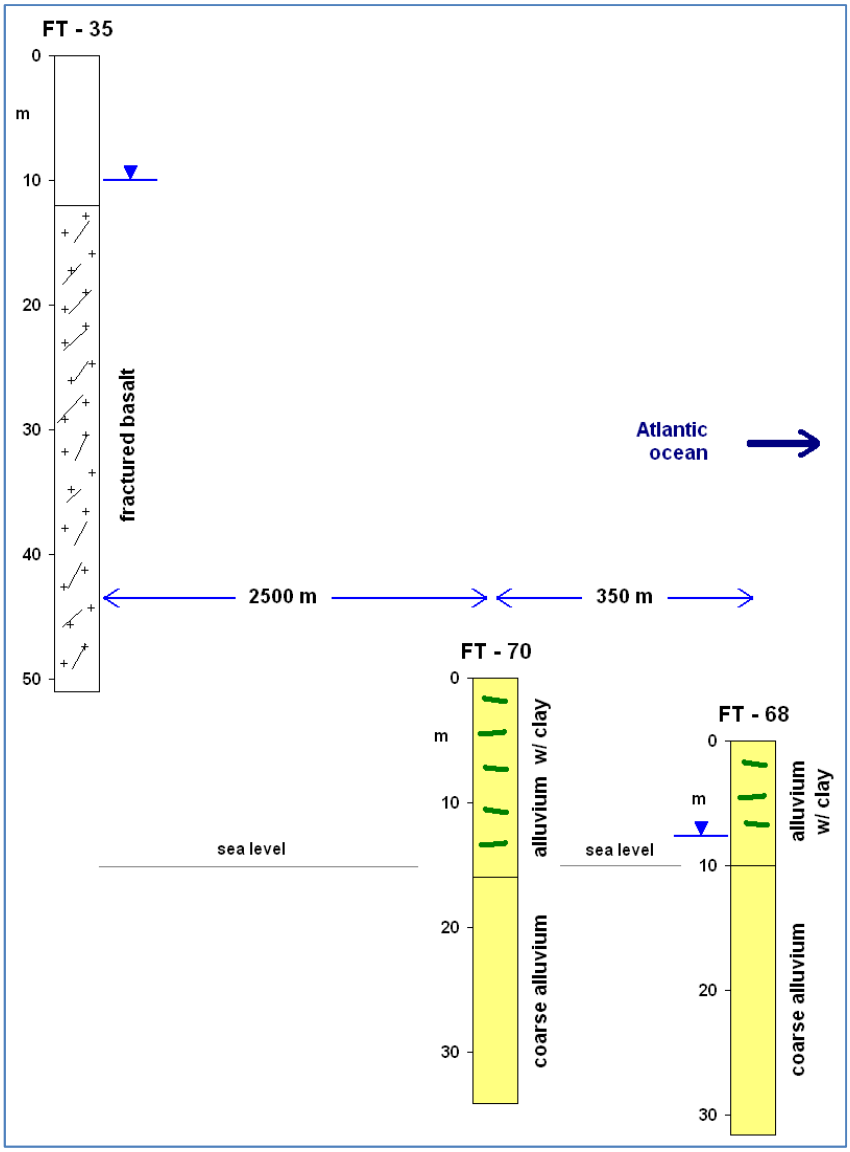

Figure 7.86 – Borehole lithologic description at S. Miguel valley (INGRH data).

With all 1D TEM sounding models, a stitched cross section was built throughout the S Miguel valley. Figure 7.87 shows this cross section and also the groundwater resistivity and level below the surface, known from wells and boreholes positions.

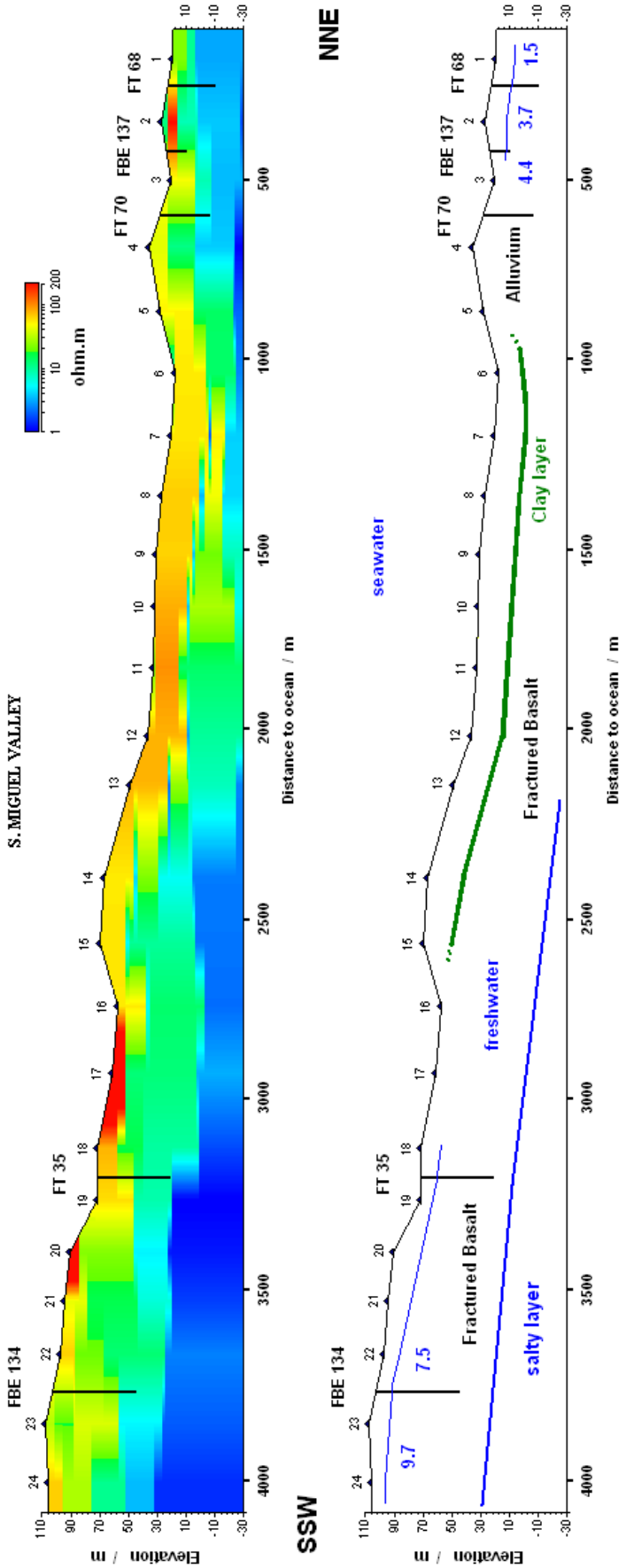

Figure 7.87 – Resistivity cross section at S. Miguel valley, from 1D TEM sounding models. Groundwater level and resistivity (ohm.m) plus interpreted geology.

7.1.4.6 – S. Miguel 2D data inversion

The TEM soundings in S. Miguel valley are rather uniformly spaced throughout the valley. The spatially constrained algorithm methodology to 1D inversion with laterally constrains (LCI) was applied again to these soundings set. The overall mean distance between soundings was 170 m. The modelling inversion tests had been carried as previously changing initial damping factor, the number of layers and lately different EDC values.

The maximum number of iterations was set to 60 and the *rms* value to 0.02. Initial model was set with resistive top layers (40 ohm.m) over a 10 ohm.m medium, with 15 layers models (till 80 m deep). Figure 7.88 display the mean *rms* misfit *versus* maximum iteration number and pairs of soundings in EDC. Misfit error is high with no lateral influence and drop with that LCI influence, to a mean value of 1.2%, with almost equal results with more iterations.

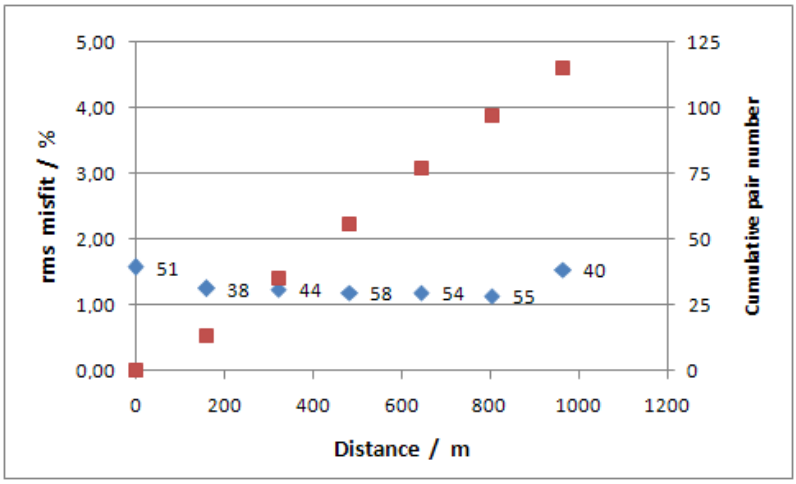

Figure 7.88 – Mean *rms* quasi-2D models misfit and iteration number (blue square), and cumulative sounding pair number (red square) for several constrained distances at S. Miguel valley. Initial damping factor set to 1.5 and 15 layers with 40 to 10 ohm.m model space.

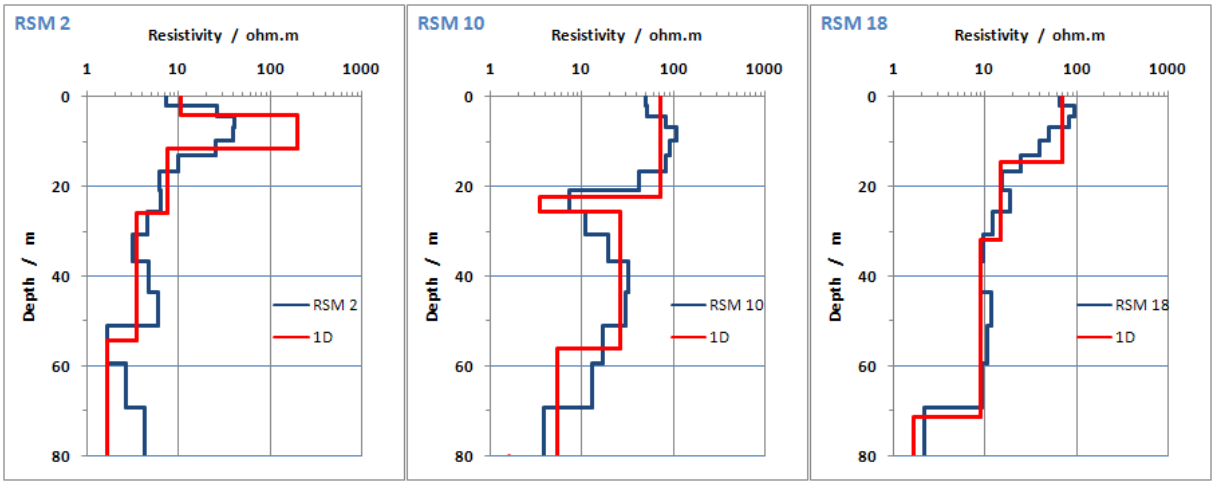

Figure 7.89 – Some Flamengos valley TEM soundings 1D model from quasi-2D inversion (blue), and corresponding 1D mean models (red).

Some of the 1D models obtained from quasi-2D inversion, and its corresponding data fit are shown in figures 7.89 and 7.90. Models are similar to those calculated from 1D individual inversion, in spite of some differences mostly related to layers fixed geometry and equivalent responses. The mean differences between both modelled sets are around 5%.

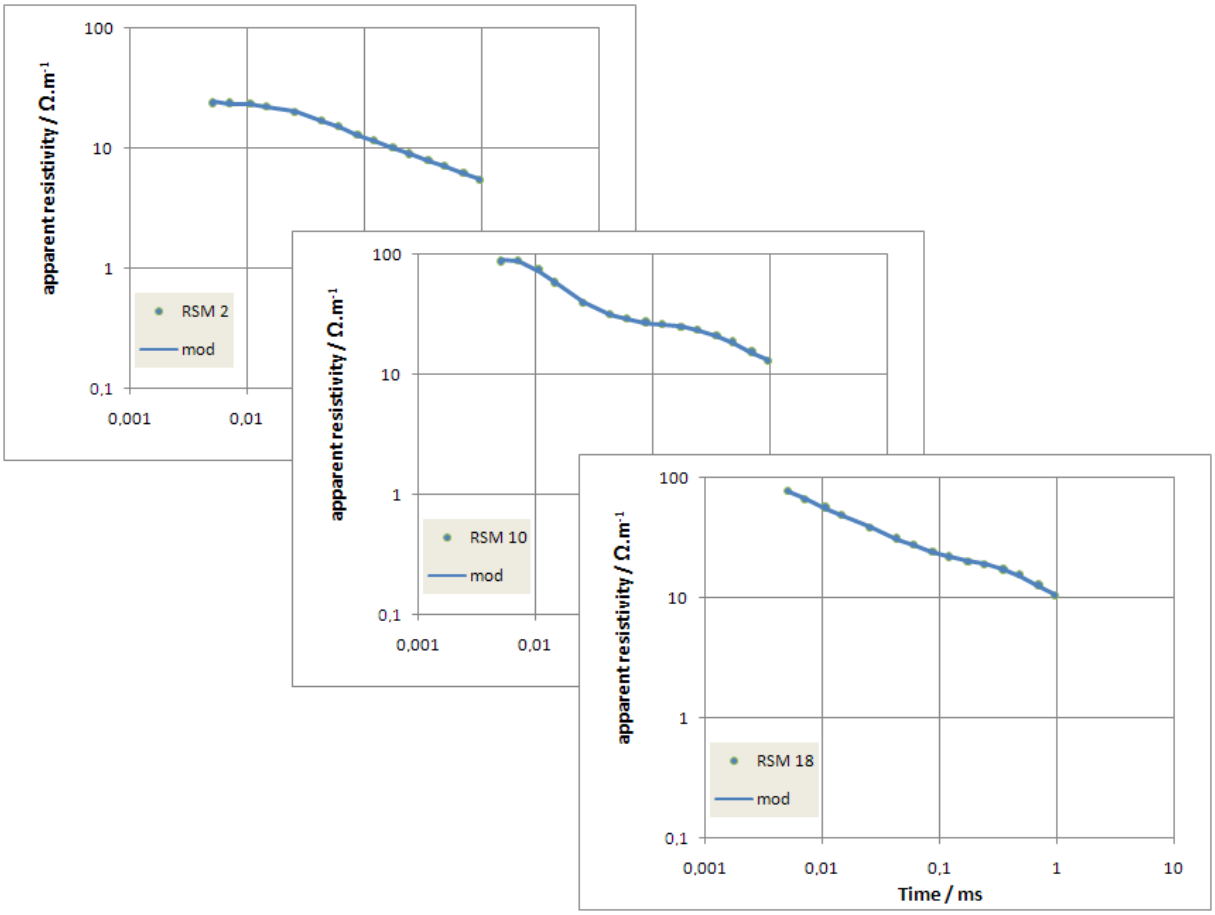

Figure 7.90 – S. Miguel valley TEM data points and 1D model fit response from quasi-2D inversion, (corresponding to figure 7.89 models).

The overall resulting structure is shown in figure 7.91. It's comparable to the previous one obtained by stitched 1D models (figure 7.87), with plotting limitations. The mean resistivities values at aquifer depth range from 10 to 20 ohm.m, as given by former 1D model results. High superficial resistivities start one km from the ocean upstream the valley. Near the coastline, a seawater influence seems to be present. Inland a relatively deep conductive layer is also detected, like happened in other valleys.

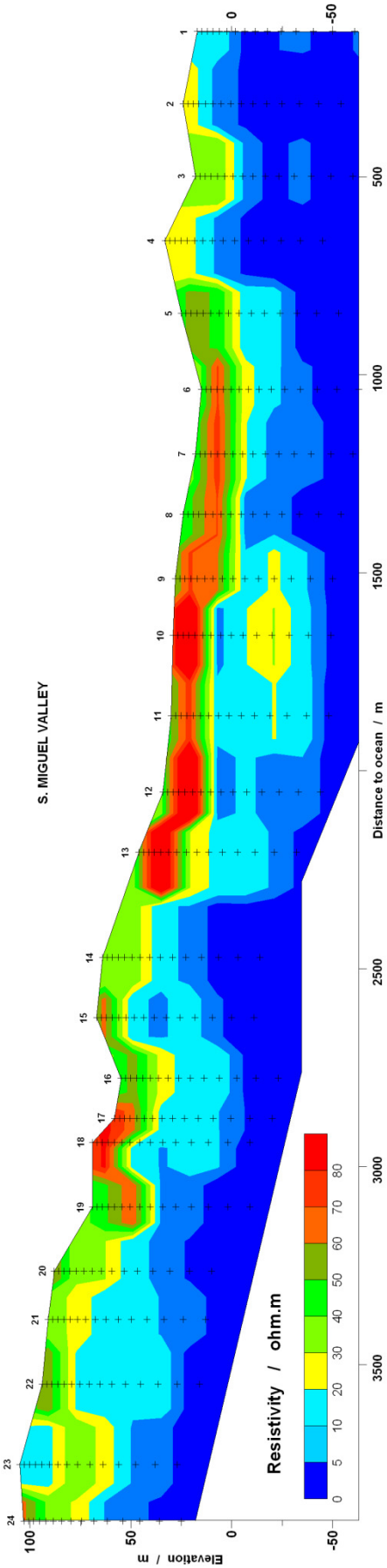

Figure 7.91 – 2D resistivity cross section from quasi-2D models, at S. Miguel valley.

7.2 – TEM data *versus* hydrologic parameters

Starting from the TEM sounding data, the obtained and modeled bulk electric resistivity at several survey places is now compared to the available hydrologic parameters. These later ones came from natural springs, manmade wells and boreholes, as mention in the previous chapter sixth. This data includes EC measures, chemistry groundwater analyses and also some boreholes lithological description (already mentioned), water levels and transmissivities from a few pumping tests. The seawater EC was also measured, as a reference. The spatial distribution of all this data is uneven throughout most valleys and Santiago Island (INGRH).

7.2.1 – Seca and Picos hydrologic parameters

At Seca and Picos valleys, only a few borehole parameters are available. Regarding to groundwater EC, the number of samples (mainly from wells) is such that allows a groundwater electric resistivity map at the region. Most of the data comes from locations at the axis of both valleys. A rather extensive data was pull together at summer 2000. Significant EC changes are not observed in the course of the years at inland regions far from the shoreline. But, nearest the ocean, some important changes are known, as shown in figure 7.92 below. Some groundwater EC measured at wells in 2005 has been compared with previous ones, from year 2000. It's clear a relationship between EC and the distance to the coastline. This behaviour is not just exclusive at Seca valley it seems to happen also at most of the farmed valleys of Santiago.

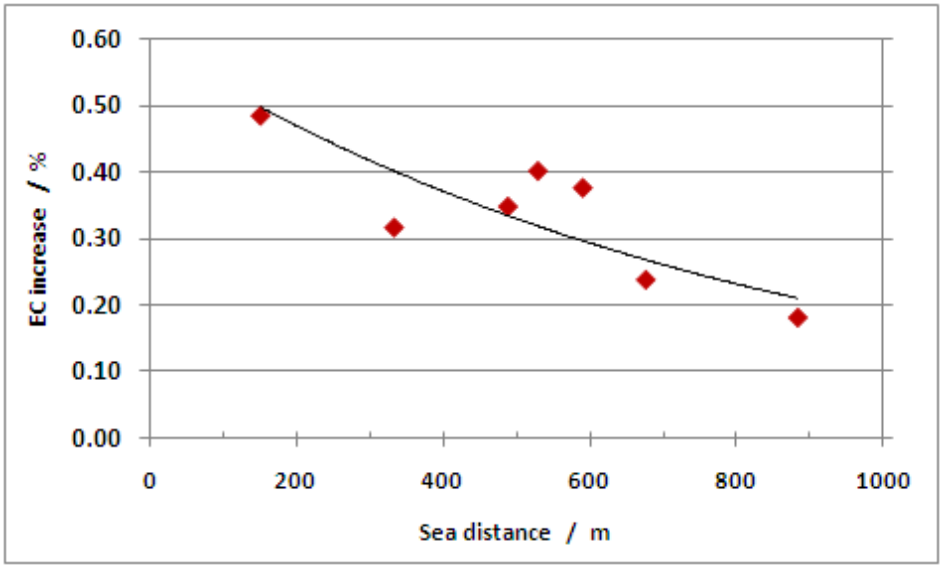

Figure 7.92 – Groundwater EC (25 ºC) increase versus sea distance, between 2000 to 2005 years, at Seca valley (from INGRH data).

Figure 7.93 presents the condition in year 2000, before the electromagnetic field work (at the year 2005). It is clear the remarkable relation between the groundwater resistivity data and points' distance to the coastline.

Taking into account the bulk resistivity values at aquifer depth (from TEM inversions) and the corresponding in-situ groundwater resistivity values, it is possible to calculate the formation factor (*F*) by expression (5.5). The table 7.2 below, exhibit such as results.

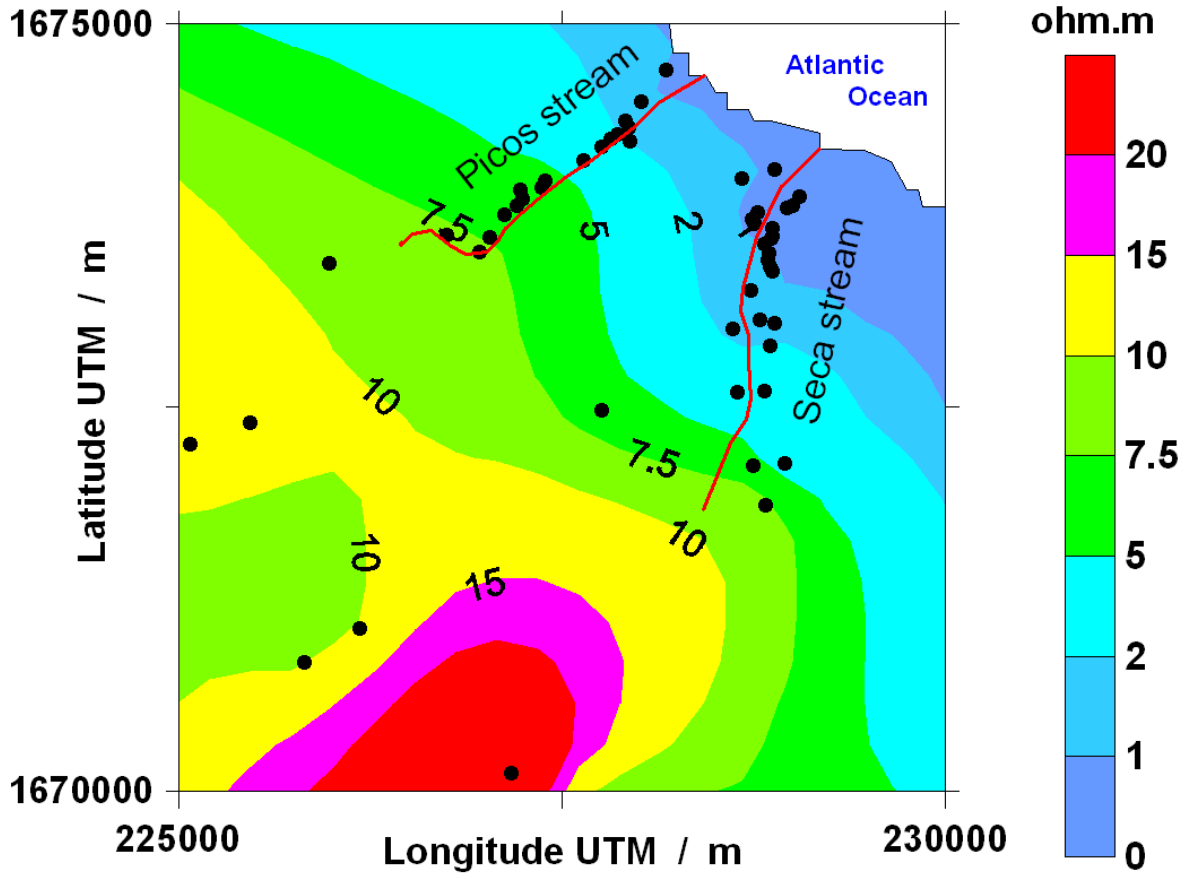

Figure 7.93 – Krigged groundwater resistivity map from manmade well and borehole data points, at Seca and Picos valleys (year 2000), (from INGRH data).

Table 7.2 – Formation factor values at Seca and Picos valleys.

Seca	**Resistivity / ohm.m**		**F**	**Picos**	**Resistivity / ohm.m**		**F**
TEM #	**bulk**	**water**		**TEM #**	**bulk**	**water**	
15	1.5	0.4	3.5	**9**	1.2	0.5	2.6
16	2.1	0.5	4.2	**10**	1.9	0.7	2.9
17	2.7	0.6	4.5	**11**	1.9	0.9	2.0
18	3.9	0.7	5.7	**12**	4.4	1.2	3.6
19	2.6	0.7	3.6	**1**	21.7	3.1	6.2
20	2.7	0.8	3.3	**2**	19.2	4.8	2.7
10	4.9	0.9	5.3	**3**	12.8	5.6	3.4
11	5.0	0.9	5.5	**4**	19.1	6.3	1.8
1	5.3	1.3	4.2	**5**	11.5	6.7	1.4
8	6.1	1.3	4.8	**6**	9.2	7.3	1.2
9	12.1	2.7	4.4	**7**	8.7	9.5	1.5
7	13.4	3.5	3.9	**8**	14.6	0.5	2.6
2	11.9	5.5	2.1	-	-	-	-
5	20.8	8.3	2.5	-	-	-	-
Mean value			**4.1**	**Mean value**			**2.7**
Standard Deviation			**1.1**	**Standard Deviation**			**1.4**

Doing a simple analysis of the calculated *F* values its worth remarking that all of them are rather small, with a mean value of 4.1 and 2.7, respectively to Seca and Picos. Apparently, there aren't significant differences between *F* values at the beginning of the profile, near the coastline were alluvium is thicker, and the end of the profile, where the alluvium is much thinner, replaced by fractured basalt. Nevertheless, seems that formation factor values are decreasing from the shoreline, upwards the valleys, figure 7.94.

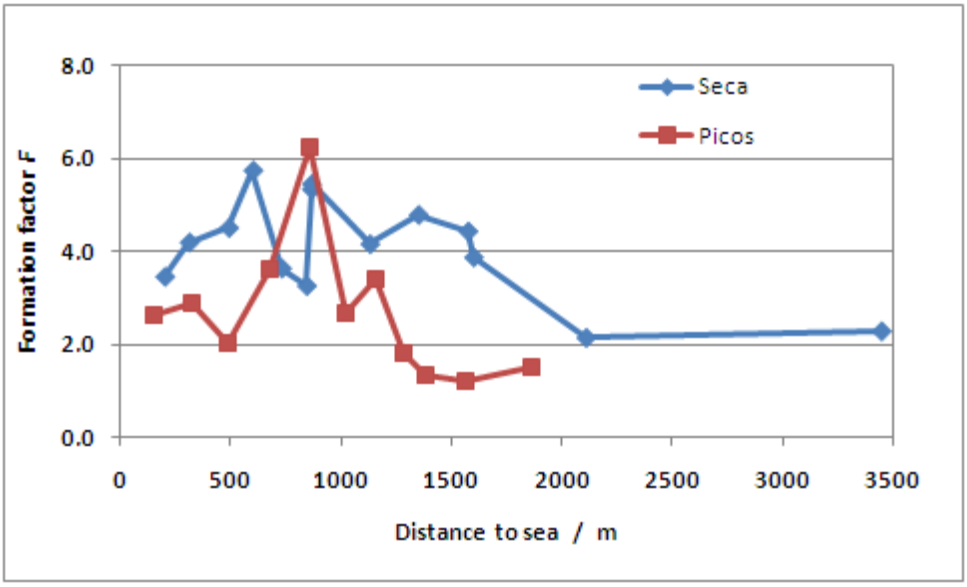

Figure 7.94 – Formation factor *versus* sea distance, for Seca and Picos valleys.

These values can be directly translated into porosities via Archie first law (5.11b). Table 7.3 summarizes this calculation with three sets of parameter's values (*a* and *m*), typical for alluvium (higher values) and fractured basalts (lower values) environments. These porosities seem rather high, especially at the lowest formation factor values, but are within the range of values published for this sort of lithology.

Table 7.3 – Mean porosities from formation factor values, at Seca and Picos valleys.

Valley	***F***	***a* = 0.6 , *m* = 1**	***a* = 1 , *m* = 1**	***a* = 1 , *m* = 1.4**
Seca	4.1	0.15	0.24	0.37
Picos	2.7	0.22	0.37	0.49

Several factors may affect the values of the formation factor. The clay content dispersion throughout alluvium, and throughout fractured basalts, and its cation exchange capacity (CEC). Or to a much lesser extent, a low bulk resistivity value due to the equivalence problems in the inversion process. Thin clay layers and clayed inclusions are reported in the alluvium and also in basaltic formations. Concerning the clay surface conductivity influence, the analyses of the bulk resistivity versus groundwater EC available data seems to indicate a real effect (figure 7.95), which will produce always a major correction at the lower groundwater EC places. At Picos the data fit is worse because it shows high data scattering at low conductivities. The surface conduction term (σ_s) has been estimated from the extrapolated intercept when groundwater EC is set to zero (Waxman and Smits, 1968), using a power fit function (see figure 7.95).

Applying Archie's second law (5.12), with the mean calculated correction, σ_S = 592 µS.cm^{-1} to Seca valley and σ_S = 653 µS.cm^{-1} to Picos valley the mean porosity values became (excluding the highest bulk resistivities ones) as following (table 7.4):

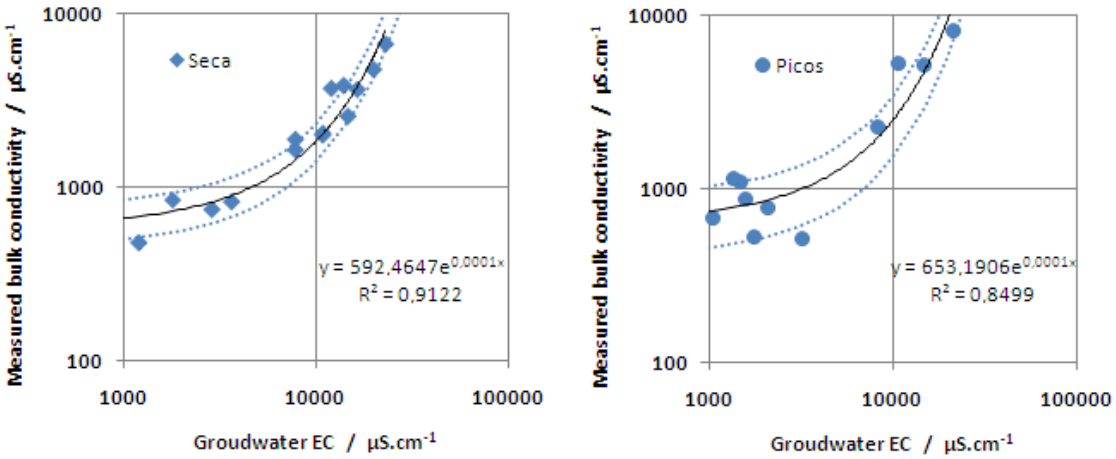

Figure 7.95 – Bulk versus groundwater EC relation, (continuous line - fit function, dotted lines - plus and less one standard deviation fit function), for Seca and Picos valleys.

Table 7.4 – Mean porosities from corrected formation factor values, at Seca and Picos valleys.

Valley	*F*	*a* = 0.6 , *m* = 1	*a* = 1 , *m* = 1	*a* = 1 , *m* = 1.4
Seca	**7.7 ± 1.7**	0.08 ± 0.02	0.13 ± 0.03	0.23 ± 0.05
Picos	**5.4 ± 2.2**	0.11 ± 0.07	0.19 ± 0.10	0.30 ± 0.12

This is assuming an effective porosity (connected porosity structure) equal to the porosity given by Archie's law. These ranges of porosity values can be compared against the available transmissivities values from pumping tests at boreholes FT-63 and FBE-169 (inland, near last TEM Seca sounding), which have both about 60 m^{2}d^{-1}. At thick alluvium formation, the transmissivities values are usually higher in one order, 600 m^{2}d^{-1} (Gomes, 2007). With the assumption of a 40 m thick aquifer system, the hydraulic permeability becomes respectively 3×10^{-12} m^2 and 3×10^{-11} m^2, (and K = 1.5 and 15 m.d^{-1}, to a confined aquifer hypothesis).

Porosity can be estimated taking the K-C relation for the sedimentary environment (expression (5.7b)), and the expression (5.6) for the fractured basalt environmental (assuming that it acts identically to granular porosity when it is densely fractured) with an equivalent grain diameter at least as 8 times the inner fractured radius channels. The results are given in table 7.5. The lithologic description of the alluvium sedimentary formation has no reference to be coarse sandy, so the porosity must be in 15 to 25% range with a mean grain particle diameter below 0.3 mm (equivalent to medium to fine sand). Sediments in Picos valley have higher porosity and fine grained materials than sediments in Seca valley. Fractures at the basaltic formations seem to exist below the 0.15 mm equivalent D_{50} value (10 µm inner radius), with porosities in the 10% (in Seca) to 20% (in Picos) range. That inner radius fractures give a specific surface area (S_p, known as SSA) around 0.1 m^{2}g^{-1}, a common value at basaltic formations (Nielsen and Fisk, 2008).

Table 7.5 – D_{50} grain size (alluvium) and equivalent D_{50} grain size (fractured basalt) in mm, to given porosities. Seca and Picos valleys.

Formation	Porosity					
	0.05	**0.10**	**0.15**	**0.20**	**0.25**	**0.30**
Alluvium	1.8	0.6	0.30	0.20	0.13	0.09
Fractured basalt	0.30	0.15	0.10	0.06	0.04	0.03

Although there is no information about the clay composition (detected at many borehole logs) an assessment of CEC amount value for the mean porosity was tried. From the W-S models and their relations (chapter 5, expressions 5.13 to 5.15) assuming a specific weight (density) of 2500 kg.m^{-3} and cementation index of 1.0, the mean CEC estimated value is: 1.7 meq^{+}/100 g to 15% porosity for Seca valley and 2.5 meq^{+}/100 g to 20% porosity for Picos valley. These are low CEC values but nevertheless, affecting bulk resistivity values. As there is an intrinsic relationship between CEC and porosity, none of them having independent measures, only a rough idea on the spatial distribution of CEC can be made (figures 7.96 and 7.97).

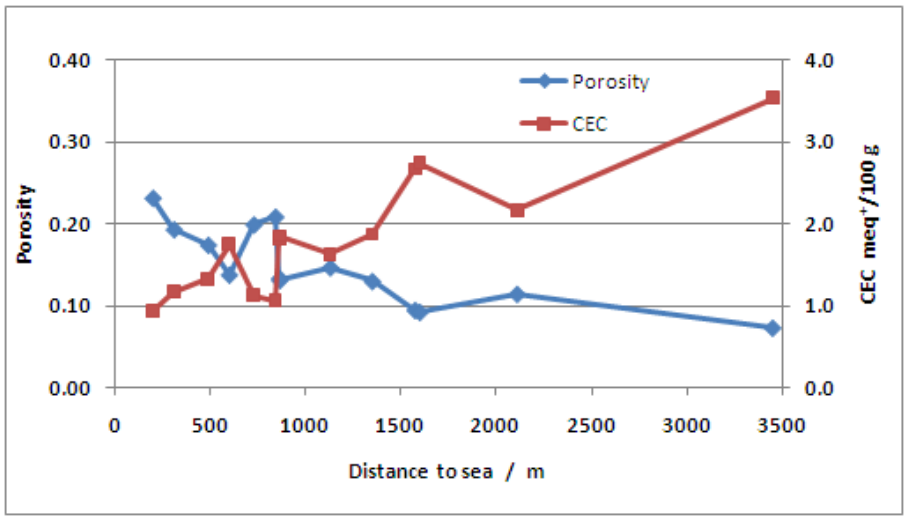

Figure 7.96 – Porosity values (CEC = 1.7 meq^{+}/100 g) and CEC values (porosity = 15%) *versus* sea distance at Seca valley.

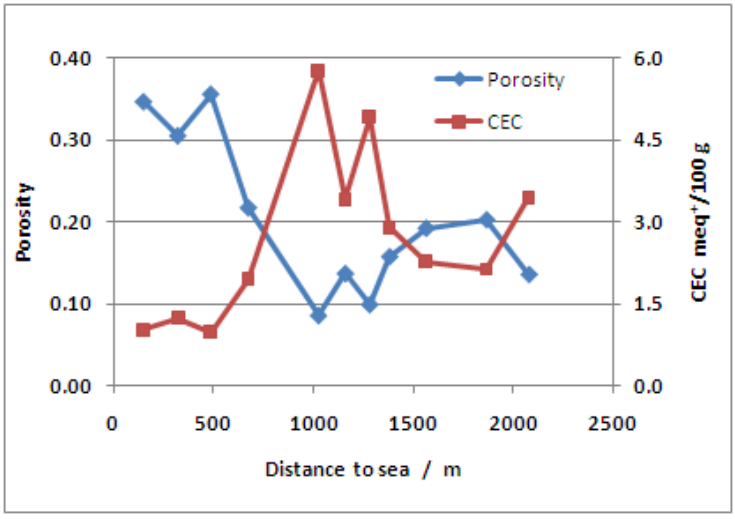

Figure 7.97 – Porosity values (CEC = 2.5 meq^{+}/100 g) and CEC values (porosity = 20%) *versus* sea distance at Picos valley.

7.2.2 – Salto, Flamengos, and S. Miguel hydrologic parameters

At Salto, Flamengos and S. Miguel valleys, a few more parameters exist, but fewer groundwater EC values measured in samples from wells and boreholes. Although the density of points per stream valley is much smaller, it allows the plotting of a groundwater electric resistivity map for the entire region. Figure 7.98 presents the condition at summer of 2000. Again, it is clear the remarkable relation between groundwater resistivity and sea distance.

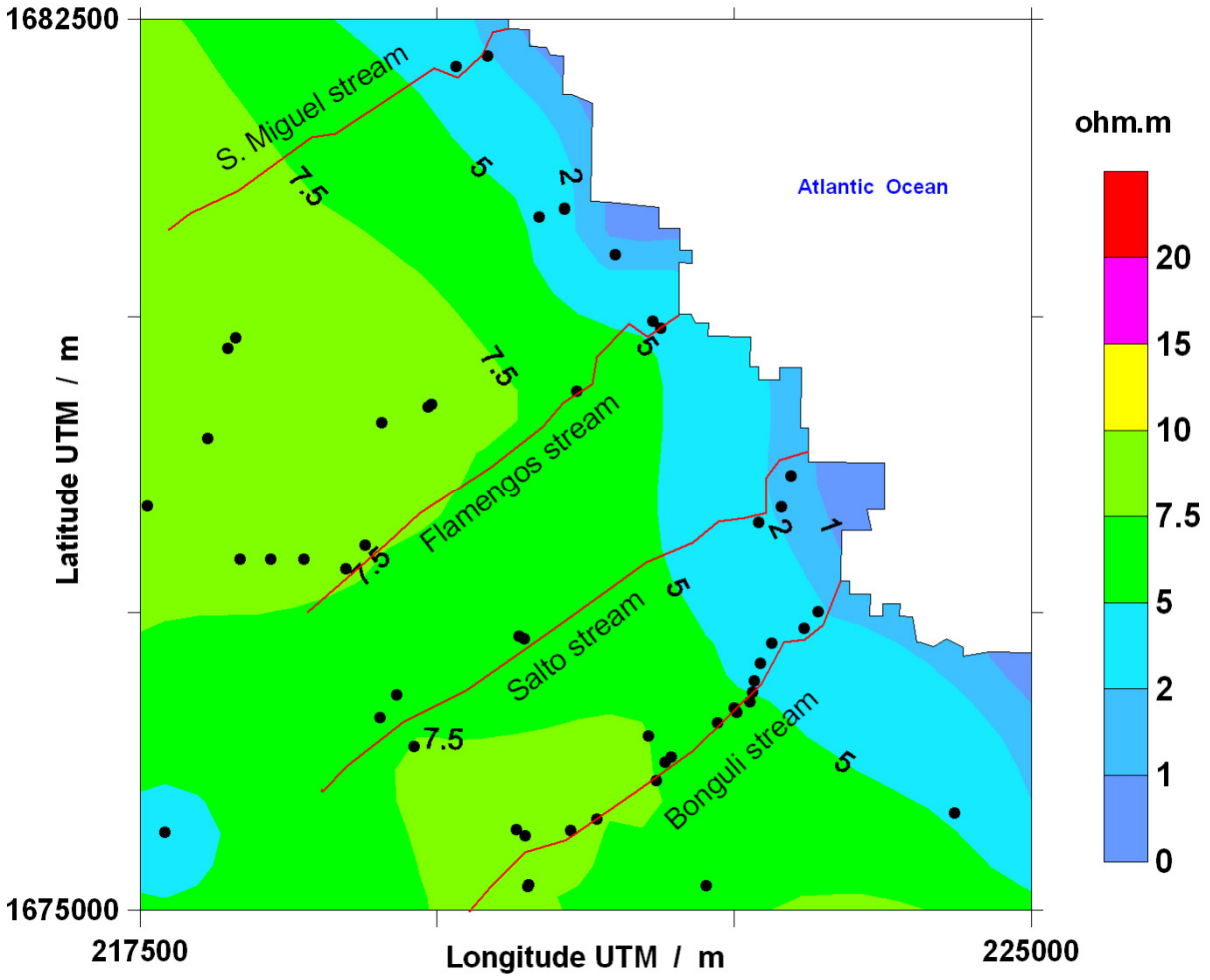

Figure 7.98 – Krigged groundwater resistivity map from manmade well and borehole data points, at Salto, Flamengos and S. Miguel valleys (year 2000), (from INGRH data).

Taking the modelled bulk resistivity values of the aquifer at each TEM sounding (closer to the well where groundwater EC is known), an estimation of the formation factor was calculated. Table 7.6 in the next page exhibits such results for those three valleys. The formation factors are again very low (near 3.0), exception of a few values at Flamengos valley. Conversion to porosities, by Archie first law, will give high to very high porosity values, as seen below in table 7.7. This table includes also the corrected formation factors by surface conductivity effect from clay dispersion throughout the lithologic formations. The bulks versus groundwater EC are plotted in figure 7.99 for the three surveyed valleys.

Table 7.6 – Formation factor values from TEM soundings and groundwater resistivities, at Salto, Flamengos (FL) and S. Miguel (SM) valleys.

Salto TEM	Res. / ohm.m		F	FL TEM	Res. / ohm.m		F	SM TEM	Res. / ohm.m		F
	bulk	water			bulk	water			bulk	water	
1	2.3	1.0	2.2	**1**	118.0	4.7	25	**1**	2.9	1.5	1.9
2	4.1	1.2	3.4	**2**	8.9	3.8	2.4	**2**	7.6	3.7	2.0
3	3.0	1.4	2.1	**3**	7.1	3.0	2.3	**3**	7.9	4.4	1.8
4	4.4	1.9	2.3	**5**	51.0	5.8	8.9	**22**	16.7	7.5	2.2
13	11.8	6.3	1.9	**6**	68.0	7.4	9.2	**24**	21.7	9.7	2.2
14	9.6	6.3	1.5	-	-	-	-	-	-	-	-
18	12.3	6.5	1.9	-	-	-	-	-	-	-	-
Mean value			**2.2**	**Mean value**			**3.9**	**Mean value**			**2.0**
Standard Deviation			**0.6**	**Standard Deviation**			**3.8**	**Standard Deviation**			**0.2**

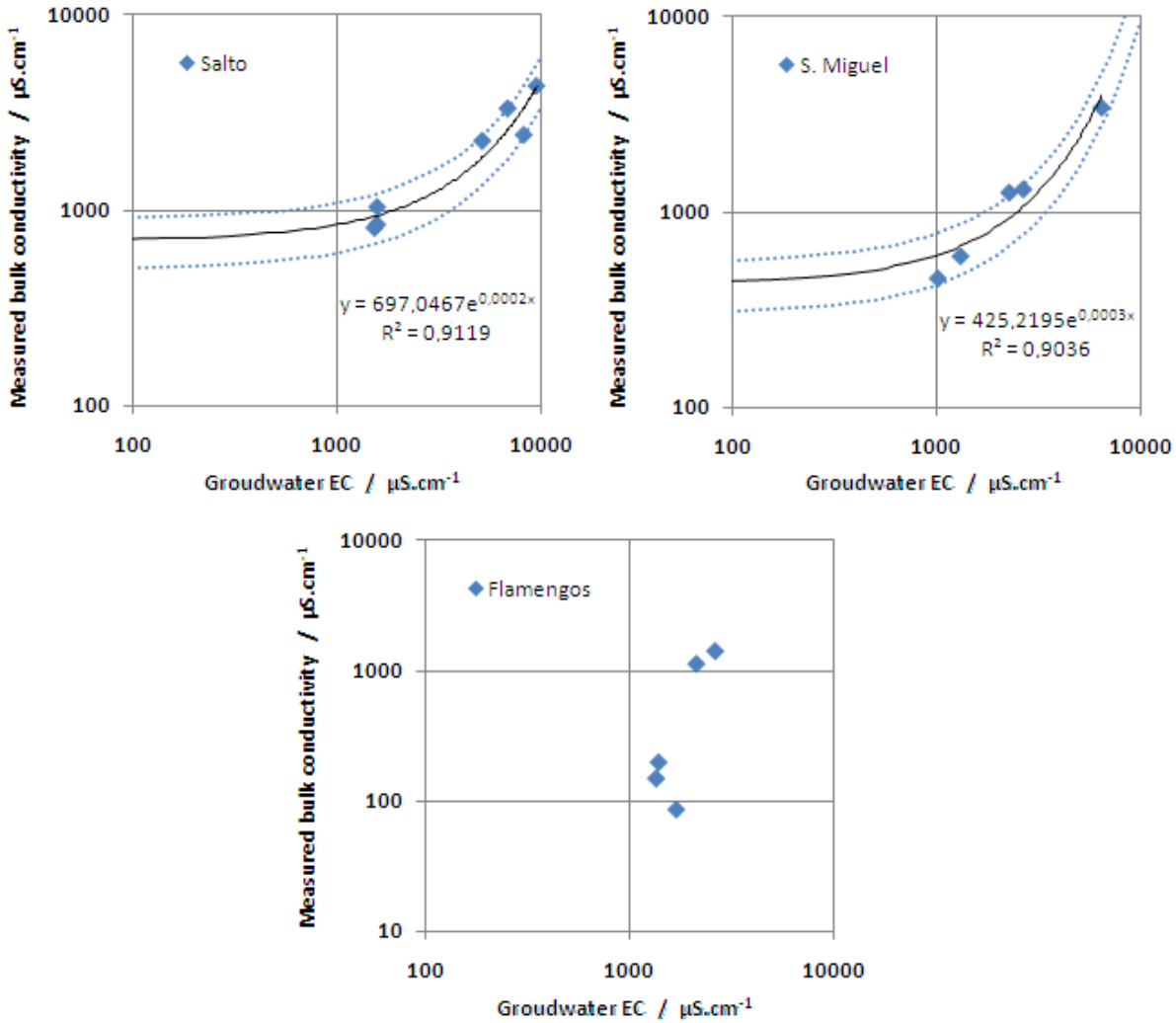

Figure 7.99 – Bulk versus groundwater EC relation, (continuous line - fit function, dotted lines - plus and less one standard deviation fit function), for Salto, Flamengos and S. Miguel valleys.

With only a handful of data points, the fits are only reasonable for Salto and S. Miguel, with respectively, σ_S = 697 µS.cm^{-1} and σ_S = 425 µS.cm^{-1}. At Flamengos an assumed correction of σ_S = 697 µS.cm^{-1} was also applied.

Table 7.7 – Mean porosities from formation factor and corrected values one, at Salto, Flamengos (FL) and S. Miguel (SM) valleys.

Valley	*F*	*a* = 0.6 , *m* = 1	*a* = 1 , *m* = 1	*a* = 1 , *m* = 1.4
Salto	**2.2**	0.27	0.45	0.57
Flamengos	**3.9**	0.15	0.26	0.38
S. Miguel	**2.0**	0.30	0.50	0.61
Corrected *F*				
Salto	**6.0 ± 2.4**	0.10 ± 0.05	0.17 ± 0.08	0.28 ± 0.11
Flamengos	**5.4 ± 1.5**	0.11 ± 0.03	0.19 ± 0.06	0.30 ± 0.08
S. Miguel	**3.9 ± 1.0**	0.15 ± 0.05	0.26 ± 0.07	0.38 ± 0.09

These porosity range values were also compared against the available transmissivities, from local pumping tests at boreholes FT-5 and FBE-145 (inland, at Flamengos valley). Both have low values at the 2 to 5 m^2d^{-1} range, which is typical for the Flamengos formation lithology (Gomes, 2007). Near the coastline, where the alluvium formations are thicker, the transmissivities are again much higher, around the 600 m^2d^{-1}. With the assumption of a 40 m thick aquifer system, the hydraulic permeability becomes 2×10^{-13} m^2 and 3×10^{-11} m^2, (and K = 0.1 and 15 $m.d^{-1}$, to a confined aquifer hypothesis), respectively.

The corresponding mean grain diameter of alluvium formation and equivalent grain diameter for fractured basaltic formation are given at table 7.8. At the alluvium sedimentary formation, porosity must be in the 20 to 30% range with particle mean size around 0.2 mm (equivalent to fine sand). Porosity seems to grow from Salto (at south) to S. Miguel, but this could be biased with this so little data amount. Fractures at basaltic formations seem to exist below the 0.06 mm equivalent D_{50} value (2 µm inner radius), with porosities in the 10 to 20% range, with Salto valley in the former limit and S. Miguel valley in the later limit. This fractures inner radius gives a SSA value around 0.3 m^2g^{-1}.

Table 7.8 – D_{50} grain size (alluvium) and equivalent D_{50} grain size (fractured basalt) in mm, to given porosities, Salto, Flamengos and S. Miguel valleys.

Formation	Porosity					
	0.10	**0.15**	**0.20**	**0.25**	**0.30**	**0.35**
Alluvium	1.8	0.6	0.30	0.20	0.13	0.09
Fractured basalt	0.06	0.04	0.02	0.010	0.008	0.006

The measured seawater EC value is of 56100 µS.cm^{-1} (25 ºC) (Mota Gomes, private communication). For this seawater conductivity, the calculated salinity is around S = 37.2, i.e. a TDS content of 37200 mg.L^{-1} (Kennish, M., 1989). This seawater 0.18 ohm.m electric resistivity value is compared with TEM soundings carried out near to sea, where apparent resistivities show deeper seawater influence other than just the shallower one. This would be always the best procedure to get better porosity results (Kafri, Goldman, 2005). At Salto the corrected and uncorrected formation factors are 9.4 and 8.4, respectively for first sounding. At Flamengos they are respectively, 12.0 and 10.3, and at S. Miguel the calculated values are 6.5 and 6.0, respectively. All these values are higher than those calculated and discussed above, by some 50% at Salto and S. Miguel. At Flamengos, the offset value is

even higher. Explanation to this could be that water is not “pure seawater”, but a rather very high saline mixture. Nevertheless, this implies that former mean formation factors must be taken at higher limit and that porosities are consequently small, and must be at the low limit as well. Table 7.9 below, summarize these values. Porosities at fractured basalts (including tuffs) must be considered with a mean value around 10 to 15%.

Table 7.9 – Mean porosities from seawater corrected formation factor values, at Salto, Flamengos and S. Miguel valleys.

Valley	***F***	***a* = 0.6 , *m* = 1**	***a* = 1 , *m* = 1**	***a* = 1 , *m* = 1.4**
Salto	**8.9 ± 0.5**	0.07 ± 0.01	0.11 ± 0.01	0.21 ± 0.02
Flamengos	**11.0 ± 1.0**	0.05 ± 0.01	0.09 ± 0.01	0.18 ± 0.01
S. Miguel	**6.3 ± 1.0**	0.10 ± 0.01	0.16 ± 0.01	0.27 ± 0.01

The consequent mean CEC value for these data sets gives the following results: 1.5 $meq^{+}/100$ g to 15% porosity at Salto valley, 2.0 $meq^{+}/100$ g to 15% porosity at Flamengos valley and 1.5 $meq^{+}/100$ g to 20% porosity to S. Miguel valley, at the same order, as previously found.

7.2.3 – S. Domingos hydrologic parameters

At S. Domingos’s valley, the numbers of manmade wells are even smaller. The few ones near the sea are dry from time to time. The only available groundwater EC measures at mid valley come from a few boreholes there, together with their lithologic description. Borehole FT-40 is at mid valley between TEM soundings 26 and 27, with a measured groundwater EC of 1375 $\mu S.cm^{-1}$. From year 2003 to 2006 FT-40 EC values had only 25 $\mu S.cm^{-1}$ variations. The modelled bulk resistivity values at aquifer depth from TEM 26 and 27 soundings are 12.2 and 11.6 ohm.m, respectively. With these values, the formation factor becomes F = 1.65, a rather small one. If a clay conductivity surface correction with σ_S = 600 ± 100 $\mu S.cm^{-1}$ is applied, regarding that similar lithology with previous valleys is found, the corrected formation factor is equal to F = 5.9 ± 1.8. This is for fractured basalt lithology formations. The related porosities are assigned in table 7.10. CEC value is about the same order, 3.0 $meq^{+}/100$ g for 20 % porosity.

Table 7.10 – Mean porosities from formation factor and corrected formation factor values at S. Domingos FT-40 borehole site.

S. Domingos	***F***	***a* = 0.6 , *m* = 1**	***a* = 1 , *m* = 1**	***a* = 1 , *m* = 1.4**
FT-40	**1.7**	0.36	0.60	0.69
Corrected *F*				
FT-40	**5.9 ± 1.8**	0.10 ± 0.04	0.17 ± 0.06	0.28 ± 0.08

Taking into account the deeper seawater intrusion from the shoreline up to 500 m inland, and the corresponding TEM models’ bulk resistivity of 1.6 ± 0.3 ohm.m, the formation factor becomes now F = 9.0 ± 1.6. This is again some 50 % plus that early simple corrected determination, although the error bands do overlap around value 7.5 (table 7.11).

Table 7.11 – Mean porosities from seawater corrected formation factor values, at S. Domingos valley.

Valley	*F*	*a* = 0.6 , *m* = 1	*a* = 1 , *m* = 1	*a* = 1 , *m* = 1.4
S. Domingos	**9.0 ± 1.6**	0.07 ± 0.01	0.11 ± 0.02	0.21 ± 0.03

The porosity range values were again compared against the known local pumping test's results, at boreholes FT-26, FT-40 and FT-42. The transmissivity is around 70 m^2d^{-1}, for the fractured basaltic formation. That means a value of 2×10^{-12} m^2 for the hydraulic permeability, with a 40 m thick aquifer system assumption (and K = 1.75 $m.d^{-1}$, to a confined aquifer hypothesis).

The corresponding equivalent grain diameter for fractured basaltic formation is given at table 7.12. Fractures at basaltic formations seem to exist below the 0.2 mm equivalent D_{50} value (6 µm inner radius), with porosities in the 10 to 20 % range. This fractures inner radius gives a SSA around 0.1 m^2g^{-1}.

Table 7.12 – Equivalent D_{50} grain size at fractured basalt (in mm) and porosities at S. Domingos valley.

Formation	Porosity		
	0.10	**0.15**	**0.20**
Fractured basalt	0.16	0.08	0.05

With these parameters and the modelled TEM bulk resistivity values at aquifer's depth, the groundwater resistivity was calculated throughout the axis valley, upstream starting from the shoreline. Results are given below in figure 7.100. The shallow groundwater resistivity is extremely low nearest to sea (0.3 to 0.8 ohm.m) and becomes progressively more resistive with sea distance. At 1000 m distance onwards, mean resistivity is near 7 ohm.m value. Similar values were measured beyond TEM 37 at borehole FT-42 and on more five wells, 3500 m from the coastline (1500 m behind this last sounding).

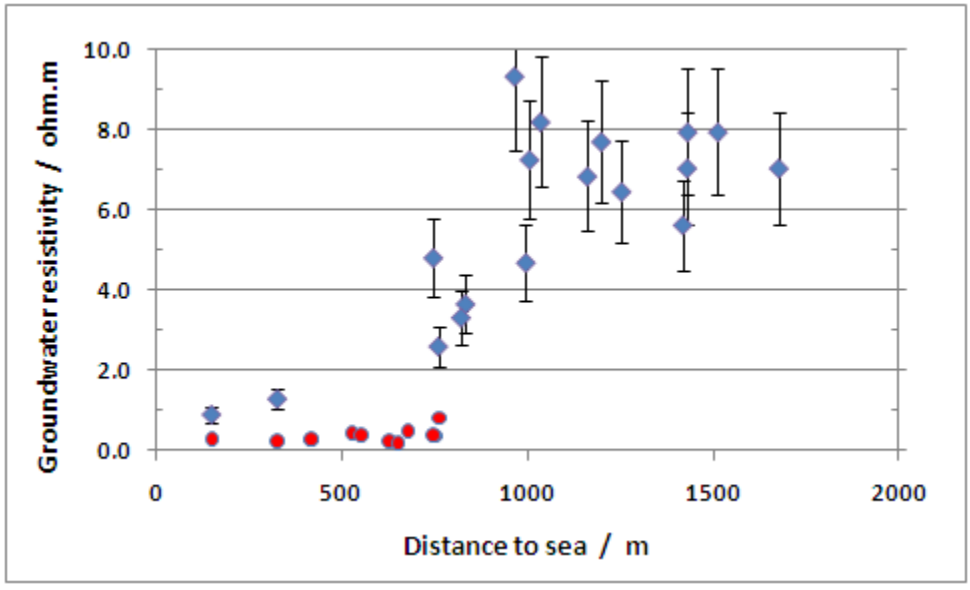

Figure 7.100 – Groundwater resistivity from TEM soundings at S. Domingos valley, with 20% error bars, (red circles – shallow water near the sea).

7.2.4 – Tarrafal and Ribeira Grande hydrologic parameters

At Tarrafal (Chão Bom) and Ribeira Grande valley only a small number of manmade wells have EC and water level's measures. These wells are all nearby each other and close to the sea, at SW Chão Bom. Some of the few boreholes have lithologic description, groundwater EC measures and only one Transmissivity value (FT-29 borehole). Figure 7.101 below, show the linear relation between groundwater resistivity versus sea distance, starting from the sea with values below one ohm.m. This must represent a fresh to seawater mixture as groundwater level is barely above the sea level at all this near sea area.

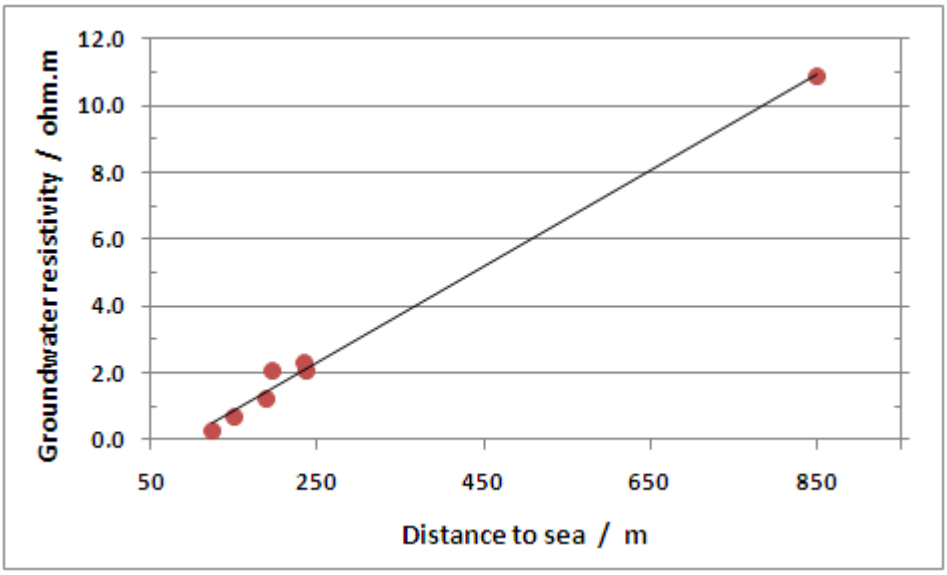

Figure 7.101 – Groundwater resistivity versus distance to the sea, at Tarrafal and Ribeira Grande valley.

Direct comparison between these water values and TEM modelled bulk resistivity gives a formation factor of F = 9.2 ± 2.8 (without any clay superficial conductivity correction) for the shallow fractured basalt. With these values, a porosity range can be calculated (table 7.13).

Table 7.13 – Mean porosities at shallow fractured basaltic formation, at Tarrafal and Ribeitra Grande valley.

Tarrafal, Rib. Grande	***F***	***a* = 0.6 , *m* = 1**	***a* = 1 , *m* = 1**	***a* = 1 , *m* = 1.4**
	9.2 ± 2.8	0.07 ± 0.02	0.11 ± 0.03	0.20 ± 0.03

Porosity for this shallow basaltic layer near the sea must be around 10%.

The available groundwater EC logging measures in SST-33 and SST-34 boreholes (Dahlin *et al.*, 1986), show that 25 to 30 m below the mean sea level values are less than 0.3 ohm.m, i.e. it is a high degree salty rich mixture water or even seawater. On this assumption, with a 0.18 ohm.m seawater resistivity value, the formation factor is calculated to this deep level, from the TEM bulk resistivity values. Mean formation factor value is F = 6.2, ranging from 2.8

to 16.7. Figure 7.102 shows the corresponding formation factor map. With these resistivity values, any correction by clay superficial conductivity adds at most some more 10 to 20%.

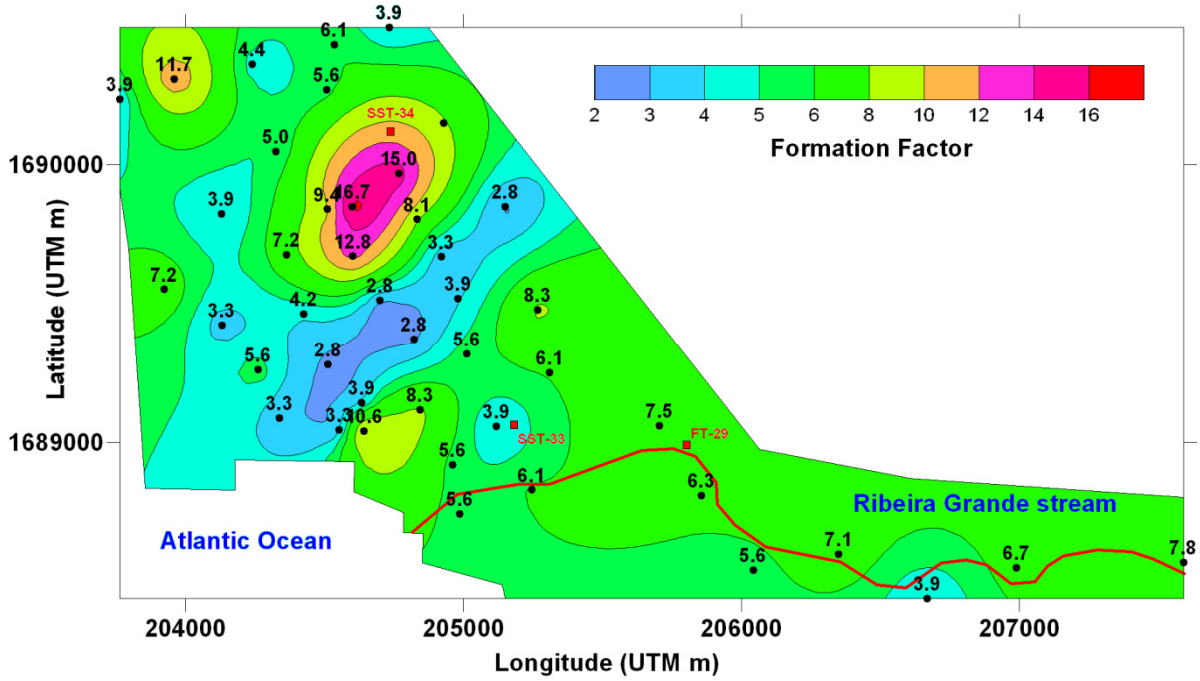

Figure 7.102 – Formation factor map at Tarrafal and Ribeira Grande valley, 30 m below sea level.

It is evident, as previous quasi-3D models showed (figure 7.61), a NE-SW oriented feature at south Chão Bom area. This must be certainly related to the lithologic variation described between SST-33 and SST-34 boreholes (figure 7.53), from deep alluvium layers (at south) to fractured basaltic and pyroclastic formations (at north).

The known transmissivity value at FT-29 is high, around 7000 m^2d^{-1} (fractured basalts). That means also a very high value of 2×10^{-10} m^2 for hydraulic permeability, with 40 m thick aquifer system assumption (and K = 175 $m.d^{-1}$, to a confined aquifer hypothesis). The analogous equivalent grain diameter for this fractured basaltic formation is around 0.5 mm, with fracture internal radius of 50 µm. This gives a porosity range between 15 to 30% and a SSA around 0.01 m^2g^{-1}. If this transmissivity value is over estimated, porosities are necessarily lower. Nevertheless, the high formation factor area at north Chão Bom is probably a low porosity zone (below 10 to 15%) and the orientated feature a higher porosity one (above 25 to 30%).

7.2.5 – Hydrologic parameters

The groundwater recharge rates for each valley were calculated knowing the basin spatial development at each bioclimatic zone and annual mean precipitation rate and recharges percentages (subchapter 6.4.1.). The annual extraction rates have been estimated approximately half of those values at most of the basins (INGRH reports). Half of this groundwater exploitation goes to agriculture land irrigation, which implies a partial water return of 10 to 20% to the soil. The natural water springs discharge can reach also 15 to 20% of annual recharge, and all these major watersheds are linked to the water-supply network of the island.

The amount of incoming and natural discharge to the sea (direct or indirect) is shown at table 7.14, assuming a steady-state flux condition. Daily mean discharge is presented, as also the hydraulic transmissivity and conductivity estimation (at basin scale), with a given shoreline wide and useful thickness of 40 m discharge, and a global 15% porosity, by simple application of Darcy's law.

Table 7.14 – Annual recharge rates and mean hydraulic transmissivities and conductivities values, at surveyed basins.

Hydrologic basin	**recharge/discharge**		**wide**	**T**	***K***
	$m^3.year^{-1}$	**$m^3.d^{-1}$**	**m**	**$m^2.d^{-1}$**	**$m.d^{-1}$**
Tarrafal	0.27×10^6	740	2000	20	0.5
Ribeira Grande	1.76×10^6	4800	1200	200	5
S. Miguel	0.87×10^6	2400	500	120	3
Flamengos	2.0×10^6	5450	400	340	9
Salto	0.7×10^6	1900	250	190	5
Picos	3.9×10^6	10700	850	320	8
Seca	5.8×10^6	15900	450	880	22
S. Domingos	1.4×10^6	3900	400	240	6

Comparison between these conductivity values and those just taken from the boreholes pumping tests, at each surveyed valleys can be done. Except for Ribeira Grande (FT-29 borehole with K = 175 $m.d^{-1}$) all the other hydraulic conductivity values are about of same magnitude; S. Miguel, Flamengos and Salto, K = 0.1 to 15 $m.d^{-1}$. Picos and Seca, K = 1.5 to 15 $m.d^{-1}$ and S. Domingos, K = 1.75 $m.d^{-1}$. Explanation for these differences can be ascribed to a changing scale factor of the hydraulic transmissivity between local and regional flow path behavior and to variable lithologic conditions at both local and regional (or borehole and basin) scales. The mean recharge rates can be overestimated, as detailed spatial parameter's description trough time is not complete and major changes are detected between the basins on the same year. Also, the deeper groundwater discharge may include a substantial fraction of submarine groundwater discharge, directly into the ocean.

7.3 – TEM versus Hydrochemical data

Several chemical analyses have been done from water samples collected at natural springs, wells and boreholes. The most important water elements and compounds were measured to assign water type and saturation conditions. Comparison to bulk modelled resistivity from TEM data is now analysed and relations between both data sets are sought after.

7.3.1 – Groundwater salt origins

The global chemical characteristic of the groundwater at Santiago Island was already presented in chapter 6. Geochemical data sub-set matching the worked valleys (and several others near the sea) show a predominant NaCl water facies. The source of this groundwater type and measured salinity could arise from seawater encroachment inland or by a different process or source mechanism. These later ones could comprise entrapped ancient (fossil) seawater, physic-chemical evaporate rock dissolution, sea-spray accumulation over time, displacement of ancient saline groundwater from adjacent aquifer or aquitard by thermal convection or natural advection, aquitards leaking through existing faults and lately by human related activities (pollution) from sewage effluents and agriculture practices and return flows. All these can contribute to groundwater salt increase, (Custodio, 1997).

The natural and starting point should be the direct comparison to local seawater composition (figure 7.103). Seawater exhibit in general a uniform chemical composition over time, with marked features like the predominance of Cl^- and Na^+ (with molar Na/Cl = 0.86), an excess of chloride over the alkali ions (Na and K) and also Mg^{2+} greatly in excess over Ca^{2+} (about four to five times). Further solute differentiation between ground- and seawater can be done, with the latter one having $Mg > HCO_3 + SO_4$. The ground meteoric waters (even with marine salt's re-solution), have Na > Cl. These waters can carry significant Ca, in excess over $HCO_3 + SO_4$ due to diagenetic carbonate or silicate reactions, (Jones *et al.*, 1999).

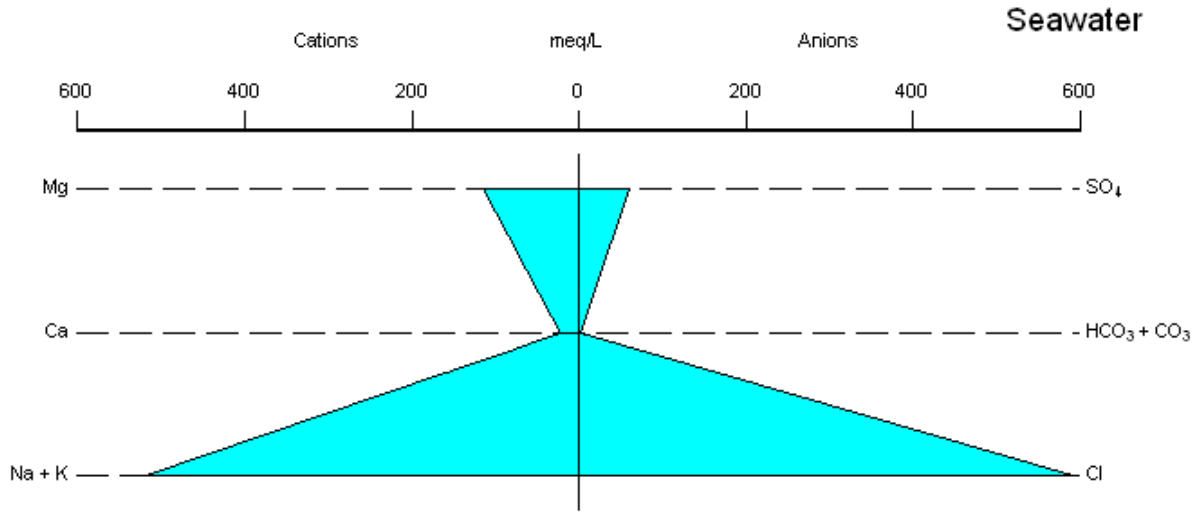

Figure 7.103 – Stiffer diagram of seawater mean major chemical specimens, around Santiago Island.

7.3.2 – Criteria to distinguish saltwater intrusions

As the groundwater salinity can have different sources, the distinction of these different salinization mechanisms is crucial to apply a correct water-resource management program, with discrimination between modern seawater intrusion and relics of entrapped brines within or underlying aquifers. The interpretation of the salinization process should be based upon geological and hydrochemical criteria and data (chemical e isotopic). Several geochemical criteria had been suggested to identify the origin of salinity, especially the detection of seawater intrusion in opposition to other salinity sources in coastal aquifers, (Jones *et al.*, 1999), and should be used altogether to clearly delineate the situation.

Salinity values – because of the contrast between marine and typical continental anion matrices, the clearest indication of a possible seawater intrusion is the increase of Chloride concentration as a proxy for salinity (although other processes may lead to a similar phenomenon). In coastal aquifers, where continuous overexploitation can cause a reduction of the piezometric level, the intrusion of seawater results in a salinity breakthrough. Thus, time-series of chloride concentrations (e.g. at seashore boreholes) can record the early evolution of a relatively rapid salinization process.

Br/Cl ratio – the Bromide to Chloride ratio can be used as a reliable tracer, because both Cl and Br usually behave conservatively (i.e., do not react with the aquifer solid matrix) except in the presence of very high amounts of organic matter (Davis *et al.*, 1998). Seawater (Br/Cl molar ratio of 0.0015) is distinguished from relics of evaporated seawater (hypersaline brines Br/Cr > 0.0015, Dead Sea = 0.011 (Starinsky *et al.*, 1983)), evaporite-dissolution products (below 0.00045) and anthropogenic sources like sewage effluents (Br/Cl above 0.00055) (Vengosh and Pankratov, 1998) or agriculture-return flows (high Br/Cl ratios). (The global analyses of groundwater Br/Cl ratio in Santiago had been written at chapter 6).

Na/Cl ratio – the Na/Cl ratio of saltwater intrusion are usually lower than the marine values (i.e., bellow molar ratio of 0.86). Thus low Na/Cl ratio, combined with other geochemical parameters, can be an indicator of the arrival of saltwater intrusion, even at relatively low Chloride concentrations during the first early stages of salinization. The low Na/Cl ratio of seawater intrusion is distinguishable from the high Na/Cl ratio (above unit), typical of anthropogenic sources, like domestic waste waters. (The global analyses of groundwater Na/Cl ratio in Santiago was also written at chapter 6).

Ca/Mg, Ca/(HCO_3 + SO_4) ratios – as already mention, one of the most conspicuous features of seawater intrusion is the enrichment of Ca over its concentration in seawater. High Ca/Mg and Ca/(HCO_3 + SO_4) ratios (>1) are further indicators of arrival of seawater intrusion. It worth mention, however, that saline water with high Ca can be originated by a different mechanism, not necessarily related to base-exchange reaction and modification of modern seawater.

O and H isotopes – linear correlations are expected from mixing of seawater with ^{18}O depleted groundwater in the correlation of $\delta^{2}H$ versus $\delta^{18}O$ or Cl versus $\delta^{18}O$. Different sources with high salinity (e.g., agriculture return-flows, sewage effluents) would result in different slopes due to evaporation processes that would change the isotopic composition of the saline end-member. (The global analyses of O and H isotopes in Santiago, was also written at chapter 6).

Boron isotopes – The Boron isotopic composition of groundwater can be a powerful tool for discrimination of salinization sources, in particular, distinguishing seawater from anthropogenic fluid such as domestic waste water. The $\delta^{11}B$ values of saltwater intrusion range over 30‰ to the seawater value ($\delta^{11}B$ = 39‰), reflecting mixing of freshwater and seawater in coastal areas.

7.3.3 – Groundwater chemical modification

As the chemical composition of a coastal salty groundwater can deviate significantly from just a simple conservative seawater-freshwater mixing (Appelo and Geirnart, 1991) the criteria mentioned above should be used with care, when looking for groundwater salt origin. Most of this deviation can be ascribed to water-rock interactions (Appelo and Postma, 1993), with the principal one being ion exchange with clay materials (Appelo and Willemsen, 1987) and also carbonate dissolution-precipitation processes (Fidelibus and Tulipano, 1986). When the concern chemical parameters behave conservatively, they can be used to estimate the different source contributions, therefore, the use of Cl, Br and Deuterium. Otherwise they can carry information on the solid matrix extended interaction (e.g. B and Sr isotopes), (Morell *et al.*, 1996). The four basic reactions associated with the hydrogeologic environmental setups of seawater intrusion are; the water mixing, and that includes evaporites associated fluids, carbonate precipitation and dolomitization, ion exchange and silicate (clay) diagenesis, and redox reactions, (Jones *et al.*, 1999).

Mixing – when freshwater and seawater mixing occur, a small amount of this latter is sufficient to overcome and dominate groundwater chemical composition. A 5% seawater contribution outputs groundwater salinity with more than 1 g $Cl.l^{-1}$. As a result, Chloride is used as a very sensitive mixing indicator and also the ionic Na/Cl ratio of seawater will dominate its chemical composition (assuming conservative behaviour). Stables O and H isotopes are also used to ascribe the mixing amount, as freshwater is in general depleted in both ^{18}O and ^{2}H relative to seawater (Manzano *et al.*, 1990 and Izbicki, 1996).

Exchange reactions in water-rock interaction – cation exchange in seawater intrusion plays a key role, and has been treated and detailed by Appelo and Postma (1993). The freshwater is usually dominated by Ca^{2+} and HCO_3^- ions (mostly from calcite dissolution). Therefore, the cation exchangers in aquifers such as clay minerals, organic matter or fine grain rock materials, have mostly Ca^{2+} absorbed at their surfaces. In contrast to this, the sediments in contact with seawater have Na^+ as the most prevalent absorbed cation (Sayles and Mangelsdorf, 1977). When seawater intrudes on a coastal freshwater aquifer, ion Na^+ replaces part of the Ca^{2+} ion at the solid surface. In such reaction, Na^+ is taken up by the solid phase, and Ca^{2+} is released and the solute composition changes from NaCl to $CaCl_2$

facies (Custodio, 1987, Appelo and Postma, 1993). Moreover, as the Chloride ion concentration remains unaffected by this trade reaction, it can be regarded as a reference parameter, as mention before. Consequently, as seawater intrudes on coastal aquifers containing freshwater, the Na/Cl ratio decreases and the (Ca + Mg)/Cl ratio increases. Under such conditions, the enrichments in Calcium and Magnesium should be balanced by the depletion of Sodium. Accordingly, the decrease in Na/Cl ratio balances the increase in (Ca + Mg)/Cl ratio (Custodio, 1987). Upon inflow of freshwater the reverse process takes place, with the increase of the Na/Cl ratio and a decrease of the (Ca + Mg)/Cl ratio value, and formation of $NaHCO_3$ fluid facies. In addition to the expected development of a $CaCl_2$ water type at the seawater front, a significant increase in Mg^{2+} also takes place. These increased levels are congruent at first, but when the Ca from exchange runs out, the trends of the two ion concentrations diverge afterwards - the Ca^{2+} decreases and Mg^{2+} increases towards its higher concentration value in seawater. In fact, because of the relatively small amount of exchanged Ca compared to even the relatively low Ca level maintained by $CaCO_3$ saturation of the saline water, the decrease of Ca content as already begun before the Chloride reaches the seawater concentrations (Appelo and Postma, 1993).

It is also known that when seawater intrusion into groundwater is primarily by diffusion rather than advection, and the cation exchange capacity of the sediment are low, the effects of ion exchange tend to be considerably reduced, and the resulting water compositions will resemble a simple mixture of fresh and saline water (Appelo and Postma, 1993).

Carbonate Diagenesis and Dolomitization – Plummer (1975) and Wigley and Plummer (1976) have shown the effects of speciation in the mixing of dilute carbonate groundwater with seawater when coastal aquifers are composed of some carbonate materials, either of calcareous clastics or of limestone. The mixing of dilute groundwater in equilibrium with calcite with common seawater that is supersaturated with respect to calcite can produce solutions of intermediate composition that are undersaturated with respect to calcite. Besides this, products in the mixture might be undersaturated with respect to calcite but supersaturated with respect to dolomite, as several authors have shown (Jones *et al.*, 1999 and references thereafter). The extent of this calcite undersaturation and dolomite supersaturation, is strongly dependent on temperature and also heavily dependent on the solubility of dolomite, which is stronger for very finned grain forms. The dolomitization process, in which calcite and dolomite are in equilibrium results in a progressive enrichment of Ca over Mg in solution (i.e., Ca/Mg ratio increases). Therefore, saline water affected by dolomitization processes should be characterized by high Ca content and by a CaCl signature (i.e., $Ca/(HCO_3 + SO_4) > 1$) (Starinsky *et al.*, 1983; Carpenter, 1978). The formation of dolomite in modern marine sediments and sediment burial to shallow depths is strongly controlled by the reaction kinetic that is slow even at high supersaturation, (Morse and Mackenzie, 1990).

Adsorption and organic matter reduction – One of the processes that modifies the seawater intrusion chemistry is adsorption onto clay minerals in the host aquifer. The elements that are sensitive to adsorption process are Potassium, Boron and Lithium. The adsorption process resulted in low K/Cl, B/Cl and Li/Cl ratios in the residual saline groundwater relative to the marine ratios (of K/Cl = 0.02 at seawater).

The seawater encroachment and the formation of a relatively static interface zone between overlying fresh and underlying saline water, may produce local low redox conditions, due to the decomposition of dissolved organic matter, of organic-rich sediment or fine suspended organic particulate, as mention by Schoeller (1956), Custodio and Liamas (1976), Hem (1985). According to Custodio *et al*., (1987), this process will cause changes in pH, and the reduction of dissolved sulfate to H_2S, resulting in low SO_4/Cl ratio. These changes shift the calcium carbonate equilibria and most commonly cause dissolution. The resulting increase in the Calcium content is frequentiy masked by exchange of Ca^{2+} for Mg^{2+} or Na^{+} on clays previously equilibrated with more seawater like cation matrices. Intense and episodic nature of rainfall, lack of soil cover, well developed fractures and fissures and shallow depth of the vadose zone, all contribute to significant inputs of organic matter to the freshwater lens, Whitaker and Smart (2007). This generates potential for dissolution considerably greater than that predicted solely by simulations of inorganic mixing between basal freshwater lens waters and underlying saline groundwaters.

Fossil Seawater intrusion – in the coastal areas, if entrapped fossil seawater exists at unflushed parts of the aquifer, they can also affect the quality of adjacent fresh groundwater. Fossil seawater could have originated from past invasions of coastal aquifers accompanying the sea level rises. However, it has been difficult do date this saline groundwater and to evaluate the timing and time rate of seawater intrusion. The evidence for ancient seawater is primarily from tritium and radiocarbon dating, as ascribed at chapter 6. The ^{l4}C content of fresh and saline groundwater is a result of complex contributions from different sources, including the original seawater, soil CO_2, carbon derived from dissolution of the carbonate matrix, and carbon derived from decomposition of organic matter. But the ^{14}C budget can be affected by the processes occurring in seawater encroachment. These include interaction of interstitial water with bottom sea sediments and with the aquifer matrix. Consequently, ^{14}C interpretation requires additional chemical and ^{13}C supporting data. Another indirect evaluation of the age of saline groundwater is $\delta^{18}O$ value of saline water. Groundwater with depleted ^{18}O lower than that of modern atmospheric recharge reflects past replenishment when the $\delta^{18}O$ of precipitation was lower. Also, groundwater dissolved noble gases (He, Ne, Ar, Kr and Xe) analyses can be applied to support and adds constraints to the radiocarbon data (Aeschbach-Hertig *et al*., 1999).

7.3.4 – Hydrochemical data at S. Domingos valley

At S. Domingos valley, groundwater chemical data have been taken from two boreholes; the FT-40 and the FT-42, at two epochs, before (June) and after (December) the traditional rain season. Table 7.15 includes some values and ratios related to water quality. Borehole FT-40 is located at mid TEM profile and FT-42 past last inland TEM sounding. Both have NaCl water types (figures 7.104 to 7.106). The measured EC, TDS, pH and Chloride are almost identical (exception for a major Cl decrease at FT-42). Both groundwaters are undersaturated relative to Calcite and Aragonite. The TDS and Chloride amounts are above the freshwater threshold limit of 0.5 $g.L^{-1}$. These values are not directly related to present time seawater intrusion, according to several ratios values. Those high values can have two different origins:: can be linked to some upwelling of trapped ancient seawater (by a diffusion

process or due to the overexploitation) and mixing into the shallow groundwater, by natural discharge from mainland, or by sewage effluents and agriculture activities, as Nitrate values are high and the pH decrease can be from organic matter origin. The measured variations agree with the shallow waters flush in the rainy season. The answer is that most certainly both situations are taking place at those places as TEM resistivity models had shown, a deeper high conductive layer exists and also because villages are placed around and above the valley. The intense overexploitation as a mean to explain the increasing salinization by mixing is taken as a hypothesis by Carreira *et al.* (2010), as a result of geochemical and isotopic analysis study of 36 inland groundwater samples. That includes also the Tritium content at FT-40 water, which is null and point to a higher residence time.

Table 7.15 – S. Domingos valley hydrochemical borehole data, (UnS - UnderSaturated).

Parameter	FT-40		FT-42	
	Jun.	Dec.	Jun.	Dec.
EC μS.cm^{-1}	1394	1400	1418	1420
TDS mg.L^{-1}	804	793	879	887
pH	7.2	7.1	7.0	6.9
Cl mg.L^{-1} (% TDS)	283.6 (35)	262.3 (33)	382.9 (43)	241.1 (27)
NO_3 mg.L^{-1}	37.5	21.5	91.2	64.4
Na/Cl	0.74	0.87	0.37	1.01
K/Cl	0.029	0.038	0.021	0.034
SO_4/Cl	0.059	0.066	0.038	0.042
Ca/Mg	0.736	0.444	0.832	0.484
(Ca + Mg)/Cl	0.529	0.491	0.407	0.558
Ca/(HCO_3 + SO_4)	0.577	0.291	0.864	0.258
Calcite	UnS	UnS	UnS	UnS
Aragonite	UnS	UnS	UnS	UnS

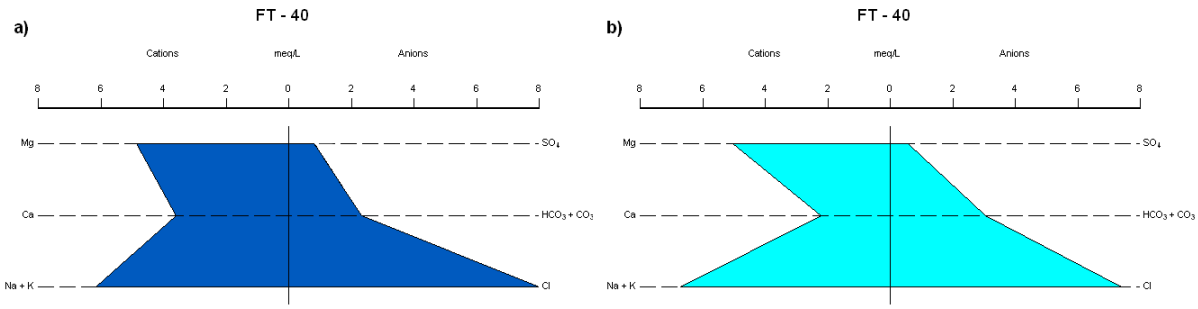

Figure 7.104 – Stiffer diagram of FT-40 water, at June a) and December b), S. Domingos valley.

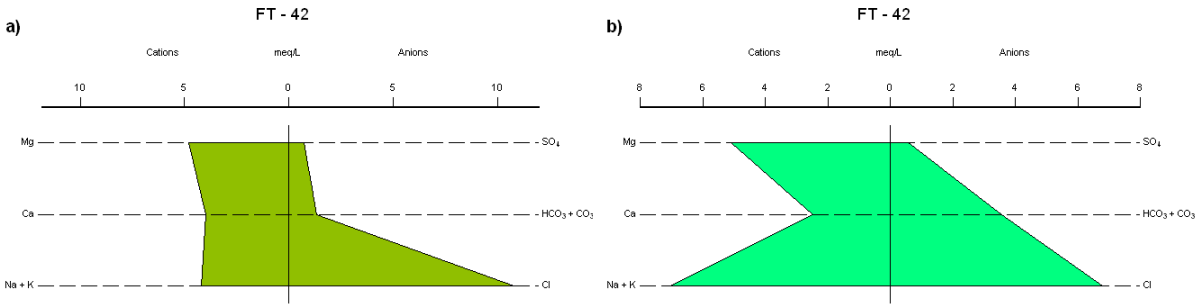

Figure 7.105 – Stiffer diagram of FT-42 water, at June a) and December b), S. Domingos valley.

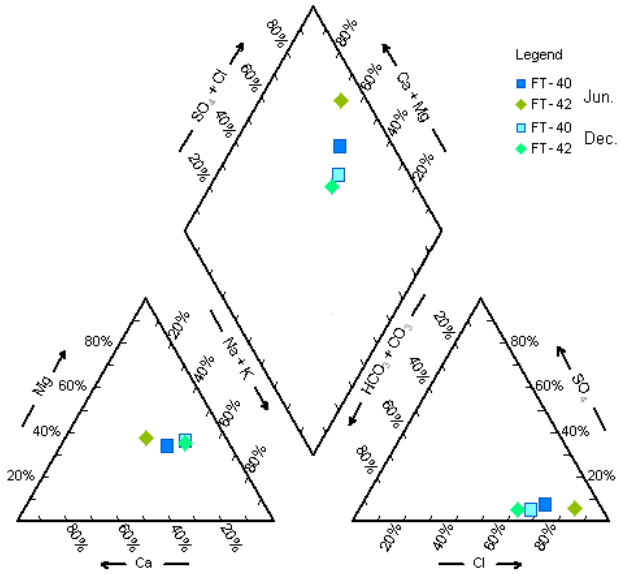

Figure 7.106 – Piper diagram of FT-40 and FT-42 waters, at both epochs, S. Domingos valley.

7.3.5 – Hydrochemical data at Seca and Picos valleys

At Seca valley, groundwater chemical analysis exists at three boreholes; FT-9 near mid TEM profile and FT-63 and FBE-169 near the last TEM sounding, (table 7.16). All are a NaCl water type with also a major Mg content (figures 7.107 to 7.110). The measured EC, TDS, pH and Chloride does not change significantly over time. All are undersaturated of Calcite and Aragonite. The measured TDS values are slightly above 0.5 $g.L^{-1}$. The majority of Na/Cl ratios are near the unit value and the ratios with Ca are low. That means that the salinity is not related to present time seawater intrusion whatsoever. The mechanism is similar to that one found in S. Domingos valley, but to a lesser extent. At Seca, agriculture practices are more intense and salinity seems to be related also to anthropogenic factors (high values of Nitrate are detected). Nevertheless, the Magnesium by Calcium ions trade can be also masking the water mixing from deep conductive salty layer.

Table 7.16 – Seca valley hydrochemical borehole data, (UnS - UnderSaturated).

Parameter	FT-9		FT-63		FBE-169	
	Jun.	Dec.	Jun.	Dec.	Jun.	Dec.
EC $\mu S.cm^{-1}$	1020	1260	1029	1150	1192	1230
TDS $mg.L^{-1}$	574	668	798	701	651	759
pH	7,1	7.0	7.1	7.0	7.1	7.0
Cl $mg.L^{-1}$ (% TDS)	141.8 (25)	157.0 (24)	156.0 (20)	170.4 (24)	184.3 (28)	199.0 (26)
NO_3 $mg.L^{-1}$	59.0	53.6	53.6	48.3	64.4	53.6
Na/Cl	1.06	0.97	1.06	1.07	0.81	0.99
K/Cl	0.051	0.057	0.058	0.058	0.054	0.059
SO_4/Cl	0.095	0.107	0.086	0.118	0.091	0.101
Ca/Mg	0.536	0.614	0.499	0.538	0.417	0.457
(Ca + Mg)/Cl	0.629	0.758	0.627	0.665	0.599	0.612
$Ca/(HCO_3 + SO_4)$	0.299	0.317	0.300	0.271	0.299	0.254
Calcite	UnS	UnS	UnS	UnS	UnS	UnS
Aragonite	UnS	UnS	UnS	UnS	UnS	UnS

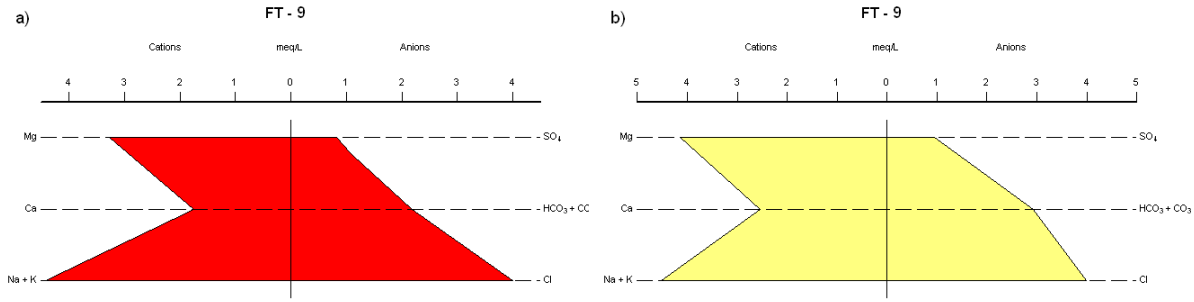

Figure 7.107 – Stiffer diagram of FT-9 water, at June a) and December b), Seca valley.

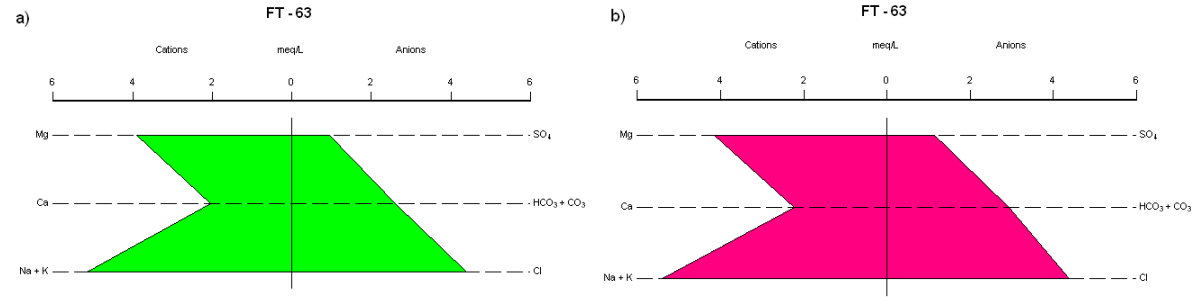

Figure 7.108 – Stiffer diagram of FT-63 water, at June a) and December b), Seca valley.

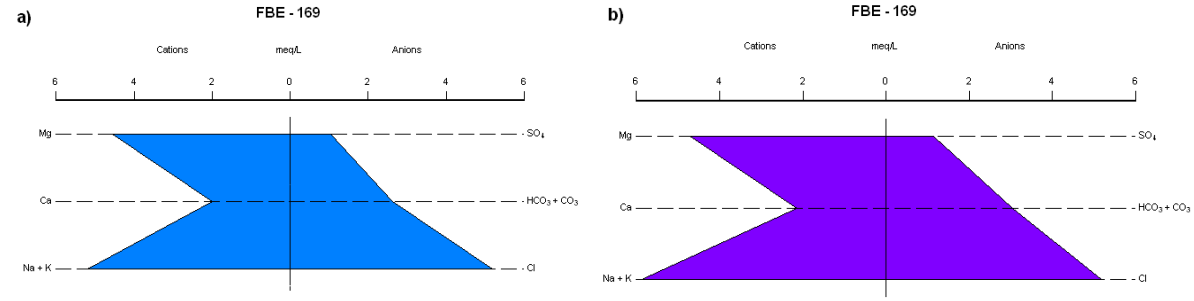

Figure 7.109 – Stiffer diagram of FBE-169 water, at June a) and December b), Seca valley.

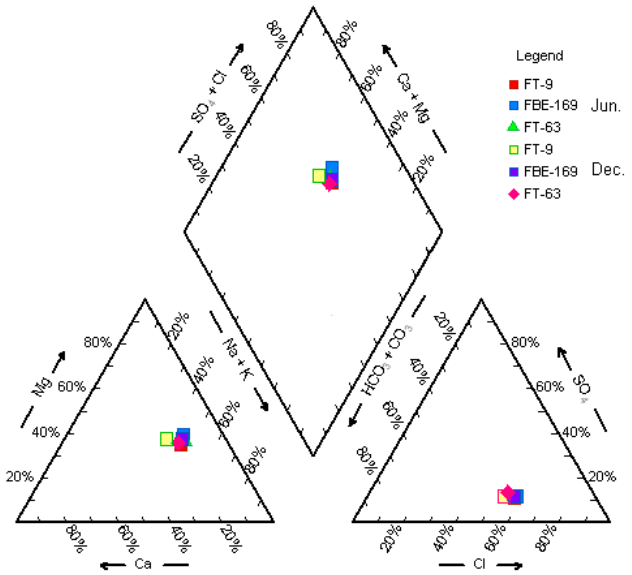

Figure 7.110 – Piper diagram of FBE-169, FT-63 and FT-9 waters, at both epochs, Seca valley.

At Picos valley, groundwater chemical analysis exists at three boreholes; FT-59 is just beyond last TEM sounding, and SP-34 and SP-39 at mid and near start TEM profile, respectively, at north, above the valley, (table 7.17). Water facies is different; the water at SP-34 is of NaCl type while the other two are of Na-, Mg- or Ca-HCO_3 types, (figures 7.111 to 7.113). In all of them, TDS values exceed the limit of 0.5 $g.L^{-1}$. SP-39 groundwater is of $NaHCO_3$ type and supersaturated of Calcite and approximately saturated of Aragonite. Although being the nearest to shoreline, it is outside the valley, and its salinization comes from a water-rock interaction process. Water facies in SP-34 and FT-59 is compatible with some deep salty water mixing. Besides this, the mixing may also indicate an influence of the agriculture activities. Tritium value is null at borehole SP-39 and less than 1 T.U. at borehole FT-59, that implies several decades of residence time (Carreira *et al.*, 2010).

Table 7.17 – Picos valley hydrochemical borehole data,
(~S - approximately Saturated, SS - SuperSaturated).

Parameter	FT-59		SP-34	SP-39
	Jun.	Dec.	Aug.	Aug.
EC $\mu S.cm^{-1}$	913	950	1297	760
TDS $mg.L^{-1}$	699	649	894	554
pH	7.0	7.1	6.9	7.9
Cl $mg.L^{-1}$ (% TDS)	113.4 (16)	118.0 (18)	181 (20)	55 (10)
NO_3 $mg.L^{-1}$	37.5	32.2	24.5	43.0
Na/Cl	1.06	1.03	0.77	1.60
K/Cl	0.079	0.084	0.038	0.181
SO_4/Cl	0.089	0.114	0.051	0.013
Ca/Mg	0.956	1.046	0.753	1.021
(Ca + Mg)/Cl	1.149	1.032	0.129	1.018
Ca/(HCO_3 + SO_4)	0.330	0.371	0.078	0.430
Calcite	~S	~S	UnS	SS
Aragonite	UnS	UnS	UnS	~S

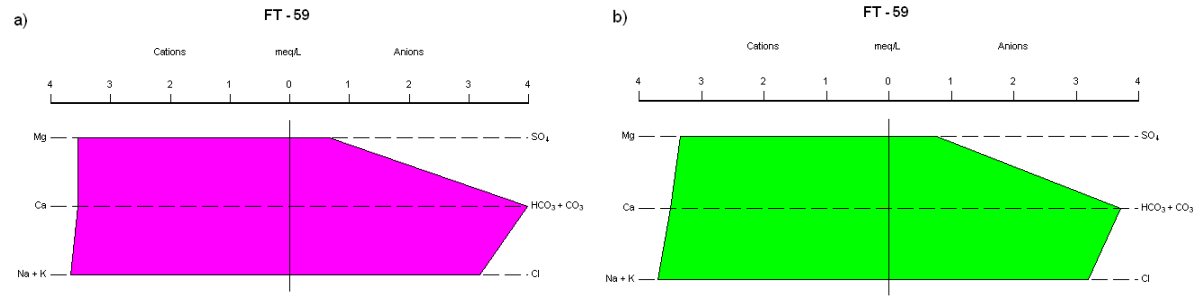

Figure 7.111 – Stiffer diagram of FT-59 water, at June a) and December b), Picos valley.

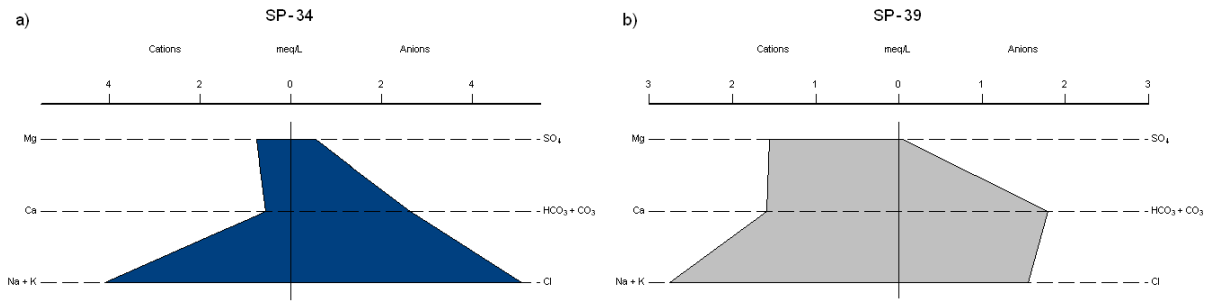

Figure 7.112 – Stiffer diagram of SP-34 water a) and SP-39 water b), Picos valley.

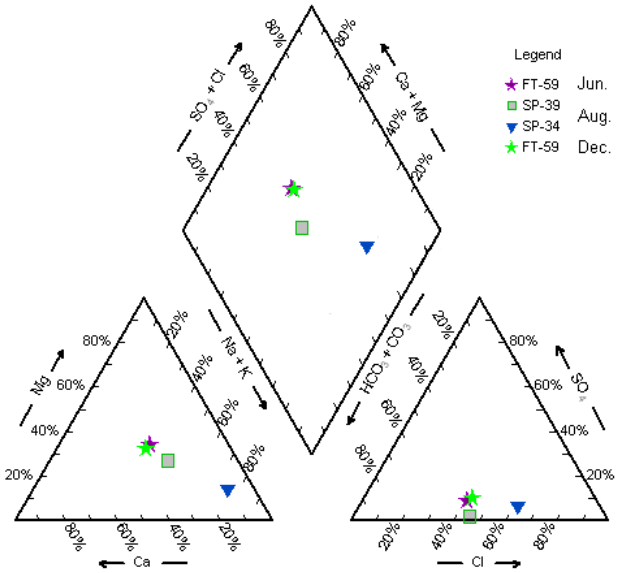

Figure 7.113 – Piper diagram of FT-59 waters, at both epochs, SP-34 and SP-39 waters, Picos valley.

7.3.6 – Hydrochemical data - Salto, Flamengos and S. Miguel valleys

At Salto valley, groundwater chemical analysis exists from two places; well 52-81 near sea and near the beginning of the TEM profile, and borehole FT-47 at mid profile, (table 7.18). The water type in the well is MgCl to CaCl and in the borehole is NaCl type, (figures 7.114 to 7.116). All samples have TDS values above the 0.5 $g.L^{-1}$ threshold. At the well, the ratios indicate a fresh-seawater mixing with Na exchange. Saturation of $CaCO_3$ is high before rain season, however, all ratios and values are in accordance with the freshwater rainy flush, after rain season. A dolomitization process seems to happen also. The water salinity is related to a water-rock interaction with agriculture activity's inputs, and it's not to exclude a deep salty layer influence too. It is very similar to S. Domingos valley.

Table 7.18 – Salto valley hydrochemical well and borehole data,
(~S - approximately Saturated, SS - SuperSaturated).

Parameter	52-81		FT-47
	Jun.	Dec.	Jun.
EC $\mu S.cm^{-1}$	7300	2760	1622
TDS $mg.L^{-1}$	6048	1454	949
pH	7.0	7.2	7.2
Cl $mg.L^{-1}$ (% TDS)	2297.2 (38)	758.6 (52)	297.8 (31)
NO_3 $mg.L^{-1}$	2.7	16.1	48.3
Na/Cl	0.26	0.38	0.91
K/Cl	0.014	0.034	0.069
SO_4/Cl	0.022	0.018	0.079
Ca/Mg	0.763	1.014	0.270
(Ca + Mg)/Cl	0.509	0.474	0.514
$Ca/(HCO_3 + SO_4)$	4.429	2.530	0.213
Calcite	SS	~S	UnS
Aragonite	~S	UnS	UnS

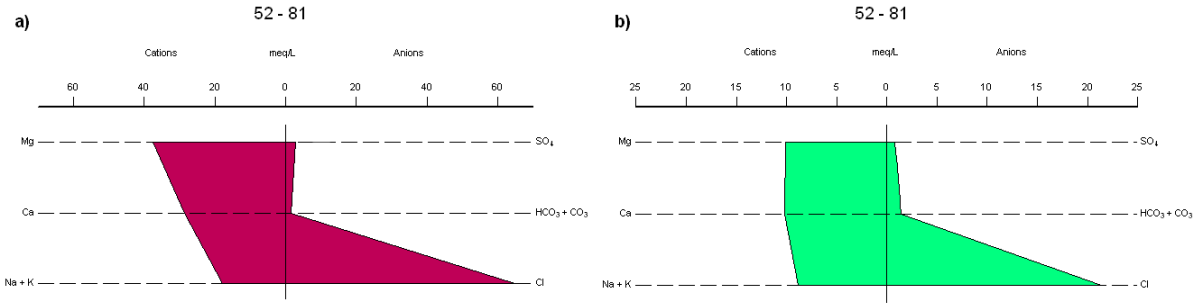

Figure 7.114 – Stiffer diagram of 52-81 water, at June a) and December b), Salto valley.

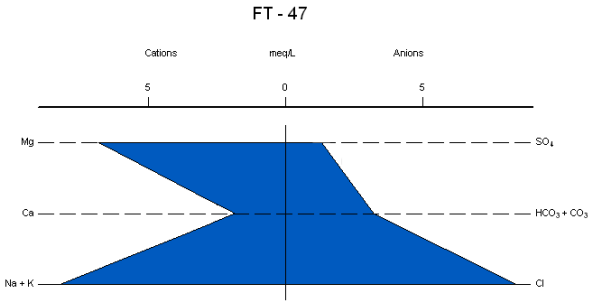

Figure 7.115 – Stiffer diagram of FT-47 water, Salto valley.

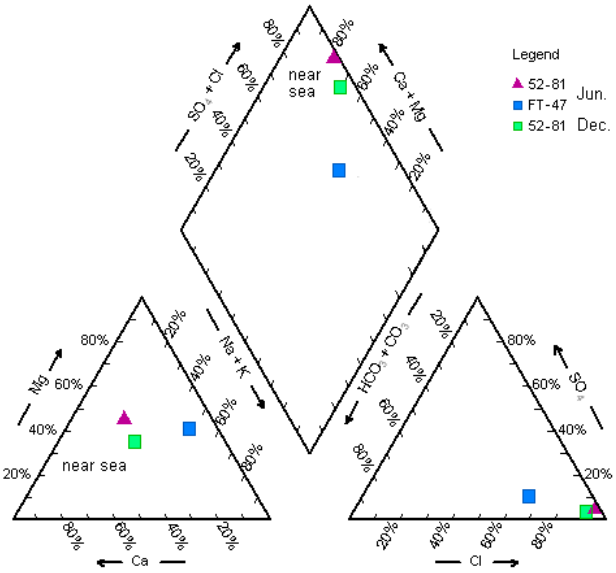

Figure 7.116 – Piper diagram of 52-81 water, at both epoch, and FT-47 water, Salto valley.

At Flamengos valley, hydrochemical analyses were taken at four boreholes; FT-62 and SP-12 near the coastline and near the beginning of the TEM profile, and FBE-145 and FT-5 further upstream beyond last TEM sounding, (table 7.19a and b). Again, all water samples have TDS values above the 0.5 $g.L^{-1}$. Water from FT-62 is MgCl changing to NaCl type, and nearby SP-12 the water is of NaCl type, wowing to salty water mixing and also to some sewage effluent effects. The inland waters are less mineralized than seashore ones and are of NaCl type and enriched with HCO_3 due to water-rock interaction process. The seasonal flush seems to decrease NaCl content from the possible deep salty layer, by mixing with shallow inland freshwater, (figures 7.117 to 7.121).

Table 7.19a – Flamengos valley hydrochemical borehole data, (UnS - UnderSaturated).

Parameter	FT-62		SP-12		FBE-145	
	Jun.	Dec.	Jun.	Dec.	Jun.	Dec.
EC µS.cm^{-1}	1975	1629	2680	2520	1380	1202
TDS mg.L^{-1}	1067	995	1383	1245	953	761
pH	6.8	6.9	6.8	6.8	7.3	7.2
Cl mg.L^{-1} (% TDS)	418.3 (39)	326.1 (33)	638.1 (46)	567.2 (46)	226.9 (24)	170.2 (22)
NO_3 mg.L^{-1}	42.9	37.5	42.9	37.5	5.4	21.5
Na/Cl	0.50	0.79	0.64	0.62	1.65	1.52
K/Cl	0.045	0.083	0.032	0.016	0.186	0.053
SO_4/Cl	0.048	0.052	0.047	0.047	0.118	0.079
Ca/Mg	0.886	0.465	0.570	0.306	0.451	0.233
(Ca + Mg)/Cl	0.569	0.465	0.415	0.362	0.281	0.462
Ca/(HCO_3 + SO_4)	0.894	0.283	1.023	0.386	0.097	0.080
Calcite	UnS	UnS	UnS	UnS	UnS	UnS
Aragonite	UnS	UnS	UnS	UnS	UnS	UnS

Table 7.19b – Flamengos valley hydrochemical borehole data, (~S - approximately Saturated).

Parameter	FT-5	
	Jun.	Dec.
EC µS.cm^{-1}	1218	769
TDS mg.L^{-1}	931	631
pH	7.2	7.5
Cl mg.L^{-1} (% TDS)	163.1 (18)	120.5 (19)
NO_3 mg.L^{-1}	16.1	16.1
Na/Cl	2.39	1.13
K/Cl	0.066	0.090
SO_4/Cl	0.309	0.112
Ca/Mg	1.261	0.364
(Ca + Mg)/Cl	0.373	0.594
Ca/(HCO_3 + SO_4)	0.154	0.102
Calcite	UnS	~S
Aragonite	UnS	UnS

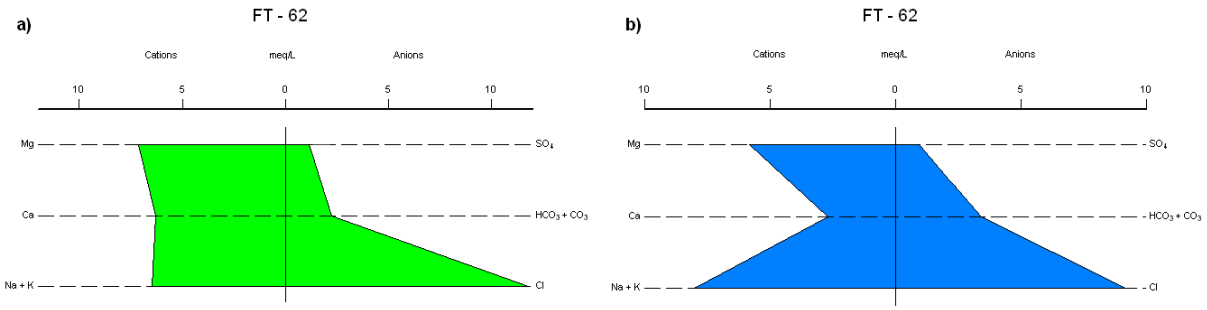

Figure 7.117 – Stiffer diagram of FT-62 water, at June a) and December b), Flamengos valley.

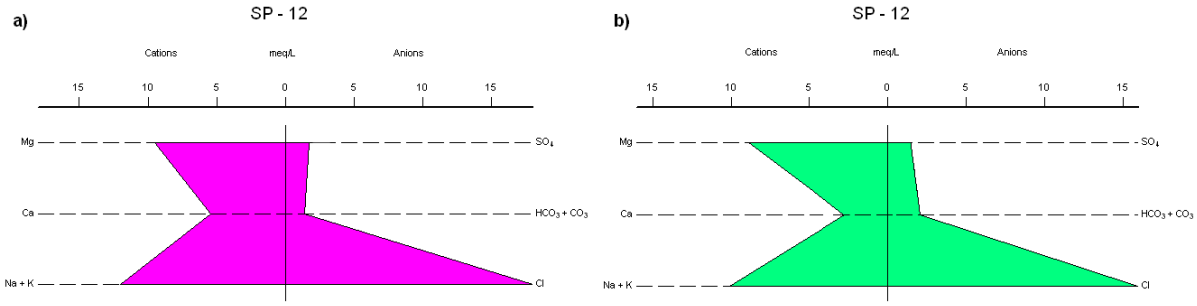

Figure 7.118 – Stiffer diagram of SP-12 water, at June a) and December b), Flamengos valley.

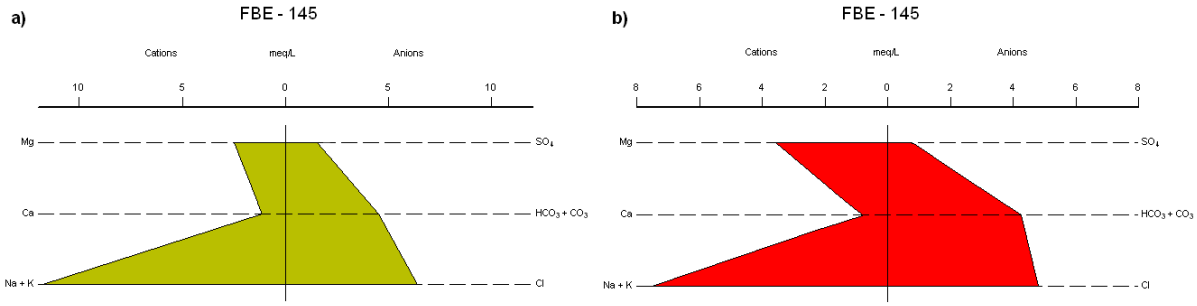

Figure 7.119 – Stiffer diagram of FBE-145 water, at June a) and December b), Flamengos valley.

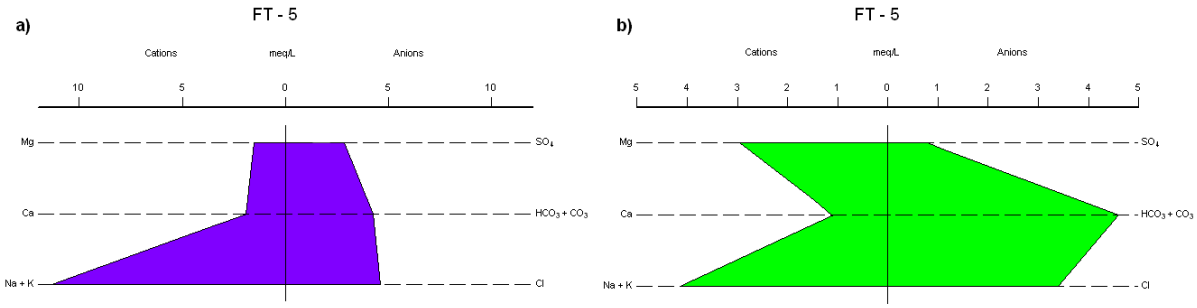

Figure 7.120 – Stiffer diagram of FT-5 water, at June a) and December b), Flamengos valley.

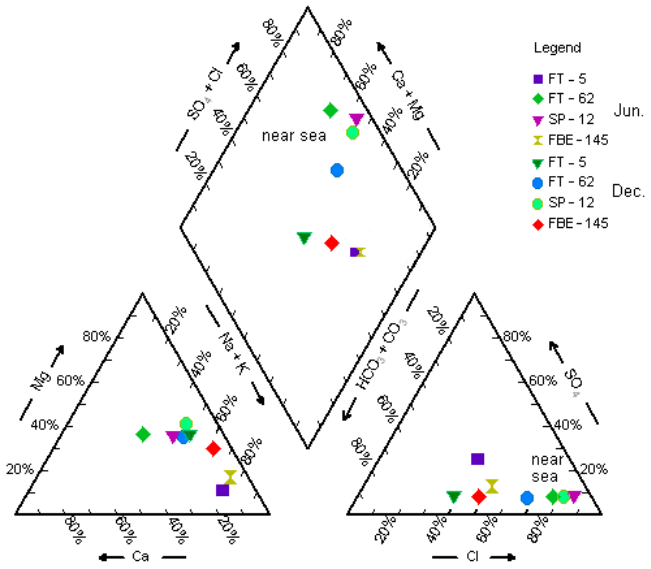

Figure 7.121 – Piper diagram of borehole's data at both epochs, Flamengos valley.

At S. Miguel valley hydrochemical analyses exist at just one well near the coastline, at the beginning of the TEM profile. The water from 52-29 well is of MgCl type, with high salinity and Chloride content (table 7.20). It is a mixture of seawater with inland freshwater, and it is approximately saturated before the seasonal flush, (figure 7.122 and 7.123).

Table 7.20 – S. Miguel valley hydrochemical well data,
(~S - approximately Saturated).

Parameter	52-29	
	Jun.	Dec.
EC $\mu S.cm^{-1}$	2500	2240
TDS $mg.L^{-1}$	1527	1254
pH	6.9	6.7
Cl $mg.L^{-1}$ (% TDS)	609.7 (40)	524.7 (42)
NO_3 $mg.L^{-1}$	21.5	37.5
Na/Cl	0.52	0.55
K/Cl	0.027	0.041
SO_4/Cl	0.044	0.051
Ca/Mg	0.879	0.430
(Ca + Mg)/Cl	0.546	0.444
$Ca/(HCO_3 + SO_4)$	0.768	0.458
Calcite	~S	UnS
Aragonite	~S	UnS

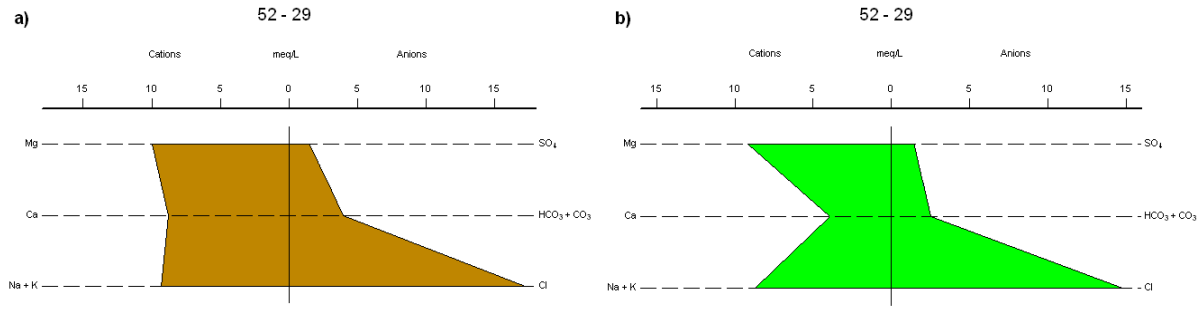

Figure 7.122 – Stiffer diagram of 52-29 water, at June a) and December b), S. Miguel valley.

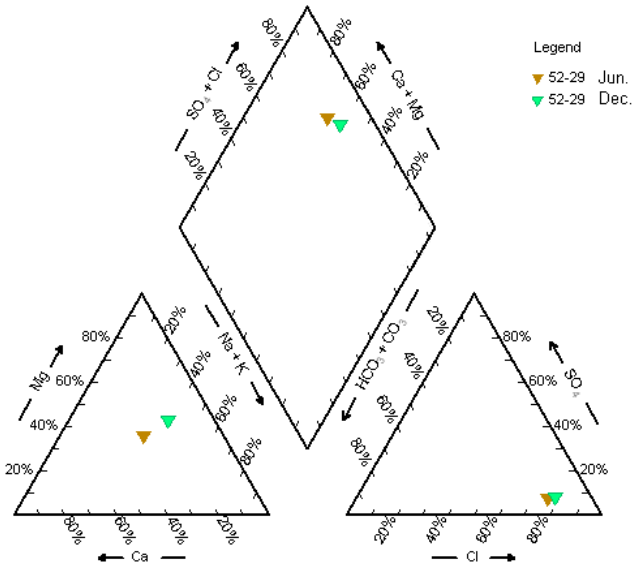

Figure 7.123 – Piper diagram of well's data at both epochs, S. Miguel valley.

At all these three valleys, the Tritium content is very low or null and point to older waters (residence time of decades) or mixing with present day shallow ones, (Carreira *et al.*, 2010).

7.3.7 – Hydrochemical data at Tarrafal and Rib. Grande valley

At Tarrafal and Ribeira Grande valley, five hydrochemical analysis exists; three boreholes and two wells. These later ones are located at Chão Bom (Tarrafal) near the sea. Waters from these wells together with the borehole in Chão Bom have high to very high EC and salinity values. The two nearby boreholes in Ribeira Grande valley are 1 km from the coastline. All the water samples are of NaCl type, and surpass the 0.5 $g.L^{-1}$ TDS limits, (table 7.21 and 7.22). The groundwater in Chão Bom is a seawater-freshwater mixing with salinity decreasing after the rainy season. The seawater amount ranges from 4% at borehole up to 7.5% at wells. TDS content in Ribeira Grande is smaller because boreholes are less deep, inland flow is higher and salinity comes most certainly from a water-rock interaction process. Anthropogenic influence seems to be also present, especially at borehole FT-27 as both boreholes are nowadays within the village, (figures 7.124 to 7.129). Eastwards of Chão Bom the Tritium value in water samples is bellow the 1 T.U., pointing again to high residence times (Carreira *et al.*, 2010).

Table 7.21 – Tarrafal (Chão Bom) hydrochemical borehole and well data, (UnS - UnderSaturated, ~S - approximately Saturated).

Parameter	SST-34		48-22		48-09
	Jun.	Dec.	Jun.	Dec.	Dec.
EC $\mu S.cm^{-1}$	4380	2706	4870	4002	6140
TDS $mg.L^{-1}$	2414	1935	2713	2668	3324
pH	6.8	6.8	7.3	7.0	7.0
Cl $mg.L^{-1}$ (% TDS)	1233.7 (51)	836.6 (43)	1375.5 (51)	1276.2 (48)	1588.2 (48)
NO_3 $mg.L^{-1}$	16.1	21.5	5.4	8.0	2.7
Na/Cl	0.82	0.91	0.80	0.75	0.82
K/Cl	0.034	0.033	0.034	0.014	0.017
SO_4/Cl	0.004	0.044	0.044	0.039	0.040
Ca/Mg	0.421	0.379	0.648	0.625	0.460
(Ca + Mg)/Cl	0.240	0.271	0.256	0.265	0.300
$Ca/(HCO_3 + SO_4)$	0.689	0.320	1.183	0.555	0.645
Calcite	UnS	UnS	~S	~S	~S
Aragonite	UnS	UnS	UnS	~S	UnS

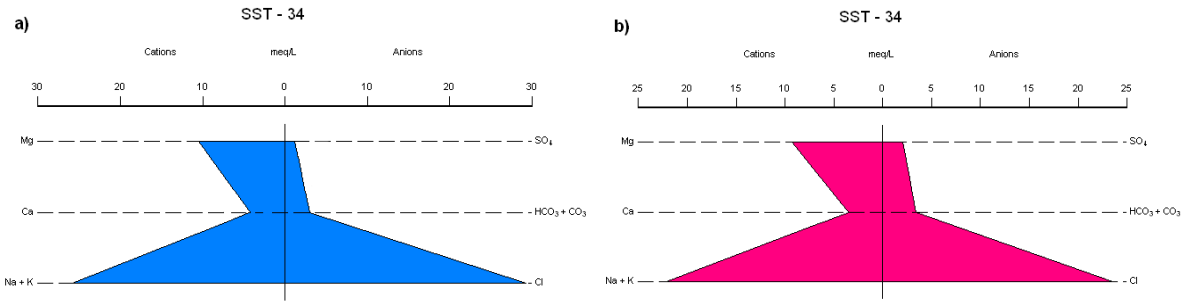

Figure 7.124 – Stiffer diagram of SST-34 water, at June a) and December b), Chão Bom.

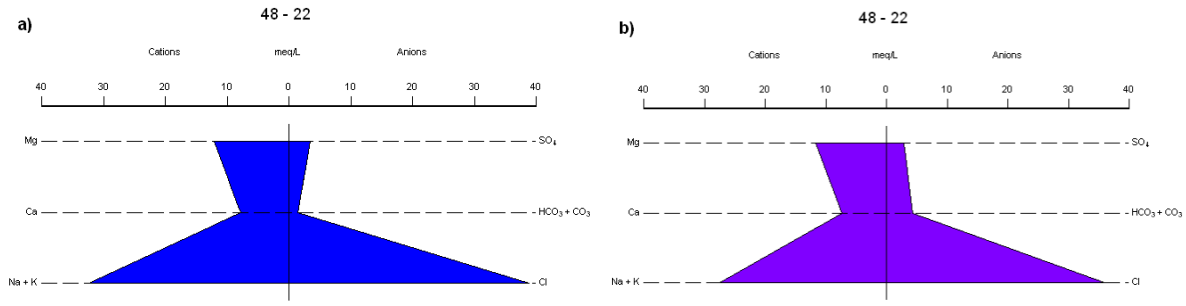

Figure 7.125 – Stiffer diagram of 48-22 well's water, at June a) and December b), Chão Bom.

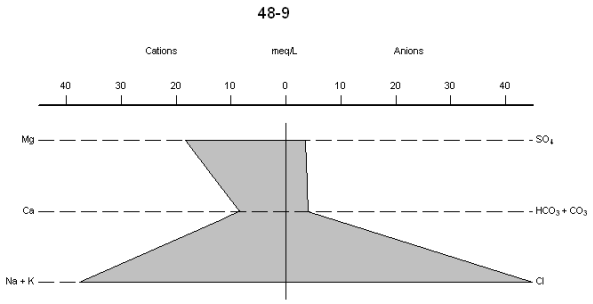

Figure 7.126 – Stiffer diagram of 48-9 well's water, December, Chão Bom.

Table 7.22 – Rib. Grande valley hydrochemical borehole data,
(~S - approximately Saturated, SS - SuperSaturated).

Parameter	FT-27		FT-29	
	Jun.	Dec.	Jun.	Dec.
EC μS.cm^{-1}	694	640	920	963
TDS mg.L^{-1}	470	540	623	670
pH	7.0	7.0	7.8	7.0
Cl mg.L^{-1} (% TDS)	98.3 (21)	99.3 (18)	191.4 (31)	170.2 (25)
NO_3 mg.L^{-1}	32.2	37.5	10.7	16.1
Na/Cl	1.36	1.53	1.10	1.34
K/Cl	0.154	0.518	0.099	0.138
SO_4/Cl	0.068	0.068	0.035	0.039
Ca/Mg	0.953	0.763	0.677	0.776
(Ca + Mg)/Cl	0.614	0.428	0.348	0.400
Ca/(HCO_3 + SO_4)	0.296	0.155	0.232	0.210
Calcite	UnS	UnS	SS	UnS
Aragonite	UnS	UnS	~S	UnS

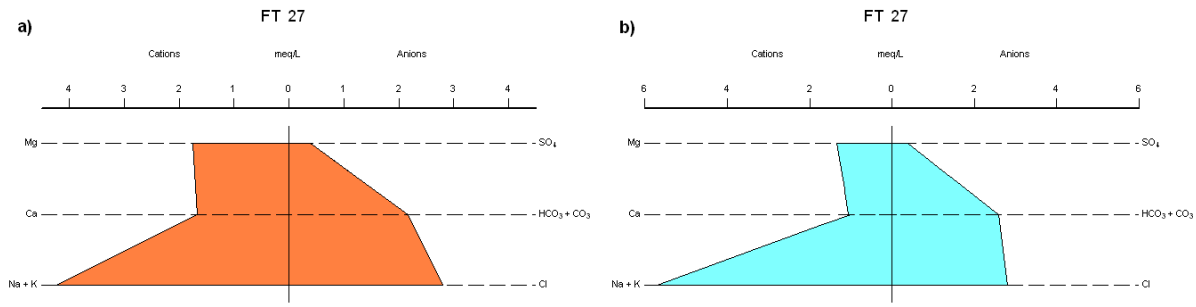

Figure 7.127 – Stiffer diagram of FT-27 water, at June a) and December b), Ribeira Grande valley.

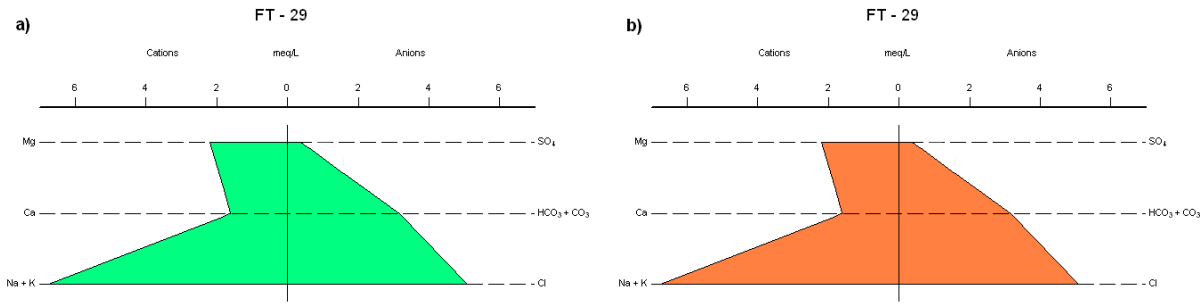

Figure 7.128 – Stiffer diagram of FT-29 water, at June a) and December b), Ribeira Grande valley.

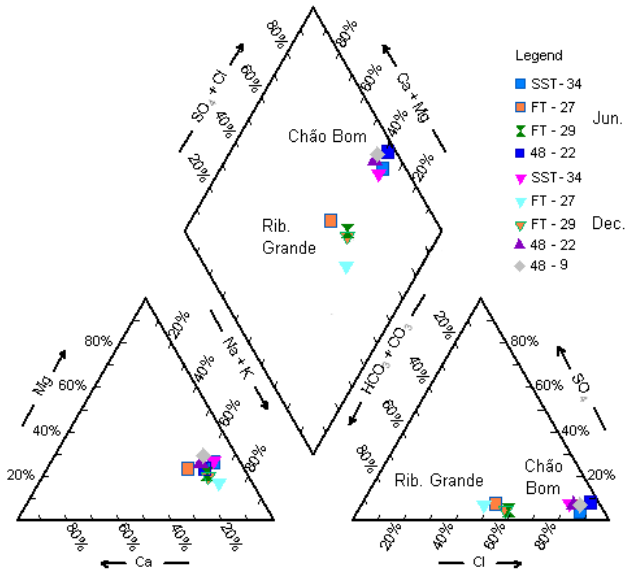

Figure 7.129 – Piper diagram of borehole and wells data at both epochs, Chão Bom and Ribeira Grande.

7.3.8 – Resistivity to hydrochemical data relations

The hydrochemical analysis showed that one of the major and the most abundant anion is Chloride, which is the reason why waters are of -Cl type. As Cl amount in the local volcanic rocks is rather low (Alves et al. 1979), the measured quantities can be seen as a benchmark of the groundwater origin and evolution in Santiago's island, with the advantage of a conservative behaviour. The other groundwater ionic elements and compounds are mostly from water-rock interaction along the underground path way. The Chloride enrichment process over the typical inland $NaHCO_3$ water is happening at valleys downstream; very near the ocean by direct fresh-seawater mixing and ion exchange when low head and flow hydraulic conditions occur and from deep salty layer influence by leaching and dissolution of ancient marine sediments, probably induced by borehole overexploitation, at mid valleys and far from the coastline. Nevertheless, the marine aerosol spray cannot be excluded as another source of salinity. Soil irrigation with brackish waters also increases the salt content at valley shallow depths.

The groundwater salinity can be thus given by Chlorinities, and related to sea distance and bulk TEM resistivity. Figure 7.130 shows waters Chloride (TDS percentage) versus sea

distance at the surveyed valleys. A linear trend can be assigned with decreasing Cl percentage inland and a shoreline value of 42% (less than pure seawater). The mean data samples offset to fit trend line is 6%.

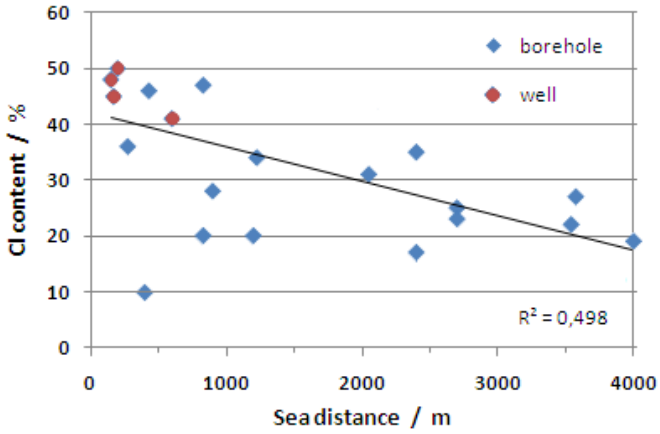

Figure 7.130 – Groundwater's Cl percentage *versus* distance to the sea.

$$\mathrm{Cl} = (42 - 0.006 \times \mathrm{distance}) \pm 6 \qquad \% \qquad (7.1)$$

with distance given in meters. Expression (7.1) is valid within the measured range distance, as gives zero Chloride percentage at 7 km from the coastline (and negative beyond that). At 5.3 km, the Cl is about 10 % of TDS amount. This is the mean measured value detected at inland locations.

A fit can be also found to the total Cl per litre amount, with a high increase going towards the sea, to around 15 g.L^{-1} at the coastline (under Cl content seawater), figure 7.131, below.

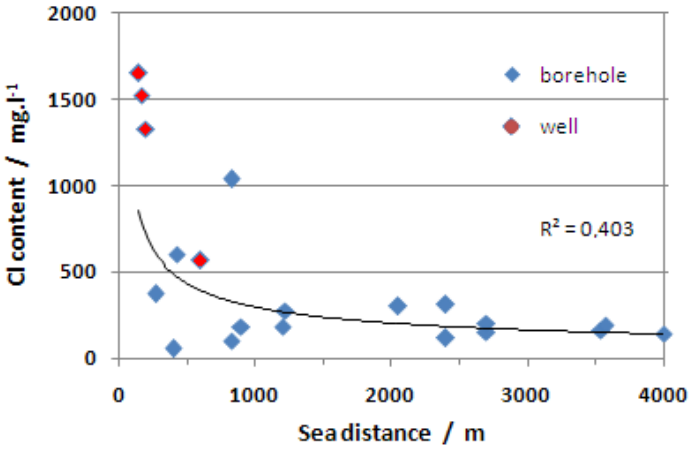

Figure 7.131 – Groundwater's Cl amount *versus* distance to the sea.

$$\mathrm{Cl} = \frac{14620}{\mathrm{distance}^{0,56}} \qquad \mathrm{mg.L^{-1}} \qquad (7.2)$$

Expression (7.2) will give lesser Cl content very near the sea, when the comparison is done against respective sample data. However it has a reasonable fit beyond that distance, within the range of distances of the data samples.

These Cl values can be directly compared against the nearby bulk modelled resistivities (from TEM sounding), as given at figure 7.132. An inverse relationship is found. With the available data, two separate sample groups are noted; the nearest to sea and high Cl content (above 1 g.L^{-1}, group I) and inland ones (Cl content below that value, group II). The former ones are detected by TEM measures within the 1.5 to 3 ohm.m range and the latter ones within the 8 to 20 ohm.m range. These values are linked to lithologic environment, notably to porosity, which can be assumed with a mean value of 15% all over the studied valleys.

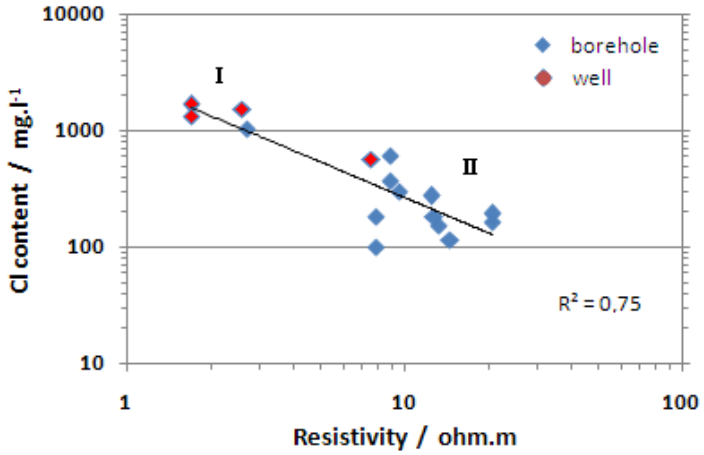

Figure 7.132 – Groundwater's Chloride *versus* bulk TEM resistivity.

$$\mathrm{Cl} = \frac{2646}{\rho_b} \quad \text{mg.L}^{-1} \qquad (7.3)$$

with a mean 25% error. The ρ_b is the modelled TEM bulk resistivity value (in ohm.m).

With this calibration factor, and taking into account that no other lithology (whether saturated or not), exhibits similar low resistivities as group I, one would expect that the hydrogeological interpretation of the TEM sounding data within and even below the above-mentioned resistivity range represents a high content of Chloride, and thus a high salinity groundwater. Some clay could exhibit similar low resistivities, like Bentonite (formed by weathered volcanic ash). Bentonite outcrops were detected at eastern Santiago (João Coroado, personal communication) but this clay type is almost Chloride free, and could not be responsible for the detected deep low electric resistivities.

With this assumption and taking expression (7.3), the deep low resistivity layer must have at least a Chloride equivalent concentration of 2.5 to 5 g per litre, and at least a TDS amount 5 to 10 g per litre.

Merging the previous expressions, the groundwater quality, given as TDS amount can be derived as a function of both TEM resistivities and sea distance:

$$\mathrm{TDS} = \frac{2646}{\rho_b} \frac{100}{42 - 0{,}006 \times \mathrm{distance}} \quad \text{mg.L}^{-1} \qquad (7.4)$$

with a mean 25% error.

Bellow, the figure 7.133 displays the TDS content throughout the S. Domingos valley using expression (7.4). The values are computed for the shallow groundwater near the sea, the seawater intrusion beneath it and for groundwater inland. As detected, seashore groundwater salinity is higher, both superficially and at depth, with seawater mixing from 5 to 12% (TDS from 3000 to 6000 $mg.L^{-1}$). At inland this salinity is lower with a mean of 650 $mg.L^{-1}$, somewhat less than the measured samples (but within the error), as it comes from a mean fit expression for all (fewer) calibration samples.

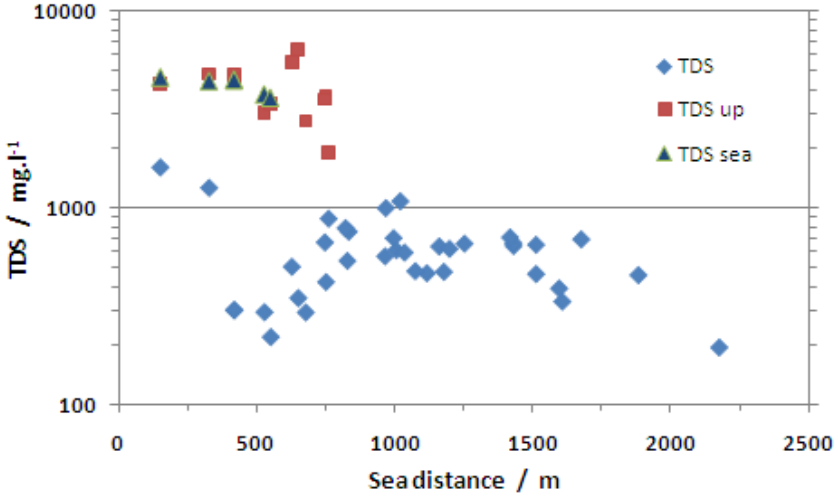

Figure 7.133 – Computed groundwater mean TDS at S. Domingos valley.

The same procedure was applied to the remaining surveyed valleys. At Seca and Picos valleys, the expected behaviour of near sea shallow influence results in high TDS content (as direct EC measures have shown) with values in the 1,5 to 5 $g.L^{-1}$ range (seawater mixing from 4 to 14%). Inland values are smaller, from 400 to 1000 $mg.L^{-1}$, figure 7.134.

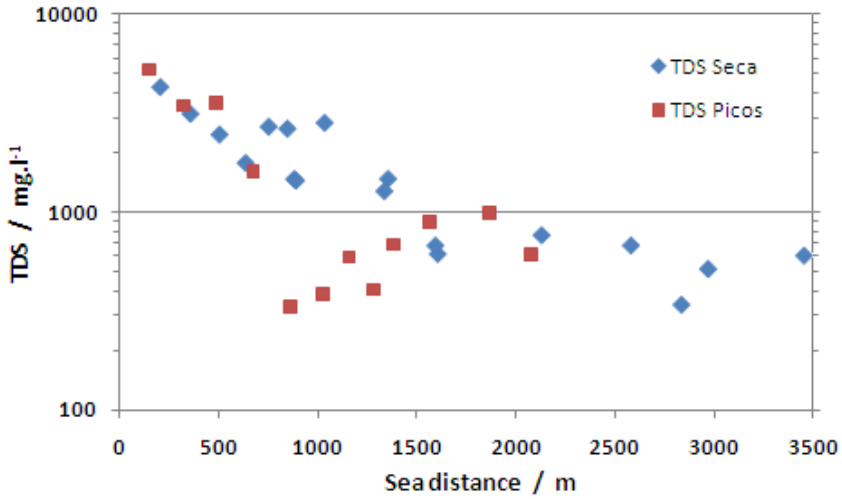

Figure 7.134 – Computed groundwater mean TDS at Seca and Picos valleys.

A “discontinuity TDS step” seems to exist at both S. Domingos and Picos valleys, after the initial decreasing values. This can be related to changing lithology (less thick Quaternary alluvium) and also to overexploitation and inducing a vertical flow of the high conductive deep layer, beyond these distances.

At Salto, Flamengos and S. Miguel, computed TDS values are all about 1000 mg.L^{-1}. Inland higher values could be related to lithologic variations, and to the boreholes influence. Near the sea, TDS values are higher too, figure 7.135.

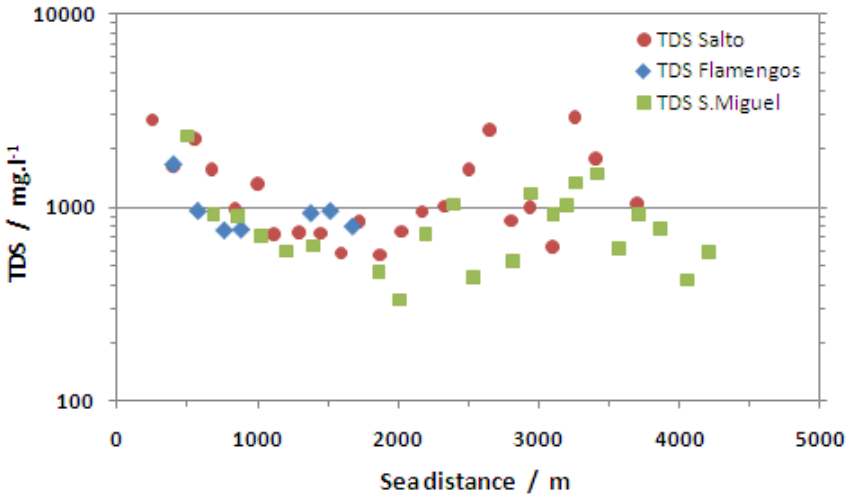

Figure 7.135 – Computed groundwater mean TDS at Salto, Flamengos and S. Miguel valleys.

The TDS content map for Tarrafal and Ribeira Grande valley is given below, in figure 7.136. The values are for 30 m below mean sea level. The NE-SW feature between Chão Bom and Ribeira Grande (already shown before, at figure 7.102), is now contoured with high TDS values. These TDS values are all above 2 g.L^{-1} at Ribeira Grande valley. That's also true for Chão Bom, except at a small area in the plateaux's middle, with smaller values. The NE-SW feature could be related with some fault/fracture and/or ancient valley filled with salty material.

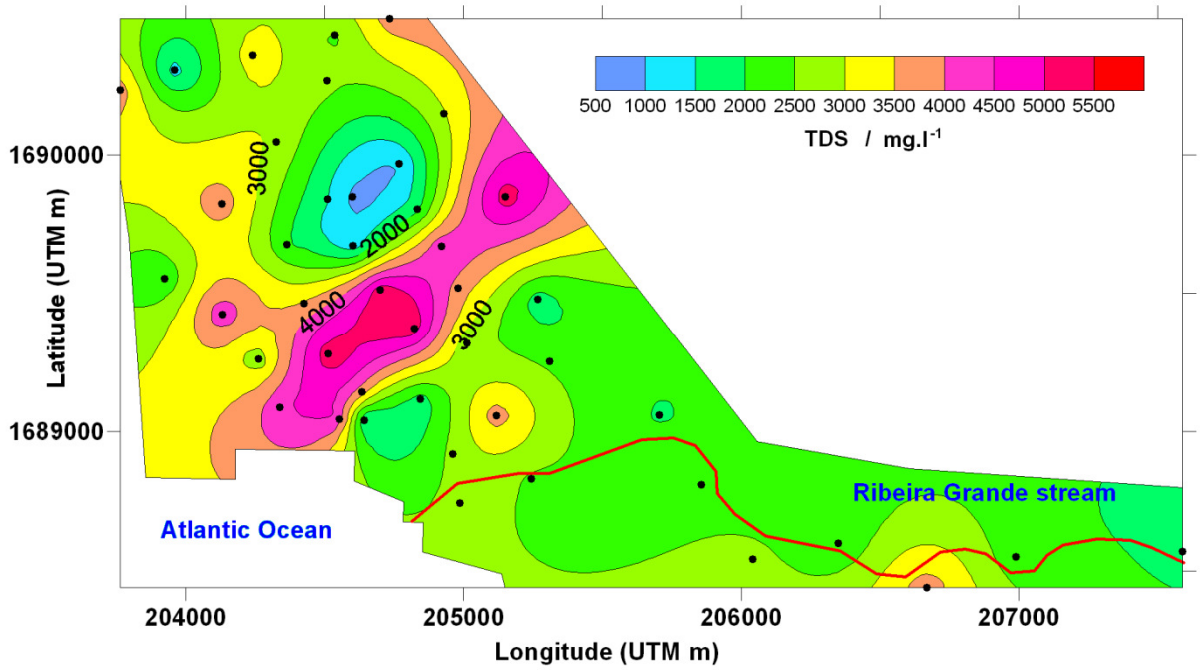

Figure 7.136 – Computed groundwater mean TDS at Chão Bom (Tarrafal) and Ribeira Grande valley.

7.4 – Simplified SUTRA models

To understand these TDS values, hydrodynamic numerical simulation has been done with the well-known and tested U.S. Geological Survey's SUTRA code. SUTRA (Saturated-Unsaturated TRAnsport) is a finite-element 3D code to solve a very general set of single-phase subsurface fluid flow and single-species transport problems, (Voss, 1984). The history and implementation of SUTRA code, as also a review of major published SUTRA applications is given in Voss (1999).

The code solves numerically two general balance equations: for variable-density single-phase saturated-unsaturated flow and for single-species solute (or energy) transport, based upon Bear (1979) formulations. First equation, for seawater intrusion (i.e. variable density saturated flow with non-reactive solute transport of TDS or Chloride) is the general fluid mass balance equation (usually referred as the *groundwater flow model*), given by:

$$\rho S_{op}\frac{\partial p}{\partial t}+\phi\frac{\partial \rho}{\partial U}\frac{\partial U}{\partial t}-\nabla\cdot\left[\left(\frac{\boldsymbol{k}\rho}{\mu}\right)\cdot(\nabla p-\rho\boldsymbol{g})\right]=Q_p \qquad (7.5)$$

where ρ is the fluid density, S_{op} is the specific pressure storativity, Φ the fractional porosity, p is the fluid pressure, U can be either solute mass fraction (C) or temperature (T), $\boldsymbol{k}$ is the permeability tensor, μ is the fluid viscosity, $\boldsymbol{g}$ is the gravity vector and Q_p is the fluid mass source (all in the International System units). The fluid density is expressed as:

$$\rho=\rho_0+\frac{\partial \rho}{\partial U}(U-U_0) \qquad (7.6)$$

where U_0 is the reference solute concentration (or temperature), ρ_0 is the fluid density at U_0.

The specific pressure storativity is given by:

$$S_{op}=(1-\phi)\alpha+\phi\beta \qquad (7.7)$$

where α is the porous matrix compressibility and β the fluid compressibility.

The fluid velocity is given by the general form of Darcy's law:

$$\boldsymbol{v}=-\frac{\boldsymbol{k}\rho}{\phi\mu}\cdot(\nabla p-\rho\boldsymbol{g}) \qquad (7.8)$$

The second equation is given with unified solute mass and energy balances, usually referred as the *transport model*, simplified for seawater intrusion conditions as:

$$\phi\rho\frac{\partial C}{\partial t}+\phi\rho\boldsymbol{v}\cdot\nabla C-\nabla\cdot[\phi\rho(D_m\mathbf{I}+\mathbf{D})\cdot\nabla C]=Q_p(C^*-C) \qquad (7.9)$$

where $\mathbf{I}$ is the identity tensor and $\mathbf{D}$ the dispersion tensor, C^* is the concentration of the fluid source, and D_m is the coefficient of molecular diffusion in medium fluid.

The dispersion tensor is defined in the classical manner by:

$$D_{ii} = |\boldsymbol{v}|^{-2}\left(d_L v_{\mathrm{i}}^2 + d_T v_{\mathrm{j}}^2 + d_T v_{\mathrm{i}}^2\right) \quad \text{diagonal elements} \quad (7.10a)$$

$$D_{ij} = |\boldsymbol{v}|^{-2}(d_L - d_T)v_i v_j \quad \text{off-diagonal elements} \quad (7.10b)$$

for i = x,y,z, j = x,y,z, but $i \neq j$, and,

$$d_L = \alpha_L|\boldsymbol{v}| \quad (7.11a)$$

$$d_T = \alpha_T|\boldsymbol{v}| \quad (7.11b)$$

where d_L is the longitudinal dispersion coefficient, d_T is the transverse dispersion coefficient, α_L is the longitudinal dispersivity, and the α_T is the transverse dispersivity.

$$\alpha_L = \frac{\alpha_{Lmax}\alpha_{Lmin}}{\alpha_{Lmin}cos^2\theta_{kv}+\alpha_{Lmax}sin^2\theta_{kv}} \quad (7.12a)$$

$$\alpha_T = \frac{\alpha_{Tmax}\alpha_{Tmin}}{\alpha_{Tmin}cos^2\theta_{kv}+\alpha_{Tmax}sin^2\theta_{kv}} \quad (7.12a)$$

where α_{Lmax} and α_{Lmin} are the longitudinal dispersivities for flow in the maximum and minimum permeability directions, respectively. The α_{Tmax} and α_{Tmin} are the transverse dispersivities for flow in the maximum and minimum permeability directions, respectively. The θ_{kv} is the angle between the maximum permeability direction to the local flow direction. These definitions allow the longitudinal and transverse dispersivities to vary in a time-dependent manner at any point depending on the flow's direction. Usually, longitudinal dispersivity is about one hundred times more intense at horizontal than by vertical direction. Transverse dispersivity is usually held constant, i.e. independent of flow direction, (Voss, 1999).

A simplified 3D model for the axial mid valley is tested with the known hydraulic parameter values to check the validity of the hypothesis of the deep conductive layer to behave as a salinity groundwater source, other than inland water-rock interaction. The near ocean shallow fresh to seawater mixing was also tested, upon the conditions detected by TEM soundings.

For the SUTRA simulation of the first situation, a uniform rectangular model with a 2000 m long (x-direction), 400 m wide (y-direction) and 70 to 50 m depth (z-direction), with the constant bottom at 50 m below msl was tested. A tridimensional mesh dimension was set with 160×20×40 finite element (rectangular elements). Applied hydraulic parameters are presented at table 7.23. Most of them are unknown to actual problem and thus initially taken from published similar cases, as the Hawaii Oahu island basaltic aquifer (Voss, 1999). A range values to the longitudinal and transverse dispersivities have been tested. From 100 to 1000 for the longitudinal dispersivity. From 0 to 10 for the transverse dispersivity.

The final and chosen values, that are compatible with observed and measured data, are given at table 7.23.

Table 7.23 – Applied hydraulic parameters at first SUTRA simulation.

Parameter	value
Freshwater density	1000 $kg.m^{-3}$
Seawater density	1026 $kg.m^{-3}$
Water compressibility	4.47×10^{-10} Pa^{-1}
Water viscosity	0.001 $kg.m^{-1}.s^{-1}$
Molecular diffusivity	1.5×10^{-9} $m^2.s^{-1}$
Matrix compressibility	2.5×10^{-9} Pa^{-1}
Horizontal hydraulic permeability	5×10^{-12} m^2
Vertical hydraulic permeability	1×10^{-12} m^2
Porosity	0.15
Horizontal Longitudinal dispersivity	250 m
Vertical Longitudinal dispersivity	25 m
Horizontal Transverse dispersivity	1,0 m
Vertical Transverse dispersivity	1,0 m

Boundary conditions were set to the inland and ocean sides, as also to the surface and bottom ones. Lateral wedge boundaries are closed to fluid flow. A flux was set from inland side, corresponding to calculated infiltration rates. At the seaward boundary, the usual hydrostatic seawater pressure is held together with seawater concentration. Top surface recharge is also included with known values. At the bottom wedge, upward flow represents the main inland regional discharge with seawater concentration's equivalent, from the high EC salty layer effect. All these values are constant over time, and an equilibrium condition (steady-state) was sought with the given hydraulic parameters, outputting a concentration spatial distribution field.

The model spatial discretization must be set in order to avoid general oscillations in the concentration distribution, with finite-element size limitation. This is related to the mesh Peclet number criterion (Voss. 1984):

$$\mathrm{Pe}_m = \frac{|\boldsymbol{v}|\Delta L_L}{(D_m+\alpha_L|\boldsymbol{v}|)} \qquad (7.13a)$$

where ΔL_L is the local distance between element sides along a streamline of flow. Stability is guaranteed in all cases when $\mathrm{Pe}_m \leq 2$. This criterion significantly affects discretization. Spatial stability is usually obtained with SUTRA when $\mathrm{Pe}_m \leq 4$, which gives a less-stringent criterion. In the case of solute transport with longitudinal dispersion primarily due to longitudinal mixing, the mesh Peclet number becomes:

$$\mathrm{Pe}_m \approx \frac{\Delta L_L}{\alpha_L} \qquad (7.13b)$$

Conditions are then defined by $\Delta L_L \leq 4\alpha_L$ and $\Delta L_L < 10\alpha_T$ (Voss and Provost, 2003).

Taking this into account and the boundary conditions, summarized in table 7.24 for two scenarios (higher and lower inland and surface recharge flow) the TDS (salinity) concentration field was computed via SUTRA. The higher to low flux is regarded as the seasonal rainy effect at shallow depth. Results for the two described scenarios are shown at figure 7.137. Variations can be noted when seasonal inland shallow flow decreases and the

deep upwards flow stays constant over time (trough salty layer). The deep layer influence is high at "dry season" and with increasing borehole pumping or overexploitation, salinity values will easily reach the mean observed 1000 mg.L^{-1} value. To confirm the effect of a borehole overexploitation, a SUTRA simulation was also done with the borehole in the centre of the model and depth position of 30 m below msl. The water sink amount was set to 1.5 kg.s^{-1}, the typical mean daily pumping rates at valleys, 13 m^3.h^{-1} for about 10 h long (INGRH data).

Table 7.24 – Applied boundary's data at first SUTRA simulation.

Boundary	Flow (kg.m^{-2}.s^{-1} , mm.yr^{-1})	Concentration (kg.L^{-1})
inland (low)	1.6×10^{-6} , 50	0.0005
inland (high)	4.8×10^{-6} , 150	0.0005
surface (low)	3.2×10^{-7} , 10	0.0001
surface (high)	9.6×10^{-7} , 30	0.0001
deep bottom	3.2×10^{-6} , 100	0.0350

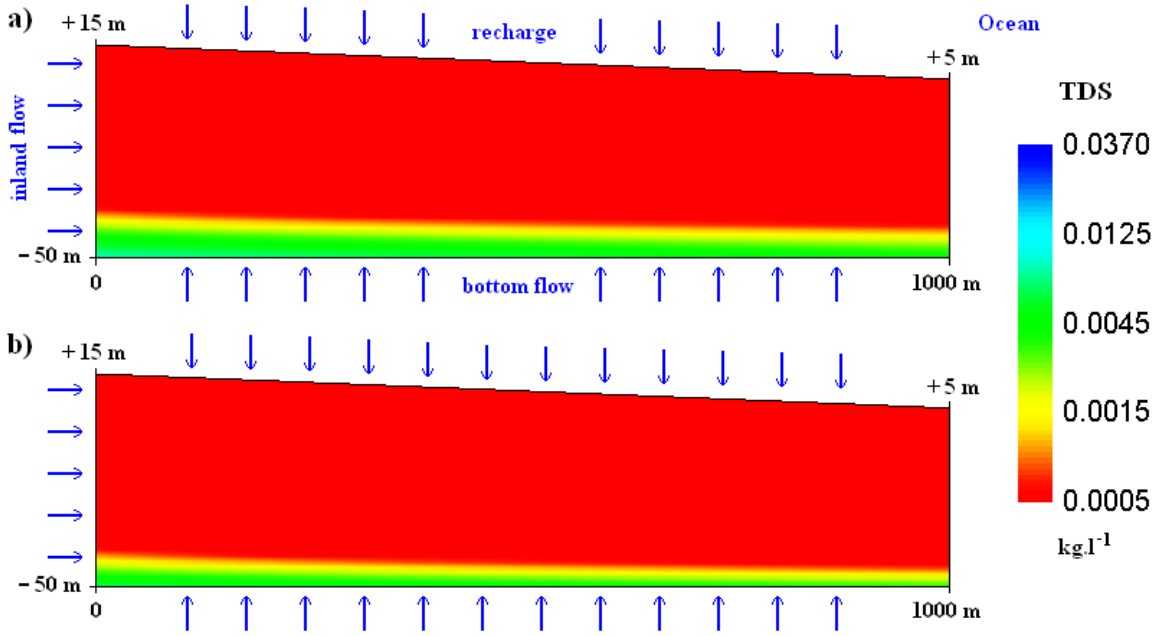

Figure 7.137 – Cross section of 3D SUTRA simulated TDS groundwater's values, throughout mid valley; at a) "dry season" and b) "rain season" scenarios.

The simulated results in figure 7.138 show that major TDS values increase near the borehole, with an "upconning" asymmetry and offset into the ocean direction. That's because borehole sink breaks and disturbs local equilibrium between the downstream horizontal and bottom upper vertical flux, with this latter overwhelming beyond this position (some small numerical instability is also superimposed). This same kind of signature seems to be present in TEM resistivity cross sections at S. Domingos valley, near boreholes FT-26 and FT-38 (fig. 7.15), and borehole FT-6 in Seca valley (fig.7.29), and could be the explanation of those geometric features.

Under these conditions, TDS asset value in the borehole is about 1500 mg.L^{-1}. This amount will change upon borehole sink rate and also with the prevailing local hydraulic parameters.

Thus, the reasonable explanation to measured groundwater TDS and Chloride content (as well the conductive TEM values) can indeed be the deep enriched salty layer. Overexploitation just induces and increases the water's salinity amount. Far from the coastline, by the prevailing dynamic conditions, it's impossible for the modern seawater to be the salinity main source.

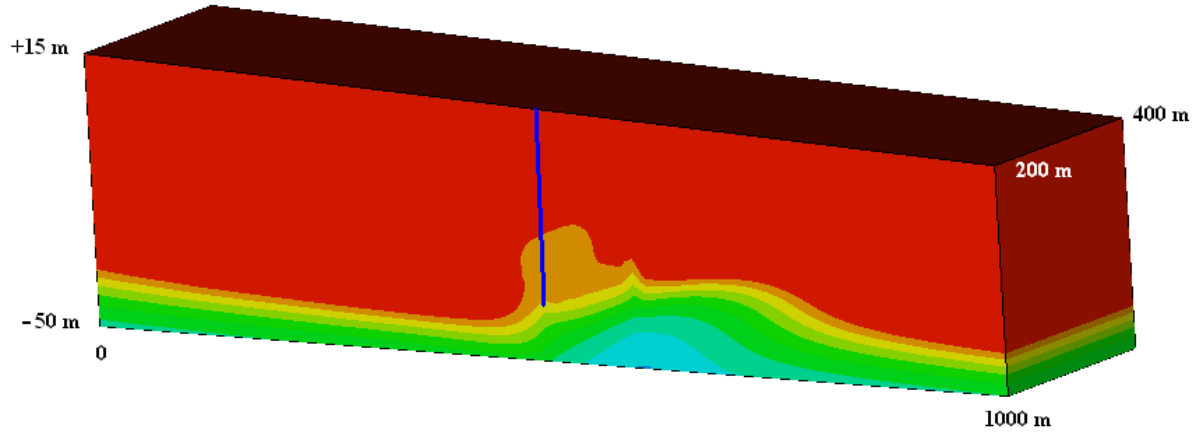

Figure 7.138 – Borehole overexploitation effect at mid valley. Cross section perspective view of 3D SUTRA simulated TDS groundwater's values, (colour scale is the same of fig. 7.137).

For the SUTRA second simulation, a uniform rectangular sheet like model with a 1600 m long (x-direction), 400 m wide (y-direction) and 37 to 35 m depth (z-direction), with the constant bottom at 35 m below msl was tested. The tridimensional mesh dimension was set with 60×10×40 finite element (rectangular elements). The tested and applied hydraulic parameters are presented at table 7.25, for the two zone layers. The remaining system parameter values are the same as the previous ones. The output TDS groundwater concentrations are much independent on the porosity values at this dispersive environment model. Under this scenario, with no groundwater withdrawal, the mixing waters reach a concentration state as shown at figure 7.139, with a 4 to 5 g.L^{-1} near the coastline and a null effect beyond 1300 m. These values are similar and compatible with the observed TDS at wells near the shoreline. This equilibrium condition ends up independent of initial concentration (when filled with fresh or seawater).

Table 7.25 – Applied boundary and hydraulic parameters data at second SUTRA simulation.

Boundary	**Flow (kg.m^{-2}.s^{-1} , mm.yr^{-1})**	**Concentration (kg.L^{-1})**
inland	4.0×10^{-7} , 12	0.0005
surface	2.0×10^{-7} , 6	0.0001
Parameter	**Zone I**	**Zone II**
Horizontal hydraulic permeability	5×10^{-11} m^2	5×10^{-11} m^2
Vertical hydraulic permeability	5×10^{-12} m^2	1×10^{-12} m^2
Horizontal Longitudinal dispersivity	1000 m	500 m
Vertical Longitudinal dispersivity	40 m	25 m
Horizontal Transverse dispersivity	1.0 m	1.0 m
Vertical Transverse dispersivity	1.0 m	1.0 m

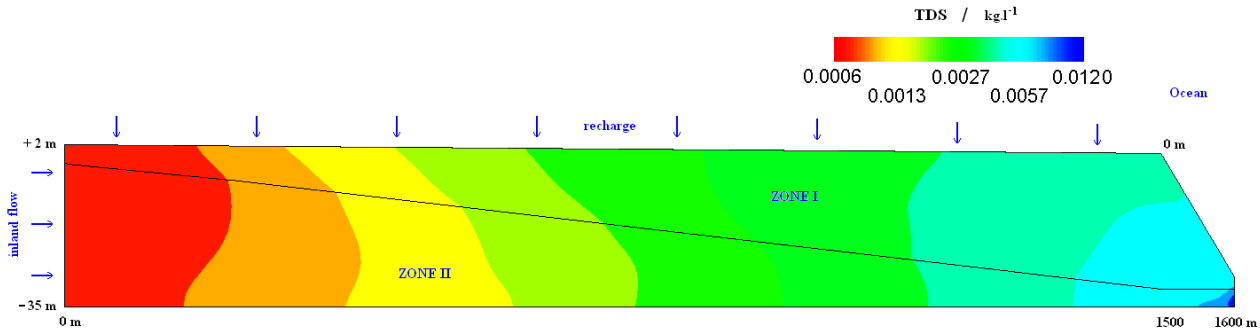

Figure 7.139 – TDS values cross section of 3D SUTRA simulation for dispersive mixing at shoreline. Vertical scale is 6 times the horizontal scale.

Standing on this result, the measured groundwater TDS values near the shoreline are due to a direct mixing between subsurface meteoric water and seawater. This is possible and provided by the particular geologic settings and groundwater level variations throughout the hydrological year; raising and flushing this underground area (diminish the TDS amount) or dropping and allowing the seawater advance inland (augmenting the TDS amount).

8
TEM DATA CHANGES OVER TIME

In this eighth chapter, the observed changes in TEM data acquired at different times are discussed within climatologic and hydrochemistry settings.

8.1 – TEM sounding repetitions

At some selected surveyed places, repetitions of several soundings were done within the available fieldwork time and local prevailed conditions. Most of the TEM soundings within the repetition's framework were acquired exactly at the same initial position. Geographic coordinates of the soundings were taken by a GPS hand unit, under the WGS84 geodetic Datum (or converted to) with a horizontal assigned error of about 10 m. After, sometimes the return to the exact site was impossible due to changes on lands motivated by agricultural works. On this occasion, the sounding's position offset from original position was small, one loop size distance at most. Some repetitions, when possible, were also acquired with a larger 50 m × 50 m single loop size. The TEM-FAST 48 time mode acquisition was not always the same, and that was chosen regarding the observed data quality and available signal power. Quality of the data soundings and curve points scattering are unequal. The high available power at the last survey's fieldwork does not mean better results. The summary of the available soundings repetitions have been summarized in table 7.1 of previous chapter.

8.1.1 – 2005-2009 S. Domingos valley TEM data

At S. Domingos valley (near Achada Baleia village), the chosen minimum number of sites (TEM soundings) that have been repeated was four, wrapping extremes and middle valley locations. They were the TEM soundings; AB02, AB12, AB26 and AB33. In 2006 fieldworks only two sites were easily accessible (AB02 and AB12) since the valley road was flooded at the time. In 2008 and 2009 TEM soundings were repeated for 10 sites.

Apparent resistivity curves and 1D mean models of each sounding are shown in figures 8.1 and 8,2, next page. Model misfit errors are about 5 to 7%. The measured apparent resistivity's changes between epochs are due to real changes in the subsurface, but loop location offset cannot be ruled out, especially at AB02 sounding's site.

The comparison of the 1D models from AB02, AB12 and AB26 sites, shows that the top layers' characteristics are roughly the same (as expected). The conductive layer underneath the shallow one, representing a seawater-groundwater mixing zone (at AB02 and AB12 sites), has a change in the resistivity that is compatible with the effect of the measured annual precipitation in those epochs, as seen in figure 8.3. The assumption that high rainfall and infiltration decrease the seawater effect at these near sea sites, increasing the shallow groundwater resistivity values seems to be confirmed.

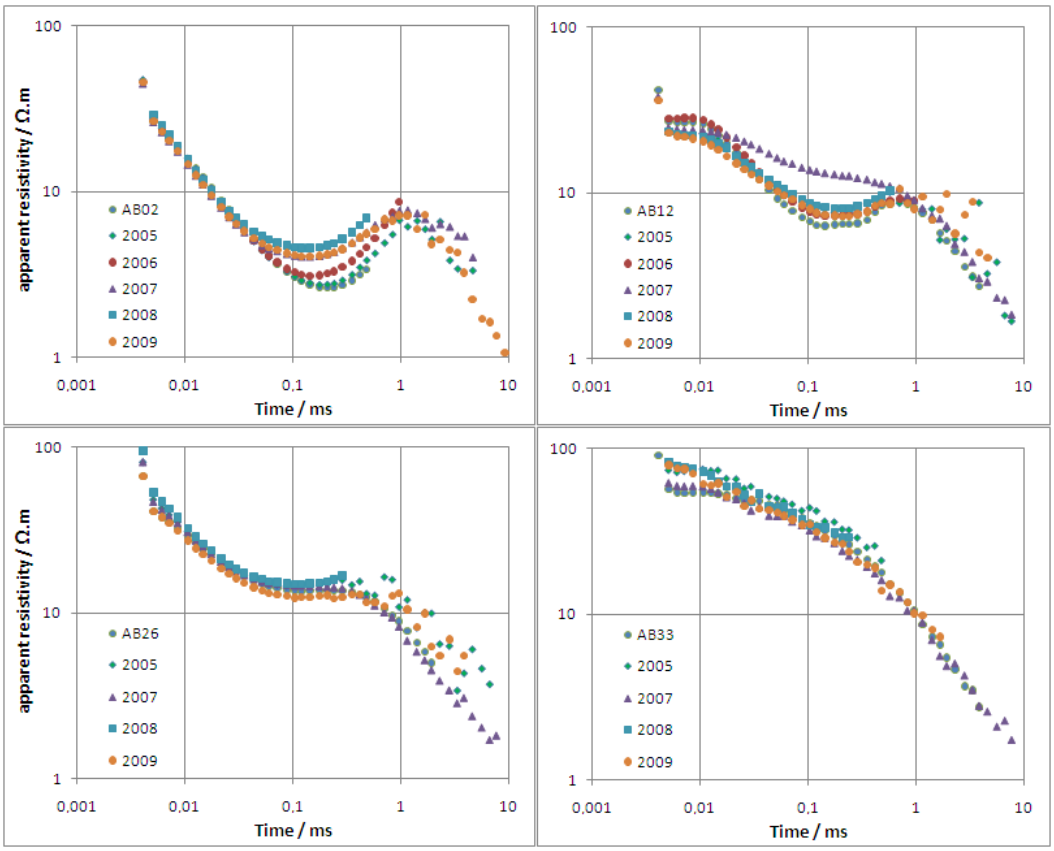

Figure 8.1 – Apparent resistivity TEM sounding curves at S. Domingos valley (AB02, -12, -26 and -33).

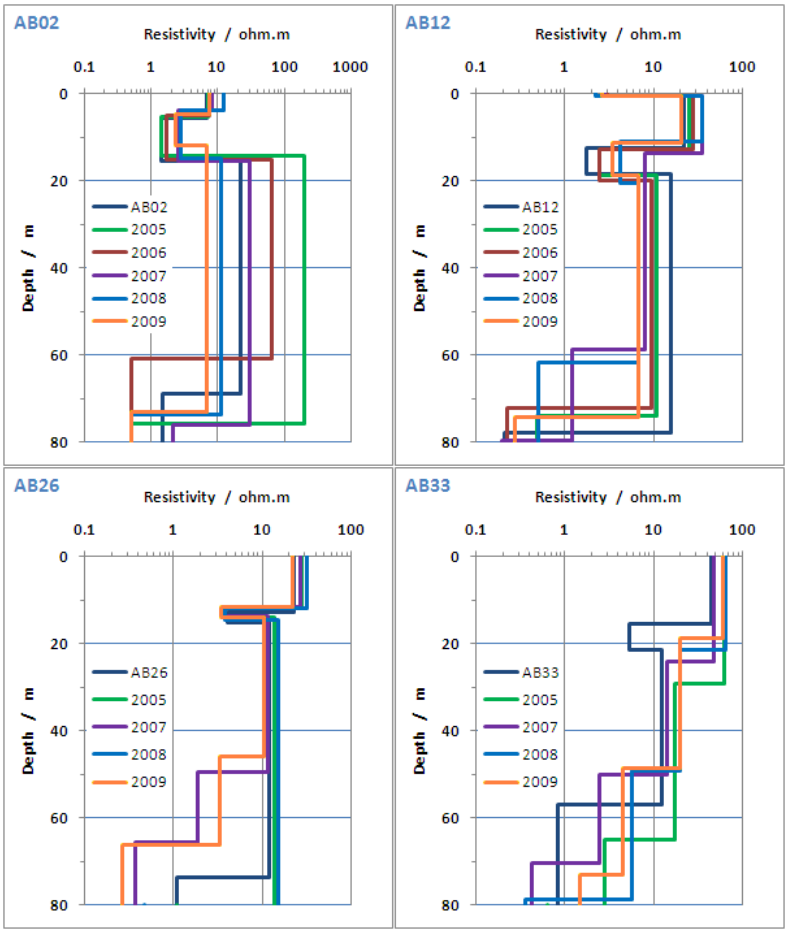

Figure 8.2 – 1D models from repetition soundings (AB02, -12, -26 and -33).

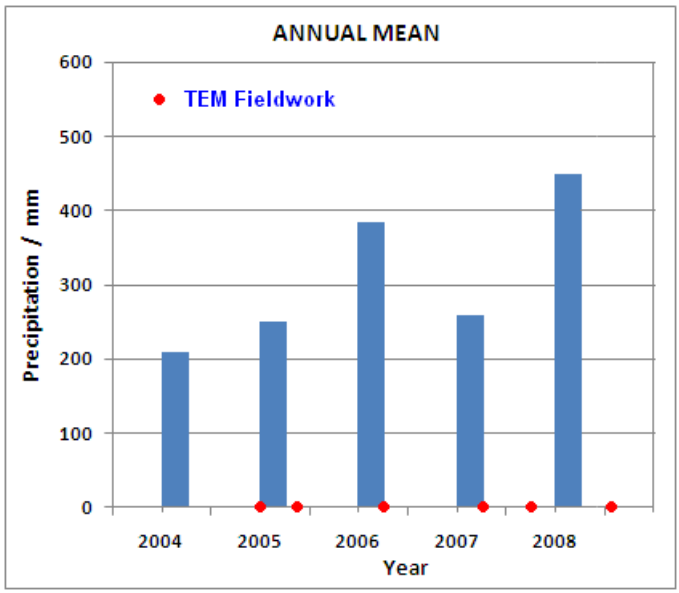

Figure 8.3 – Annual mean precipitation at Santiago's Island (2004-2008) and EM fieldwork epochs (2005-2009). (INMG).

The resistivity of this shallow groundwater should be proportional to rain amount (R) and inversely proportional to spanned time (ΔT) after the rainy season. Comparison is done against annual precipitation registered at S. Jorge dos Orgãos meteorological station, at middle Island, affecting S. Domingos hydropraphic basin (INMG data). For the given time span, the two data sets show an increasing trend with a 0.010 ± 0.001 $\Omega.m.mm^{-1}$ for the AB02 and AB12 soundings. This is a mean value, since figure 8.4 suggests that a 1 to 2 years time lag can exist between the two data sets, with the resistivity response delay implying a flow velocity in the shallow groundwater of about 20 $m.day^{-1}$ throughout the valley.

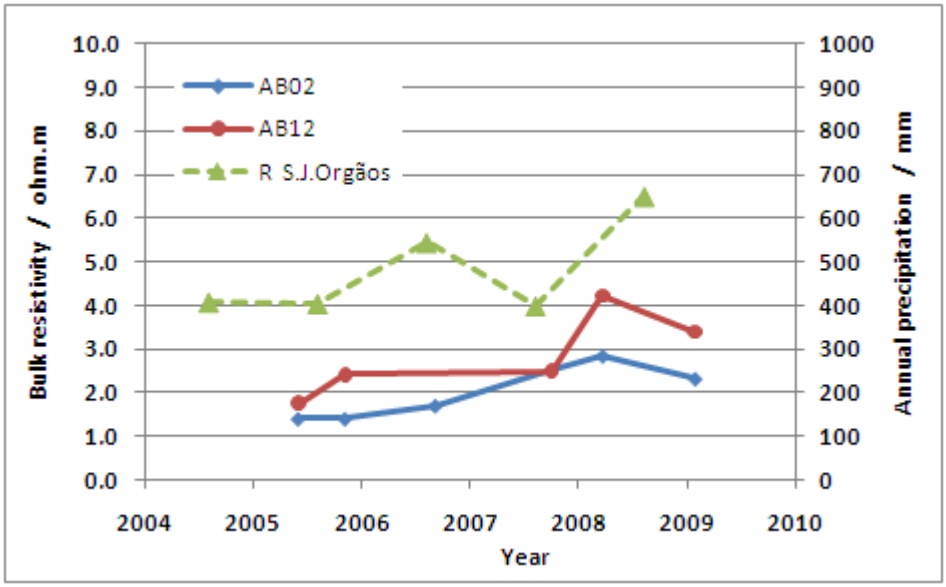

Figure 8.4 – Bulk resistivity values (2005-2009) of the shallow aquifer layer AB02 and AB12 sites *versus* annual precipitation at S. Jorge dos Orgãos meteorological station (2004-2008).

Beneath the mixing layer, the high resistivity that corresponds to the basaltic aquifer, is not well constrained by TEM data AB02 models, by less accurate data curves. It is much more

limited at soundings AB12 and AB26, within 7 to 14 and 10 to 14 Ω.m, respectively. A "reverse pattern" and "trend" is detected at these three TEM soundings (AB02, AB12 and AB26). The trend shows that the low resistivity values seem to follow the rainiest seasons and that more water should be interacting or dissolving more salts becaming more conductive. The deep conductive layer was not always clearly detected, and that is a function of data quality. At AB02 and AB12 layer depth is compatible with fresh-seawater interface position. At sounding AB26 the conductive layer is located at 50 to 60 m below msl. The TEM sounding AB33 exhibits a high scatter at shallow layer depth positions and also at deep conductive layer depth position. The most probable explanation is that the very nearby unattended borehole FT26 was extracting groundwater during sounding's acquisition, and disturbing the free water level and the deep mixing interface. The bulk resistivity ranges from 12 to 20 Ω.m.

These resistivity values are converted to groundwater salinity (TDS) using equation (7.4) and presented in figure 8.5. It's notorious that, although some seasonal variations, computed salt content stays between 410 and 725 mg.L^{-1} in inland locations, while it changes to higher values, 1700 to 4800 mg.L^{-1}, at shallow depths near the sea. In between these, at transition zone, the deep groundwater shows a salinity increase trend. As observed in the previous sub-chapter 7.3.8, these inland computed values are underestimated and can have an error of 25-30%. Knowing this and the groundwater chemistry (NaCl type) at valley, this can be translated to a groundwater Chloride content of between 200 and 350 mg.L^{-1} and also equivalent contemporary seawater mixing of 1 to 2%.

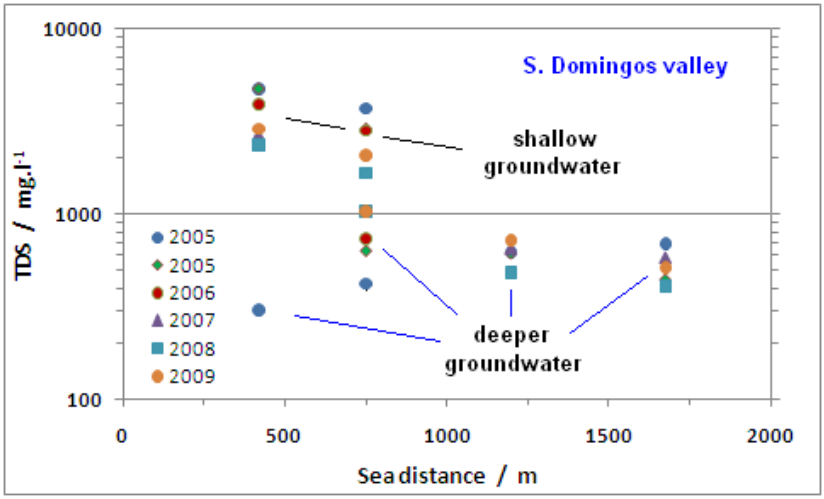

Figure 8.5 – Computed groundwater TDS amounts (2005-2009), at S. Domingos valley.

8.1.2 – 2005-2009 Seca and Picos valleys TEM data

At Seca valley, the number of repeated TEM soundings at exactly the same sites were two; sounding SECA16 near the sea and sounding SECA21 at shallow seawater influence transition zone. Also between these sounding's locations, two more extra soundings were done and repeated during the two last survey epochs (SECA17A and 18A). At Picos valley there were three repeated sites; sounding PICOS04, PICOS10 and PICOS12, at mid valley, with the last two ones not covering all survey period.

Data curves and 1D models for each of those soundings are presented in figures 8.6 and 8.7, for Seca valley and in figures 8.9 and 8,10 for Picos valley. In the year 2008 the TEM soundings SECA16 and 21 were acquired with 50 m × 50 m loop. Mean model misfit errors are about 6 and 7% for Seca and Picos soundings, respectively.

The near to sea SECA16 sounding models exhibit greater variability, notoriously that one repeated in 2008 (an incorrect site location is a possible cause). The shallow groundwater resistivity layer varies from 2 to 6-8 Ω.m, and groundwater mixing seems to be rather independent of time, probably from greater well water exploitation, reducing the natural outflow to the sea. Underneath this, basaltic aquifer layer resistivity ranges from 2 to 10 Ω.m, and the deep conductive layer is detected at roughly 50 m below msl. The models for soundings SECA21, SECA17A and 18A are much more invariant over time with shallow groundwater layer resistivity from 4 to 6 Ω.m. The basaltic aquifer layer bellow is less resistive with values from 2 to 3 Ω.m. The deep conductive layer can be detected at the best sounding data curves, with resistivity values under 1 Ω.m, but not well constrained.

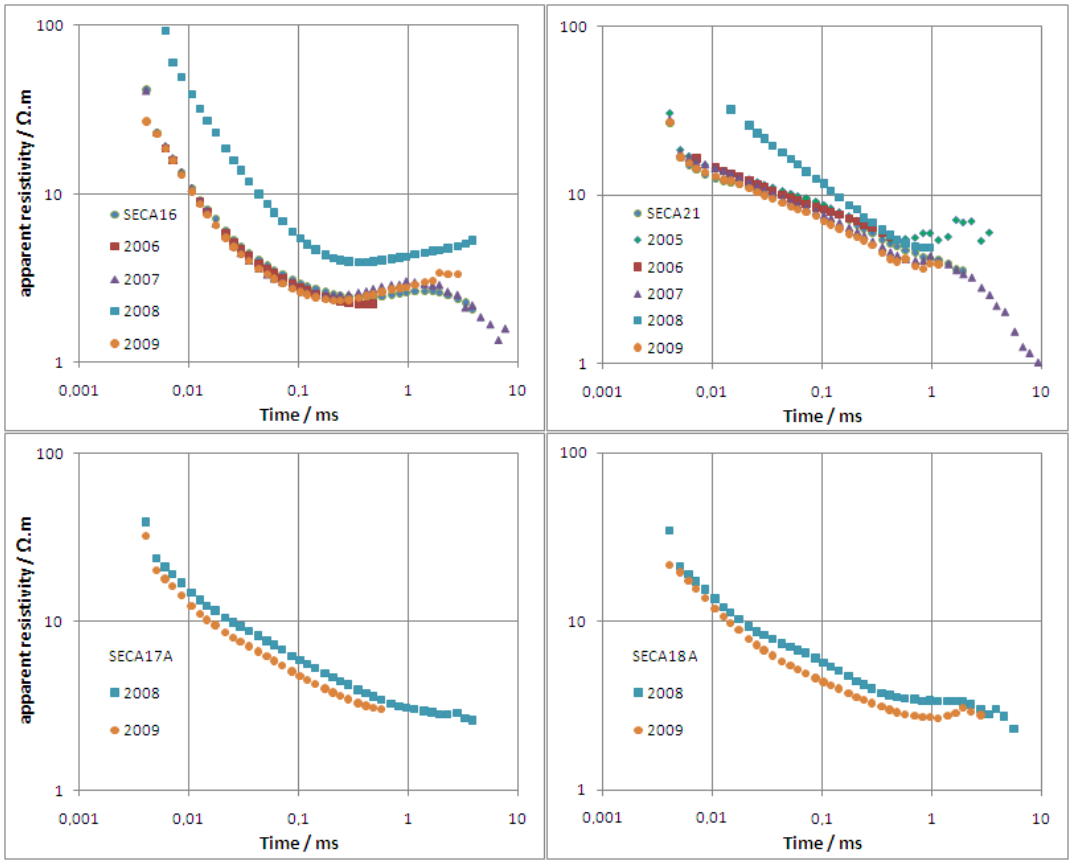

Figure 8.6 – Apparent resistivity TEM sounding curves at Seca valley (SECA16, 17A, 18A and 21).

As before, a comparison against the precipitation at S. Jorge dos Orgãos meteorological station, located at Seca hydropraphic basin head, was done. Variation in resistivity has a less expressive slope at SECA16 site, with an increasing trend of just 0.002 Ω.m.mm^{-1} and a decreasing 0.010 Ω.m.mm^{-1} trend at SECA21 site, figure 8.8. This behaviour is explained by the fact that groundwater extraction is more significant at those places, especially near SECA21 location.

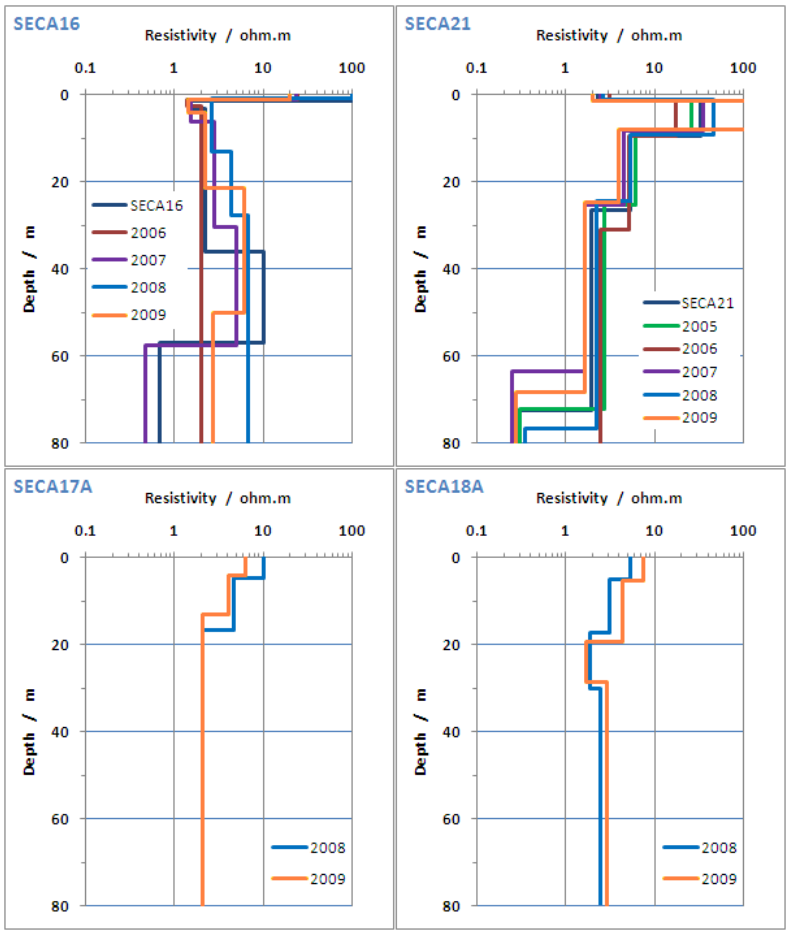

Figure 8.7 – 1D models from repetition soundings (SECA16, 17A, 18A and 21).

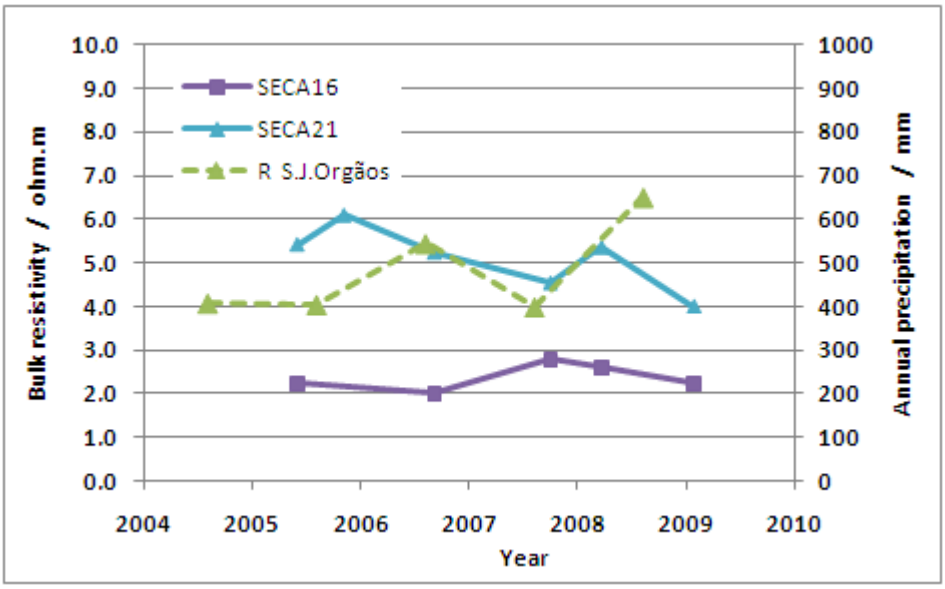

Figure 8.8 – Bulk resistivity values (2005-2009) of the shallow aquifer layer SECA16 and SECA21 sites, *versus* annual precipitation at S. Jorge dos Orgãos meteorological station (2004-2008).

At Picos valley the nearest to sea soundings (PICOS10 and PICOS12) exhibit again a shallow low resistivity layer with values ranging from 1 to 3 Ω.m, followed by a more resistive basaltic aquifer layer with values from 3 to 6 Ω.m. At mid of the TEM profile (PICOS04 sounding) the superficial basaltic aquifer layer shows resistivity values from 11 to 13 Ω.m, followed by lower resistive values 2 to 5 Ω.m. Insights to deep conductive layer, beyond 50 m below msl, is given at some soundings.

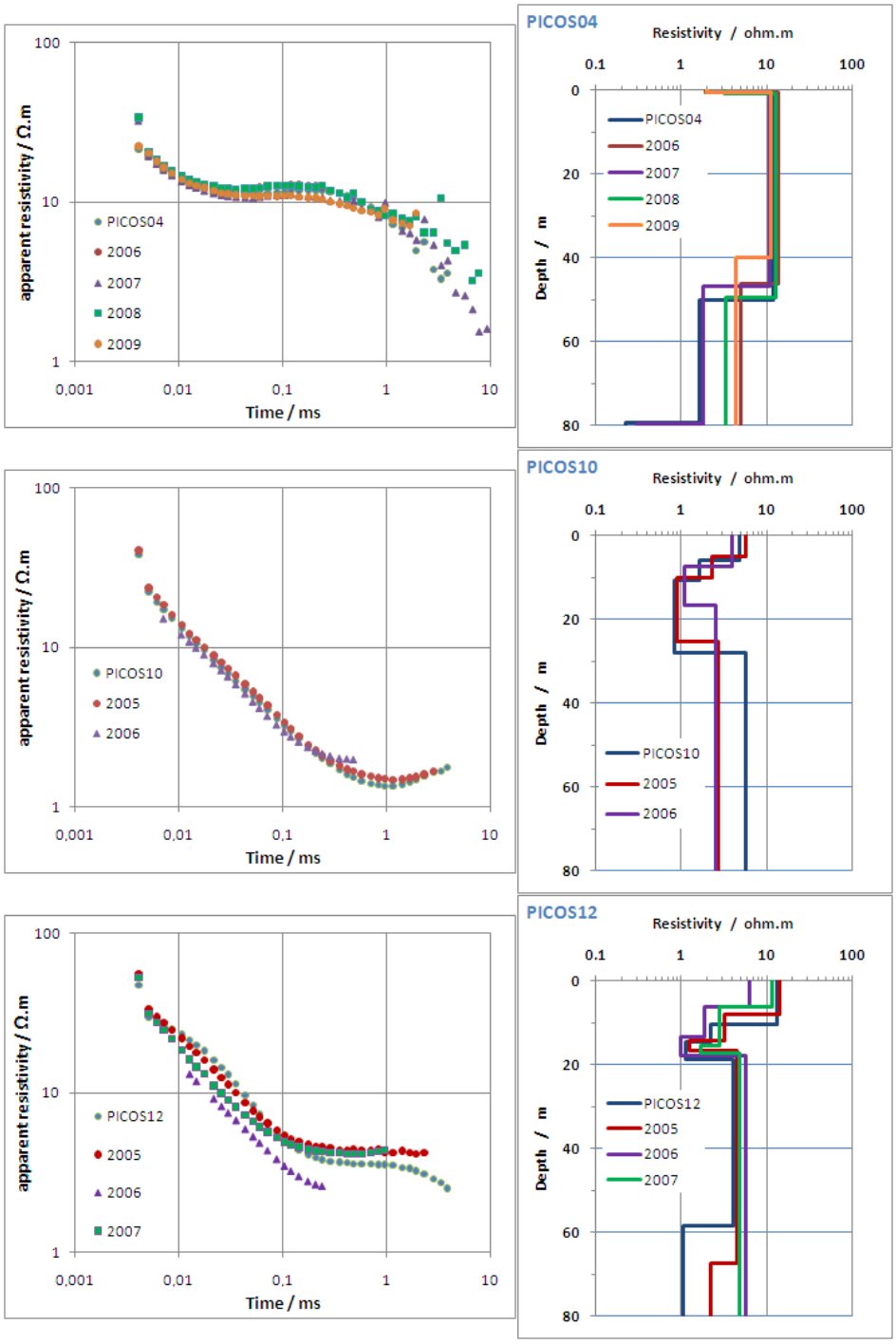

Figure 8.9 – Apparent resistivity TEM sounding curves and 1D models from repetition sites at Picos valley, (PICOS04, 10 and 12).

Results of the calculated bulk resistivity values to groundwater salinity (TDS) conversion are shown in figure 8.10 and 8.11, for Seca and Picos valleys, respectively. Almost all these computed values are high above the 1000 $mg.L^{-1}$. At both valleys, the shallow groundwater TDS content decreases inland, in accordance with direct measure's indications. Underneath this, at Seca valley deep waters are even more salty to inland, over this distance range. At Picos valley, the behaviour is similar with deeper groundwater becoming also more salty to inland.

At Picos valley computed TDS values (from bulk resistivity) at shallow groundwater exhibit high scatter than values from Seca valley, with no conclusive TDS trend in time. To this NaCl water type, the highest TDS values correspond to a mean Chloride content of 500 and 800 $mg.L^{-1}$, respectively, for Seca and Picos shallow groundwaters, and slightly higher at greater depths, near the coastline. This corresponds to equivalent (contemporary) seawater mixing of 2.5 and 4% at shallow waters, respectively for Seca and Picos. Beyond this sea distance, TDS values are known to diminish, in accordance with the remaining TEM soundings and direct measures (subchapter 7.3.8).

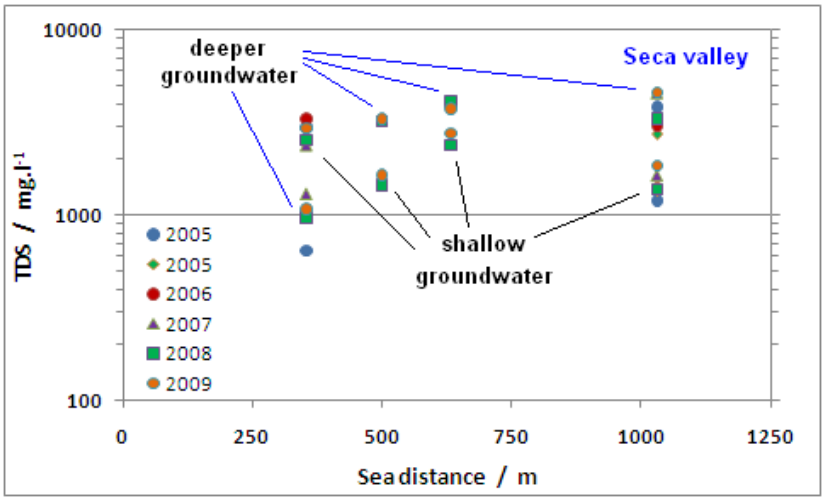

Figure 8.10 – Computed groundwater TDS amounts (2005-2009), at Seca valley.

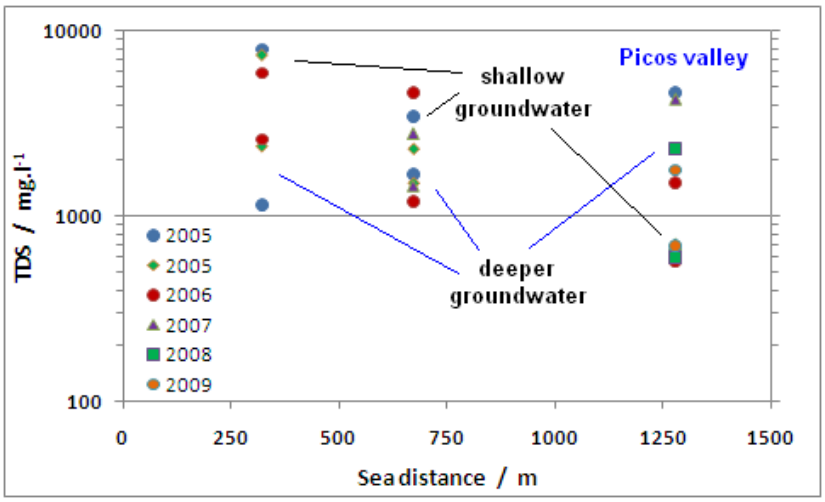

Figure 8.11 – Computed groundwater TDS amounts (2005-2009), at Picos valley.

8.1.3 – 2006-2009 Salto, Flamengos and S.Miguel valleys TEM data

At Salto valley, four TEM soundings have been repeated at the same site: soundings SALTO03, SALTO04, SALTO06 and SALTO07, in the years 2008 and 2009. At Flamengos valley, three soundings (FL02, FL05 and FL06), were repeated since 2007. For S. Miguel valley, three soundings (SM01, SM04 and SM08) were repeated at each year subsequent to initial survey (2007).

Apparent resistivity curves and 1D models for each of those soundings are shown in figures 8.12 to 8.15. The mean misfit errors range from 5 to 10%, for TEM acquired at Salto, and are about the same order for Flamengos and S.Miguel. Soundings from 2008 are observed to be noisier, with higher scatter in the late time points.

The SALTO03 and SALTO04 soundings were always done at exactly the same site. The other two soundings, SALTO06 and SALTO07, due to landscape conditions and lack of useful landmarks, were repeated as close as possible to the original ascribed coordinates. These latter soundings show a greater variability that can be, to some extent, committed to that offset, revealing local 2D or 3D geometry effects, figures 8.12 to 8.13. At Flamengos these behaviours were not observed, with rather smooth and similar soundings, figure 8.14. The same sounding localization difficulties were present at S.Miguel TEM sounding SM08.

In Salto, the soundings nearest to the sea (SALTO03 and SALTO04) show almost no change, with shallow groundwater resistivity layer staying between 3 and 4 Ω.m. At roughly 40 m below msl, the resistivity increases to about 7 Ω.m. This latter value is better constrained at SALTO03 sounding. The other two repeated soundings are much more problematic; at SALTO06 the resistivity of the basaltic aquifer layer varies between 6 and 17 Ω.m and at SALTO07 is even higher, between 14 and 36 Ω.m. In both these soundings the resistivity decreases with depth to low values, not well constrained by models, but below the 7 Ω.m.

Soundings in Flamengos are much alike, with shallow groundwater resistivity staying between 3 and 4 Ω.m (FL02), 6 to 9 Ω.m (FL05) and about 8 Ω.m (FL06). Both, first survey and repetitions have been taken just after the rain season, with 2006 season being rainiest than 2007 one (resistivities for 2006 are accordingly higher). Deeper at about 50 m bellow msl, the resistivity also decreases to low values, bellow 3 Ω.m.

At S. Miguel valley, the SM01 and SM04 soundings and models are much alike with major differences in deeper layers, arising from the scatter in the data, figure 8.15. The shallow groundwater resistivity values are estimated between 7 and 10 Ω.m, and the basaltic aquifer resistivity is about 3 Ω.m. A deep conductive layer is detected at about 50 m bellow msl, with resistivity values between 0.5 to 4 Ω.m,

The superficial unsaturated layers at these valleys are always much more resistive than any other observed layer and had stayed in a practically unchanged trough the time.

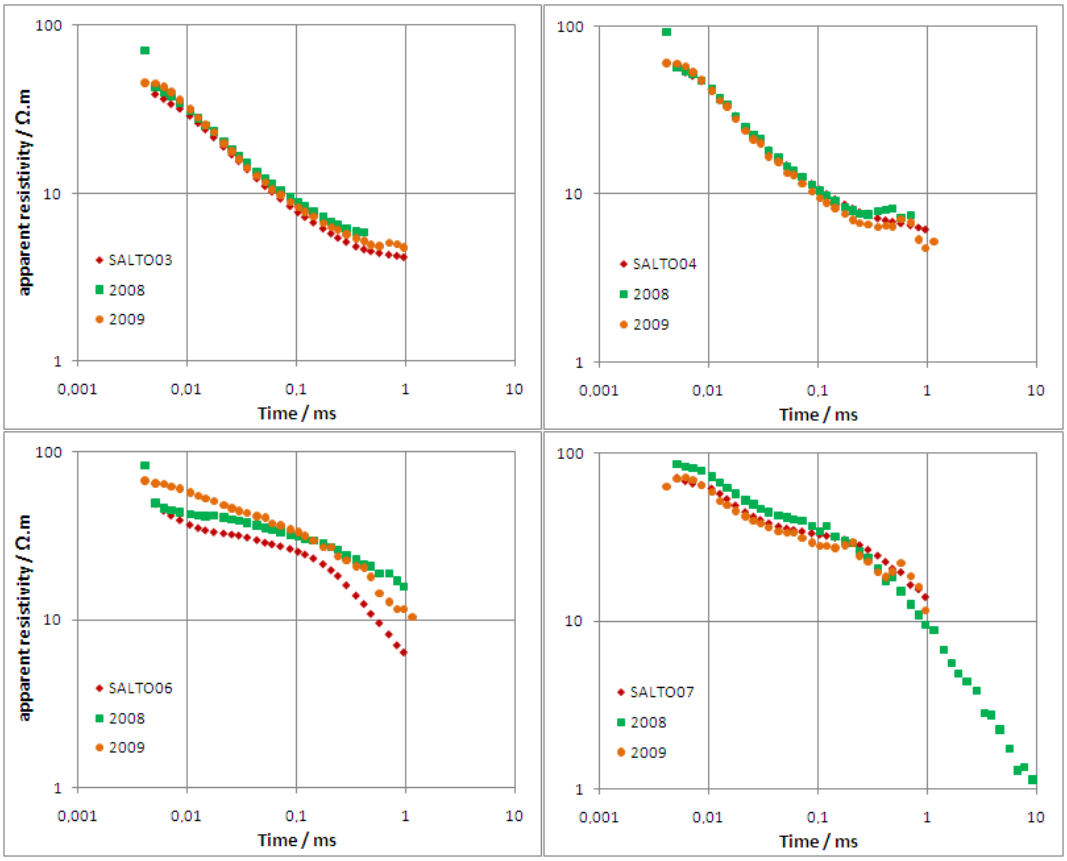

Figure 8.12 – Apparent resistivity TEM sounding curves at Salto valley (SALTO03, 04, 06 and 07).

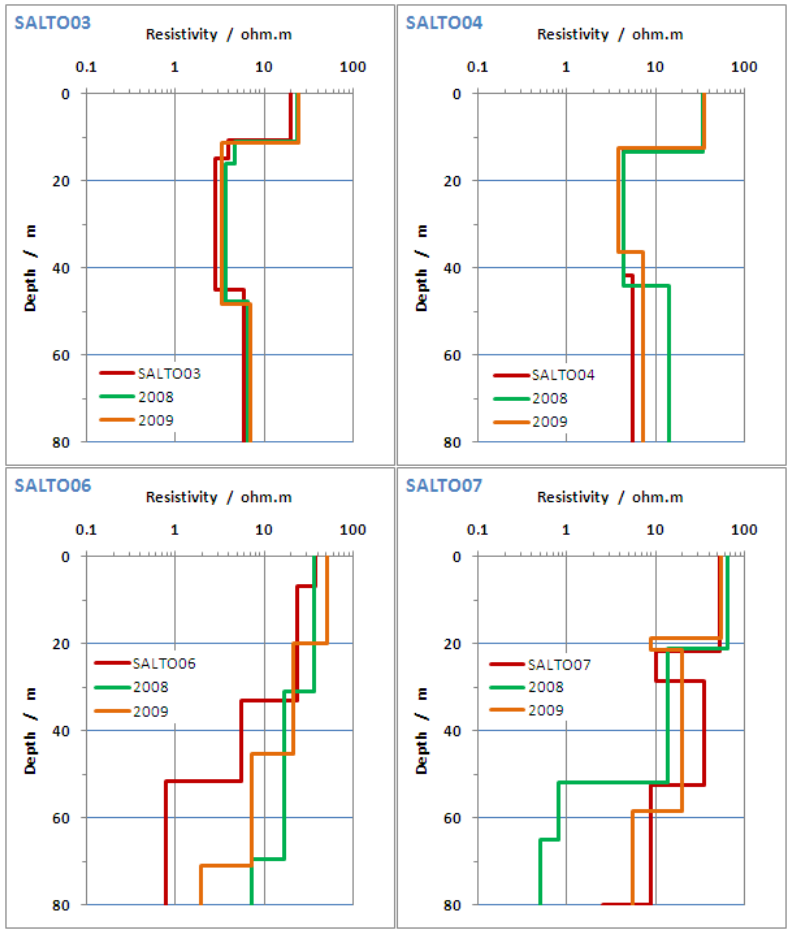

Figure 8.13 – 1D models from repetition soundings (SALTO03, 04, 06 and 07).

From these bulk resistivity values, the groundwater salinity (TDS) conversion gives the results, shown in figure 8.16 to 8.18, respectively for Salto, Flamengos and S.Miguel valleys. At Salto, salinity decrease inland with values staying more or less constant over time (2000 to 600 mg.L^{-1}). The inland samples show a decreasing trend. From the groundwater type and chemical composition, these values are translated to a mean Chloride content of 1000 to 300 mg.L^{-1}, (with the greater values closest to shoreline) or to a equivalent contemporary seawater mixing from 5 to 1.5%.

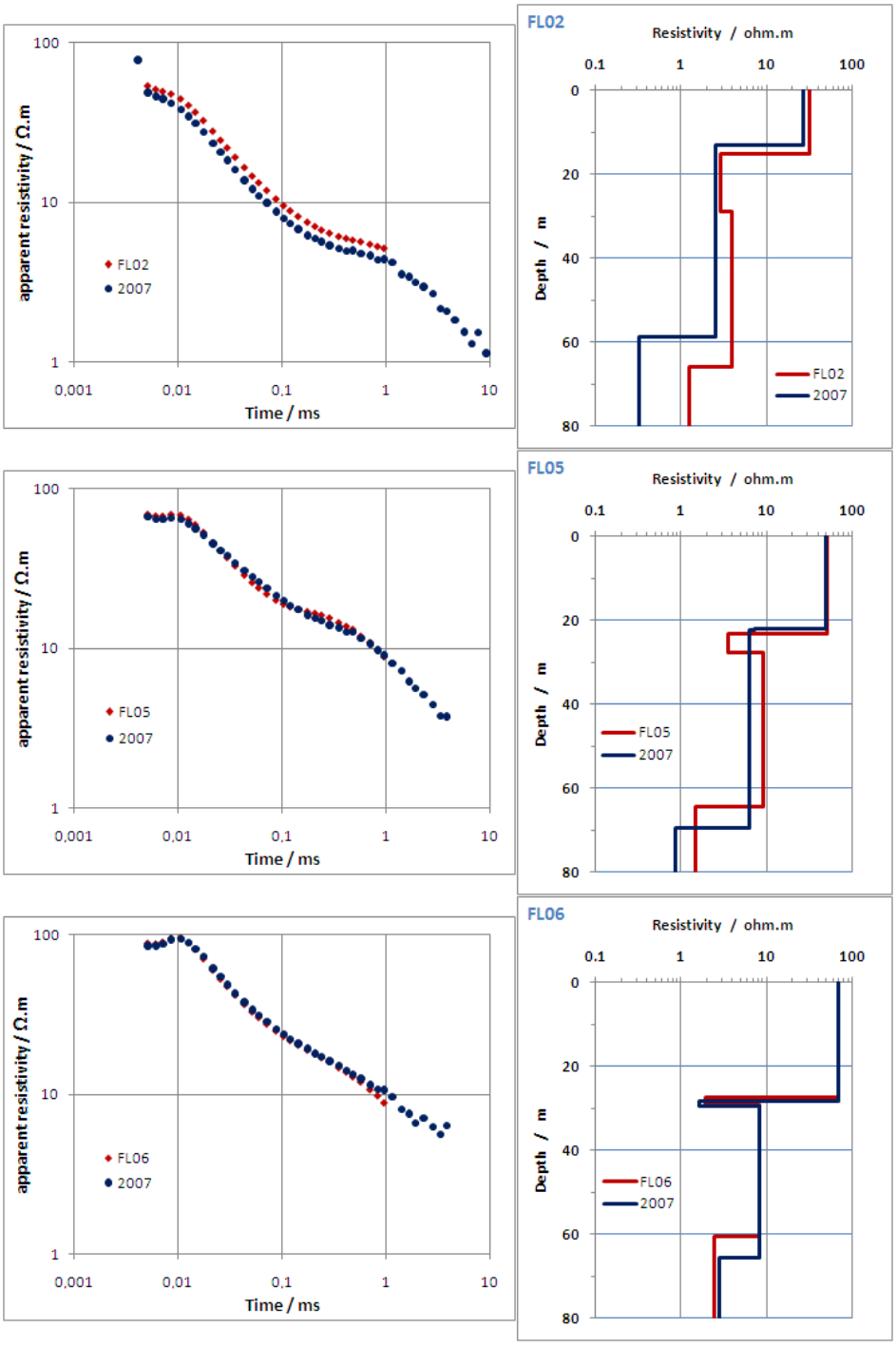

Figure 8.14 – Apparent resistivity TEM sounding curves and 1D models from repetition sites at Flamengos valley, (FL02, 05 and 06).

At Flamengos valley, the same trend is observed, with TDS decreasing inland, between 2000 and 1000 mg.L^{-1}, and being higher in the repeated soundings of 2007. This stands in agreement to a greater infiltration and water flush in year 2006. These salinity values are translated to a mean Chloride content ranging from 800 to 400 mg.L^{-1}, with higher values being found nearest to the coastline. This corresponds to an equivalent contemporary seawater mixing of 4 to 2%. The deepest detected conductive layer, assuming the same kind of aquifer behaviour, must have salinity greater than 3 g.L^{-1} and Chloride content greater than 1.2 g.L^{-1} and equivalent contemporary seawater mixing of at least 6%.

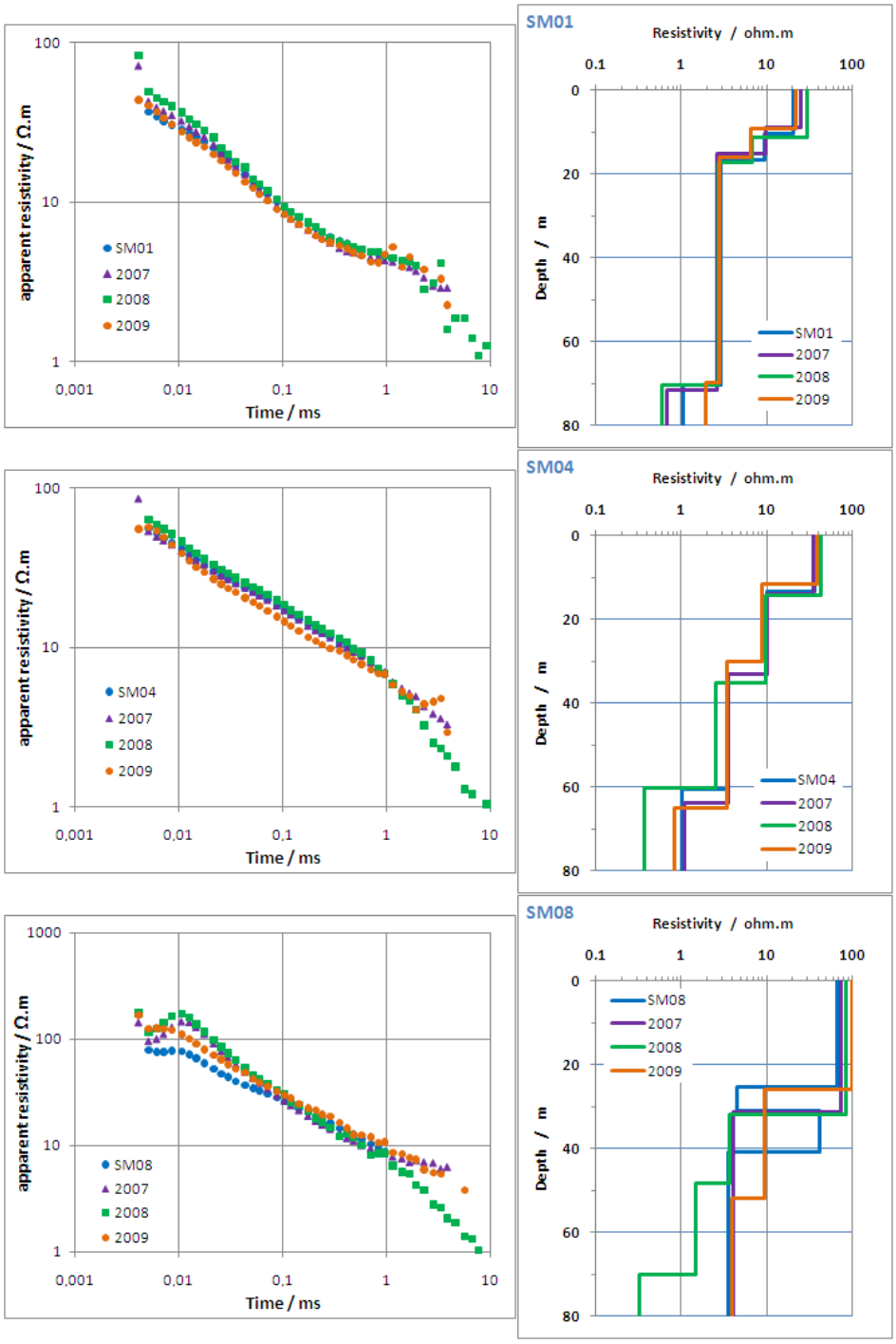

Figure 8.15 – Apparent resistivity TEM sounding curves and 1D models from repetition sites at S.Miguel valley, (SM01, 04 and 08).

At S.Miguel valley, the inland decreasing TDS tendency is also present. Salinity values are between 2500 and 800 mg.L^{-1}, and almost unchanged with time. This corresponds to a Chloride content of 1000 to 300 mg.L^{-1}, and to equivalent contemporary seawater mixing of 5 to 1.5%. The deepest conductive layer must also have a salinity greater than 3 g.L^{-1} and Chloride greater than 1.2 g.L^{-1}.

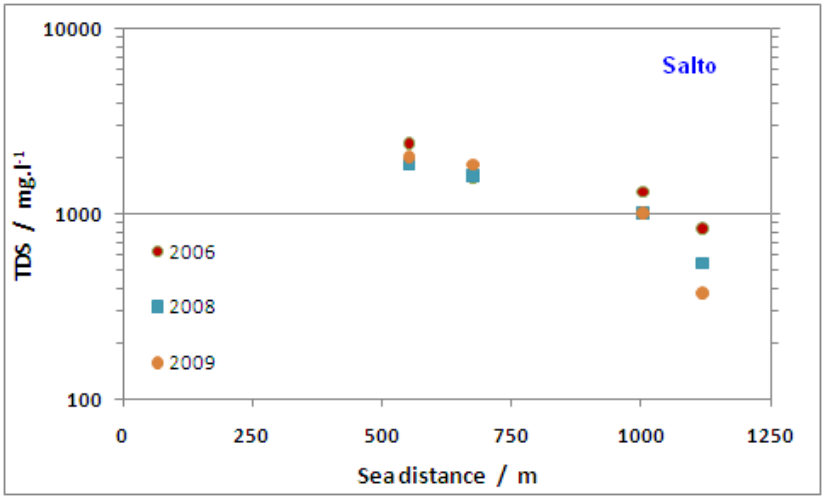

Figure 8.16 – Computed groundwater TDS amounts (2006-2009), at Salto valley.

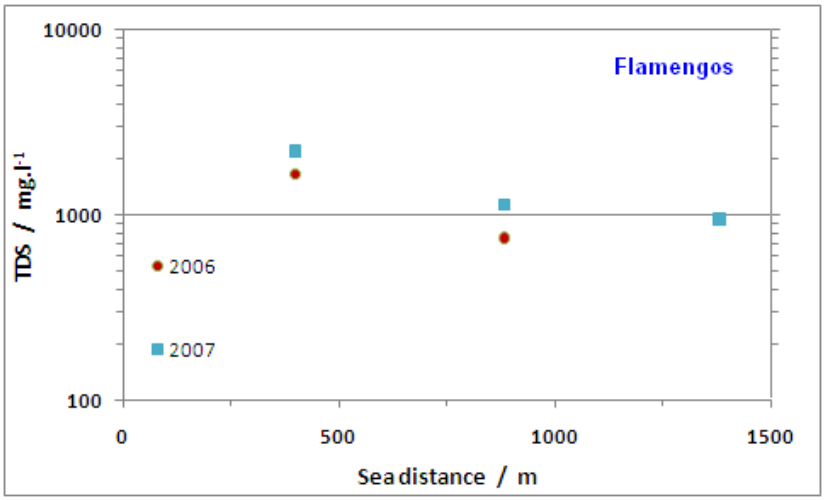

Figure 8.17 – Computed groundwater TDS amounts (2006-2007), at Flamengos valley.

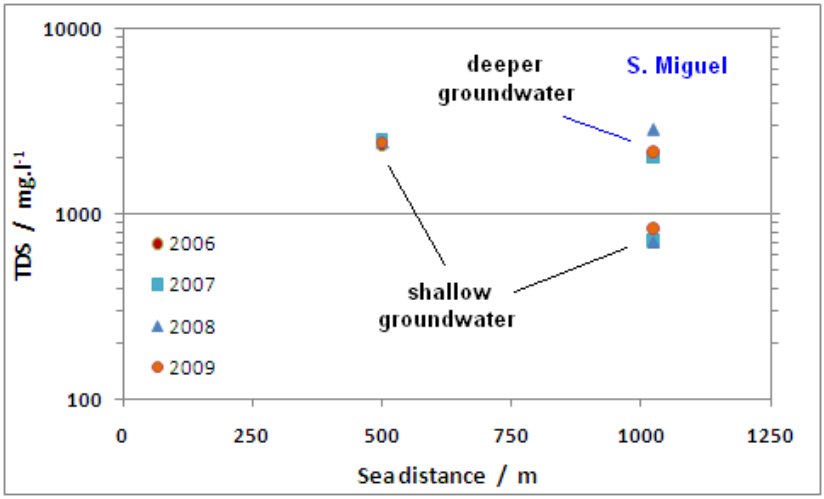

Figure 8.18 – Computed groundwater TDS amounts (2006-2009), S. Miguel valley.

8.1.4 – 2005-2009 Tarrafal TEM data

At Tarrafal (Chão Bom plateaux), the number of TEM soundings that were repeated varies between 3 and 5. All have been taken along a profile line at Chão Bom north side, over TAR02 to TAR06 initial sounding's direction, each year after 2005 (to the exception of 2008) as plotted at figure 8.19.

The mean 1D model was obtained for each TEM sounding, shown in figure 8.20. The corresponding resistivity cross section, done by stitching the models, is shown in figure 8.21. The figure includes all the four-year profiles with their relative position to each other, all with the same resistivity colour scale. The model's responses to data curve's misfit are about 4 to 8%.

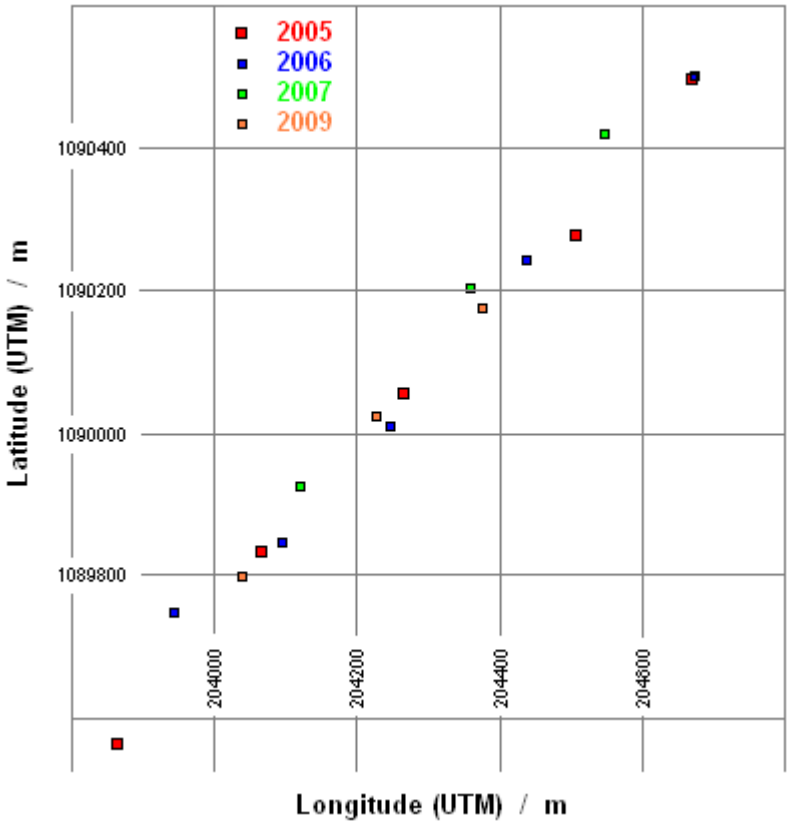

Figure 8.19 – Location of original (2005) and repetition soundings at northwest Tarrafal (Chão Bom), (2006-2009).

As expected, the overall layer's geometry seems to be mostly unchanged, but some real resistivity variations are detected trough the time (that couldn't be ascribed to models' equivalence or error misfit). The major changes take place at the deepest layer, with higher resistivity values in 2006 and 2009 years, figure 8.22. Those changes mean that TDS values at depth 30 m below msl oscillated between about 3000 to 1500 $mg.L^{-1}$, or 1 to 0.5 $g.L^{-1}$ Chloride content, respectively.

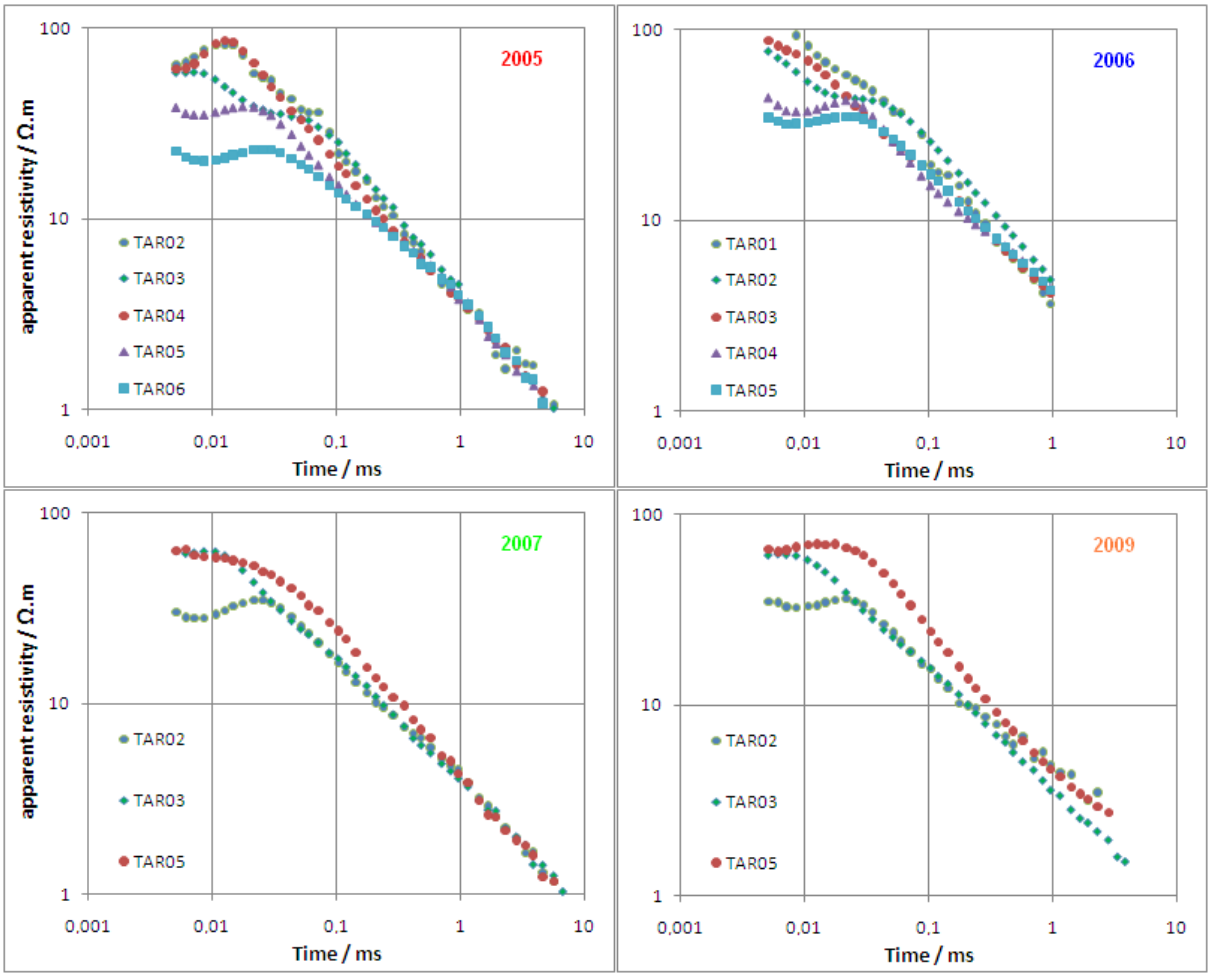

Figure 8.20 – Apparent resistivity TEM sounding curves at northwest Tarrafal (Chão Bom) from 2005 to 2009.

Although the measured resistivity variations seem to be directly correlated with the registered precipitation amounts (figure 8.3), the groundwater mixing with this rainwater infiltration flush would turn out into higher resistivity values in the inland side, gradually decreasing resistivity towards the sea. That is partially verified at shallow layers but not completely fulfilled at all profile's length and depth. One hypothesis to explain this behaviour is the already mentioned mechanism of mixing of groundwater with upcoming flux from the deep salty enrichment older waters, as no disturbance by groundwater exploitation is done at or near these TEM sounding.

A two to one water mixing ratio, with the higher value being from the deep conductive layer, and the smaller from the shallow layer, is sufficient to justify the observed variations, assuming that deep layer has the suggested present day equivalent seawater salinity. An even smaller mixing ratio will be verified if the deep layer is under brine like condition.

At groundwater depths, where borehole screens are usually installed, it is expected that the TDS observed changes aren't directly linked to recent rainfall events.

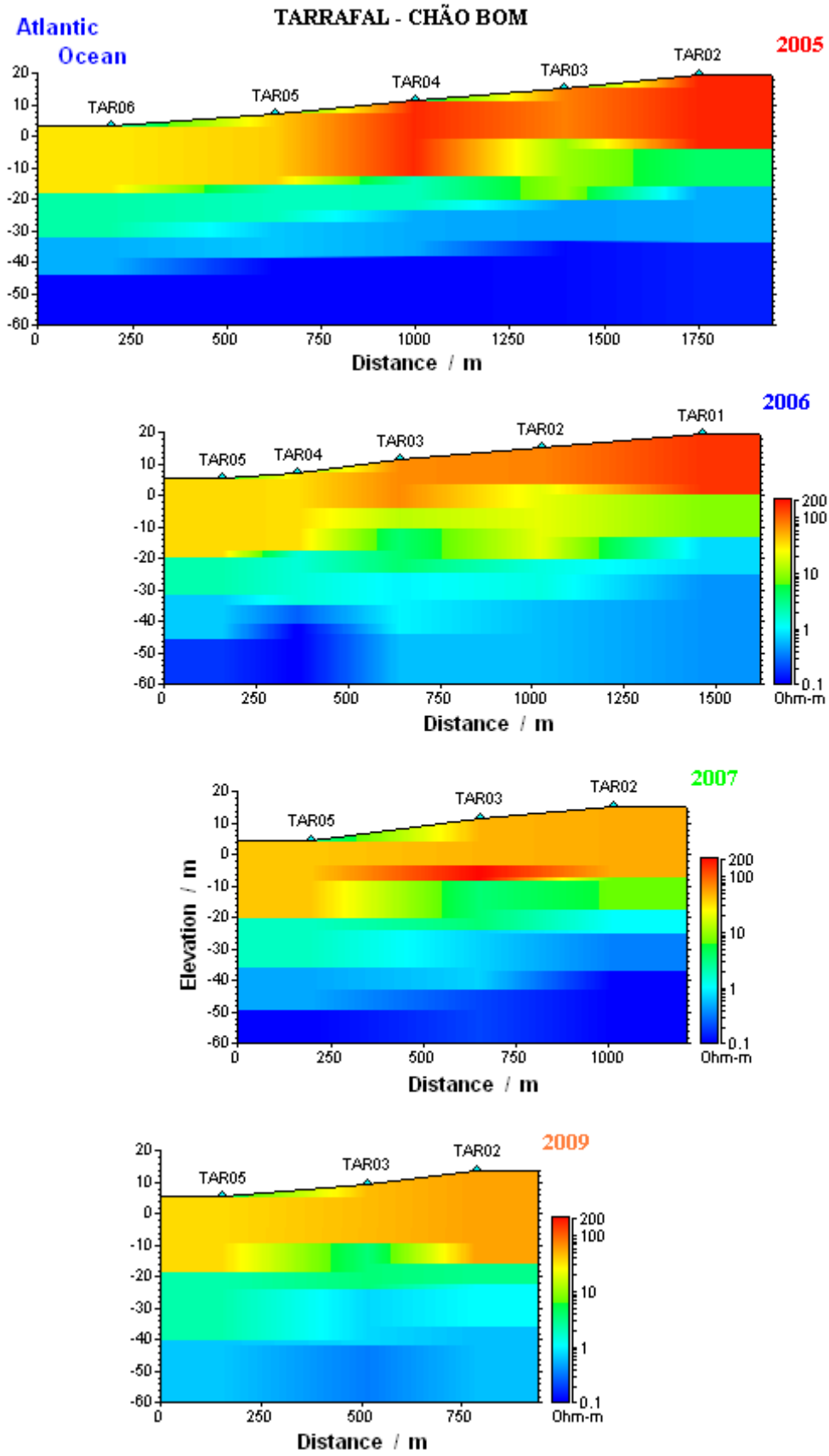

Figure 8.21 – Resistivity cross sections at northwest Tarrafal (Chão Bom), 2005-2009.

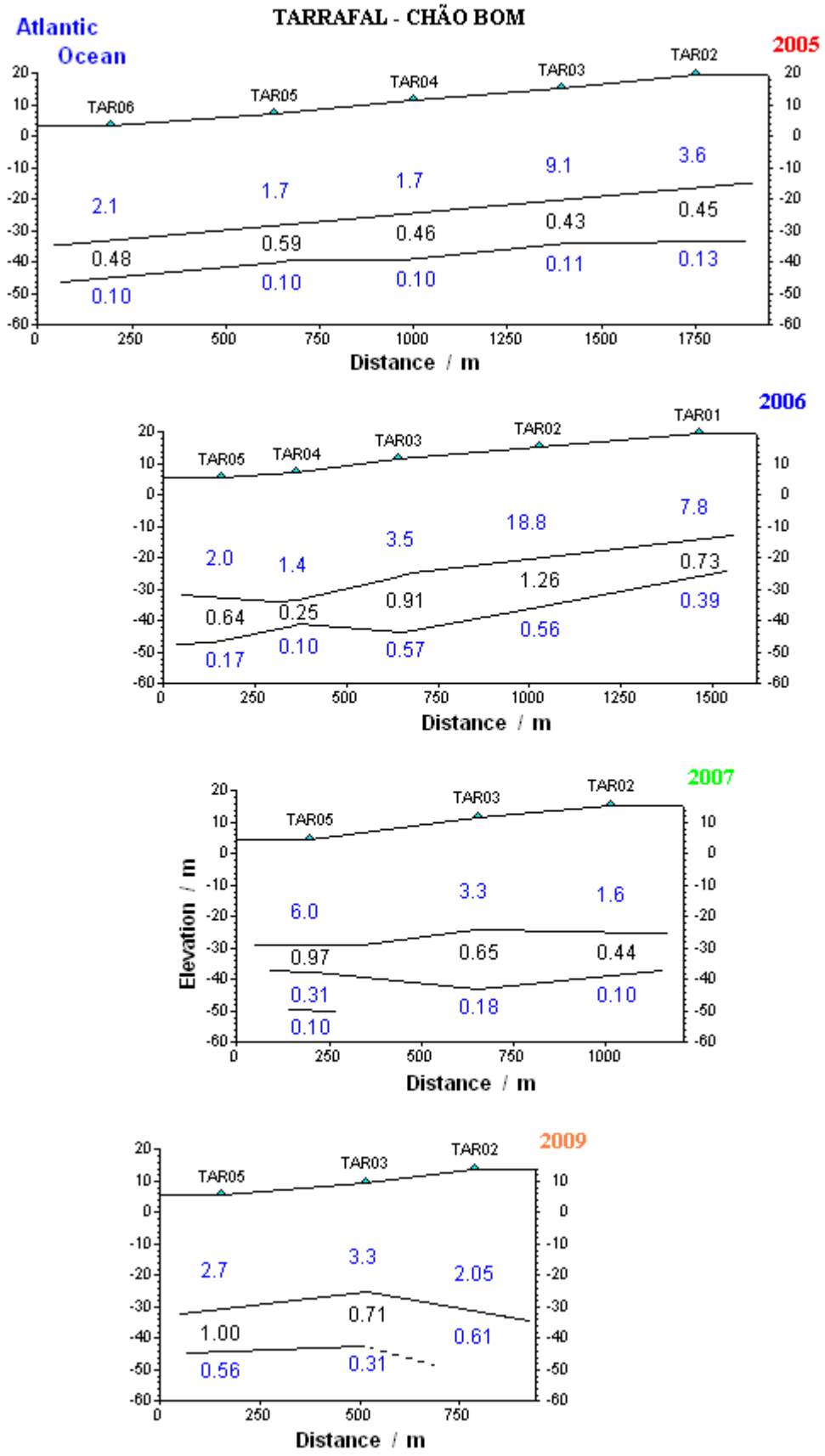

Figure 8.22 – Cross sections resistivities values (ohm.m)
at northwest Tarrafal (Chão Bom), 2005-2009.

8.2 – TEM versus Rainfall correlation

The relation between the registered precipitation and the time measured bulk electric resistivity changes to the groundwater layers (water's TDS) are seen to be of different origin, in respect to near sea shallow groundwater and to deep groundwater.

In S. Domingos, Seca and Picos valleys, the near coastline shallow groundwaters quality (i.e. salinity or TDS content) are directly related to the correspondent rainfall quantities in the respective hydrographic basin. This is controlled by local confining or semi-confining layers that allow the seawater to encroach into inland and mix with freshwater when the groundwater table is below the upper confining layer limit. That can happen by; groundwater overexploitation, natural system discharges depression long after the rainy season or under a prevailing wet condition. The relation between rainfall and bulk resistivity of the shallow layer is of the order of 0.010 $\Omega.m.mm^{-1}$.

The bulk resistivity variations in the basaltic aquifer are due to the groundwater resistivity. This groundwater is a mixing from the sub-superficial inland waters, already changed by rock interaction, and deep upward flow of waters with high dissolved salt's content. The measured groundwater EC value depends on its ionic content, and that can be changed by the mixing of different inland waters. The time changes come only from the time changes on the recharge rates, and that can be difficult to track when mixing occurs, as isotopic measures showed. Nevertheless, those resistivity time changes can be compared against the available precipitation time series, back to the early 60 of last century, figure 8.23. The simple Pearson correlation coefficient between the short resistivity time sets and the wider rainfall ones was done for the several soundings' repetitions. For some valleys, the correlation was poor and no apparent relations between the two data sets were found. "Conclusive results" come from the S. Domingos valley, were the four soundings spanning the 2005-2009 period. The results seem to indicate a spatial flow evolution where a strong negative Pearson coefficient is detected (-0.90 to -0.98 range).

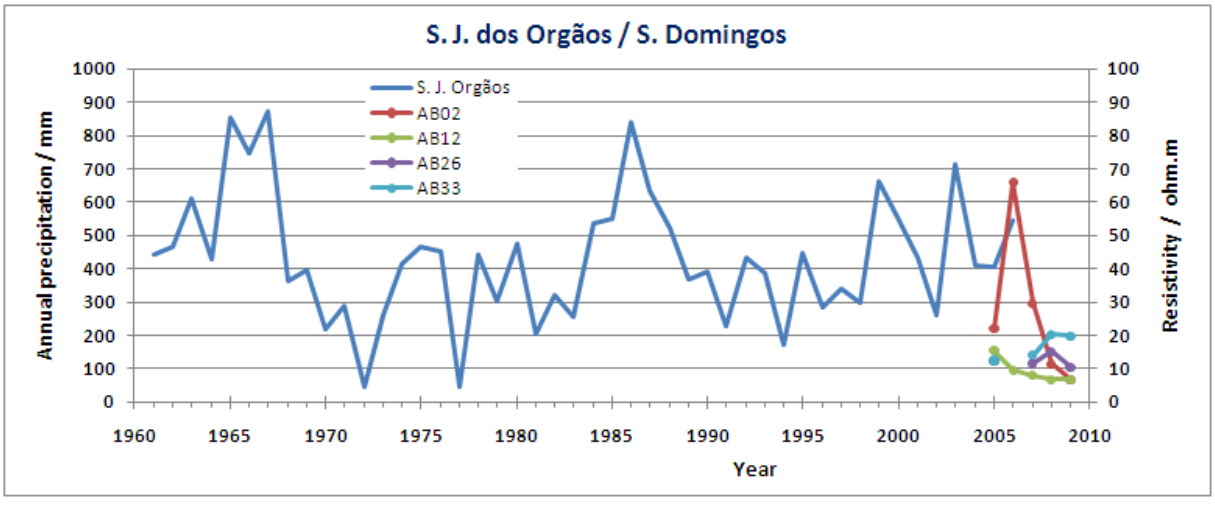

Figure 8.23 – Annual S. J. dos Orgãos precipitation station values and S. Domingos valley repetitions TEM soundings resistivities, (left and right axis, respectively).

The negative correlation means, as expected, that a rainfall increase implies a bulk resistivity decreasing, or a TDS increasing. The observed correlation holds like described in table 8.1, with the corresponding year and time delay getting higher as distance to hydrographic head basin increases. The travel mean time for this deep upstream flow influence is of about 30 years, which is a similar and compatible result to the ascribed values in chapter 6. A piston like mechanism seems to be present between the inland central mountains' recharge, and the near sea discharges.

Table 8.1 – Coefficient and year for the rainfall *versus* resistivity correlations, at S. Domingos.

TEM Sounding	**AB02**	**AB12**	**AB26**	**AB33**
Year (time lag)	1971 (34)	1972 (33)	1976 (29)	1978 (27)
Pearson coefficient	-0.98	-0.98	-0.97	-0.90

From this computed delay time, and for the implicated distances (groundwaters path), with a minimum length of 15 km and a possible maximum of about 20 km, an average linear velocity of 1.5 ± 0.3 $m.d^{-1}$ are estimated. Applying the Darcy law with a hydraulic gradient of 0.04, results into hydraulic conductivity (for the several porosities values), given at table 8.2.

Table 8.2 – Hydraulic conductivity *versus* porosity for the observed data at S. Domingos valley.

Porosity	**0.05**	**0.10**	**0.15**	**0.20**
K **/ m.d^{-1}**	1.9 ± 0.4	3.8 ± 0.8	5.6 ± 1.1	7.6 ± 1.6

Assuming that deep groundwater path way goes through the middle and more compact bottom geologic units, with smaller porosities, the corresponding regional hydraulic conductivity must be in the 4 ± 2 $m.d^{-1}$ range. These values agree and are of the same order of those ones previously computed (in subchapter 7.2.5) from the field data. The same order of delay time is obtained at SECA21 TEM sounding, with a Pearson coefficient of -0.90 for a lag of 29 years, and a hydraulic conductivity of 3.5 $m.d^{-1}$.

For Salto valley the bulk resistivity variations, under the strong influence of the central island Assomada region, the correlation between data sets give a wider time lag ranging from 29 to 40 years, figure 8.24.

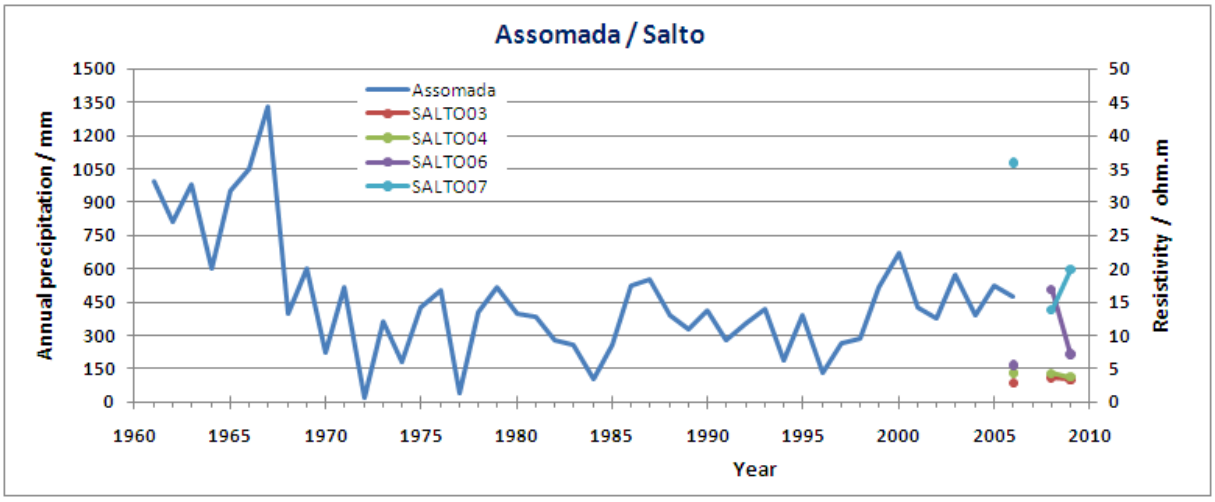

Figure 8.24 – Annual Assomada precipitation station values and Salto valley repetitions TEM soundings resistivities, (left and right axis, respectively).

The Table 8.3 summarizes the computed correlation values. From these delay times and for the concerned groundwater path distances, with a minimum length of 12 km and a possible maximum of about 15 km, an average linear velocity of 1.1 ± 0.3 $m.d^{-1}$ are calculated. Applying again the Darcy law with a hydraulic gradient of 0.04 (and various porosities) results in hydraulic conductivity as given in table 8.4. The mean regional hydraulic conductivity in the region is then in the 3 ± 1 $m.d^{-1}$ range.

Table 8.3 – Coefficient and year for the rainfall *versus* resistivity correlations, at Salto.

TEM Sounding	**SALTO03**	**SALTO04**	**SALTO06**	**SALTO07**
Year (time lag)	1966 (40)	1972 (34)	1975 (31)	1977 (29)
Pearson coefficient	-1.00	-0.96	-1.00	-1.00

Table 8.4 – Hydraulic conductivity *versus* porosity for the observed data at Salto valley.

Porosity	**0.05**	**0.10**	**0.15**	**0.20**
K **/ m.d^{-1}**	1.4 ± 0.4	2.8 ± 0.8	4.1 ± 1.1	5.6 ± 1.6

For northwest Tarrafal, the observed resistivity variations when compared against Chão Bom precipitation time series (figure 8.25) (although this meteorological station isn't located at hydraulic basin beginning, but rather near the coastline), gives a mean regional hydraulic conductivity of 2 ± 1 $m.d^{-1}$, from the data shown at tables 8.5 and 8.6.

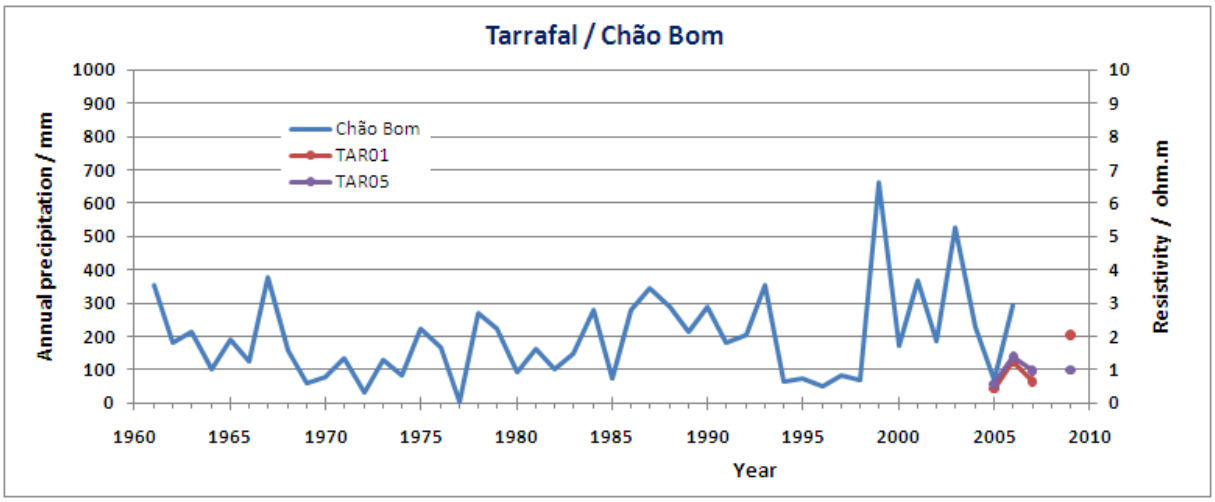

Figure 8.25 – Annual Chão Bom precipitation station values and northwest Chão Bom plateaux repetitions TEM soundings resistivities, (left and right axis, respectively).

Table 8.5 – Coefficient and year for the rainfall *versus* resistivity correlations, at Tarrafal.

TEM Sounding	**TAR01**	**TAR05**
Year (time lag)	1981 (24)	1979 (26)
Pearson coefficient	-0.98	-0.99

Table 8.6 – Hydraulic conductivity *versus* porosity for the observed data at Tarrafal.

Porosity	**0.05**	**0.10**	**0.15**	**0.20**
K **/ m.d^{-1}**	1.2 ± 0.2	2.4 ± 0.5	3.6 ± 0.7	4.8 ± 1.0

Although these hydraulic conductivity values and estimated time lags are similar to observed and expected ones, all these values have to be taken and regarded with care, as the TEM data set has only a few years range, and observed resistivity variations are small.

9
CONCLUSIONS

On this night chapter, the conclusions about the work are described, with some recommendations and future work's applications.

9.1 – Concluding remarks and outlook

The application of the EM transient method as an evaluation tool of groundwater quality, if properly calibrated against known information from the wells and boreholes (namely the chemical water composition), proved to be feasible to the semi-arid Cape Verde environmental condition. That is especially important for areas where the watershed points are sparse.

To this purposes the TEM data spatial density is higher than local watersheds, giving altogether information about deep layers, beyond the depth of the existent boreholes. At Santiago Island, the present study showed that groundwater quality in coastline valleys, regarding to salinity, has two distinct origins.

From the available data and their analysis, the conclusion is that groundwater quality, i.e. its TDS content (furthermore its usefulness), apart from rock interaction enrichment, is naturally affected by the rainfall amount at each hydrographic basin.

In Santiago, the shallow seashore aquifer system, especially in the south-eastern coastline valleys, are under direct influence of seawater and attains a strong seasonal salinity variation effect. This effect is a consequence of valley's lithological geometry, with local impervious to semi-pervious layers allowing the seawater shallow mixing, as simulation had shown. The problem increases by the groundwater overexploitation at the annual dry period or under long time waterless condition, when groundwater salinity is high. Land irrigation from these wells and shallow boreholes, enhances even further the soil and water salinity. This procedure has changed the soil in these fertile valleys, into unproductive or low productive ones. The solution to decrease land salty content is to start irrigation with less salty inland sources, like from springs, boreholes, water dam reservoir or desalinized waters. Another solution, already tested with success at a small scale in the valleys between Picos and Salto, is to insert a deep concrete wall, side to side near the end of the valley to stop the seawater encroachment and its mixing with fresh or brackish water (António Pina, personal communication).

Concerning the deep groundwater, available in boreholes, its extraction usually starts 1 km from the coastline, onward. The TEM survey data have shown in most valleys a conductive layer below mean sea level (at roughly 50 m depth). These low resistivity values can be associated to seawater salt's deposition (evaporites) in the course of ancient low level seawater episodes. This deep layer can be also the source to the higher Chloride water content. The shallow direct infiltration of recent meteoric waters and the deeper and older

ones with larger-scale time and path way from central mountain regions, mix in the valleys ends. The mixing is certainly not constant because both groundwater flows (deep and shallow) must be changing with precipitation recharge rates over the years. The data seems compatible with a deep groundwater flow of about 30 years long (although care must be taken regarding the analyses from the few TEM variability data set). This mixing can be also induced by the overexploitation conditions in boreholes, increasing the water salt content from upward flow across salty layers, as the numerical flow simulations showed. There is no direct and easy solution to this problem. The action is to impose a groundwater extraction limit at each borehole in these valleys, compatible with a given allowed TDS maximum value. Each borehole groundwater extraction rate should change throughout seasons and also from year to year. Monitoring the groundwater EC periodically could easily give the desired information to assign that extraction rate limit. However, the observed and actual reality, is that the local authorities have been unsuccessful, applying to boreholes and wells a number of hours per day extraction limits.

For irrigation purposes, the present groundwater chemical characterization is adequate. It could help to delineate, altogether with soil classification, the agricultural specimens to achieve the best yields with the available water quality. The condition is that present yields are progressively decreasing for traditional plants because the water and soil salinity within valleys is increasing.

But available groundwater chemical data is insufficient to search out finer details about shallow and deeper waters. The mixing conditions on borehole water sampling surely had affected the joint TEM and hydrochemistry interpretation, superimposing a higher scatter on the data. In the present conditions, most of the boreholes have multi screens placed at several depths producing a groundwater extra mixing. Taking this into account, care must be also taken with future chemical water sampling. If possible, the use of water grab samplers in the boreholes from several depths is preferable. Borehole continuous water EC logging profiles would also be very useful to help interpretation. Furthermore, an accurate topographic levelling with centimetres precision of the watersheds (wells and boreholes) is desired, to achieve a better knowledge about groundwater levels. This could be a task to carry out after the responsible authority's conclusion of the Santiago Island watersheds' catalogue.

Concerning a possible future electromagnetic field work, a higher spatial density and a powerful transient equipment is recommendable. That will overcome the (present work) weak input signal and enhance the SNR, reaching easily to greater depths. Water sampling for chemical analyses, but especially water parameters (like EC, pH and temperature), as also water depth measures should be carried out altogether with upcoming TEM survey. The sounding's inversion and modelling will profit from this and also with continuous profiling, collated or very nearby soundings, to better fulfil the needs of the 2D and 3D interpretation methods, tested in this work.

The applied algorithm, for the quasi-2D and quasi-3D inversion, proved to be useful, with some intrinsic and natural limitations. The 2D approximation being a LCI method was only applied to those surveyed valleys where the TEM soundings were acquired in succession

along an almost constant direction. Those 2D starting models were always resistive uniform with fixed thickness layers. The 2D inversion results gave similar structures and resistivity values when compared against the simple collated 1D inversion tool from native equipment software, which gives confidence to the inversion outputs. In general, the global fit between model result's output and field data gets better with growing lateral distance influence. That inclusion of more nearby sounding's data follows the expected behaviour, with smaller *rms* misfit values at the expense of slightly smoothing each sounding model. Beyond the imposed number of fixed layer's geometry, the distance between soundings (spatial soundings density) is a more relevant issue. When neighbours soundings are further apart, naturally are not to expect a really true continuity influence, hence the blocky output observed in some model's parts.

The 3D approximation being a SCI method was consequently applied only to the surveyed wide areas of S. Domingos and Tarrafal plateaux. The kind of performance from the inversion algorithm is similar to the 2D approximation. The misfit *rms* tends to be smaller with more soundings inclusion to the inversion, unless the medium owns a more heterogeneous structure, like from the Tarrafal area.

From these achieved electric resistivity values, relations between this data and the available hydrological and groundwater chemical data were found. Those relations are satisfactory and hold relatively well, concerning the present amount of data. Relations like the TDS inland distributions are based upon the deducted porosity, around 15 to 20 %, to both sedimentary shallow layers and altered and fractured basalts. Upon this and from measured electric resistivity values, acquired by electromagnetic (or DC) methods, TDS values and groundwater quality can be deduced.

With nowadays data, the exact Santiago Island hydrologic water balance is difficult to reach. Only the bound's value can be estimated. Nevertheless, it seems that the major problem that Santiago is faced with, does not concern only to the water available quantity, but as more to do with the available quality, especially at the agricultural land irrigation areas.

REFERENCES

Aeschbach-Hertig W., Peeters, F., Beyerle, U., Kipfer, R., 1999. Interpretation of Dissolved Atmospheric Noble Gases in Natural Waters. *Water Resources*, 35, 2779-2792.

Akiti, T., 1985. Environmental isotope study of the groundwaters of the island of Santiago (Cape Verde). *Report Project CVI/82/004 PNUD. International Atomic Energy Agency, Division of Research and Laboratories, Section of Isotope Hydrology*, Vienna. 26.

Ali, M. Y., Watts, A. B., Hill, I., 2003. A seismic reflection profile study of lithospheric flexure in the vicinity of the Cape Verde Islands. *Journal Geophysical Research*. 108, 2239-2262.

Allison, G. B. and Hughes M. W., 1978. The use of environmental tritium and chloride to estimate total local recharge to an unconfined aquifer. *Australian Journal of Soil Sciences*. 16, 181-195.

Alves, M. C. A., Macedo, J. R., Silva, L. C., Serralheiro, A., Peixoto Faria, A. F., 1979. *Estudo geológico, petrológico e vulcanológico da ilha de Santiago (Cabo Verde).* Garcia de Orta 3, 1-2, 47-74, (in Portuguese).

Amaral, I., 1964. *Santiago de Cabo Verde - A Terra e os Homens.* Junta de Investigações do Ultramar. Lisboa, 444, (in Portuguese).

Anders Vest Christiansen, A. V., 2003. Application of airborne TEM methods in Denmark and layered 2D inversion of resistivity data. PhD thesis. Department of Earth Sciences, University of Aarhus, Denmark.

Anderson, W. L., 1979. Numerical integration of related Hankel transforms of order 0 and 1 by adaptative digital filtering. *Geophysics*. 44, 1287-1305.

Antonov, E. Y., Shein, A. N., 2008. Improving inversion quality for IP-affected TDEM data. *Russian Geology and Geophysics.* 49, 790-802.

ANZECC - Australian and New Zealand Environment Conservation Council - National Water Quality Management Strategy Guideline Documents, *Australian and New Zealand Guidelines for Fresh and Marine Water Quality* (revised 2000)

Appelo, C. A. J. and Geirnart, W., 1991. Processes accompanying the intrusion of salt water. In Hydrogeology of salt water intrusion – A selection of SWIM papers, II. 291-304.

Appelo, C. A. J. and Postma, D., 2005. *Geochemistry, groundwater and pollution*, 2nd Ed., A. A. Balkema Publishers. Leiden, The Netherlands; 634.

Appelo, C. A. J. and Willemsen, A., 1987. Geochemical calculations and observations on salt water intrusions, a combined geochemical/mixing cell model. *Journal of Hydrology*. 94, 313-330.

Applied Electromagnetic Research (AEMR), 2006. TEM-FAST 48 – Manual, Version 7.3, (Ed. Fainberg). The Netherlands.

Archie, G. E., 1942. The electrical resistivity log as an aid in determining some reservoir characteristics. *Petroleum Transactions of AIME*. 146, 54-62.

Arps, J. J., 1953. The effect of temperature on the density and electrical resistivity of sodium chloride solutions. *Petroleum Transactions of AIME*. 198, 327.

Aster, R. C., Thurber, C. H., Borchers, B., 2005. *Parameter estimation and inverse problems*. Elsevier Academic Press; 301.

Auken, E., 1995. 1D time domain electromagnetic interpretations over 2D and 3D structures. *Proceedings of the Symposium on the Application of Geophysics to Engineering and Environmental Problems*. Orlando, USA. EEGS. 329-338.

Auken, E. and Christiansen, A. V., 2004. Layered and laterally constrained 2D inversion of resistivity data. *Geophysics*. 69, 752-761.

Auken, E., Christiansen, A. V., Jacobsen, B. H., Foged, N., Sørensen, K. I., 2005a. Piecewise 1D laterally constrained inversion of resistivity data. *Geophysical Prospecting*. 53, 497-506.

Auken, E., Christiansen, A. V., Jacobsen, L., Sørensen, K. I., 2005b. Laterally constrained 1D inversion of 3D TEM data. *Symposium on the Application of Geophysics to Engineering and Environmental Problems*. SAGEEP Proceedings. 519-524.

Auken, E., Christiansen, A. V., Jacobsen, L. H., Sørensen, K. I., 2008. A resolution study of buried valleys using laterally constrained inversion of TEM data. *Journal of Applied Geophysics*. 65, 10-20.

Auken, E., Foged, N., Sørensen, K. I., 2002. Model recognition by 1-D laterally constrained inversion of resistivity data. *Proceedings of the 8th Meeting Environmental and Engineering Geophysics*, Matias, M. S., Grangeia, C. (Eds.), EEGS-ES, University of Aveiro, Portugal, 241-244.

Auken, E., Pellerin L., Christensen, N. B., Sørensen, K., 2006. A survey of current trends in near-surface electrical and electromagnetic methods. *Geophysics*. 71-5, 249-260.

Auken, E., Sørensen, K. I., Danielsen, J. E., Pellerin, L., 2001. Mutually constrained inversion (MCI) of electrical and electromagnetic data from Skaro, Denmark. EEGS-ES Birmingham U.K., 94-95.

Averyanov, V. S., 1965. Role of magnetic crystallographic anisotropy in the process of viscous magnetization of ferrites, Izvestiya. *Physics of the Solid Earth*. 82-89.

Azevedo, J. M. M., 1998. *Geologia e hidrogeologia da Ilha das Flores (Açores - Portugal)*. PhD thesis, Departamento de Ciências da Terra. Universidade de Coimbra, 403. (in Portuguese).

Bahr, K., 1991. Geological noise in magnetotelluric data: a classification of distortion types. *Physics of the Earth and Planetary Interiors*. 60, 24-38.

Barker, R. D., 1981. The offset system of electrical resistivity and its use with a multicore cable. *Geophysical Prospecting*. 29, 128-143.

Barmen, G., Carvalho, V., Querido, A., 1990. Groundwater-related geological and isotopic investigations on the island of Fogo: an overview. Report LUTVDG/TVTG-90/3027, Lund Institute of Technology. Lund, Sweden, 72.

Barmen, G., Joseffson, G., Magnusson, M., Wernersson, H., 1984. A hydrogeological investigation on Santiago, Cape Verde Islands, Report TVTG-5009, Lund Institute of Technology. Lund, Sweden. 43.

Barsukov, P. and Fainberg, E., 2001. Superparamagnetic effect over gold and nickel deposits. *European Journal of Environmental and Engineering Geophysics*. 6, 61-72.

Barsukov, P. O., Fainberg, E. B., Khabensky, E. O., 2003. The Antenna Polarization Effect in Transient Electromagnetic Sounding, Izvestiya. *Physics of the Solid Earth*. 39-11, 949-954.

Barsukov, P. O., Fainberg, E. B., Khabensky, E. O., 2007. Shallow Investigations by TEM-FAST Technique: Methodology and Examples, chapter 3. Methods in Geochemistry and Geophysics, 40, in Spichak V. V. (Ed.), *Electromagnetic Sounding of the Earth's Interior*. Elsevier. 55-77.

Bear, J., Cheng, A., Sorek, S., Ouazar, D., Herrera, I., (Eds.), 1999. *Seawater Intrusion in Coastal Aquifers - Concepts, Methods and Practices. Theory and Applications of Transport in Porous Media*, Kluwer Academic Publishers, 14, 625.

Bebiano, J. B., 1932. *A geologia do Arquipélago de Cabo Verde, Comunicações dos Serviços Geológicos de Portugal*. 18-1, 275. (in Portuguese).

Bishop, J. and Reid, J., 2003. Some Positive thoughts about Negative TEM Responses. *ASEG 16th Geophysical Conference and Exhibition*, Adelaide

Bosscher, A., 1981. *Groundwater availability in selected areas of Cabo Verde*. ITC. Praia

BURGEAP, 1974. *La Mise en Valeur des Eaux Souterraines dans l`Archipel du Cap Vert, Rapport de Fin de Mission*, Praia

BURGEAP, 1983. *Étude générale du massif du Pico da Antónia (Santiago)*, Praia

Buselli, G., 1982. The effect of near-surface superparamagnetic material on electromagnetic measurements. *Geophysics*. 47, 1315-1385.

Buselli, G., Barber, C., Davis, G. B., Salama, R. B., 1990. Detection of ground water contamination near waste disposal sites with transient electromagnetic and electrical methods. Geotechnical and Environmental Geophysics. 2. In Ward S. H. (Ed.), Environmental and Groundwater, Society of Exploration Geophysicists, Investigations in Geophysics 5, Tulsa, Oklahoma, 27-39.

Carman, P. C., 1937. Fluid flow through granular beds. *Trans Inst Chem Eng.* 15, 150-166.

Carman, P. C., 1939. Permeability of saturated sands, soils and clays, *J. Agric. Sci*. 29, 262-273.

Carpenter, A. B., 1978. Origin and chemical evolution of brines in sedimentary basins. (eds. K. S. Johnson and J. R. Russell) in 13th Industrial Minerals Forum Oklahoma, *Geol. Surv. Circular*. 79, 60-77.

Carreira, P. M., Marques, J. M., Pina, A., Gomes, A. M., Fernandes, P. A. G., Santos, F. M., 2010. Groundwater Assessment at Santiago Island (Cabo Verde): A Multidisciplinary Approach to a Recurring Source of Water Supply. *Water Resource Manage*. 24, 1139-1159.

Carreira, P. M., Pina, A. F. L., Gomes, A.M., Marques, J. M., Almeida, E., Monteiro Santos, F., 2007a. Assessment of groundwater salinization mechanisms in Santiago Island (Cabo Verde), an environmental isotopic approach. Vienna, Austria.

Carreira, P. M., Pina, A. F. L., Gomes, A. M., Marques, J. M., Gonçalves, R., Almeida, E., Valério, P., Monteiro Santos, F., 2007b. *Utilização dos teores em Trítio na caracterização dos sistemas aquíferos da ilha de Santiago, Cabo Verde*, Revista da Universidade de Cabo Verde, (in Portuguese).

Carrier, W. D., 2003. Goodbye, Hazen; Hello, Kozeny-Carman. *Journal of Geotechnical and Geoenvironmental Engineering, Technical Notes*, 129-11, 1054-1056.

Cartwright, I., Weaver, T. R., Fifield, L. K., 2006. Cl/Br ratios and environmental isotopes as indicators of recharge variability and groundwater flow: An example from the southeast Murray Basin, Australia. *Chemical Geology*. 231, 38-56.

Carvalho, J., Cabral, J. Gonçalves, R., Torres, T., Mendes-Victor, L., 2006. Geophysical methods applied to fault characterization and earthquake potential assessment in the Lower Tagus Valley, Portugal. *Tectonophysics*. 418, 277-297.

Cazenave, A., Dominh, K., Rabinowicz, M., Ceuleneer, G., 1988. Geoid and depth anomalies over ocean swells and troughs: evidence of an increasing trend of the geoid to depth ratio with age of plate. *Journal Geophysical Research*. 93, 8064-8077.

Christensen, B. P., Holm, P. M., Jambon, A., Wilson, J. R., 2001. Helium, Argon and Lead isotopic composition of volcanics from Santo Antão and Fogo, Cape Verde Islands. *Chem. Geol*. 178, 127-142.

Christensen, N. B. and Sorensen, K. I., 1998. Surface and borehole electric and electromagnetic methods for hydrogeophysical investigations. *European Journal Environmental Engineering Geophysics*. 3-1, 75-90.

Christensen, N. B.: 1995. *Den transiente elektromagnetiske sonderingsmetode*, Lecture notes, Department of Earth Sciences, University of Aarhus, 38.

Christiansen, A. V., 2003. Application of airborne TEM methods in Denmark and layered 2D inversion of resistivity data, PhD thesis. University of Aarhus, Denmark.

Christiansen, A. V., Auken, E., Sørensen, K., 2006. The transient electromagnetic method, chapter 6, Kirsch, R. (Ed.) in Groundwater Geophysics, A Tool for Hydrogeology. Spring, 493.

Coduto, D. P., 1999. *Geotechnical engineering: Principles and practice*. Prentice-Hall. New Jersey, 800.

Cole, K. S. and Cole, R. H., 1941. Dispersion and Absorption in Dielectrics - I Alternating Current Characteristics. *Journal of Chemical Physics*. 9, 341-351.

Cole, K. S. and Cole, R. H., 1942. Dispersion and Absorption in Dielectrics - II Direct Current Characteristics. *Journal of Chemical Physics*. 10, 98-105.

Condesso de Melo, M.T.; Silva, J.; Lobo de Pina, A.; Mota Gomes, A., Almeida, F.; Moura, R.; Marques da Silva, M.A., 2008. Use of geochemical tools to study groundwater salinization in volcanic islands: a case study in the Porto Santo (Portugal) and Santiago (Cape Verde) islands. *Proceedings of 20th Salt Water Intrusion Meeting*, Florida. 23-27.

Constable, S. C., Parker, R. L., Constable, C. G., 1987. Occam's inversion: a practical algorithm for generating smooth models from electromagnetic sounding data. *Geophysics*. 52, 289-300.

Correia, E., 1998. *Sobre a variabilidade da precipitação e o tempo das águas em Cabo Verde*. Lisboa. Garcia de Orta, Série de Geografia. 16, 1-2, 49-61.

Costa, F. L., 1995. *Erosion, risques naturels et conservation du sol au Cap Vert. Colloque Crues Versants et Lits Fluviaux.* Ministère de l'Enseignement Supérieur et de la Recherche, Laboratoire de Géographie Physique, C.N.R.S.-U.R.A. 141, Université de Paris.

Courtney, R. C. and White, R. S., 1986. Anomalous heat flow and geoid across the Cape Verde Rise: evidence for dynamic support from a thermal plume in the mantle. *Geophysical Journal Research*. *Astronomical Society*. 87, 815-867.

Craig, H., 1961. Standard for reporting concentration of Deuterium and Oxygen-18 in natural waters. *Science*. 133, 1702-1703.

Cunha, F. R., 1964. *O problema da captação da água do nevoeiro em Cabo Verde.* Estudos Agronómicos. Junta de Investigações do Ultramar. Lisboa, 5-4, 121-172. (in Portuguese)

Custodio, E., 1975. *Hidrogeologia de formaciones volcánicas*. Proceedings 3rd UNESCO - ESA - AIH Symposium on Groundwater, Palermo, 23-69. (in Castellano).

Custodio, E., 1978. *Hidrologia de las rocas volcanicas*. Proceedings III Congresso Internacional de Águas Subterrâneas. Ponencia General. UNESCO – ESA – AIH, 33-69. Palermo. (in Castellano).

Custodio, E., 1986. Groundwater characteristic and problems in volcanic rock terrains. In Isotopic techniques in the study of the hydrology of fractured and fissured rocks, International Atomic Energy Agency. Vienna. 87-137.

Custodio, E.: 1987. Ground Water problems in coastal areas. In Studies and Reports in Hydrology, UNESCO-IHP, 14-112.

Custodio, E., 1997. Studying, monitoring and controlling seawater intrusion in coastal aquifers; Guidelines for study, monitoring and control, *FAO Water Reports*, 11, 7-23.

Custodio, E., 2004. Hydrogeology of volcanic rocks. In Kovalevsky, V. S., Kruseman, G. P. and Rushton, K. R. (Eds.) – An international guide for hydrogeological investigations. IHP-IV, Series on Groundwater, 3, UNESCO. Paris

Custodio, E., and Llamas, M. R., 2001. *Hidrologia subterrânea*. I and II, Omega, S.A, Barcelona. 2350. (in Castellano).

Dahlin, T., Ferreira, A., Per-Gursson, 1986. *Resistivity measurements in arid areas and volcanic formations, a field study on Santiago Cape Verde Islands*. Department of Engineering Geology Lund University, Instituto Nacional de Investigação Tecnologica Cabo Verde, LUTVDG/(TVTG-3010)/1-49, 49.

Danielsen, J. E., Auken, E. and Sørensen, K. I., 2001. *HITEM – a high moment/high production TEM system.* The HydroGeophysics Group, Department of Earth Sciences, University of Aarhus, Denmark.

Danielsen, J. E., Auken, E., Jørgensen, F., Søndergaard, V., Sørensen, K. I., 2003. The application of the transient electromagnetic method in hydrogeophysical surveys. *Journal of Applied Geophysics*. 53, 181-198.

Darwin, C., 1844. *Geological Observations on the Volcanic Islands*. Smith, Elder and Co. London; 674.

Dash, B. P. Ball, I. M. M., King, I. G. A., Butler, L. W., Rona, F. P. A., 1976. Geophysical investigation of the Cape Verde Archipelago. *Journal Geophysical Research*. 81-B29, 5249-5259.

Davis, S. N., Cecil, L. D., Zreda, M., Moysey, S., 2001. Chlorine-36, Bromide, and the origin of spring water. *Chemical Geology*. 179, 3-16.

Davis, S. N., Wittemore, D. O. and Febryka-Martin, J., 1998. Uses of Chloride/Bromide ratios is studies of potable water. *Ground Water*, 36-2, 338-350.

De Paepe, P., Klerkx, J., Hertogen, J., Plinke, P., 1974. Oceanic tholeiites on the Cape Verde Islands - petrochemical and geochemical evidence. *Earth Planet. Sci. Lett*. 22, 347-354.

Dittrich, I., 1982: *Délimitation des composants du bilan hydrique pour Santiago: Un modèle semi-déterministique*. Praia, Cap Vert

DNR. 1997. DNR Water Facts: Irrigation water quality, salinity and soil structure stability. *Department of Natural Resources*, N. W55, Brisbane, Australia

Doucelance, R., Escrig, S., Moreira, M., Gariépy, C., Kurz, M. D., 2003. Pb–Sr–He isotope and trace element geochemistry of the Cape Verde Archipelago. *Geochim. Cosmochim. Acta*. 67, 3717-3733.

Drever, J. I., 1997. *The Geochemistry of Natural Waters: Surface and Groundwater Environments*. Prentice-Hall. New Jersey, USA; 436.

Dullien, F. A. L., 1979. *Porous media, fluid transport and pore structure*. Academic Press, New York; 396.

Duprat, H. i:, Friis, J., Holm, P. M., Grandvuinet, T., Sørensen, R. V., 2007. The volcanic and geochemical development of São Nicolau, Cape Verde Islands: constraints from field and 40Ar/39Ar evidence. *J. Volcanol. Geotherm. Res*. 162, 1-19.

Edmunds, W. M., 2001. Palaeowaters in European coastal aquifers - the goals and main conclusions of the PALAEAUX Project, Geological Society, London Special Publication 189, 1-16.

Effersø F., Auken, E., Sørensen, K. I., 1999. Inversion of band-limited TEM responses, *Geophysical Prospecting*. 47, 551-564.

Effersø, F., 2000. Resolution of Cole-Cole parameters based on induced polarization data. In Hansen, C., Jacobsen, B. H., Mosegaard K. (Eds.). Methods and Applications of Inversion Lecture Notes in Earth Sciences. Springer. 92.

El-Kaliouby, H., 2001. Extracting IP Parameters from TEM Data, Ch 17. In Poulton, M. M. (Ed.). Computational neural networks for geophysical data processing. Handbook of Geophysical Exploration – Seismic Exploration. 30, 307-326.

Epstein, S., Mayeda, T., 1953. Variation of ^{18}O content of waters from natural sources. *Geochimica Cosmochimica Acta*. 4, 213-224.

Eriksson, E. and Khunakasem, V., 1969. Chloride concentration in groundwater, recharge rate and rate of deposition of chloride in the Israel Coastal Plain. *Journal of Hydrology*. 7, 178-197.

Everett, M. E. and Weiss, C. J., 2002. Geological noise in near-surface electromagnetic induction data. *Geophysical Research Letters*. 29.

Everett, M. E., Meju, M., A., 2005. Near-Surface Controlled-Source Electromagnetic Induction: Background and recent advances. In Rubin Y. and Hubbard S. S. (Ed.), Hydrogeophysics. Springer. 157-183.

Falkland, A. and Custodio, E., 1991. Hydrology and water resources of small islands: a practical guide. Studies and Reports on Hydrology. 49. UNESCO, Paris; 630.

Fernandopullé, D., 1977. *Aperçu sur les ressources en eau et les possibilités d'aménagement hydrauliques Iles du Cap Vert*. Projet CTP-CVI/75/001. Praia; 41.

Fernandopullé, D., 1979. *Recherche et mise en valeur des eau souterraines. Rapport terminal*. Projet CVI-75/001. PNUD-DTCD, Praia.

Fetter, C. W., 2001. *Applied Hydrogeology*, 4th ed., Prentice Hall, New Jersey; 598.

Fidelibus, M. D. and Tulipano. L., 1986. Mixing phenomena owing to sea water intrusion for the interpretation of chemical and isotopic data of discharge waters in the Apulian coastal carbonate aquifer (southern Italy). Proceedings, 9th SWIM, Delft University of Technology. 591-600.

Fishman, M. J. and Friedman, L. C., 1989. Methods of determination of organic substances in water and fluvial sediments. Techniques of Water-Resource Investigations of the U.S. Geological Survey, book 5, chapter A1. 545.

Fitterman, D. V., and Anderson, W. L., 1987. Effect of transmitter turn-off time on transient soundings. *Geoexploration*. 24, 131-146.

Fittermann, D. V. and Stewart, M. T., 1986. Transient electromagnetic sounding for groundwater. *Geophysics*. 51, 995-1005.

Flint, L. E. and Selker, J. S., 2003. Use of porosity to estimate hydraulic properties of volcanic tuffs. *Advances in Water Resources*. 26, 561-571.

Flis, M. F., Newman, G. A. and Hohmann, G. W., 1989. Induced polarization effects in time-domain electromagnetic measurements. *Geophysics*. 54, 514-523.

Fontes, J. C. G., 1999. *Comportamento Hidrológico dos Solos Agrícolas da Ilha Terceira, Avaliação e Simulação com o Modelo OPUS*. PhD thesis, Departamento de Ciências Agrárias. Universidade dos Açores. 330. (in Portuguese).

Friedman, I., 1953. Deuterium content of natural waters and other substances. *Geochimica Cosmochimica Acta*. 4, 89-103.

Friedman, S. P., 1998. Simulation of a potential error in determining soil salinity from measured apparent electrical conductivity. *Soil Sci. Soc. Am. J*. 62, 593-599.

Gallardo, L. A. and Meju, M. A., 2003. Characterization of heterogeneous near-surface materials by joint 2D inversion of dc resistivity and seismic data. *Geophys. Res. Lett*. 30-13, 1658.

Gallardo, L. A. and Meju, M. A., 2004. Joint two-dimensional dc resistivity and seismic traveltime inversion with cross-gradients constraints. *J. Geophys. Res*. 109.

Geonics Ltd. Technical Note 5, 1980. *Electrical Conductivity of Soils and Rocks*

Georgi, D. T. and Menger, S, K., 1994. Reservoir quality, porosity and permeability relationships, Proceedings 14th Mintrop Seminar. Münster.

Gerlach, D. C., Cliff, R. A., Davies, G. R., Norry, M., Hodgeson, N., 1988. Magma sources of the Cape Verdes Archipelago - isotopic and trace element constraints. *Geochim. Cosmochim. Acta*. 52, 2979-2992.

Ghosh, D. P., 1971a. The application of linear filter theory to the direct interpretation of geoelectrical resistivity sounding measurements. *Geophysical Prospecting*. 19, 192-217.

Ghosh, D. P., 1971b. Inverse filter coefficients for the computation of apparent resistivity standard curves for a horizontally stratified earth. Geophysical Prospecting. 19, 769-775.

Gingerich, S. B., and Oki, D. S., 2000. Ground water in Hawaii. *US Geol Surv Fact Sheet* 126-00, 6.

Goldman, M. M. and Fitterman, D. V., 1987. Direct time domain calculation of the transient response for a rectangular loop over a two-layer medium. *Geophysics*. 52, 997-1006.

Goldman, M., Gilad, D., Ronen, A., Melloul, A., 1991. Mapping of seawater intrusion into the coastal aquifer of Israel by the Time Domain Electromagnetic Method. *Geoexploration*, 28, 153-174.

Goldman, M., Tabarovsky, L., Rabinovich, M., 1994. On the influence of 3-D structures in the interpretation of transient electromagnetic sounding data. *Geophysics*. 59, 889-901.

Golub, G. H.; Reinsch, C., 1970. Singular value decomposition and least squares solutions, *Numerische Mathematik*. 14-5, 403-420.

Gomes, A. M., 2007. Hidrogeologia *e recursos hídricos da ilha de santiago (Cabo Verde)*, PhD Thesis, Departamento de Geociências, Universidade de Aveiro, 296. (in Portuguese).

Gonfiantini, R. Roche, M. A. Olivry, J. C., Fontes, J. C., Zuppi, G. M., 2001. The altitude effect on the isotopic composition of tropical rains. *Chem Geol*. 181, 1-4, 147-167.

Grant, F. S., and West, G. F., 1965. *Interpretation Theory in Applied Geophysics*, McGraw-Hill; 583.

Grindley, J., 1967. The estimation of soil moisture deficits. *Meteorol. Mag.*, 96, 97-108.

Harinarayana, T., 1999. Combination of EM and DC measurements for upper crustal studies. *Surveys in Geophysics*. 20, 257-278.

Harrington, R. F., 1961. *Time-harmonic electromagnetic fields*, McGraw-Hill Book Co.

Hayashi, M., 2004. Temperature-electrical conductivity relation of water for environmental monitoring and geophysical data inversion. *Environmental Monitoring and Assessment*. 96, 119-128.

Hazen, A., 1892. Some physical properties of sands and gravels, with special reference to their use in filtration. 24th Annual Rep., Massachusetts State Board of Health, Pub. Doc. 34, 539-556.

Hazen, A., 1911. Discussion of Dams on sand foundations by A. C. Koenig. *Trans. Am. Soc. Civ. Eng.* 73, 199-203.

Heiland, C. A., 1968. *Geophysical exploration*. Hafner Publishing Co., New York; 1013.

Heilweil, V. M., Solomon, D. K., Gingerich, S. B., Verstraeten, I. M., 2009. Oxygen, Hydrogen, and Helium isotopes for investigating groundwater systems of the Cape Verde Islands. *West Africa Hydrogeology Journal*. 17, 1157-1174.

Hem, J. D., 1985. Study and interpretation of the chemical characteristics of natural water. U.S. Geological Survey Water-Supply Paper 2254, 263.

Herczeg, A. L., Dogramaci, S. S., Leaney, F. W., 2001. Origin of dissolved salts in a large, semi-arid groundwater system: Murray Basin, Australia. *Marine and Freshwater Resources*. 52, 41-52.

Hestenes M. R. and Stiefel, E., 1952. Methods of Conjugate Gradients for Solving Linear Systems, *Journal of Research of the National Bureau of Standards*. 49-6, 409-436.

Hildenbrand, A., Marlin, C., Conroy, A., Gillot, P., Filly, A., Massault, M., 2005. Isotopic approach of rainfall and groundwater circulation in the volcanic structure of Tahiti-Nui (French Polynesia). *Journal Hydrology*. 302, 187-208.

Hoekstra, P. and Blohm, M. W., 1990. Case histories of time domain electromagnetic soundings in environmental geophysics, In Geotechnical and Environmental Geophysics, 2 - Environmental and Groundwater. Ward S. H. (Ed.). Society of Exploration Geophysicists. Investigations in Geophysics 5, Tulsa, Oklahoma.1-16.

Holm, P. M., Grandvuinet, T., Friis, J., Wilson, J. R.,Barker, A. K., Plesner, S., 2008. An 40Ar–39Ar study of the Cape Verde hot spot - temporal evolution in a semistationary plate environment. *Journal Geophysical Research*. 113

Hölting, B., 1989. *Hydrogeologie*, 3rd Ed. Ferdinand Enke, Stuttgart; 326.

Holtz, R. D. and Kovacs, W. D., 1981. *An introduction to geotechnical engineering*, Prentice-Hall, Englewood Cliffs, New Jersey; 733.

Hördt, A. and Scholl, C., 2004. The effect of local distortions on time-domain electromagnetic measurements, *Geophysics*l. 68, 87-96.

Hoversten, G. M. and Morrison, H. F., 1982. Transient field of a current loop source above a layered earth. *Geophysics*. 47, 1068-1077.

Huntley, D., 1986. Relations between permeability and electrical resistivity in granular aquifers. *Ground Water*. 24, 466-474.

INE - Instituto Nacional de Estatística, 2000. *Recenseamento Geral da População e Habitação de Cabo Verde*, Praia. (in Portuguese)

INGRH – Cape Verde hydrological data base.

INGRH – Cooperacion Española, 1994, *Síntesis geo-hidrologica de Cabo Verde*. Praia, 1-51.

INMG – Cape Verde meteorological data base.

Izbicki, J. A., 1996. Seawater intrusion in a coastal California aquifer. U.S. Geological Survey Fact Sheet. 125-96.

Izuka, S. K., Gingerich, S. B., 2003. A thick lens of fresh groundwater in the southern Lijue Basin, Kauia, Hawaii. USA. *Hydrogeol J*. 11-2, 240-248.

Jackson, D. B., Lenat, J. F., 1989. High-level water tables on Hawaiian type volcanoes and intermediate depth geoelectric structures, Kilauea Volcano, Hawaii and Piton de la Fournaise Volcano, Isle de la Reunion. General assembly of the International Association of Volcanology and Chemistry of the Earth's Interior, Santa Fe, New Mexico. Bull New Mexico Bur Geol Min Resour. 131-142.

Jackson, D. D., 1972. Interpretation of inaccurate, insufficient, and inconsistent data, *Geophysical Journal of the Royal Astronomical Society*. 28, 97-109.

Jackson, D. D., 1979. The use of a priori information to resolve non-uniqueness in linear inversion. *Geophysical Journal of the Royal Astronomical Society*. 57, 137-157.

Jackson, P. D., Smith, D. T., Stanford, P. N., 1978. Resistivity-porosity-particle shape relationships for marine sands. *Geophysics*. 43, 1250-1268.

Joakim Arnfeldt Westergaard, J. A., 2003. *Integrated interpretation of transient electromagnetic and seismic data.* MSc thesis, Department of Earth Sciences, University of Aarhus, Denmark.

Jones, B. F., Vengosh, A., Rosenthal, E., Yechieli, 1999. Seawater Intrusion in Coastal Aquifers - Concepts, Methods and Practices, Theory and Applications of Transport in Porous Media, Ch. 3, Geochemical investigations, (Y. Bear, J., Cheng, A., Sorek, S., Ouazar, D., Herrera, I., Eds.), Kluwer Academic Publishers. 14, 625.

Jørgensen, F., Sandersen, P., Auken, E., 2003. Imaging buried Quaternary valleys using the transient electromagnetic method. *Journal of Applied Geophysics*. 53, 199-213.

Jupp, D. L. B. and Vozoff, K., 1977. Resolving anisotropy in layered media by joint inversion. *Geophysical Prospecting*. 45, 460-470.

Juvik, J. O., 1988. Fog cloud water recovery systems for agricultural and domestic use in Cape Verde Islands. University of Hawai, USA

Kafri, U. and Goldman, M., 2005. The use of the time domain electromagnetic method to delineate saline groundwater in granular and carbonate aquifers and to evaluate their porosity. *Journal of Applied Geophysics*. 57, 167-178.

Kafri, U. and Goldman, M., 2007. Are the lower subaquifers of the Mediterranean coastal aquifer of Israel blocked to seawater intrusion? Results of a TDEM (time domain electromagnetic) study. *Isr. J. Earth Sci*. 55.

Kallrén, L., Schreiber, I., 1988. Groundwater survey on western Fogo, Cape Verde. Report TVTG-5019. Lund Institute of Technology. Lund, Sweden. 83.

Karmis, P., Papadopoulos T., Louis, I. F., 2003. Applicability study of coincident loop transient EM soundings. *Journal Balkan Geophysical Society*. 6-2, 88-100.

Kaufman, A. A., 1979. Harmonic and transient fields on the surface of a two-layer medium. *Geophysics*. 44, 1208-1217.

Kearey, P., Brooks M., and Hill I., 2002. *An Introduction to Geophysical Exploration*. 3rd Ed. Blackwell Science Ltd. 262.

Keller, G.V., and Frischknecht, F.C., 1996. *Electrical methods in geophysical prospecting*. Pergamon, London.

Kennish, M. J., 1989. *CRC Practical handbook of marine science*. CRC Press, Boca Raton, Florida

King, W. P., Smith, S. G., 1981. *Antennas in Matter: Fundamentals, Theory, and Applications*. MIT Press, Cambridge; 875.

Kirsch, R., 2006. *Groundwater geophysics, a tool for hydrogeology*. (Kirsch, R., Ed), Springer-Verlag; Berlin; 493.

Knight, J. H. and Raiche, A. P., 1982. Transient electromagnetic calculations using the Gaver-Stehfest inverse Laplace transform method. *Geophysics*. 47, 47-50.

Koefoed, O., 1970. A fast method to determining the layer contribution from the raised kernel function in geoelectric sounding. *Geophysical Prospecting*. 18, 564-570.

Koefoed, O., 1979. Geosounding Principles 1, Resistivity Sounding Measurements, Methods in Geochemistry and Geophysics, 14A. Elsevier Scientific Publishing Company, Amsterdam. 276.

Koefoed, O., Ghosh, D. P., Polman, 1972. Computation of type curves for electromagnetic depth soundings with horizontal transmitting coil by means of a digital linear filter. *Geophysical Prospecting*. 20, 407-420.

Kozeny, J. A., 1928. *Die Durchlässigkeit des Bodens*, Der Kulturtechniker. 35, 478-486.

Lameli, C. H., 2001. *Caracterización Hidrogeoquímica del Macizo de Bentacuria, Fuerteventura, Archipiélago de Canarias*. PhD thesis, Escola Técnica Superior D'Enginyers de Camins, Universitat Politécnica de Catalunya. 219, (in Castellano).

Lancelot, Y. and Seibold, E., 1977. Initial Reports of the Deep Sea Drilling Project 41, United States Government Printing Office, Washington D.C. 1259.

Lanczos, C., 1958. Linear systems in self-adjoint form. *Am. Math. Mon.*, 65, 665-679.

Langmuir, D., 1997. *Aqueous environmental geochemistry*. Prentice Hall, New Jersey. 600.

Lee, T. and Lewis, R., 1974. Transient response of a large loop in layered ground. *Geophysical Prospecting*. 22, 430-444.

Lee, T., 1981. Transient electromagnetic response of a polarized ground. *Geophysics*. 46, 1037-1041.

Lesmes, D. P. and Friedman, S. P., 2005. *Hydrogeophysics*, Water Science and Technology Library. 50, (Rubin, Y. and Hubbard, S. S.,Ed.), Springer, The Netherlands; 523.

Levi, E., Goldman, M., Hadad, A., Gvirtzman, H., 2008. Spatial delineation of groundwater salinity using deep time domain electromagnetic geophysical measurements: A feasibility study. *Water Resources Research*. 44, 14.

Linacre, E., 1992. *Clima data and resources*. Routledge, New York; 366.

Lodge, A., Helffrich, G., 2006. Depleted swell root beneath the Cape Verde Islands. *Geology*. 34, 449-452.

Maas, E. V., 1984. Salt tolerance of plants. In The Handbook of Plant Science in Agriculture. (Christie, B. R., Ed.), CRC Press, Boca Raton, Florida

Macdonald, G. A., Abbott, A. T., Peterson, F. L., 1983. *Volcanoes in the sea: the geology of Hawaii*, 2nd Ed., University of Hawaii Press, Honolulu; 517.

Madeira, J., Mata, J., Mourão, C., Brum da Silveira, A., Martins, S., Ramalho, R., Hoffmann, D. L., 2010. Volcano-stratigraphic and structural evolution of Brava Island (Cape Verde) based on 40Ar/39Ar, U–Th and field constraints. *Journal of Volcanology and Geothermal Research*. 196, 219-235.

Mandelbrot, B. B., 1998. *The Fractal Geometry of Nature*. W. H. Freeman; 468.

Mannaerts, C. and Gabriels, D., 2000. Rainfall erosivity in Cape Verde. *Soil and Tillage Research*. 55, 207-212.

Mansoor, N., Slater, L., Artigas, F., Auken, E., 2006. High-resolution geophysical characterization of shallow-water wetlands. *Geophysics*. 71-4, B101-B109.

Manzano, M., Custodio, E. and Jones, B. F., 1990. Progress in the understating of groundwater flow through the aquitard of Llobregat delta, Barcelona, Spain. In: Livro de homenagem a Carlos Romariz. A. C. A. de Matos (prefacer), University of Lisbon, Applied and Economic Geology. 115-126.

Marques, M. M., 1987. *Ensaios de cartas de declives médio para a ilha de Santiago (República de Cabo Verde).* Garcia de Orta, Série de Estudos Agronómicos, Lisboa. (in Portuguese).

Marques, M. M., 1990. *Caracterização das grandes unidades geomorfológicas da ilha de Santiago (República de Cabo Verde). Contribuição para o estudo da compartimentação da paisagem*. Centro de Estudos de Pedologia (IICT), Lisboa. (in Portuguese)

Martins, S., 2003. *Petrologia e geoquímica das lavas da ilha de Santiago (Cabo Verde)*, MSc Thesis, Faculdade de Ciências, Universidade de Lisboa. 233. (in Portuguese).

Mata, J., Moreira, M., Doucelance, R., Ader, M., Silva, L. C., 2010. Noble gas and Carbon isotopic signatures of Cape Verde oceanic carbonatites - implications for carbon provenance. *Earth Planet. Sci. Lett*. 291, 1-4, 70-83.

Matthess, K. and Ubell, G., 1981. *Allgemeine Hydrogeologie - Grundwasserhaushalt, Borntraeger*. Berlin, Stuttgart.

Mazor, E., 2004. *Chemical and Isotopic Groundwater Hydrology*, 3rd Ed., Marcel Dekker, Inc., New York and Basel.

McNeill, J. D., 1980a. *Electromagnetic terrain conductivity measurement at low induction number*. Geonics Ltd, Technical Note TN-6.

McNeill, J. D., 1980b. *Applications of transient electromagnetic techniques*. Geonics Ltd, Technical Note TN-17.

Meju, M. A., 1994a. Biased estimation: a simple framework for parameter estimation and uncertainty analysis with prior data. *Geophysical Journal International*. 119, 521-528.

Meju, M. A., 1994b. Geophysical data analysis, understanding inverse problem theory and practice, Society of Exploration Geophysicists Course Notes Series 6, SEG Publishers, Tulsa, Oklahoma. 296.

Meju, M. A., 1995. Simple effective resistivity-depth transformations for in-field or real-time data processing. *Computer and Geosciences*. 21, 985–992.

Meju, M. A., 1996. Joint inversion of TEM and distorted MT soundings, some effective practical considerations. *Geophysics*. 61, 56-65.

Meju, M. A., 2005. Simple relative space–time scaling of electrical and electromagnetic depth sounding arrays: implications for electrical static shift removal and joint DC-TEM data inversion with the most-squares criterion. *Geophysical Prospecting*. 53, 463-479.

Meju, M. A., Gallardo, L. A., Mohamed, A. K., 2003. Evidence for correlation of electrical resistivity and seismic velocity in heterogeneous near-surface materials. *Geophysical Research Letters*. 30-7, 1373, 4.

Meneses, J. G. A., 1977. *O Arquipélago dos Açores. Bases para o seu estudo hidrológico*, V Simpósio Internacional de Geologia Aplicada e do Meio Ambiente. 55. (in Portuguese).

Meneses, J. G. A., 1993. *Hidrologia e Hidrogeologia da Ilha Terceira - Grandes Condicionantes*. Comunicação apresentada no Seminário Recursos Hídricos e o Ambiente na Região Autónoma dos Açores. Câmara Municipal de Angra do Heroísmo, 1-56. (in Portuguese).

Menke, W., 1984. *Geophysical data analysis, discrete inverse theory*, Academic Press; 260.

Metropolis, N., Rosenbluth, A. W., Rosenbluth, M. N., Teller, A. H., Teller, E., 1953. Equations of state calculations by fast computing machines. *Journal of Chemical Physics*. 21-6, 1087-1092.

MIF - Ministério de Infraestruturas e Transporte, 2006: *Distribuição dos Concelhos da Ilha de Santiago*. Praia. (in Portuguese).

Millet, M.-A., Doucelance, R., Schiano, P., David, K., Bosq, C., 2008. Mantle plume heterogeneity versus shallow–level interactions: a case study, the São Nicolau Island, Cape Verde archipelago. *J. Volcanol. Geotherm. Res*. 176, 265-276.

Mink, J. F., 1963. Water development tunnels in a dike complex. *Trans Am Geophys Union*. 44-1, 46.

Misac N. Nabighian (Ed.), 1988. *Electromagnetic Methods in Applied Geophysics – theory*, 1. Investigation in Geophysics 3, Society of Exploration Geophysicists

Mitchell-Thomé, R. C., 1972. Outline of the geology of the Cape Verde Archipelago, *Geologische Rundschau*. 61-3, 1087-1109.

Mitchell-Thomé, R. C., 1976. Cape Verde Islands, Geology of the Middle Atlantic Islands. *Beitr. Reg. Geol. Erde*. 12, I-IX, 247-319.

Montelli, R., Nolet, G., Dahlen, F., Masters, G., 2006. A catalogue of deep mantle plumes - new results from finite-frequency tomography. *Geochem. Geophys. Geosyst*. 7.

Morell, I., Medina, J., Pulido, A., Fernandez-Rubio, R., 1996. The use of Bromide and Strontium as indicators of marine intrusion in the aquifer of Oropesa-Torreblanca, Proceedings, 14th SWIM. Malmo, Sweden. 629-640.

Morrison, H. F., Phillips, R. J. and O'Brien, D. P., 1969. Quantitative interpretation of transient electromagnetic fields over a layered half space. *Geophysical Prospecting*. 17, 82-107.

Morse, J. W., Mackenzie, F. T., 1990. Geochemistry of sedimentary carbonates. *Developments in Sedimentology*. 48, 707.

Mourão, C., Mata, J., Moreira, M., Doucelance, R., Madeira, J., 2007. Further Helium isotopic evidence for a lower mantle contribution to the Cape Verde plume. *Geochim. Cosmochim. Acta*. 71, 15S, 691.

Müller, R. D., Sdrolias, M., Gaina, C., Roest, W. R., 2008. Age, spreading rates, and spreading asymmetry of the world's ocean crust. *Geochem. Geophys. Geosyst*. 9.

Nabighian, M. N., 1979. Quasi-static transient response of a conducting half-space – An approximate representation. *Geophysics*. 44, 1700-1705.

Nabighian, M. N., and Macnae, J. C., 1991. Time domain electromagnetic prospecting methods, in Nabighian, M. N. (Ed.), Electromagnetic Methods in Applied Geophysics, 2A, Society of Exploration Geophysicists. 427-520.

Nadler, A., 1982. Estimating the soil water dependence of the electrical conductivity soil solution/electrical conductivity bulk soil ratio, *Soil Sci. Soc. Am. J.* 46, 722-726.

Nagata, T., 1961. *Rock Magnetism*. Plenum Press, New York; 350.

Néel, L. C. R., 1949a. Ann. Geophysique, (C.N.R.S.). 5, 99-136.

Nekut, A. G., 1987. Direct inversion of time-domain electromagnetic data. *Geophysics*. 52, 1431-1435.

Nelson, P. H., 1994. Permeability-porosity relationships in sedimentary rocks. *The Log Analyst*. 35, 38-61.

Neuman, S. P., 1994. Generalized scaling of permeabilities - validation and effect of support scale. *Geophysical Research Letters*. 21, 349-352.

Newman, G. A. and Alumbaugh, D. L., 1997. Three-dimensional massively parallel electromagnetic inversion 1, Theory. *Geophysical Journal Interiors*. 128, 345-354.

Newman, G. A., Anderson, W. L., Hohmann, G. W., 1987. Interpretation of transient electromagnetic soundings over three-dimensional structures for the central-loop configuration. *Geophysical Journal of the Royal Astronomical Society*. 89, 889-914.

Newman, G. A., Recher S., Tezkan B., Neubauer, F. M., 2003. 3-D inversion of a scalar radio magnetotelluric field data set. *Geophysics*. 68, 791-802.

Nielsen, M. and Fisk, M. 2008. Data report, specific surface area and physical properties of subsurface basalt samples from the east flank of Juan de Fuca Ridge. Proceedings of the Integrated Ocean Drilling Program. 301.

Nobes, D. C., 1996. Troubled waters - environmental applications of electrical and electromagnetic methods. *Surveys of Geophysics*. 17, 393-454.

Oki, D. S., Gingerich, S. B., Whitehead, R. L., 1999. Hawaii. In: Groundwater atlas of the United States: Alaska, Hawaii, Puerto Ricoand the US Virgin Islands. US Geol Surv Invest Altas 730-N, segment 13, N12-N22.

Oldenburg, D. W. and Li, Y., 1994. Inversion of induced polarization data. *Geophysics*. 59, 1327-1341.

Olivry, J. C., 1981. *Estudo de precipitacões em São Nicolau, República das Ilhas de Cabo Verde*, Office de la Recherche Scientifique et Technique outre mer centre ORSTOM, Dakar, Senegal, 55.

Oster, J. D. and Schroer, F. W., 1979. Infiltration as influenced by irrigation water quality. *Soil Sci. Soc. Amer. J.* 43, 444-447.

Palacky, G. J., and West, G. F., 1991. Airborne electromagnetic methods, in Nabighian, M. N. (Ed.), Electromagnetic Methods in Applied Geophysics, 2B. Society of Exploration Geophysics. 811-879.

Pape, H., and Schopper, J. R., 1988. Relations between physically relevant geometrical properties of a multifractal porous system, Characterization of porous solids, (Unger, K. K., Rouquerol, J., Sing, K. S. W., Kral, H., Eds.). Elsevier Science Publ. Co., 473-482.

Pape, H., Riepe, L., Schopper, J. R., 1987. Theory of self-similar network structures in sedimentary and igneous rocks and their investigation with microscopical methods. *J. Microscopy*. 148, 121-147.

Parker, R. L., 1994. *Geophysical inverse theory*, Princeton University Press; 400.

Patra, H. P., 1970. Central frequency sounding in shallow engineering and hydro-geological problems. *Geophysical Prospecting*. 18, 236-254.

Pelton, W., Sill, W., Smith, B., 1983. Interpretation of complex resistivity and dielectric data, Part I. *Geophysical Transactions*. 29-4, 297-330.

Pelton, W., Sill, W., Smith, B., 1984. Interpretation of complex resistivity and dielectric data, Part II. *Geophysical Transactions*. 30-1, 11-45.

Penman, H. L., 1950. The water balance of the Stour catchment area. *J. Inst. Water Eng*. 4, 457-469.

Person, M., Raffensperger, J. P., Ge, S., Garven, G., 1996. Basin-scale hydrogeologic modeling. *Reviews of Geophysics*. 34, 61-87.

Peterson, F. L., 1972. Water development on tropical volcanic islands: type example: Hawaii. *Ground Water*, 10-5, 18-23.

Pim, J., Peirce, C., Watts, A. B., Grevemeyer, I., Krabbenhoeft, A., 2008. Crustal structure and origin of the Cape Verde Rise. *Earth Planet. Sci. Lett*. 272, 422-428.

Pina, A. F. L., 2009. *Hidroquímica e qualidade das águas subterrâneas da ilha de Santiago - Cabo Verde*, PhD Thesis, Departamento de Geociências, Universidade de Aveiro. 209. (in Portuguese).

Plummer, L. N., Parkhurst D. L., Kosiur, D. R., 1975. MIX2, a computer program for modelling chemical reactions in natural waters. US Geo. Survey, Water-Resources Inv., Report 61-75, 68.

PNUD - JRH, 1992. *Schema Directeur pour le secteur eau et assainissement, République du Cap Vert*. Programation sectoriel 1993-2005. Projet CVI/87/001, Praia.

Porrat, D., Bannister, P. R. and Fraser-Smith, A. C., 2001. Modal phenomena in the natural electromagnetic spectrum below 5 kHz. *Radio Science*. 36, 499-506.

Powers, M. H., 1997. Modeling frequency-dependent GPR. *The Leading Edge*. 16, 1657-1662.

Prada, S. N., da Silva, M. O., Cruz, J. V., 2005. Groundwater behavior in Madeira, volcanic island (Portugal). *Hydrogeol J*. 13, 5–6, 800-812.

Press, W. H., Teukolsky S. A., Vetterling W. T., Flannery B. P., 1992. Numerical recipes in Fortran, the art of scientific computing (2nd Ed.). Cambridge Univ. Press.

Purvance, D. T. and Andricevic, R., 2000. On the electrical-hydraulic conductivity correlation in aquifers. *Water Resour. Res*. 36, 2905-2913.

Qian, W. and Boerner, D. E., 1995. Electromagnetic modelling of buried line conductors using an integral equation. *Geophysical Journal International*. 121, 203-214.

Rabinovich, M. B., 1995. Errors of 1-D interpretation of 3-D TDEM data in the application of mapping saltwater/freshwater contact. *Journal of Applied Geophysics*. 34, 23-34.

Rai, S. S. and Sarma, G, S., 1986. In loop pulse EM response of stratified earth. *Geophysical Prospecting*. 34-2, 232-239.

Raiche, A. P. and Spies, B. R., 1981. Coincident loop transient electromagnetic master curves for interpretation of two-layered earths. *Geophysics*. 46, 53-64.

Raiche, A. P., Jupp, D. L. B., Rutter, H., Vozoff, K., 1985. The joint use of coincident loop transient electromagnetic and Schlumberger sounding to resolve layered structures. *Geophysics*. 50, 1618-1627.

Ramalho, R., Helffrich, G., Schmidt, D., Vance, D., 2010a. Tracers of uplift and subsidence in the Cape Verde Archipelago. *J. Geol. Soc. (London)*. 167, 519-538.

Ramalho, R., Helffrich, G., Cosca, M., Vance, D., Hoffmann, D., Schmidt, D. N., 2010b. Vertical movements of ocean island volcanoes: insights from a stationary plate. *Mar. Geol.* 275, 8-95.

Rhoades, J. D. and Merrill, S. D., 1976. Assessing the suitability of water for irrigation: Theoretical and empirical approaches, In: Prognosis of Salinity and Alkalinity, FAO Soils Bulletin 31. FAO, Rome. 69-110.

Rhoades, J. D., 1974. Drainage for salinity control. In: Drainage for Agriculture, (Van Schilfgaarde, Ed.), *Amer. Soc. Agron. Monograph*, 17, 433-462.

Rhoades, J. D., 1977. Potential for using saline agricultural drainage waters for irrigation. Proc. Water Management for Irrigation and Drainage, ASCE, Reno, Nevada. 85-116.

Richards, L. A., 1954. Diagnosis and improvement of saline and alkali soils. USDA Agricultural Handbook, 60. US. Department of Agriculture, Washington DC. 160.

Rigassi, D. A., 1975. Micropaleontological investigations in Cabo Verde archipelago. Proceedings. Colóquio Geologia Africana. Leeds

Rocha Faria, J. M., 1971. Frequency Analysis of the Annual highest values of the daily precipitation in some Portuguese overseas sites. Fomento. Lisbon, 9-3, 237-270.

Rodrigues, F. C., 1993. *Estudo Hidrogeológico da Ilha Terceira: contributo para o seu conhecimento*. MSc thesis, Universidade dos Açores, Departamento de Ciências Agrárias, Angra do Heroísmo. (in Portuguese).

Rodrigues, F. C., 2002. *Hidrogeologia da Ilha Terceira (Açores–Portugal)*. PhD thesis, Universidade dos Açores. Departamento de Ciências Agrárias, Angra do Heroísmo. 395. (in Portuguese).

Rodrigues, R., 1995: *Hidrologia de Ilhas Vulcânicas*. Tese para obtenção de grau de especialista, Laboratório Nacional de Engenharia Civil, Lisboa, 397. (in Portuguese).

Rothman, D. H., 1985a. Large near-surface anomalies, seismic reflection data, and simulated annealing. Ph.D. thesis. Stanford University.

Rothman, D. H., 1985b. Nonlinear inversion, statistical mechanics, and residual statics estimation. *Geophysics*. 50, 2797-2807.

Rothman, D. H., 1986. Automatic estimation of large residual statics corrections. *Geophysics*. 51, 332-346.

Routh, P. S. and Oldenburg, D. W., 2001. Electromagnetic coupling in frequency-domain induced polarization data: a method for removal. *Geophysical Journal International*. 145, 59-76.

Sabino, A. A., 2004. Experiments Conducted in Cape Verde. Constraints on Fog Collection Development Projects. Proceedings to the 3rd International Conference on Fog, Fog Collection and Dew. Cape Town, South Africa.

Santos, F. A. M., 2004. 1-D laterally constrained inversion of EM34 profiling data. *Journal of Applied Geophysics*. 56, 123-134.

Santos, F. A. M., Almeida, E. P., Gomes, M., Pina, A., 2006. Hydrogeological investigation in Santiago Island (Cabo Verde) using magnetotellurics and VLF methods. *Journal of African Earth Sciences*. 45, 4-5, 421-430.

Santos, F. A. M., Gonçalves, R., El-Kaliouby, H. M., Meju, M. A., 2010. Spatially-contrained joint inversion of VES and TDEM data, Proceedings of 20th International Electromagnetic Induction Workshop, Giza, Egypt.

Santos F. A. M., Triantafilis, J., Bruzgulisand, K., 2011a. Case History - A spatially constrained 1D inversion algorithm for quasi-3D conductivity imaging: Application to DUALEM-421 data collected in a riverine plain. *Geophysics*. 76-2, B43-B53.

Santos F. A. M. and El-Kaliouby, H. M., 2011b. Quasi-2D inversion of DCR and TDEM data for shallow investigations. *Geophysics*. 76-4, 239-250.

Sasaki, Y., 1989. Two-dimensional joint inversion of magnetotelluric and dipoledipole resistivity data. *Geophysics*. 54, 254-262.

Sayles, F. L. and Mangelsdorf, P. C., 1977. The equilibrium of clay minerals with sea water: exchange reactions. *Geochim. Cosmochim. Acta*. 41, 951-960.

Scales, J. A., Smith, M. L., Treitel, S., 2001. Introductory Geophysical Inverse Theory. Samizdat Press, Colorado School of Mines. 193.

Scheidegger, A. E., 1974. *The Physics of Flow through Porous Media*. 3rd ed., University of Toronto Press; 353.

Schoeller, H., 1956. *Geochemie des eaux souterraines, Application aux eaux des gisements de petrole*. Soc. Des Editions Technique. Paris; 213.

Schön, J. H., 1996. Physical properties of rocks - fundamentals and principles of petrophysics. Handbook of Geophysical Exploration, Seismic Exploration, Elsevier Science Ltd., 18, 379-478.

Sen, P. N., Goode, P. A., Sibbit, A., 1988. Electrical conduction in clay bearing sandstones at low and high salinities. *J. Appl. Phys*. 63, 4832-4840.

Serra, O., 1984. *Fundamentals of well-log interpretation: 1 - The acquisition of data*. Elsevier Science Publ. Co.

Serralheiro, A., 1976a. *A geologia da Ilha de Santiago (Cabo Verde)*, PhD Thesis, Faculdade Ciências da Universidade de Lisboa. 218. (in Portuguese).

Serralheiro, A., 1976b. *Carta geológica da Ilha de Santiago (Cabo Verde) na escala 1:25000. (folhas 48 a 59)*. Junta de Investigações Científicas do Ultramar, Laboratório de Estudos Petrológicos e Paleontológicos do Ultramar. Lisboa. (in Portuguese).

Serralheiro, A., 1977. *Carta geológica da Ilha de Santiago (Cabo Verde) na escala 1:100000*. Junta de Investigações Científicas do Ultramar, Laboratório de Estudos Petrológicos e Paleontológicos do Ultramar. Lisboa. (in Portuguese).

Sharma, P. V., 1997. *Environmental and Engineering Geophysics*. Cambridge University Press, 475.

Shashwati R., and Tarafdar, S., 1997. Archie's law from a fractal model for porous rocks. *Phys. Rev. B*, 55, 8038-8041.

Shepherd, R. G., 1989. Correlations of permeability and grain size. *Ground Water*. 27-5, 633-638.

Siegel, D. I., Jenkins, D. T., 1987. Isotopic analysis of groundwater flow systems in a wet alluvial fan, southern Nepal. *Isotope Techniques in Water Resources Development*. IAEA. Vienna. 475-482.

Simões, M. M. M., 1998. *Contribuição para o conhecimento hidrogeológico do cenozóico na bacia do baixo Tejo.* PhD thesis, Universidade Nova de Lisboa. (in Portuguese).

Simpson, H. J., Herczeg, A. L.,1994. Delivery of marine chloride in precipitation and removal by rivers in the Murray–Darling Basin, Australia. *Journal of Hydrology*. 154, 323-350.

Singh, N. P., Utsugi, M. and Kagiyama, T., 2009. TEM Response of a Large Loop Source over a Homogeneous Earth Model: A Generalized Expression for Arbitrary Source-Receiver Offsets. *Pure and Applied Geophysics*. 166, 2037-2058.

Sleep, N. H., 1990. Hotspots and mantle plumes - some phenomenology. *Journal Geophysical Research*. 95, 6715-6736.

Smith, R. S. and West, G. F., 1988. An explanation of abnormal TEM responses: Coincident-loop negatives and the loop effect. *Exploration Geophysics*. 19-3, 435-446.

Smith, R. S. and West, G. F., 1989. Field examples of negative coincident transient electromagnetic responses modelled with polarizable half-planes. *Geophysics*. 54, 1491-1498.

Smith, R. S., Edwards, R. N., and Buselli, G., 1994. An automatic technique for presentation of coincident-loop, impulse-response, transient electromagnetic data. *Geophysics*. 59, 1542-1550.

Sørensen, K. I., 1996. Pulled Array Continuous Electrical Profiling. *First Break*. 14, 85-90.

Spies, B. R. and Raiche, A. P., 1980. Calculation of apparent conductivity for the transient electromagnetic (coincident loop) method using a HP 67 calculator. *Geophysics*. 45, 1862-1878.

Spies, B. R., and Frischknecht, F. C., 1991. Electromagnetic Sounding. Electromagnetic Methods in Applied Geophysics, 2A, in Nabighian, M. N. (Ed.). Society of Exploration Geophysics. 285-425.

Spitzer, K., 2001. Magnetotelluric static shift and direct current sensitivity. *Geophysical Journal International*. 144, 289-299.

Starinsky A., Bielsky M., Lazar B., Steinitz G., and Raab M., 1983. Strontium isotope evidence on the history of oilfield brines, Mediterranean Coastal Plain, Israel. *Geochim. Cosmochim. Acta*. 47, 687-695.

Stefanesco, S. S., Schlumberger, C. and Schlumberger, M., 1930. *Sur la distribution électrique potentielle autour d'une prise de terre ponctuelle dans un terrain à couches horizontales, homogènes et isotropes*. Le Journal de Physique et le Radium, Tome 1, Série VII, 4, 132-140.

Stefansson, V., Axelsson, G., Sigurdsson, O., 1982. Resistivity logging of fractured basalt. Proceedings Eighth Workshop Geothermal Reservoir Engineering. Stanford University. 189-195.

Strack, K. M., 1992. Exploration with deep transient electromagnetic. *Methods in Geochemistry and Geophysics*. 30, 373.

Stratton, J. A., 1941. *Electromagnetic theory*, McGraw-Hill Book Co.

Suarez, D. L., 1981. Relation between pHc and Sodium Adsorption Ratio (SAR) and an alternate method of estimating SAR of soil or drainage waters. *Soil Sci. Soc. Amer. J*. 45, 469-475.

Swift, C. M., 1988. Electromagnetic Theory for Geophysical Applications, Electromagnetic Methods in Applied Geophysics, 1, in Nabighian, M. N. (Ed.). Society of Exploration Geophysicists. 5-10.

Tarantola, A. and Valette, B., 1982. Generalized nonlinear inverse problems solved using least squares criterion. *Reviews of Geophysics & Space Physics*. 20, 219-232.

Tarantola, A., 2005 Inverse problem theory and methods for model parameter estimation. *Society for Industrial and Applied Mathematics*. Philadelphia. 342.

Telford, W. M., Geldart L. P., and Sheriff R. E., 1990. *Applied Geophysics*, 2nd Edition. Cambridge University Press; 770.

Tezkan, B., 1999. A review of environmental quasi-stationary electromagnetic techniques. *Surveys of Geophysics*. 20, 279-308.

Toft, M. W., 2001. *Three-dimensional TEM modelling of near-surface resistivity variations*. MSc thesis, Department of Earth Science, University of Aarhus, Denmark.

Torres, P. C., Silva, L. C., Serralheiro, A., Tassinari, C., Munhá, J., 2002. *Enquadramento geocronológico pelo método K/Ar das principais sequências vulcano-estratigráficas da Ilha do Sal - Cabo Verde*, Garcia de Orta, 18, 1-2, 9-13. (in Portuguese).

Twomey, S., 1977. *An introduction to the mathematics of inversion in remote sensing and indirect measurements*. Elsevier Scientific Publishing Company.

Vailleux, Y. and Bourguet, L., 1974. *La mise en valeur des eaux souterraines dans l'archipel du Cap Vert. Rapport de fin de mission.* Ministério de Coordenação Interterritorial, Brigada de Águas Subterrâneas de Cabo Verde. Praia. 291.

Vanysek, P., 2002. *Ionic conductivity and diffusion at infinite dilution*. CRC Handbook of Chemistry and Physics. 83rd Ed. (Lide, D. R., Ed), CRC Press, Boca Raton

Vengosh, A. Pankratov, I., 1998. Chloride/Bromide and Chloride/Fluoride Ratios of Domestic Sewage Effluents and Associated Contaminated Ground Water. *Ground Water*. 36-5, 815-824.

Verma, R. K. and Mallick, K., 1979. Detectability of intermediate conductive and resistive layers by timedomain electromagnetic sounding. *Geophysics*. 44, 1862-1878.

Viezzoli, A., Christiansen, A. V., Auken E., Sørensen K., 2008. Quasi-3D modeling of airborne TEM data by spatially constrained inversion. *Geophysics*. 73-3, 105-113.

Vogel, H. J., Cousin I. and Roth, K., 2002. Quantification of pore structure and gas diffusion as a function of scale. *European Journal of Soil Science*. 53, 465-473.

von Hippel, A. R., 1954a. *Dielectric materials and applications*. John Wiley and Sons, MIT Press.

von Hippel, A. R., 1954b. *Dielectrics and waves*, John Wiley and Sons, MIT Press.

Voss, C. I., 1984. SUTRA, A finite-element simulation model for saturated-unsaturated fluid density-dependent ground-water flow with energy transport or chemically-reactive single-species solute transport, US Geological Survey Water-Resources Investigations Report 84-4369. 409.

Voss, C. I., 1999. Seawater Intrusion in Coastal Aquifers - Concepts, Methods and Practices, Theory and Applications of Transport in Porous Media, Ch. 9. In USGS SUTRA code – History, Practical use, and Application in Hawaii, (Y. Bear, J., Cheng, A., Sorek, S., Ouazar, D., Herrera, I., Eds.), Kluwer Academic Publishers. 14, 625.

Voss, C. I. and Provost, A. M., 2003. SUTRA, A Model for Saturated-Unsaturated, Variable-Density Ground-Water Flow with Solute or Energy Transport. US Geological Survey Water-Resources Investigations Report 02-4231. 250.

Vozoff, K., and Jupp, D. L. B., 1975. Joint inversion of geophysical data. *Geophysical Journal of the Royal Astronomical Society*. 42, 977-991.

Wait, J.R., 1962. *Electromagnetic Waves in Stratified Media*. Pergamon

Wait, J. R., 1982. *Geo-electromagnetism*. Academic Press. 268.

Ward, S. H., and Hohmann, G. W., 1988. Electromagnetic Theory for Geophysical Applications. Electromagnetic Methods in Applied Geophysics, 1 - theory. in Nabighian, M. N. (Ed.), Investigation in Geophysics 3, Society of Exploration Geophysicists. 131-311.

Waxman, M. H. and Smits, L. J. M., 1968. Electrical conductivities in oil-bearing shaly sands, *Soc. Pet. Eng. J.* 8, 107-122.

Weast, R. C., (ed.), 1983. *CRC Handbook of Chemistry and Physics*, 63rd ed., CRC Press. Boca Raton, Florida.

West, G. F., and Macnae, J. C., 1991. Physics of the electromagnetic induction exploration method, in Nabighian, M. N. (Ed.), Electromagnetic Methods in Applied Geophysics, 2A, Society of Exploration Geophysics. 1-45.

Whitaker, F. F. and Smart, P. L., 2007. Geochemistry of meteoric diagenesis in carbonate islands of the northern Bahamas, 1 - Evidence from field studies. *Hydrological Processes*, 21, 949-966.

Wigley, T. M. L. and Plummer, L. N., 1976. Mixing of carbonate waters. *Geochim. Cosmochim. Acta*. 40-9, 989-995.

Williams, C. A., Hill, I. A., Young, R., White, R. S., 1990. Fracture zones across the Cape Verde Rise, NE Atlantic. *J. Geol. Soc. (London)*. 147, 851-857.

Winter, C. L. and Tartakovksy, D. M. 2001. Theoretical foundation for conductivity scaling. *Geophysical Research Letters*. 28, 4367-4369.

Worthington, A. E., Hedges, J. H., Pallatt, N., 1990. SCA guidelines for sample preparation and porosity measurement of electrical resistivity samples: Part I - Guidelines for preparation of brine and determination of brine resistivity for use in electrical resistivity measurements. *The Log Analyst*. 31, 20.

Y. Yechieli, Y., Kafri, U., Goldman, M., Voss, C. I., 2001. Factors controlling the configuration of the fresh–saline water interface in the Dead Sea coastal aquifers: synthesis of TDEM surveys and numerical groundwater modeling. *Hydrogeology Journal*. 9, 367-377.

Zhao, D., 2007. Seismic images under 60 hotspots - search for mantle plumes. *Gondwana Res.* 12, 335-355.

Zhdanov M. S., 2009. Geophysical Electromagnetic Theory and Methods. Methods in Geochemistry and Geophysics. 43. Elsevier. Amsterdam.

Zhdanov, M. S. and Keller, G. V., 1994. *The Geoelectrical Methods in Geophysical Exploration*. Elsevier. Amsterdam. 884.